frontiers | Research Topics

Fluid and heat transfer in unconventional reservoirs

Edited by
Biao Shu, Ranjith Pathegama, Dawei Hu and Wenjing Lin

Published in
Frontiers in Earth Science

ISSN 1664-8714
ISBN 978-2-83250-530-4
DOI 10.3389/978-2-83250-530-4

About Frontiers

Frontiers is more than just an open access publisher of scholarly articles: it is a pioneering approach to the world of academia, radically improving the way scholarly research is managed. The grand vision of Frontiers is a world where all people have an equal opportunity to seek, share and generate knowledge. Frontiers provides immediate and permanent online open access to all its publications, but this alone is not enough to realize our grand goals.

Frontiers journal series

The Frontiers journal series is a multi-tier and interdisciplinary set of open-access, online journals, promising a paradigm shift from the current review, selection and dissemination processes in academic publishing. All Frontiers journals are driven by researchers for researchers; therefore, they constitute a service to the scholarly community. At the same time, the *Frontiers journal series* operates on a revolutionary invention, the tiered publishing system, initially addressing specific communities of scholars, and gradually climbing up to broader public understanding, thus serving the interests of the lay society, too.

Dedication to quality

Each Frontiers article is a landmark of the highest quality, thanks to genuinely collaborative interactions between authors and review editors, who include some of the world's best academicians. Research must be certified by peers before entering a stream of knowledge that may eventually reach the public - and shape society; therefore, Frontiers only applies the most rigorous and unbiased reviews. Frontiers revolutionizes research publishing by freely delivering the most outstanding research, evaluated with no bias from both the academic and social point of view. By applying the most advanced information technologies, Frontiers is catapulting scholarly publishing into a new generation.

What are Frontiers Research Topics?

Frontiers Research Topics are very popular trademarks of the *Frontiers journals series*: they are collections of at least ten articles, all centered on a particular subject. With their unique mix of varied contributions from Original Research to Review Articles, Frontiers Research Topics unify the most influential researchers, the latest key findings and historical advances in a hot research area.

Find out more on how to host your own Frontiers Research Topic or contribute to one as an author by contacting the Frontiers editorial office: frontiersin.org/about/contact

Fluid and heat transfer in unconventional reservoirs

Topic editors

Biao Shu — Central South University, China

Ranjith Pathegama — Monash University, Australia

Dawei Hu — Institute of Rock and Soil Mechanics, Chinese Academy of Sciences (CAS), China

Wenjing Lin — Institute of Hydrogeology and Environmental Geology, Chinese Academy of Geological Sciences, China

Citation

Shu, B., Pathegama, R., Hu, D., Lin, W., eds. (2023). *Fluid and heat transfer in unconventional reservoirs*. Lausanne: Frontiers Media SA.

doi: 10.3389/978-2-83250-530-4

Table of contents

frontiers in Earth Science

ORIGINAL RESEARCH
published: 17 February 2022
doi: 10.3389/feart.2022.849361

Fracture Characteristics and Reservoir Inhomogeneity Prediction of the Gaoyuzhuang Formation in the Xiong'an New Area: Insights From a 3D Discrete Fracture Network Model

Gaofan Yue[1,2,3], *Guiling Wang*[2,3]*, *Feng Ma*[2,3], *Xi Zhu*[2,3], *Hanxiong Zhang*[2,3], *Jianwei Zhou*[1] *and Jin Na*[4]

[1]School of Environmental Studies, China University of Geosciences, Wuhan, China, [2]Institute of Hydrogeology and Environmental Geology, Chinese Academy of Geological Sciences, Shijiazhuang, China, [3]Technology Innovation Center of Geothermal and Hot Dry Rock Exploration and Development, Ministry of Natural Resources, Shijiazhuang, China, [4]College of Resources and Environment, Yangtze University, Wuhan, China

The Xiong'an new area in northern China is rich in geothermal resources. The Gaoyuzhuang Formation in the Proterozoic Jixian system is an important recently discovered geothermal reservoir. The Gaoyuzhuang reservoir has been affected by multiple stages of tectonic movement. The fractures are very well developed, resulting in strong heterogeneity in the reservoir's porosity and permeability. Few studies have been conducted on the fractures and heterogeneity of the Gaoyuzhuang reservoir. In this study, interpretation of data from image logs was used to summarize the characteristics of the fractures, including the fractures' strikes, dips, and lengths. The permeability distribution of the reservoir in the vicinity of the borehole was predicted. The hydro-thermal (TH) coupling model was used to reproduce the process of pumping tests, and the simulation results were found to be in good agreement with the field test data. In addition, the relationship between the fracture aperture and length was obtained, $d_{max} = 4.2 \times 10^{-5} \cdot L^{0.5}$. The results of this study provide data and technical support for further reservoir research and evaluation of the geothermal resources of the Gaoyuzhuang reservoir.

Keywords: fractures and heterogeneity, the gaoyuzhuang formation, discrete fracture network, hydro-thermal (TH) coupling, The xiong'an new area

OPEN ACCESS

Edited by:
Dawei Hu,
Institute of Rock and Soil Mechanics (CAS), China

Reviewed by:
Yanjun Zhang,
Jilin University, China
Zhihong Zhao,
Tsinghua University, China

***Correspondence:**
Guiling Wang
ihegwangguiling@sina.com

Specialty section:
This article was submitted to Structural Geology and Tectonics, a section of the journal Frontiers in Earth Science

Received: *06 January 2022*
Accepted: *19 January 2022*
Published: *17 February 2022*

Citation:
Yue G, Wang G, Ma F, Zhu X, Zhang H, Zhou J and Na J (2022) Fracture Characteristics and Reservoir Inhomogeneity Prediction of the Gaoyuzhuang Formation in the Xiong'an New Area: Insights From a 3D Discrete Fracture Network Model. Front. Earth Sci. 10:849361. doi: 10.3389/feart.2022.849361

1 INTRODUCTION

Solving the problem of energy shortage and optimization of the energy structure is the key to sustainable global development (Dincer, 2000; Ahmad et al., 2020). Geothermal energy has become a hotspot in research on new energy sources due to its wide distribution, large reserves, good stability, and clean and environmentally friendly characteristics (Lu, 2018; Zhang et al., 2019; Gong et al., 2020; Wang et al., 2020; Dincer and Ozturk, 2021). Research has shown that geothermal energy can provide 3.9% of global energy and reduce CO_2 emissions by 800 million tons by 2050 (Pan et al., 2019b). Globally, for both hot dry rock and hydrothermal geotherm type geothermal energy, deep geothermal reservoirs are often fractured. A large number of densely distributed fractures control the flow path of the underground fluid. The existence of fractures not only changes the mechanical

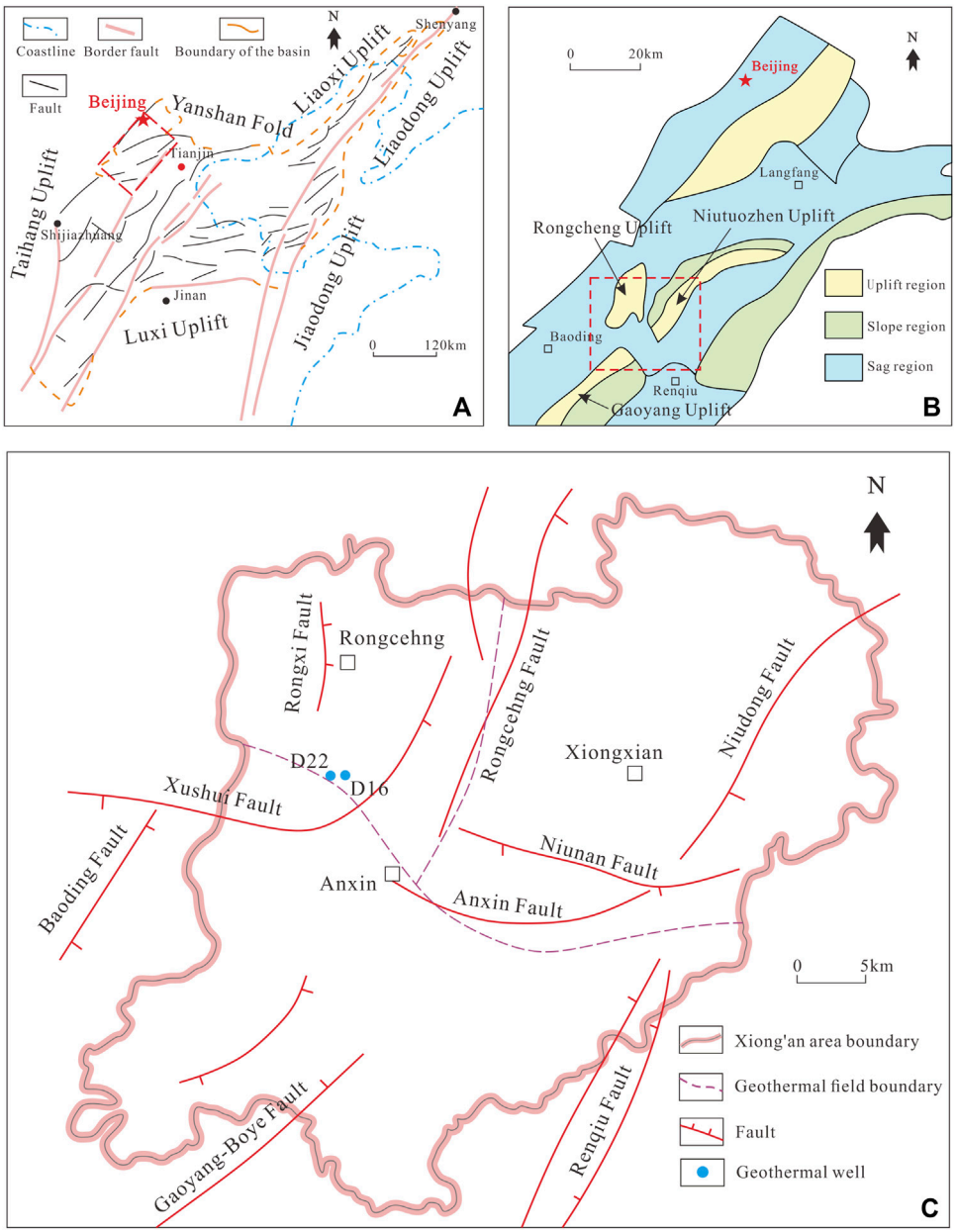

FIGURE 1 | (A) Basic tectonic map of the Bohai Bay Basin; **(B)** Basic tectonic map of the Jizhong depression (from He et al., 2018); **(C)** Distributions of the major faults, geothermal fields, and boreholes in the Xiongan New Area.

parameters of the surrounding rock, but it also controls the distribution characteristics of the hydraulically fractured fracture network.

China is rich in geothermal resources, especially high-temperature hydrothermal geothermal energy resources (Chen, 1988; Wang et al., 2017; Wang and Lin, 2020). The best geothermal fields in the Beijing–Tianjin–Hebei region are distributed in the Xiong'an New Area. The Wumishan Formation in the Jixian system is the most representative hydrothermal reservoir in northern China (Pang, 2018; Wu et al., 2018; Ma et al., 2020). Since 2018, the China Geological Survey has conducted detailed exploration of the deep geothermal reservoir in the Xiong'an New Area and has found a second reservoir in the Gaoyuzhuang Formation (Wang et al., 2018; Ma et al., 2020). The Gaoyuzhuang Formation contains a large number of natural fractures, and the reservoir is very heterogeneous, which greatly effects future geothermal development. For example, the water production rate of well D22 in the original state is very low and cannot meet the requirements for development. It is urgent that a regional model be developed to guide the next stage for exploitation.

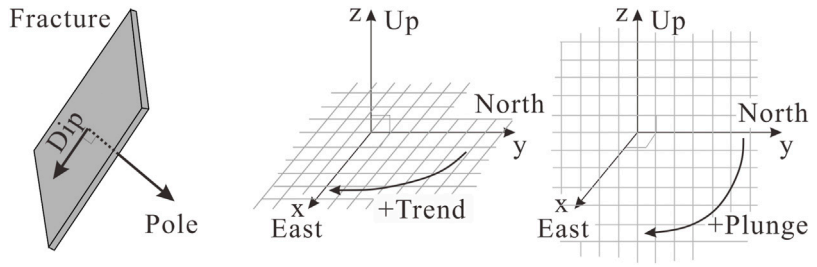

FIGURE 2 | (A) Vertical fracture dip and pole, both pointing downward; **(B)** the pole trend in the x-y plane; and **(C)** a pole plunge in the y-z (or x-z) plane.

Discrete fracture network (DFN) models are commonly used to describe fracture networks. It uses deterministic or stochastic methods to generate a series of discrete fracture patches in order to quantitatively describe the size, strike, and strength of the fractures (Pan et al., 2019a; Barcelona et al., 2020; Giuffrida et al., 2020). The number of fractures in the reservoir is large, and the fractures range from a few microns to tens of meters, which cannot be simply described in a deterministic manner. The stochastic method uses the statistical results to describe the fracture network. There is no exact correspondence between individual fractures in reality, but in a representative body, the overall properties of the fracture network are the same as the real situation (Li et al., 2016; Gottron and Henk, 2021). The DFN model usually consists of three models: a distribution model, a dimensional model, and a spatial distribution model (Dowd et al., 2009). The normal vector is usually used to describe the strike and dip angle of the fractures. The probability density functions mainly include the Fisher distribution, Bingham distribution, binary normal distribution, and empirical probability distribution (Gottron and Henk, 2021). In practical applications, the Fisher distribution is the model that is most commonly used to describe the fracture direction. The model parameters mainly come from statistics of field observation data. For example, Pan et al., 2019a established a local fracture network model of a limestone mine using outcrop fracture measurements obtained using non-contact measurement techniques (such as 3D laser scanning and photometry). For deep reservoirs, image logging can be used to identify fractures more accurately and can provide important parameters such as the linear fracture density, direction, and pore diameter (Ozkaya, 2021; Nian et al., 2022). Tang et al. (2020) obtained statistics of the distribution characteristics of image logging fractures and gained a better understanding of the fractures in the Wumishan geothermal reservoir in the Jixian system in the Xiong'an new area. However, the fracture characteristics of the Gaoyuzhuang Formation have not been reported.

In this study, the characteristics of the fractures were analyzed quantitatively using image logging data. Using a geostatistical method, a regional discrete fracture network model was constructed, and the porosity and permeability distributions of the Gaoyuzhuang reservoir were calculated. A hydro-thermal (TH) coupling numerical model was established to validate the accuracy of the DFN model by fitting the field pumping test data.

2 GEOLOGIC SETTING OF THE XIONG'AN NEW AREA

The Xiong'an new area is located in the middle of the Jizhong depression in the Bohai Basin (**Figures 1A,B**). According to previous studies, the Bohai Basin has experienced four stages of tectonic movement since the Archean (Qi et al., 2003; Chang et al., 2016; Qiu et al., 2017; Wang et al., 2019a). In particular, in the Mesozoic, the strata were uplifted and then strongly eroded (Zheng et al., 1999). The bedrock undulations have resulted in the secondary tectonic units in this area being developed, including the Niutuozhen uplift, Rongcheng uplift, and Gaoyang uplift (Qi et al., 2003; Cai et al., 2007). The faults in this area are well developed, including the Rongdong fault, Xushui fault, Niudong fault, Niunan fault, and Gaoyang fault (**Figure 1C**). The depths of the faults vary greatly, and some of them even reach the crystalline basement (Zhang et al., 2002). The study area is located in the southern part of the Rongcheng uplift near the Xushui Fault. The Xushui Fault is a normal fault with a dip angle of about 45°, and it is generally W–E trending, with a NE deflection near the Rongcheng uplift (Lu et al., 2019; Hu et al., 2020).

Many stages of tectonic movement and karstification occurred from the Late Indosinian to the Himalayan, forming a large number of fractures in the geothermal reservoir. For example, the image logging of well Dawang1 shows that two main stages of fracture systems are developed in the Wumishan Formation, which is obviously similar to the trends of the Rongcheng fault and the Niudong fault. The high angle fractures control the vertical migration of the groundwater from bottom to top (Tang et al., 2020). In contrast to the development of the karst fractures in the Wumishan Formation, the Gaoyuzhuang Formation is mainly characterized by structural fractures due to its large burial depth and the weak influence of karstification. Wells D22 and D16 in the Rongcheng uplift encounter the Gaoyuzhuang Formation at a depth of about 3,200 m. The image logging results for well D22 show that the microfracture orientation is consistent with that of the large fault. A detailed analysis of the results will be presented in the subsequent sections.

Based on this, the heat accumulation mechanism in the Xiong'an New Area was determined. Affected by the westward subduction of the Pacific Plate, the eastern part of the North China Craton was obviously destroyed. The thickness of the lithosphere and crust was greatly reduced, and the Moho

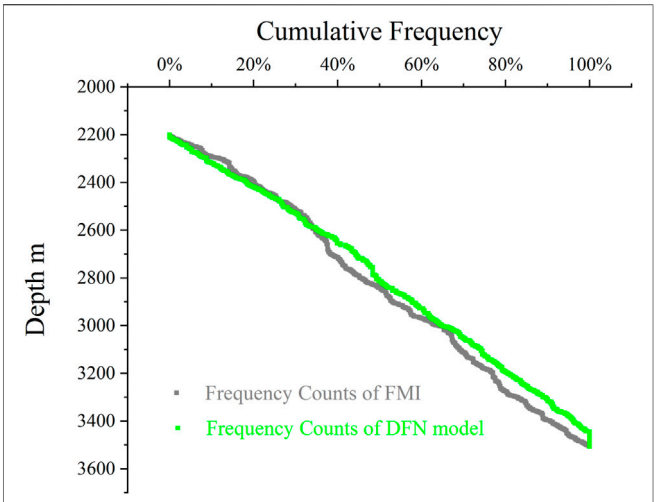

FIGURE 3 | Cumulative density distribution of the measured and simulated fractures in well D22.

surface at the bottom of the study area was significantly uplifted, which is conducive to the conduction of mantle heat to the shallow part of the crust (Wang et al., 2019b). Deep faults cut through the upper crust, which is conducive to the upward intrusion of deep mantle thermal materials and magma into the crust. Under the thermal refraction effect, the heat accumulated in the concave area with a low thermal conductivity and was transferred to the convex area with a high thermal conductivity (Wang et al., 2020). The fault structure is very conducive to deep circulation heating of the groundwater (Pang, 2018). In addition, the internal temperature of the reservoir is homogenized due to the density flow of the water. Moreover, the intrusion of magma from the mantle provided radioactive material, and the heat from the subsequent radioactive decay created positive anomalies in the local geothermal field (Li H. et al., 2017a; Pang, 2018; Wang et al., 2021).

3 METHODS

First, we analyzed the image logging results for well D22 in the Rongcheng uplift. In addition, we obtained the fracture density, fracture strike, dip angle, and other parameters. The fracture length was difficult to determine. Even image logging cannot accurately judge the lengths of fractures well. Based on a previous analysis of the entire Jizhong depression (Li et al., 2017b), we assumed that the fracture length had a normal distribution. Research has shown that there is an exponential relationship between the fracture aperture and length. Based on Fisher's fractal statistical theory, a 3D DFN model of the Gaoyuzhuang reservoir around well D22 was established, and the fracture information was upscaled to a square grid using ODA theory. The random fractures result in great uncertainty. In order to reduce this uncertainty, we established a hydrothermal coupling model. Based on the field pumping test data for well D16 (well D16 is located about 200 m to the east of well D22), the model was verified, which greatly improved the correspondence between the model and the actual geological conditions.

3.1 Discrete Fracture Network Setting

3.1.1 Geometric Characteristics of Fractures

The disk shape has the greatest advantage in establishing mathematical expressions. In this study, it was assumed that the fractures in the 3D DFN model (rectangular fractures have an equivalent radius) were disk shaped. To quantitatively describe a fracture, its diameter (d), central position (x, y, z), poles (trends and folds), and aperture 1) need to be determined. It should be noted that poles and dip vectors are terms used to define the orientation of a plane in a space. The fractures were modeled as planar polygons and the poles or dips were used to describe their orientations (**Figure 2A**). The pole is a vector normal to the fracture plane, and it usually (by convention) points downward. The dip vector is a vector normal to the pole, and it lies in the plane pointing in the direction of the maximum slope gradient. The trend and plunge describe the orientation of the vector. The trend is the horizontal angle in the x-y plane away from north (positive *y*-axis) (**Figure 2B**). The plunge is the vertical angle in space away from the horizontal (x-y plane) (**Figure 2C**). The orientation of a dip or pole vector is completely specified by its trend and plunge (Golder Associates, 2019; Gläser et al., 2020).

It was assumed that the spatial position of the fracture exhibits a Poisson distribution, that is, the center of the fracture is randomly distributed in 3D space. This assumption requires that the rock mass does not contain bedding planes, fault zones or geological structures (Baecher et al., 1977). This process can be described using the Baecher model. The Baecher model (Baecher, 1983) was one of the first well-characterized discrete fracture models. In this model, the fracture centers are located uniformly in space, and using a Poisson process, the fractures are generated as disks with a given radius and orientation. The enhanced Baecher model extends the Baecher model by providing the provision of the fracture terminations and more general fracture shapes. The enhanced Baecher model utilizes fracture shapes that are initially generated as polygons with three to sixteen sides. These polygons can be equilateral (aspect ratio of one) or elongate, and the aspect ratio (ratio of the major to minor axis size and orientation) is defined.

It was assumed that the fracture direction obeys a Fisher distribution. The univariate Fisher distribution is the analog of the normal (Gaussian) distribution on a sphere, and it is theoretically justified when the sum of multiple, uncorrelated variations in the rock's properties and stress conditions cause variations in the fracture orientation. It is relatively easy to fit and easy to explain. However, its major drawback is that it requires symmetric variation of the orientation around the mean pole.

The Fisher distribution is defined by the probability density function (Gottron and Henk, 2021):

$$f(\varphi', \phi') = \frac{\kappa sin\varphi' e^{xcos\phi'}}{2\pi(e^{\kappa} - 1)}, 0 \le \phi' \le \pi, 0 \le \varphi' \le 2\pi$$

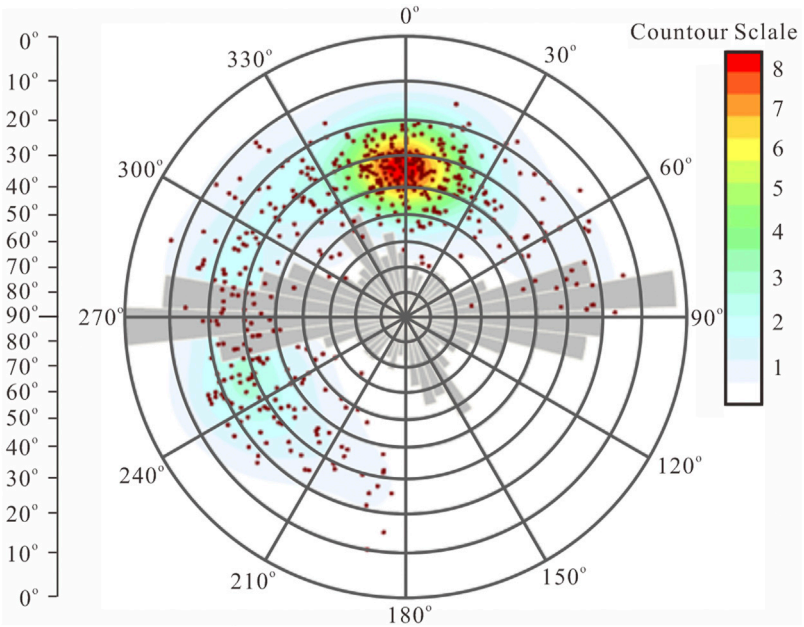

FIGURE 4 | Well logging fracture rose diagram and Fisher fractal statistical results for well D22 (the rose diagram represents the fracture trend, and the scattered points are the projection of the trend and the plunge of each fracture).

where κ is the distribution parameter, i.e., the concentration, and $\phi^{'}$ is the angle of the deviation from the mean pole. This distribution is unimodal and symmetric about the $\varphi^{'}$ axis. Increasing κ produces a distribution more concentrated around the $\varphi^{'}$ axis.

The Fisher concentration parameter κ is generally approximately defined as

$$\kappa \approx \frac{N_F}{N_F - |R|}$$

where $|R|$ is the magnitude of the vector sum of the unit vectors for orientation, and N_F is the number of fractures. This approximation is only valid for κ values of greater than five. The uniform dispersion corresponds to $\kappa = 0$.

The fracture length exhibits significant fractal characteristics on the outcrop scale, which has also confirmed in many previous studies (Bertrand et al., 2018; Gong et al., 2021). However, the burial depth of the Gaoyuzhuang reservoir is more than 3,000 m, and the outcrop fractures are poorly representative of the *in situ* fractures in the reservoir after later karstification and other geological processes. We assumed that the fractures between 5 and 30 m play a major role in the migration of the groundwater (Lu et al., 2019; Tang et al., 2020; Wang et al., 2020), and the fracture length has a lognormal distribution. The lognormal distribution is specified by the probability density function (Golder Associates, 2019; Gläser et al., 2020):

$$f(x) = \frac{1}{xln(10)y_\sigma\sqrt{2\pi}}\exp\left(-\frac{1}{2}\left(\frac{logx - \bar{y}}{y_\sigma}\right)^2\right)$$

where $\bar{y}$ and y_σ are the mean and standard deviation in log10 space. The truncated lognormal distribution has two additional parameters (x_-, x_+), the minimum and maximum values. Although FracMan uses the mean and standard deviation values above (i.e., for the un-truncated distribution), the actual mean $\overline{x'}$ of the truncated lognormal distribution is

$$\overline{x'} = log\bar{x} + \sqrt{\frac{2}{\pi}}logx_\sigma\frac{e^{-y_-^2} - e^{-y_+^2}}{erf(y_+) - erf(y_-)}$$

where $y_- = \frac{logx_- - log\bar{x}}{\sqrt{2}logx_\sigma}$, and $y_+ = \frac{logx_+ - log\bar{x}}{\sqrt{2}logx_\sigma}$.

The term fracture intensity can mean different things to different people, including the intensity, density, and frequency. A wide variety of methods are available for quantifying the intensity of fractures, such as the area of the fractures per unit volume (P32), the volume of the fractures per unit volume (P33), the number of fractures (NF), and the number of fractures per unit length of the borehole (P10) (Golder Associates, 2019; Gläser et al., 2020). The linear fracture intensity is expressed as the number of fractures per unit length. P10 is a 1-D measurement, and it is typically recorded as the position of the fracture intersection along a line in space, such as the core axis for boreholes, the well centerline for image log data, and the scanline on a surface outcrop or tunnel wall. We used P10 to describe the fracture density in well D22, which is the most direct and stable method.

The degree of elongation is specified in terms of the aspect ratio, which can either be set as a constant or specified as a uniform distribution. An aspect ratio of 2.5 was used.

3.1.2 Relationship Between Fracture Aperture and Length

The fracture aperture has been demonstrated to control the fluid flow and solute transport. Due to the rough surface of the

TABLE 1 | Fisher fractal statistical results for well D22.

Distribution	Fisher distribution
WE set	
Fracture Count	171
Relative Intensity	68.95%
Mean Pole (tr/pl)	357.972, 35.100
K	8.2538
KS Probability	88.57%
NW set	
Fracture Count	77
Relative Intensity	31.05%
Mean Pole (tr/pl)	240.608, 29.904
K	5.2616
KS Probability	41.69%
Total Fracture Count	**248**

fracture, the aperture of the fracture is non-uniform and is not the only determined value. In a natural fracture system, it is difficult to describe each of the fracture aperture distributions. Therefore, the maximum aperture (d_{max}) or the average aperture ($d_{ave} = \pi d_{max}/4$) is often used to represent the aperture of a single fracture. Then, the permeability of the fracture can be calculated using the cubic law (Witherspoon et al., 1980; Ghanbarian et al., 2019):

$$k_f = \frac{d_{ave^2}}{12}$$

The determination of the fracture aperture has been a research hotspot during the past few decades. It is generally believed that the fracture aperture follows a lognormal distribution or power-law distribution (Walmann et al., 1996; Renshaw and Park, 1997; Ghanbarian et al., 2019). In nature, larger fractures have larger permeabilities than smaller fractures, so it is reasonable to assume that the fracture aperture is related to the fracture length (Baghbanan and Jing, 2007). However, even if the effects of the shear history, weathering, and filling are ignored, it is difficult to establish the exact quantitative relationship between the aperture and length. Researchers have attempted to obtain a linear (Vermilye and Scholz, 1995) or power-law correlation (Hatton et al., 1994; Renshaw and Park, 1997) between the fracture aperture and length. Olson (2003) proposed a nonlinear power-law relationship:

$$d_{max} = \alpha L^n$$

where L is the fracture length, and n is the power law exponent. α is the parameter related to the mechanical properties of the surrounding rock:

$$\alpha = \frac{K_{lc}(1-\nu)^2}{E}\frac{\sqrt{8}}{\sqrt{\pi}}$$

where K_{lc} is the fracture toughness, ν is Poisson's ratio of the rock, and E is the Young's modulus of the rock, all of which are constant material properties of the rock. Olson (2003) further pointed out that the mechanical interaction between closely spaced fractures causes the exponent n to vary with the fracture spacing and suggested that a value of $n > 0.5$ could result from post-jointing relaxation or other secondary effects.

A large number of statistical measurements (Olson, 2003; Schultz et al., 2008) have revealed that $0.22 < n < 0.69$, with a mean value of 0.5 and α ranging from 10^{-1} to 10^{-5}. We assumed that $n = 0.5$, and α was determined through sensitivity analysis.

3.2 Hydrothermal Coupling Model

3.2.1 Grid Permeability Calculations

Due to the limitation of the scientific computing capability, we could not use the full DFN simulation to perform calculations for hundreds of thousands of fractures. It is most economical and reliable to approximate a reservoir as a porous medium and to coarsen the fracture properties to finite grids.

Oda analysis calculates the permeability and/or hydraulic conductivity tensors in three dimensions and all directions for each cell in a given grid. The Oda tensor represents a simplification of Darcy's Law for laminar flow through an isotropic porous medium. It works by projecting the fracture's isotropic permeability (k) onto the plane of the fracture, then scaling it using the ratio between the fracture volume (from porosity analysis) and the volume of the simulation grid cell. The result is a 3 × 3 matrix describing the directional permeability in each fracture. These matrices can be summed to obtain a net permeability tensor (k_{net}) for the grid cell. The principal permeabilities and flow directions (K_i, K_j, and K_k) can be found through eigenvector analysis of the net permeability tensor.

Oda's (1985) method begins by considering the orientation of fractures in a grid cell, which is expressed as a unit normal vector n. By integrating the fractures over all of the unit normals N, the mass moment of the inertia of the fracture normals distributed over a unit sphere is obtained:

$$N = \int_{\Omega/2} n_i n_j E(n) d\Omega,$$

where N is the number of fractures in Ω, n_i, n_j are the components of a unit normal to the fracture n. $E(n)$ is the probability density function that describes the number of fractures whose unit vectors n are oriented within a small solid angle $d\Omega$. Ω is the entire solid angle corresponding to the surface of a unit sphere.

For a specific grid cell with known fracture areas A_k and transmissivities T_k, which are obtained from the DFN model, an empirical fracture tensor can be calculated by adding the individual fractures weighted by their area and transmissivity:

$$F_{ij} = \frac{1}{V}\sum_{k=1}^{N} A_k T_k n_{ik} n_{jk}$$

where F_{ij} is the fracture tensor, V is the grid cell volume, and N is the total number of fractures in the grid cell. A_k and T_k are area and transmissivity of fracture k, respectively. n_{ik}, n_{jk} are the components of a unit normal to the fracture k.

Oda's permeability tensor is derived from F_{ij} by assuming that F_{ij} expresses the fracture flow as a vector along the fracture's unit normal. Assuming that the fractures are impermeable in the direction parallel to their unit normal, F_{ij} must be rotated into the planes of the permeability:

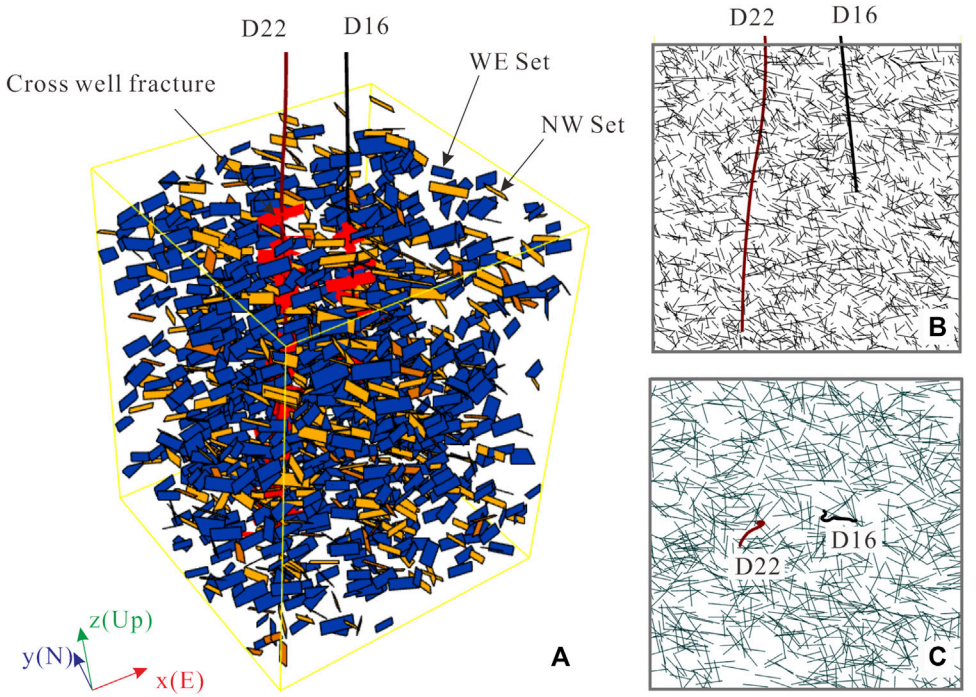

FIGURE 5 | (A) Three-dimensional DFN fracture modeling results the red pieces represent the logged fractures in well D22 and the black line represents well D16. Only 1% of the generated fractures are displayed. Blue denotes the EW set, and orange denotes the NW set; **(B)** EW vertical profile fracture trace map through D22 and D16; **(C)** Horizontal fracture trace map at the depth of 3000 m.

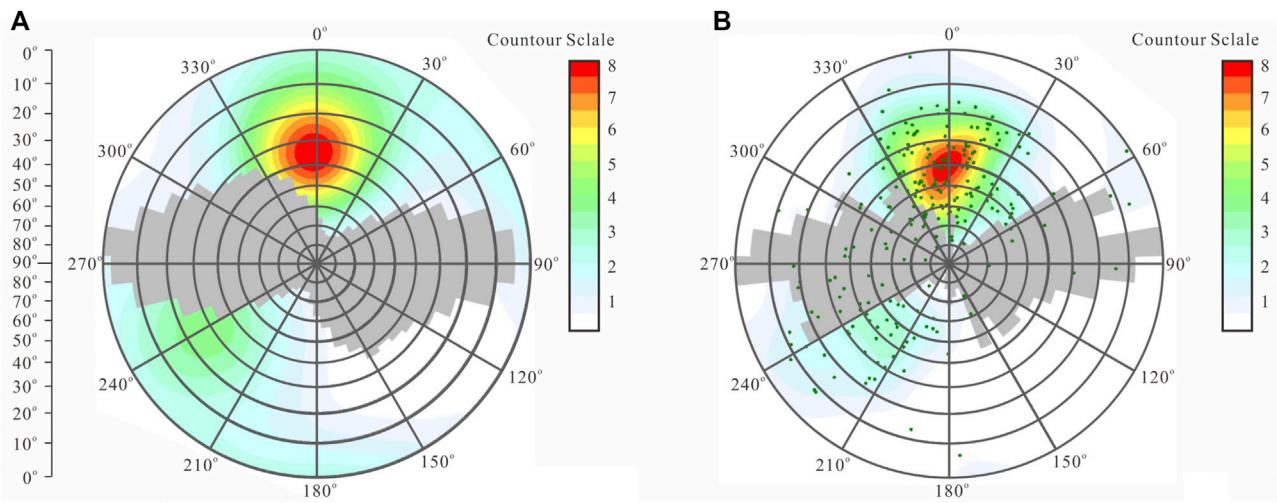

FIGURE 6 | (A) Rose diagrams of all of the fractures in the DFN model, and **(B)**the fractures that cut through well D22.

$$k_{ij} = \frac{1}{12}\left(F_{kk}\delta_{ij} - F_{ij}\right)$$

where k_{ij} is the permeability tensor, F_{ij} is the fracture tensor, and δ_{ij} is Kroenecker's delta.

However, the permeability estimated using Oda method is often overestimated, and the results calibrated using the actual flow model have a higher reliability.

3.2.2 Hydrothermal Coupled Flow in Porous Media

We used the TOUGH2 EOS1 program to perform the hydrothermal coupling simulations (Pruess, 1991). TOUGH2 has been demonstrated to be effective in geothermal porous media. All of the flow and transport equations have the same structure, and they can be derived based on the principle of the conservation of mass

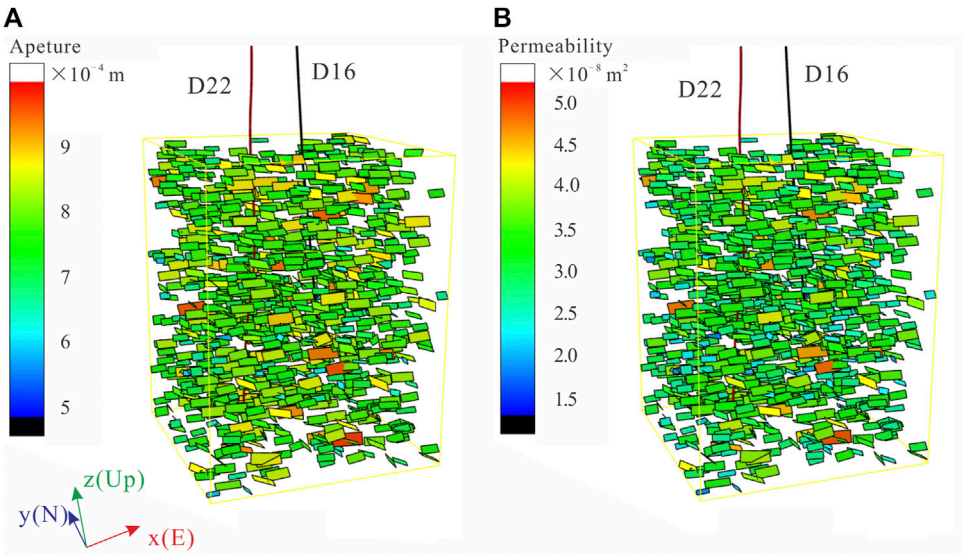

FIGURE 7 | (A) Distribution of the fracture aperture, and **(B)** permeability for the 3D DFN model.

(or energy). The models for fluid and heat flow have been discussed in detail by Pruess (1991) and Pruess et al. (1999):

$$\frac{\partial M_\kappa}{\partial t} = -\nabla F_\kappa + q_\kappa$$

For Water

$$M_w = \phi\left(S_l\rho_l X_{wl} + S_g\rho_g X_{wg}\right)$$
$$F_w = X_{wl}\rho_l \boldsymbol{u}_l + X_{wg}\rho_g \boldsymbol{u}_g$$
$$q_w = q_{wl} + q_{wg}$$

For Heat

$$M_h = \phi\left(S_l\rho_l U_l + S_g\rho_g U_g\right) + (1-\phi)\rho_s U_s$$
$$F_h = \sum_{\beta=l,g} h_\beta\rho_\beta \boldsymbol{u}_\beta - \lambda\nabla T + q_h$$
$$\boldsymbol{u}_\beta = -k\frac{k_{r\beta}}{\mu_\beta}\left(\nabla P_\beta - \rho_\beta g\right)\beta = l, g \quad \text{(Darcy's Law)}$$

where M is the mass accumulation (kg/m^3), F is the mass flux ($kg/(m^2 \cdot s)$), and q is the source/sink. ϕ is the porosity, S is saturation, and X is the mass fraction. ρ is the density (kg/m^3), $\boldsymbol{u}$ is the Darcy velocity (m/s). U is the internal energy (J/kg), λ is the heat conductivity ($\frac{W}{m\cdot K}$), T is the temperature (K), and P is the pressure (Pa). k is the permeability (m^2), and k_r is the relative permeability. The subscripts w, g, l, and s denote water, gas phase, liquid phase, and solid phase, respectively. h is heat, and κ and β are the governing equation index and phase index, respectively. In the Gaoyuzhuang reservoir, the pressure is much higher than the saturated vapor pressure of water, and there is no gas phase. Therefore, the term containing the subscript g can be ignored in the equation.

4 RESULTS AND DISCUSSION

4.1 Fracture Characteristics From Image Logging

A total of 248 fractures were interpreted through image logging in well D22. The cumulative fracture density distribution map (**Figure 3**) shows that the fracture density in the reservoir is relatively uniform without obvious stratification characteristics. The same line density (P10) can be used for the construction of the DFN model. The linear density of the fractures (P10) in the entire logging section is 0.3894 m^{-1}.

According to Fisher's fractal analysis, the fractures near well D22 were mainly divided into two subsets (**Figure 4**): a nearly east–west trending fracture set (hereinafter referred to as the EW set) and a north–west trending fracture set (hereinafter referred to as the NW set). According to the statistics, there are more fractures in the EW fracture set, with a total of 171 fractures. The relative density is 68.95%, and the P10 value is 0.2685 m^{-1}. The distribution is relatively concentrated. The mean poles (trends and pluges) are 357.9° and 35.1°, and the Fisher concentration is 62.05. The NW fracture set includes 77 fractures, with a relative density of 31.05% and a P10 value of 0.1209 m^{-1}. The distribution is relatively scattered, with mean poles (trends and pluges) of 240.6° and 29.9°. They have different trend distributions, and a Fisher concentration of 26.55. The detailed results of the Fisher analysis are presented in **Table 1**.

4.2 Three-Dimensional DFN Model and Fracture Parameters

Based on the Fisher's fractal statistics, it was assumed that the fracture length ranged from 5 to 30 m and obeyed a lognormal distribution (Li et al., 2017b). The average fracture length was 10 m and the variance was 5 m. The length to height ratio of the

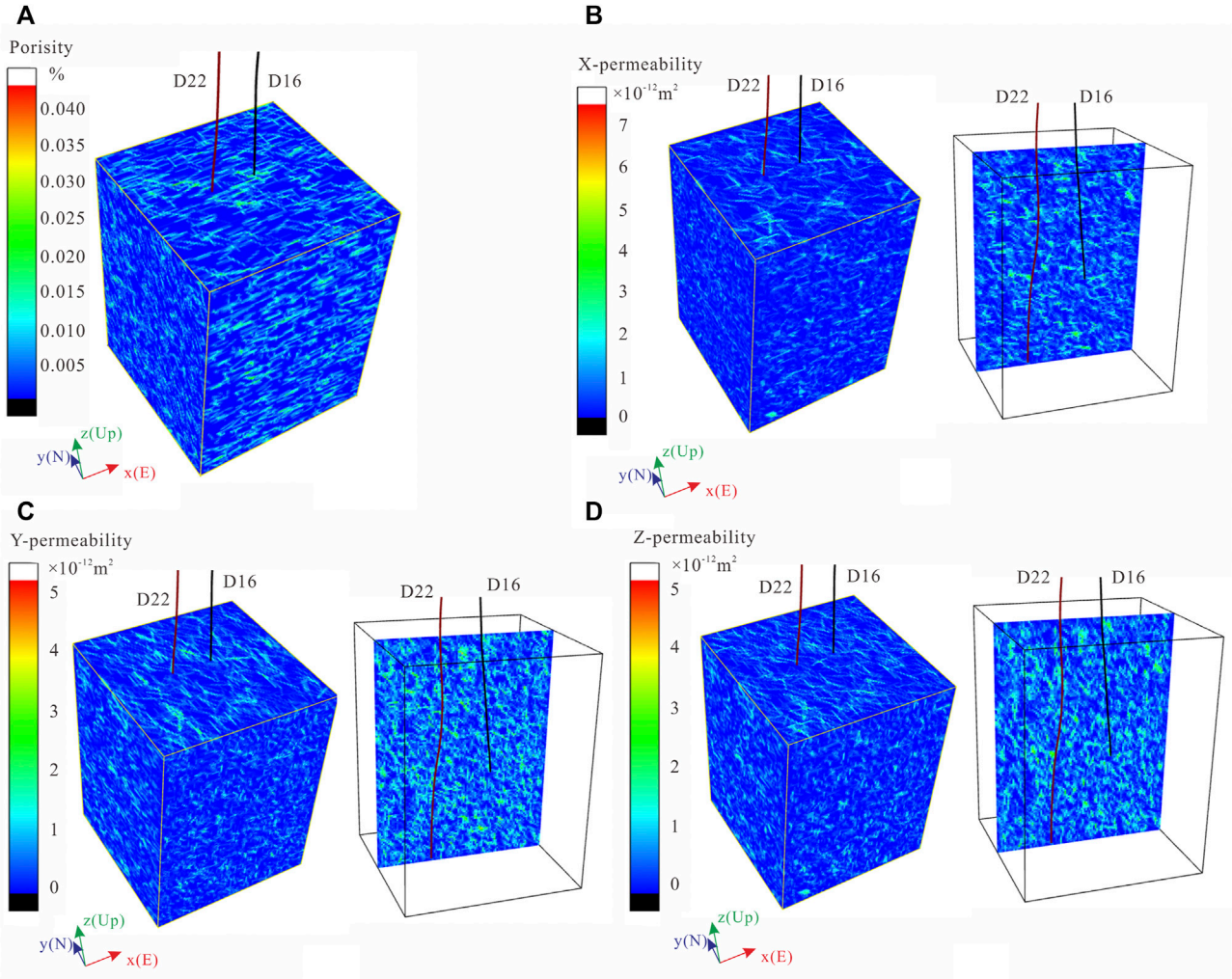

FIGURE 8 | (A) Calculated porosity and permeability **(B–D)** in the reservoir grid. Earch of the permeability map contains a slice through D22 and D16.

fractures was 2.5:1. About 30% of all of the logged fractures had flow conductivity. As has been described in *Relationship Between Fracture Aperture and Length* Section, the aperture of the fracture directly affects its permeability. This section mainly presents the modeling results for $\alpha = 10^{-4}$.

Taking well D22 as the center, the horizontal range was $1000\,m \times 1000\,m$ and the vertical range was $2200 - 3500\,m$. The fractures were randomly generated in this space. **Figure 5** shows the fracture distribution of the 3D DFN model. The EW and NW fracture sets were generated completely according to the statistical results. The number of fractures in the EW set was significantly larger than that in the NW set, which was controlled by their P10 values.

In order to determine the coincidence between the random fracture model and the actual fracture network, we drew a rose diagram of all of the fractures, a rose diagram of the fractures passing through well D22, and a cumulative density map of the fractures passing through well D22. **Figure 6A** shows the statistics of all of the fractures in the model, and **Figure 6B** shows the statistics of the model through the well fractures. The distributions of these two fracture sets, for both fracture strike and concentration, are very similar to the results of the statistical analysis of the actual logged fractures. The cumulative density distribution of the simulated fractures through the well also has the same slope as the measured value. We believe that the 3D DFN model established using this method adequately represents the actual fracture network.

The purpose of establishing a fracture network model is to predict the reservoir's flow capacity. Before this, we needed to obtain the parameters for a single fracture, such as the aperture and permeability. Using the process described in *Relationship Between Fracture Aperture and Length* Section, we obtained the fracture aperture and permeability parameters of the 3D DFN model. In our DFN model, the maximum fracture aperture was 0.9 mm (**Figure 7A**) and the maximum permeability was $5 \times 10^{-8}\,m^2$ (**Figure 7B**). The corresponding relationship between the fracture permeability and the fracture aperture was very obvious.

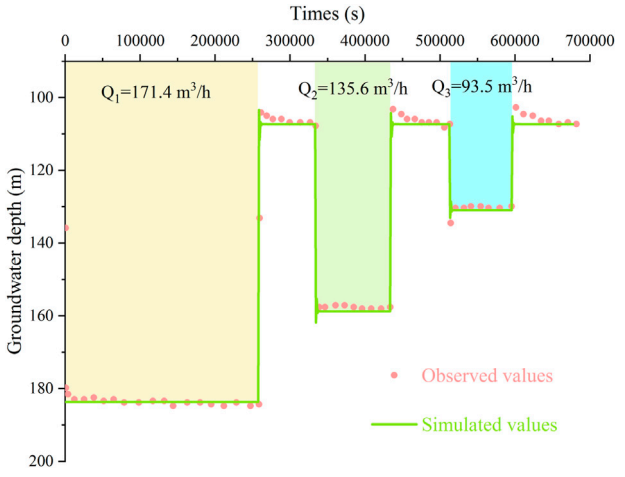

FIGURE 9 | Fitting of simulated and pumping test water levels in well D16.

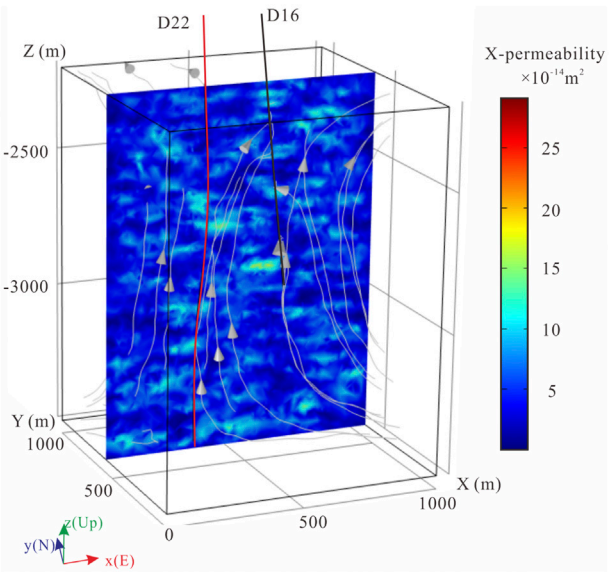

FIGURE 10 | Calculated permeability in the *x* direction and the pumping streamline distribution.

4.3 Prediction of Reservoir Permeability Distribution

We discretized the above range into $10\,m \times 10\,m \times 10\,m$ cubic grids, with a total of 130,000,000 grids. The east–west, north–south, and vertical directions were represented by the x, y, and z axes, respectively. The porosity and permeability tensors of each grid were obtained using the Oda method. Although there were many fractures, their contribution to the grid porosity was very small. The maximum porosity caused by the fractures was only 0.04%, which is negligible compared with the 1% porosity of natural dolomite. However, the fractures had a great impact on the grid permeability. Due to the differences in the fracture density, direction, aperture, and permeability, the permeability of the reservoir in the three orthogonal directions was very different. The permeability was large in the dense fracture area and along the fractures' strike. Most of the fractures strike east-west and had high dip angles, so the permeability of the reservoir was larger in the *x* and *z* directions and smaller in the *y* direction. The maximum permeability in the *x* direction reached 7×10^{-12} m^2, and the permeability in most of the high permeability areas was about 2×10^{-12} m^2 (**Figure 8**). In this way, we obtained the distributions of the porosity and permeability of the reservoir. We found that the existence of fractures resulted in the reservoir being highly heterogeneous, which also explains the fact that a consistent water production was not obtained for a single well during the geothermal development.

4.4 Model Calibration Based on Pumping Test

As previously mentioned, the Oda method tends to overestimate the conductivity of fractures. In terms of the parameters, it can be considered that α has a great uncertainty. We evaluated the value of α based on a fixed DFN model. Well D16 is located about 200 m to the east of well D22, which is also within our modeling range. If the simulated pumping test results are consistent with the *in situ* test results, the permeability model can be considered to be accurate.

Pumping tests for about 190 h were conducted for well D16 in June 2018, including 124 h of continuous pumping and 65 h of water level recovery. The pumping test results were divided into three stages, with durations of 72, 28, and 24 h. Initially, the water level was 101.61 m below the surface, the water level drawdowns during stages 1–3 were 82.09, 55.79, and 27.91 m, respectively, and the corresponding water inflow values were 171.4 m^3/h, 135.6 m^3/h, and 93.5 m^3/h, respectively. The entire pumping test process was reproduced *via* hydrothermal coupling numerical simulation. The fitting results are shown in **Figure 9**. The pumping tests during the three stages are well fitted. For the best fitting case, α is 4.2×10^{-5}. At this time, the maximum *x* -direction permeability of the thermal reservoir is about $25 \times 10^{-14}\,m^2$, and the permeability of the fracture zone is mainly $15 \times 10^{-14}\,m^2$ (**Figure 10**), which is also close to the effective permeability of the fracture zone identified *via* conventional logging.

5 CONCLUSION

The fractures control the convection and mass transfer processes in the reservoir. The Gaoyuzhuang Formation in the Jixian system in the Xiong'an new area has a great development potential. After analyzing the fracture distribution interpreted through image logging of D22 well, it was found that the fractures around the well are affected by the Xushui fault, and the fractures mainly strike east-west, followed by northwest. Most of the fractures are high angle fractures, which is very conducive to

the vertical migration of hot water. This is the main reason for the low temperature gradient in the geothermal reservoir.

Via statistical methods, a random 3D DFN model of the Gaoyuzhuang Formation was established for the first time. This model describes the characteristics of the fracture distribution, fracture length, fracture aperture, and fracture permeability in detail. The distributions of the porosity and permeability were obtained through further calculations. The increase in the porosity caused by the fractures can be ignored, but the fractures directly control the distribution of the reservoir's permeability. In our model, the maximum predicted reservoir permeability reached $25 \times 10^{-14}\, m^2$, which corresponds well with the logging results.

The prediction of the fracture aperture is particularly important in the modeling process. It is a function of the fracture length, and the parameter α has a large influence on the calculation results. Based on the field pumping tests conducted in well D16 and through water level fitting, the empirical relationship between the fracture aperture and length for the Gaoyuzhuang Formation was obtained: $d_{max} = 4.2 \times 10^{-5} \cdot L^{0.5}$.

DATA AVAILABILITY STATEMENT

The raw data supporting the conclusions of this article will be made available by the authors, without undue reservation.

AUTHOR CONTRIBUTIONS

GY was responsible for numerical simulation and overall paper writing. GW put forward the research idea. FM provides funding and site support. XZ and HZ conducted well logging and pumping tests. JZ and JN gave guidance to fracture modeling.

FUNDING

The authors acknowledge the financial support provided by National Key R&D Program of China (2019YFB1504101), National Natural Science Foundation of China (41807208), and Natural Science Foundation of Hebei Province (D2021504041).

REFERENCES

Ahmad, T., Zhang, H., and Yan, B. (2020). A Review on Renewable Energy and Electricity Requirement Forecasting Models for Smart Grid and Buildings. *Sust. Cities Soc.* 55, 102052. doi:10.1016/j.scs.2020.102052

Baecher, G. B., Lanney, N. A., and Einstein, H. H. (1977). Statistical Description of Rock Properties and Sampling. (OnePetro). Available at: https://onepetro.org/ARMAUSRMS/proceedings/ARMA77/All-ARMA77/ARMA-77-0400/128963 (Accessed August 18, 2021).

Baecher, G. B. (1983). Statistical Analysis of Rock Mass Fracturing. *Math. Geology.* 15, 1–20. doi:10.1007/bf01036074

Baghbanan, A., and Jing, L. (2007). Hydraulic Properties of Fractured Rock Masses with Correlated Fracture Length and Aperture. *Int. J. Rock Mech. Mining Sci.* 44, 704–719. doi:10.1016/j.ijrmms.2006.11.001

Barcelona, H., Maffucci, R., Yagupsky, D., Senger, M., and Bigi, S. (2020). Discrete Fracture Network Model of the Vapor Zone Leakages at the Copahue Geothermal Field. *J. Struct. Geology.* 140, 1–14. doi:10.1016/j.jsg.2020.104155

Bertrand, L., Jusseaume, J., Géraud, Y., Diraison, M., Damy, P.-C., Navelot, V., et al. (2018). Structural Heritage, Reactivation and Distribution of Fault and Fracture Network in a Rifting Context: Case Study of the Western Shoulder of the Upper Rhine Graben. *J. Struct. Geology.* 108, 243–255. doi:10.1016/j.jsg.2017.09.006

Cai, X., Zhu, J., Cao, J., and Cheng, X. (2007). 3D Structure and Dynamic Types of the Lithospheric Crust in continental china and its Adjacent Regions. *Geology. China* 34, 543–557. (in Chinese with English abstract).

Chang, J., Qiu, N., Zhao, X., Xu, W., Xu, Q., Jin, F., et al. (2016). Present-day Geothermal Regime of the Jizhong Depression in Bohai Bay Basin,East China. *Chin. J. Geophys.* 59, 1003–1016. (in Chinese with English abstract).

Chen, M. (1988). *Geothermics of North China*. 1st ed. Beijing, China: Science Press of China.

Dincer, I., and Ozturk, M. (2021). *Geothermal Energy Systems*. Elsevier.

Dincer, I. (2000). Renewable Energy and Sustainable Development: a Crucial Review. *Renew. Sust. Energ. Rev.* 4, 157–175. doi:10.1016/S1364-0321(99)00011-8

Dowd, P. A., Martin, J. A., Xu, C., Fowell, R. J., and Mardia, K. V. (2009). A Three-Dimensional Fracture Network Data Set for a Block of Granite. *Int. J. Rock Mech. Mining Sci.* 46, 811–818. doi:10.1016/j.ijrmms.2009.02.001

Ghanbarian, B., Perfect, E., and Liu, H.-H. (2019). A Geometrical Aperture-Width Relationship for Rock Fractures. *Fractals* 27, 1940002. doi:10.1142/S0218348X19400024

Giuffrida, A., Agosta, F., Rustichelli, A., Panza, E., La Bruna, V., Eriksson, M., et al. (2020). Fracture Stratigraphy and DFN Modelling of Tight Carbonates, the Case Study of the Lower Cretaceous Carbonates Exposed at the Monte Alpi (Basilicata, Italy). *Mar. Pet. Geology.* 112, 104045. doi:10.1016/j.marpetgeo.2019.104045

Gläser, D., Flemisch, B., Class, H., and Helmig, R. (2020). Frackit: a Framework for Stochastic Fracture Network Generation and Analysis. *JOSS* 5, 2291. doi:10.21105/joss.02291

Golder Associates (2019). *FracMan Interactive Discrete Feature Data Analysis, Geometric Modeling and Exploration Simulation*. User Documentation.

Gong, H., Wang, B., Liang, H., Luo, Z., and Cao, Y. (2020). Strategic Analysis of China's Geothermal Energy Industry. *Front. Eng. Manag.* 8, 390–401. doi:10.1007/s42524-020-0106-4

Gong, L., Gao, S., Liu, B., Yang, J., Fu, X., Xiao, F., et al. (20212021). Quantitative Prediction of Natural Fractures in Shale Oil Reservoirs. *Geofluids* 2021, 1–15. doi:10.1155/2021/5571855

Gottron, D., and Henk, A. (2021). Upscaling of Fractured Rock Mass Properties - an Example Comparing Discrete Fracture Network (DFN) Modeling and Empirical Relations Based on Engineering Rock Mass Classifications. *Eng. Geology.* 294, 106382. doi:10.1016/j.enggeo.2021.106382

Hatton, C. G., Main, I. G., and Meredith, P. G. (1994). Non-universal Scaling of Fracture Length and Opening Displacement. *Nature* 367, 160–162. doi:10.1038/367160a0

He, D., Shan, S., Zhang, Y., Lu, R., Zhang, R., and Cui, Y. (2018). 3-D Geologic Architecture of Xiong 'an New Area :Constraints from Seismi Reflection Data. *Sci. China Earth Sci.* 49, 1207–1222. (in Chinese with English abstract).

Hu, Q., Gao, J., Ma, F., Zhao, Z., Liu, G., Wang, G., et al. (2020). Dynamic Prediction of Geothermal Recoverable Resources in the Rongcheng Uplift Area of the Xiong'an New Area. *Acta Geologica Sinica* 94, 2013–2025. (in Chinese with English abstract). doi:10.19762/j.cnki.dizhixuebao.2020230

Li, H., Yu, J., Lv, H., and Xiao, P. (2017a). Gravity and Aeromagnetic Responses and Heat-Control Lng Structures of Xiongxian Geothermal Area. *Geophys. Geochemical Exploration* 41, 242–248. (in Chinese with English abstract). doi:10.11720/wtyht.2017.2.08

Li, S., Zhang, S., Yu, G., and Xu, A. (2017b). An Equivalent Fracture Modeling Method. *IOP Conf. Ser. Earth Environ. Sci.* 104, 012007. doi:10.1088/1755-1315/104/1/012007

Li, Y., Hou, J., and Li, Y. (2016). Features and Classified Hierarchical Modeling of Carbonate Fracture-Cavity Reservoirs. *Pet. Exploration Dev.* 43, 655–662. doi:10.1016/S1876-3804(16)30076-3

Lu, K., Bao, Z., Ji, H., Liu, J., Wang, G., and Ma, F. (2019). Characteristics, Main Controlling Factors and Favorable Area Prediction of Karstic Geothermal Reservoirs of the Jixian Wumishan Formation in Xiong an New Area. *J. Palaeogeogr.* 21, 885–900. (in Chinese with English abstract).

Lu, S.-M. (2018). A Global Review of Enhanced Geothermal System (EGS). *Renew. Sust. Energ. Rev.* 81, 2902–2921. doi:10.1016/j.rser.2017.06.097

Ma, F., Wang, G., Zhang, W., Zhu, X., Zhang, H., and Yue, G. (2020). Structure of Geothermal Reservoirs and Resource Potential in the Rongcheng Geothermal Field in Xiong'an New Area. *Acta Geologica Sinica* 94, 1981–1990. (in Chinese with English abstract). doi:10.19762/j.cnki.dizhixuebao.2020217

Nian, T., Wang, G., Cang, D., Tan, C., Tan, Y., and Zhang, F. (2022). The Diagnostic Criteria of Borehole Electrical Imaging Log for Volcanic Reservoir Interpretation: An Example from the Yingcheng Formation in the Xujiaweizi Depression, Songliao Basin, China. *J. Pet. Sci. Eng.* 208, 109713. doi:10.1016/j.petrol.2021.109713

Oda, M. (1985). Permeability Tensor for Discontinuous Rock Masses. *Géotechnique* 35, 483–495. doi:10.1680/geot.1985.35.4.483

Olson, J. E. (2003). Sublinear Scaling of Fracture Aperture versus Length: An Exception or the Rule? *J. Geophys. Res.* 108. doi:10.1029/2001JB000419

Ozkaya, S. I. (2021). Geometry of Layer-Bound Fractures Based on Fracture Density and Aperture-Depth Plots from Resistivity Image Logs of Deviated wells. *J. Struct. Geology.* 149, 104372. doi:10.1016/j.jsg.2021.104372

Pan, D., Li, S., Xu, Z., Zhang, Y., Lin, P., and Li, H. (2019a). A Deterministic-Stochastic Identification and Modelling Method of Discrete Fracture Networks Using Laser Scanning: Development and Case Study. *Eng. Geology.* 262, 105310. doi:10.1016/j.enggeo.2019.105310

Pan, S.-Y., Gao, M., Shah, K. J., Zheng, J., Pei, S.-L., and Chiang, P.-C. (2019b). Establishment of Enhanced Geothermal Energy Utilization Plans: Barriers and Strategies. *Renew. Energ.* 132, 19–32. doi:10.1016/j.renene.2018.07.126

Pang, J. (2018). *A Study on the Responsing Mechanism of Karstic Geothermal Reservoir to Large Scale Production and Reinjection in Niutuozhen Geothermal Field*.

Pruess, K., Oldenburg, C. M., and Moridis, G. J. (1999). *TOUGH2 User's Guide Version 2*. Berkeley, CA (United States: Lawrence Berkeley National Lab. (LBNL. doi:10.2172/751729

Pruess, K. (1991). *TOUGH2: A General Purpose Numerical Simulator for Multiphase Fluid and Heat Flow*. UNIVERSITY OF CALIFORNIA: Lawrence Berkeley Laboratory.

Qi, J., Yu, F., Lu, K., Zhou, J., Wang, Z., and Yang, Q. (2003). Conspectus on Mesozoic Basins in Bohai bay Province. *Earth Sci. Front.* 10, 199–206. (in Chinese with English abstract). doi:10.3321/j.issn:1005-2321.2003.z1.028

Qiu, N., Xu, W., Zuo, Y., Chang, J., and Liu, C. (2017). Evolution of Meso-Cenozoic thermal Structure and Therma-Rheological Structure of the Lithosphere in the Bohai Bay Basin, Eastern North China Craton. *Earth Sci. Front.* 24, 13–26. (in Chinese with English abstract). doi:10.13745/j.esf.2017.03.002

Renshaw, C. E., and Park, J. C. (1997). Effect of Mechanical Interactions on the Scaling of Fracture Length and Aperture. *Nature* 386, 482–484. doi:10.1038/386482a0

Schultz, R. A., Soliva, R., Fossen, H., Okubo, C. H., and Reeves, D. M. (2008). Dependence of Displacement-Length Scaling Relations for Fractures and Deformation Bands on the Volumetric Changes across Them. *J. Struct. Geology.* 30, 1405–1411. doi:10.1016/j.jsg.2008.08.001

Tang, B., Zhu, C., Qiu, N., Cui, Y., Guo, S., and Chen, C. (2020). Characteristics of the Karst thermal Reservoir in the Wu Misha nFormation in the Xiong'an New Area. *Acta Geologica Sinica* 94, 2002–2012. (in Chinese with English abstract). doi:10.19762/j.cnki.dizhixuebao.2020232

Vermilye, J. M., and Scholz, C. H. (1995). Relation between Vein Length and Aperture. *J. Struct. Geology.* 17, 423–434. doi:10.1016/0191-8141(94)00058-8

Walmann, T., Malthe-Sørenssen, A., Feder, J., Jøssang, T., Meakin, P., and Hardy, H. H. (1996). Scaling Relations for the Lengths and Widths of Fractures. *Phys. Rev. Lett.* 77, 5393–5396. doi:10.1103/PhysRevLett.77.5393

Wang, G., Li, J., Wu, A., Zhang, W., and Hu, Q. (2018). A Study of the Thermal Storage Characteristics of Gao Yu Zhuang Formation, A New Layer System of Thermal Reservoir in Rong Cheng Uplift Area, Hebei Province. *Acta Geoscientica Sinica* 39, 533–541. (in Chinese with English abstract). doi:10.3975/cagsb.2018.071901

Wang, G., and Lin, W. (2020). Main Hydro-Geothermal Systems and Their Genetic Models in China. *Acta Geologica Sinica* 94, 1923–1937. (in Chinese with English abstract). doi:10.19762/j.cnki.dizhixuebao.2020224

Wang, G., Liu, Y., Zhu, X., and Zhang, W. (2020). The Status and Development Trend of Geothermal Resources in China. *Earth Sci. Front.* 27, 001–009. (in Chinese with English abstract). doi:10.19762/j.cnki.dizhixuebao.2020235

Wang, G., Zhang, W., Lin, W., Liu, F., Zhu, X., Liu, Y., et al. (2017). Research on Formation Mode and Development Potential of Geothermal Resources in Beijing-Tianjin-Hebei Region. *Geology. China* 44, 1074–1085. (in Chinese with English abstract). doi:10.12029/gc20170603

Wang, S., Zhang, B., Li, Y., Xing, Y., Yuan, W., Li, J., et al. (2021). Heat Accumulation Mechanism of Deep Ancient Buried hill in the Northeast of Gaoyang Geothermal Field, Xiong'an New Area. *Bull. Geol. Sci. Tech.* 40, 12–21. (in Chinese with English abstract). doi:10.19509/j.cnki.dzkq.2021.0319

Wang, Z., Jiang, G., Zhang, C., Tang, X., and Hu, S. (2019a). Estimating Geothermal Resources in Bohai Bay Basin, Eastern China, Using Monte Carlo Simulation. *Environ. Earth Sci.* 78, 355. doi:10.1007/s12665-019-8352-7

Wang, Z., Zhang, C., Jiang, G., Hu, J., Tang, X., and Hu, S. (2019b). Present-day Geothermal Field of Xiongan New Area and its Heat Source Mechanism. *Chin. J. Geophys.* 62, 4313–4322. (in Chinese with English abstract). doi:10.6038/cjg2019M032

Witherspoon, P. A., Wang, J. S. Y., Iwai, K., and Gale, J. E. (1980). Validity of Cubic Law for Fluid Flow in a Deformable Rock Fracture. *Water Resour. Res.* 16, 1016–1024. doi:10.1029/WR016i006p01016

Wu, A., Ma, F., Wang, G., Liu, J., Hu, Q., and Miao, Q. (2018). A Study of Deep-Seated Karst Geothermal Reservoir Exploration and Huge Capacity Geothermal Well Parameters in Xiongan New Area. *Acta Geologica Sinica* 39, 523–532. (in Chinese with English abstract). doi:10.3975/cagsb.2018.071104

Zhang, C., Zhang, X., Zhao, J., Ren, Q., Zhang, J., and Hai, Y. (2002). Study and Review on Crust-Mantle Velocity Structure in Bohai Bay and its Adjacent Areas. *Acta Seismologica Sinica* 24, 428–435+448. (in Chinese with English abstract). doi:10.3321/j.issn:0253-3782.2002.04.011

Zhang, W., Wang, G., Liu, F., Xing, L., and Li, M. (2019). Characteristics of Geothermal Resources in Sedimentary Basins. *Geology. China* 46, 255–268. (in Chinese with English abstract). doi:10.12029/gc20190204

Zheng, J., Lu, F., O'Reilly, S. Y., Griffin, W. L., and Zhang, M. (1999). Comparison between Palaeozoic and Cenozoic Lithospheric Mantle in the Eastern Part of the North China Block -with a Discussion of Mantle Evolution. *Acta Geologica Sinica* 73, 47–56. (in Chinese with English abstract).

Conflict of Interest: The authors declare that the research was conducted in the absence of any commercial or financial relationships that could be construed as a potential conflict of interest.

frontiers in Earth Science

ORIGINAL RESEARCH
published: 25 February 2022
doi: 10.3389/feart.2022.816960

Lithologic Hydrocarbon Accumulations in the Upper Jurassic Kalazha Formation in the Foreland Slope, the South Marginal Junggar Basin, Northwest China

Gang Liu[1], Xue-Feng Qi[1], Jian-Zhong Li[1], Ming Zhu[2], Bo Yuan[2] and Zhi-Chao Pang[2]*

[1]Research Institute of Petroleum Exploration and Development, China National Petroleum Corporation, Beijing, China, [2]Research Institute of Petroleum Exploration and Development, Xinjiang Oilfield, China National Petroleum Corporation, Karamay, China

The foreland slope in the south marginal Junggar Basin (SMJB) is geologically favorable for mass lithologic oil and gas reservoir accumulation. Based on outcrops, thin sections, individual-well facies, and cross-well stratigraphic correlation, the stratigraphic distribution and features of the Upper Jurassic Kalazha Formation were investigated in the SMJB. There are two sedimentary sources in the southwest and southeast Kalazha Formation, which thin out from south to north and vanish in the northern slope. Fan deltas occur in the southwest, and braided river deltas occur in the southeast. Kalazha reservoir rocks and sedimentary facies were predicted using joint 2D and 3D seismic impedance inversion. According to the overall analysis, the Kalazha Formation in the foreland slope is favorable for hydrocarbon accumulation, considering structural highs as the destination of long-term hydrocarbon migration and the updip wedge-out zone in the north with potential lithologic traps. The accumulation model was established with source rocks, reservoir rocks, caprocks, and migration systems for the lithologic hydrocarbon reservoirs in the Kalazha Formation in the SMJB. As per the model and regional stratigraphic and structural features, Kalazha lithologic hydrocarbon reservoirs mainly formed in the annular updip wedge-out zone in the foreland slope. Our deliverables may provide useful information for mass lithologic hydrocarbon accumulation in the foreland slope and deep to ultra-deep hydrocarbon exploration in the SMJB.

Keywords: Kalazha Formation, lithologic hydrocarbon reservoir, foreland slope, south marginal Junggar Basin, accumulation condition, accumulation model

OPEN ACCESS

Edited by:
Wenjing Lin,
Institute of Hydrogeology and Environmental Geology (CAGS), China

Reviewed by:
Binfeng Cao,
Institute of Geology and Geophysics (CAS), China
Changyu Fan,
Northwest University, China

****Correspondence:***
Gang Liu
584670774@qq.com

Specialty section:
This article was submitted to Solid Earth Geophysics, a section of the journal Frontiers in Earth Science

Received: *17 November 2021*
Accepted: *17 January 2022*
Published: *25 February 2022*

Citation:
Liu G, Qi X-F, Li J-Z, Zhu M, Yuan B and Pang Z-C (2022) Lithologic Hydrocarbon Accumulations in the Upper Jurassic Kalazha Formation in the Foreland Slope, the South Marginal Junggar Basin, Northwest China. Front. Earth Sci. 10:816960. doi: 10.3389/feart.2022.816960

INTRODUCTION

Lithologic reservoirs, especially large and extremely large lithologic oil and gas fields (provinces), are important to hydrocarbon exploration and reserves and production increases, the proved reserves of which account for 80% of the total reserves (Yuan et al., 2003; Jia et al., 2007; Tao et al., 2017). There are fewer and fewer structural reservoirs, which are less challenging for exploration, and hydrocarbon exploration is now focusing more on elusive lithologic reservoirs (Fu et al., 2020; Liang and Li, 2020).

The slope zone in a foreland basin is among the primary areas deposited with clastic lithologic reservoirs. According to the theory of structure-sequence-dominated hydrocarbon accumulations in

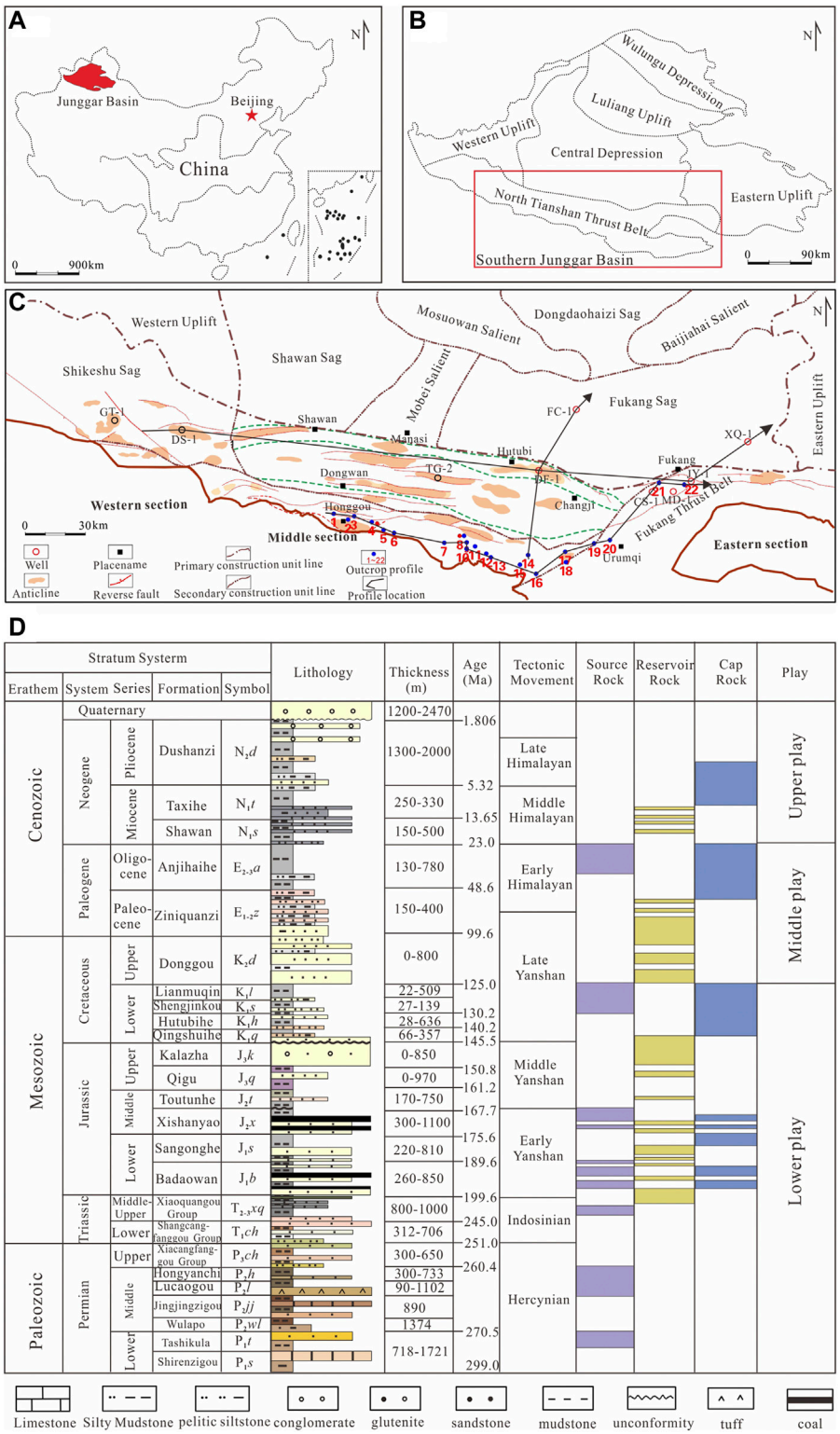

FIGURE 1 | (A) Regional location of the Junggar Basin in northwest China. **(B)** Tectonic units and the south marginal Junggar Basin (SMJB). **(C)** Location of the subunits, typical wells, and cross-sections. **(D)** Composite stratigraphic column in the MSTB.

a continental foreland basin, the occurrence of lithologic traps is dominated by six boundaries, such as lithologic pinch-out boundary, and four surfaces, such as fault surface. The distribution of lithologic reservoirs is dominated by three surfaces (maximum flooding, unconformity, and fault surfaces). Mass lithologic-stratigraphic hydrocarbon accumulation is related to the fans in the thrust belt, deltaic plains, and fronts in the slope zone in a continental foreland basin (Jia et al., 2008; Tao et al., 2017). Based on a portfolio of proven techniques for the exploration and evaluation of lithologic-stratigraphic reservoirs, elusive lithologic reservoir exploration in the thrust belt could be effectively performed in the slope zone, in addition to the structural belt. Recent hydrocarbon exploration has focused more on deep to ultra-deep zones. Moreover, large deep-seated structures and clastic lithologic reservoirs in the slope zones in foreland basins will become important targets for large-scale reserves increases. Most foreland basins in China are multicyclic superimposed basins with multi-phase tectonic movements and complicated hydrocarbon accumulation. Limited by deep to ultra-deep data, it is challenging to pinpoint lithologic reservoirs in deep to ultra-deep slope zones in foreland basins.

The south marginal Junggar Basin (SMJB) (**Figure 1**) is rich in hydrocarbon resources (Zhen et al., 2019), where large hydrocarbon reservoirs may occur. Exploration activities in the SMJB began in 1936 and have targeted shallow zones, including the Paleogene and Cretaceous Systems before 2008, where some small gas-rich fields were discovered. Since 2008, exploration has turned to deep-seated large structural traps in and below the Cretaceous System. Successes in Well GT1 at the beginning of 2019 (Du et al., 2019) indicated substantial exploration potential in the SMJB. Given the large area and promising accumulation conditions, large lithologic reservoirs may continuously occur in the slope zone in the foreland basin; thus, the slope zone may become an important reserves successor (Zhang and Liu, 2002).

We focused on the sedimentation, reservoirs, and hydrocarbon accumulation in the Jurassic Kalazha Formation in the SMJB; a model of lithologic hydrocarbon accumulation was established in the slope zone of the foreland basin and predicted promising areas rich in lithologic reservoirs. Research findings may provide useful information for hydrocarbon exploration in this region.

GEOLOGIC SETTING

The SMJB went through multi-phase tectonic-sedimentary evolution after the Permian Period, including foreland basin evolution from the Permian Period to Triassic Period, fault subsidence and compresso-shear in the Jurassic Period, intracontinental depression evolution from the Cretaceous Period to Paleogene Period, and rejuvenated foreland basin evolution from the Neogene Period to Quaternary Period (Wu et al., 2002; Wu et al., 2005; Wan et al., 2005; He et al., 2018). Foreland basin evolution may also occur in the late Jurassic Period as per the Qigu anticline and intense denudation in the Middle and Upper Jurassic Series (Kuang and Qi, 2006). Due to multi-phase tectonic-sedimentary processes in the SMJB, the slope zone in the thrust belt was geologically favorable for mass lithologic hydrocarbon accumulation (Zhang and Liu, 2002; Liu et al., 2019).

The SMJB has several packages of Permian-Paleogene source rocks (**Figure 1D**) (Tian et al., 2017; Wei et al., 2010) and major source rocks, including dark mudstones, carbonaceous mudstones, and coals, occurring in the Jurassic Badaowan (J_1b), San'gonghe (J_1s), and Xishanyao (J_2x) Formations (Qiu et al., 2008; Chen et al., 2017; Chen et al., 2019). The source center extends widely in the Fukang sag, Shawan sag, piedmont thrust belt, and Sikeshu sag (Wei et al., 2007; Wang et al., 2013; Chen et al., 2015). Source rocks, 600–800 m thick, are mature to post mature.

Several packages of effective reservoir rocks are developed in the deep Cretaceous Qingshuihe Formation and Jurassic Kalazha and Toutunhe Formations in the SMJB (Lei et al., 2012; Tian et al., 2017). Stable basal sandy conglomerates in the Qingshuihe Formation are laterally connected, favorable for lateral hydrocarbon migration (Liu et al., 2018). Kalazha reservoir rocks are mainly thick, blocky sandy conglomerates and sandstones of hundreds of meters thick with the sedimentary source in the south (Schneider et al., 1992; Shan et al., 2014; Gao et al., 2020).

The upper, middle, and lower reservoir-seal assemblages are separated by the regional mudstones in the Taxihe Formation (N_1t), Anjihaihe Formation ($E_{2\text{-}3}a$), and Tugulu Group (K_1tg) in the SMJB (Li et al., 2003; Li et al., 2006). Oil and gas are mainly concentrated in the middle assemblage (Xiao et al., 2011; Kuang et al., 2012). The Kalazha Formation, with promising accumulation conditions for hydrocarbon preservation, is covered with 500–1,000-m-thick Tugulu mudstones in the lower assemblage. The overpressure in the Tugulu Group, with a pressure coefficient above 1.8, will further enhance the sealing performance of mudstones (Tigert and Al-Shaieb, 1990; Magara, 1993; Darby et al., 1996). In addition to structural reservoirs in the Qingshuihe Formation, large lithologic reservoirs may be found in the Kalazha Formation.

STRATIGRAPHIC DISTRIBUTION

Well data are insufficient for the study of stratigraphic distribution because only a limited number of wells were drilled into the Kalazha Formation. Thus, we made full use of piedmont outcrop, well, and 2D and 3D seismic data to investigate stratigraphic distribution in the Kalazha Formation. Due to the influence of compressional tectonic movements in the Middle and Late Jurassic Epochs, the Kalazha Formation has been intensely denuded and is limited within Hutubi, Fukang, and some piedmont areas in the middle and eastern parts of the SMJB.

In the area of interest, the Kalazha Formation was drilled by some exploratory wells, i.e., DF-1, JY-1, JY-2, CS-1, and MD-1. Well DF-1 did not penetrate the Kalazha Formation. As per log data, the Kalazha Formation consists of gray and brown conglomerates, sandy conglomerates, and medium-to-fine-grained sandstones sandwiched with thin siltstones and pelitic siltstones (**Figure 2**).

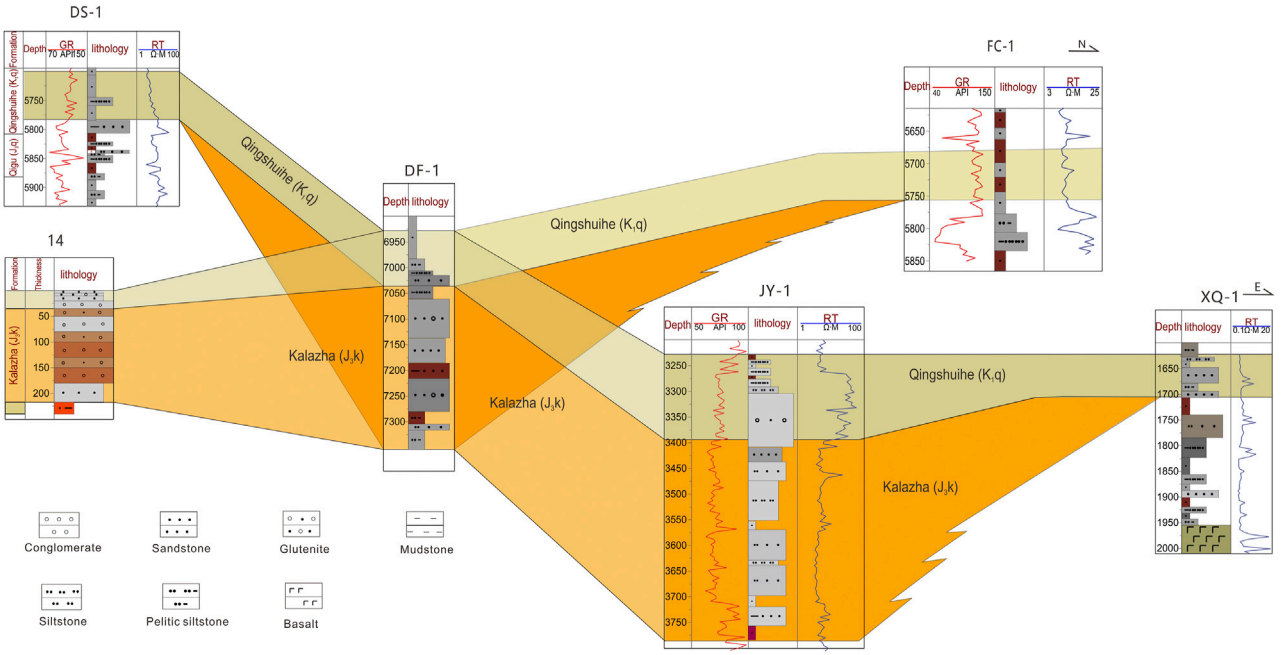

FIGURE 2 | Fence diagram showing cross-well stratigraphic correlation of the Kalazha Formation in the SMJB (location in **Figure 1**).

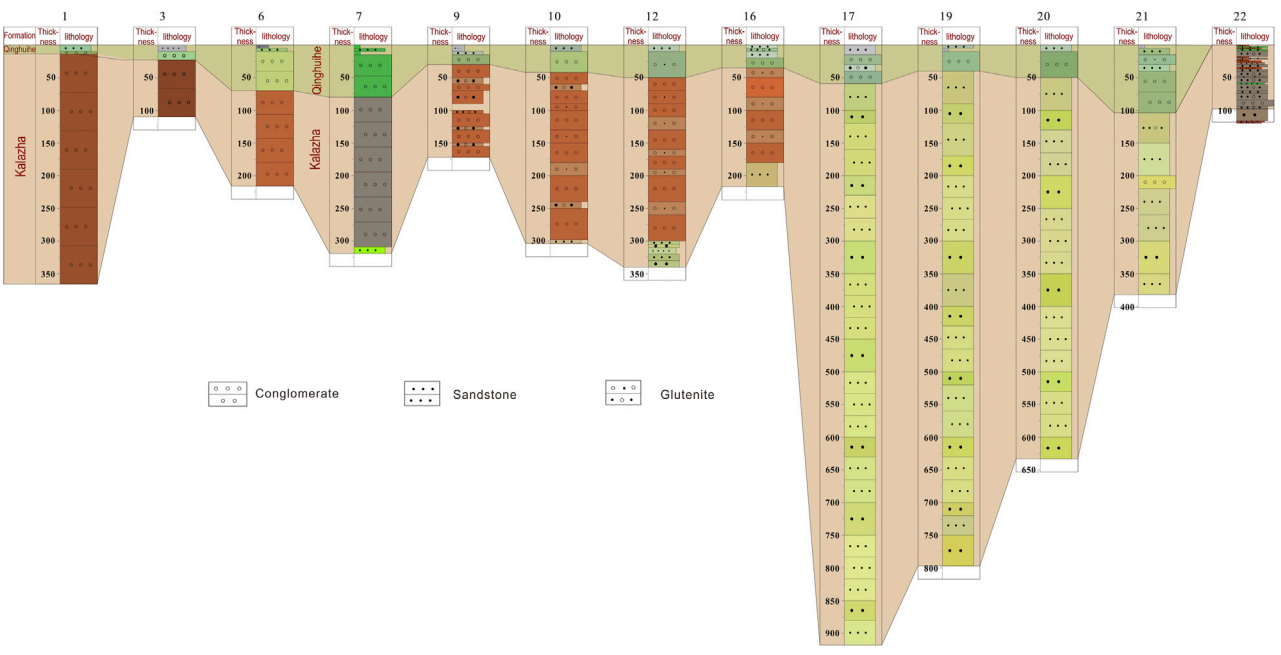

FIGURE 3 | Outcrop stratigraphic correlation of the Kalazha Formation in the SMJB (location in **Figure 1**).

The Kalazha Formation at Well JY-1 is 390 m thick and mainly composed of medium-to-fine-grained sandstones and some conglomerates. As per the east-west and north-south cross-well stratigraphic correlation sections (**Figure 2**), the Kalazha Formation pinches out to the east of Well JY-1 and the west of Well XQ1 in the east, between Wells DF-1 and DS-1 in the west, and the south of Well FC-1 in the north. According to outcrop observation, the Kalazha Formation lithologically consists of conglomerates and sandy conglomerates in the southern piedmont area and finestones and siltstones toward the north.

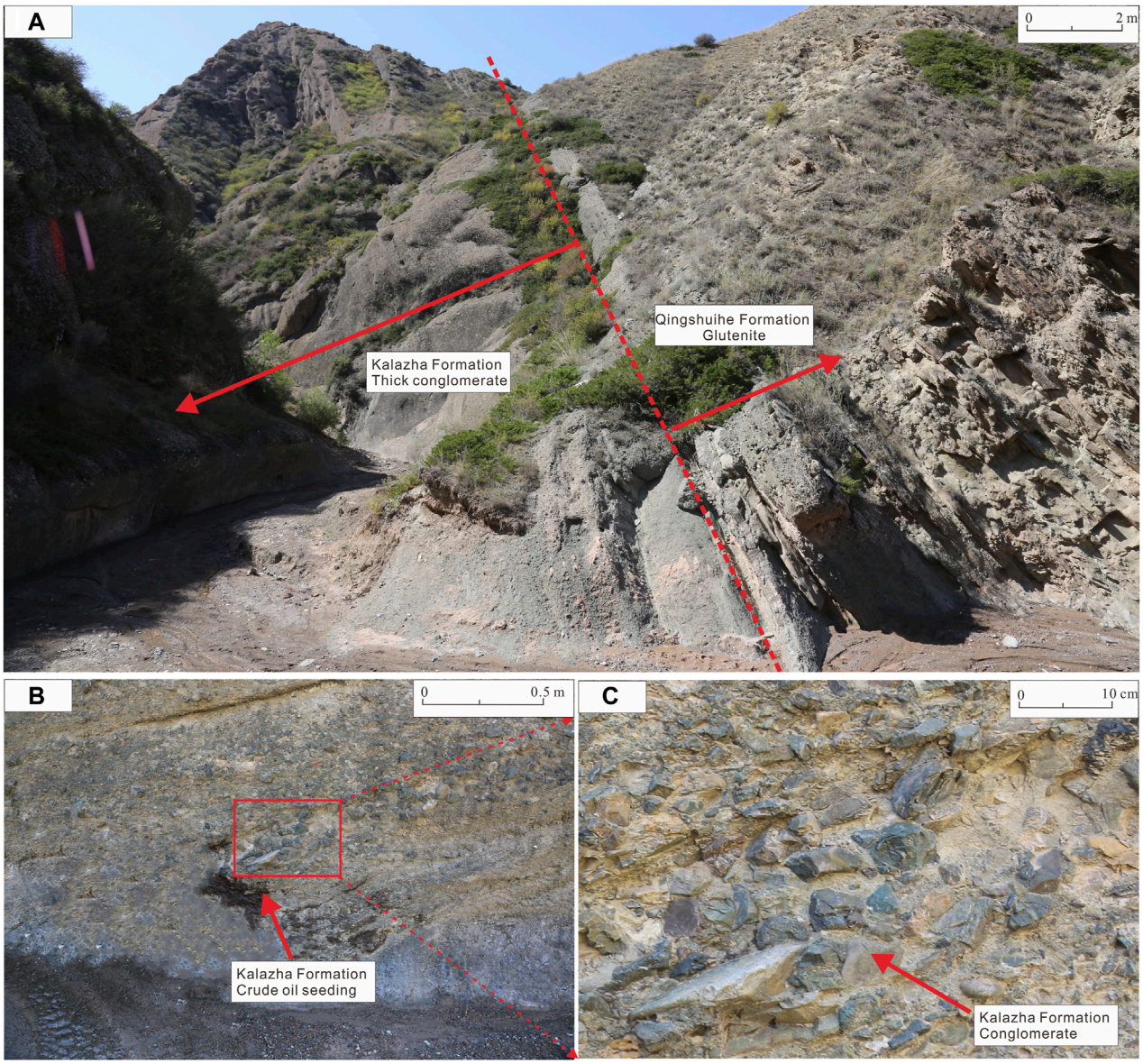

FIGURE 4 | (A) The Kalazha Formation in the Honggou section, SMJB (location in **Figure 1**), **(B)** crude oil seedlings in the Kalazha Formation, **(C)** boulders of conglomerate stone in the Kalazha Formation.

To further investigate the stratigraphic distribution and reservoir properties in the Kalazha Formation, we made a stratigraphic column based on the observation, measurement, and sampling of 22 outcrop sections in the area of interest (**Figure 1**) and performed stratigraphic correlation (**Figure 3**). The Kalazha Formation in the outcrop area is lithologically composed of thick, blocky brown, gray, and grayish green conglomerates; sandy conglomerates; and medium-to-coarse-grained sandstones (**Figure 4A**) 80–860 m thick. The largest thickness occurs in the Toutunhe section across the Kalazha anticline, where the Kalazha Formation is 860 m thick. Formation thickness decreases from east to west.

As per outcrop correlation, the Kalazha Formation consists of brown and gray conglomerates from the Ziniquanzi section in the west-east direction (no. 1 outcrop section) to the section across the south flank of the Aketun syncline between the Changji river and Toutunhe river (no. 16 outcrop section). Angular pebbles of various diameters occur chaotically with a low degree of roundness and high shale content (**Figures 4B,C**), which indicate near-source alluvial fan deposition (Shan et al., 2014; Guan et al., 2020). On the east of the section across the north flank of the Kalazha anticline in Toutunhe (no. 17 section), the Kalazha Formation consists of grayish green coarse sandstones and medium-to-fine-

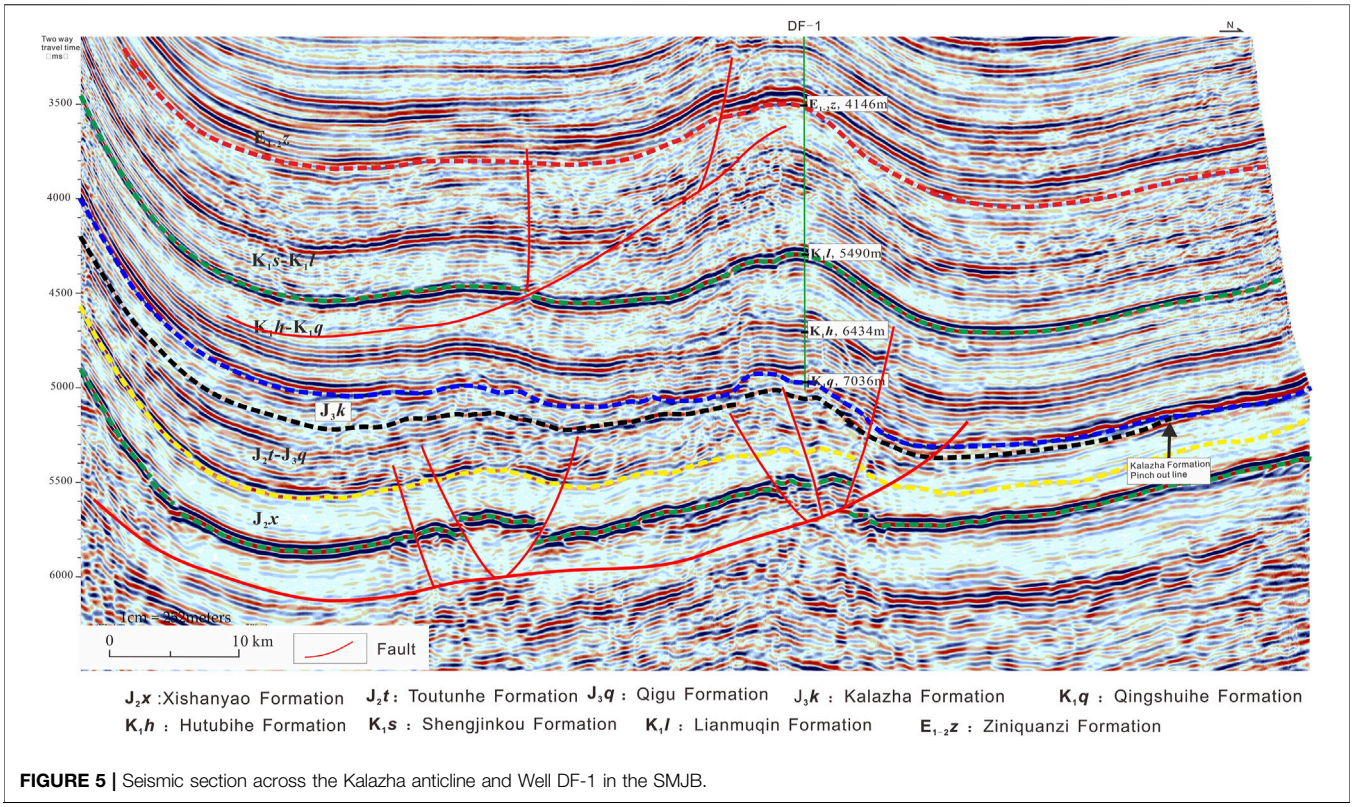

FIGURE 5 | Seismic section across the Kalazha anticline and Well DF-1 in the SMJB.

grained sandstones with increased thickness (**Figure 3**), inferred to be braided river delta deposition (Si et al., 2018; Gao et al., 2020). In general, the Kalazha Formation in the area of interest is lithologically varied in the lateral direction. Conglomerates mainly occur in the southwestern piedmont area, especially west of Changji. Additionally, particle size decreases toward the north. Sandstones of braided river delta deposition turn up in the southeast, e.g., in Urumchi and Fukang, close to the Bogeda Mountain; this lithologically differs greatly from the sandy conglomerates of alluvial fan deposition in the southwest.

Using 2D and 3D seismic data and well-tie calibration, we located the Kalazha Formation in seismic sections and performed horizon interpretation based on seismic facies and cross-well stratigraphic correlation. The Kalazha Formation features weak reflections inside the region and chaotic reflections in the piedmont area (**Figure 5**), related to thick less-layered blocky sandy conglomerates. The lateral continuity of seismic reflections increases from the piedmont area to the north. As shown in several framework sections, the Kalazha Formation mainly extends in Manas, the Qigu faulted fold belt, Hutubi, and Fukang with topographically high areas in the north and low areas in the south. The Kalazha Formation wedges out in the updip direction from the piedmont area to the north (**Figure 5**) and was denuded at the east and west sides.

The Kalazha Formation is thick, laterally stable, and continuous. With respect to tectonic features, the structurally high piedmont thrust belt in the south changes into the structurally low piedmont depressed zone, with a large, buried depth and slope zone and small, buried depth in the north. The formations incline in a monoclinal geometry toward the south with a small, buried depth in the south.

RESERVOIR PROPERTIES AND PREDICTION

We measured reservoir porosity and permeability using Kalazha core and outcrop samples acquired from the area of interest, including eight sandstone samples from Well CS-1 and more than 20 sandy conglomerate and sandstone samples from outcrops. As per cast thin sections from the Toutunhe section (no. 17 outcrop section) and Well CS-1, Kalazha sandstones have suitable reservoir properties with abundant highly interconnected pores, mainly intergranular pores and adequate particle sorting and roundness (**Figures 6A,B**). Kalazha conglomerates are of relatively poor reservoir properties. Cast thin sections of conglomerates from the Qingshuihe section (no. four outcrop section) showed a limited number of intergranular pores (**Figure 6C**) with poor connectivity and poor pebble sorting and roundness. Siltstones and finestones with small particle sizes turn up toward the lake basin in the north (**Figures 6D,E**). These deeply buried sandstones are tight in spite of the high sorting degree. For siltstone and finestone core samples acquired from Well HS1, the average porosity was tested to be 5.6%, and the average permeability was tested to be 0.028×10^{-3} μm^2. Kalazha sandstones are generally superior to

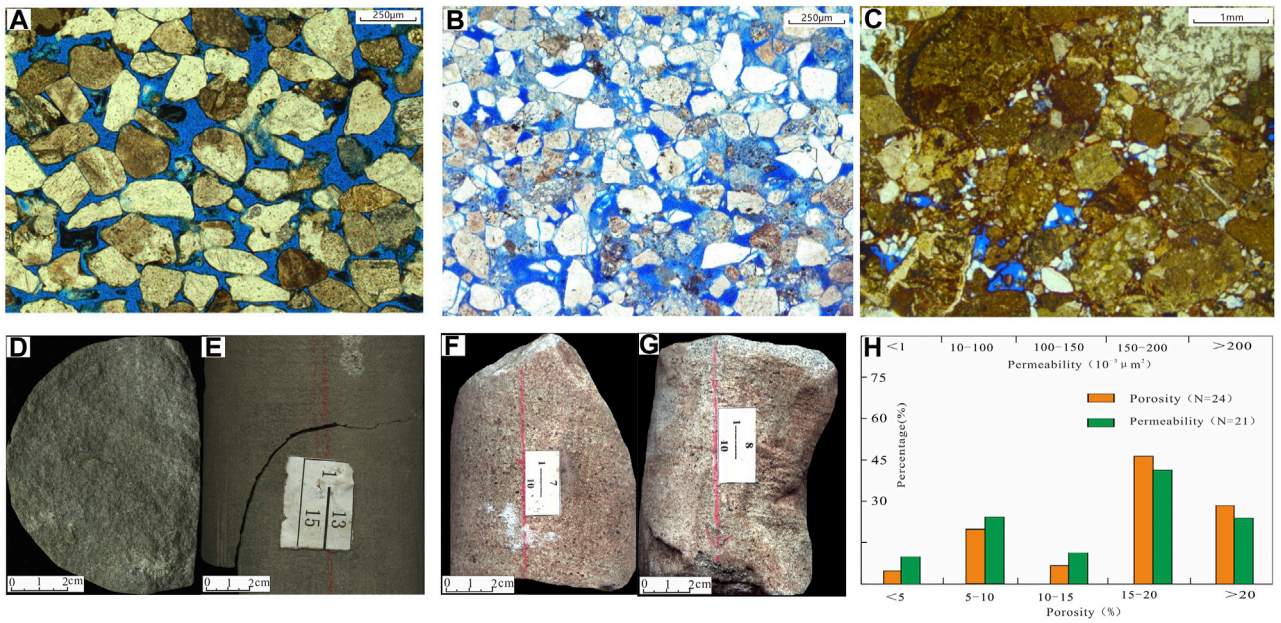

FIGURE 6 | Photos of cast thin sections **(A–C)** and cores **(D–G)** and histograms of petrophysical properties **(E)**, and histogram of porosity and permeability **(H)**, the Kalazha Formation, and the SMJB.

TABLE 1 | Impedance variation with lithology and buried depth in the SMJB.

Depth (m)	Impedance (g/cm^3 × m/s)		
	Sandstone	Mudstone	Sandy conglomerate
<2,000	6,500–9,000	9,000–11,000	>11,000
2,000–4,500	7,500–10,000	10,000–12,000	>12,000
>4,500	9,000–12,000	12,000–13,000	>13,000

conglomerates in reservoir properties. Kalazha reservoir rocks in the Toutunhe section and Well CS-1 are mainly thick, medium-to-coarse-grained sandstones with massive bedding (**Figures 6F,G**). The porosity ranges from 5.7% to 25.7% with an average of 17.69%. The samples with the porosity above 15% account for 72% of the total samples. The permeability ranges from 0.8 to 260 × 10^{-3} μm^2 with an average of 175 × 10^{-3} μm^2. The samples with a permeability above 150 × 10^{-3} μm^2 account for 67% of the total samples (**Figure 6H**).

As per the correlation between lithology and impedance for the Kalazha Formation and Middle and Upper Jurassic Series at Wells JY-1, JY-2, CS-1, and XH-1, impedance generally increases with buried depth (Li et al., 2002). Within a specific depth range, the impedance varies with the lithologic association. Sandy conglomerates exhibit the largest impedance, followed by mudstones; sandstones exhibit the smallest impedance. Given the change in buried depth and impedance, the Kalazha Formation was divided into three intervals (above 2,000 m, between 2,000 and 4,500 m, and below 4,500 m) for the study of lithology–impedance relation.

At the interval shallower than 2,000 m, the data of Well CS-1 show sandstone impedance of 6,500–9,000 g/cm^3 × m/s, mudstone impedance of 9,000–11,000 g/cm^3 × m/s, and sandy conglomerate impedance over 11,000 g/cm^3 × m/s (**Table 1**). At the interval of 2,000–4,500 m, the data of Wells JY-1 and JY-2 show sandstone impedance of 7,500–10,000 g/cm^3 × m/s, mudstone impedance of 10,000–12,000 g/cm^3 × m/s, and sandy conglomerate impedance over 12,000 g/cm^3 × m/s. At the interval deeper than 4,500 m, the Kalazha Formation was drilled by only one well, i.e., DF-1. No deep-zone well logging was performed due to engineering issues, and thus, log data are unavailable. We used the data of Well XH1 drilled in a neighboring area, showing sandstone impedance of 9,000–12,000 g/cm^3 × m/s, mudstone impedance of 12,000–13,000 g/cm^3 × m/s, and sandy conglomerate impedance over 13,000 g/cm^3 × m/s.

1) Toutunhe section, Kalazha formation, medium sandstone; 2) Changshan 1,764.16 m, Kalazha formation, medium fine sandstone; 3) Qingshuihe section, Kalazha formation, glutenite (Si et al., 2020; internal communication); 4) Hutan 17,365.3 m, Kalazha formation, silty fine sandstone; 5) Hutan 17,366.45–7,366.5 m, Kalazha formation, siltstone; 6) Changshan 1,764.5–764.6 m, Kalazha formation, fine sandstone; 7) Changshan 1,764.6–764.7 m, Kalazha formation, fine sandstone; and 8) physical property histogram of sandstone reservoir of Kalazha formation.

According to the impedance variations with lithology and buried depth in the Kalazha Formation, we used 2D and 3D seismic data for impedance inversion and reservoir prediction. As per joint 2D and 3D inversion results, blocky Kalazha reservoirs are generally over 100 m thick and extend consistently in the lateral direction with suitable inter-connectivity. Formation thickness decreases from south to north and finally vanishes.

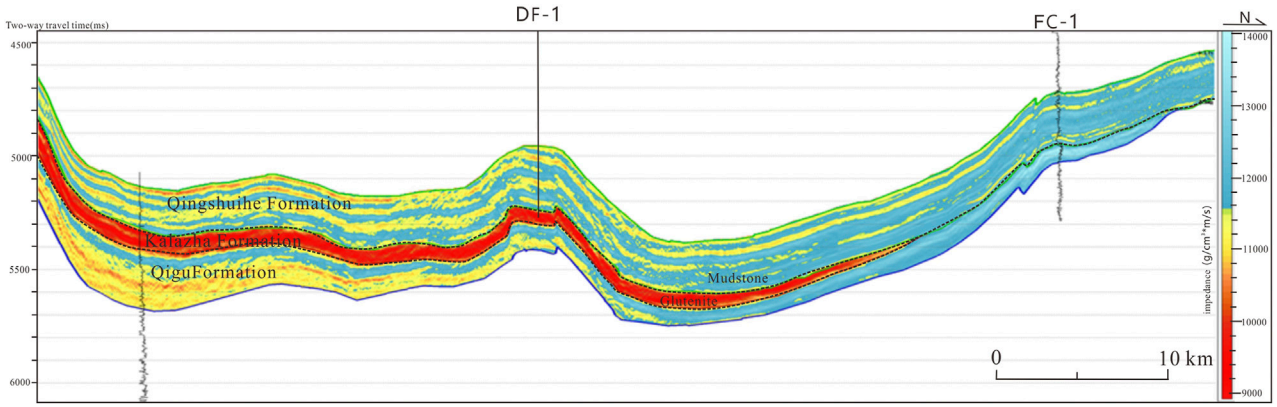

FIGURE 7 | Inverted impedance section across Wells DF-1 and FC-1 in the SMJB.

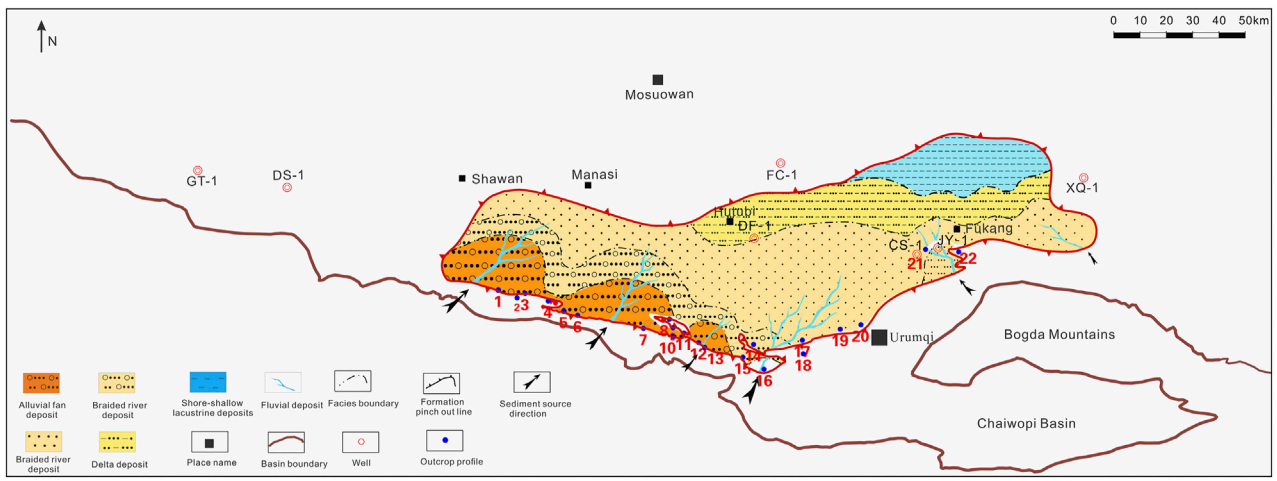

FIGURE 8 | Stratigraphic distribution of the Jurassic Kalazha Formation in the SMJB.

Reservoir rocks are overlain and underlain with mudstones (**Figure 7**). Sandstone reservoirs mainly occur in the northeast, e.g., Fukang on the north of the Bogeda Mountain. Sandy conglomerate reservoirs mainly occur in the southwest piedmont area, e.g., the Qigu faulted fold belt and Manas (**Figure 8**).

The study of Kalazha sedimentation was based on seismic inversion and reservoir prediction and well drilling and outcrop data. As per the sedimentation in the outcrop sections, the Kalazha Formation has different lithologic associations. On the west of the section across the south flank of the Aketun syncline between the Changji river and Toutunhe river (no. 16 outcrop section), the Kalazha Formation is composed of thick blocky brown or grayish brown conglomerates and sandy conglomerates of typical alluvial fan deposition with chaotically arranged pebbles, a low sorting degree, and high shale content, as mentioned above. A lake basin system occurs in the north with enhanced water power and fine-grained sandstones and siltstones deposited (**Figures 6D,E**). In the outcrop area on the east of the section across the north flank of the Kalazha anticline in Toutunhe (no. 17 section), the Kalazha Formation is mainly composed of sandstones with basal scouring structure. Trough cross-bedding and massive bedding shown in the cores from Well CS-1 (**Figures 6F,G**) indicate underwater distributary channel deposition in the braided river deltaic front (Si et al., 2018). Sand particle size decreases toward the northwest. It is hard to delineate the alluvial fan system or the braided river deltaic system in the lake basin for lack of deep-well data. Thus, we inferred the intrafacies and their boundary (**Figure 8**), according to the depositional model and lithology-varied impedance. Detailed sedimentary microfacies will be classified using more well data.

As shown on the sedimentary system map, the Kalazha Formation in the southwest piedmont area is mainly composed of conglomerates (**Figure 8**) with large impedance,

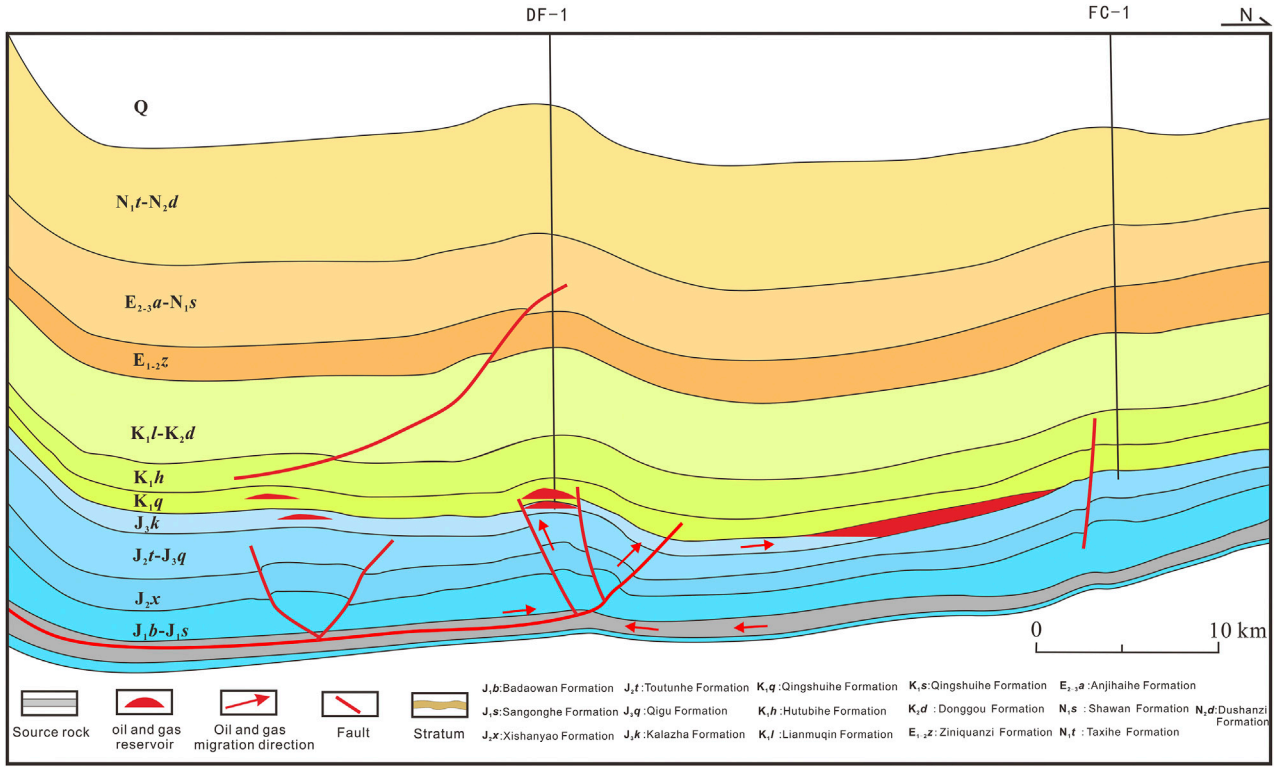

FIGURE 9 | A model showing hydrocarbon accumulation in Jurassic Kalazha lithologic reservoirs, the SMJB.

which change into medium-to-fine-grained sandstones and siltstones with small impedance in the north and vanish at last. Conglomerates seldom occur in the southeast. The formation is mainly composed of thick, layered sandstones of nearly 400 m thick with suitable reservoir properties, small impedance, and consistent lateral extension. High-graded reservoirs exhibit medium to low impedance. Shore-lake to shallow lacustrine argillaceous sediments were predicted to occur in the northeast.

ACCUMULATION MODEL AND PROMISING PROSPECTS

The Jurassic Kalazha Formation in the SMJB is among the most important exploration targets in the lower assemblage due to its promising hydrocarbon accumulation conditions. Kalazha reservoirs are underlain with several packages of deeply buried multi-type Middle and Lower Jurassic source rocks. The Lower Jurassic Badaowan Formation was deposited with dark mudstones 200–300 m thick, carbonaceous mudstones, and coals. Dark mudstones in the San'gonghe Formation are 50–300 m thick. Dark mudstones and carbonaceous mudstones in the Middle Jurassic Xishanyao Formation are 75–150 and 2–15 m thick, respectively. Crude oil originating from the Jurassic System in the Qigu and Kayindike oilfields (Wang et al., 2013; Chen et al., 2015) demonstrated wide extension and credibility of Jurassic source rocks in the SMJB. Mature to post-mature source rocks may generate sufficient oil and gas for overlying reservoirs. Thus, the Kalazha Formation is rich in oil and gas resources.

Kalazha sandstone and sandy conglomerate reservoirs feature large thickness and suitable properties, favorable for hydrocarbon accumulation. The overlying regional capping bed in the Cretaceous Tugulu Group extends consistently in the lateral direction, where high to extremely high formation pressure enhances the sealing performance of mudstone overburden for the preservation of Kalazha oil and gas reservoirs. As shown in the Honggou outcrop section (**Figure 8**), oil seepage with large viscosity could be observed frequently in the Kalazha Formation (**Figure 4**), which evidences the promising accumulation conditions in the Kalazha Formation in the area of interest.

We established an accumulation model for Jurassic Kalazha lithologic reservoirs in the SMJB, according to the source rocks, reservoir rocks, caprocks, and migration system (**Figure 9**). Source conditions are promising in view of mature to highly mature coal-measure source rocks in the Middle and Lower Jurassic System. Downward detachment faults and associated secondary faults inside Lower Jurassic coal measures strata and unconformable surfaces constitute an effective migration system. Due to a high degree of plasticity in coal measures strata, detachment and deformation tend to occur in the process of compressional

overthrusting to form fractures. Detachment faults and associated faults constitute a vertical migration system in the Kalazha Formation (**Figures 5**, **9**). The Jurrasic Kalazha Formation lies unconformably below the Cretaceous Qingshuihe Formation. Thick sandy conglomerates at the bottom of the Qingshuihe Formation extend consistently in the lateral direction and could function as the lateral carrier bed (Kuang and Jia, 2005; Li et al., 2006).

Sediments from the south sedimentary source in the Kalazha Formation were unloaded and accumulated in the fore-deep sags in the thrust belt to form thick sands, which wedge out in the updip direction toward the north. Thus, the slope zone in the thrust belt is geologically favorable for lithologic traps.

In conclusion, the Kalazha Formation has favorable hydrocarbon accumulation conditions. Mass oil and gas generated by Middle and Lower Jurassic source rocks may migrate into reservoir rocks along microcracks in the source rocks and into shallow zones and structural highs along the system composed of detachment faults. Oil and gas may migrate laterally along continuous inter-connected sands in the Kalazha Formation. Owing to the effect of buoyancy force, oil and gas will flow toward the shallow zones in the north along laterally connected sands in the Kalazha Formation and accumulate in those lithologic traps with top mudstone overburden to form lithologic hydrocarbon reservoirs.

According to the accumulation model and stratigraphic and structural features of the Kalazha Formation, the promising prospects were anticipated to be lithologic traps in the annular zone, wedging out in the updip direction of the north slope, which has been the destination of hydrocarbon migration in a long period and is covered with thick mudstones in the updip direction. Lithologic reservoirs may concentrate in this zone. The area with the Kalazha Formation is also important for gas exploration in view of highly to post-mature Jurassic source rocks for gas generation in deep zones. We should make full use of 2D and 3D seismic data to perform lithologic trap identification and prediction and offer support to gas exploration.

CONCLUSION

The following conclusions can be drawn:

1) The stratigraphic distribution and features of the Jurassic Kalazha Formation were revealed in the SMJB based on individual-well analysis, cross-well stratigraphic correlation, well-tie calibration, and seismic reflections. Due to intense denudation, the Kalazha Formation is limited within Manas, Hutubi, Fukang, and Qigu faulted fold belt in the SMJB. It pinches out from the piedmont area to the north in the updip direction and was denuded in the east and west. The formation exhibits a monoclinal geometry with structurally high areas in the north and structurally low areas in the south.
2) The relations were established between impedance and different lithologies, i.e., sandstone, mudstone, and sandy conglomerate, at different depths in the Kalazha Formation based on individual-well lithology–impedance correlation. Reservoir distribution in the Kalazha Formation was predicted using joint 2D and 3D seismic impedance inversion, showing major Kalazha reservoir rocks, i.e., sandy conglomerates and sandstones, 100–400 m thick. According to seismic inversion and outcrop sections, the Kalazha Formation in the southwest was diagnosed as a fan deltaic deposition with sandy conglomerate reservoirs close to the piedmont source area and fine-grained reservoir rocks in the north. The Kalazha Formation in the southeast was diagnosed as a braided river deltaic deposition with sandstone reservoirs of suitable petrophysical properties.
3) According to the study of source rocks, reservoir rocks, caprocks, and migration system, the Kalazha Formation in the SMJB was geologically favorable for large-scale hydrocarbon accumulation in lithologic reservoirs, establishing an accumulation model for lithologic reservoirs. Based on the accumulation model, the promising prospects were predicted to be lithologic traps in the annular wedge-out zone in the north foreland slope. Efforts should focus on lithologic trap identification and prediction in this region.

DATA AVAILABILITY STATEMENT

The raw data supporting the conclusion of this article will be made available by the authors, without undue reservation.

AUTHOR CONTRIBUTIONS

GL (first author and corresponding author) made significant contributions in the writing—original draft and manuscript revision, research ideas, sample collection, experimental analysis, and data analysis. J-ZL put forward and improve the research process and ideas. X-FQ made significant contributions in the reservoir-forming process simulation. MZ helped with sample collection. BY made significant contributions in the reservoir sample collection and data analysis. Z-CP made significant contributions in drawing the figures and data analysis. All authors contributed to the article and approved the submitted version.

FUNDING

This study was supported by the advanced research fund project of CNPC (No. 2019D-500801) and the Major Science and Technology project of CNPC (No. kt2020-0404).

ACKNOWLEDGMENTS

We are particularly grateful to the editorial department and the reviewers for their patience and hard work.

REFERENCES

Chen, J. P., Wang, X. L., Deng, C. P., Zhao, Z., Ni, Y. Y., Sun, Y. G., et al. (2015). Geochemical Features of Source Rocks in the Southern Margin, Junggar Basin, Northwest China. *Acta Petrol. Sin.* 36 (7), 767–780. doi:10.7623/syxb201507001

Chen, J., Deng, C., Wang, X., Ni, Y., Sun, Y., Zhao, Z., et al. (2017). Formation Mechanism of Condensates, Waxy and Heavy Oils in the Southern Margin of Junggar Basin, NW China. *Sci. China Earth Sci.* 60, 972–991. doi:10.1007/s11430-016-9027-3

Chen, J. P., Wang, X. L., Ni, Y. Y., Xiang, B. L., Liao, F. R., Liao, J. D., et al. (2019). Genetic Type and Source of Natural Gas in the Southern Margin of Junggar Basin, NW China. *Pet. Explor. Develop.* 46, 461–472. doi:10.1016/S1876-3804(19)60029-7

Darby, D., Stuart Haszeldine, R., and Couples, G. D. (1996). Pressure Cells and Pressure Seals in the UK Central Graben. *Mar. Pet. Geol.* 13 (8), 865–878. doi:10.1016/s0264-8172(96)00023-2

Du, J. H., Zhi, D. M., Li, J. Z., Yang, D. S., Tang, Y., Qi, X. F., et al. (2019). Major Breakthrough of Well Gaotan 1 and Exploration Prospects of Lower Assemblage in Southern Margin of Junggar Basin, NW China. *Pet. Explor. Develop.* 46 (02), 15–25. doi:10.1016/s1876-3804(19)60003-0

Fu, X., Du, X. F., Guan, D. Y., Wang, Q. M., and Ye, M. S. (2020). Depositional System, Plane Distribution and Exploration Significance of Fan-Delta Mixed Siliciclastic-Carbonate Sediments in Lacustrine Basin: An Example of Member1-2 of Shahejie Formation in Offshore Bohai Bay, Eastern China. *Earth Sci.* 45 (10), 3706–3720. doi:10.3799/dqkx.2020.173

Gao, Z. Y., Feng, J. R., Cui, J. G., Zhou, C. M., and Shi, Y. X. (2020). Comparative Analysis on Sedimentary and Reservoir Characteristics of Jurassic to Cretaceous between Foreland Basins in Southern and Northern Tianshan Mountains. *Xin Jiang Pet. Geol.* 41 (1), 80–90. doi:10.7657/XJPG20200110

Guan, X. T., Wu, C. D., Wu, J., Zhou, J. Q., Jiao, Y., Zhou, R., et al. (2020). Sedimentary Sequence and Sedimentary Environment Evolution of Upper Jurassic and Lower Cretaceous in the Southern Margin of Junggar Basin. *Xinjiang Pet. Geol.* 041 (001), 67–79. doi:10.7657/XJPG20200109

He, D. F., Zhang, L., Wu, S. T., Li, D., and Zhen, Y. (2018). Tectonic Evolution Stages and Features of the Junggar Basin. *Oil Gas Geol.* 39 (05), 5–21. doi:10.11743/ogg20180501

Jia, C. Z., Zhao, W. Z., Zou, C. N., Feng, Z. Q., Yuan, X. J., Chi, Y. L., et al. (2007). Geological Theory and Exploration Technology for Lithostratigraphic Hydrocarbon Reservoirs. *Pet. Explor. Develop.* 34 (3), 257–272. Available at http://www.cpedm.com/CN/article/openArticlePDF.jsp?id=1474.

Jia, C. Z., Zhao, W. Z., and Zou, C. N. (2008). *LithologicStratigraphic Reservoir Geology Theory and Exploration Technique*. Beijing: Petroleum Industry Press, 162–180.

Kuang, J., and Jia, X. Y. (2005). Relationship between Himalayan Movement and Hydrocarbon Accumulation in Southern Margin of Junggar Basin. *Xinjiang Pet. Geol.* 26 (02), 17–21. doi:10.3969/j.issn.1001-3873.2005.02.003

Kuang, J., and Qi, X. F. (2006). The Structur Al Character Istics and Oil-Gas Explorative Direction in Junggar Foreland Basin. *Xinjiang Pet. Geol.* 27 (1), 5–9. doi:10.3969/j.issn.1001-3873.2006.01.002

Kuang, L. C., Wang, X. L., Zhang, J., and Xia, H. P. (2012). Structural Modeling of the Huoerguoshi-Manashi-Tugulu Thrust belt at the Southern Margin of the Junggar Basin and the Discovery of the Mahe Gas Field. *Nat. Gas Industry* 32 (2), 11–15. doi:10.3787/j.issn.1000-0976.2012.02.003

Lei, D. W., Chen, N. G., Li, X. Y., and Zhang, Y. C. (2012). The Major Reservoirs and Distribution of Lower Combination in Southern Margin of Jungar Basin. *Xinjiang Pet. Geol.* 33 (6), 648–650. Available at http://www.zgxjpg.com/CN/abstract/abstract1132.shtml.

Li, L. C., Wu, J., Zhang, S., Zhuang, X. J., Zou, Y. P., and Wang, W. Z. (2002). Application of Seismic Wave Resistance Inversion in Sequence Stratigraphy Research-An Example of Junggar Basin. *Xinjiang Pet. Geol.* 23 (03), 70–81. doi:10.3969/j.issn.1001-3873.2002.03.020

Li, X. Y., Shao, Y., and Li, T. M. (2003). Three Oil-Reservoir Combinations in South Marginal of Jungar Basin, Northwest China. *Pet. Explor. Develop.* 30 (6), 32–34. doi:10.3321/j.issn:1000-0747.2003.06.009

Li, X. Y., Wang, B., and Chen, Y. (2006). The Fracture Patterns and Oil-Controlled Process in Piedm on the Bruchfalten Zone Southern Margin of Junggar Basin. *Xinjiang Pet. Geol.* 27 (3), 285–287. doi:10.3969/j.issn.1001-3873.2006.03.006

Liang, W., and Li, X. P. (2020). Lithological Exploration and Potential in Mixed Siliciclastic-Carbonate Depositional Area of Eastern Pearl River Mouth Basin. *Earth Sci.* 45 (10), 3870–3884. doi:10.3799/dqkx.2020.174

Liu, G., Wei, Y. Z., Luo, H. C., Chen, G., Gong, D. Y., Wang, F., et al. (2018). Sand-body Structure and Reservoir Forming Control of Jurassic Sangonghe Formation in Well Block Shinan 13, Luxi Area, Junggar Basin. *Acta Petrol. Sin.* 39 (9), 1006–1018. doi:10.7623/syxb201809005

Liu, G., Wei, Y. Z., Chen, G., Jia, K. F., Gong, D. Y., Wang, F., et al. (2019). Forming Mechanism, Distribution Characteristics of Jurassic-Cretaceous Secondary Reservoirs in the central Junggar Basin. *Acta Petrol. Sin.* 40 (8), 914–927. doi:10.7623/syxb201908003

Magara, K. (1993). Pressure Sealing: An Important Agent for Hydrocarbon Entrapment. *J. Pet. Sci. Eng.* 9 (1), 67–80. doi:10.1016/0920-4105(93)90029-E

Nansheng, Q., Zhihuan, Z., and Ershe, X. (2008). Geothermal Regime and Jurassic Source Rock Maturity of the Junggar basin, Northwest China. *J. Asian Earth Sci.* 31, 464–478. doi:10.1016/j.jseaes.2007.08.001

Schneider, W., Zhao, X. F., Long, N. L., Zhao, Y. S., and Long, N. L. (1992). Sedimentary Environment and Tectonic Implication of Jurassic in Toutunhe Area, Junggar Basin. *Xinjiang Geol.* 10 (3), 191–201.

Shan, X., Yu, X. H., Li, S. L., Li, S. L., Li, W., and Wang, Z. X. (2014). The Depositional Characteristics and Model of Kalazha Formation in Shuimogou profile,Junggar basin. *J. China Univ. Mining Techn.* 43 (2), 262–270. doi:10.13247/j.cnki.jcumt.2014.02.005

Si, X. Q., Yuan, B., Guo, H. J., Xu, Y., and Chen, N. G. (2020). Bloomberg Reservoir Characteristics and Main Controlling Factors of Qingshuihe Formation in the Southern Margin of Junggar Basin. *Oil and Gas Geology* 41 (01), 38–45. doi:10.7657/XJPG20200106

Si, X. Q., Shen, J. L., Chen, N. G., Xu, Y., Guo, H. J., and Yuan, B. (2018). "Sedimentary Characteristics and Model of Jurassic Kalazha Formation in Southern Margin of Junggar Basin," in Abstracts of the 15th National Conference on Palaeogeography and Sedimentology, Chengdu, China, 2018 (Petroleum geology Committee of Chinese Petroleum Society)

Tao, S. Z., Yuan, X. J., Hou, L. H., Zhang, G. S., Yang, F., Tao, X. W., et al. (2017). The Regularities of Formation and Distribution of Giant Litho-Stratigraphic Oil and Gas Field. *Nat. Gas Geosci.* 28 (11), 1613–1624. doi:10.11764/j.issn.1672-1926.2017.10.002

Tian, X. R., Zhuo, Q. G., Zhang, J., Hu, H. W., and Guo, Z. J. (2017). Sealing Capacity of the Tugulu Group and its Significance for Hydrocarbon Accumulation in the Lower Play in the Southern Junggar Basin, Northwest China. *Oil Gas Geol.* 38 (2), 334–344. doi:10.11743/ogg20170213

Tigert, V., and Al-Shaieb, Z. (1990). Pressure Seals:their Diagenetic Banding Patterns. *Earth Sci. Rev.* 29 (1), 227–240. doi:10.1016/0012-8252(90)90039-x

Wan, L. G., Liu, D. M., and Hou, L. G. (2005). Structural Characteristics of Foreland Thrust belt in the Southern Junggar Basin. *Pet. Geophys. Explor.* 40 (b11), 40–45. doi:10.3321/j.issn:1000-7210.2005.z1.008

Wang, X. L., Zhi, D. M., and Wang, Y. T. (2013). *Source Rocks and Hydrocarbon Geochemistry in Junggar Basin*. Beijing: Petroleum Industry Press, 1–565.

Wei, D. T., Jia, D., Zhao, Y. C., Yang, H. B., Chen, T., Wu, L. Y., et al. (2007). Geochemical Characteristics of Crude Oil in the Southern Margin of Junggar Basin. *Oil and Gas Geology* 2007 (03), 433–440. 0253-9985(2007)03-0433-08

Wei, D. T., Zhao, Y. C., Abuli, M. T., Chen, T., Yang, H. B., Wu, L. Y., et al. (2010). Difference of Hydrocarbon Accumulation in the Foreland Thrust-fold Belt of the Southern Junggar Basin. *Geol. J. China Univ.* 16 (3), 339–350. doi:10.3969/j.issn.1006-7493.2010.03.007

Wu, J. H., Xiang, S. Z., Wu, X. Z., Chen, W., and Wu, J. (2002). Structures in East Part of Southern Margin in Junggar Basin and Their Formation Mechanism. *Xinjiang Pet. Geol.* 23 (3), 208–210. doi:10.3969/j.issn.1001-3873.2002.03.009

Wu, K. Y., Zha, M., Wang, X. L., Qu, J. X., and Chen, X. (2005). Further Researches on the Tectonic Evolution and Dynamic Setting of the Junggar Basin. *Acta Geosci. Sin.* 26 (3), 217–222. doi:10.3975/cagsb.2005.03.04

Xiao, L. X., Chen, N. G., Zhang, J., Shen, J. L., and Zhang, S. C. (2011). Sedimentary Systems of Paleogene Ziniquanzi Formation, South Edge of Junggar Basin. *Nat. Gas Geosci.* 22 (03), 58–63. doi:10.3969/j.issn.1674-151x.2015.19.020

Yuan, X. J., Xue, L. Q., Chi, Y. L., Chen, Z. M., and Qu, Y. H. (2003). Sequence Stratigraphic and Subtle-Trap Characteristics of Lacustrine Depression

basin. *Acta Pet. Sin.* 24 (3), 11–15. doi:10.3321/j.issn:0253-2697.2003.03.003

Zhang, Y. J., and Liu, G. D. (2002). Characteristics and Evolution of Composite Petroleum Systems and the Exploration Strategy in Junggar basin, Northwest China. *Pet. Explor. Develop.* 29 (1), 36–39. doi:10.3321/j.issn:1000-0747.2002.01.009

Zhen, M., Li, J. Z., Wu, X. Z., Wang, S. J., Guo, Q. L., Chen, X. M., et al. (2019). Potential of Oil and Natural Gas Resources of Main Hydrocarbon-Bearing Basins and Key Exploration Fields in China. *Earth Sci.* 44 (03), 833–847. doi:10.3799/dqkx.2019.957

Conflict of Interest: Authors GL, J-ZL, X-FQ are employed by China National Petroleum Corporation, and in the PetroChina Research Institute of Petroleum Exploration and; Development. Authors MZ, BY, and Z-CP are employed by China National Petroleum Corporation, and in the Research Institute of Petroleum Exploration and; Development, Xinjiang Oilfield.

The authors declare that the research was conducted in the absence of any commercial or financial relationships that could be construed as a potential conflict of interest.

Publisher's Note: All claims expressed in this article are solely those of the authors and do not necessarily represent those of their affiliated organizations, or those of the publisher, the editors and the reviewers. Any product that may be evaluated in this article, or claim that may be made by its manufacturer, is not guaranteed or endorsed by the publisher.

frontiers in Earth Science

ORIGINAL RESEARCH
published: 21 March 2022
doi: 10.3389/feart.2022.865322

Geochemical Characteristics of Rare Earth Elements in the Chaluo Hot Springs in Western Sichuan Province, China

Shuaichao Wei[1,2], *Feng Liu*[1,2,3], *Wei Zhang*[1,2]*, *Hanxiong Zhang*[1,2], *Rouxi Yuan*[1,2], *Yuzhong Liao*[1,2] *and Xiaoxue Yan*[1,2]

[1]*The Institute of Hydrogeology and Environmental Geology, Chinese Academy of Geological Sciences, Shijiazhuang, China,* [2]*Technology Innovation Center of Geothermal and Hot Dry Rock Exploration and Development, Ministry of Natural Resources, Shijiazhuang, China,* [3]*China University of Geosciences (Beijing), Beijing, China*

OPEN ACCESS

Edited by:
Dawei Hu,
Institute of Rock and Soil Mechanics (CAS), China

Reviewed by:
Qixin Wu,
Guizhou University, China
Santosh Kumar Rai,
Wadia Institute of Himalayan Geology, India

***Correspondence:**
Wei Zhang
18879003@qq.com

Specialty section:
This article was submitted to Geochemistry, a section of the journal Frontiers in Earth Science

Received: *29 January 2022*
Accepted: *02 March 2022*
Published: *21 March 2022*

Citation:
Wei S, Liu F, Zhang W, Zhang H, Yuan R, Liao Y and Yan X (2022) Geochemical Characteristics of Rare Earth Elements in the Chaluo Hot Springs in Western Sichuan Province, China. Front. Earth Sci. 10:865322. doi: 10.3389/feart.2022.865322

High-temperature hydrothermal activity areas in western Sichuan Province, China are ideal objects for studying deep Earth science, extreme ecological environments, and comprehensive geothermal utilization. To understand the geochemical characteristics of rare Earth elements (REEs) in the Chaluo hot springs in western Sichuan Province, the authors analyzed the composition and fractionation of REEs in the hot springs through hydrochemical analysis, REE tests, and North American Shale Composite-normalized REE patterns. Moreover, the composition and complex species of REEs in the geothermal water in the Chaluo area were determined through calculation and simulation analysis using the Visual MINTEQ 3.0 software. The results are as follows. In terms of hydrochemical type, all geothermal water in the Chaluo area is of the Na-HCO_3 type. The cations in the geothermal water are mainly controlled by water-rock interactions and evaporation, the anions are determined by water-rock interactions, and the hydrochemical processes are primarily controlled by the dissolution of silicate minerals. The total REE content of the geothermal water in the Chaluo hot springs is 0.306 ± 0.103 ug/L. It is low compared to the Kangding area and is primarily affected by the reductive dissolution of Fe oxides/hydroxides, followed by pH. The geothermal water in the Chaluo area is rich in light rare Earth elements (LREEs) because of the presence of Fe oxides. It shows positive Eu and Ce anomalies due to the combined effects of the dissolution of Eh and Mn oxides and surface water. Furthermore, the positive Eu anomalies are also caused by the water-rock interactions between the Qugasi Formation and deep geothermal water. Similar to alkaline water bodies, the complex species of REEs in the geothermal water mainly include $Ln(CO_3)_2^-$, $LnCO_3^+$, and $LnOH^{2+}$, which is caused by the stability constants of complexation reactions.

Keywords: Chaluo hot springs, rare earth elements, North American shale standardized REE distribution patterns, Eu anomaly, complexes of the species

INTRODUCTION

Western Sichuan Province is located at the easternmost end of the Mediterranean-Himalayan geothermal zone and at the boundary of the collision between the Eurasian Plate and the African and Indian plates (Royden et al., 2008; Xu et al., 2011; **Figure 1A**). This region is mainly composed of three strike-slipping faults-the Xianshuihe, Ganzi-Litang, and Jinshajiang faults (Dewey et al., 1988; Xu et al., 2005; Yan and Lin, 2015), the Songpan-Ganzi fold belt, and the Yidun arc (SBGMR, 1991; Xu et al., 1992; Zhang et al., 2013; Tang et al., 2017; **Figure 1B**). It is characterized by strong neotectonic movements, frequent earthquakes, active hot springs, and geothermal anomalies (Tang et al., 2017; Zhang Jian. et al., 2017). Statistics reveal that 248 hot springs are distributed in this region (Luo, 1994). Similar to the Yangbajing geothermal field in Tibet and the Rehai geothermal field in Tengchong City, Yunnan Province (Tong et al., 1981; Tong and Zhang, 1989), the high-temperature geothermal resources in western Sichuan Province have various geothermal manifestations including geysers, boiling springs, and boiling spouters, hydrothermal explosions, and hydrothermal alterations (Fan et al., 2019; **Figure 1B**). The hot springs in western Sichuan Province are mainly controlled by the Jinshajiang, Dege-Xiangcheng, Ganzi-Litang, and Xianshuihe faults in the giant structure in the shape of Chinese character "歹", which reach as deep as the Moho (Zhang Jian. et al., 2017; **Figure 1B**). Medium- and high-temperature hot springs are intensively exposed in the Kangding, Batang, and Litang areas. They exhibit strong hydrothermal activities, bear rich high-temperature thermal energy, and therefore have considerable potential for geothermal resource development (Fu and Yin, 2009). These high-temperature hydrothermal activity areas, which are ideal for understanding deep Earth science, extreme ecological environments, and the comprehensive utilization of geothermal energy, have attracted the attention of domestic and foreign experts and researchers in geothermal, geological, geochemical, and ecological fields.

Previous hydrogeochemical studies on the hot spring system in western Sichuan Province have mainly focused on the material origin and the recharge, runoff, and discharge conditions of hot springs, the characteristics and genetic mechanisms of geothermal reservoirs, and the structure, formation, and evolution of crust-mantle heat flow (Zhang Jian. et al., 2017; Yuan et al., 2017; Zhang Y. et al., 2018; Li et al., 2018; Zhang et al., 2019; Cao et al., 2021). Zhao J. Y. et al. (2019) analyzed the evolution of geothermal water in the Batang area by calculating the thermal storage temperature, cold water mixing ratio, and thermal circulation depth. Cao et al. (2021) studied the recharge sources, recharge elevation, geothermal water circulation depth, and geothermal storage temperature of the Chaluo geysers. Yuan et al. (2017) concluded that the differences in hydrochemical characteristics in western Sichuan Province are primarily caused by the dissolution and precipitation of minerals and cation exchanges. Previous research methods are mostly limited to traditional water chemistry and hydrogen and oxygen isotopes, and lack of combined analyses of macronutrients, trace elements and rare Earth elements, which make it difficult to accurately reflect the complex hydrogeochemical evolution of water-rock processes in deep and large fractured geothermal systems. Therefore, the combined hydrochemical and rare-earth element analyses are used in this study to provide a more detailed picture of the water-rock interaction in hot springs.

REEs consist of a group of elements with similar physicochemical properties (Hederson, 1984). They generally do not break in geochemical processes and thus have been widely used to trace the processes such as water-rock interactions in surface water (Goldstein and Jacobsen, 1988; Ménager et al., 1992; Johannesson et al., 1997; Dia et al., 2000; Göb et al., 2013). However, there are relatively few studies on the application of REEs in geothermal systems (Möller, 2000; Wood and Shannon, 2003; Sanada et al., 2006). Since REEs serve as a valuable tool for retrospectively studying the origin of geothermal fluids, the study of REEs is fundamental to understanding fluid-rock systems. Therefore, it is necessary to study the geochemical characteristics of REEs in geothermal fluids to improve the understanding of the behavior of geothermal fluids. This study analyzed the composition, fractionation, and key affecting factors of REEs in the geothermal system in the Chaluo hot springs. It will improve the understanding of the genesis of the geothermal system and provide guidance for increasing the development and utilization efficiency of local geothermal resources.

REGIONAL GEOTHERMAL GEOLOGICAL CHARACTERISTICS

The study area is located in the Jinshajiang fault and has cut downward to the upper mantle (Zhang Jian. et al., 2017; Zhang, 2020). In this area, the Late Yanshanian-Himalayan faults are superimposed on the earlier tectonic traces and cut through earlier structures. As a result, a checkerboard structural pattern with obvious fracture zones and fracture surfaces has been formed, providing favorable channels for the recharge and runoff of geothermal water. Meanwhile, the checkerboard structural pattern noticeably restricts hydrothermal activities, and the hot springs mostly spread along the fracture zones. By contrast, Indonesian structures in the study area are long and deep. They control the magmatic activities in the area and further control deep hydrothermal convection in the study area. The intersections of these structures of different eras show intensive high-temperature hydrothermal activities. The Rekeng and Reshuitang hot springs in Chaluo Town investigated in this study are also located at the intersections.

The study area lies in a hilly plateau subject to tectonic erosion. The mountains show high-grade slopes, and valleys are wide and gentle, with middle and lower parts downcutting deeply. The height differences between mountain peaks and valley bottom are generally less than 500 m. The rainfall in the Batang area is low and shows an uneven spatial-temporal distribution. It is mainly concentrated from June to September, with an average annual rainfall of 474 mm (Zhang, 2020). The Baqu River with plenty and stable water is the main river in the study area. It is a first-order tributary of the Jinsha River, with a length of 144 km and an annual runoff of about 800 million m^3. It is mainly recharged by precipitation and a small amount of snowmelt.

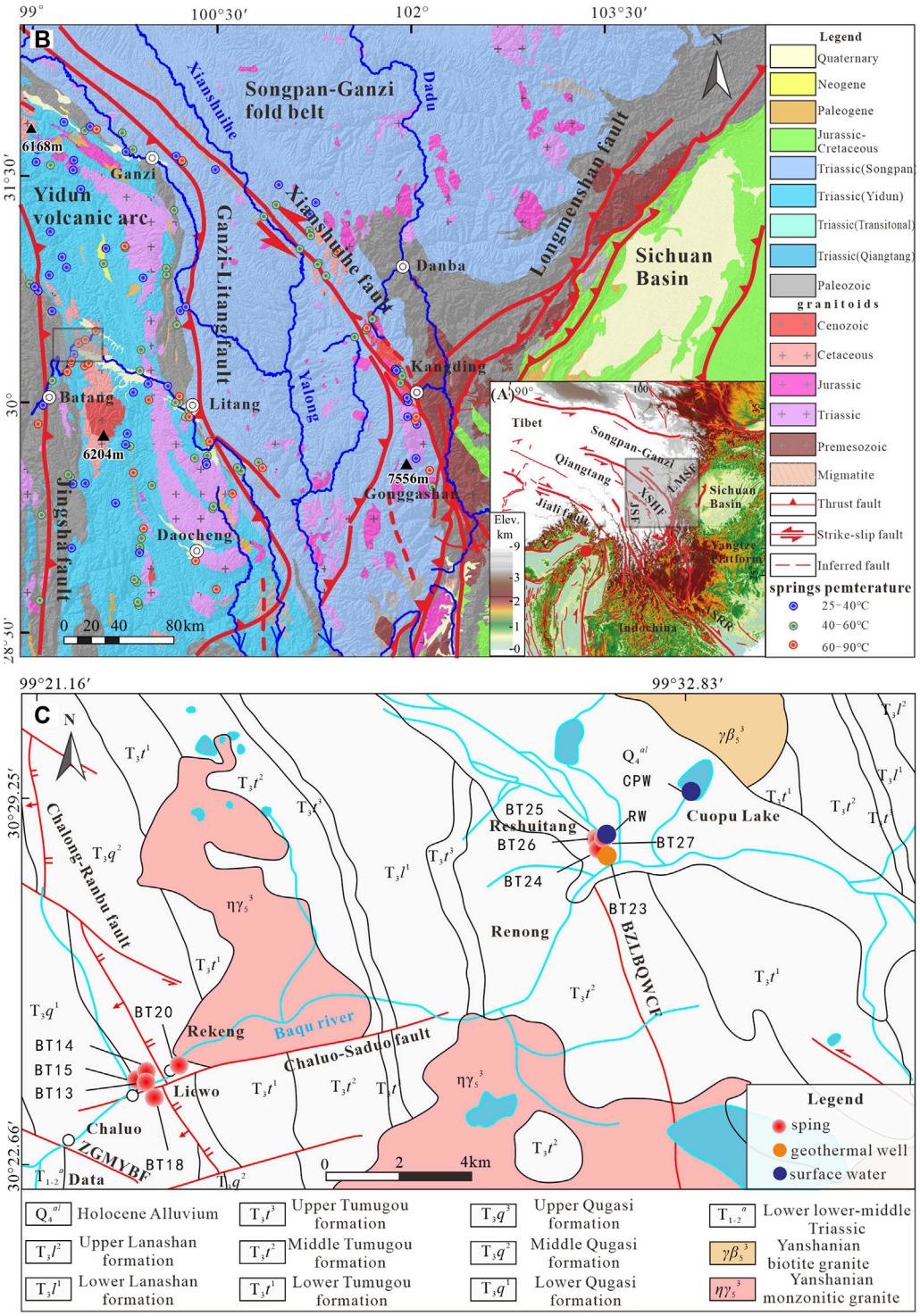

FIGURE 1 | (A) Topographic map of southwest China; **(B)** Geological map of the southeastern margin of the Tibetan Plateau (according to Zhang Y.-Z. et al., 2017; Tang and Johnnesson, 2010). **(C)** Geological map of the Chaluo area, Batang County, western Sichuan Province.

The study area features stratigraphic discontinuity, where Mesozoic strata dominated by Triassic strata (especially Upper Triassic strata) are widely distributed and outcrops also include Yanshanian biotite granites and monzonitic granites (**Figure 1C**). Hot springs in the study area are exposed in the Triassic Tumugou and Qugasi formations. The Qugasi Formation

FIGURE 2 | Field photo of Chaluo hot spring. **(A)** Hot pit spring mouth lower development of spring water; **(B)** Hot pit boiling spring waterfall; **(C)** Hot pit boiling spring; **(D)** Hot water pond boiling spring; **(E)** Geothermal well near hot water pond; **(F)** Baqu River water.

(T_3q) is exposed in the central part of the study area and spreads along Chaluo and Leiwo villages in the NS direction. With the Chalong-Ranbu fracture as a boundary, the Qugasi Formation can be roughly divided into the upper and lower members (**Figure 1C**). The upper member (T_3q^2) has a thickness of 2,295 m and is mainly composed of miscellaneous quartz conglomerates, sandy slates, slates, and dolomitic crystalline tuffs. Meanwhile, lamellibranchia and ammonite fossils occur in this member. The lower member (T_3q^1) has a thickness of 1,558 m. It is composed of light gray—dark gray crystalline tuffs, metamorphic sandstones, and slates and is interbedded with quartz conglomerates. The fossils occurring in this member include lamellibranchia, brachiopoda, and coral. The Tumugou Formation (T_3t), which is widely distributed in the study area, is a set of intermediate-acidic volcanic-sedimentary rock assemblages consisting of neritic-facies volcanic conglomerates, metamorphic sandstones, argillaceous argillites, and crystalline tuffs containing various types of volcanic conglomerates. This formation is in conformable contact with the overlying Lanashan Formation. It can be divided is divided into the upper, middle, and lower members. The upper member (T_3t^3) of the formation has a thickness of 972–4,832 m and is composed of sandstones and slates interbedded with intermediate and basal volcanic rocks and crystalline tuffs. The middle member (T_3t^2) has a thickness of 579–4,852 m. It is composed of interlayers with different thicknesses consisting of grayish-black lithic feldspar-quartz sandstones and dark slates, interbedded with rhyolites and limestones. The lower member (T_3t^1) has a thickness of 1,830 m and is composed of metamorphic sandstones and argillites. It bears conglomerates in most phase zones and is interbedded with acidic volcanic rocks locally. Moreover, it is in unconformable contact with the underlying strata in local areas.

The Chaluo hot springs refer to a group of hot springs distributed along both sides of the Baqu River in the NE direction from Chaluo Town to the Cuopu Lake in Batang County. They are mainly affected by the Zamagang-Maoyaba, Biezonglongba-Quwengcuo, Chaluo-Saduo, and Chalong-Ranbu faults (Zhang, 2020) and are mostly distributed in the shape of bands along the fault zones in the low-lying areas of the river valley, especially in the area between the Rekeng and Reshuitang areas (**Figure 1C**).

The hot springs in the Rekeng area (also referred to as the Rekeng hot springs) occur as a spring group. Their water mostly violently boils since its temperature is higher than the local boiling point (89°C; Cao et al., 2021). The hot and boiling springs have temperatures of 80–89°C and their fumaroles have a temperature of up to 99°C. The Rekeng hot springs are composed of more than a thousand springs in an area with a length of about 1,000 m, a width of 100–200 m, and an area of 0.15 km^2. Their outlets are mainly composed of strongly weathered zones consisting of elluvium-proluvium, pebble gravel, and bedrock. A large amount of calcareous tufa occurs below the outlets (**Figure 2A**), and its surrounding rocks are oxidized and brown. Meanwhile, a large area of tufa waterfalls is also present below the spring outlets (**Figure 2B**), with a height of about 50 m and a maximum thickness of 3 m. Local geothermal manifestations include boiling spouters, many boiling springs,

fumaroles, steaming ground, hot springs, and geysers (**Figure 2C**).

The hot springs in the Reshuitang area (also referred to as the Reshuitang hot springs) are also present as a spring group. Their temperatures are 27°C–89°C dominated by 80°C–87°C, mostly exceeding the local boiling point. These hot springs are primarily located on the high platform of a floodplain. The platform is made of calcareous tufa and spreads in the EW direction in the shape of an oval with a long axis of about 250 m and a short axis of about 150 m in length. The top of the platform is about 10 m above the water level. Hot and boiling springs are concentrated in an area of about 100 × 60 m^2 in the upper part of the high platform. They are composed of more than one hundred springs, each of which shows small water bubbles at dozens of positions. In addition, a few springs are distributed along the edge of the river valley. The surface geothermal manifestations include boiling spouters, many boiling springs, fumaroles, bubbling ground, and hot springs (**Figure 2D**). They are accompanied by a large amount of gas overflow and a small amount of H_2S odors, with milky white calcified sediments occurring in surrounding areas. In addition, geothermal wells (**Figure 2E**) and the Baqu River (**Figure 2F**) are also distributed near the Reshuitang hot springs.

SAMPLING AND TESTS

Samples were collected in September 2016. They include 10 samples collected from the Rekeng and Reshuitang hot springs in the area from Chaluo Village to the Cuopu Lake, one geothermal water sample and some core samples taken from the geothermal well next to the Reshuitang hot springs (the geothermal well was subsumed into the Reshuitang hot spring system), and two surface water samples collected from the Cuopu Lake and the Baqu River. The pH, Eh, total dissolved solids (TDS), and temperature of water were measured on site using portable water quality analyzers. 500 ml polyethylene bottles were used to collect the water samples after being cleaned and rinsed. The hydrochemical analysis of the water samples was conducted at the Key Laboratory of Groundwater Science and Engineering of the Ministry of Natural Resources, the Institute of Hydrogeology and Environmental Geology, Chinese Academy of Geological Sciences. The REE content of the water and rock samples was determined at the Central South Mineral Resources Supervision and Testing Center, Ministry of Land and Resources. The water samples used for tests of cations, trace elements, and isotopes were acidized until their pH was <2 by adding some drops of concentrated hydrochloric acid, while water samples used for anion tests were not acidified. Before tests, hydrochloric acid was added into the water samples using the titration method to eliminate the impacts of microorganisms and other impurities. Cations, anions, and trace elements were determined primarily using ICP-MS as per GB/TB 538-2008 Methods for examination of drinking natural mineral water. The REE contents of the water samples were tested using a plasma mass spectrometer, with analytical accuracy of better than 5%.

RESULTS AND DISCUSSION

Hydrochemical Characteristics

The hydrochemical compositions of the water samples are shown in **Table 1**. The Schöeller diagram (**Figure 3**) can be used to reflect the physicochemical properties of geothermal water from hot springs and geothermal wells and surface water from lakes and rivers. The geothermal water is neutral to alkaline and surface water is alkaline, and they have similar chemical compositions. However, the geothermal water contains higher concentrations of major ions, especially Na ions, than the surface water (**Figure 3**). The TDS content of the surface water and the geothermal water is 75.61–98.98 mg/L and 305.5–1,179 mg/L, respectively. For most water samples, the anions are dominated by HCO_3^-, and their contents are in the order of $HCO3- > SO42- > Cl-$. Meanwhile, cations in the water samples mainly included Na+, and their contents are in the order of $Na+ > K+ > Ca2+ > Mg2+$. The total dissolved cations ($TZ+ = Na+ + K+ 2Mg2+ + 2Ca2+$) and total dissolved anions ($TZ- = Cl- + 2SO42- + HCO3- + 2CO32-$) are well balanced: all samples have normalized inorganic charge balance, $NICB = (TZ+ - TZ-)/TZ+$, and all samples have NICB ≤10% (**Table 1**) (Moon et al., 2007). The Piper diagram of the water samples (Piper, 1994; **Figure 4**) illustrates the distribution of these cations and anions and the hydrochemical classification of the water samples. According to this diagram, three hydrochemical types were identified. All the geothermal water is of Na-HCO_3 type, the river water is of the mixed Ca-Na-HCO_3 type, and lake water is of Ca-HCO_3 type. Moreover, the greater concentrations of major ions and the higher TDS content in the geothermal water indicate a longer retention time and stronger water-rock interactions of the geothermal water (Zhang Y. et al., 2018).

Hydrochemical Processes

Soluble ions in water originate from various natural processes, such as precipitation, water-rock interactions, and evaporation, and these different processes can be distinguished using Gibbs diagrams (Gibbs, 1970). In the Gibbs diagram of TDS versus $Na^+/(Na^+ + Ca^{2+})$ and $Cl^-/(Cl^- + HCO^{3-})$ of the geothermal water (**Figure 5**), the $Na^+/(Na^+ + Ca^{2+})$ ratio is 0.87–0.99, falling in the zones of water-rock interactions and evaporation. Meanwhile, the $Cl^-/(Cl^- + HCO_3^-)$ ratio of the geothermal water is 0.05–0.17, falling into the water-rock interaction zone. These results indicate that cations in the geothermal water are mainly controlled by water-rock interactions and evaporation, while the anions in the geothermal water are dominated by water-rock interactions. The surface water samples fall in the water-rock interaction zone in the Gibbs diagram (**Figure 5**), indicating that the hydrochemical composition of the surface water is controlled by water-rock interactions.

The hydrochemical processes of water-rock interactions can be reflected from the correlation between the anion and cation

TABLE 1 | Hydrochemical composition of water samples in the study area (mg/L).

Sample	Location	T(°C)	Eh(mv)	pH	K^+	Na^+	Ca^{2+}	Mg^{2+}
BT13	Rekeng	89	−514.5	9.18	34.53	358.9	1.34	0.02
BT14	Rekeng	89	−574	9.27	29.81	317	0.81	0.013
BT15	Rekeng	90	−413.4	8.43	27.62	290.8	4.02	0.21
BT18	Rekeng	89	−517	8.97	28.86	343.8	0.65	0.013
BT20	Rekeng	53	45.1	8.26	2.41	90.24	11.61	0.81
BT23	Reshuitang	86	−550	8.19	26	353.2	6.41	2.92
BT24	Reshuitang	90	−442.1	9.1	26.23	351.6	0.77	0.1
BT25	Reshuitang	90	55.8	7.76	26.8	358.2	1.67	0.2
BT26	Reshuitang	90	64.8	8.03	25.24	345.2	0.8	0.1
BT27	Reshuitang	70	45.3	7.64	30.51	380.4	7.77	2.51
CPH	Cuopu Lake	15	75	8.96	0.75	0.65	19.55	1.81
RW	Baqu River	13	90	8.2	2.3	14.71	10.95	2.51

Sample	Cl^-	SO_4^{2-}	HCO_3^-	CO_3^{2-}	TDS	NICB[a] (%)	Fe	Mn
BT13	19.19	32.84	379.1	222.5	1,079	10	0.242	0.032
BT14	39.1	30.17	365	194.2	991.2	2.79	0.012	0.032
BT15	42.65	42.06	617.5	42.09	909	−0.21	0.021	0.032
BT18	51.9	25.45	428	180.4	1,041	4.48	0.012	0.001
BT20	8.89	20.74	217	—	305.5	8.50	0.036	0.006
BT23	33.77	19.47	904.9	18.04	1,071	−1.21	0.17	0.011
BT24	23.1	20.3	679.3	114.3	1,039	−0.03	0.425	0.009
BT25	33.77	42.62	885.9	—	1,071	0.04	0.381	0.004
BT26	33.06	42.09	862.1	—	1,033	−1.46	0.512	0.009
BT27	32.7	25.9	1,015	—	1,179	−0.98	0.016	0.01
CPH	1.78	22.89	42.8	—	75.61	−4.80	0.01	0.004
RW	1.78	17.95	61.75	—	98.98	1.08	0.162	0.003

[a]*NICB, normalized inorganic charge balance = $(TZ^+–TZ^-)/TZ^+ \times 100\%$.*

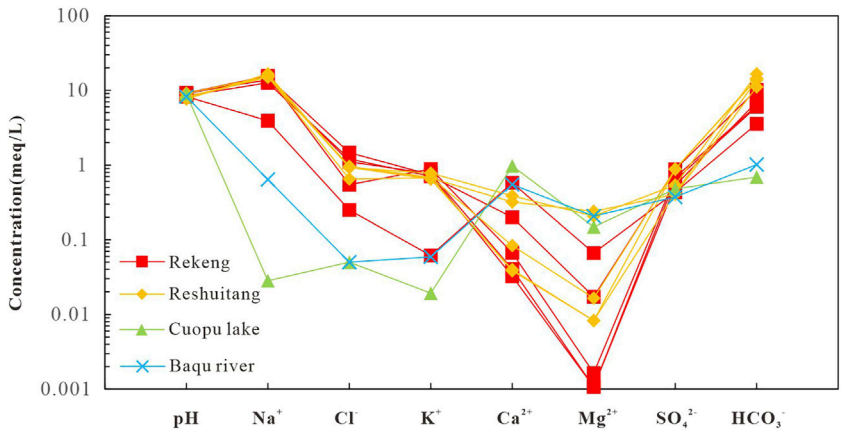

FIGURE 3 | Schöeller's diagram for different water samples in the study area.

contents (Li et al., 2020). According to the lithology of the strata in the study area, the rock formations contain minerals such as silicates, carbonates, sulphates and halides, and the main ions in the water samples originate from the dissolution of these minerals. Among these ions, Cl^- is rarely altered by water-rock interactions and mineral adsorption, even under high temperature and pressure conditions. Therefore, the correlation between Cl^- and other ions can account for the hydrochemical process in the geothermal water cycle (Li et al., 2020). If Na^+ is derived from halite dissolution, the molar ratio of Na^+ to Cl^- should be 1:1. **Figure 6A** shows that the surface water samples are distributed near the origin of coordinates in which the Na^+/Cl^+ ratios for CPW and RW were 0.56, 12.74 respectively. While the geothermal water shows a Na^+/Cl^- molar ratio of much higher than 1, implying that the excess Na^+ in the geothermal water may originate from silicate weathering (Zhang Y. et al., 2018). Ca^{2+} and SO_4^{2-} in groundwater are affected by the dissolution and precipitation of gypsum. If merely gypsum dissolves and precipitates in groundwater, as shown in **Eq. 1**, the molar ratio of Ca^{2+} to SO_4^{2-} should be 1:1. In the plot of Ca^{2+}

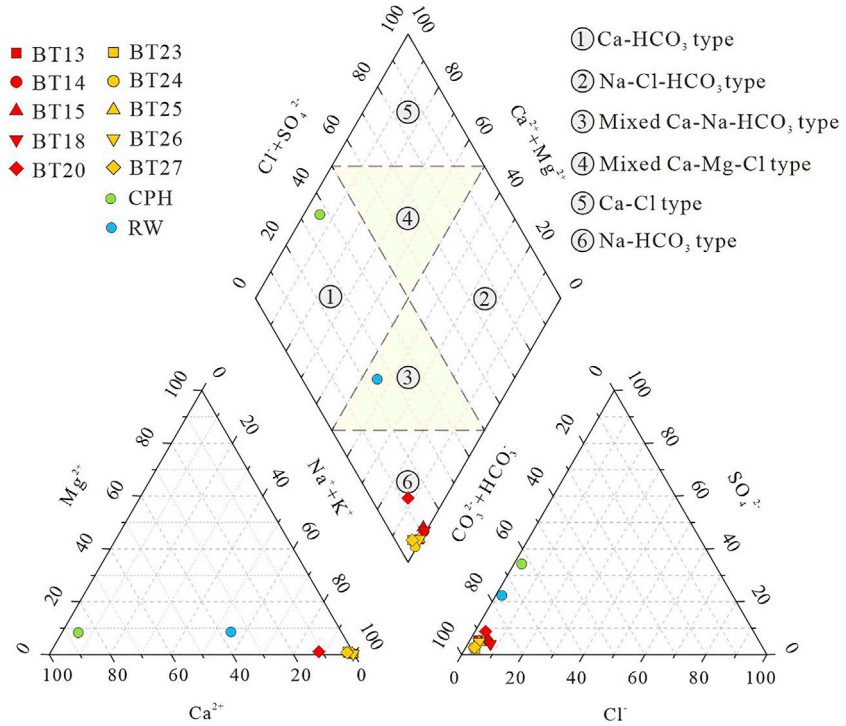

FIGURE 4 | Piper plot of water samples (modified from Piper, 1994; Zhang Y. et al., 2018).

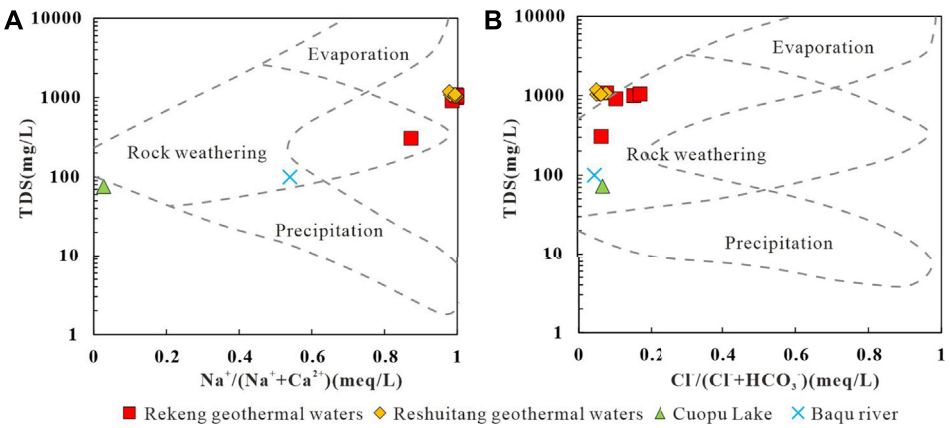

FIGURE 5 | Gibbs illustration of water samples in the study area. Rock weathering: the hydrochemical composition within the region is mainly influenced by rock weathering and dissolution; Evaporation: the hydrochemical composition within the region is mainly influenced by evaporation and concentration; Precipitation: the hydrochemical composition within the region is mainly influenced by atmospheric precipitation factors.

versus SO_4^{2-} (**Figure 6B**), only a few geothermal water and river water samples are distributed along the line with a slope of 1:1, and most of the geothermal water samples fall below the line with a slope of 1:1. These results indicate that the excess Ca^{2+} may originate from the dissolution of carbonate and silicate minerals. In addition, the relatively high SO_4^{2-} of some samples from the geothermal water and the Cuopu Lake may be influenced by human activities (Zhang Y. et al., 2018).

If the molar ratio of Ca^{2+} to HCO_3^- is 1:2, Ca^{2+} in groundwater originates from the dissolution of carbonate minerals (**Eq. 2**; Guo et al., 2020). In the plot of Ca^{2+} versus HCO_3^- (**Figure 6C**), the samples of river water and Cuopu Lake are distributed along the line with a slope of 1:2, and the molar ratio of Ca^{2+} to HCO_3^- of samples from the geothermal water are much less than 1:2. These results indicate that the Ca^{2+} in the geothermal water are derived from the dissolution of silicate minerals, while the Ca^{2+} in the

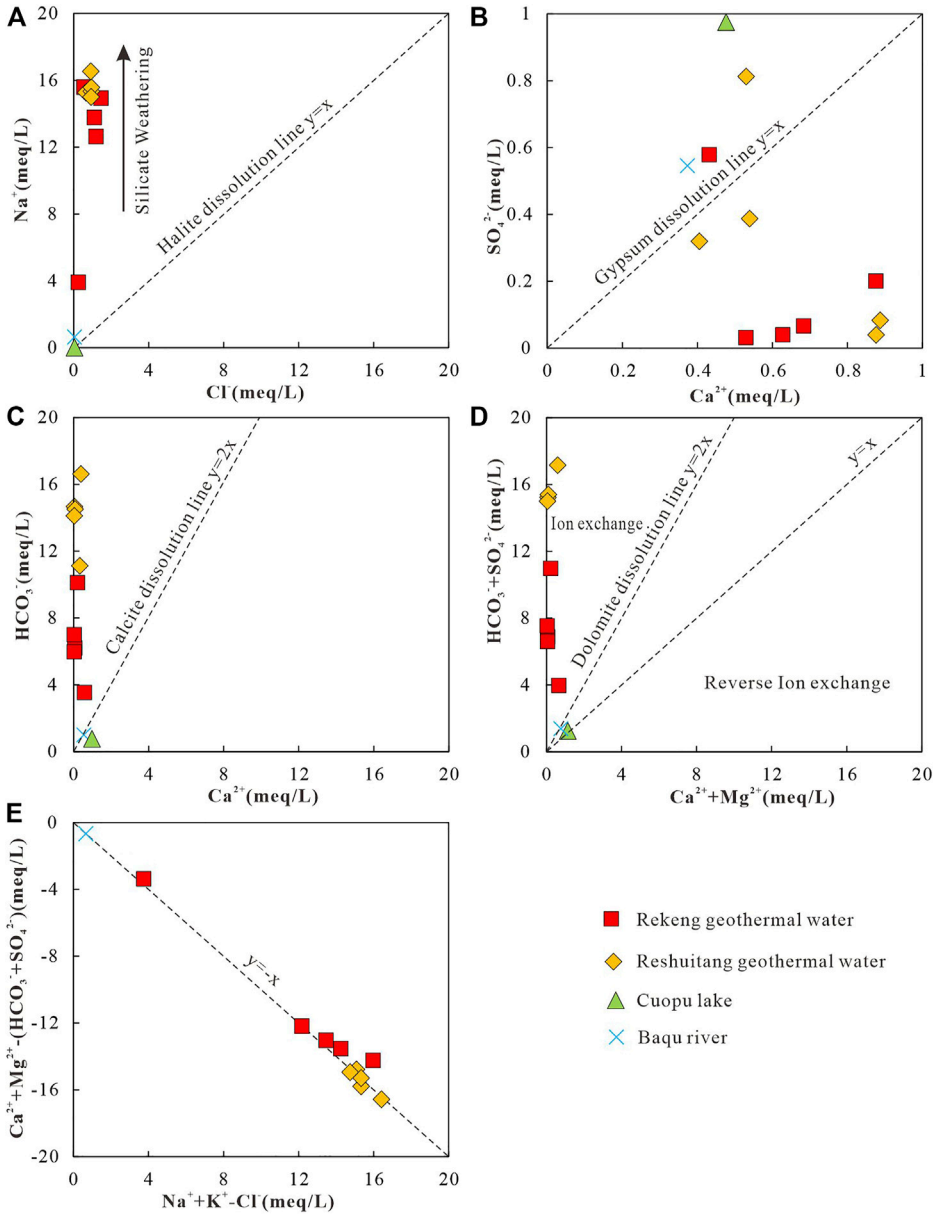

FIGURE 6 | Diagram of the determination of hydrochemical processes based on the molar ratio among the main ions in water. **(A)** Cl- vs. Na+, **(B)** Ca^{2+} vs. SO_4^{2-}, **(C)** Ca^{2+} vs. HCO_3^-, **(D)** (Ca^{2+}+Mg^{2+}) vs. (HCO_3^- + SO_4^{2-}), and **(E)** (Na^++K^+)-Cl^- vs. (Ca^{2+}+Mg^{2+})-(SO_4^{2-} + HCO_3^-).

river water and Cuopu Lake are derived from the dissolution of carbonate minerals.

The origin of Ca^{2+}, Mg^{2+}, HCO_3^-, and SO_4^{2-} in groundwater can be reflected from the molar ratio of (Ca^{2+} + Mg^{2+}) to (HCO_3^- + SO_4^{2-}) in water. Specifically, a molar ratio of 1:1 indicates that these ions are obtained from the dissolution of carbonate rocks and sulfate minerals, a molar ratio of greater than 1:1 indicates that ion exchange process dominates (**Eq. 3**), and a molar ratio of less than 1:1 indicates the presence of reverse ion exchange (**Eq. 4**). As shown in plot of (Ca^{2+} + Mg^{2+}) versus (HCO_3^- + SO_4^{2-}) of the water samples (**Figure 6D**), the samples of river water and Cuopu Lake are distributed along the line with a slope of 1:1, while the water samples of the geothermal water are distributed below the line. Meanwhile, the concentration of Ca^{2+} is far higher than that of Mg^{2+} in the geothermal water. Therefore, it can be inferred that the relatively depleted Ca^{2+} in the geothermal water may be affected by ion exchange (**Eq. 3**), which is caused by silicate weathering.

In the diagram of (Na^+ + K^+)-Cl^- versus (Ca^{2+} + Mg^{2+})-(SO_4^{2-} + HCO_3^- + CO_3^{2-}) (**Figure 6E**), all samples are essentially distributed along a 1:1 line. These results indicate that the hydrochemical processes of the geothermal water and the surface water are mainly controlled by cation exchanges and adsorption in the dissolution of silicate minerals (Li et al., 2020).

TABLE 2 | Rare Earth element composition of geothermal water in the study area (ug/L).

Sample	Location	La	Ce	Pr	Nd	Sm	Eu	Gd	Tb	Dy
BT13	Rekeng	0.05	0.17	0.007	0.021	0.004	0.017	0.005	0.004	0.002
BT14	Rekeng	0.03	0.3	0.004	0.016	0.001	0.008	0.002	0.004	0.004
BT15	Rekeng	0.034	0.13	0.005	0.007	0.002	0.008	0.003	0.004	0.005
BT18	Rekeng	0.021	0.12	0.006	0.008	0.005	0.006	0.002	0.004	0.005
BT20	Rekeng	0.054	0.18	0.007	0.028	0.0035	0.008	0.0035	0.004	0.0025
BT23	Reshuitang	0.036	0.14	0.004	0.011	0.002	0.015	0.002	0.004	0.003
BT24	Reshuitang	0.061	0.18	0.007	0.034	0.009	0.01	0.004	0.004	0.001
BT25	Reshuitang	0.059	0.17	0.009	0.03	0.008	0.014	0.006	0.0005	0.002
BT26	Reshuitang	0.11	0.26	0.017	0.067	0.013	0.008	0.015	0.003	0.009
BT27	Reshuitang	0.032	0.13	0.004	0.009	0.004	0.022	0.006	0.003	0.008
CPH	Cuopu Lake	0.018	0.093	0.001	0.004	—	—	—	—	—
RW	Baqu River	0.078	0.16	0.007	0.028	0.003	0.007	0.005	0.004	0.005
Sample	Ho	Er	Tm	Yb	Lu	∑REE	LREE/HREE	(La/Yb)N	δCe	δEu
BT13	0.003	0.002	0.004	0.003	0.006	0.298	9.28	1.61	1.98	16.69
BT14	0.003	0.003	0.004	0.003	0.006	0.388	12.38	0.97	5.96	24.84
BT15	0.003	0.004	0.004	0.005	0.006	0.22	5.47	0.66	2.17	14.34
BT18	0.003	0.003	0.004	0.005	0.006	0.198	5.19	0.41	2.33	8.33
BT20	0.0025	0.0025	—	0.0045	—	0.3	14.38	1.16	2.02	10.04
BT23	0.003	0.002	0.003	0.003	0.005	0.233	8.32	1.16	2.54	32.93
BT24	0.003	0.002	0.004	0.002	0.005	0.326	12.04	2.95	1.90	7.32
BT25	0.002	0.002	0.004	0.003	0.005	0.3145	12.08	1.91	1.61	8.87
BT26	0.002	0.029	0.003	0.007	0.005	0.548	6.51	1.52	1.31	2.52
BT27	0.001	0.005	0.003	0.004	0.005	0.236	5.74	0.78	2.50	19.72
CPH	—	—	—	—	—	0.116		—	4.77	—
RW	0.002	0.003	0.003	0.002	0.005	0.312	9.76	3.78	1.49	7.94

Cation exchanges and adsorption in the geothermal water result in a decrease in Ca^{2+} and Mg^{2+} concentrations and an increase in Na^{+} concentration (**Figure 3**, Wang et al., 2021). According to the molar ratio diagrams of the major ions in water, the hydrochemical processes in the study area are mainly controlled by the dissolution of silicate minerals.

$$CaSO_4 \cdot 2H_2O \leftrightharpoons Ca^{2+} + SO_4^{2-} + 2H_2O \quad (1)$$

$$CaCO_3 + H_2CO_3 \rightarrow Ca^{2+} + 2HCO^{3-} \quad (2)$$

$$Ion\ exchange:\ 2Na^{+} - Clay + Ca^{2+} \rightarrow 2Na^{+} + Ca^{2+} - Clay_2 \quad (3)$$

$$Reverse\ ion\ exchange:\ 2Na^{+} + Ca^{2+} - Clay_2 2Na^{+} - Clay + Ca^{2+} \rightarrow 2Na^{+} - Clay + Ca^{2+} \quad (4)$$

Characteristics and Controlling Factors of Rare Earth Element Contents in Geothermal Water

The composition of REEs in geothermal water in the study area is shown in **Table 2**. The contents of REEs (except for Yttrium) in the Chaluo hot springs are lower than those of the hot springs around the Kangding area in western Sichuan Province. They are 0.306 ± 0.103 ug/L and 0.669 ± 0.367 ug/L, respectively (Zhang, 2018b). In addition, the water in the Cuopu Lake has low REE contents, while the river water has high REE contents. The difference in the REE contents between the surface water and the geothermal water may be related to the material exchanges between water and rocks (Fan et al., 2021).

Studies have shown that REEs in water bodies are derived from the weathering or dissolution of minerals, the reductive dissolution of Fe and Mn oxides in sediments, the leaching and dissolution of secondary minerals, and human activities (Markert and Zhang, 1991; Dia et al., 2000; Tweed et al., 2006; Kynicky et al., 2012). The dominant factors of these REE sources include pH, oxidation-reduction potential (OPR), and mineral adsorption/dissolution (Leybourne et al., 2000; Noack et al., 2014; Gruau et al., 2004; Koeppenkastrop and De Carlo, 1992; Coppin et al., 2002). pH can control the REE contents by directly influencing the chemical weathering or adsorption/precipitation of REE minerals and by indirectly affecting the complexation (Namely, inorganic ions in the water column such as CO_3^{2-}, PO_4^{3-}, F^{-}, SO_4^{2-}, Cl^{-}, NO_3^{-} as ligands combine with rare Earth elements to form complexes) or adsorption of REEs (Millero, 1992; Noack et al., 2014). Generally, there is a close negative correlation between the pH and the REE contents of water bodies (Noack et al., 2014). **Figure 7A** shows almost no correlation between the pH and ∑REE (R^2 = 0.02) of geothermal water in the study area. However, the ∑REE tends to increase with a decrease in pH when pH < 9, and there is a significant positive correlation between the ∑REE and pH (R^2 = 0.84) when pH > 9. These results are consistent with the study of Noack et al. (2014). It is speculated that the adsorption-absorption regulation of REEs decreases as alkalinity increases in the water bodies. Meanwhile, the increase in the dissolution of CO_2 increases ∑REE through complexation reactions (Zhu, 2006; Liu, 2018). OPR can directly affect redox-sensitive REEs such as Ce and Eu and can indirectly affect REEs by influencing the precipitation or dissolution of Fe and Mn oxides/hydroxides (Guo et al., 2010). Fe and Mn oxides/hydroxides adsorb REEs in an oxidizing environment but

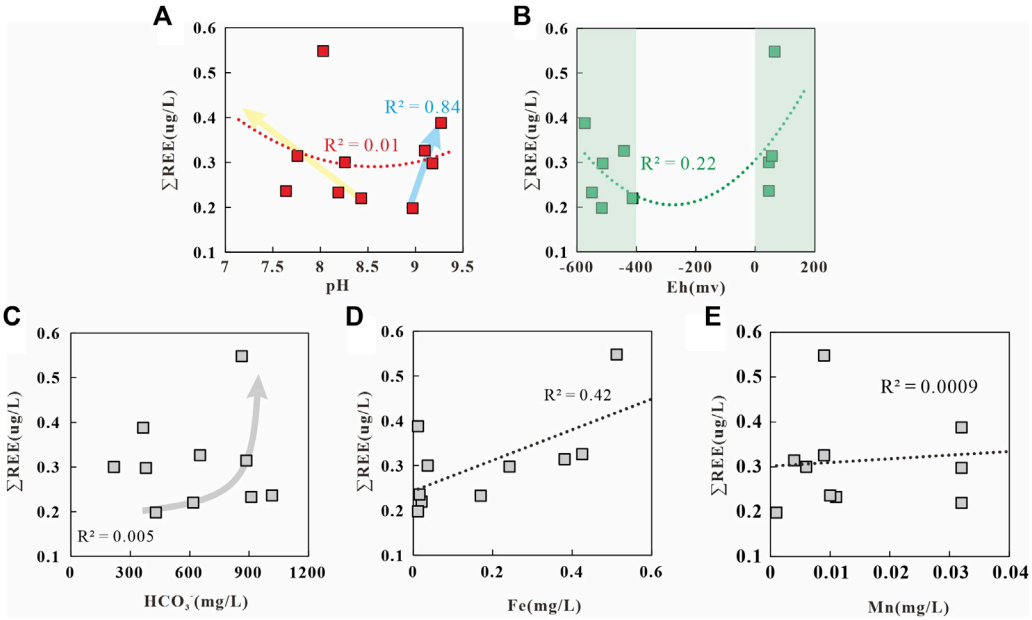

FIGURE 7 | Relationship between ∑REE and pH **(A)**, Eh **(B)**, HCO_3^- **(C)**, Fe **(D)** and Mn **(E)** in the geothermal water of Chaluo.

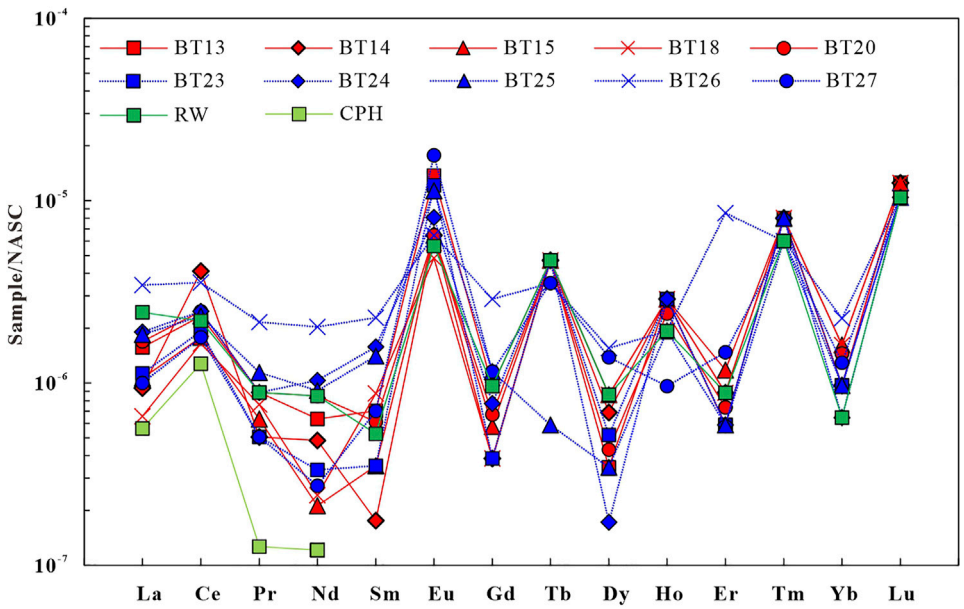

FIGURE 8 | North American shale standardized partitioning pattern of geothermal water and surface water rare Earth elements in the study area.

dissolve and release REEs in a reducing environment. As shown in the diagram of Eh versus ∑REE of the study area (**Figure 7B**), there is essentially no correlation between the Eh and ∑REE, reflecting the fact that REEs are barely influenced by Eh. In alkaline water bodies, HCO_3^- occurs in the form of $LnCO_3^+$ and $Ln(CO_3)_2^-$ after experiencing complexation reactions with REEs (Wood, 1990). **Figure 7C** shows that there is no correlation between HCO_3^- and ∑REE. However, in geothermal water with a high HCO_3^- content, the ∑REE tends to increase with an increase in HCO_3^-. This finding indicates that high HCO_3^- content is favorable for REE enrichment (Xie et al., 2012). In geothermal water with a low HCO_3^- content, however, REEs may be liable to be affected by other factors such as pH. The diagrams of Fe versus ∑REE and Mn versus ∑REE (**Figures 7D,E**) show a certain positive correlation between Fe and ∑REE and no significant correlation between Mn and ∑REE. These results indicate that the reductive dissolution of Fe oxides/

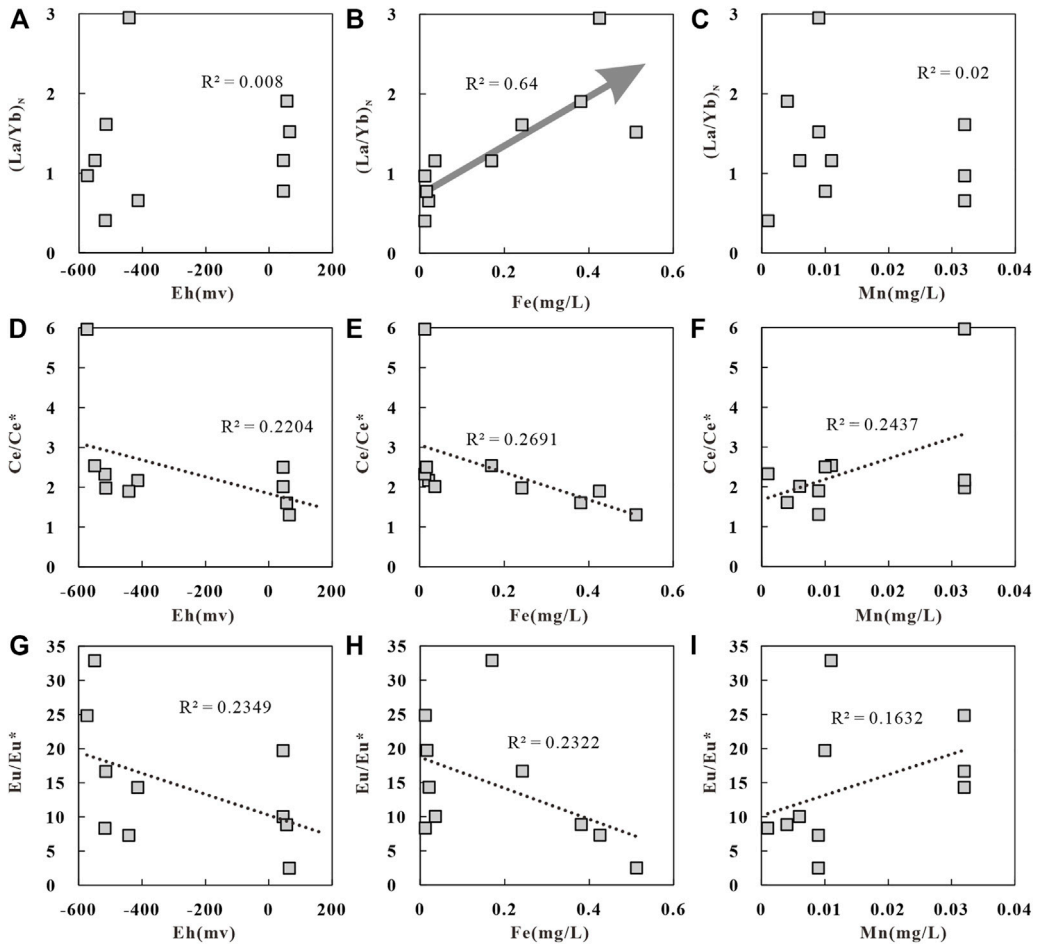

FIGURE 9 | Correlation of geothermal water in the study area, **(A)** $(La/Yb)_N$ versus Eh, **(B)** $(La/Yb)_N$ versus, **(C)** $(La/Yb)_N$ versus Mn, **(D)** Ce/Ce* versus Eh, **(E)** Ce/Ce* versus, **(F)** Ce/Ce* versus Mn, **(G)** Eu/Eu* versus Eh, **(H)** Eu/Eu* versus, **(I)** Eu/Eu* versus Mn.

hydroxides in geothermal water accounts for the increase in the REE content. Overall, the REE contents depend on the reductive dissolution of Fe oxides/hydroxides, followed by pH.

Rare Earth Element Fractionation in Geothermal Water and Controlling Factors

The North American Shale Composite (NASC) (Haskin et al., 1968) normalized REE patterns of the geothermal water in the study area (**Figure 8**) take the shape of gentle sawteeth (Haley et al., 2004). The LREE(La-Eu)/HREE(Gd-Lu) ratio of geothermal water varies from 5.19 to 14.38. The $(La/Yb)_N$ ratio is generally used to replace the LREE(La-Eu)/HREE(Gd-Lu) ratio to characterize the relative enrichment of LREEs in geothermal water (Zhao Y. Y. et al., 2019). The $(La/Yb)_N$ ratio of the geothermal water in the study area is 0.41–2.95, with an average of 1.31, reflecting the enrichment of LREEs. **Figure 9A** shows no significant correlation between Eh and $(La/Yb)_N$, indicating that Eh does not directly affect the REE contents. Studies show that Fe and Mg preferentially adsorb LREEs in the process of oxidation-induced precipitation, leading to the relative enrichment of HREEs. Meanwhile, Fe and Mg oxides will release LREEs after reductive dissolution, leading to a relative enrichment of LREEs in water bodies (Tang and Johanesson, 2010). **Figure 9B** shows a significant positive correlation between Fe and $(La/Yb)_N$. That is, as the Fe content increases, $(La/Yb)_N$ increases significantly and gradually and the REE fractionation enhances. In contrast, **Figure 9C** shows that this is almost no correlation between Mn and $(La/Yb)_N$. These occur possibly for the following reasons. Fe and Mg oxides have different absorption capacities of LREEs and HREEs. The Fe concentration is higher than the Mn concentration in the geothermal water, and Fe oxides release more LREEs after reductive dissolution. As a result, the geothermal water is richer in LREEs than in HREEs.

The redox-sensitive Ce and Eu elements are also commonly used to reflect the fractionation of REEs. Ce exists in both +3 and +4 valence states. In an oxidizing environment, Ce^{3+} in water bodies converts into Ce^{4+} after losing electrons, which will be preferentially adsorbed by Fe and Mn oxides and is then separated from other REEs in the +3 valence state, leading to Ce depletion in water bodies. In a reducing environment, adsorbed Ce^{4+} is reduced to Ce^{3+} and enters water bodies due to the dissolution of Fe and Mn oxides, resulting in Ce enrichment (Byrne and Sholkovitz, 1996).

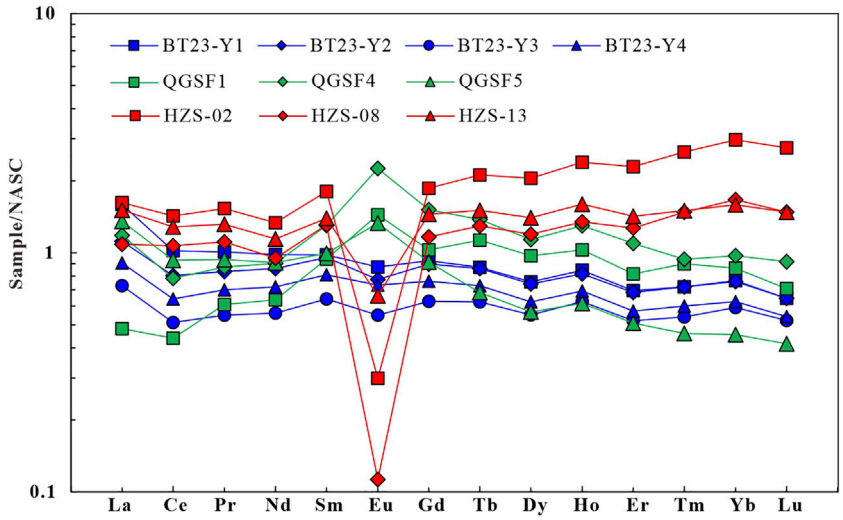

FIGURE 10 | Standardized allotment map of North American shales in the study area rocks (Qugasi Formation data (QGSF1, 4, 5) according to Wang H Y, 2017; HZS data according to Zhang F. Y. et al, 2018).

Eu normally occurs in the Eu^{3+}valence state. In a reducing environment, Eu^{3+} converts into Eu^{2+} after extracting electrons, which will separate from the other REEs in the +3 valence state due to chemical differences, thus resulting in Eu depletion. Among various equations used to calculate Ce/Ce* and Eu/Eu* ratios (Zhao Y. Y. et al., 2019), the following equations (Guo et al., 2010) are used in this study:

$$Ce/_{Ce*} = CeN/_{(LaN*\mathrm{Pr}N)} \cdot 0.5 \quad (5)$$

$$Eu/_{Eu*} = EuN/_{(SmN*GdN)} \cdot 0.5 \quad (6)$$

The Ce/Ce* ratio of the geothermal water in the study area is 1.31–5.96, with an average of 2.43, reflecting positive Ce anomalies. The Eu/Eu* ratio of the geothermal water is 2.52–32.93, with an average of 14.56, indicating positive Eu anomalies. Factors affecting Ce anomalies in water bodies usually include OPR and mineral adsorption/dissolution or the weathering of the surrounding rocks (Elderfield et al., 1990). There is a weak negative correlation between Eh and the Ce/Ce* ratio in the geothermal water in the study area (**Figure 9D**). That is, a lower Eh suggests a higher Ce/Ce* ratio, indicating that the positive Ce anomalies in water bodies are caused by the redox environment. Specifically, Ce^{4+} converts into Ce^{3+} with the dissolution of Fe and Mn oxides, resulting in positive Ce anomalies (Xie et al., 2012). In contrast, **Figure 9E** shows a certain negative correlation between Fe and the Ce/Ce* ratio, and **Figure 9F** shows a certain positive correlation between Mn and the Ce/Ce* ratio. These results indicate that the dissolution of Mn oxides in water bodies leads to positive Ce anomalies.

To further investigate the REE fractionation in water-rock interactions, this study obtained NASC-normalized REEs patterns of the Tumugou and Qugasi formations and Yanshanian granites (**Figure 1C**) in the study area. According to the NASC-normalized REE patterns, the rocks of the Qugasi Formation show positive Eu anomalies (Wang, 2017; **Figure 10**). In contrast, rocks of the Tumugou Formation and especially the Yanshanian granites show negative Eu anomalies (Zhang F. Y. et al., 2018). All types of rocks show slightly negative Ce anomalies, from which it can be inferred that the weathering of surrounding rocks roughly does not cause positive Ce anomalies. The surface water near the geothermal water shows positive Ce anomalies (**Figure 8**), with a Ce/Ce* ratio of 1.49–4.77, with an average of 3.13. This value is slightly higher than the Ce/Ce* ratio of the geothermal water, indicating that the geothermal water may be influenced by the positive Ce anomalies of the surface water (Barrat et al., 2000). Therefore, the positive Ce anomalies in the geothermal water result from both the dissolution of Eh and Mn oxides and surface water. **Table 3**.

TABLE 3 | Rare Earth element composition of geothermal well cores in the study area (ug/g).

Sample	La	Ce	Pr	Nd	Sm	Eu	Gd
BT23-Y1	51	74.5	7.96	32.4	5.58	1.08	4.82
BT23-Y2	35.7	58.6	6.61	28.4	5.44	0.96	4.67
BT23-Y3	23.3	37.3	4.33	18.5	3.66	0.68	3.26
BT23-Y4	29	46.9	5.54	23.8	4.62	0.91	3.96
Sample	Tb	Dy	Ho	Er	Tm	Yb	Lu
BT23-Y1	0.74	4.39	0.88	2.36	0.36	2.37	0.31
BT23-Y2	0.73	4.3	0.85	2.32	0.36	2.35	0.31
BT23-Y3	0.53	3.19	0.65	1.77	0.27	1.83	0.25
BT23-Y4	0.62	3.62	0.72	1.94	0.3	1.94	0.26

The negative correlation between Eh and the Eu/Eu* ratio in the geothermal water (**Figure 9G**) indicates that the positive Eu anomalies in the geothermal water are caused by the reducing environment. Meanwhile, the correlations between Fe and the Eu/Eu* ratio (**Figure 9H**) and between Mn and the Eu/Eu* ratio (**Figure 9I**) indicate that the dissolution of Mn oxides promotes the positive Eu anomalies. As mentioned above, the NASC-normalized

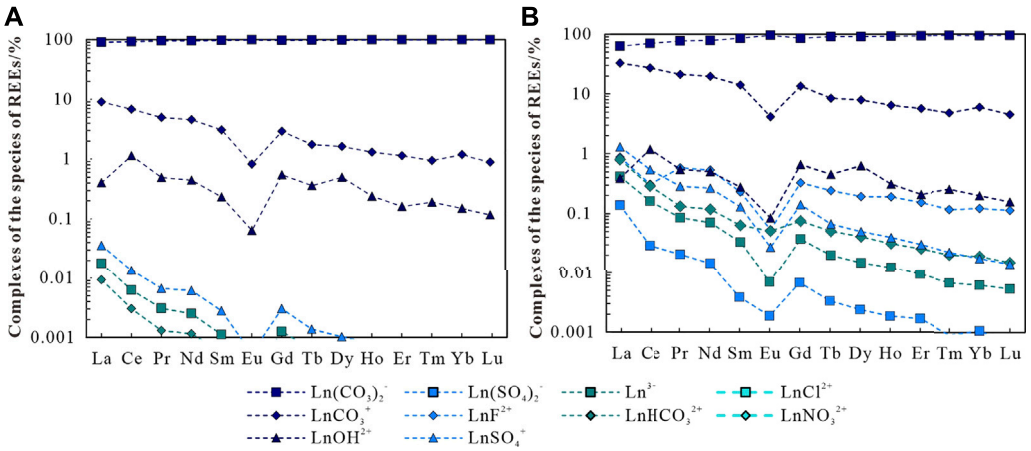

FIGURE 11 | Percentage of each inorganic complexation form of rare Earth elements in geothermal water BT15 **(A)** and BT25 **(B)** in the study area.

REE patterns (**Figure 10**) show that only rocks in the Qugasi Formation show positive Eu anomalies, while the rocks in the Tumugou Formation and Yanshanian granites show negative Eu anomalies. It can be inferred from these results that water-rock interactions between the Qugasi Formation and deep geothermal water also cause positive Eu anomalies. The Eu/Eu^{*} ratio of the surface water is 7.94 and shows significant positive Eu anomalies which indicating positive Eu anomalies in surface water was inherited from the rock of Qugasi Formation (Dong et al., 2017). It is lower than that of the geothermal water, suggesting that the geothermal water is affected by the surface water. In addition, the dissolved feldspar minerals in water bodies also lead to positive Eu anomalies and calcite precipitation (Lee et al., 2003; Liu et al., 2016). The surrounding rocks in the study area are rich in feldspar minerals and the geothermal water in the Batang area is supersaturated with calcite (Zhang, 2020). Therefore, the dissolution of feldspar in the surrounding rocks in the study area promotes the Eu enrichment. Overall, the Eu positive anomalies in the geothermal water result from the combined effects of the reducing environment, surrounding rocks, water bodies, and feldspar dissolution.

Distribution of Rare Earth Element Complexes in Geothermal Water

In this study, the composition and forms of REEs in water sample BT15 from the Rekeng hot springs and the water sample BT25 from the Reshuitang hot springs were determined through

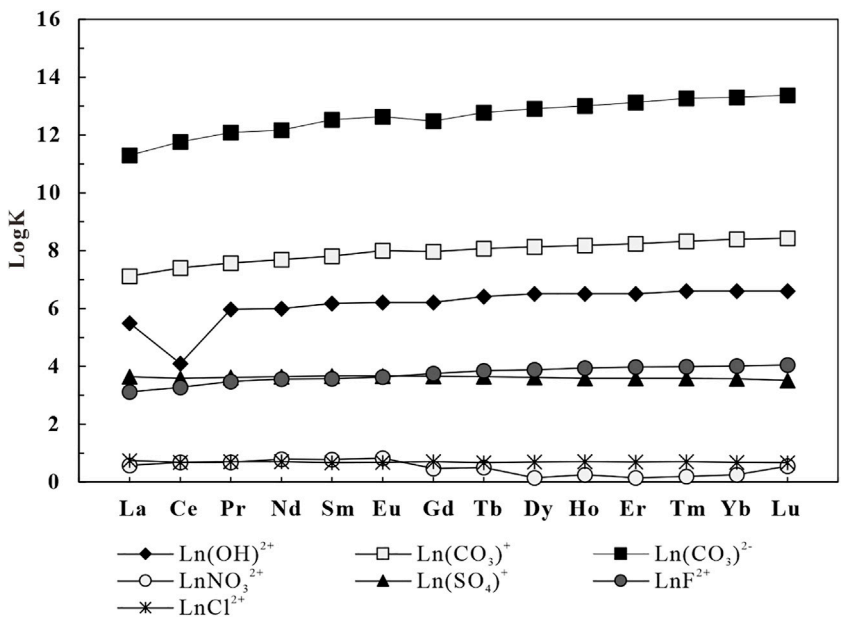

FIGURE 12 | Variation of complexation stability constants of different complexes of rare Earth elements with increasing elemental order (temperature 25°C) (Lee and Byrne, 1992; Millero, 1992; Luo and Byrne, 2001, 2004; Schijf and Byrne, 2004).

calculation and simulation analysis using the Visual MINTEQ 3.0 software. Specifically, measured temperatures, pH, major anions, and REE concentrations were input to MINTEQ to determine the inorganic complex species of REEs in the water samples. The simulation results show that the complex species in the geothermal water mainly include $Ln(CO_3)_2^-$, $LnCO_3^+$, and $LnOH^{2+}$ (Ln signifies the REE). This finding is roughly consistent with the complex species in partially alkaline water bodies (Liu et al., 2021). As shown in **Figure 11**, the inorganic complexes in the Rekeng geothermal water are dominated by $Ln(CO_3)^{2-}$, which accounts for 90.47–99.11% of the total mass concentration of inorganic complexes. They also include $LnCO_3^+$ and $LnOH^{2+}$, which account for 0.82–9.06% and 0.06–1.14%, respectively, and other complexes account for less than 0.01%. The complexes in the Reshuitang geothermal water mainly include $Ln(CO_3)_2^-$ and $LnCO_3^+$, which account for 62.89–95.22% and 4.47–33.18%, respectively. They also include $LnSO_4^+$, which accounts for 0.013–1.31%, and other complexes account for less than 0.1%.

As shown in **Figure 11**, with an increase in the atomic number of the REEs in the geothermal water, the percentage of $Ln(CO_3)_2^-$ gradually increases but the percentages of other complexes such as $LnCO_3^+$ gradually decrease (Liu et al., 2021). This occurs because the stability constants (lgK) of different REE complexes increase as the atomic order of REEs increases. The LgK of $(CO_3)_2^-$is higher than that of other complexes, and therefore the percentage of $Ln(CO_3)_2^-$ increases with an increase in the atomic number of REEs (**Figure 12**).

CONCLUSION

This study determined the hydrochemical characteristics and REE contents of water samples collected from the Chaluo hot springs and rock samples from the surrounding areas through analysis and tests, obtaining the following conclusions:

1) In terms of hydrochemical types of the Chaluo hot springs, the geothermal water is of Na-HCO_3 type, the river water is of mixed Ca-Na-HCO_3 type, and the lake water is of Ca-HCO_3 type. The cations in the geothermal water are mainly controlled by water-rock interactions and evaporation, the anions are primarily determined by water-rock interactions, and the hydrochemical composition of the surface water is controlled by water-rock interactions. Overall, the hydrochemical processes in the water bodies of the study area are mainly controlled by the dissolution of silicate minerals.
2) The total REE content in the geothermal water is 0.306 ± 0.103 ug/L. Studies reveal that the REE contents are primarily affected by the reductive dissolution of Fe oxides/hydroxides, followed by pH.
3) The LREE/HREE and $(La/Yb)_N$ ratios of the geothermal water are 5.19–14.38 and 0.41 to 2.95, respectively, indicating the relative enrichment of LREEs. They are mainly affected by Fe oxides. In addition, the geothermal water shows positive Eu and Ce anomalies, which are caused by both the dissolution of Eh and Mn oxides and surface water. Furthermore, the water-rock interactions between the Qugasi Formation and deep geothermal water also contribute to the positive Eu anomalies.
4) According to the results of the calculation and simulation analysis using the Visual MINTEQ 3.0 software, the complex species of REEs in the geothermal water mainly include $Ln(CO_3)_2^-$, $LnCO_3^+$, and $LnOH^{2+}$. This finding is roughly consistent with the complex species of REEs in alkaline water and is caused by the stability constants of complexation reactions.

DATA AVAILABILITY STATEMENT

The original contributions presented in the study are included in the article/Supplementary Material, further inquiries can be directed to the corresponding author.

AUTHOR CONTRIBUTIONS

SW: Drafting the manuscript, analysis and interpretation of data. FL: Acquisition of data. WZ: Analysis and interpretation of data. HZ: Acquisition of data. RY: Verify data. YL: Participate in mapping. XY: Check the manuscript.

FUNDING

This study was financially supported by the grants from the geothermal survey project of the China Geological Survey (Grant No. DD20190128) and basic Research Operations Project of the Institute of Hydrogeology and Environmental Geology, Chinese Academy of Geological Sciences (SK202212).

REFERENCES

Barrat, J. A., Boulègue, J., Tiercelin, J. J., and Lesourd, M. (2000). Strontium Isotopes and Rare-Earth Element Geochemistry of Hydrothermal Carbonate Deposits from Lake Tanganyika, East Africa. *Geochimica et Cosmochimica Acta* 64 (2), 287–298. doi:10.1016/s0016-7037(99)00294-x

Byrne, R. H., and Sholkovitz, E. R. (1996). "Chapter 158 Marine Chemistry and Geochemistry of the Lanthanides," in *Handbook on the Physics and Chemistry of Rare Earth*. Editors K. A. Gschneidner and L. Eyring (Amsterdam: Elsevier), 497–593. doi:10.1016/s0168-1273(96)23009-0

Cao, R. W., Zhou, X., Chen, B. H., and Li, Z. (2021). Hydrogeochemical Characteristics and Genetic Analysis of the Chaluo hot springs and Geysers in the Batang County of Sichuan Province. *Earth Sci. Front.* 28 (4), 361–372. doi:10.13745/j.esf.sf.2020.6.35

Coppin, F., Berger, G., Bauer, A., Castet, S., and Loubet, M. (2002). Sorption of Lanthanides on Smectite and Kaolinite. *Chem. Geology.* 182 (1), 57–68. doi:10.1016/s0009-2541(01)00283-2

Dewey, B. J. F., Shackleton, R. M., Chang, C. F., and Sun, Y. Y. (1988). The Tectonic Evolution of the Tibetan Plateau. *Phil Trans. R. Soc. Lond.* 327, 379–413.

Dia, A., Gruau, G., Olivié-Lauquet, G., Riou, C., Molénat, J., and Curmi, P. (2000). The Distribution of Rare Earth Elements in Groundwaters: Assessing the Role

of Source-Rock Composition, Redox Changes and Colloidal Particles. *Geochimica et Cosmochimica Acta* 64 (24), 4131–4151. doi:10.1016/s0016-7037(00)00494-4

Dong, L. X., Jiang, Y. B., Zhang, H. Y., Ji, H. B., Wu, Y. K., Wang, P., et al. (2017). Geochemistry of Dissolved Rare Earth Elements in Watershed at Northern Mount Huangshan Landscape. *J. Chin. Soc Rare Earth* 35 (2), 283–293. doi:10.11785/S1000-4343.20170216

Elderfield, H., Upstill-Goddard, R., and Sholkovitz, E. R. (1990). The Rare Earth Elements in Rivers, Estuaries, and Coastal Seas and Their Significance to the Composition of Ocean Waters. *Geochimica et Cosmochimica Acta* 54 (4), 971–991. doi:10.1016/0016-7037(90)90432-k

Fan, L. J., Zou, S. Z., Xie, Q. L., Lu, L., Lin, Y. S., and Pei, J. G. (2021). Rare Earth Element Geochemical Characteristics of Karst Groundwater in Heqing Basin, Yunnan Province. *J. Chin. Soc Rare Earth* 39 (5), 805–815. doi:10.11785/S1000-4343.20210514

Fan, Y., Pang, Z., Liao, D., Tian, J., Hao, Y., Huang, T., et al. (2019). Hydrogeochemical Characteristics and Genesis of Geothermal Water from the Ganzi Geothermal Field, Eastern Tibetan Plateau. *Water* 11 (8), 1631. doi:10.3390/w11081631

Fu, G. H., and Yin, J. C. (2009). A Study on the Distribution and General Mechanism about the Hot spring as Well as Tourism Development in Ganzi of Sichuan Province. *J. Northwest. Univ. (Nat Sci. Ed.* 1, 148–154. doi:10.16152/j.cnki.xdxbzr.2009.01.047

Gibbs, R. J. (1970). Mechanisms Controlling World Water Chemistry. *Science* 170, 1088–1090. doi:10.1126/science.170.3962.1088

Göb, S., Loges, A., Nolde, N., Bau, M., Jacob, D. E., and Markl, G. (2013). Major and Trace Element Compositions (Including REE) of mineral, thermal, Mine and Surface Waters in SW Germany and Implications for Water-Rock Interaction. *Appl. Geochem.* 33, 127–152. doi:10.1016/j.apgeochem.2013.02.006

Goldstein, S. J., and Jacobsen, S. B. (1988). Rare Earth Elements in River Waters. *Earth Planet. Sci. Lett.* 89 (1), 35–47. doi:10.1016/0012-821x(88)90031-3

Gruau, G., Dia, A., Olivié-Lauquet, G., Davranche, M., and Pinay, G. (2004). Controls on the Distribution of Rare Earth Elements in Shallow Groundwaters. *Water Res.* 38 (16), 3576–3586. doi:10.1016/j.watres.2004.04.056

Guo, H., Zhang, B., Wang, G., and Shen, Z. (2010). Geochemical Controls on Arsenic and Rare Earth Elements Approximately along a Groundwater Flow Path in the Shallow Aquifer of the Hetao Basin, Inner Mongolia. *Chem. Geol.* 270 (1-4), 117–125. doi:10.1016/j.chemgeo.2009.11.010

Guo, Y., Wei, J. C., Gui, H., Zhang, Z., and Hu, M. (2020). Evaluation of Changes in Groundwater Quality Caused by a Water Inrush Event in Taoyuan Coal Mine, China. *Environ. Earth Sci.* 79 (24), 1–15. doi:10.1007/s12665-020-09243-5

Haley, B. A., Klinkhammer, G. P., and McManus, J. (2004). Rare Earth Elements in Pore Waters of marine Sediments. *Geochimica et Cosmochimica Acta* 68 (6), 1265–1279. doi:10.1016/j.gca.2003.09.012

Haskin, L. A., Haskin, M. A., Frey, F. A., and Wildeman, T. R. (1968). Relative and Absolute Terrestrial Abundances of the Rare Earths. *Origin and Distribution of the Elements*, 889–912. doi:10.1016/b978-0-08-012835-1.50074-x

Hederson, P. (1984). "General Geochemical Properities and Abundances of Rare Earth Elements," in *Rare Earth Element Geochemistry*. Editor P. Henderson (Amsterdam: Elsevier), 1–32.

Johannesson, K. H., Stetzenbach, K. J., and Hodge, V. F. (1997). Rare Earth Elements as Geochemical Tracers of Regional Groundwater Mixing. *Geochimica et Cosmochimica Acta* 61 (17), 3605–3618. doi:10.1016/s0016-7037(97)00177-4

Koeppenkastrop, D., and De Carlo, E. H. (1992). Sorption of Rare-Earth Elements from Seawater onto Synthetic mineral Particles: An Experimental Approach. *Chem. Geol.* 95 (3-4), 251–263. doi:10.1016/0009-2541(92)90015-w

Kynicky, J., Smith, M. P., and Xu, C. (2012). Diversity of Rare Earth Deposits: the Key Example of China. *Elements* 8 (5), 361–367. doi:10.2113/gselements.8.5.361

Lee, J. H., and Byrne, R. H. (1992). Examination of Comparative Rare Earth Element Complexation Behavior Using Linear Free-Energy Relationships. *Geochimica et Cosmochimica Acta* 56, 1127–1137. doi:10.1016/0016-7037(92)90050-s

Lee, S.-G., Lee, D.-H., Kim, Y., Chae, B.-G., Kim, W.-Y., and Woo, N.-C. (2003). Rare Earth Elements as Indicators of Groundwater Environment Changes in a Fractured Rock System: Evidence from Fracture-Filling Calcite. *Appl. Geochem.* 18 (1), 135–143. doi:10.1016/s0883-2927(02)00071-9

Leybourne, M. I., Goodfellow, W. D., Boyle, D. R., and Hall, G. M. (2000). Rapid Development of Negative Ce Anomalies in Surface Waters and Contrasting REE Patterns in Groundwaters Associated with Zn-Pb Massive Sulphide Deposits. *Appl. Geochem.* 15 (6), 695–723. doi:10.1016/s0883-2927(99)00096-7

Li, J., Yang, G., Sagoe, G., and Li, Y. (2018). Major Hydrogeochemical Processes Controlling the Composition of Geothermal Waters in the Kangding Geothermal Field, Western Sichuan Province. *Geothermics* 75, 154–163. doi:10.1016/j.geothermics.2018.04.008

Li, X., Huang, X., Liao, X., and Zhang, Y. (2020). Hydrogeochemical Characteristics and Conceptual Model of the Geothermal Waters in the Xianshuihe Fault Zone, Southwestern China. *Ijerph* 17 (2), 500. doi:10.3390/ijerph17020500

Liu, H., Guo, H., Xing, L., Zhan, Y., Li, F., Shao, J., et al. (2016). Geochemical Behaviors of Rare Earth Elements in Groundwater along a Flow Path in the North China Plain. *J. Asian Earth Sci.* 117, 33–51. doi:10.1016/j.jseaes.2015.11.021

Liu, H. Y. (2018). *Distribution of Groundwater Rare Earth Elements in the Typical Region of the North China Plain and Modeling Study on Their Complexation with Iron and Manganese*. Beijing: China University of Geosciences.

Liu, H. Y., Liu, M. H., Zhang, W. M., Sun, Z. X., Wang, Z., Wu, T. H., et al. (2021). Distribution and Fractionation of Rare Earth Elements in High-Fluoride Groundwater from the North China Plain. *Earth Sci. Front* 117, 1–16. doi:10.13745/j.esf.sf.2021.7.24

Luo, L., L. (1994). Inquisition of the Distribution and Cause of the Hot Springs in Western Sichuan. *J. Chongqing Teach. Coll. (Nat Sci. Ed.* 11 (2), 39–47.

Luo, Y.-R., and Byrne, R. H. (2004). Carbonate Complexation of Yttrium and the Rare Earth Elements in Natural Waters. *Geochimica et Cosmochimica Acta* 68, 691–699. doi:10.1016/s0016-7037(03)00495-2

Luo, Y.-R., and Byrne, R. H. (2001). Yttrium and Rare Earth Element Complexation by Chloride Ions at 25°C. *J. Solution Chem.* 30 (9), 837–845. doi:10.1023/a:1012292417793

Markert, B., and Deli, Z. (1991). Natural Background Concentrations of Rare-Earth Elements in a forest Ecosystem. *Sci. Total Environ.* 103 (1), 27–35. doi:10.1016/0048-9697(91)90350-n

Ménager, M., Menet, C., Petit, J., Cathelineau, M., and Côme, B. (1992). Dispersion of U, Th, and REE by Water-Rock Interaction Around an Intragranitic U-Vein, Jalerys Mine, Morvan, France. *Appl. Geochem.* 7, 239–252.

Millero, F. J. (1992). Stability Constants for the Formation of Rare Earth-Inorganic Complexes as a Function of Ionic Strength. *Geochimica et Cosmochimica Acta* 56, 3123–3132. doi:10.1016/0016-7037(92)90293-r

Möller, P. (2000). "Rare Earth Elements and Yttrium as Geochemical Indicators of the Source of mineral and thermal Waters," in *Hydrogeology of Crystalline Rocks*. Editors I. Stober and K. Bucher (Dordrecht, Netherlands: Kluwer Academic Publishers), 227–246.

Moon, S., Huh, Y., Qin, J., and van Pho, N. (2007). Chemical Weathering in the Hong (Red) River basin: Rates of Silicate Weathering and Their Controlling Factors. *Geochimica et Cosmochimica Acta* 71 (6), 1411–1430. doi:10.1016/j.gca.2006.12.004

Noack, C. W., Dzombak, D. A., and Karamalidis, A. K. (2014). Rare Earth Element Distributions and Trends in Natural Waters with a Focus on Groundwater. *Environ. Sci. Technol.* 48, 4317–4326. doi:10.1021/es4053895

Piper, A. M. (1994). A Graphic Procedure in the Geochemical Interpretation of Water-Analyses. *T-am Geophys. Union* 25, 914–928.

Royden, L. H., Burchfiel, B. C., and van der Hilst, R. D. (2008). The Geological Evolution of the Tibetan Plateau. *Science* 321, 1054–1058. doi:10.1126/science.1155371

Sanada, T., Takamatsu, N., and Yoshiike, Y. (2006). Geochemical Interpretation of Long-Term Variations in Rare Earth Element Concentrations in Acidic Hot spring Waters from the Tamagawa Geothermal Area, Japan. *Geothermics* 35 (2), 141–155. doi:10.1016/j.geothermics.2006.02.004

SBGMR (Bureau of Geology and Mineral Resource of Sichuan Province) (1991). *Regional Geology of Sichuan Province*. Beijing: Geological Publishing House.

Schijf, J., and Byrne, R. H. (2004). Determination of SO4β1 for Yttrium and the Rare Earth Elements at I = 0.66 M and T = 25°C-Implications for YREE Solution Speciation in Sulfate-Rich Waters. *Geochimica et Cosmochimica Acta* 68 (13), 2825–2837. doi:10.1016/j.gca.2003.12.003

Tang, J., and Johannesson, K. H. (2010). Rare Earth Elements Adsorption onto Carrizo Sand: Influence of strong Solution Complexation. *Chem. Geology.* 279, 120–133. doi:10.1016/j.chemgeo.2010.10.011

Tang, X., Zhang, J., Pang, Z., Hu, S., Tian, J., and Bao, S. (2017). The Eastern Tibetan Plateau Geothermal belt, Western China: Geology, Geophysics, Genesis, and Hydrothermal System. *Tectonophysics* 717, 433–448. doi:10.1016/j.tecto.2017.08.035

Tong, W., and Zhang, M. T. (1989). *Geothermal Resources in Tengchong*. Beijing: Science Press.

Tong, W., Zhang, M. T., Zhang, Z. F., Liao, Z. J., You, M. Z., Zhu, M. X., et al. (1981). *Geothermal Resources in Tibet*. Beijing: Science Press.

Tweed, S. O., Weaver, T. R., Cartwright, I., and Schaefer, B. (2006). Behavior of Rare Earth Elements in Groundwater during Flow and Mixing in Fractured Rock Aquifers: an Example from the Dandenong Ranges, Southeast Australia. *Chem. Geol.* 234 (3), 291–307. doi:10.1016/j.chemgeo.2006.05.006

Wang, H. Y. (2017). *Geological Characteristics Study of the Qugasi Formation in Baisong-Bendu Area, Sichuan Province*. Chengdu: Chengdu University of Technology.

Wang, Z., Guo, H. M., Xing, S. P., and Liu, H. Y. (2021). Hydrogeochemical and Geothermal Controls on the Formation of High Fluoride Groundwater. *J. Hydrol.* 598. doi:10.1016/j.jhydrol.2021.126372

Wood, S. A., and Shannon, W. M. (2003). Rare-earth Elements in Geothermal Waters from Oregon, Nevada, and California. *J. Solid State. Chem.* 171 (1), 246–253. doi:10.1016/s0022-4596(02)00160-3

Wood, S. A. (1990). The Aqueous Geochemistry of the Rare-Earth Elements and Yttrium. *Chem. Geology.* 82, 159–186. doi:10.1016/0009-2541(90)90080-q

Xie, X. J., Wang, Y. X., Li, J. X., Su, C. L., Wu, Y., Yu, Q., et al. (2012). Characteristics and Implications of Rare Earth Elements in High Arsenic Groundwater from the Datong Basin. *Earth Sci-j China Univ. Geosci.* 37 (2), 381–390.

Xu, X. W., Zhang, P. Z., Wen, X. Z., Qin, Z. L., Chen, G. H., and Zhu, A. L. (2005). Characteristics of Active Tectonics and Models of Earthquake Recurrence in Western Sichuan. *Seismol Geol.* 27 (3), 446–461.

Xu, Z. Q., Hou, L. W., Wang, Z. X., Fu, X. F., and Huang, M. H. (1992). *Orogeic Processes of the Songpan-Ganze Orogenic belt of China*. Beijing: Geological Publishing House.

Xu, Z. Q., Yang, J. S., Li, H. B., Ji, S. C., Zhang, Z. M., and Liu, Y. (2011). On the Tectonics of the India-Asia Collision. *Acta Geol. Sin* 85 (1), 1–33.

Yan, B., and Lin, A. (2015). Systematic Deflection and Offset of the Yangtze River Drainage System along the Strike-Slip Ganzi-Yushu-Xianshuihe Fault Zone, Tibetan Plateau. *J. Geodynamics* 87, 13–25. doi:10.1016/j.jog.2015.03.002

Yuan, J. F., Deng, G. S., Xu, F., Tang, Y. Q., and Li, P. Y. (2017). Hydrogeochemical Characteristics of Groundwater in the Xide Geothermal Field, Southwest Sichuan, China. *Geoscience* 31 (1), 200–208.

Zhang, F. Y., Lai, S. C., and Qin, J. F. (2018c). Petrogenesis and Geological Significance of the Late Cretaceous Haizishan Monzogranite from the Yidun Island Arc. *Geol. J. China Univ.* 24 (3), 340–352. doi:10.16108/j.issn1006-7493.2017129

Zhang, Jian., Li, W. Y., Tang, X. C., Tian, J., Wang, Y. C., Guo, Q., et al. (2017a). Geothermal Data Analysis at the High-Temperature Hydrothermal Area in Western Sichuan. *Sci. China Earth Sci.* 47 (8), 899–915. doi:10.1007/s11430-016-9053-2

Zhang, K., Zhang, Y., Tang, X., and Xia, B. (2013). Late Mesozoic Tectonic Evolution and Growth of the Tibetan Plateau Prior to the Indo-Asian Collision. *Earth-sci Rev.* 114 (3-4), 236–249.

Zhang, W. (2020). *The Formation and Geochemical Response Mechanism of Medium-High Temperature Geothermal System in Western Sichuan*. Beijing: Chinese Academy of Geological Sciences.

Zhang, W., Wang, G., Xing, L., Li, T., and Zhao, J. (2019). Geochemical Response of Deep Geothermal Processes in the Litang Region, Western Sichuan. *Energy Exploration & Exploitation* 37 (2), 626–645. doi:10.1177/0144598718812550

Zhang, Y.-Z., Replumaz, A., Leloup, P. H., Wang, G.-C., Bernet, M., van der Beek, P., et al. (2017b). Cooling History of the Gongga Batholith: Implications for the Xianshuihe Fault and Miocene Kinematics of SE Tibet. *Earth Planet. Sci. Lett.* 465, 1–15. doi:10.1016/j.epsl.2017.02.025

Zhang, Y. H. (2018b). *Research on Genesis and Development of the Geothermal System in the Kangding-Moxi Segment of the Xianshuihe Fault*. Chengdu: Chengdu University of Technology.

Zhang, Y., Xu, M., Li, X., Qi, J., Zhang, Q., Guo, J., et al. (2018a). Hydrochemical Characteristics and Multivariate Statistical Analysis of Natural Water System: A Case Study in Kangding County, Southwestern China. *Water* 10 (1), 80. doi:10.3390/w10010080

Zhao, J. Y., Zhao, W., Zhang, H. X., Qu, Z. W., Li, M., and Yue, G. F. (2019a). Hydrogeochemical Characteristics and Genesis of the Geothermal fields in Batang of Sichuan. *Hydrogeol Eng. Geol.* 46 (4), 81–89. doi:10.16030/j.cnki.issn.1000-3665.2019.04.11

Zhao, Y. Y., Li, S. Z., Li, D., Guo, L. L., Dai, L. M., and Tao, J. L. (2019b). Rare Earth Element Geochemistry of Carbonate and its Paleoenvironmental Implications. *Geotectonica et Metallogenia* 43 (1), 141–167. doi:10.16539/j.ddgzyckx.2019.01.011

Zhu, Z. Z. (2006). *The Geochimal Character and Environmental Effect of Rare Earth Elements in Lakes, Upper and Lower Reaches of Yangtze River, China*. Guiyang: Institute of Geochemistry Chinese Academy of Sciences.

Conflict of Interest: The authors declare that the research was conducted in the absence of any commercial or financial relationships that could be construed as a potential conflict of interest.

Publisher's Note: All claims expressed in this article are solely those of the authors and do not necessarily represent those of their affiliated organizations, or those of the publisher, the editors and the reviewers. Any product that may be evaluated in this article, or claim that may be made by its manufacturer, is not guaranteed or endorsed by the publisher.

frontiers | Frontiers in Earth Science

ORIGINAL RESEARCH
published: 26 April 2022
doi: 10.3389/feart.2022.898414

Occurrence Mechanism of Convective Geothermal Systems in Jiaodong Peninsula, China

Meng Shi[1], *Fengxin Kang*[2,3,4,5]*, *Tao Yin*[1], *Song Gao*[1], *Haibo Sui*[4,6], *Xu Guo*[1] *and Xiaojing Yu*[1]

[1]Shandong No. 3 Exploration Institute of Geology and Mineral Resources, Yantai, China, [2]Shandong Provincial Bureau of Geology and Mineral Resources (SPBGM), Jinan, China, [3]Shandong University of Science and Technology, Qingdao, China, [4]Shandong Provincial Research Center of Geothermal Resources, Dezhou, China, [5]Shandong Provincial Research Center of Groundwater Conservation and Restoration, Jinan, China, [6]801 Hydrogeological and Engineering Geological Institute of SPBGR, Jinan, China

Previous studies have shown that on the surface, Jiaobei uplift and Weihai uplift have higher heat flow values than Jiaolai depression. However, the mechanism by which the deep heat flow migrates and the exposure of geothermal resources are still unclear. In this study, the geothermal field distribution, thermal conductivity, temperature logging data, and chemical composition of the geothermal fluid in the Jiaodong Peninsula were analyzed. Regarding the thermal field's characteristics and their controlling factors, a conceptual model of heat flow diversion-accumulation between the uplift and basin areas in the Jiaodong Peninsula is proposed. The lithology of the uplift area is mainly composed of intrusive rocks and metamorphic rocks with high thermal conductivities. The lithology of the basin mainly consists of sandstone with a low thermal conductivity. The bottom of the basin, which has a low thermal conductivity and low permeability, serves as a heat insulation and water insulation roof, which causes the heat flow and the heat-carrying fluids and gases from the deep crust to be refracted and redistributed at the bottom of the basin area. As a result, the bottom of the uplift areas has a higher heat flow. In particular, the axial position in the uplift area has the highest heat flow. In addition, the geothermal resources in the Jiaodong Peninsula are mainly distributed in the V-shaped area where the upper block of the NE- and NW-trending faults intersect, and the scope of the exposure of the geothermal resources is very limited.

Keywords: Jiaodong Peninsula, uplift and basin, refraction and redistribution, V-shaped area, heat flow accumulation

OPEN ACCESS

Edited by:
Wenjing Lin,
Chinese Academy of Geological Sciences, China

Reviewed by:
Bo Feng,
Jilin University, China
Shengbiao Hu,
Institute of Geology and Geophysics (CAS), China

***Correspondence:**
Fengxin Kang
kangfengxin@126.com

Specialty section:
This article was submitted to Structural Geology and Tectonics, a section of the journal Frontiers in Earth Science

Received: *17 March 2022*
Accepted: *04 April 2022*
Published: *26 April 2022*

Citation:
Shi M, Kang F, Yin T, Gao S, Sui H, Guo X and Yu X (2022) Occurrence Mechanism of Convective Geothermal Systems in Jiaodong Peninsula, China. Front. Earth Sci. 10:898414. doi: 10.3389/feart.2022.898414

INTRODUCTION

Geothermal resources can be considered to be renewable on the time scales of technological systems and do not require geological time scales to regenerate, as fossil fuel reserves do (coal, oil, and gas) (Rybach et al., 1999; Rybach et al., 2000). Compared with traditional fossil fuel energy, geothermal resources have obvious advantages, and various countries have accelerated the exploration and utilization of geothermal resources (Sanyal, 2004; Kang, 2013). Analyzing the thermal structure and heat flow transfer mechanism of the Earth can provide a better understanding of the formation mechanism of geothermal resources and help guide us in the exploration of geothermal resources. Low-medium temperature convective geothermal systems are widely distributed in China, especially in the eastern coastal area affected by plate collisions. This area has no additional heat source, such as

intrusions, and these resources are mainly distributed in fracture zones with a normal or slightly higher thermal background. Although the Jiaodong Peninsula is rich in geothermal resources, in the actual geothermal exploration process, the exploration failure rate is high. As early as the 1880s, Chinese scholars began systematically studying the geothermal heat flow and the occurrence mechanism of geothermal resources using numerical simulations to simulate the geothermal temperature field, and they proposed the refraction and redistribution of terrestrial heat flow (Xiong and Gao, 1982; Zhang et al., 1982; Xiong and Zhang, 1984). Xie and Yu (1988) summarized the temperature field characteristics of the Sichuan Basin using temperature data from 460 wells in the Sichuan Basin, and they found that the temperature in the uplift region at the interface between the marine stratum and the continental stratum is higher, while the temperature in thee depressions is lower, and thus, the structure determines the location of the geothermal resources. This is because the uplift and basin in the same tectonic zone have different structural forms. This difference causes the heat flow to redistribute in each layer Chen et al. (1990) explored the relationship between the geothermal and geological structures and the tectonic-thermal evolution using the temperature and terrestrial heat flow data for the North China Basin. Hu and Wang (1994) conducted a comprehensive study of the terrestrial heat flow characteristics of many orogenic belts using 125 reliable datasets from south-eastern China. They found that the heat flow distribution was significantly affected by the thermal conductivity structure of the shallow crust. They investigated the effects of the thermal properties of the rocks and the fracture development on the current temperature field.

Based on previous research results, in this study, the regional geology and structure, geothermal reservoir, wellbore temperature data and temperature field, different thermal properties of the rocks, and fluid chemistry of the geothermal systems in the Jiaodong Peninsula were analyzed. In this study, the occurrence mechanism of the geothermal resources and the characteristics of and relationships between the temperature fields in the Jiaobei uplift, the Jiaolai basin, and the Weihai uplift were systematically investigated. A V-shaped structural control and thermal conductivity model, a heat flow model, and a conceptual model suitable for the Jiaodong Peninsula were developed. These results can be used to guide geothermal exploration in the Jiaodong Peninsula, thereby increasing the success rate of geothermal resource exploration.

GEOLOGICAL AND RESERVOIR TEMPERATURE BACKGROUND

Geological and Tectonic Setting

The Jiaodong Peninsula is located on the eastern margin of the North China Craton, in the Pacific Ocean tectonic area, and it is part of the Pacific Rim tectonic-magmatic belt (**Figure 1**) (Chen, 2009; Qiu et al., 2014). In addition to the wide distribution of geothermal resources, the gold resources in the Jiaodong Peninsula are extensive. The most important common feature of the geothermal resources and gold resources is that they are both controlled by the regional faults. The widely distributed regional faults not only provide the tectonic space and migration channels for the gold deposits (Lv et al., 2015), but they also provide a channel for the deep migration and upward-flow of geothermal liquids (Jin et al., 1999). Previous studies on the mineralization mechanism of the gold resources investigated the basic geology and structure of the Jiaodong Peninsula in detail, providing detailed geological data for the study of the heat flow related to the geothermal resources in the Jiaodong Peninsula.

The study area has many medium-intensity intrusive rocks related to the oceanic subduction from the Jurassic to the Early Cretaceous (Liu et al., 2018). The dikes are very well developed. The intrusive rocks were formed in different periods, with an average density of 10 intrusions per km^2. There was no obvious mixing of crustal material during their ascent. They originated from the lithospheric mantle rather than the asthenosphere mantle (Tan et al., 2006).

The crystalline basement of the platform in this area was formed in the Archean-Proterozoic. The sedimentary caprock of the platform was formed in the Paleozoic. Before this period, the Jiaodong Peninsula was a stable continental block, and the terrestrial heat flow was low. The destruction of the North China Craton (NCC) and the lithospheric thinning had not yet occurred (Lin et al., 2013; He, 2015; Hu et al., 2021). The Late Mesozoic destruction of the eastern NCC and the accompanying magmatism were controlled by prolonged thermomechanical-chemical erosion due to low-angle subduction, steepening, and rollback of the Paleo-Pacific Oceanic lithosphere (Liang et al., 2020). The Mesozoic and Cainozoic era were important stages of intense crustal activity in the Jiaodong area. In particular, during the Yanshanian, the upper mantle was strongly active, and this activity was accompanied by crustal movement, forming a series of NE-SW and NNE-SSW trending compressive-torsional faults and NW-SE trending tensional faults. These faults are considered to be secondary faults in the regional Tanlu fault zone (Mao et al., 2005). For example, the regional Muping-Jimo fault zone is an important fault that controls the boundary of the Jiaolai Basin, and its extension in the Cretaceous controlled the formation and development of the Jiaolai Basin. The Taocun Fault is inferred to be a deep-cutting fault that cuts through the Moho based on seismic detection (Pan et al., 2015). The tectonic activity and intrusive rocks determine the distribution of the tectonic units in the Jiaodong Peninsula, and they clearly divide the Jiaodong Block into three structural units: the Jiaobei uplift, Weihai uplift, and Jiaolai depression. The geology, structure, thermal properties of the rocks, and crustal structure of the three different structural units indirectly determine the geothermal background in the Jiaodong Peninsula.

It can be seen from **Figure 2** that the lithologies of the Jiaobei uplift and Weihai uplift mainly consist of Archean and Proterozoic metamorphic rocks and Mesozoic intrusive rocks. The lithology of the Jiaolai Basin is mainly Cretaceous sandstone, and the thickness of the sediments in some areas is greater than 7 km. The depth of the detachment system is 8–10 km, and it controls the origin of the Jiaolai Basin (Zhang et al., 2006). The sedimentary age of the

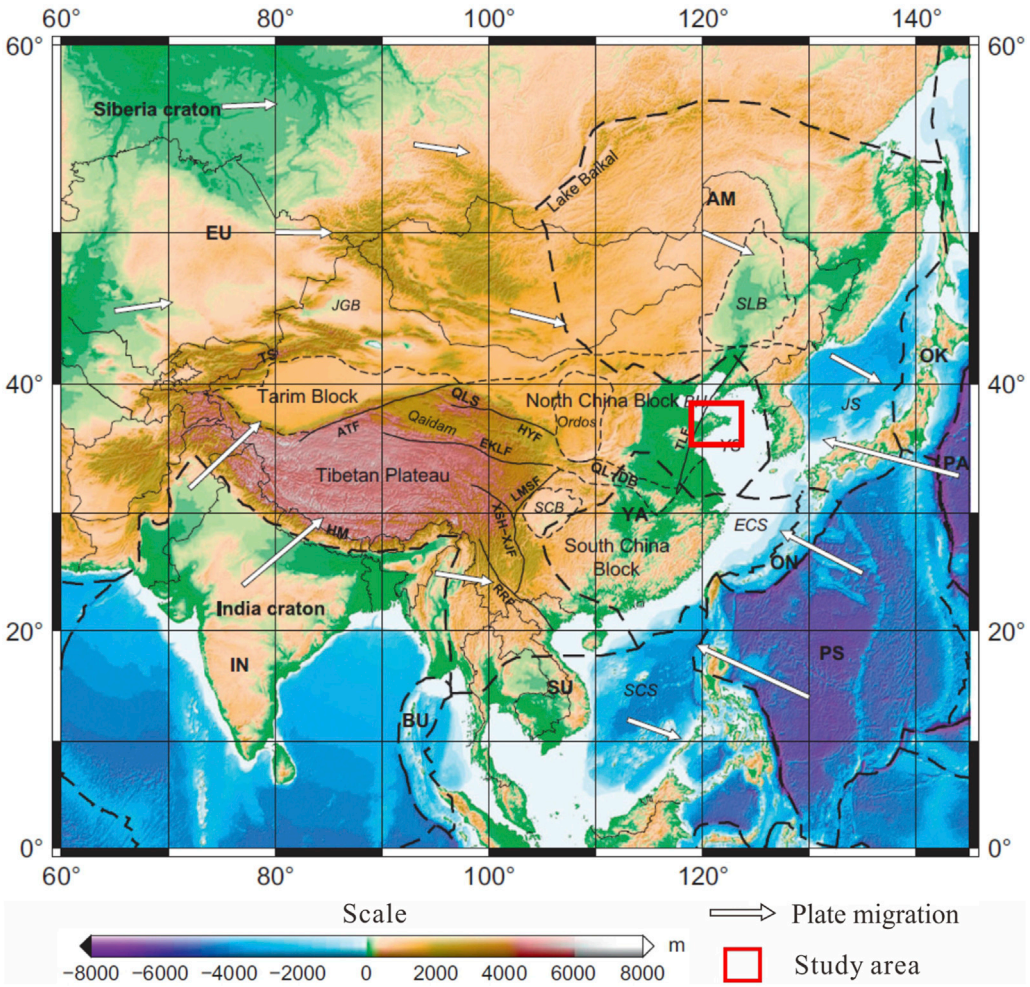

FIGURE 1 | Location of the Jiaodong Peninsula (modified from Chen et al., 2013).

Wawukuang Formation at the bottom of the Jiaolai Basin is Early Cretaceous. The source of these sediments was mainly the denudation-transport-deposition of the metamorphic rocks in the early Jiaobei uplift and Weihai uplift.

Reservoir Temperature Background Based on Silica Content

Terrestrial heat flow is considered to be an important parameter for studying the geodynamic processes of the formation and evolution of orogenic belts (Lee, 1970; Sclater and Francheteau, 2010; Majorowicz and Wybraniec, 2011). Based on heat flow data from the Precambrian shields in North America and South Africa, Jaupart and Mareschal (1999) found that large-scale variations in the bulk crustal heat production are well-documented and imply significant differences in the deep lithospheric thermal structure. In thick lithosphere, surficial heat flow measurements record the time averaged heat production in the lithospheric mantle, which is not in equilibrium with the instantaneous heat production.

In China, Hu et al. (2000) created a new compilation of heat flow data for the continental area of China, including 862 observations from different sites. The relationships between the heat flow and geological ages based on this new dataset indicate that the surface heat flow is obviously more dependent on the most recent tectonic-thermal activity than on the age of the orogeny. Different tectonic units have different heat flow backgrounds owing to their different tectonic-thermal evolutions. Terrestrial heat flow is also an important basis for understanding the regional temperature field. Based on its geothermal and geological background, the Jiaodong Peninsula lies in the high heat flow zone on the west coast of the Pacific Rim, which is the junction zone between the North China Plate and the Yangtze Plate. The structures and intrusive rocks are well developed, which provide a good channel for the formation, conduction, and storage of geothermal resources. In general, the Jiaodong Peninsula was a stable rock platform before the Mesozoic, and during this period, the terrestrial heat flow of the entire Jiaodong Peninsula was low. Since the Mesozoic, the Jiaodong Peninsula has entered a stage of

FIGURE 2 | Regional geological map of the Jiaodong Peninsula.

rift development and has begun a slow warming process. From the Late Cretaceous to the Early Tertiary, the Jiaodong Peninsula was in a higher temperature stage. Since the Late Tertiary, the temperature conditions in the Jiaodong Peninsula have gradually begun to decline, but the high geothermal background developed in the previous period has been retained (Chen et al., 1988).

The temperature field can reflect the characteristics of the heat energy in the upper crust. Studying the characteristics of the temperature field is conducive to enhancing our understanding of the distribution of the heat energy in the crust. Li et al. (1997) created a 1:200,000 heat flow contour map of the Jiaodong Peninsula based on the SiO_2 values of 578 reliable water samples from the Jiaodong Peninsula (**Figure 3**). It can be seen from **Figure 3** that the heat flow values in the Jiaobei uplift and Weihai uplift are obviously higher than those in the Jiaolai depression. The values of the silica heat flow in the uplift areas are generally greater than 60 mW/m^2, with a maximum of 85 mW/m^2, while the values in the basin are generally less than 60 mW/m^2. Compared with the geothermal heat flow of 47.15 mW/m^2 in northern China, the Jiaodong Peninsula has a higher background terrestrial heat flow, especially in the anticlinal axis of the Jiaobei uplift and Weihai uplift where the

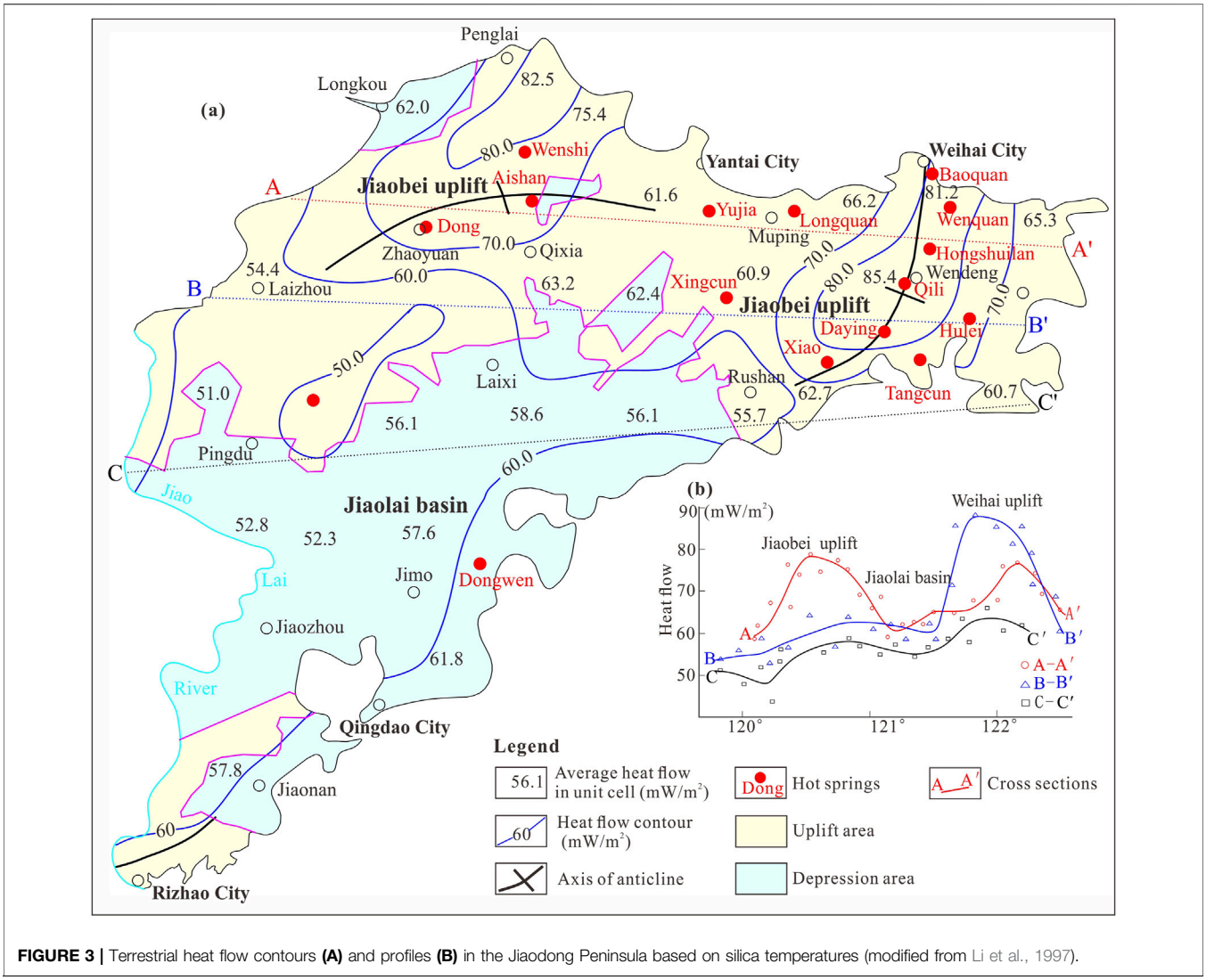

FIGURE 3 | Terrestrial heat flow contours **(A)** and profiles **(B)** in the Jiaodong Peninsula based on silica temperatures (modified from Li et al., 1997).

heat flow is the highest (>80 mW/m^2). In addition, Jiang et al. (2016) used two boreholes in Jiaodong Peninsula to calculate the heat flow in this area, and their results indicate that the Bohai Bay Basin has high heat-flow values. The regional distribution pattern of high heat flow values exhibits NE-SW and NNE-SSW trends, which is basically consistent with the strikes of the NE-SW and NNE-SSW faults in the Jiaodong Peninsula. In addition, it can be seen that the average heat flow decreases gradually with increasing distance from the anticlinal axis, and eventually, it becomes almost the same as the regional average heat flow value.

According to the temperature of natural hot springs in the Jiaodong Peninsula, it was found that the closer to the center of the axis of the uplift area, the higher the temperature of the hot springs. The Baoquan hot spring (67°C), Hongshuilan hot spring (71°C), and Qili hot spring (66°C) are located along the axis of the Weihai uplift area and have significantly higher temperatures than the Tangcun hot spring (51°C) and the Xingcun hot spring (28°C), which are located farther from the axis. The temperature of the Xingcun hot spring, which is located near the contact zone between the Jiaolai Basin and Weihai uplift, is only 30°C (**Table 1**). Based on this, there are obvious differences in the surface heat flow in the different tectonic units such as the Jiaobei uplift, Jiaolai Basin, and Weihai uplift, and the terrestrial heat flow in different regions of the same tectonic unit also vary.

DATA AND METHODS

Geological Survey, Geochemistry, and Geophysics

The Jiaodong Peninsula contains 16 hot springs. To determine the distribution of the geothermal resources, a 1:2,000 geological survey of the 16 geothermal fields was conducted, and we identified the main thermal conduction fault and water conduction fault. In addition, the reservoir channel was also identified. Geological survey and geophysical explanation methods were used to identify the locations of the faults controlling the distribution of the geothermal field. Temperature logging was used to delineate the

TABLE 1 | Wellhead temperature and SiO_2 concentration of the hot springs in the Jiaodong Peninsula.

Name of spring	Wellhead temperature (°C)	SiO_2 (mg/L)	Name of spring	Wellhead temperature (°C)	SiO_2 (mg/L)
Baoquan	67	67.69	Longquan	59	59.00
Wenquan	59	85.54	Yujia	46	69.54
Hongshuilan	71	105.00	Xingcun	28	63.77
Qili	66	105.00	Dongwen	62	82.38
Hulei	60	108.54	Aishan	52	70.77
Tangcun	51	54.85	Wenshi	54	98.69
Daying	62	58.77	Dong	81	89.62
Xiao	56	60.62	Jiudian	61	103.60

distribution range of the geothermal field, with the 25°C isotherm as the boundary of the geothermal fields (**Figures 4**, **8**).

In addition, we collected samples of the geothermal fluids from these 16 hot springs in accordance with the sampling specifications, and then, we sent the water samples to the laboratory for water quality analysis. The geochemistry data were used to calculate the reservoir temperatures of the geothermal fields (**Table 1**).

It can be seen from **Figure 4** that the lithology of the geothermal field is relatively simple, mainly including the monzogranite from the Late Yanshanian in the Mesozoic. The surface of the geothermal field is covered by the fine sand of the Yihe Formation and the coarse sand of the Linyi Formation. There are three main faults controlling the geothermal field. F1 is the main fault zone in this area. Its strike is NW-SE, its dip is NE, its inclination is 60–70°, its width is about 20 m, and there are breccia and fault mud in the fault zone, so it is a water-blocking fault F2 also strikes NW-SE. Its dip is NE, and its width is about 10 m. It is a secondary fault of the F1 fault, and the former is a water-conducting fault. F3 is a NNE-SSW-oriented compression-torsion fault, and it is a heat-conducting fault. The high-permeability fracture zone formed by the intersection of the F2 fault and F3 fault provides a channel for the upward flow of the geothermal fluids, which forms the geothermal fluid channel of the Yujia hot spring. In this study, we define the boundary of the geothermal field as the 25°C isotherm. The geothermal wells in this geothermal field are mainly distributed to the north of F2 and the west of F1, and there is no obvious geothermal anomaly in the foot walls of F1 and F3.

Temperature Logging

In past decades, to identify more geothermal fields in the Jiaodong Peninsula, many boreholes have been drilled in the geothermal field, and most of the boreholes were drilled without finding geothermal resources. In this study, we collected the temperature logs of 18 wells to estimate the temperature conditions in this area. The temperature logging was conducted at least 1 month after the completion of the drilling. Thus, the temperature was considered to be stable. **Figure 6** shows the positions of the wells in the area, and **Figure 7** shows the temperature logs with depth.

To better compare the differences between the wells in the geothermal fields and the wells outside of the geothermal fields, in **Figures 5**, **6**, we plotted the Yujia, Zhaoyuan, and Wendeng hot springs for comparison (No. 13, No. 17, and No. 18, respectively).

Three-Dimensional Geothermal Model

Leapfrog Geothermal is a 3D modeling visualization and resource management software developed by ARANZ Geo (Applied Research Associates Ltd.). It includes geoscientific input from GNS Science and meets the 3D computing needs of the geothermal industry. Leapfrog Geothermal is based on implicit modeling methods that represent the geology, structure, geophysical, and reservoir data using fitted mathematical functions. Complex geological models are built by combining measured field data, specialist interpretations, and user editing. The Leapfrog software is easy to use, and it allows the quick and efficient creation of 3D models. It is also routinely updated (Alcaraz et al., 2011; Tri et al., 2017; Wulaningsih et al., 2017).

The area of the Jiaodong Peninsula is very large, so we just take the Weihai uplift area as an example to illustrate the heat distribution of the hot springs and wells in the Jiaodong Peninsula (**Figure 7**). In **Figure 7**, the modeled area is shown by the blue square, and the faults, hot springs, and boreholes distribution are within the modeled section.

For the surface data, the 1:500,000 scale geological map was used. The faults in this area are mainly the Mishan fault, the Wenquan fault, and the Xizicheng fault, and the hot springs and borehole wellhead locations (coordinates) were also input into the Leapfrog software. The subsurface information consists of the lithology of the Weihai uplift, which is relatively simple, with a very thin Quaternary sand layer at the surface and granite below. In this area, we mainly used nine hot springs and three boreholes with temperature logs and lithology data to build the model. The boundaries of the model are listed in **Table 2**.

RESULTS

Occurrence Mechanism

The tertiary structural units in the study area mainly include the Jiaobei uplift, Jiaolai Basin, and Weihai uplift. The main structural traces include the Rushan-Weihai anticline, Qixia anticline, and Jiaolai syncline. The anticline structure is ridge-type with a narrow upper part and wide lower part, which is beneficial to the lateral migration and redistribution of geothermal fluids (Zhao et al., 2017). The overall strike of the

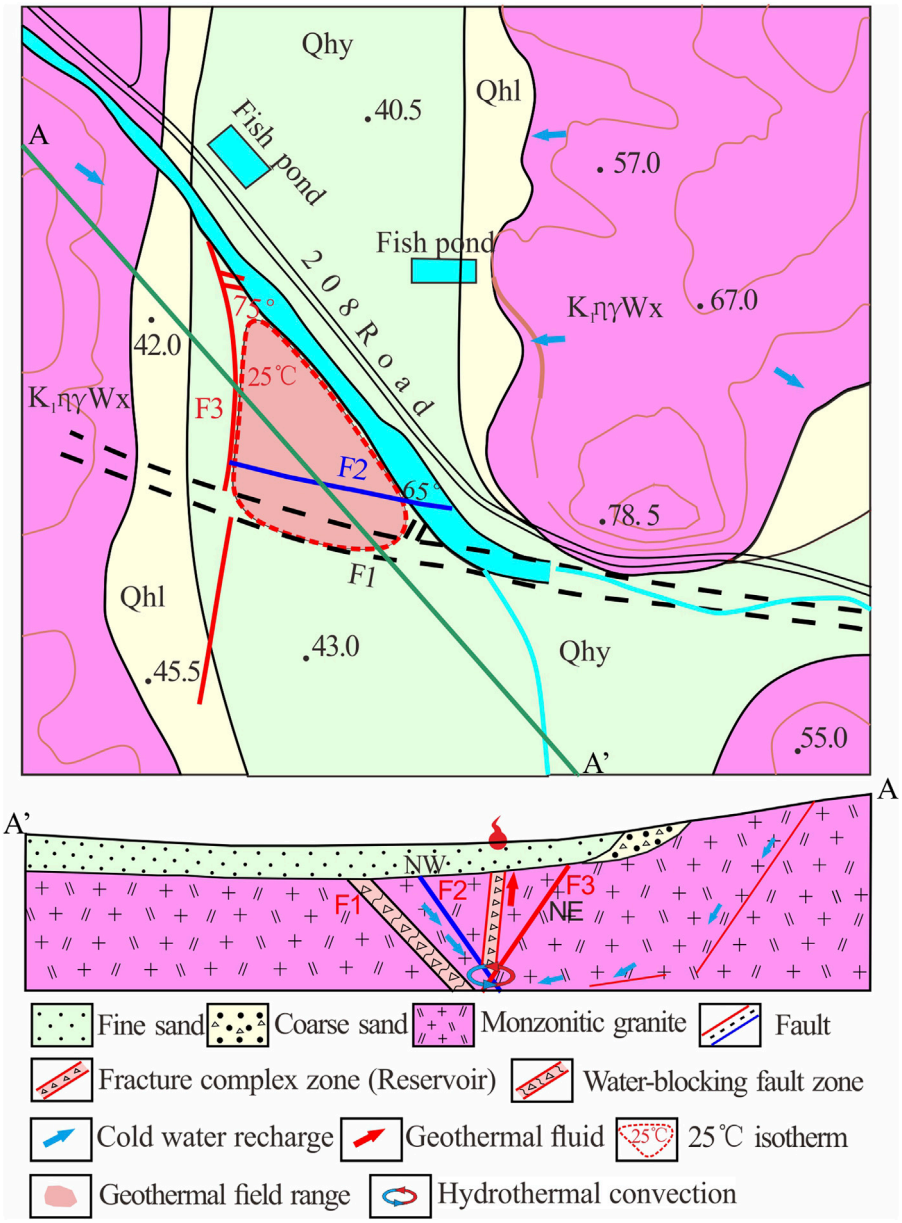

FIGURE 4 | Geologic map of the Yujia hot spring area and profile of the geothermal field.

faults is consistent with the strain at the boundary between the Eurasian Plate and Pacific Plate, which easily causes earthquakes (Chen et al., 2004). The NE-SW and NNE-SSW trending faults mainly compressive faults and torsional faults and mainly conduct heat. The NW-SE faults are mainly tensional or tensional-shear faults and mainly conduct water.

Figure 8 presents a typical geothermal field distribution map of the Jiaodong Peninsula, including the Hongshuilan, Wenshi, Daying, and Xiao hot springs, with the 25°C isotherm as the boundary of the geothermal fields. It can be seen from **Figure 8** that the distribution range of the geothermal fields, such as the Hongshuilan, Wenshi, Daying, and Xiao hot springs, are mainly distributed within the V-shaped area where the upper block of the NE- and NW-trending faults intersect. The geothermal reservoir is controlled by the NE- and NW-trending faults and has an irregular columnar shape.

It can be seen from the 1:2,000 geological geothermal survey of the 16 geothermal fields that the geothermal resources in the Jiaodong Peninsula are mainly distributed in the V-shaped area where the upper block of the NE-SW and NW-SE trending faults intersect (**Figure 8**). The geothermal reservoir is controlled by the NE-SW and NW-SE trending faults and has an irregular columnar shape. Using Visual Modflow, in this study, a V type structural control and thermal conductivity model was

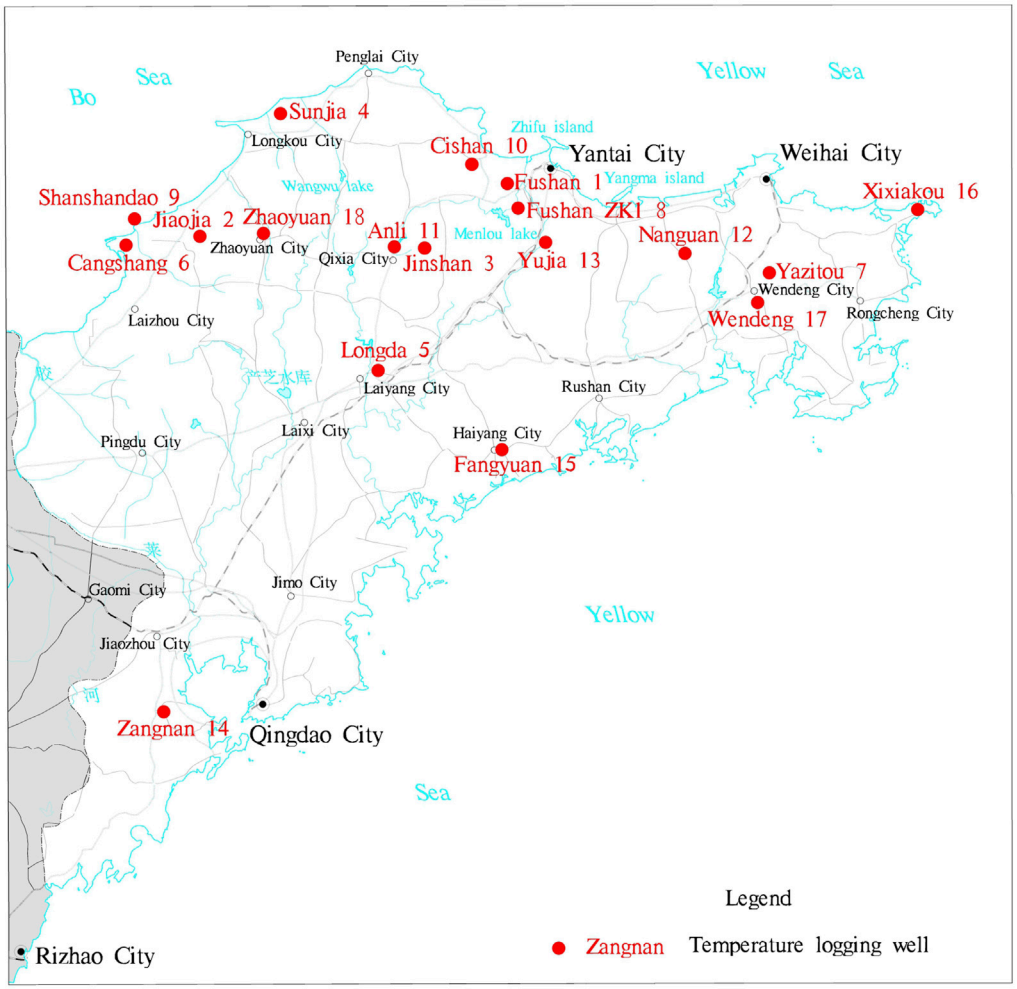

FIGURE 5 | Locations of the temperature logging wells (**Figure 6**).

developed (**Figure 9**). As can be seen from **Figure 8**, A-A' and B-B' are faults with different trends. Fault A-A' is water conducting and fault B-B' is thermal conducting. The surface water goes into the crust with the deep circulation, and when the water reaches the intersection of the water conducting and thermal conducting faults, the cool water is heating *via* heat convention. Then, the hot water flows upward along the fracture zone.

Temperature Conditions

In the Weihai uplift area, the granite is widely distributed, and the Quaternary sand layer is very thin, i.e., less than 50 m in the geothermal field. Thus, in this stratigraphic model the lithology can be divided into two layers: an upper thin sand layer and a lower granite layer. Since the sand layer is very thin compared to the granite layer, it is not possible to show the sand layer in this model. The main faults are the Mishan fault, the Wenquan fault, and the Xizicheng fault (**Figure 10**).

The temperature data were used to create a 3D temperature model, which sheds light on the importance of the major geological structures and their relationships to the heat flow (**Figure 11**).

It can be seen from **Figure 11** that in the Weihai uplift, the hot springs are mainly distributed around the Wenquan fault, and the hot springs are distributed almost on a line along it. The temperature along the Wenquan fault is much higher than in other locations in the model area. In addition, along the Wenquan fault, the temperature is the highest at the Hongshuilan hot spring (**Figure 12**).

DISCUSSION

Heat Source of Geothermal Resources in the Jiaodong Peninsula

To study the reservoir temperature characteristics of the hot springs in the Jiaodong Peninsula and to preliminarily

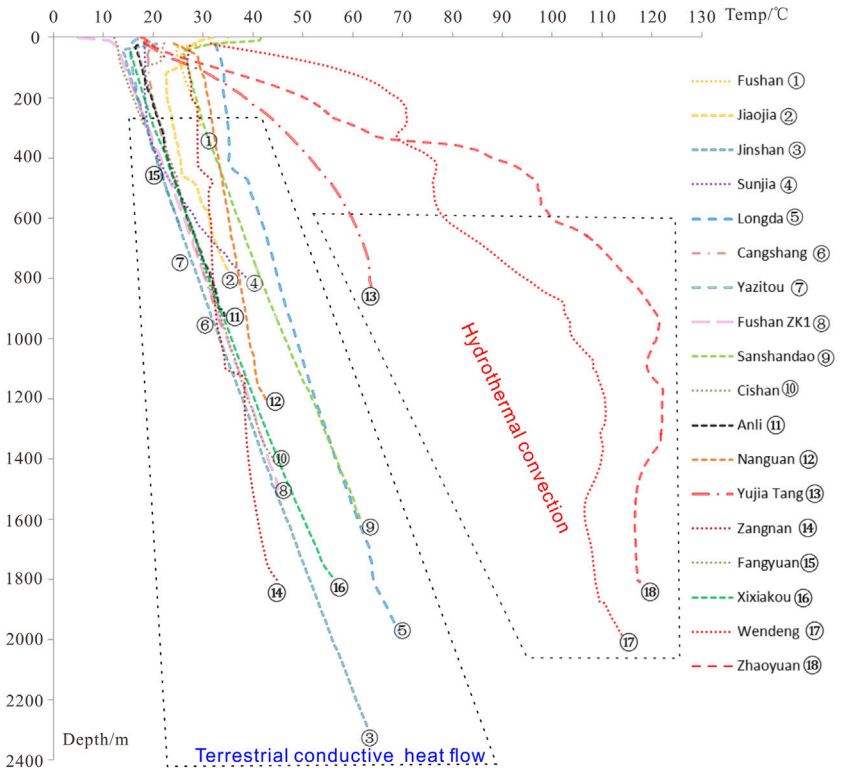

FIGURE 6 | Temperature logging curves (**Figure 5**).

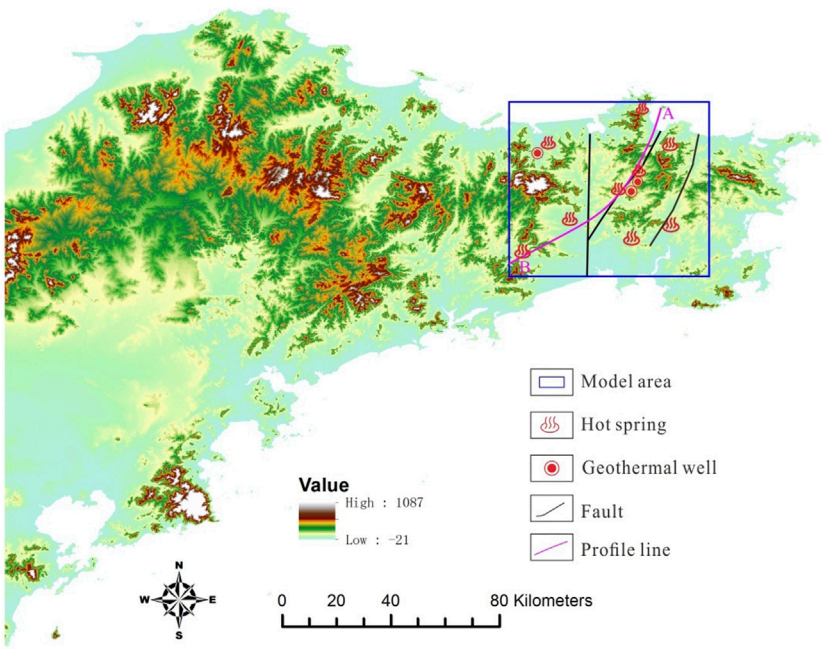

FIGURE 7 | Modeled area of the Weihai uplift.

TABLE 2 | Boundaries of the modeling area.

Items	Min	Max
X (East)	380861.6	448932.7
Y (North)	4096220.0	4154780.0

determine their temperature, geothermal fluid samples were collected from 16 natural hot springs in the Jiaodong Peninsula and the water was analyzed. Owing to the mixing of seawater, the water samples from some of the hot springs not only contained a large amount of Cl^- but also large amounts of Na^+ and K^+. The Na^+, K^+, and other cations are not easy to

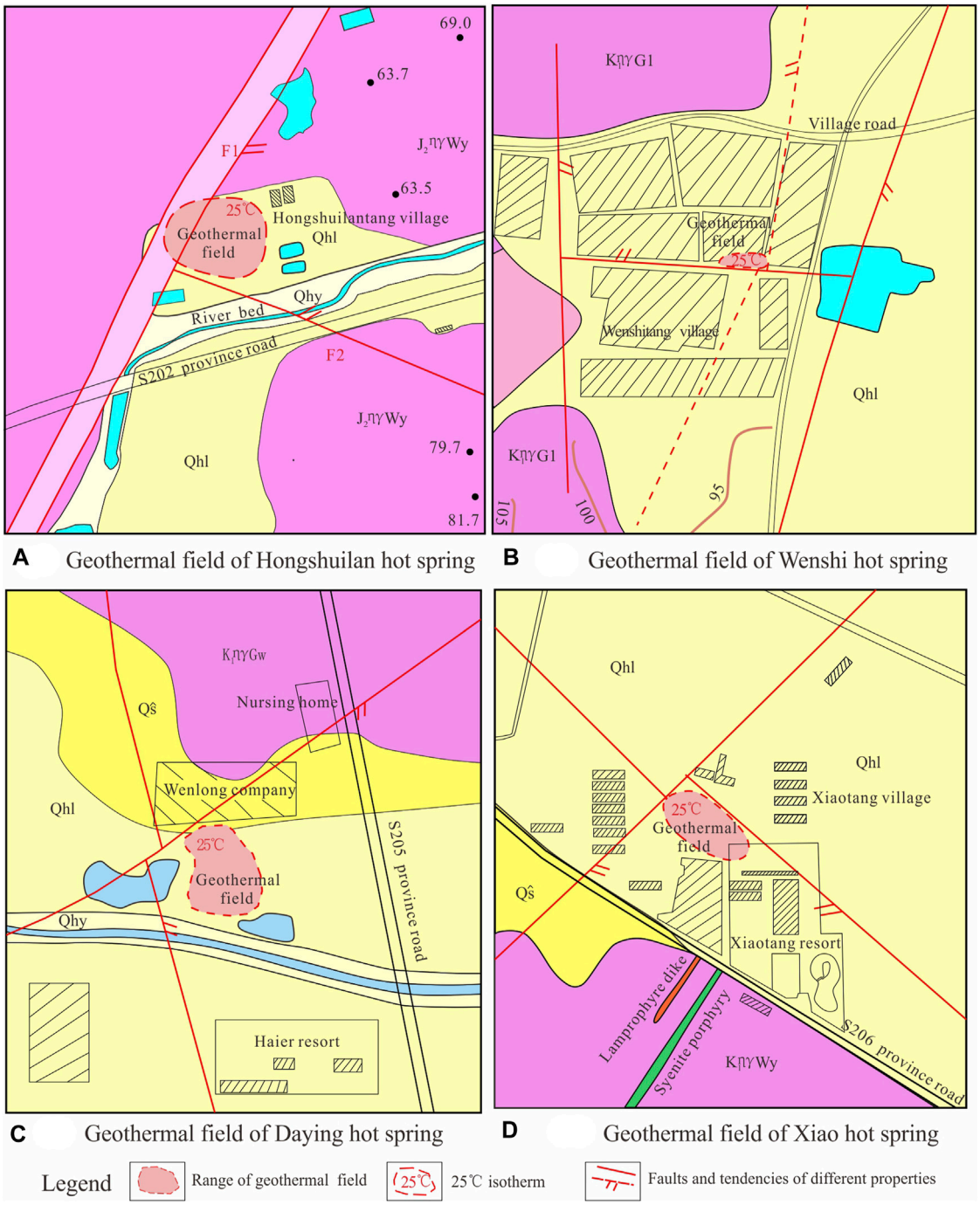

FIGURE 8 | Typical geothermal field distribution in the Jiaodong Peninsula: **(A)** Hongshuilan, **(B)** Wenshi, **(C)** Daying, and **(D)** Xiao hot springs.

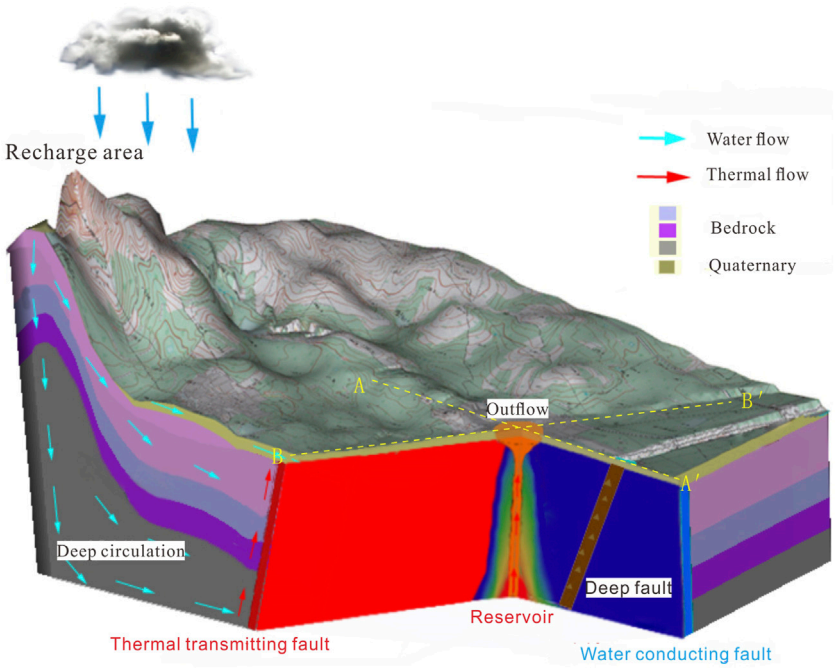

FIGURE 9 | Fracture controlled geothermal conceptual model of the Jiaodong Peninsula.

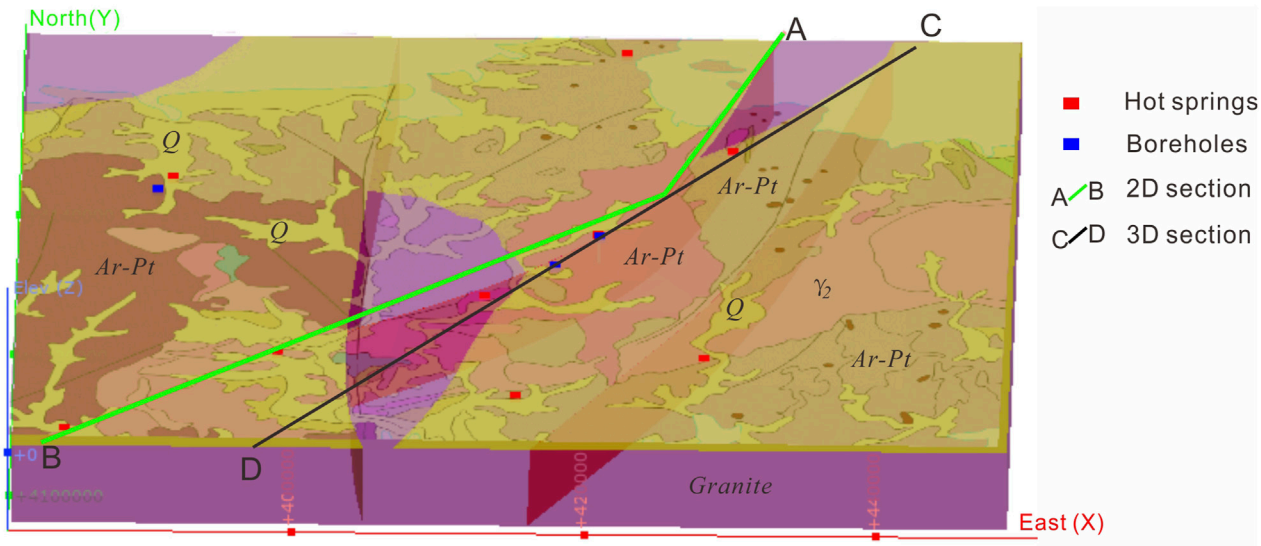

FIGURE 10 | Stratigraphic model of the Weihai uplift area (see **Figure 8**).

balance with the surrounding rock. Therefore, in this study, the cation temperature scale method could not be used and the SiO_2 temperature scale (silica temperature) was used to calculate the reservoir temperature.

The formula for calculating the reservoir temperature T (°C) based on the SiO_2 temperature scale is as follows:

$$T\,(℃) = \frac{1522}{5.75 - \log S} - 273.15$$

where S is the SiO_2 concentration of the water (mg/L).

According to the SiO_2 temperature scale, the reservoir temperature range of the hot springs is 106–137°C (**Table 3**),

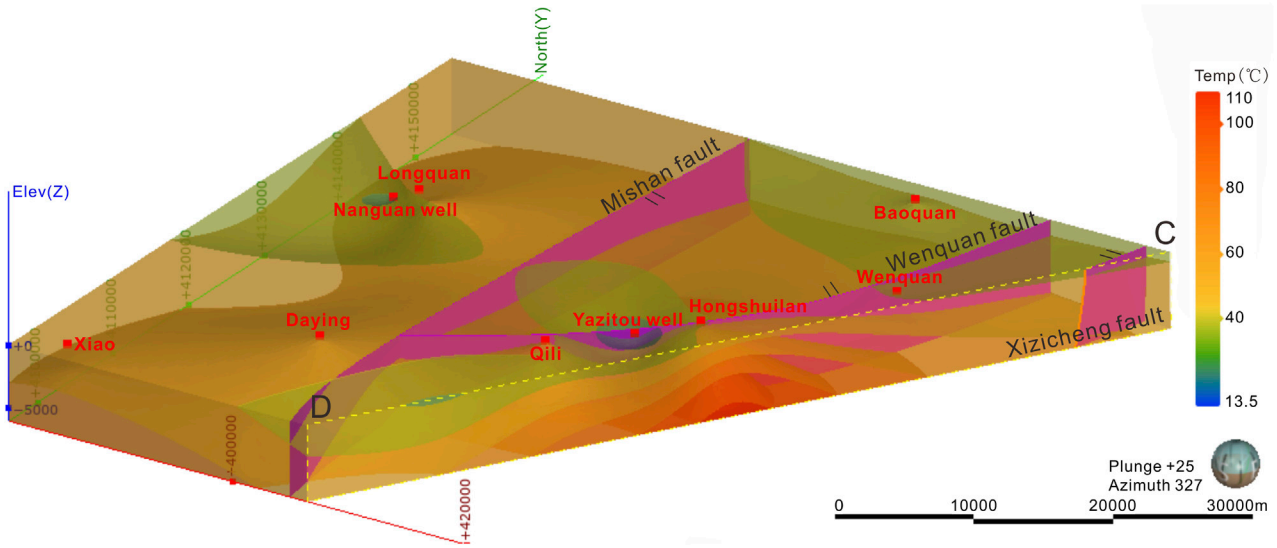

FIGURE 11 | 3D temperature model of the Weihai uplift, including the Mishan fault, the Wenquan fault, and the hot springs (**Figure 10**).

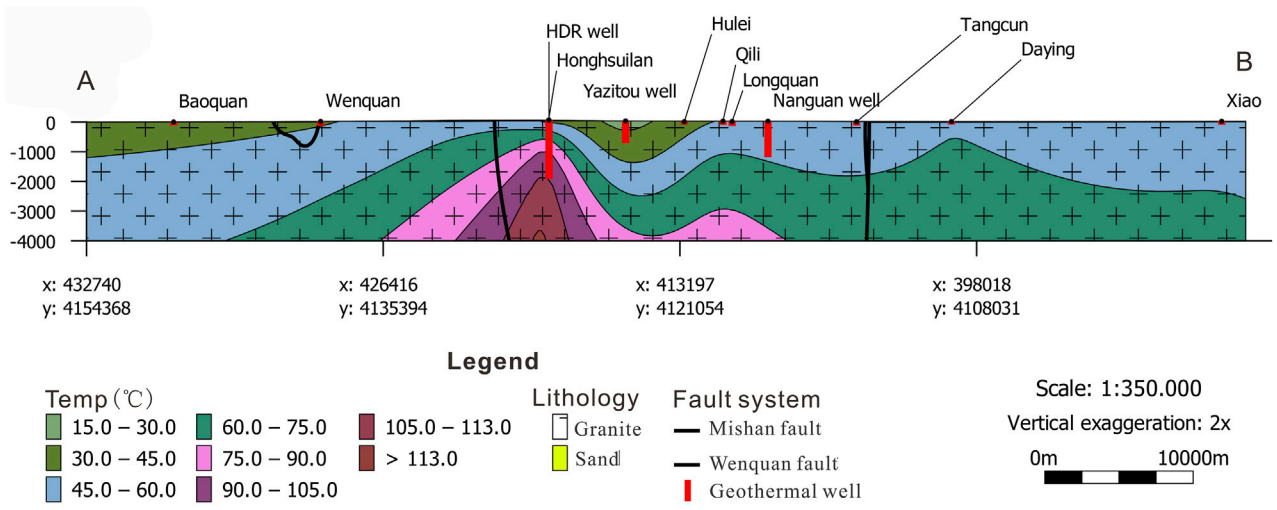

FIGURE 12 | Temperature profile A-B (**Figure 10**).

so all of the reservoir temperatures are lower than 150°C, making this a low-medium temperature geothermal system. This means up to now there is no high-temperature heat source similar to magmatic intrusions in this region through which the geothermal water flows.

Figure 13 shows the lithology and temperature logs for the Zangnan well (No. 14 in **Figures 6**, **7**). As can be seen from **Figure 13**, the cap rock is gravel sand, and the cap is very thin (only 10 m). The lithology is mainly monzonitic granite. In fact, in the Jiaodong Peninsula, the cap rocks of all of the geothermal fields are mainly composed of gravel sand, and the caps are very thin, with thicknesses of mostly less than 50 m.

As can be seen from **Figure 7**, the temperature curve of the well in the geothermal field is not linear, but the temperature logs of the wells outside of the geothermal fields are linear. This indicates that outside of the geothermal fields, there are no obvious anomalies in the geothermal gradient for this type of well, and it is mainly based on the normal terrestrial heat flow heating the groundwater. The temperature gradient outside of the geothermal fields mainly ranges from 1.9°C/100 m to 2.3°C/100 m.

Based on the above analysis, the boreholes outside of the geothermal fields have normal geothermal gradients. No high temperature heat source such as magma was found in this area, and no obvious geothermal heat anomalies were found in the

TABLE 3 | Characteristics of the geothermal reservoir in the Jiaodong Peninsula.

Name of spring	SiO_2 (mg/L)	Silica temp (°C)	Spring temp (°C)	Name of spring	SiO_2 (mg/L)	Silica temp (°C)	Spring temp (°C)
Baoquan	67.69	115.16	67	Longquan	59.00	109.34	59
Wenquan	85.54	125.50	59	Yujia	69.54	116.33	46
Hongshuilan	105.00	135.02	71	Xingcun	63.77	112.61	28
Qili	105.00	135.02	66	Dongwen	82.38	123.80	62
Hulei	108.54	136.60	60	Aishan	70.77	117.09	52
Tangcun	54.85	106.32	51	Wenshi	98.69	132.09	54
Daying	58.77	109.18	62	Dong	89.62	127.63	81
Xiao	60.62	110.47	56	Jiudian	103.60	135.68	61

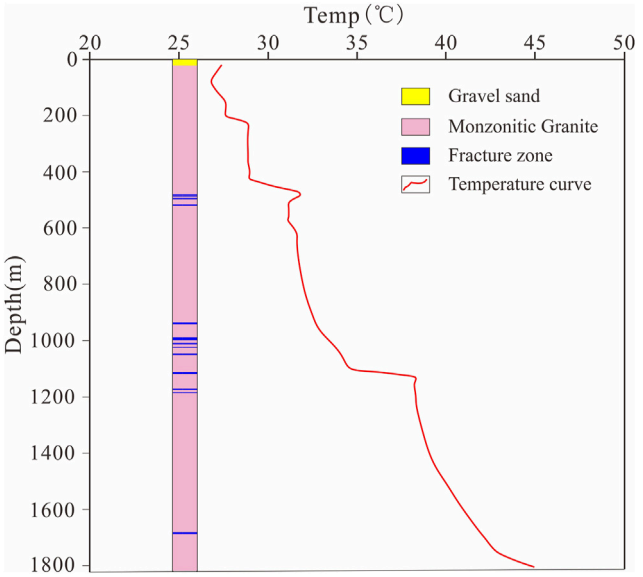

FIGURE 13 | Temperature logging and lithology for the Zangnan well (No. 14 in **Figures 6**, **7**).

deep crust. Most of the heat anomalies in the boreholes come from the geothermal fluids. The main heat source of the water was the terrestrial heat flow and heat-conducting faults.

The thermal structure of the lithosphere controls many of the properties of and processes in Earth's crust (Furlong and Chapman, 2013). Based on comparative analysis of the temperature conditions in the geothermal anomaly area and the non-geothermal anomaly area, it is proposed that the geothermal fluid heat accumulation mode in the Jiaodong area is mainly a three-source heat accumulation mode. Here, we take the Wenquan hot spring as an example to analyze the heat source of the geothermal fields in the Jiaodong Peninsula. The heat source of the geothermal liquids mainly comes from 1) hydrothermal convection within the thermal conducting faults. This is the most important heat source for the geothermal fields in the Jiaodong Peninsula. 2) The second source is heat conduction via the terrestrial heat flow. It can be seen in **Figure 3** that the heat flow values in the Jiaobei uplift and Weihai uplift are obviously higher, which provides the basic heat for this area. 3) The third heat source is conduction-convection during groundwater migration. When the surface water flows downward and deep migration occurs, the water absorbs the heat from the surrounding rock (**Figure 14**). The most important heat source is the hydrothermal convection heat accumulation in the thermal conduction fault zone. In particular, the deep and large cross-crust faults conduct the heat from the crust and upper mantle. Because these faults have stronger water conductivity, the faults become strong water-rich and water-conducting channels. The deep heat flow is absorbed by the deep fluids along these channels, so this is the main heat source of the natural hot springs in this area. The second heat source is conduction heat accumulation from terrestrial heat flow, which mainly occurs when there is no obvious thermal anomaly. This is the main heat source of the geothermal resources in the non-geothermal anomaly areas. The third heat source is groundwater transport and conduction-convective heat accumulation. The surface water supplied by rainfall migrates to deeper depths, the heat from the surrounding rock is continuously absorbed, and heat is continuously accumulated. These three heat sources are the main heat accumulation methods of the geothermal resources in the Jiaodong Peninsula.

Diversion and Accumulation Mode of Heat Flow in the Jiaodong Peninsula

The outflow of heat from the Earth's interior, i.e., the terrestrial heat flow, and the temperature field at depth are determined by deep-seated tectonic processes. Analyzing the regional heat flow pattern is a useful tool for studying the structures of the crust and lithospheric (Horai and Shankland, 1987; David, 1994). The factors influencing the shallow temperature field in the Jiaodong Peninsula include the structural distribution, the thermal properties of the different strata, the heat storage distribution, and groundwater activity (Rhee, 1975; Roy et al., 1981; Rybach and Bunterbarth, 1982; Blackwell and Steele, 1989; Pribnow et al., 2013).

Owing to the strong activity in the upper mantle and the crustal movements during the Yanshanian, during the formation of the Jiaobei uplift and the Weihai uplift, the central axis became more fractured relative to the two-wings due to the compressive stress. There are a series of NE-SW, NNE-SSW, and NW-SE faults, and the lithology is mainly Mesozoic, Archean and Proterozoic monzonitic granites. Previous studies have shown that the thermal conductivity

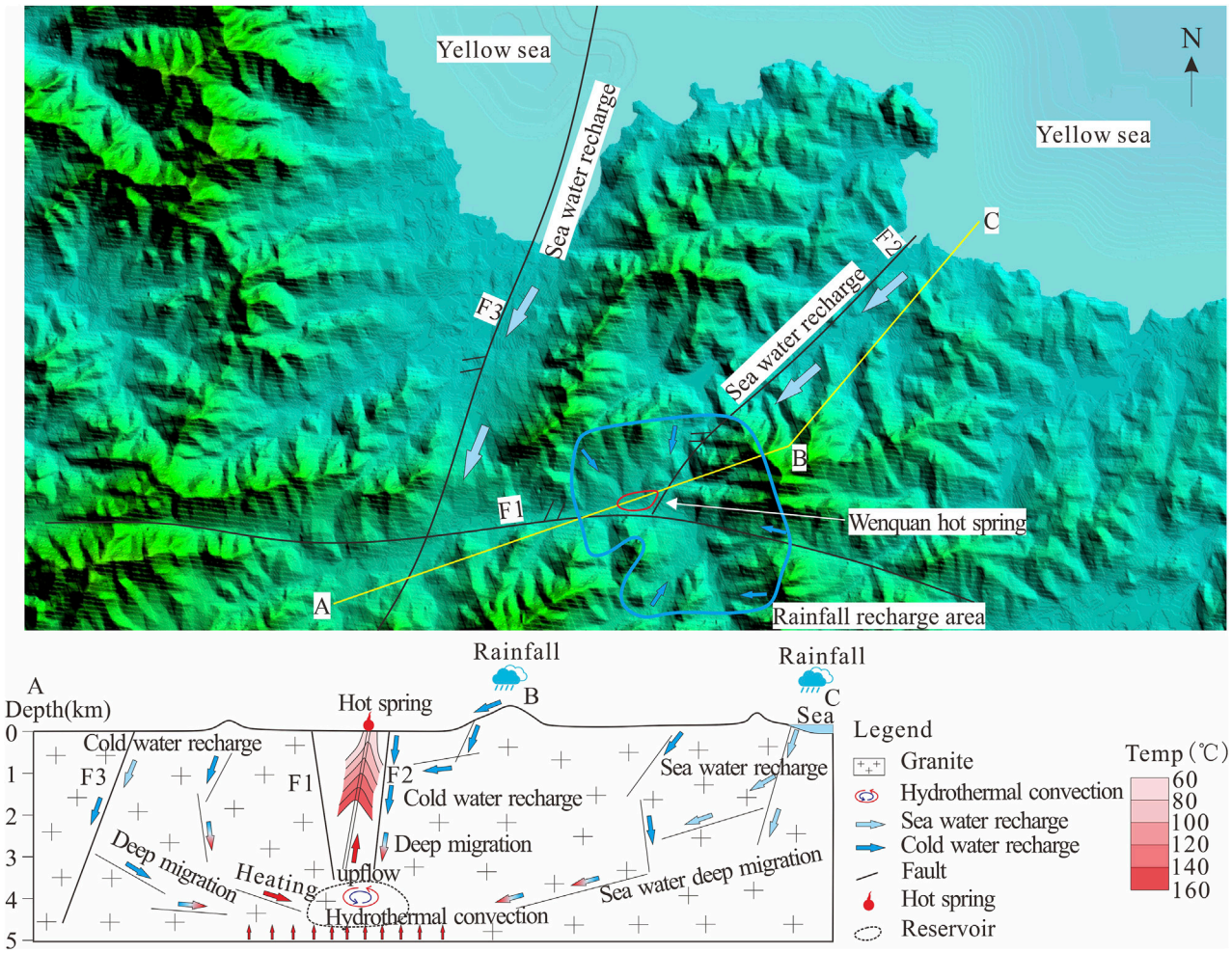

FIGURE 14 | Recharge, runoff, drainage, and heat sources of the Wenquan hot springs geothermal field.

increases with increasing pressure, and it increases nonlinearly with increasing axial pressure. The higher the porosity is, the higher the thermal conductivity of the granite is (Zhao et al., 1995; Durutürk et al., 2002; Chen et al., 2016). Therefore, in the Jiaodong Peninsula where granite is widely distributed, the more fractured uplift axis and the fault zone are characterized by higher thermal conductivities and faster heat transfer. The fracture zone provides a channel for the upwelling of the deep heat flow.

The thermophysical parameters of rocks mainly refer to physical properties such as the thermal conductivity, thermal diffusivity, specific heat capacity, and radioactive heat generation rate, which are important indicators for characterizing the thermophysical properties of rocks (Xu, 1992). The thermophysical properties of rocks directly affect the thermal generation, storage, and transmission of heat between the various layers. They are indispensable parameters for studying the temperature distribution and heat transfer (Song et al., 2019).

The lithology of the Jiaobei uplift and Weihai uplift is dominated by granitic intrusive rocks. The average thermal conductivity of the granite in the Sanshandao borehole in Laizhou, Jiaobei uplift, is 2.64–3.56 W/m•K and that of gneiss is 2.24–3.12 W/m•K (Jiang et al., 2016). The thermal conductivities of 32 granite samples measured in the Dong hot spring area are 2.34–3.68 W/m•K. The thermal conductivities of 20 granite samples measured in the Tangbo hot dry rock exploration hole in the Weihai uplift area are 2.29–3.63 W/m•K. It can be seen that the thermal conductivities of the granitic rocks in the Jiaodong uplift area are 2.2–3.6 W/m•k, while the thermal conductivity of the granite in the Zhangzhou area of the eastern part of China is 3.19 W/m•K. The thermal conductivity of felsic and mafic rocks is 2.52 W/m•K (Wang et al., 2015), which is similar to the thermal conductivity of the granite in the Jiaodong Peninsula. The Jiaolai Basin is dominated by sandstone. The thermal conductivity of sandstone (1.84 W/m•K) is generally lower than that of granite (Zhou et al., 2011). In

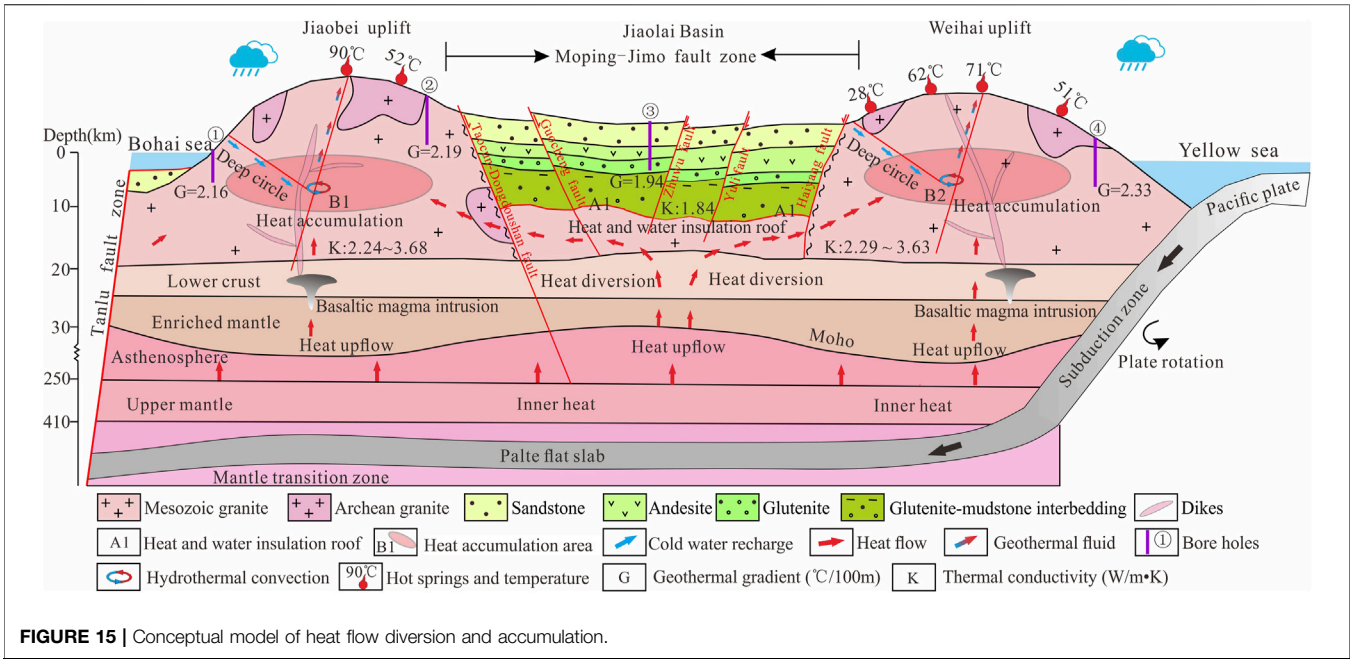

FIGURE 15 | Conceptual model of heat flow diversion and accumulation.

addition, the sandstone has a much lower permeability than the granite.

The shape of the reservoir and the movement of the geothermal fluids are also the main factors affecting the distribution of the local temperature field. The reservoir's shape determines the flow space of the fluids inside the Earth. The geothermal fluid carrying the heat also affects the distribution of the temperature around the reservoir. This is also the main reason for the local thermal anomalies on the surface of the Jiaodong Peninsula.

As can be seen from **Figure 15**, during upwelling, the heat flow from the interior of the Earth reaches the Moho surface first and then enters the crust. The undulations of the Moho surface are opposite to those of the surface. When the deep heat flow reaches this interface, there is no obvious difference. However, because the lithology in the uplift area is granite and that in the basin is sandstone, the difference in the thermal conductivities and permeabilities of the different rocks lead to the bottom (A1) becoming a heat insulating and water insulating surface. When the heat flow reaches to the bottom (A1) of the Jiaolai Basin, the heat flow changes direction and is redistributed along the bottom of A1 toward both sides of the uplifts, which have a higher thermal conductivity. The rising heat flow accumulates at a certain depth in the crust (areas B1 and B2), which results in the uplift area having a higher temperature. This explains why the silica heat flow value in the uplift area is higher than the silica heat flow value in the basin (**Figure 3**).

CONCLUSION

Through geothermal geological survey and heat conduction and water conduction structural analysis of the 16 hot springs in the Jiaodong Peninsula, the mechanisms of the geothermal resources in Jiaodong Peninsula were comprehensively analyzed. We propose a V-type structural control and thermal conductivity model. Based on the heat flow distribution, the logging data for the wells, and the thermophysical parameters of the rocks in the Jiaodong Peninsula, a 3D model of the temperature and lithology and a conceptual model were established. The main conclusions of this study are as follows.

(1) The geothermal resources in the Jiaodong Peninsula are mainly distributed in the V-shaped area where the upper block of the NE- and NW-trending faults intersect. The geothermal reservoir is controlled by the NE- and NW-trending faults and has an irregular columnar shape.

(2) The lithology in the uplift area is mainly granite, that in the basin is mainly sandstone, and the heat flow value in the uplift area is much higher than that in the basin. Due to the differences between the thermophysical parameters of the different rocks, the heat flow changes direction at the bottom of the basin and redistributes toward both sides to the uplifts, which results in the uplift area having a higher heat flow value. This demonstrates the diversion and accumulation mode of the heat flow in the deep crust in the Jiaodong Peninsula.

(3) For the geothermal fluids in the Jiaodong Peninsula, the heat is mainly supplied by the terrestrial heat flow and the heat-conducting faults. Up to now, there is no high-temperature heat source similar to magmatic intrusions in this area. The heat of the geothermal liquids mainly comes from three sources: hydrothermal convection in the thermal conducting faults, heat conduction via

terrestrial heat flow, and conduction-convection during groundwater migration.

DATA AVAILABILITY STATEMENT

The original contributions presented in the study are included in the article/Supplementary Material, further inquiries can be directed to the corresponding author.

AUTHOR CONTRIBUTIONS

Conceptualization, MS and FK; investigation, MS, TY, SG, XG, and XY; writing—original draft preparation, MS; writing—review and editing, FK; supervision, FK; project administration, MS; funding acquisition, FK. All authors have read and agreed to the published version of the article.

FUNDING

This research was supported by the National Natural Science Foundation of China (grant numbers U1906209, 42072331) and financial foundation of Yantai City (SDGP37600202102000097).

ACKNOWLEDGMENTS

We thank UNU Geothermal Training Programme for applying for 6 months free use of leapfrog for me, and thank Vivi Dewi Mardiana Nusantara who comes from PT Pertamina Geothermal Energy, Indonesia and Erick Jiménez for their help in the establishment of the leapfrog model, and also thank LetPub for its linguistic assistance during the preparation of this manuscript. We are grateful to editors and reviewers for their constructive comments and valuable suggestions that significantly improved this manuscript.

REFERENCES

Alcaraz, S. A., Lane, R., Spragg, K., Milicich, S. D., and Bignall, G. (2011). "3-D Geological Modelling Using New Leapfrog Geothermal Software," in Proceedings, 36th Workshop on Geothermal Reservoir Engineering. doi:10.3901/JME.2008.10.294

Blackwell, D., and Steele, J. (1989). *Thermal Conductivity of Sedimentary Rocks: Measurement and Significance*. New York: Springer. doi:10.1007/978-1-4612-3492-0-2

Chen, B., Chen, C., Kaban, M. K., Du, J., Liang, Q., and Thomas, M. (2013). Variations of the Effective Elastic Thickness over China and Surroundings and Their Relation to the Lithosphere Dynamics. *Earth Planet. Sci. Lett.* 363, 61–72. doi:10.1016/j.epsl.2012.12.022

Chen, L. (2009). Lithospheric Structure Variations between the Eastern and central North China Craton from S- and P-Receiver Function Migration. *Phys. Earth Planet. Interiors.* 173, 216–227. doi:10.1016/j.pepi.2008.11.011

Chen, M., Huang, G., and Xiong, L. (1988). *North China Geothermal*. Beijing: Science Press.

Chen, M., Wang, J., Wang, J., Xiao, D., Yang, S., Xiong, L., et al. (1990). The Characteristics of the Geothermal Field and its Formation Mechanism in the North China Down-Faulted basin (In Chinese with English Abstract). *Acta Geologica Sinica.* (1), 80–91.

Chen, Y., Franco, P., and Lai, Y. (2004). Metallogenic Time and Tecctonic Setting of the Jiaodong Gold Province, Eastern china (In Chinese with English Abstract). *Acta Petrologica Sinica.* 20 (4), 907–922.

Chen, Z., Wu, X., Chen, F., Wang, H., and Sun, D. (2016). Research of thermal Conductive Characteristics of Granite under Uniaxial Compression. *Coal Eng.* 48 (9), 113–116.

Deming, D. (1994). Estimation of the thermal Conductivity Anisotropy of Rock with Application to the Determination of Terrestrial Heat Flow. *J. Geophys. Res.* 99 (B11), 22087–22091. doi:10.1029/94jb02164

Durutürk, Y. S., Demirci, A., and Keçeciler, A. (2002). Variation of thermal Conductivity of Rocks with Pressure. *CIM Bull.* (95), 67–71. Available at: https://www.researchgate.net/publication/290823333.

Furlong, K. P., and Chapman, D. S. (2013). Heat Flow, Heat Generation, and the thermal State of the Lithosphere. *Annu. Rev. Earth Planet. Sci.* 41, 385–410. doi:10.1146/annurev.earth.031208.100051

He, L. (2015). Thermal Regime of the north china Craton: Implications for Craton Destruction. *Earth-Science Rev.* 140, 14–26. doi:10.1016/j.earscirev.2014.10.011

Horai, K., and Shankland, T. (1987). 8. Thermal Conductivity of Rocks and Minerals. *Methods Exp. Phys.* 24 (1), 271–302. doi:10.1016/S0076-695X(08)60589-X

Hu, S., He, L., and Wang, J. (2000). Heat Flow in the continental Area of China: a New Data Set. *Earth Planet. Sci. Lett.* 179 (2), 407–419. doi:10.1016/S0012-821X(00)00126-6

Hu, S., and Wang, J. (1994). Heat Flow Characteristics of Orogenic Belts in southeastern China (In Chinese with English Abstract). *Geol. Rev.* 40 (5), 387–394.

Hu, Y., Liu, S., Fu, J., Sun, G., Gao, L., and Guo, R. (2021). Neoarchean-early Paleoproterozoic Granitoids, the Geothermal Gradient and Geodynamic Evolution in the Hengshan Terrane, north china Craton. *Gondwana Res.* 94 (2), 143–163. doi:10.1016/j.gr.2021.03.004

Jaupart, C., and Mareschal, J. C. (1999). The thermal Structure and Thickness of continental Roots. *Lithos.* 48, 93–114. doi:10.1016/S0419-0254(99)80007-X

Jiang, G., Tang, X., Rao, S., Gao, P., Zhang, L., Zhao, P., et al. (2016). High-quality Heat Flow Determination from the Crystalline Basement of the South-East Margin of North China Craton. *J. Asian Earth Sci.* 118, 1–10. doi:10.1016/j.jseaes.2016.01.009

Jin, B., Zhang, Y., and Luan, G. (1999). Characteristics of Geothermal Resources in Jiaodong Peninsula (In Chinese with English Abstract). *Ludong Univ. J. (Natural Sci. Edition).* 15 (4), 297–301. doi:10.16030/j.cnki.issn.1000-3665.2000.05.010

Kang, F. (2013). Sustainable Yield and its Assessment of Geothermal Reservoirs in china. *Trans. - Geothermal Resour. Counc.* 37 (4), 843–852.

Lee, W. H. K. (1970). On the Global Variations of Terrestrial Heat-Flow. *Phys. Earth Planet. Interiors* 2 (5), 332–341. doi:10.1016/0031-9201(69)90026-0

Li, X., Liu, B., Sun, X., and Wang, Y. (1997). Relationship between the Silica Heat Flow and Regional Geological Conditions in Shandong Peninsula (In Chinese with English Abstract). *J. Ocean Univ. Qingdao* 27 (1), 75–83. doi:10.16441/j.cnki.hdxb.1997.01.011

Liang, Y., Guo, W., Ma, Y., and Zhao, E. (2020). Geochemical Evidence for Thickening and Thinning of Lower Crust beneath the Jiaodong Peninsula: Implications for Late Mesozoic Destruction of the Eastern North China Craton. *Lithosphere.* 2020 (1), 1–17. doi:10.2113/2020/8831664

Lin, Z. T., Zhu, B., Lin, X., Chen, Y., and Liu, Y. Z. (2013). Study on the Mechanism of the Anodic Oxidation of PAN-Based Carbon Fibers by Cyclic Voltammetry. *Adv. Mater. Res.* 774-776 (5), 832–835. doi:10.4028/www.scientific.net/amr.774-776.832

Liu, C., Deng, J., Li, S., Xiao, Q., Jin, T., Sun, H., et al. (2018). Discussions on Crust-Mantle Structure during the Formation of Yanshanian of Large-Super Large Scale Deposits in the Jiaodong Gold Ore District: Constraints from Ore-Forming Igneous Assemblage (In Chinese with English Abstract). *Earth Sci. Front.* 25 (6), 296–307. doi:10.13745/j.esf.sf.2018.11.16

Lv, C., Wu, G., and Boyko, K. J. (2015). A Study of Distribution and Charge of Regional Tectonic Fluid in Goldfields of Jiaodong Peninsula (In Chinese with English Abstract). *Earth Sci. Front.* 22 (4), 113–121. doi:10.13745/j.esf.2015.04.013

Majorowicz, J., and Wybraniec, S. (2011). New Terrestrial Heat Flow Map of Europe after Regional Paleoclimatic Correction Application. *Int. J. Earth Sci. (Geol Rundsch)* 100 (4), 881–887. doi:10.1007/s00531-010-0526-1

Mao, J., Li, H., Wang, Y., Zhang, C., and Wang, Y. (2005). The Relationship between Mantle-Derived Fluid and Gold Ore-Formation in the Eastern Shandong Peninsula: Evidences from D-O-C-S Isotopes. *Acta Geologica Sinica.* 79 (6), 839–857. doi:10.1360/gs050303

Pan, S., Wang, F., Zheng, Y., Duan, Y., Liu, L., Deng, X., et al. (2015). Crustal Velocity Structure beneath Jiaodong Peninsula and its Tectonic Implications (In Chinese with English Abstract). *Chin. J. Geophys.* 58 (9), 3251–3263. doi:10.6038/cjg20150920

Pribnow, D., Williams, C. F., Sass, J. H., and Keating, R. (2013). Thermal Conductivity of Water-saturated Rocks from the KTB Pilot Hole at Temperatures of 25 to 300 °C. *Geophys. Res. Lett.* 23 (4), 391–394. doi:10.1029/95gl00253

Qiu, N., Zuo, Y., Chang, J., and Li, W. (2014). Geothermal Evidence of Meso-Cenozoic Lithosphere Thinning in the Jiyang sub-basin, Bohai Bay Basin, Eastern North China Craton. *Gondwana Res.* 26 (3-4), 1079–1092. doi:10.1016/j.gr.2013.08.011

Rhee, S. K. (1975). Porosity-Thermal Conductivity Correlations for Ceramic Materials. *Mater. Sci. Eng.* 20 (1), 89–93. doi:10.1016/0025-5416(75)90134-2

Roy, R. F., Beck, A. E., and Touloukian, Y. S. (1981). Thermophysical Properties of Rocks. *Phys. Prop.Rocks Min.* 2 (2), 409–502.

Rybach, L., and Buntebarth, G. (1982). Relationships between the Petrophysical Properties Density, Seismic Velocity, Heat Generation, and Mineralogical Constitution. *Earth Planet. Sci. Lett.* 57 (2), 367–376. doi:10.1016/0012-821x(82)90157-1

Rybach, L., Mégel, T., and Eugster, W. J. (2000). "At what Time Scale Are Geothermal Resources Renewable?" in *World Geothermal Congress 2000* (Japan: Kyushu-Tohoku), 867–872.

Rybach, L., Mégel, T., and Eugster, W. J. (1999). How Renewable Are Geothermal Resources? *Trans. - Geothermal Resour. Counc.* 23, 563–566.

Sanyal, S. K. (2004). Sustainability and Renewability of Geothermal Power Capacity. *Trans. - Geothermal Resour. Counc.* 28, 804–817. doi:10.1007/978-1-4614-5820-3-229

Sclater, J. G., and Francheteau, J. (1970). The Implications of Terrestrial Heat Flow Observations on Current Tectonic and Geochemical Models of the Crust and Upper Mantle of the Earth. *Geophys. J. Int.* 20 (5), 509–542. doi:10.1111/j.1365-246X.1970.tb06089.x

Song, X., Jiang, M., Peng, Q., and Xiong, P. (2019). Thermal Property Parameters and Influencing Factor Analysis of Main Rock Strata in Guizhou Province (In Chinese with English Abstract). *Acta Geologica Sinica.* 93 (8), 2092–2103. doi:10.19762/j.cnki.dizhixuebao.2019116

Tan, J., Wei, J., Yang, C., Feng, B., Tan, W., and Guo, D. (2006). Geochemstry and Tectonic Setting of Dikes in the Guocheng Area, Jiaodong Peninsula. *Acta Geologica Sinica* 80 (8), 1177–1188. doi:10.1111/j.1745-4557.2006.00081.x

Wang, A., Sun, Z., Liu, J., Hu, B., Wan, J., and Yang, L. (2015). Radiogenic Heat Production of Rocks from Zhangzhou, Southeast China and its Implications for thermal Regime of Lithosphere. *Sci. Technology Rev.* 33 (24), 41–45. doi:10.3981/j.issn.1000-7857.2015.24.007

Wulaningsih, T., Fujii, Y., and Tsutsumi, S. (2017). "A 3D Model of the Yamagawa Geothermal System: Insights into Reservoir Structure and Future Field Management," in Proceedings 39th New Zealand Geothermal Workshop.

Xie, X., and Yu, H. (1988). The Characteristics of the Regional Geothermal Field in Sichuan Basin (In Chinese with English Abstract). *J. Chengdu Coll. Geology.* (4), 110–117.

Xiong, L., and Gao, W. (1982). Characteristics of Geothermal in Uplift and Depression (In Chinese with English Abstract). *Acta Geophysica Sinica.* 25 (5), 60–68.

Xiong, L., and Zhang, J. (1984). Mathematical Simulation of Refract and Redistribution of Heat Flow (In Chinese with English Abstract). *Chin. J. Geology.* (4), 445–454.

Xu, Z. (1992). A Discussion of Factors Influencing Thermophysical Characteristics of Rocks and Their Mechanisms (In Chinese with English Abstract). *Pet. Exploration Development* 19 (6), 85–89.

Zhang, J., Sun, H., and Xiong, L. (1982). Mathematical Simulating of Regional Geothermal Field and Case Analysis (In Chinese with English Abstract). *Chin. J. Geology.* (3), 315–321. doi:10.1007/BF01033890

Zhang, Y., Li, J., Liu, Z., Ren, F., and Yuan, J. (2006). Detachment Systems in Deep of Jiaolai basin and Their Regional Tectonic Significance. *Oil Gas Geology.* 27 (4), 504–511. doi:10.11743/ogg20060410

Zhao, X., Li, F., Zeng, J., and Jin, F. (2017). The Geological Characteristics and Origin of Deep Geothermal Water in Baxian Sag. *Earth Sci. Front.* 24 (3), 210–218. doi:10.13745/j.esf.2017.03.019

Zhao, Y., Yang, S., Zhang, W., Liang, X., and Ma, L. (1995). An Experimental Study of Rock thermal Conductivity under Different Temperature and Pressure (In Chinese with English Abstract). *Prog. Geophys.* 10 (1), 104–113.

Zhou, Y., Ji, Y., Zhang, S., and Wan, L. (2011). Characteristics and Controlling Factors on Physical Properties of Low-Permeability sandstone of the Laiyang Formation in the Laiyang Sag, Jiaolai Basin (In Chinese with English Abstract). *Acta Petrolei Sinica* 32 (4), 611–620. doi:10.1007/s12182-011-0123-3

Conflict of Interest: The authors declare that the research was conducted in the absence of any commercial or financial relationships that could be construed as a potential conflict of interest.

Publisher's Note: All claims expressed in this article are solely those of the authors and do not necessarily represent those of their affiliated organizations, or those of the publisher, the editors and the reviewers. Any product that may be evaluated in this article, or claim that may be made by its manufacturer, is not guaranteed or endorsed by the publisher.

frontiers | Frontiers in Earth Science

ORIGINAL RESEARCH
published: 27 April 2022
doi: 10.3389/feart.2022.885000

Laboratory Hydraulic Fracturing of Large-Scale Granite Characterized by Acoustic Emission Under Different Confining Conditions

Huang Wang[1,2,3], *Guiling Wang*[3,4]*, *Yuedu Chen*[5], *Lu Liu*[3,4,6], *Zhihong Zhao*[5] and *Haonan Gan*[3,4]

[1]School of Environmental Studies, China University of Geosciences, Wuhan, China, [2]China Geological Survey, Ministry of Natural Resources, Beijing, China, [3]Technology Innovation Center for Geothermal & Hot Dry Rock Exploration and Development, Ministry of Natural Resources, Shijiazhuang, China, [4]Institute of Hydrogeology and Environmental Geology, Chinese Academy of Geological Sciences, Shijiazhuang, China, [5]Department of Civil Engineering, Tsinghua University, Beijing, China, [6]State Key Laboratory of Biogeology and Environmental Geology, China University of Geosciences, Wuhan, China

Hydraulic fracturing (HF) technology is crucial to form connected fracture network within the low-permeability geothermal reservoir. However, the HF process and failure mechanism in this process are only partly understood. A series of true triaxial hydraulic fracturing tests on large-scale natural granite samples were conducted under different confining conditions, combining with acoustic emission monitoring to evaluate the initiation and propagation of hydraulic fractures. Results show that a main hydro-fracture was formed in three samples during the first fracturing process. Many AE events occurred during the first pump period. The proportion of tensile fractures during the hydraulic fracturing accounted for more than 85% of all fractures. The test results could provide a new understanding of the effect of HF under different stress conditions. And implied that field engineering should pay attention to the initial HF, which may determine the main fracture framework of the field at the first pump procedure.

Keywords: hydraulic fracturing, enhanced geothermal system, acoustic emission, confining stress, granite

OPEN ACCESS

Edited by:
Wenjing Lin,
Chinese Academy of Geological Sciences, China

Reviewed by:
Bo Feng,
Jilin University, China
Jeoung Seok Yoon,
DynaFrax UG Limited, Germany

***Correspondence:**
Guiling Wang
ihegwangguiling@sina.com

Specialty section:
This article was submitted to Solid Earth Geophysics, a section of the journal Frontiers in Earth Science

Received: *27 February 2022*
Accepted: *07 April 2022*
Published: *27 April 2022*

Citation:
Wang H, Wang G, Chen Y, Liu L, Zhao Z and Gan H (2022) Laboratory Hydraulic Fracturing of Large-Scale Granite Characterized by Acoustic Emission Under Different Confining Conditions. Front. Earth Sci. 10:885000. doi: 10.3389/feart.2022.885000

1 INTRODUCTION

Geothermal energy shows significant potential as a renewable energy because of its huge resource reserve, clean, and low-carbon characteristics. The geothermal heat source has been widely applied in power generation and heat supply uses (Moya et al., 2018). China has gradually increased its policy support for geothermal energy development in recent years. According to the outline of the 14th Five-Year Plan (2021–2025) for national economic and social development and vision 2035, China plans to develop and utilize geothermal energy in accordance with local conditions (Xinhua News Agency is authorized to release, 2021). The State Council released an action plan for reaching carbon dioxide peak before 2030, which proposed to explore ways of expanding the exploitation and utilization of geothermal energy (State Council Report, 2021). Hot dry rock (HDR) energy is an important part of geothermal energy, and is considered to be the future energy due to its huge reserves and development prospects (MIT-Led Report, 2006). Enhanced geothermal system (EGS) is essential for the extraction of geothermal heat from HDR, and a number of EGS sites have been carried out worldwide [(Lu, 2018) and references therein]. A series of EGS tests is conducted by the China Geological Survey (CGS) in Qinghai Province since 2018, and aim to establish a demonstration project in the next few years (Zhang et al., 2019).

Reservoir construction by Hydraulic fracturing (HF) for EGS is a key technology (Fan and Zhang, 2014; Wu et al., 2017; Tomac and Sauter, 2018). A network of hydraulic fractures can provide a path for fluid flow and heat exchange with the surrounding hot rock. The injected geothermal fluid (usually water) flows through the fractures and exchanges heat with the HDR reservoir.

The monitoring of HF and laboratory simulations have been intensively studied (Kumari et al., 2018; Liu et al., 2018; Xing et al., 2019; Zhou et al., 2019; Shan et al., 2021). The HF process of reservoir rocks can be monitored with the help of laboratory tests, and the propagation of fractures can be directly observed. This provides an understanding of the fracturing characteristics, rock fracture mechanism, and hydraulic fracture network distribution of HDR reservoirs at the given sites. The fracture initiation and propagation behavior of HF are mainly studied using true triaxial hydraulic fracturing physical simulation experiments. The influence of pre-existing fractures on HF in the EGS project has been proven in many previous studies (Guo, 2016; Mao et al., 2017; Kolawole and Ispas, 2020; Zhou et al., 2020; Liu et al., 2021). The extension path of hydraulic fractures in the HDR reservoir is simple and extending only in the direction of the maximum principal stress; however, because of the influence of the weak surface of the rock, hydraulic fractures prefer to extend along the weak surface, creating a complicated fracture network (Liu et al., 2021). Mao et al. (2017) conducted HF tests on granite with prefabricated fractures under different confining pressures, and found that the extension path of the hydraulic fractures obviously influenced by the magnitude of the horizontal stress difference, and the larger the horizontal stress difference, the greater the curvature of the hydraulic fracture extension path.

Previous studies have divided the process during HF into five stages (Caulk et al., 2016; Lei et al., 2019). 1) The steel wellbores of the sample were gradually filled with water, and the rock samples were not affected by the water pressure; 2) continued injection of water resulted in a rapid increase in pressure; 3) accumulation of pressure caused the rock to be hydrofractured; and 4) pressure of the induced hydraulic fracture was gradually released along the induced hydraulic fracture. In this process, under the same injection rate, there was almost no change in the water pressure, which is defined as the residual pressure that induces cracks. The residual pressure can be regarded as the corresponding minimum confining pressure; 5) post-fracture stage.

Acoustic emission (AE) systems are used to monitor fracture propagation and energy release activities in rocks (Matsunaga et al., 1993; Ishida, 2001; Zhou et al., 2019). Significant energy is released during HF fracture propagation, and AE events are generated (Ishida, 2001; Shan et al., 2021). Laboratory and field studies have shown that during HF the failure mechanism is not unique. The stress and direction of natural cracks control the dominant failure mechanism for HF (Fischer and Guest, 2011; Yamamoto et al., 2019). The failure mechanism can be distinguished by specific AE parameters, and cracks are classified into tensile and shear cracks (Yuyama et al., 1999; Ohtsu, 2010). The order of tension and shearing depends on the specific microcrack in granite (Li and Einstein, 2019).

However, for granites that are commonly applied to geothermal energy utilization, the HF process and failure mechanism are only partly understood, which merits further study. Additionally, fracturing experiments for large-scale granite samples are few.

In this study, a series of true triaxial hydraulic fracturing experiments were performed to evaluate the impact of the fracture on the HF process under different compressive pressures on natural granite rock samples. During the fracturing process, an acoustic emission monitoring system was used to record the acoustic emission events during the HF of the rock samples. The

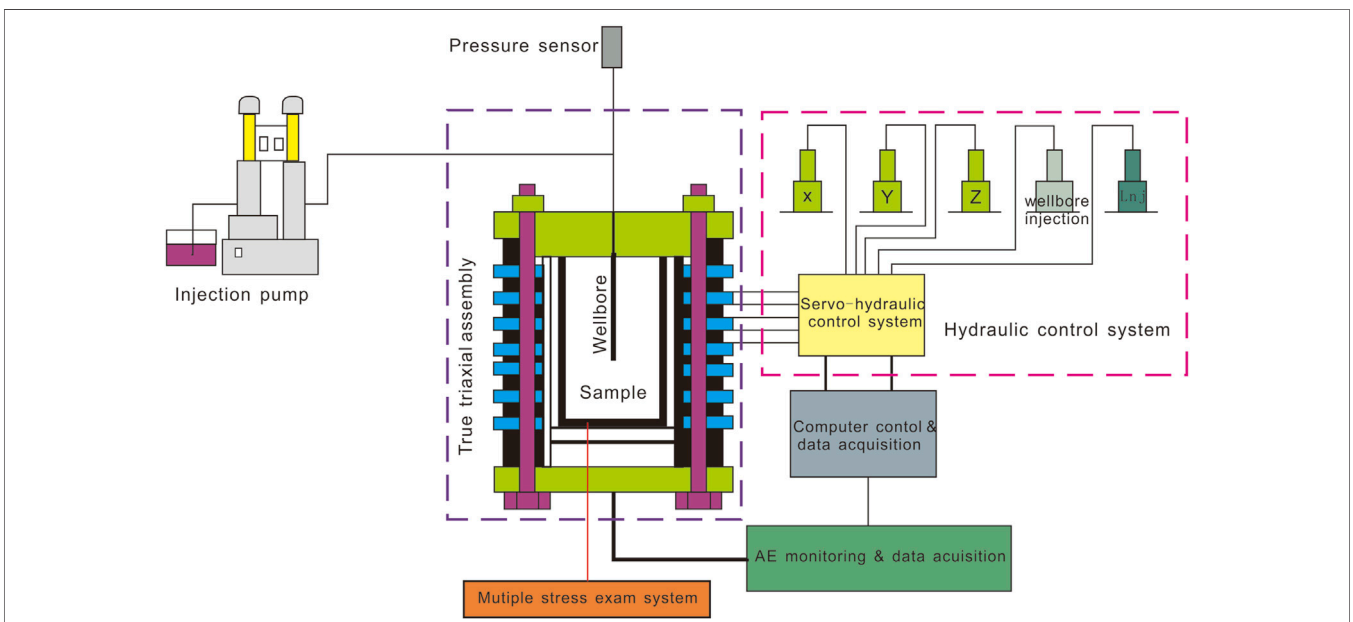

FIGURE 1 | Schematic diagram of the true triaxial hydraulic fracturing system.

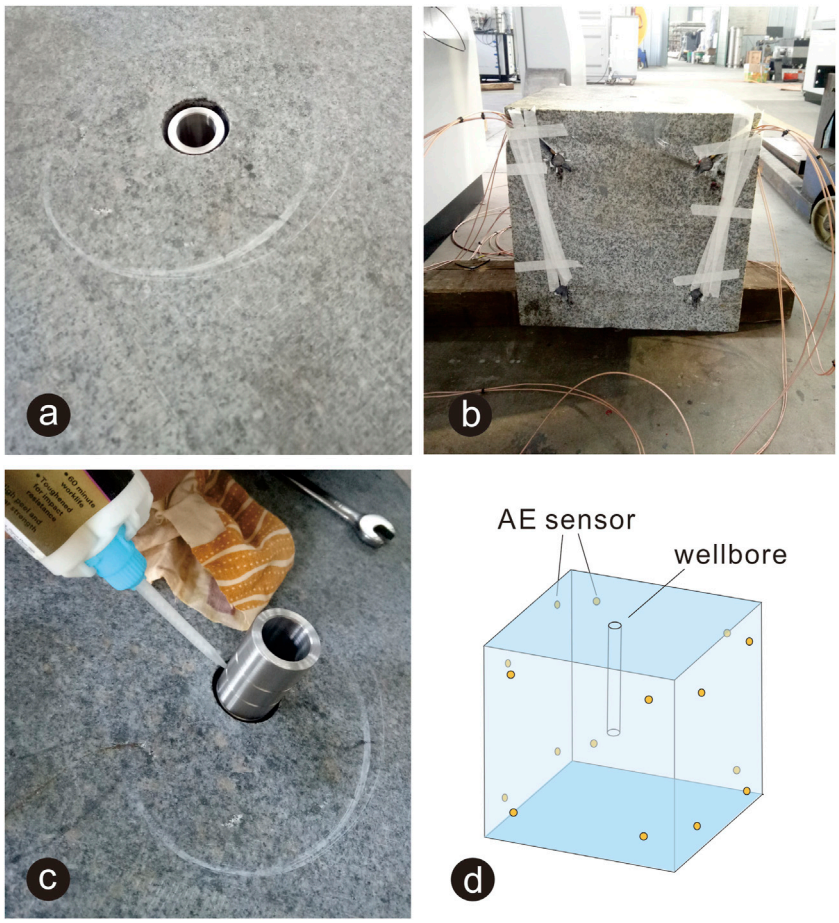

FIGURE 2 | Sample preparation **(A)** intact surface of samples; **(B)** arrangements of AE sensor; **(C)** wellbore sealed with glue; **(D)** AE sensors layout on cubic samples.

TABLE 1 | Experimental programs and results.

Sample id	Target confining pressure (MPa)			Temperature (°C)	Constant flow (ml/min)	Breakdown pressure (MPa)	Residual pressure (MPa)	With obvious natural cracks
	X	Y	Z					
HDR400-1	10	20	15	23	20	24.91	——	No
HDR400-2	15	25	20		20	32.15	17.0	No
HDR400-4	35	40	30		20	34.57	16.0	No

experiments show the AE-based fracturing behavior reveals the notable characteristics of hydraulic fractures. This study is useful for understanding the effect of HF in granite reservoirs under different stress conditions.

2 EXPERIMENTAL PROCEDURES

2.1 Experiment Setup

The equipment used in this experiment was a true triaxial hydraulic fracture propagation simulation system developed by Jiangsu Huaan Scientific Reasarch Devices Co., Ltd. The equipment can carry a maximum sample size of 600 mm × 600 mm × 600 mm, and the triaxial pressure can be automatically and uniformly loaded separately. The maximum loading pressure is 70 MPa. To accurately detect the development of fractures, an acoustic emission probe is directly installed on the surface of the rock sample. During the test preparation stage, the rock sample was opened and slotted for the monitoring probe.

The equipment included a true triaxial pressure control system and a pressure monitoring system (**Figure 1**) as well as

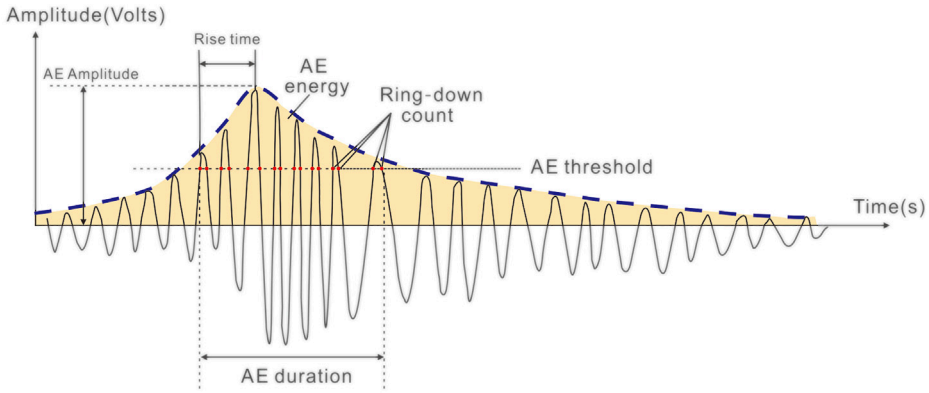

FIGURE 3 | AE hit feature extraction [Modified from (Fischer and Guest, 2011)].

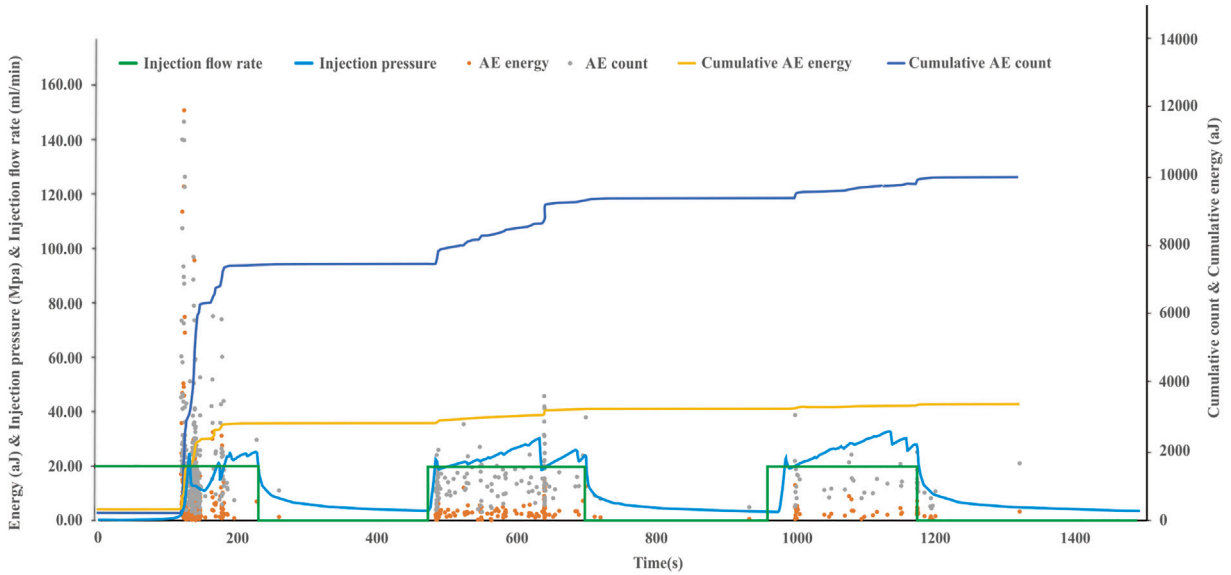

FIGURE 4 | Result of the injection pressure and AE energy and count of HDR400-1.

an acoustic emission monitoring system in addition to the fracturing main part, which can monitor the pressure and acoustic emission data in real time during the experiment, to identify the fracture development, and the fluid used for fracturing. The maximum injection pressure is up to 120 MPa.

2.2 Sample Preparation

The samples used in the HF experiments were all outcropping Permian strata and Middle-Late Triassic granodiorite and granite from Qinghai Province, northwestern China. The samples were gray, medium-grained biotite granite, with a massive structure. The sample size was 400 mm × 400 mm × 400 mm cubes, all of which were polished in order to reduce uneven stress of the samples during the test. Three samples were prepared to study the influence of the injection pressure on the HF and AE parameters. Distilled water was used as the fracturing fluid during the fracturing process.

Before processing, we carefully checked for natural cracks on each end surface of the sample, recorded, and described them. The samples were relatively intact, and no obvious natural cracks were observed (**Figure 2A**). The samples were then perforated and slotted, including injection wells (bore diameter is 30 mm, hole depth is 200 mm, which equals 1/2 of the sample side length) and holes for acoustic emission probe placement (**Figure 2B**). The reason for the designed length of the injection well is to attempt to keep the fracturing extension and AE events as centrally located as possible. After completing the drilling, the wellbore was placed in a well, sealed the wellbore with glue, and dried for at least 24 h to ensure the sealing effect (**Figure 2C**).

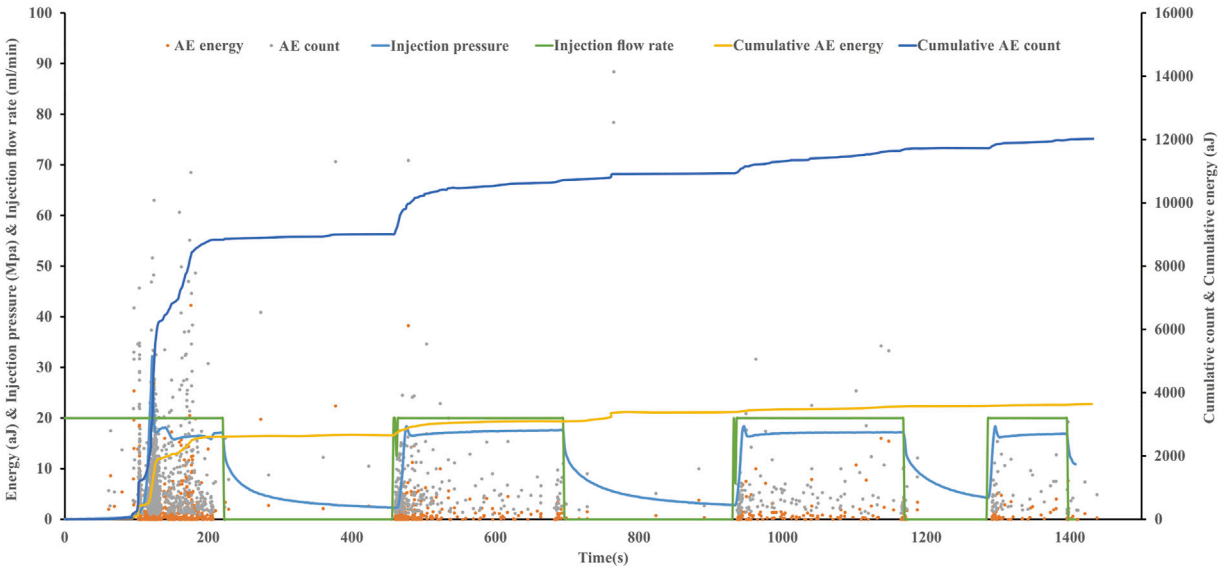

FIGURE 5 | Result of the injection pressure and AE energy and count of HDR400-2.

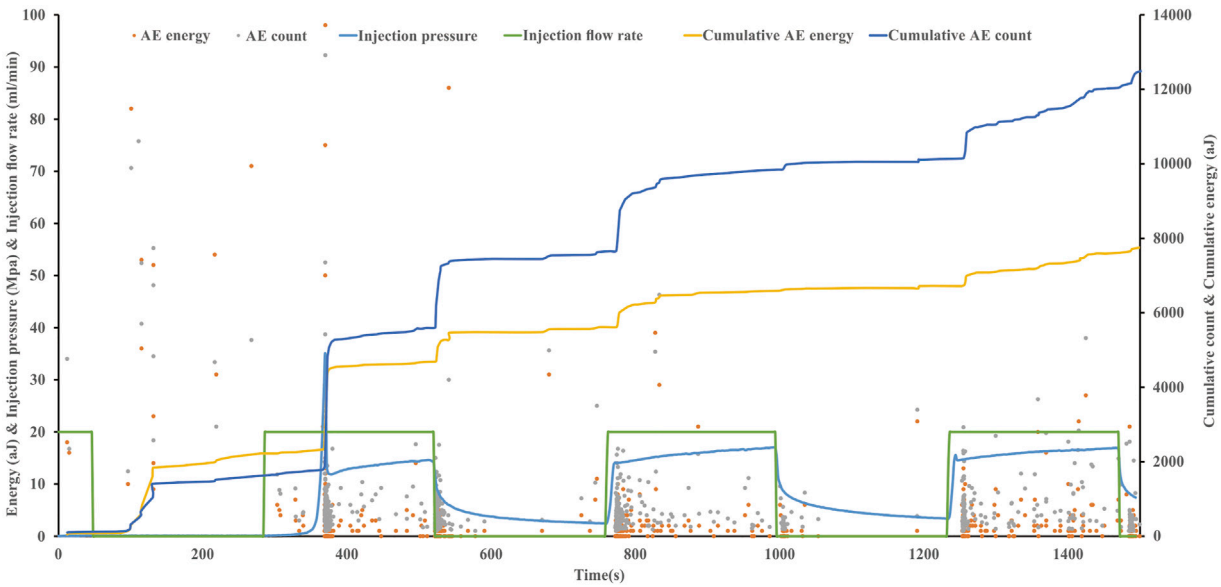

FIGURE 6 | Result of the injection pressure and AE energy and count of HDR400-4.

2.3 Testing Procedure

Considering that the scale of the rock sample is very small compared to *in-situ* fracturing, large confining pressure cannot be set for HF when the confining pressure is added in the early stage of the test. The value of the pressure begins to increase gradually, and a relatively large confining pressure difference owing to the strength of the granite, which makes the effect of the confining pressure on the fracture more obvious.

Before the start of the experiment, the confining pressure system, fracturing fluid injection pump, pressure monitoring system, and AE monitoring system were turned on. The target confining pressure value was entered on the display of the confining pressure system, and pressurizing was started. The pressure and AE monitoring start time are recorded and used to adjust the data to the same timeline for corresponding analysis. Comparing with the thermal reservoir condition in the field, an injection rate of 20 ml/min was adopted for the experiment. Different triaxial pressures were applied for each sample (**Table 1**), which are the equal proportional reduction of the situ geological stresses. We set the vertical confining pressure

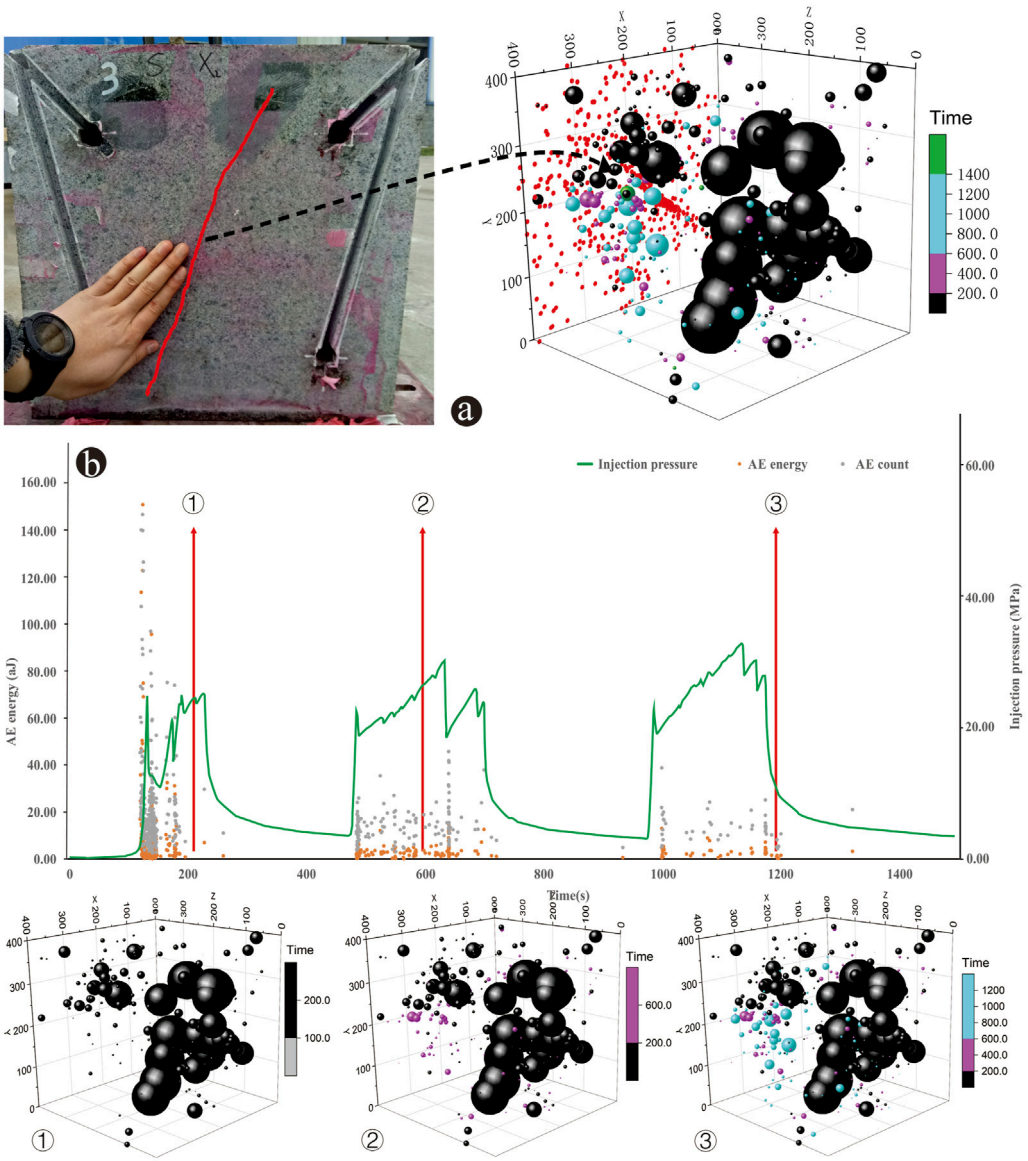

FIGURE 7 | AE spatial distribution characteristics of HDR400-1 **(A)** AE spatial distribution compared with the surface appearance of the sample. Each sphere represents a single AE event, and the size of the spheres represent the value of AE energy. The red scatter points are the projection of the AE events on the X-Y plane; **(B)** AE spatial distribution of each pump periods, and ①–③ represent the first to third pump periods.

(Y) as the maximum stress, while there is a difference of 5 MPa between the horizontal confining pressure (X and Z). The value of the confining pressures of the samples are increased in sequence, which is used to simulate the fracture propagation of the field HF process. The experiment was processed under 23°C. i.e., the room temperature in the laboratory. Pressurizing was stopped and maintained after the confining pressure value was stable. Then the injection pressure was started, and simultaneously recording pressure and acoustic emission data. When the injection pressure in the boreholes stabilized, data collection was complete and the experiment was finished.

2.4 Acoustic Emission Monitoring

The AE signal detecting part includes three eight-channel AE signal processing systems (PCI-2). The AE system is from the American physical acoustics company (PAC), which has an operating frequency range from 20 to 1,500 kHz. The trigger threshold of AE was set to 40 dB. The sensors were separated into four groups, which were adhered to the surrounding surfaces of the samples, respectively (**Figure 2D**). Sixteen AE sensors are used to enhance source location accuracy in this study. The location coordinates of the AE events were determined by the arrival time differences between different sensors, the sensor arrangement geometry, and the propagation velocity through

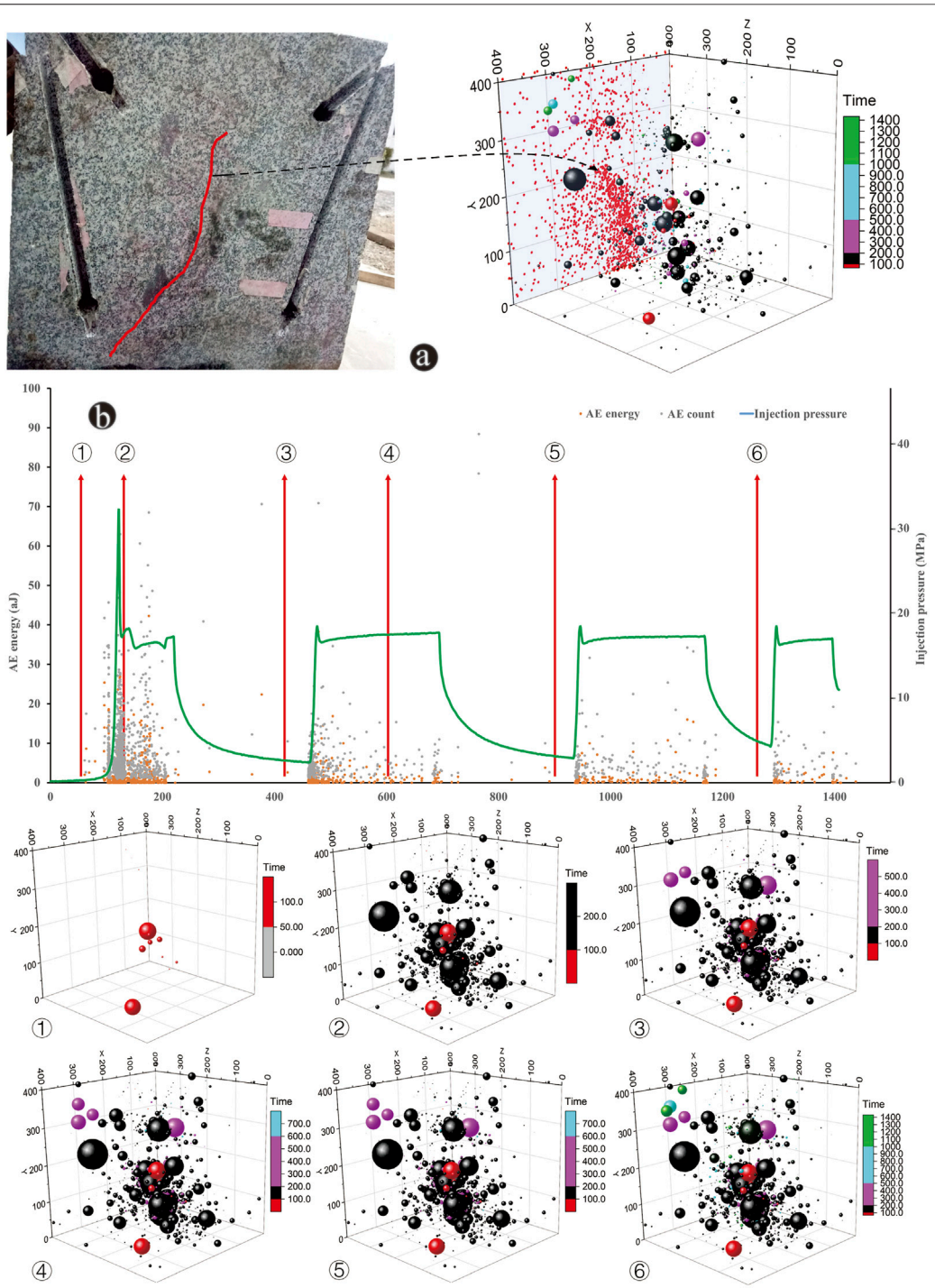

FIGURE 8 | AE spatial distribution characteristics of HDR400-2 **(A)** AE spatial distribution compared with the surface appearance of the sample; **(B)** AE spatial distribution of each pump period. ①–⑥ represent the spatial distribution characteristics of AE for different section of the pressure curve corresponding to the time increasing. See **Figure 7** for detailed figure description.

the granite (Shang et al., 2021). After installation, the probe was connected to the acoustic emission system according to the serial number, and the upper adapter plate, pressure injection joint, and longitudinal pressure pump head. The upper pressure plate was then fixed with a nut.

The detected AE signal was analyzed by the rise time, AE counts, AE amplitude, and AE duration (Mao et al., 2017), which is illustrated in **Figure 3**. The injection pressure and AE parameters were combined to evaluate the propagation of the hydraulic fracture (Landis and Baillon, 2002).

3 RESULTS

3.1 Injection Pressure and AE Characterizations

The experiment results are presented in **Table 1**. The samples showed different HF characteristics under different confining pressure conditions, with the same flow rate and temperature. The confining pressures, AE parameters, and spatial distribution characteristics showed differences during the experimental process. In order to better observe the trend of AE parameters during the hydraulic fracturing experiment, we eliminated several very-high values (>300 aJ) of AE energy events, most of which were occurred once the rock fractured, and the elimination would not influence the distribution trend of AE energy and count.

3.1.1 Sample HDR400-1

The injection pressure of HDR400-1 started to rise rapidly 2 min after the injection began, and reached a breakdown pressure of 24.91 MPa (**Figure 4**). Once the rock fractured, the injection pressure quickly dropped to 10.57 MPa. During this process, the AE activity increased significantly, and the AE energy and count reached the maximum of the entire experimental process. Dense AE activity still occurred in the case of a sudden drop in the injection pressure. Subsequently, the injection pressure continued to rise at a relatively rapid rate until it reached 21.39 MPa, and breakdown occurred again; the pressure dropped rapidly to 14.43 MPa. During the second fracture process, the AE activity was also dominant, but compared with the first fracture process, the AE energy and count were weakened. Subsequently, the pressure rapidly increased, and the third fracture process occurred. The breakdown pressure was 24.78 MPa, which was remarkably close to the breakdown pressure of the first time, whereas the pressure dropped to 21.75 MPa. During the third fracture process, there was no obvious AE activity, and the AE energy and count were also significantly reduced, indicating that no obvious cracks were formed in the process.

After the pump was filled with water and injection continued, the pressure increased again and reached a breakdown pressure of 22.63 MPa. After re-pumping, the breakdown pressure was lower than the pressure during the first pumping period. After the breakdown, the injection pressure dropped to 18.16 MPa and then slowly increased to 29.86 MPa. During this process, the AE activity continued to appear, which may represent the continuous occurrence of small-scale cracks causing decompression and injection pressurization during the crack extension.

Cracks occurred when the injection pressure dropped sharply, and a large amount of AE activity was generated simultaneously. The pressure drop occurred because the injection water gradually filled the fractures suddenly formed by fracturing, forming a short-time decompression space. When the crack is filled with water, the pressure increases, forcing the cracks to expand. The subsequent breakdown pressure of the second and third pump periods continued to increase, indicating the continuous expansion of the cracks; however, the AE energy and count were less than those of the first pump period. It can be seen from the cumulative AE energy and count that during the first fracture process, more than half of the AE energy accumulation was completed quickly. The accumulation of AE energy and count was relatively smooth during the subsequent pumping periods.

3.1.2 Sample HDR400-2

After the injection started, the injection pressure increased rapidly (**Figure 5**). The breakdown pressure was 32.15 MPa. Afterwards, the pressure dropped sharply to 17.13 MPa, and the pressure increases to 18.15 MPa. A second fracture occurred, and the pressure dropped to 15.78 MPa. The pressure then increased slowly and steadily, indicating that the continuous water injection after the fracture occurred caused the cracks to propagate. After the pressure increased to 17.15 MPa, the pump refilled water, and the pressure decreased to 2.38 MPa during this process.

The pressure curves in the 2–4 pump periods were similar. The breakdown pressure is 18.39–18.43 MPa. It can be explained that the required breakdown pressure cannot reach 32.15 MPa because the cracks have been opened before. The injection pressure stabilizes at approximately 17 MPa, which is similar to the 17.15 MPa of the first pump period. This suggests that the very first fracture process is the most important fracture process in the entire hydraulic fracture experiment, and a long extended fracture framework may have been formed. This can be verified by the spatial distribution characteristics of acoustic emission (**Figure 5**). The fracture expands along the direction of the first fracture process under a stable pressure of 17 MPa during subsequent pump periods.

3.1.3 Sample HDR400-4

After the sample HDR400-4 injected water to fill the wellbore, the injection pressure increased rapidly and fracture occurred (**Figure 6**). The breakdown pressure was 34.57 MPa. Subsequently, the pressure decreased sharply to 11.86 MPa, and the pressure increased slowly to 14.40 MPa until the pump refilled water, and the pressure decreased to 2.49 MPa.

The pressure curve patterns in the 2–3 pumps are similar, and the pressure rises rapidly after re-pumping. As the cracks steadily expand, the injection pressure steadily increases from approximately 14–17 MPa, which is higher than the residual pressure of the first pump at 14.40 MPa. This may be because the injection water was exhausted before the residual pressure increased to 17 MPa.

The cumulative AE energy and count did not show a rapid increase during the first pump period. Instead, there was a rapid increase during the second pump period.

3.2 Spatial Distribution Characteristics of AE

3.2.1 Sample HDR400-1

The AE spatial distribution of sample HDR400-1 shows that the HF produced a main fracture that is parallel to the direction of the maximum principal stress, and projects a relatively concentrated fracture distribution on the XY plane. It can be seen that the locations of the AE events are aligned with the hydraulic fracture (**Figure 7A**).

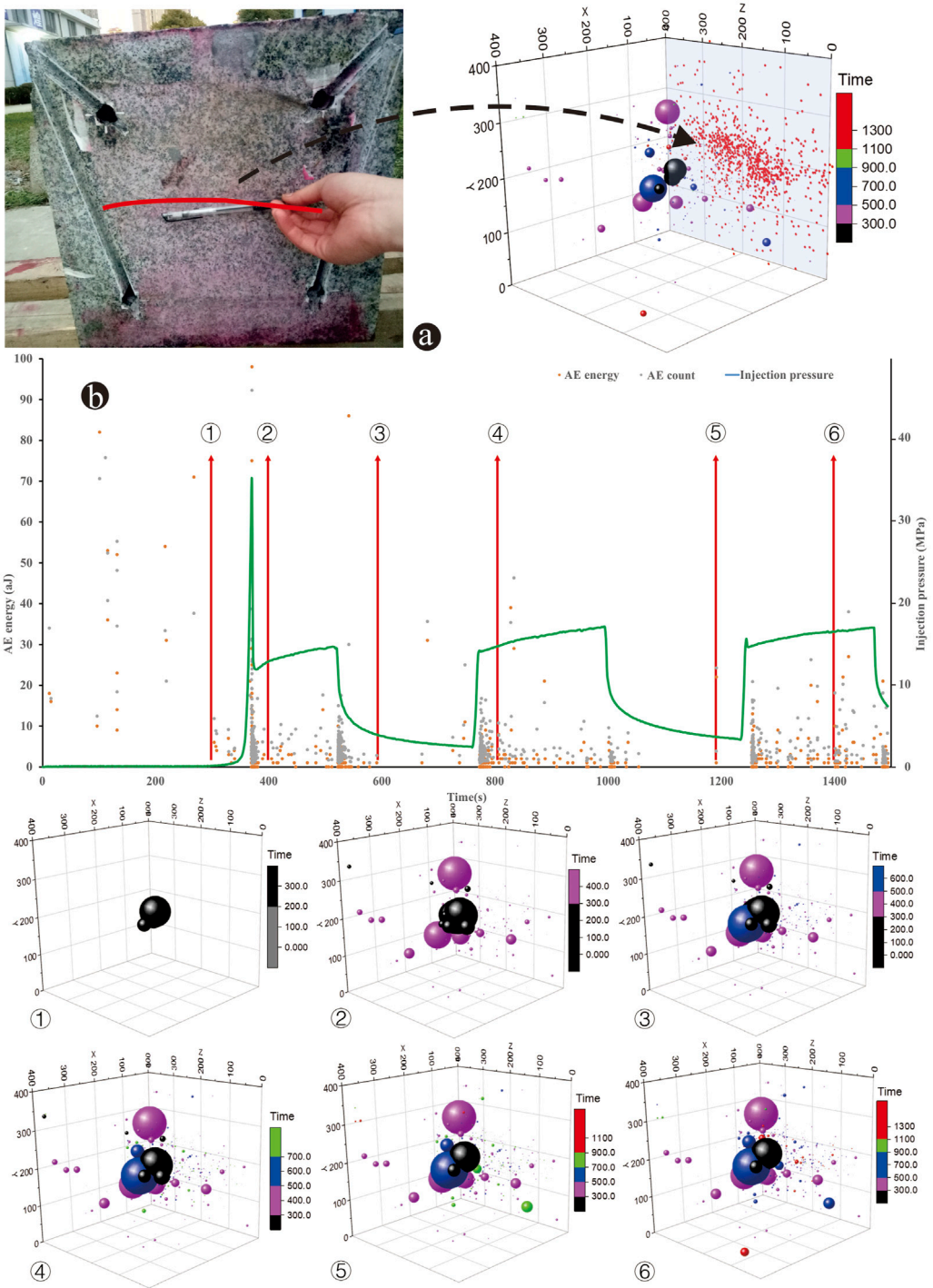

FIGURE 9 | AE spatial distribution characteristics of HDR400-4 **(A)** AE spatial distribution compared with the surface appearance of the sample; **(B)** AE spatial distribution of each pump periods. See **Figure 7** for detailed figure description.

The AE energy and count during the first pump period were high, mainly on one side of the well pipe, and constituted the fracture framework (**Figure 7B**). The AE energy and count of each subsequent pump period were less than those of the first pump period, and the spatial distribution of AE events extends to the other side of the well pipe, showing a lower energy and denser distribution. Overall, sample HDR400-1 shows that the first pump period formed the main fracture framework.

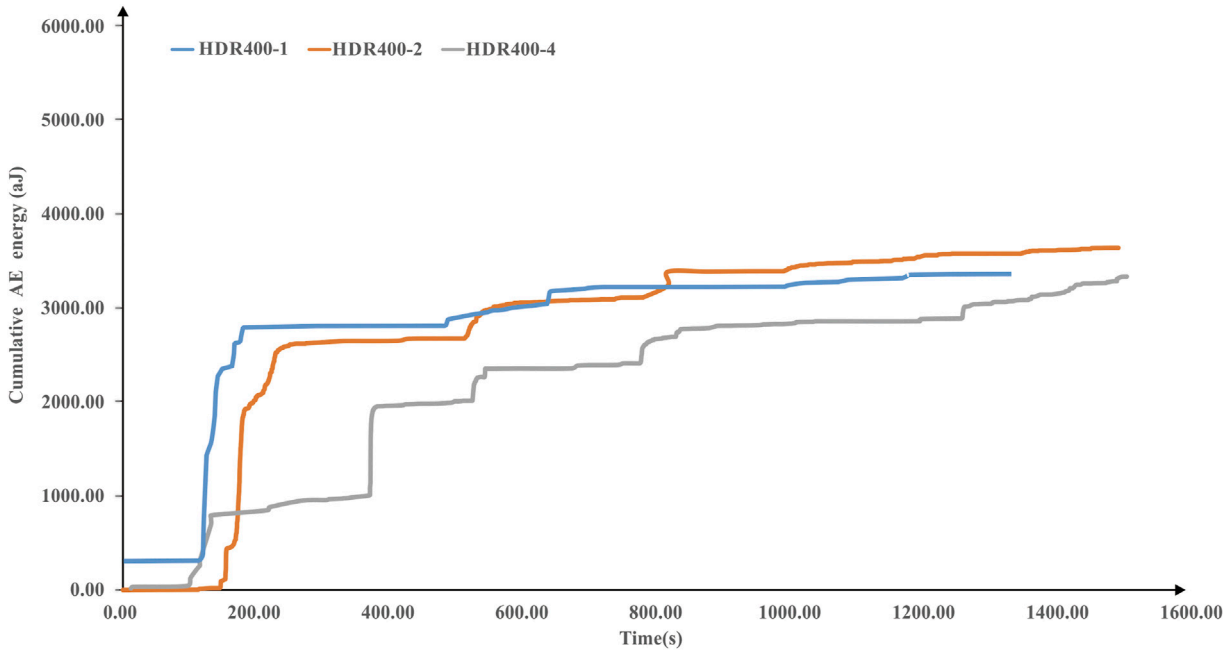

FIGURE 10 | Cumulative AE energy over time.

3.2.2 Sample HDR400-2

The AE spatial distribution of sample HDR400-2 appeared to be relatively dense, and the main fracture direction was parallel to the maximum principal stress direction (**Figure 8A**). The main fracture channel is projected onto the X-Y plane, with a relatively large fracture width (**Figure 8A**). From the temporal and spatial distribution of AE, the fracture process during the first pump period was mainly concentrated around the well pipe and formed the main fracture framework (**Figure 8B**). During the subsequent 2–4 pump injection periods, the cracks gradually spread to the outside. The extended AE events are still mainly in the range of the main fracture, which is equivalent to the extension of the main fracture. Owing to its larger confining pressure compared to HDR400-1, the fracture extension speed is slow, causing the injected water to accumulate in the main fracture.

3.2.3 Sample HDR400-4

The fractures produced by sample HDR400-4 formed a dense main channel (**Figure 9A**). The AE events with larger energy at the first fracture process are mainly parallel to the direction of the maximum principal stress, whereas the denser small-energy AE events are almost horizontally distributed, approximately perpendicular to the direction of the maximum principal stress, which coincides with the fractures appearing on the surface of the sample. It is possible that this phenomenon is related to the influence of the weak layers inside the rock sample; that is, the larger energy events are new cracks formed by HF, and the nearly horizontal dense AE events may have been formed by the weak layers. Therefore, the energy released by the dense horizontal AE events was relatively small. The fractures formed during the first pump period were mainly concentrated in the vertical and horizontal planes at the bottom of the wellbore (**Figure 9B**). During the second and third pumping periods, the fractures mainly extended to the plane of the wellbore and slightly upwards, representing the main fractures extending far away.

4 DISCUSSION

4.1 Analysis of AE Parameters During Hydraulic Fracturing

4.1.1 AE Events During Hydraulic Fracturing

When the injection pressure drops sharply after the peak pressure, the hydraulic fractures rapidly spread, and many AE events occur in the form of stress waves due to the release of potential strain energy (Lei et al., 2019). Similar situation is reported by Ishida et al. (1997) that after injecting high-pressure water into the granite, with the sudden drop of pressure, the AE count increased sharply and the cracks expanded rapidly (Ishida et al., 1997). A main fracture framework was formed in all three samples during the first fracturing process. Under low confining pressures (e.g., sample HDR400-1), the main fractures relatively extend longer, and in the subsequent pump periods, the formation and expansion of fractures occur in the blank areas where no cracks occurred before. However, for the high confining pressure cases (e.g., samples HDR400-2 and HDR400-4), the propagation of fractures in the subsequent pump periods was the continuous reconstruction of the main fractures. Usually, the direction of fracture propagation is perpendicular to the direction of the minimum principal stress (Shang et al., 2021), however the spatial distribution of the AE events in three samples indicates

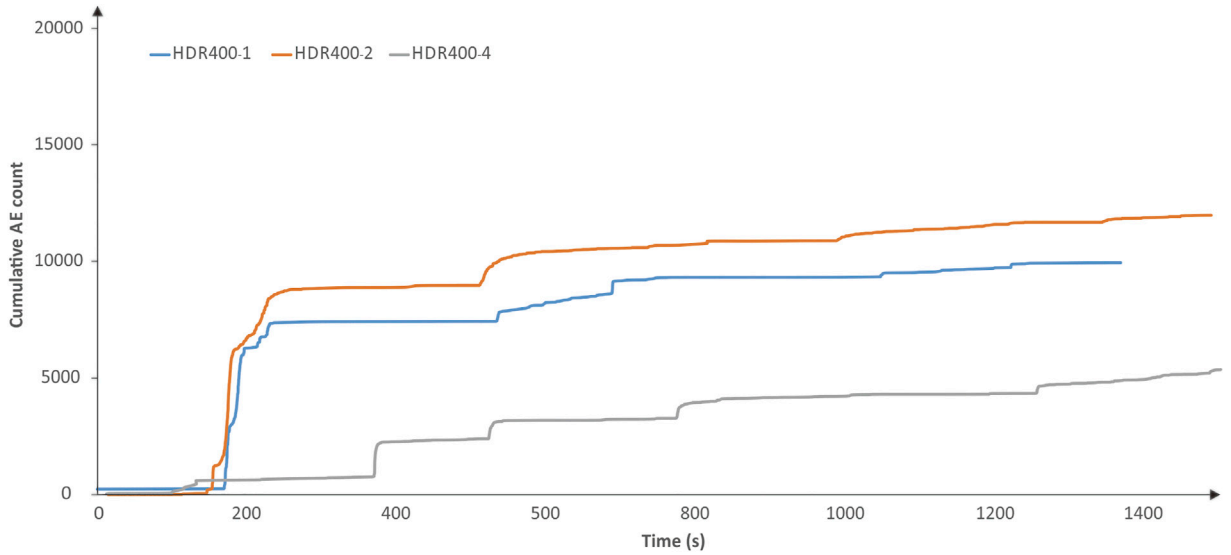

FIGURE 11 | Cumulative AE count over time.

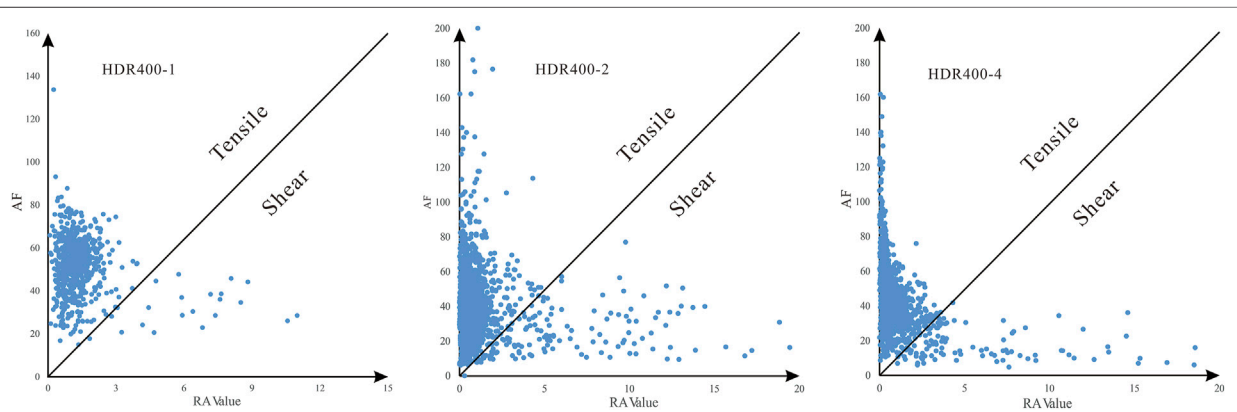

FIGURE 12 | Classification of tensile and shear fracture.

that the direction of the main fractures does not exactly coincide with the maximum stress directions. We speculate that the reason may be due to the artificial damage inside the rock samples during the transportation to the laboratory and the sample-cutting process.

4.1.2 Accumulative AE Energy and Counts During Hydraulic Fracturing

The cumulative AE energy changes before and after the breakdown pressure shows the energy required for the rock fracturing, and the propagation of the fracture caused a release of energy during the fracturing process. For the samples HDR400-1 and HDR400-2, the AE energy accumulates rapidly during the first pump period, and then slowly increases for the subsequent pump periods (**Figure 10**), which is consistent with the observations of Xing et al. (Shan et al., 2021). However, the sample HDR400-4 shows a difference variation trend that the accumulated AE energy is small for the first pump period, and then increased progressively during the subsequent pump periods, perhaps indicating that the condition of high confining pressure limits the rock fracturing during the first pump period. Similarly, the variation of cumulative AE count has a good corresponding with the cumulative AE energy (**Figure 11**).

4.1.3 Analysis of Failure Mechanism

The characteristics of the AE signals are evaluated primarily by the RA value and the average frequency (AF) (Ohtsu, 2010), which are defined as follows:

$$RA\ value = \frac{Rise\ time}{Maximum\ amplitude} \quad (4-1)$$

$$Average\ frequency\ (AF) = \frac{AE\ ringdown\ counts}{Duration\ time} \quad (4-2)$$

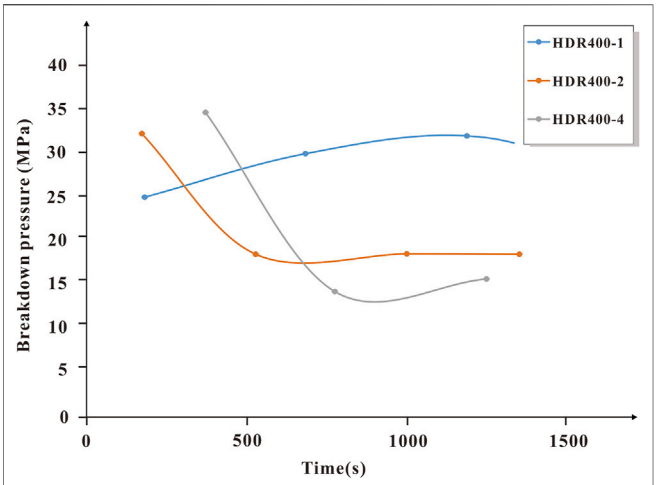

FIGURE 13 | Comparison of sample breakdown pressure curves over time.

The RA value of AE events can be used to distinguish the failure mechanisms, where the RA value of shear failure is generally higher than the RA value of tensile failure (Yue et al., 2019). According to the relationship between the RA value and AF, the detected AE events can be divided into tensile and shear fractures based on the method of JCMS-III B5706 (Ohtsu, 2010; Mao et al., 2017).

As can be seen in **Figure 12** that the percentages of tensile events are 96.9, 90.5, and 91.9%, respectively, for the samples HDR400-1, HDR400-2, and HDR400-4. Although it is necessary to note that the approach based on RA value and AF is kind of empirical method, it can be interoperate that tensile crack dominates in all tests [(Zhang et al., 2021) and references therein]. This result was well in accordance with Jiang et al. (2020), which reported tensile crack comprised over 94% of the cracks. It can be explained that tensile cracks are commonly observed in the initial loading and failure preparatory phase (Zhuang and Zang, 2021), which concentrates most of the AE events.

4.2 Analysis of Confining Pressure on Hydraulic Fracturing

Through comparing three samples it can be found that the initial breakdown pressure increases correspondingly with the confining pressure increases (**Figure 13**), indicating that the high confining pressure has a limiting effect on the rock fracturing. Once the rock is fractured, the higher confining pressure caused the increasing of the fracture surface roughness (Hu et al., 2019; Liu et al., 2021). This may contribute to the fracture remaining open, which results in significantly lower breakdown pressure for subsequent pumping. In addition, after the hydraulic fractures occurring, the residual pressure decreases gradually with the increase of confining pressure, indicating the hydraulic pressure required to maintain the fracture propagation is low at high confining pressure. The samples HDR400-2 and HDR400-4 exhibit similar variation trends of breakdown pressure, in which a high breakdown pressure occurs at first and then the pressure rapidly decrease and stabilize in a lower level. In contrast, the variation of the sample HDR400-1 was different that the pressure maintained at a higher level at whole fracturing process (**Figure 13**). This may be due to the pressure increase caused by the continuous formation of new cracks in the unfractured area during the expansion of the sample HDR400-1.

In order to verify the reliability of the measured breakdown pressure, the empirical equations established by Haimson and Fairhurst (1967) (H&F) and Anderson et al. (1973) were used to calculate the HF breakdown pressures.

$$P_b = 3\sigma_h - \sigma_H + \sigma_T \tag{4-3}$$

$$P_b = \frac{2\nu}{1-\nu}\left(P_{ob} - \alpha P_p\right) + \alpha P_p \tag{4-4}$$

Where P_b represents the breakdown pressure, σ_h represents the minimum horizontal pressure, σ_H represents the maximum horizontal pressure, σ_T represents the rock tensile strength

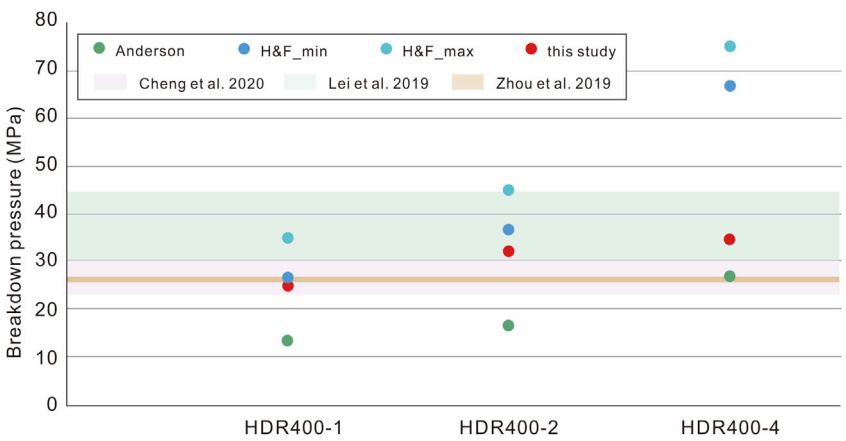

FIGURE 14 | Comparison between measured HF breakdown pressure and relative literature results in Qinghai.

with the range of 11.5–19.9 MPa (Lei et al., 2019), ν represents the Poisson's ratio of 0.25 (Lei et al., 2019), P_{ob} represents the overlying rock pressure, P_p represents the pore pressure of zero (considering the extremely low permeability of the rock), and α represents the Biot coefficient with the range of 0.2–0.6.

The results showed that the breakdown pressures calculated by **Eq. 4-3**) are relatively high compared with the measured values, while the breakdown pressures calculated by **Eq. 4-4**) are lower than the measured values. That is, the measured HF breakdown pressures fall in the middle range of the calculated results of these two empirical equations.

We compared with measured values of other studies in Qinghai Province, and the results show consistency (**Figure 14**). Lei et al. (2019) obtained the HF breakdown pressures of monzogranite at room temperature of 30.6–44.3 MPa. Zhou et al. (2019) reported the HF breakdown pressures of granite of 26.49–26.65 MPa. Cheng et al. (2020) obtained the HF breakdown pressures of 23.07–30.28 with the temperatures range of 30–120°C. Since the measured HF breakdown pressure is influenced by the sample size, confining pressure, injection flow rate, temperature, etc. (Lei et al., 2019; Cheng et al., 2020), we speculate that the deviations between former studies and our results may be due to the different experimental conditions.

4.3 Implication for Field Fracturing

Although the number of samples in our HF test is small, all three samples exhibit the formation of the main fracture framework during the first pumping, which indicates that the initial HF operation would likely has a large impact on field reservoir construction. And high confining pressure will cause the fracture modification to be concentrated near the borehole, but lower confining pressure help to the main fractures to extend longer (Warpinski et al., 1982). This suggests that HF at shallow depths (low confining pressure) may result in greater reservoir space, while the deeper depths (high confining pressure) is likely to create smaller reservoir space, but with more adequate reservoir construction effect. The HF experiments also indicate that selecting a field site with relatively low geological stress is more beneficial for fracture expansion (Cheng et al., 2020). The failure mechanism of all samples revealed a dominate character of tensile crack, suggesting that tensile crack occurs first when HF is processing at field site of Qinghai.

5 CONCLUSION

We find that a main hydro-fracture was formed during the first fracturing process. Under high confining pressure, a larger breakdown pressure is required for rock fracturing, meanwhile the residual pressure gradually decreased. After the fracture formation, the pressure required to maintain crack extension was lower under higher confining pressure. Many AE events with greater energy occurred during the first pump period. The accumulated energy is slowly and stable at the subsequent pump periods. The proportion of tensile fractures during the hydraulic fracturing ac the effect of HF counted for more than 85% of all fractures. The subsequent fracture extension is mainly concentrated in the wellbore, rather than extending to the distant region to form new fractures. Therefore, we suggest that field engineering should carefully launch the initial HF, which may determine the main fracture framework of the field at the first pump procedure.

DATA AVAILABILITY STATEMENT

The raw data supporting the conclusion of this article will be made available by the authors, without undue reservation.

AUTHOR CONTRIBUTIONS

WH: Writing original draft. WG: Conceptualization and Investigation. CY: Software and Visualization. LL: Investigation and Methodology. ZZ: Supervision and Methodology. GH: Visualization.

FUNDING

This work was supported by the National Key Research and Development Program of China (2019YFB1504203), China Geological Survey Project (DD20221676), the Fundamental Research Funds of the Chinese Academy of Geological Sciences Project (SK201906), National Natural Science Foundation of China (41807208), and S&T Program of Hebei (20374201D).

REFERENCES

Anderson, R. A., Ingram, D. S., and Zanier, A. M. (1973). Determining Fracture Pressure Gradients from Well Logs. *J. Pet. Techn.* 25, 1259–1268. doi:10.2118/4135-pa

Caulk, R. A., Ghazanfari, E., Perdrial, J. N., and Perdrial, N. (2016). Experimental Investigation of Fracture Aperture and Permeability Change within Enhanced Geothermal Systems. *Geothermics* 62, 12–21. doi:10.1016/j.geothermics.2016.02.003

Cheng, Y., Zhang, Y., Yu, Z., Hu, Z., and Yang, Y. (2020). An Investigation on Hydraulic Fracturing Characteristics in Granite Geothermal Reservoir. *Eng. Fracture Mech.* 237, 107252. doi:10.1016/j.engfracmech.2020.107252

Fan, T.-g., and Zhang, G.-q. (2014). Laboratory Investigation of Hydraulic Fracture Networks in Formations with Continuous Orthogonal Fractures. *Energy* 74, 164–173. doi:10.1016/j.energy.2014.05.037

Fischer, T., and Guest, A. (2011). Shear and Tensile Earthquakes Caused by Fluid Injection. *Geophys. Res. Lett.* 38, a–n. doi:10.1029/2010GL045447

Guo, L. L. (2016). *Test and Model Research of Hydraulic Fracturing and Reservoir Damage Evolution in Enhanced Geothermal System [dissertation]*. Jilin: Jilin University. (in Chinese with English abstract).

Haimson, B., and Fairhurst, C. (1967). Initiation and Extension of Hydraulic Fractures in Rocks. *Soc. Petrol. Engng J.* 7, 310–318. doi:10.2118/1710-pa

Hu, D., Li, J., Zhou, H., Lu, J., Ma, D., and Zhang, F. (2019). Gas Permeability Evolution of Granite under Confining Pressure Unloading Tests. *Eur. J. Environ. Civil Eng.* 25, 1915–1928. doi:10.1080/19648189.2019.1610073

Ishida, T. (2001). Acoustic Emission Monitoring of Hydraulic Fracturing in Laboratory and Field. *Construction Building Mater.* 15 (5–6), 283–295. doi:10.1016/S0950-0618(00)00077-5

Ishida, T., Chen, Q., and Mizuta, Y. (1997). Effect of Injected Water on Hydraulic Fracturing Deduced from Acoustic Emission Monitoring. *Pure Appl. Geophys.* 150, 627–646. doi:10.1007/s000240050096

Jiang, Z., Li, Q., Hu, Q., Liang, Y., Xu, Y., Liu, L., et al. (2020). Acoustic Emission Characteristics in Hydraulic Fracturing of Stratified Rocks: A Laboratory Study. *Powder Techn.* 371, 267–276. doi:10.1016/j.powtec.2020.05.050

Kolawole, O., and Ispas, I. (2020). Interaction between Hydraulic Fractures and Natural Fractures: Current Status and Prospective Directions. *J. Petrol. Explor Prod. Technol.* 10 (4), 1613–1634. doi:10.1007/s13202-019-00778-3

Kumari, W. G. P., Ranjith, P. G., Perera, M. S. A., Li, X., Li, L. H., Chen, B. K., et al. (2018). Hydraulic Fracturing under High Temperature and Pressure Conditions with Micro CT Applications: Geothermal Energy from Hot Dry Rocks. *Fuel* 230, 138–154. doi:10.1016/j.fuel.2018.05.040

Landis, E. N., and Baillon, L. (2002). Experiments to Relate Acoustic Emission Energy to Fracture Energy of Concrete. *J. Eng. Mech.* 128128 (6), 6986–7702. doi:10.1061/(ASCE)0733-939910.1061/(asce)0733-9399(2002)128:6(698)

Lei, Z., Zhang, Y., Hu, Z., Li, L., Zhang, S., Fu, L., et al. (2019). Application of Water Fracturing in Geothermal Energy Mining: Insights from Experimental Investigations. *Energies* 12 (11), 2138. doi:10.3390/en12112138

Li, B. Q., and Einstein, H. H. (2019). Direct and Microseismic Observations of Hydraulic Fracturing in Barre Granite and Opalinus Clayshale. *J. Geophys. Res. Solid Earth* 124 (11), 11900–11916. doi:10.1029/2019JB018376

Liu, X., Feng, B., Liu, Y., and Yuan, Y. (2021). Hydraulic Conductivity Characteristics of Hot Dry Rocks under Different Fracture Modes. *Acta Geologica Sinica (Eng)* 95 (6), 1915–1925. doi:10.1111/1755-6724.14872

Liu, Z., Wang, S., Zhao, H., Wang, L., Li, W., Geng, Y., et al. (2018). Effect of Random Natural Fractures on Hydraulic Fracture Propagation Geometry in Fractured Carbonate Rocks. *Rock Mech. Rock Eng.* 51 (2), 491–511. doi:10.1007/s00603-017-1331-y

Lu, S.-M. (2018). A Global Review of Enhanced Geothermal System (EGS). *Renew. Sustain. Energ. Rev.* 81, 2902–2921. doi:10.1016/j.rser.2017.06.097

Mao, R., Feng, Z., Liu, Z., and Zhao, Y. (2017). Laboratory Hydraulic Fracturing Test on Large-Scale Pre-cracked Granite Specimens. *J. Nat. Gas Sci. Eng.* 44, 278–286. doi:10.1016/j.jngse.2017.03.037

Matsunaga, I., Kobayashi, H., Sasaki, S., and Ishida, T. (1993). Studying Hydraulic Fracturing Mechanism by Laboratory Experiments with Acoustic Emission Monitoring. *Int. J. Rock Mech. Mining Sci. Geomechanics Abstr.* 30 (7), 909–912. doi:10.1016/0148-9062(93)90043-D

Mit-Led Report (2006). *The Future of Geothermal Energy: Impact of Enhanced Geothermal System (EGS) on the United States in 21st Century*. MIT-led interdisciplinary panel.

Moya, D., Aldás, C., and Kaparaju, P. (2018). Geothermal Energy: Power Plant Technology and Direct Heat Applications. *Renew. Sustain. Energ. Rev.* 94, 889–901. doi:10.1016/j.rser.2018.06.047

Ohtsu, M. (2010). Recommendation of RILEM TC 212-ACD: Acoustic Emission and Related NDE Techniques for Crack Detection and Damage Evaluation in concrete*. *Mater. Struct.* 43 (9), 1187–1189. doi:10.1617/s11527-010-9640-6

Shan, K., Zhang, Y., Zheng, Y., Cheng, Y., and Yang, Y. (2021). Effect of Fault Distribution on Hydraulic Fracturing: Insights from the Laboratory. *Renew. Energ.* 163, 1817–1830. doi:10.1016/j.renene.2020.10.083

Shang, D., Chen, Y., Zhao, Z., Shangguan, S., and Qi, X. (2021). Mechanical Behavior and Acoustic Emission Characteristics of Intact Granite Undergoing Direct Shear. *Eng. Fracture Mech.* 245, 107581. doi:10.1016/j.engfracmech.2021.107581

State Council Report (2021). Action Plan for Carbon Dioxide Peaking before 2030. Information on Available at: http://www.gov.cn/zhengce/content/2021-10/26/content_5644984.htm.

Tomac, I., and Sauter, M. (2018). A Review on Challenges in the Assessment of Geomechanical Rock Performance for Deep Geothermal Reservoir Development. *Renew. Sustain. Energ. Rev.* 82, 3972–3980. doi:10.1016/j.rser.2017.10.076

Warpinski, N. R., Schmidt, R. A., and Northrop, D. A. (1982). *In-situ* Stresses: the Predominant Influence on Hydraulic Fracture Containment. *J. J. Pet. Techn.* 34, 653–664. doi:10.2118/8932-pa

Wu, B., Zhang, G., Zhang, X., Jeffrey, R. G., Kear, J., and Zhao, T. (2017). Semi-Analytical Model for a Geothermal System Considering the Effect of Areal Flow between Dipole Wells on Heat Extraction. *Energy* 138, 290–305. doi:10.1016/j.energy.2017.07.043

Xing, Y., Zhang, G., Luo, T., Jiang, Y., and Ning, S. (2019). Hydraulic Fracturing in High-Temperature Granite Characterized by Acoustic Emission. *J. Pet. Sci. Eng.* 178, 475–484. doi:10.1016/j.petrol.2019.03.050

Xinhua News Agency is authorized to release (2021).Outline of the 14th Five-Year Plan (2021-2025) for National Economic and Social Development and Vision 2035. Information on Available at: http://www.gov.cn/xinwen/2021-03/13/content_5592681.htm (Accessed March 13, 2021).

Yamamoto, K., Naoi, M., Chen, Y., Nishihara, K., Yano, S., Kawakata, H., et al. (2019). Moment Tensor Analysis of Acoustic Emissions Induced by Laboratory-Based Hydraulic Fracturing in Granite. *Geophys. J. Int.* 216 (3), 1507–1516. doi:10.1093/gji/ggy493

Yue, Y., Peng, S., Liu, Y., and Xu, J. (2019). Investigation of Acoustic Emission Response and Fracture Morphology of Rock Hydraulic Fracturing under True Triaxial Stress. *Acta Geophys.* 67 (4), 1017–1024. doi:10.1007/s11600-019-00299-x

Yuyama, S., Li, Z. W., Ito, Y., and Arazoe, M. (1999). Quantitative Analysis of Fracture Process in RC Column Foundation by Moment Tensor Analysis of Acoustic Emission. *Construction Building Mater.* 13 (1–2), 87–97. doi:10.1016/S0950-0618(99)00011-2

Zhang, Q., Zhang, X.-P., and Sun, W. (2021). A Review of Laboratory Studies and Theoretical Analysis for the Interaction Mode between Induced Hydraulic Fractures and Pre-existing Fractures. *J. Nat. Gas Sci. Eng.*, 86, 103719. doi:10.1016/j.jngse.2020.103719

Zhang, Y., Ma, Y., Hu, Z., Lei, H., Bai, L., Lei, Z., et al. (2019). An Experimental Investigation into the Characteristics of Hydraulic Fracturing and Fracture Permeability after Hydraulic Fracturing in Granite. *Renew. Energ.* 140, 615–624. doi:10.1016/j.renene.2019.03.096

Zhou, Z., Jin, Y., Zeng, Y. J., Zhang, X. D., Zhou, J., Wang, W. Z., et al. (2019). Experimental Study on Hydraulic Fracturing Physics Simulation, Crack Initiation and Propagation in Hot Dry Rock Geothermal Reservoir in Gonghe Basin, Qinghai. *J. Jilin Univ. (Earth Sci. Edition)* 49 (5), 1425. doi:10.13278/j.cnki.jjuese.20180204

Zhou, Z., Jin, Y., Zeng, Y., Zhang, X., Zhou, J., Zhuang, L., et al. (2020). Investigation on Fracture Creation in Hot Dry Rock Geothermal Formations of China during Hydraulic Fracturing. *Renew. Energ.* 153, 301–313. doi:10.1016/j.renene.2020.01.128

Zhuang, L., and Zang, A. (2021). Laboratory Hydraulic Fracturing Experiments on Crystalline Rock for Geothermal Purposes. *Earth-Science Rev.* 216, 103580. doi:10.1016/j.earscirev.2021.103580

Conflict of Interest: The authors declare that the research was conducted in the absence of any commercial or financial relationships that could be construed as a potential conflict of interest.

Publisher's Note: All claims expressed in this article are solely those of the authors and do not necessarily represent those of their affiliated organizations, or those of the publisher, the editors and the reviewers. Any product that may be evaluated in this article, or claim that may be made by its manufacturer, is not guaranteed or endorsed by the publisher.

frontiers | Frontiers in Earth Science

ORIGINAL RESEARCH
published: 18 May 2022
doi: 10.3389/feart.2022.858748

Inversion of the Temperature and Depth of Geothermal Reservoirs Using Controlled Source Audio Frequency Magnetotellurics and Hydrogeochemical Method

Gui Zhao[1,2], Yanguang Liu[1,3], Longhua Hu[4], Kai Bian[1]*, Shenjun Qin[1], Feng Liu[2,3] and Jing Hu[5]*

[1]Key Laboratory of Resource Exploration Research of Hebei Province, Hebei University of Engineering, Handan, China, [2]Institute of Hydrogeology and Environmental Geology, Chinese Academy of Geological Sciences, Shijiazhuang, China, [3]Technology Innovation Center for Geothermal and Hot Dry Rock Exploration and Development, Ministry of Natural Resources, Shijiazhuang, China, [4]The Nuclear Industry Geological Survey, Xingan, China, [5]Jiangsu University of Science and Technology, Jiangsu, China

OPEN ACCESS

Edited by:
Dawei Hu,
Institute of Rock and Soil Mechanics (CAS), China

Reviewed by:
Xianchun Tang,
Chinese Academy of Geological Science, China
Bo Feng,
Jilin University, China
Andong Wang,
East China University of Technology, China

***Correspondence:**
Yanguang Liu
gaoyuanzhixing@163.com
Kai Bian
biankai@hebeu.edu.cn

Specialty section:
This article was submitted to Solid Earth Geophysics, a section of the journal Frontiers in Earth Science

Received: 20 January 2022
Accepted: 17 March 2022
Published: 18 May 2022

Citation:
Zhao G, Liu Y, Hu L, Bian K, Qin S, Liu F and Hu J (2022) Inversion of the Temperature and Depth of Geothermal Reservoirs Using Controlled Source Audio Frequency Magnetotellurics and Hydrogeochemical Method. Front. Earth Sci. 10:858748. doi: 10.3389/feart.2022.858748

The detection of the depth and temperature of deep geothermal reservoirs suffers great uncertainty if it is completed using the simple combination of traditional geophysical and geochemical methods. Given this, this study investigated the combined utilization of multiple methods including the multi-information joint detection using the controlled source audio frequency magnetotellurics (CSAMT) method and geothermometers in the Qutan geothermal field. First, the reservoir temperature and the depth of geothermal water circulation in the geothermal field were estimated using the geochemical method. Afterward, the relationship between the CSAMT resistivity and temperature of strata was explored through borehole temperature measurement. Based on this, the depth and temperature of geothermal reservoirs in the geothermal field were estimated again. According to the comprehensive analysis and comparison of the thermal reservoir temperatures and depths obtained using the two methods, the shallow reservoirs in the Qutan geothermal field have a top burial depth of approximately 423 m, a thickness of about 300 m, a temperature of about 79°C, and a fluid circulation depth of about 1959 m.

Keywords: CSAMT, geothermometer, borehole temperature measurement, geothermal reservoir temperature, geothermal reservoir depth

INTRODUCTION

Geothermal resources are greatly potential clean energy with zero carbon emissions (Long et al., 2021; Long et al., 2022). Usually, these geothermal reservoirs are buried deep in the ground, and it is difficult to predict their depth, thickness, and temperature. Accurately determining these characteristics of thermal reservoirs in advance can greatly increase the rate of drilling and reduce the extraction costs of geothermal resources. At present, geophysical methods such as CSAMT that are used to detect formation depth and thickness cannot directly reflect the distribution of reservoir temperature (Wu et al., 2012; Hu et al., 2013). Although geothermometers and other geochemical methods can be used to calculate the temperatures of deep geothermal reservoirs through inversion, they are difficult to determine the burial depth of geothermal reservoirs (Zhou

et al., 2008; Huang et al., 2017). However, the two different types of methods can be used in combination to detect the depths and temperatures of geothermal reservoirs with improved accuracy (Wang et al., 2020).

CSAMT is a method commonly used in geothermal exploration (Li et al., 2016; Cao et al., 2018; Cui et al., 2018; Dong et al., 2018). It can be used to investigate shallow geothermal reservoirs at depths of less than 2000 m (Aykaç, et al., 2015; Basokur et al., 1997). In comparison with other electromagnetic methods such as high-density resistivity and transient electromagnetics, CSAMT is better suited for identifying deep strata, electrical anomalies, and geothermal reservoir depth (Pellerin et al., 1996; Xiong and Mao 2005; Wu et al., 2014). Remarkable achievements have been made in the relationship between CSAMT and formation temperature. Former Soviet scientist Г.А. Cheremensky (1982) revised the general variation law between formation temperature and formation resistivity and established a corresponding expression. The study of Meng Yinsheng et al. (2011) indicated that formation resistivity is closely related to groundwater salinity and temperature and that formation resistivity is significantly affected by the changes in temperature when the groundwater salinity is low. Based on these findings, they developed the CSAMT resistivity-temperature method, by which they successively determined the geothermal reservoir temperature of a geothermal field in Beijing through inversion. Meng Yinsheng et al. (2010) used the resistivity-temperature method and obtained the temperature of deep geothermal resources through the inversion using CSAMT resistivity. The obtained temperature was roughly consistent with the measured temperature of geothermal wells. Therefore, the resistivity-temperature method can improve the exploration accuracy of deep geothermal reservoirs.

In actual exploration, the temperature of thermal reservoirs is usually predicted using geophysical detection combined with geothermometers to improve the detection accuracy of geothermal reservoir characteristics (Yan et al., 2018). Geothermometers, generally including cationic geothermometers and silica geothermometers, are widely used in the estimation of geothermal reservoir temperature (Giggenbach et al., 1994; Zhang et al., 2015; Ba et al., 2018). Barcelona et al. (2019) estimated the temperature of the Gollette geothermal field using cation geothermometers, and the estimates were consistent with the results obtained using multiple mineral equilibrium diagrams. Xu et al. (2019) considered silica geothermometers more suitable for the estimation of geothermal reservoir temperature than the silica-enthalpy mixing model and used them to estimate the temperature of the Xi'an geothermal field. Sun et al. (2015) used the SiO_2 solubility curve to determine the minerals in a solution that controlled the SiO_2 concentration and further effectively estimated the geothermal reservoir temperature. By using the Na-K-Mg ternary diagram, Zhao et al. (2018) demonstrated that the geothermal water in Batang had not reached the ionic equilibrium state and revealed the formation water salinity, both of which play an important role in further study of the relationship between formation resistivity and temperature.

Taking into consideration the findings of previous research on the subject, this study further investigated the formation resistivity-temperature method. Firstly, the geothermal reservoir temperature and the depth of geothermal water circulation were estimated using a geochemical method. Then, the relationship between the CSAMT resistivity and temperature of geothermal reservoirs was explored using the borehole temperature measurement. Finally, the depth and temperature of the geothermal reservoirs in the Qutan geothermal field were estimated. As the results presented in this paper suggest, this method can improve the detection accuracy of geothermal reservoirs.

GEOLOGICAL SETTING

The Jinggang Mountains are located in the northern part of the South China Fold Belt. They border the Cathaysia and Yangtze plates, are next to the Shaoxing-Jiangshan-Pingxiang fault zone in the north, and are connected to the Ganjiang fault zone in the east (**Figure 1**). The Qutan geothermal field lies in the southwestern part of the Jinggang Mountains. Over time, the Qutan area has formed a complicated geological structure pattern, which consists of the following four types of structures according to their main distribution directions, namely NE-trending structures, NS-trending structures, NEE-trending structures, and NS-trending structures. Of them, the NE-trending structures are the most developed. They are dominated by the Huang'ao fault, which extends northeastward and is 50–400 m wide. A silicified fractured zone has developed in the Huang'ao fault and constantly narrows from southwest to northeast.

The western part of the study area is composed of Caledonian and Yanshanian granites. Ordovician and Cambrian slates and sandstones mainly comprise the eastern and southern parts. Part of the area is composed of Quaternary clays and sandy gravels. Because of the diversity of lithologic characteristics, the resistivity of rocks in this area greatly differs (**Table 1**). The Quaternary clays and sandy gravels in the study area have low resistivity, which is about 20–80 Ω m. The Ordovician-Cambrian metamorphic sandstones have average resistivity of about 1,136 Ω m and a the resistivity range of 928–1,345 Ω m. The biotite granites have average resistivity of 4,267 Ω m, which greatly differs from that of metamorphic sandstones. However, their resistivity varies in a wider range of 563–7,971 Ω m. The silicified zone has the highest average resistivity of 16,674 Ω m, and its range of variation is even wider than those of the abovementioned rocks. The resistivity of the various rocks is significantly different from that of the silicified zone. This difference is conducive to the detection of fault structures and provides a basis for determining the geothermal reservoir locations.

Relevant content has been added according to this comment. Bedrock fissure water is dominant in the Qutan area, with water-bearing rocks consisting of clastic rocks, epimetamorphic rocks, and granites. Bedrock fissure water in this area is primarily recharged by atmospheric

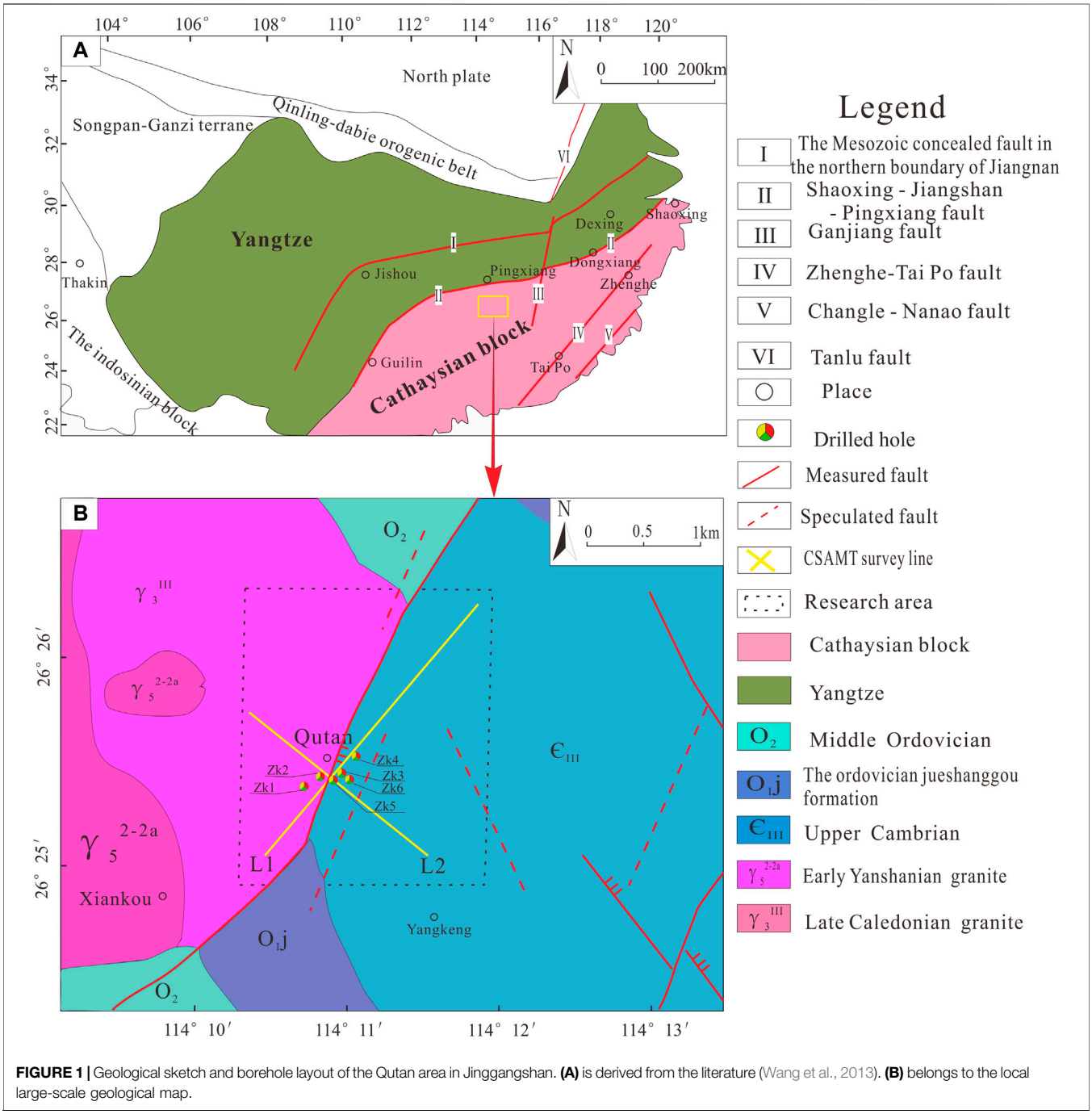

FIGURE 1 | Geological sketch and borehole layout of the Qutan area in Jinggangshan. **(A)** is derived from the literature (Wang et al., 2013). **(B)** belongs to the local large-scale geological map.

TABLE 1 | List of physical properties of rock specimens.

Lithologic Characters	Sample Number	Average Resistivity/ Ω · m	Variation Range/ Ω · m	Temperature/°C
Clays and sandy gravels	-	50	20–80	23
Granites	30	4,267	563–7,971	23
Silicified zone	30	16,674	6,451–26,896	23
Metamorphic sandstones	31	1,136	928–1,345	23

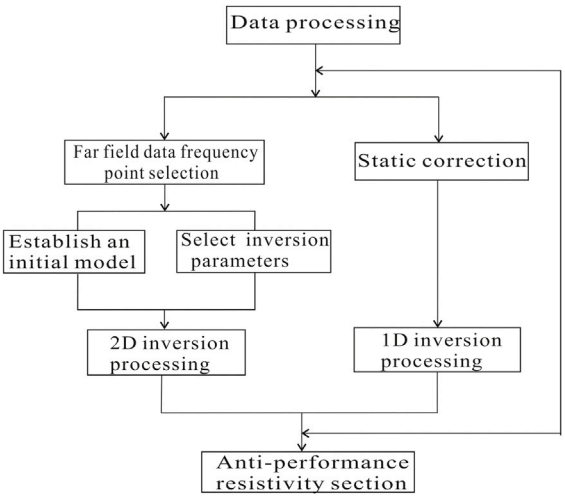

FIGURE 2 | CSAMT data processing flow.

precipitation or laterally recharged by bedrock fissures. It is exposed in the form of springs or discharged to the ground surface in the form of undercurrents. The bedrock fissure water has hydrochemical facies of mainly HCO_3-K + Na type, pH of less than 7, and salinity of 70–120 mg/L. Therefore, it is freshwater.

Geothermal wells are described as follows (**Figure 1**). Representative geothermal wells in the study area include ZK2 and ZK5. The two wells are close to each other and slightly differ in strata. The lithology revealed by well ZK2 includes brownish-yellow gravel layer, grayish-white and brownish-yellow coarse-grained biotite granites, gray and light gray siliceous breccias, and grayish-black metamorphic sandstones from top to bottom. The lithology revealed by well ZK2 provides an important scientific basis for the CSAMT results.

No hot spring is exposed in the Jinggangshan area. The complex geological structures in this area create difficulties for the detection of geothermal reservoirs. The geothermal exploration in the Qutan area has also undergone a long process, until wells ZK3, ZK5, and ZK6 at the intersections of the Huangao fault and the NW-trending fault revealed geothermal water with a temperature of 38–42 C (**Figure 1**). These three wells have a depth of 377.85, 446, and 450.2 m, respectively. This discovery lays a foundation for the geothermal surveys in Qutan and even the Jinggangshan area.

METHODOLOGY

CSAMT

The GDP-32 controllable source audio magnetotelluric acquisition system produced by the ZONGE company of the United States was adopted for CSAMT sounding in this study. It had an effective acquisition frequency of 0.125–8,192 Hz and an exploration depth of 1,500 m. The CSAMT data processing process is shown in **Figure 2**. First, conduct smoothing and interpolation of mutation data under constraints of adjacent measuring points. Second, conduct static displacement correction and topographic correction based on the known geological data, sections, and topographic relief and establish a primary model using appropriate inversion parameters selected. Finally, adopt a smooth inversion program to reduce the errors caused by initial parameters that were artificially set by referring to one-dimensional resistivity inversion. Since CSAMT is restricted by the transmitting power, near-field effect tends to occur. Therefore, man-machine interaction was adopted in the data processing in this study.

Two CSAMT survey lines (i.e., L1 and L2) were deployed in the study area and each of them had a length of 5 km. A total of 102 measuring points were set, with an interval of 50 m. L1, which ran parallel to the Huangao fault, was mainly used to detect the distribution of Yanshanian granites and their surrounding secondary faults. L2, which ran vertically along the Huangao fault, was primarily used to explore the distribution of the Huangao fault and Yanshanian granites and their surrounding secondary faults (**Figure 1**).

Sample Collection and Analysis

Relevant content has been added according to this comment. Geothermal water samples were obtained from previous literature. They were divided into two groups numbered ZK2 and ZK5. Samples for total chemical analysis were collected using 2.5 L plastic bottles. The total chemical analysis of water samples was completed as per GB/T8538-2008 Methods for Examination of Drinking Natural Mineral Water at the Nanchang Supervision Testing Center for Mineral Resources, the Ministry of Land and Resources.

In terms of lithology, the study area mainly shows the distribution of granites, metamorphic sandstones, and well-developed silicification zones, for each of which at least 30 samples of physical properties were studied (**Table 1**). The resistivity was measured using instrument Sample Core IP Tester (SCIP) produced by the Canadian manufacturer Instrumentation GDD Inc. The resolution and accuracy were 1 μV and 0.2%, respectively for the voltage measurement, were 1 nA and 0.2%, respectively for the current measurement, and were 1 nV/V and 0.3%, respectively for the polarizability measurement. Spot checks were conducted for 91 samples. The samples that were repeatedly measured in spot checks accounted for 4.8% of the total samples, with a relative error of resistivity of 6.4%. Therefore, the measurement in this study met the requirements of DD 2006-03 Technical Regulations for Physical Property Investigation of Rocks.

Estimation of Geothermal Reservoir Temperature

Water-Rock Equilibrium State

The Na-K-Mg ternary diagram is used to determine the equilibrium state of geothermal water, namely fully equilibrated waters, partially equilibrated water, and immature water (Fahrurrozie et al., 2015). It can be used to assess the

equilibrium state between geothermal water and its surrounding rock and predict the mixing trend of them. This study adopted the Na-K-Mg ternary diagram to determine the equilibrium state and the salinity of geothermal water, thus laying a foundation for development of the resistivity-temperature method and geothermometers.

The Na-K-Mg ternary diagram is mainly based on two chemical reactions (Shi et al., 2019): namely (1) $NaAlSi_3O_8+K^+ = KalSi_3O_8+Na^+$ and (2) $2.8\ KAlSi_3O_8+1.6H_2O + Mg^{2+} = 0.8$ mica $+0.2$ chlorite $+5.4SiO_2+2K^+$. When the reactions (1) and (2) reach the water-rock equilibrium state, Na^+ and K+concentrations remain stable. When the local geothermal water flows upward to the ground surface, the temperature of the geothermal water decreases, the equilibrium state is broken, and Na^+ and K^+ concentrations enter an equilibrated state. When a new equilibrium state is reached, Na^+ and K^+ are partially balanced.

Resistivity-Temperature Method

Massive previous studies have found that temperature changes have a significant influence on formation resistivity (Du, 2011). The general variation between rock resistivity and rock temperature can be expressed by the following equation.

$$\rho_t = \rho_0 / [1 + \alpha(T - 20)] \tag{1}$$

where ρ_0 is the resistivity when the formation temperature is 20 ˚C, and it is considered the approximate initial value of formation resistivity; ρ_t is the resistivity when the formation temperature is T˚C, and it is the surveyed resistivity; α is the rock temperature coefficient, which is usually set at 0.02 and is actually determined using drilling data.

The expression of the geothermal reservoir temperature can be obtained by transforming **Eq. 1** into the following.

$$T = 20 + (\rho_0/\rho_t - 1)/a \tag{2}$$

Formation resistivity can be obtained through inversion using the CSAMT sounding results. Strata can be divided into multiple areas using existing drilling data. After setting the initial resistivity values of various areas and the rock temperature coefficient, the temperature of geothermal reservoirs can be calculated using **Eq. 2**.

Geothermometers

Geothermometers can be used to assess the temperature of a deep geothermal reservoir using an empirical formula representing the relationship between the contents of some chemical components in geothermal fluids and the deep reservoir temperature. The general principle of a geothermometer is as follows. Some chemical components in deep geothermal fluid reach a dissolution equilibrium state with surrounding rocks. During the upwelling of geothermal water, the temperature of geothermal water decreases but the chemical composition of geothermal water remains almost unchanged (Yan, et al., 2019).

In this study, the Na-K-Mg ternary diagram was used to exclude cation geothermometers. Then, the chalcedony geothermometer was selected according to the SiO_2 dissolution curve.

The dissolution of SiO_2 is mainly controlled by quartz, chalcedony, and amorphous silica. The SiO_2 dissolution curve can be used to determine the minerals that control the SiO_2 content of a solution, which serves as a basis for the selection of quartz or chalcedony geothermometers. Using this method, this study concluded that the SiO_2 content of the geothermal water in the Qutan area is mainly controlled by chalcedony. Therefore, it is suitable to select chalcedony geothermometers to estimate the geothermal reservoir temperature in the Qutan area. The formula applied in chalcedony geothermometers is **Eq. 3**.

$$T = \frac{1032}{4.69 - \lg(C_{SiO_2})} - 273.15 \tag{3}$$

where T is the estimated geothermal reservoir temperature (˚C) and C_{SiO_2} is the mass concentration of SiO_2 in water (*mg/l*).

The formula of SiO_2 content is **Eq. 4**.

$$C_{SiO_2} = M_{SiO_2} \times C_{H_2SiO_3} / M_{H_2SiO_3} \tag{4}$$

where C_{SiO_2} and $C_{H_2SiO_3}$ represent the concentrations of SiO_2 and H_2SiO_3, respectively, in geothermal water (mg/l); M_{SiO_2} is the relative molecular mass of SiO_2, which is 60; and $M_{H_2SiO_3}$ is the relative molecular mass of H_2SiO_3, which is 78.

Circulation Depth Calculation

At present, the commonly used methods for calculating the depth of geothermal fluid circulation include the formula method (Gan et al., 2019) and the isotope method. Since the temperature measurement curves of the study area were collected in this study, the authors used the formula method to calculate the depth of geothermal water circulation. The formula for depth of geothermal water circulation is **Eq. 5**.

$$Z = G(T_Z - T_0) + Z_0 \tag{5}$$

where Z is the depth of geothermal water circulation (m); G is the geothermal degree (i.e., the reciprocal of geothermal gradient; m/°C); T_z is the geothermal reservoir temperature (˚C); T_0 is the annual average temperature in the study area (˚C), and Z_0 is the depth of the constant temperature zone (m).

RESULTS AND DISCUSSIONS

Analyses of CSAMT Inversion Sections

Two CSAMT survey lines were deployed in the study area, namely L1 and L2 (**Figure 1**). The two lines are perpendicular to each other, and their intersection is located in the Qutan geothermal field, where four geothermal wells were drilled, namely, ZK1, ZK2, ZK4, and ZK5. Integrated interpretations were carried out for the two survey lines based on the two-dimensional inversion results of resistivity and frequency, as well as existing drilling data. The sections obtained from the two-dimensional integrated interpretation of the two lines are shown in **Figures 3**, **4**. **Figures 3**, **4** show the NE- and SW-trending underground lithologic distribution and local structures in the Qutan geothermal field, respectively, in order to further reveal the distribution of strata and

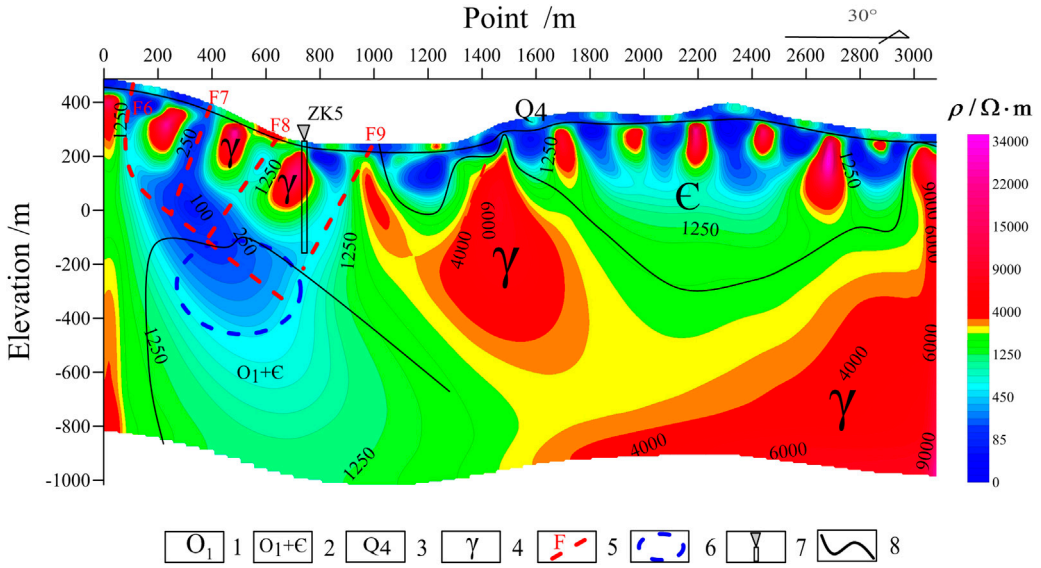

FIGURE 3 | CSAMT integrated interpretation section of survey line L1. 1-Ordovician; 2-Lower Ordovician-Cambrian; 3-Quaternary; 4-Granite; 5-inferred secondary fault; 6-inferred geothermal reservoir; 7-borehole; 8-inferred contact zone.

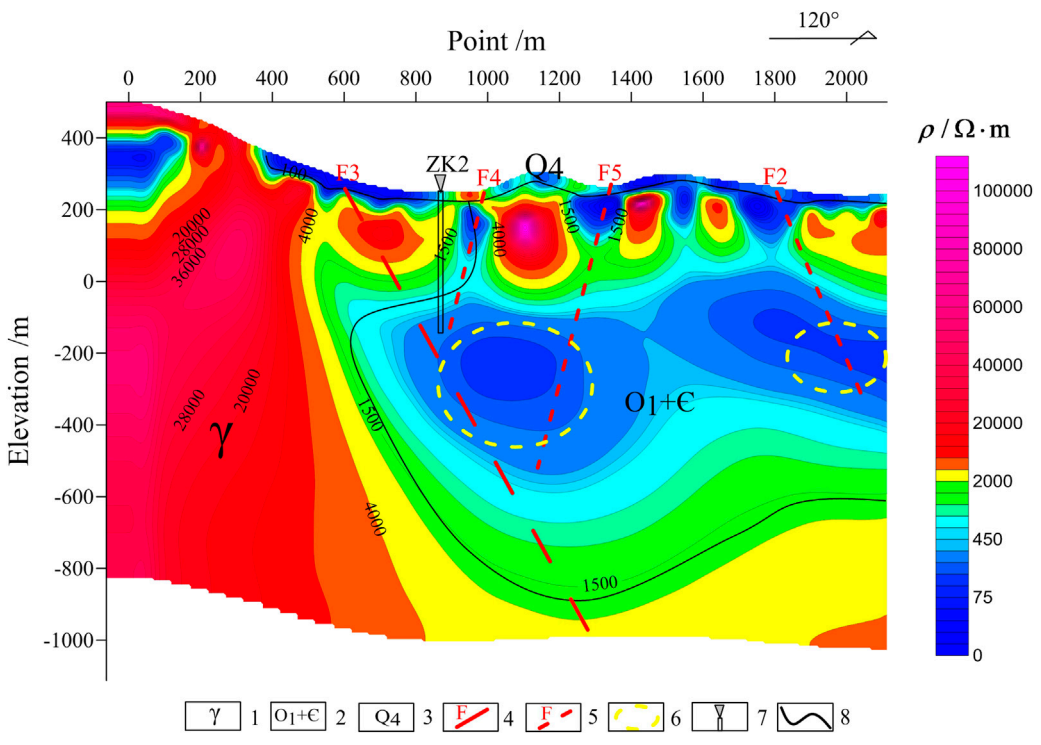

FIGURE 4 | CSAMT integrated interpretation section of survey line L2. 1-Granite; 2-Lower Ordovician-Cambrian; 3-Quaternary; 4-inferred Huangao fault; 5-inferred secondary fault; 6-inferred geothermal reservoir; 7-borehole; 8-inferred contact zone.

underground structures in the study area. Overall, the study area shows simple rock masses, and the deep bedrock and surrounding rocks are roughly dominated by granites and metamorphic sandstones. The Huangao fault is noticeably distributed, and the secondary faults are distributed in a staggered manner.

The CSAMT integrated interpretation section of survey line L1 is a simple two-layer geoelectric structure (**Figure 3**). The low

resistivity bodies on the ground surface along this section are inferred to be the Quaternary overlying layer and weathered layer. In the shallow part, faults are relatively developed and prominent high resistivity strata are distributed in the southwest. The high resistivity strata in the shallow part are inferred to be composed of Ordovician granites. The deep medium-high resistivity of 2,500–30,000 Ω m is induced by complete and dense Cambrian- Ordovician metamorphic sandstones, slates, and granites. In addition, this section shows apparent vertical zoning. The resistivity of points with low numbers (0–100) determined through inversion is greater than 1,500 Ω m, and the corresponding high resistivity bodies are inferred to be granites. The low resistivity areas in the middle part of points with high numbers (100–3,000) are speculated to be composed of carbonaceous slates and metamorphic sandstones. The surrounding areas of points Nos. 50–100, 400–450, 700–750, and 950 show a low resistance zone. The electrical characteristics on both sides of the low resistance zone show a distinct boundary and clear characteristics of an anomaly zone, which is inferred to comprise secondary faults F6, F7, F8, and F9.

Deep rock masses in the study area serve as geothermal sources, and the secondary faults are the rising channels of geothermal water. It can be inferred that the geothermal reservoirs in the study area lie in the low resistance area of points Nos. 350–800, which corresponds to an elevation of −200 to −500 m.

The CSAMT integrated interpretation section of survey line L2 is also a simple two-layer geoelectric structure (**Figure 4**). The high resistivity bodies at points with small numbers (−50–1,000) are inferred to be composed of granites. The low resistance area of points with high numbers (1,000–2,100) is inferred to consist of carbonaceous slates or metamorphic sandstones. The deep high resistance area is composed of granites, with resistivity of 2,500–100,000 Ω m. Intensive gradient anomaly zones occur near points Nos. 650–700, 1,000, 1,350, and 1,800. They show distinct characteristics and are inferred to be secondary faults F2, F4, F5, and Huangao fault F3. Points Nos. 800–2000 correspond to two low resistance area at the elevation of -100 to -400 m. This area is composed of broken rocks, enjoys favorable aquiferous conditions, and thereby is inferred to be a favorable part of geothermal reservoirs.

The following conclusions can be drawn from the analysis of the above two sections and existing drilling data.

(1) The faults in the study area primarily consist of the Huangao fault and multiple parallel secondary faults.
(2) Low-resistivity traps occur at the intersections of faults, and the overlying metamorphic sandstones and granites provide moderate thermal insulation conditions. The Huangao fault and multiple secondary faults are interlaced, providing water channels for the accumulation of geothermal reservoirs. Therefore, it can be inferred that fault intersections are favorable positions for the accumulation of geothermal reservoirs.
(3) The geothermal reservoirs revealed by the CSAMT integrated interpretation section of L1 have a top burial depth of 430 m and a thickness of about 280 m. The geothermal reservoirs revealed by the CSAMT integrated interpretation section of L2 have a top burial depth of t 415 m and a thickness of about 320 m. The horizontal projection centers of the geothermal reservoirs revealed by the two sections are only 300 m apart. Therefore, the burial depth and thickness of the geothermal reservoirs in the Qutan area can be considered the average depth and thickness of the geothermal reservoirs revealed by the two sections. That is, the shallow geothermal reservoirs in the Qutan area determined by CSAMT have a burial depth of 423 m and a thickness of 300 m.

Estimation of Geothermal Reservoir Temperature

Hydrogeochemical Characteristics of Geothermal Water

The salinity of geothermal water is closely related to the water-rock equilibrium state. The water-rock equilibrium state indicates stronger water-rock interactions and higher salinity of geothermal water compared to the non-equilibrium state. The Na-K-Mg ternary diagram is an effective tool for determining the water-rock equilibrium. **Table 2** shows the chemical analysis results of geothermal water from wells ZK2 and ZK5 (Yang et al., 2018). The salinity of geothermal water from ZK2 and ZK5 is 233.05 mg/L and 283.57 mg/L, respectively. The Na-K-Mg ternary diagram in **Figure 5** shows that the sodium and potassium feldspars in the geothermal water from both wells are in the area of unequilibrated water, indicating that the geothermal water in both wells is in the primary stage of water-rock interactions and has not yet reached an equilibrium state.

Calculating Geothermal Reservoir Temperature Through Inversion of Resistivity

The resistivity of geothermal reservoirs mainly depends on the lithology, porosity, groundwater salinity, and ambient temperature of strata. For a geothermal field with a small exploration scope, it can be assumed that the lithology, porosity, and groundwater salinity of the deep strata remain unchanged. In this case, the resistivity of the geothermal reservoirs is only related to temperature and the broken degree of formation (Zhang et al., 2011). With an increase in temperature, the density and viscosity of groundwater decrease and the solubility of groundwater increases. As a result, the salinity and ionic activity of groundwater increase and the resistivity of groundwater decreases. Therefore, the increasingly high temperature indicates increasingly low resistivity for the same fractured zone. Overall, the resistivity of geothermal reservoirs contains information about the broken degree of formation and the temperature and salinity of groundwater.

The formation resistivity is closely related to groundwater salinity and temperature. Deng et al. (2000) determined the relationships between the resistivity of water-bearing rock samples, temperature, and the salinity of aqueous solution through experiments (**Figure 6**). According to **Figure 6A**, under the same temperature, the resistivity of water-bearing rock samples decreases with an increase in the salinity of the aqueous solution. However, when the salinity of the aqueous solution reaches a certain value, the increase in the salinity of the aqueous solution has an increasingly weak influence on the resistivity of water-bearing rock samples. Under the same salinity of the aqueous solution, the resistivity of water-bearing

TABLE 2 | Results of chemical analysis of the geothermal water in wells ZK2 and ZK5.

Analyzed Item $\rho(B^{z\pm})/(mg \cdot L^{-1})$	ZK2 $mg \cdot L^{-1}$	ZK5 $mg \cdot L^{-1}$	Analyzed Item $\rho(B^{z\pm})/(mg \cdot L^{-1})$	ZK2 $mg \cdot L^{-1}$	ZK5 $mg \cdot L^{-1}$
Na^+	21.35	18.65	H_2SiO_3	73.84	74.90
K^+	3.70	4.29	Free CO_2	14.65	10.31
Mg^{2+}	1.26	0.65	P^H	8.2	7.9
Ca^{2+}	23.81	20.66	Mn	0.046	0.048
Fe^{2+}	0.00	0.00	Cu	0.001	<0.001
Cl^-	3.43	6.54	Total Cr	0.002	0.002
SO_4^{2-}	10.00	15.00	Ba	0.016	0.006
HCO_3^-	105.17	140.22	Li	0.178	0.182
CO_3^{2-}	0.00	0.00	Ni	0.002	<0.001
F^-	7.00	8.60	Mo	0.006	0.005
NO_3^-	0.50	1.00	TDS	233.02	283.57

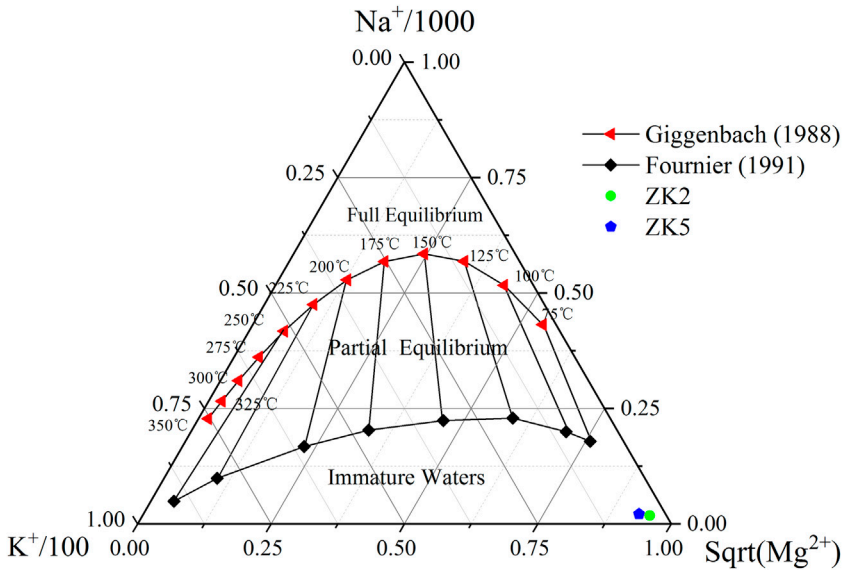

FIGURE 5 | Na-K-Mg ternary diagram.

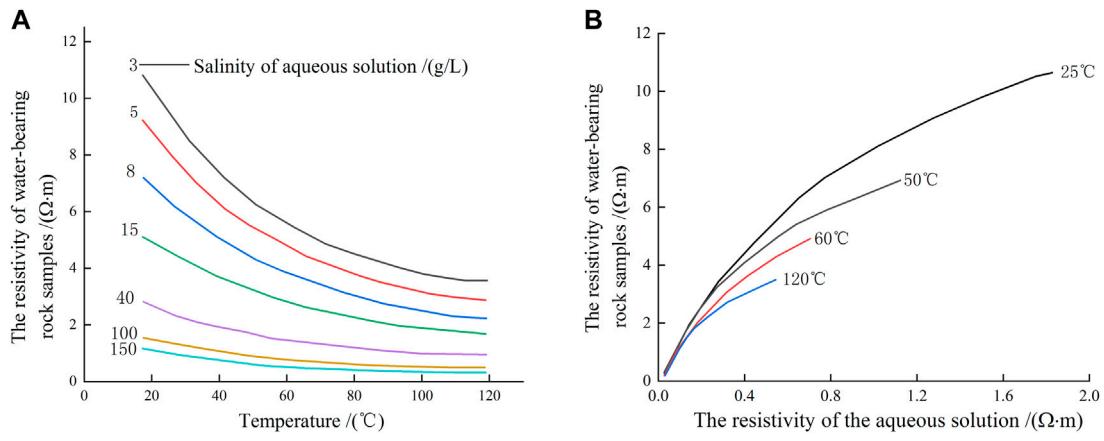

FIGURE 6 | Relationship curves of the resistivity of water-bearing rock samples, temperature, and the salinity of aqueous solution. **(A)** is the relationship curves of temperature and resistivity of water-bearing rock sample under different salinity of aqueous solution. **(B)** is the relationship curves of the resistivity of aqueous solution and the resistivity of water-bearing rock samples at different temperatures.

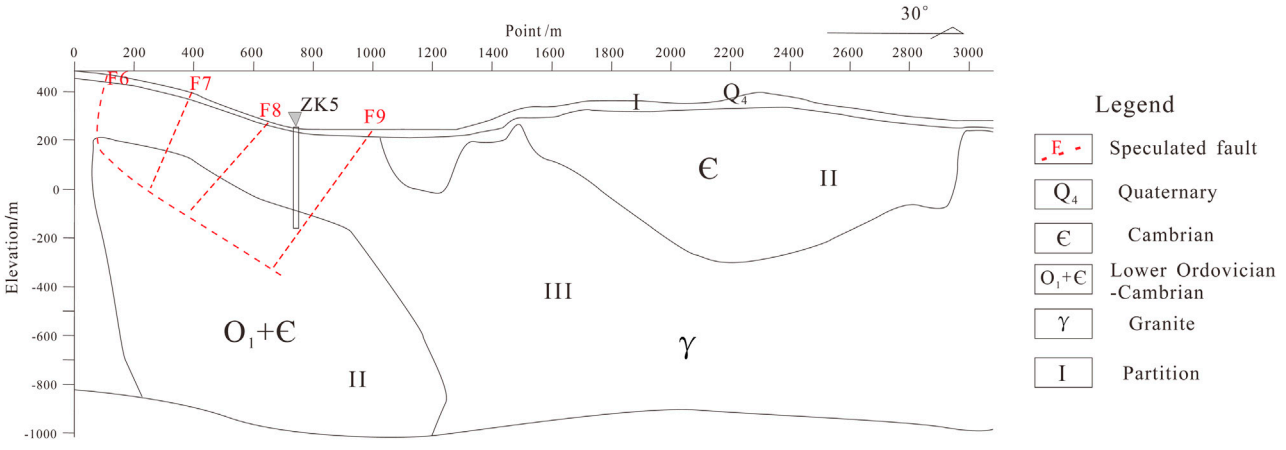

FIGURE 7 | CSAMT integrated interpretation section of survey line L1 and its regions.

rock samples decreases with an increase in temperature. However, when the temperature reaches a certain value, the increase in the temperature has an increasingly weak influence on the resistivity of water-bearing rock samples.

As **Figure 6B** shows, under the same resistivity of the aqueous solution, the resistivity of water-bearing rock samples decreases significantly with an increase in temperature. The Na-K-Mg ternary diagram (**Figure 5**) and **Table 2** indicate unequilibrated geothermal water and low water-rock interactions in the study area. Therefore, the groundwater salinity is also low. The salinity values fall in the area where formation resistivity is sensitive to temperature change. Therefore, the formation resistivity in the study area is significantly affected by temperature change.

The formation lithology and groundwater salinity in different regions show complex changes. Therefore, the resistivity-temperature calculation results are difficult to compare between different regions. To obtain an accurate temperature distribution of a geothermal field, it is necessary to select a small-scale fault zone to conduct the geothermal exploration. Assuming that the study area has the same geological conditions and similar groundwater salinity, the resistivity-temperature calculation method was used for geological interpretation.

For the inversion of geothermal reservoir temperature using resistivity, it is necessary to understand the lithological distribution along sections and the initial and surveyed resistivity of lithological layers. The L1 and L2 sections (**Figures 3**, **4**) reveal that the strata in the study area include the Quaternary and weathered crusts and Cambrian-Ordovician metamorphic sandstones and granites from young to old ages. The L1 and L2 sections can be divided into three regions (I-III) according to lithological differences. Specifically, region I is composed of Quaternary sandy gravels and weathered crusts, weathered crustregion II consists of metamorphic sandstones, and region III is comprised of granites (**Figures 7**, **8**).

As shown in the list of the physical properties of rock specimens (**Table 1**), the initial formation resistivity (ρ0) at 23 ˚C is as follows: Quaternary and weathered crust: 50 Ω m; metamorphic sandstones: 1,136 Ω m, and granites: 4,267 Ω m. The rock temperature coefficient (α) was set at 0.04 based on available borehole temperature. In practical applications, the initial resistivity of a region tends to be set at the average resistivity of the region's various partitions. For regions where the resistivity gradually increases with an increase in depth, their initial resistivity at different depths is calculated using the linear interpolation method in order to eliminate the influence of depth change. The initial resistivity of other regions are is at the average resistivity of various portions and is appropriately adjusted based on existing rock resistivity and borehole temperatures. Based on the resistivity obtained through the CSAMT inversion of survey lines L1 and L2, initial resistivity, and temperatures obtained by applying **Eq. 2**, the temperature sections of L1 and L2 survey lines were obtained using the geology software Surfer (**Figures 9**, **10**).

As shown in **Figure 9**, the shallow surface of the temperature section of L1 shows high temperature, which is caused by the Quaternary and weathered crust according to the CSAMT integrated interpretation section of L1. The temperatures near points Nos. 400, 600, and 1,100 are high and continue deep downward, for which the possible reasons are as follows. These points are located near faults F7, F8, and F9. Therefore, they have broken rocks and high water content. Correspondingly, the resistivity decreases, and the temperature increases at these points, which conforms to the resistivity-temperature method. Two high-temperature zones exist in areas with surface point nos. of 400–800 at elevations of 0–800 m. One zone has a temperature of 120–160˚C, which is greatly different from the bottom temperature of well ZK5 (36.7˚C). This great difference possibly results from the low resistivity caused by faults and the intense surface water seepage. The other high-temperature zone has a temperature of 70–80˚C, which is higher than the bottom temperature of well ZK5. The possible reason for this difference is the relatively low resistivity caused by relatively broken rocks.

As seen in **Figure 10**, the temperature anomalies reflect a noticeable geothermal reservoir structure, and the temperatures near fault fracture zones show high values. Points Nos. 800–2000, which correspond to an elevation of −200 to −400 m, show high temperatures (160–200˚C). This result is consistent with low resistivity revealed by the CSAMT

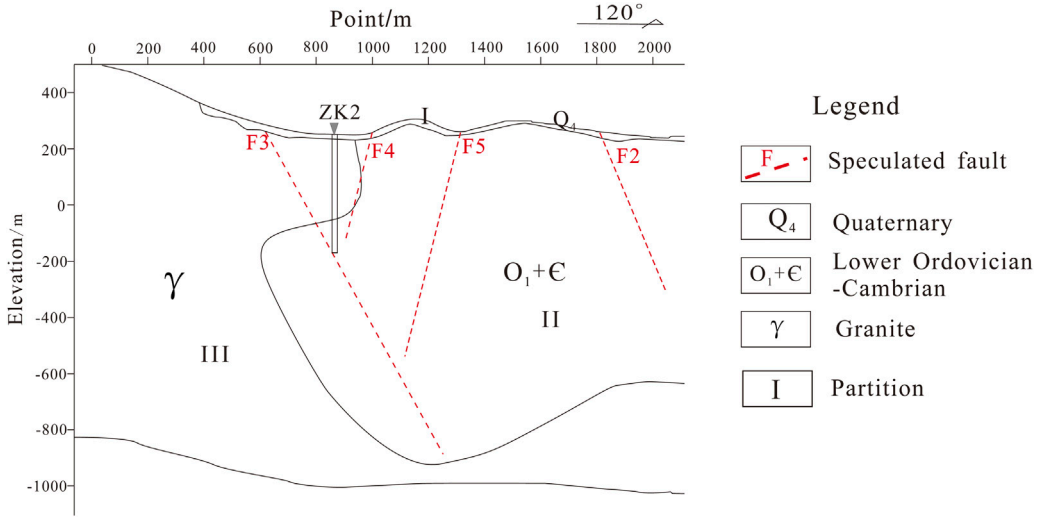

FIGURE 8 | CSAMT integrated interpretation section of survey line L2 and its regions.

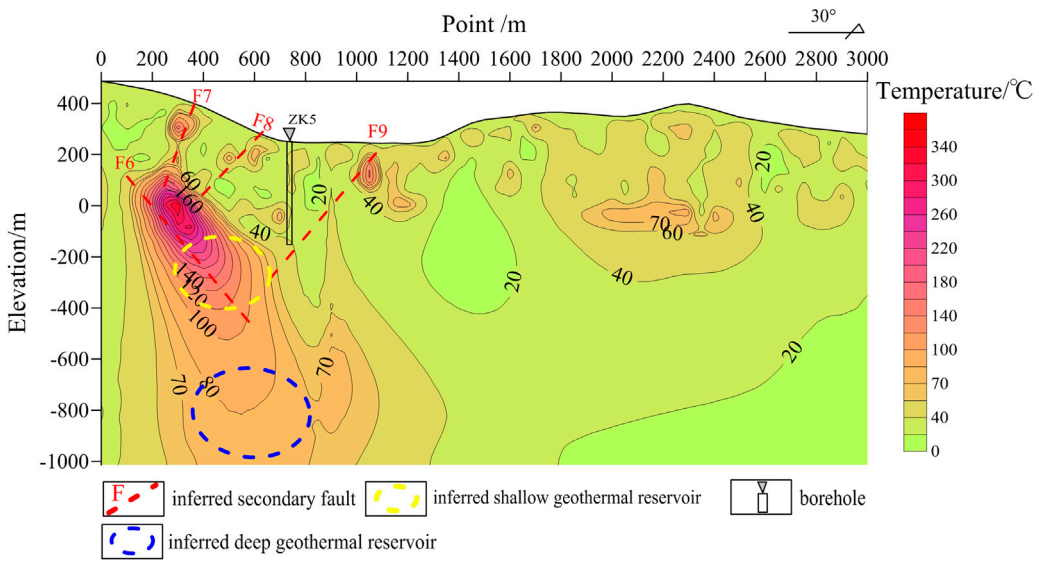

FIGURE 9 | Temperature section of survey line L1.

integrated interpretation section of L2. However, this high temperature is quite different from the bottom temperature of well ZK2 (35.6°C), which is likely affected by faults and surface water infiltration. Banded high temperatures are present near Points Nos. 1,000 and 1,400. They are formed by faults F4 and F5 revealed by the CSAMT integrated interpretation section of L2. The deep part of the L2 line temperature profile shows overall temperature of 0–40°C. This occurs because the area is close to the deep granite area, resulting in a higher resistivity of 2000–4,000, which leads to a decrease in the calculated temperatures. Therefore, this section is not suitable for obtaining geothermal reservoir temperatures through the inversion of resistivity.

Geothermometers

At present, the most commonly used geothermometers include sodium-potassium geothermometers, quartz geothermometers, and chalcedony geothermometers (Arnórsson et al., 1983). Each type of thermometer is applicable to specific conditions. For example, because the geothermal water in the study area is

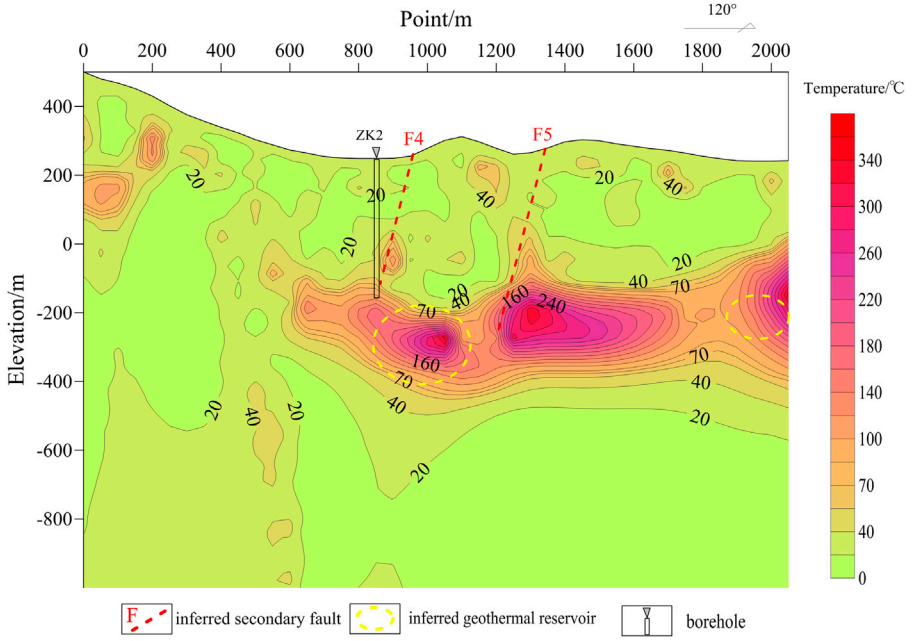

FIGURE 10 | Temperature section of survey line L2.

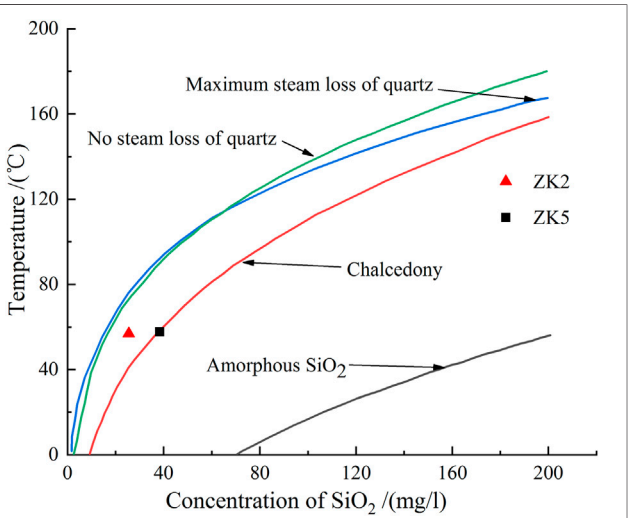

FIGURE 11 | Solubility curve of SiO_2.

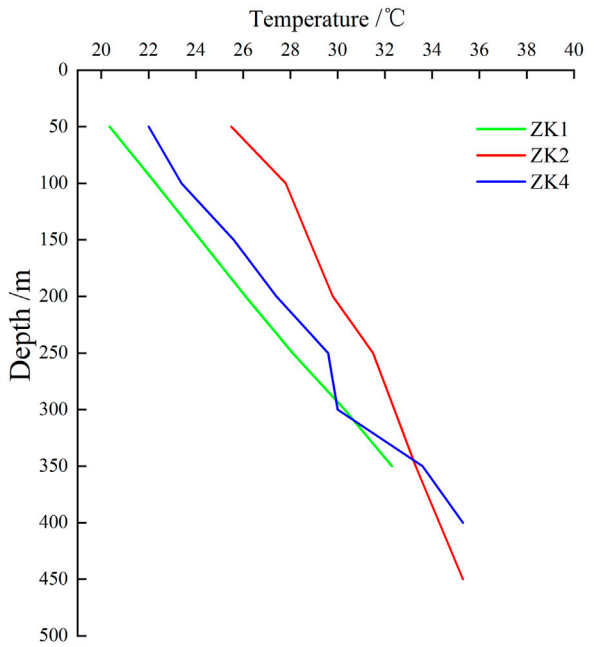

FIGURE 12 | Temperature measurement curves of wells ZK1, ZK2, and ZK4.

undersaturated with sodium and potassium feldspars, sodium and potassium geothermometers are not suitable.

SiO_2 is generally not affected by the formation and volatile component loss of other ions and complexes. As the heat flow cools, the precipitation rate of SiO_2 in the heat flow decreases, but the SiO_2 content of the heat flow can still indicate that of deep geothermal fluids (Xu and Guo, 2009).

The solubility curve of SiO_2 can qualitatively determine the controlling minerals of SiO_2 dissolution in geothermal water, which allows for selecting appropriate geothermometers. Using the solubility curve of SiO_2, this study determined that the chalcedony geothermometers are suitable for the Qutan area. The temperatures measured using chalcedony geothermometers were basically consistent with the estimates of geothermal reservoir temperature obtained by resistivity inversion.

The dissolution of SiO_2 in water is mainly controlled by quartz, chalcedony, and amorphous SiO_2 (Ellis, 1979). **Figure 11** reflects the primary minerals that affect the dissolution of SiO_2 in geothermal water and thus can be used to estimate the reservoir temperature. According to this figure, the geothermal water is mostly concentrated near the chalcedony line, indicating that chalcedony plays a role in controlling the dissolution of SiO_2 in geothermal water. Therefore, chalcedony may be the optimal mineral for assessing the reservoir temperature. According to **Table 2**, the contents of H_2SiO_3 in geothermal water of wells ZK2 and ZK5 are 73.8 *mg/l* and 74.9 *mg/l*, respectively. According to **Eq. 4**, the concentrations of SiO_2 in the geothermal water of wells ZK2 and ZK5 are 56.9 *mg/l* and 57.7 *mg/l*, respectively. As calculated using the chalcedony geothermometer equation, the geothermal reservoir temperatures of wells ZK2 and ZK5 are 78 and 79°C, respectively. These temperatures are basically consistent with the geothermal reservoir temperature estimated by the resistivity-temperature method (70–80°C), indicating that the inversion of geothermal reservoir temperature using resistivity is feasible.

Depth of Geothermal Water Circulation

The depth of geothermal water circulation refers to the vertical distance from the ground surface to the bottom plate of the aquiclude of deep geothermal fluids. It reflects the update speed of geothermal resources and can be used as a reference for determining the recharge-runoff-discharge characteristics of groundwater systems. In the Qutan area, the geothermal fluids tend to be warmed by deep heat sources during deep circulation (Long et al., 2019), and the geothermal water temperature is directly proportional to the circulation depth.

At present, the geothermal water circulation formula is commonly used to calculate the depth of geothermal fluid circulation (Mohammadi et al., 2010). The average annual temperature in the study area is 15°C. According to the temperature measurement curves with good linear characteristics of wells ZK1, ZK2, and ZK4 (**Figure 12**), the Qutan geothermal field has an average geothermal gradient of about 3.3 °C/100 m and an average geothermal degree of 30.3 m/°C. Meanwhile, the depth of the constant temperature zone was set at 20 m (Wang et al., 2015). Based on these data and the abovementioned data such as the geothermal reservoir temperature of 79°C, the depth of geothermal water circulation was determined to be 1959 m. This depth differs greatly from the top burial depth (423 m) of the Qutan shallow geothermal reservoirs obtained by the analysis of CSAMT integrated integration sections. This finding indicates that CSAMT is primarily suitable for the exploration of shallow geothermal reservoirs, while the geothermal water circulation formula can be applied to the exploration of deep geothermal reservoirs in general.

CONCLUSION

1) As shown by the geothermal reservoir characteristics revealed by CSAMT and geochemical characteristics of geothermal fluids, the Qutan geothermal field is located at the intersection of multiple faults and has a complex geological structure and intense granite intrusion. As a deep fault, the Huangao fault intersects several secondary faults, resulting in convenient geothermal water migration. Moreover, the geothermal water migration may also be accompanied by the heat flow generated by the decay of radioactive elements in granites. The shallow geothermal reservoirs in the Qutan geothermal field have a top burial depth of 423 m, a thickness of about 300 m, a geothermal reservoir temperature of about 79°C, and a geothermal water circulation depth of 1959 m.
2) In a small-scale fault zone in the geothermal field exploration, the inversion of geothermal reservoir temperature using CSAMT resistivity can better determine the distribution of the formation temperature field. The results of this method are roughly consistent with the borehole temperature measurement results and the estimates of chalcedony geothermometers, indicating that the inversion of geothermal reservoir temperature using resistivity is feasible.

OUTLOOK

This study further verified the reliability of the inversion of geothermal reservoir temperature using CSAMT resistivity by investigating and analyzing the intrinsic relationships between hydrogeochemical and geophysical explorations and using geothermal well temperature measurements. Geophysical and geochemical explorations have both played an important role in geothermal exploration. However, the limitations of using a single exploration method are increasingly noticeable, and any single exploration method or the simple combination of exploration methods has great uncertainty in the exploration of the temperature and depth of geothermal reservoirs. Exploring the intrinsic connections between various methods and accordingly extracting the implicit stratigraphic information have become important directions for future research.

Formation lithology and groundwater salinity show complex changes and may greatly differ between different regions. It is difficult to conduct correlation and comparative analyses on the resistivity-temperature calculation results of different regions. To obtain the accurate distribution of geothermal field temperature, it is necessary to further study the selection of parameters used in the resistivity-temperature calculation formula under different geological conditions. This will also improve the operability of the resistivity-temperature calculation formula.

DATA AVAILABILITY STATEMENT

The original contributions presented in the study are included in the article/Supplementary Material, further inquiries can be directed to the corresponding authors.

AUTHOR CONTRIBUTIONS

KB: Conceptualization, Methodology. GZ: Data curation, Writing-Original draft preparation. LH: Visualization, Investigation. SQ: Supervision. FL: Project administration. YL: Writing-Reviewing and Editing.

FUNDING

This study was supported by S&T Program of Hebei China (No. 20374201D), Chinese Academy of Geological Sciences Fund (No. SK202104), Natural Science Foundation of Hebei province China (No. D2019330003), and Geological survey project of China (No. DD20190128).

REFERENCES

Arnórsson, S., Gunnlaugsson, E., and Svavarsson, H. (1983). The Chemistry of Geothermal Waters in Iceland. III. Chemical Geothermometry in Geothermal Investigations. *Geochimica Et Cosmochimica Acta* 47, 567–577. doi:10.1016/0016-7037(83)90278-8

Aykaç, S., Timur, E., Sari, C., and Çaylak, Ç. (2015). CSAMT Investigations of the Caferbeyli (Manisa/Turkey) Geothermal Area. *J. Earth Syst. Sci.* 124, 149–159. doi:10.1007/s12040-014-0521-1

Ba, J., Su, C., Li, Y., and Tu, S. (2018). Characteristics of Heat Flow and Geothermal fields in Ruidian, Western Yunnan Province, China. *Ijht* 36, 1203–1211. doi:10.18280/ijht.360407

Barcelona, H., Lelli, M., Norelli, F., Peri, G., and Winocur, D. (2019). Hydrochemical and geological model of the Bañitos-Gollete geothermal system in Valle del Cura, main Andes Cordillera of San Juan, Argentina. *J. South Am. earth Sci.* 96, 1023781–1102378.15. doi:10.1016/j.jsames.2019.102378

Basokur, A. T., Rasmussen, T. M., Kaya, C., Altun, Y., and Aktas, K. (1997). Comparison of Induced Polarization and Controlled-source Audio-magnetotellurics Methods for Massive Chalcopyrite Exploration in a Volcanic Area. *Geophysics* 62, 1087–1096. doi:10.1190/1.1444209

Cao, Y. l., Cheng, G. J., Zhao, C. l., Wang, T., and Jiang, H. Y. (2018). Application of CSAMT in Hydrogeology Exploration in Shandong Province–An Example from Geothermal Exploration in Changdao County (South Four Islands). *J. Groundwater Sci. Eng.* 6 (1), 58–64. doi:10.19637/j.cnki.2305-7068.2018.01.007

Cheremensky, Γ. A. (1982). *Practical Geothermal Science*. Beijing: Geological Publishing House, 161–162.

Cui, Y. F., Zhang, J., Yin, T., Shi, M., and Bi, J. X. (2018). Discussion on Distribution of Geothermal Resources and Locating wells Methods of Geothermal Exploration in Eastern Shandong Province. *Geol. Surv. China* 5 (2), 86–92. (in Chinese with English abstract). doi:10.19388/j.zgdzdc.2018.02.13

Deng, S. G., Bian, R. X., Liu, B. K., and Zhang, L. P. (2000). The Effect of Reservoir Temperature on theParameters of Archie Formula. *WLT* 24 (2), 88–91. (in Chinese with English abstract). doi:10.3969/j.issn.1004-1338.2000.02.002

Dong, L., Li, D.-q., and Jiang, F.-b. (2018). A Two-Stage CO-PSO Minimum Structure Inversion Using CUDA for Extracting IP Information from MT Data. *J. Cent. South. Univ.* 25, 1195–1212. doi:10.1007/s11771-018-3818-4

Du, B. R. (2011). M.Sc. thesis in *The Study of Electrical Prospecting in the Deep Geothermal Investigation* (Chengdu: Chengdu Univerisity of Technology), 3–4. (in Chinese with English abstract)

Ellis, A. J. (1979). Chemical Geothermometry in Geothermal Systems. *Chem. Geology*. 25 (3), 219–226. doi:10.1016/0009-2541(79)90143-8

Fahrurrozie, A., Saputra, M. P., and Nugraha, T. (2015). The Application of Na-K-Mg, Na-K/Mg-Ca and K-Mg/Quartz Diagrams to Evaluate Water Geochemistry in West Java Geothermal Prospects. *Indonesia* 8 (2), 102–109.

Fournier, R. O., and Pang, Z. H. (1991). Geothermometer: Analysis of Na-K-Mg Relationship in Geothermal Water. *Foreign Geology. (Beijing)* (5), 34–37. (in Chinese).

Gan, H. N., Wang, G. L., Wang, X., Lin, W. J., and Yue, G. F. (2019). Research on the Hydrochemistry and Fault Control Mechanism of Geothermal Water in Northwestern Zhangzhou Basin. *Geofluids* 2019, 1–15. doi:10.1155/2019/3925462

Giggenbach, W. F. (1988). Geothermal Solute Equilibria. Derivation of Na-K-Mg-Ca Geoindicators. *Geochimica Et Cosmochimica Acta* 52, 2749–2765. doi:10.1016/0016-7037(88)90143-3

Giggenbach, W., Sheppard, D., Robinson, B., Stewart, M., and Lyon, G. (1994). Geochemical Structure and Position of the Waiotapu Geothermal Field, New Zealand. *Geothermics* 23, 599–644. doi:10.1016/0375-6505(94)90022-1

Hu, X., Peng, R., Wu, G., Wang, W., Huo, G., and Han, B. (2013). Mineral Exploration Using CSAMT Data: Application to Longmen Region Metallogenic belt, Guangdong Province, China. *Geophysics* 78 (3), B111–B119. doi:10.1190/GEO2012-0115.1

Huang, Y. H., Liu, H. L., Song, S. R., and Chen, H. F. (2018). An Ideal Geothermometer in Slate Formation: A Case from the Chingshui Geothermal Field, Taiwan. *Geothermics* 74, 319–326. doi:10.1016/j.geothermics.2017.11.002

Li, D. q., Xie, W., Di, Q. y., and Wang, M. y. (2016). Forward Modeling for "Earth-Ionosphere" Mode Electromagnetic Field. *J. Cent. South. Univ.* 23, 2305–2313. doi:10.1007/s11771-016-3288-5

Long, X., Liu, F., Xie, H., Lin, W., Liu, Y., and Li, C. (2022). Seismic Geothermal Resource Exploration Based on CPU/GPU Collaborative Parallel Prestack Time Migration. *Acta Geologica Sinica (Eng)*. doi:10.1111/1755-6724.14895

Long, X., Xie, H., Deng, X., Wen, X., Ou, J., Ou, R., et al. (2021). *Geological and Geochemical Characteristics of the Geothermal Resources in Rucheng*. China. Lithosphere. doi:10.2113/2021/1357568

Long, X., Zhang, K., Yuan, R., Zhang, L., and Liu, Z. (2019). Hydrogeochemical and Isotopic Constraints on the Pattern of a Deep Circulation Groundwater Flow System. *Energies* 12 (3), 404. doi:10.3390/en12030404

Meng, Y. S., Yao, C. L., Liu, R. D., and Huang, L. J. (2011). The Prediction of the Geothermal Field Temperature by Means of Resistivity Inversion. *Geophys. Geochemical Exploration* 35, 58–57. (in Chinese with English abstract).

Meng, Y. S., Zhang, G. Z., and Liu, R. D. (2010). The Deep Temperature Prediction by Resistivity in Exploration of the Geothermal Field System. *Comput. Tech. Geophys. geochemical exploration* 32 (1), 31–34. (in Chinese with English abstract). doi:10.3969/j.issn.1001-1749.2010.01.006

Mohammadi, Z., Bagheri, R., and Jahanshahi, R. (2010). Hydrogeochemistry and Geothermometry of Changal thermal Springs, Zagros Region, Iran. *Geothermics* 39, 242–249. doi:10.1016/j.geothermics.2010.06.007

Pellerin, L., Johnston, J. M., and Hohmann, G. W. (1996). A Numerical Evaluation of Electromagnetic Methods in Geothermal Exploration. *Geophysics* 61, 121–130. doi:10.1190/1.1443931

Shi, M., Zhang, J., Yin, T., Yang, N., and Jiang, H. Y. (2019). Hydrochemistry Characteristic Analysis of Low-Medium Temperature Convective Geothermal Resources in Jiaodong Peninsula. *Acta Geologica Sinica* 93 (S1), 138–148. (in Chinese with English abstract). doi:10.19762/j.cnki.dizhixuebao.2019221

Sun, H. l., Ma, F., Lin, W. J., Liu, Z., Wang, G. L., and Nan, D. W. (2015). Geochemical Characteristics and Geothermother Application in High Temperature Geothermal Field in Tibet. *Geol. Sci. Technol. Inf.* 34 (3), 171–177. (in Chinese with English abstract).

Wang, G. L., Liu, F., and Wang, W. L. (2015). Research on the Spatial Distribution and Law of Shallow Geothermal Field in My Country's Land Area (2). *Heat. cooling* (3), 60–61. (in Chinese).

Wang, Y., Tong, J., Li, X. L., Fang, J. F., Deng, L. R., and Qi, L. (2020). Geological Characteristics and Generation Mechanism of Qunaihai Hot spring in Qing Hai Province. *J. East China Univ. Tech. (Nat. Science)* 43 (3), 248–256. (in Chinese with English abstract). doi:10.3969/jissn.1674-3504.2020.03.006

Wang, Y., Zhang, A., Fan, W., Zhang, Y., and Zhang, Y. (2013). Origin of Paleosubduction-Modified Mantle for Silurian Gabbro in the Cathaysia Block: Geochronological and Geochemical Evidence. *Lithos* 160-161, 37–54. doi:10.1016/j.lithos.2012.11.004

Wu, C. P., Zhang, X. P., Du, L. Z., and Wang, Y. (2014). Study on the Application of CSAMT in Geothermal Exploration in Jilin Province. *Amm* 556-562, 2174–2177. doi:10.4028/www.scientific.net/amm.556-562.2174

Wu, G., Hu, X., Huo, G., and Zhou, X. (2012). Geophysical Exploration for Geothermal Resources: An Application of MT and CSAMT in Jiangxia, Wuhan, China. *J. Earth Sci.* 23, 757–767. doi:10.1007/s12583-012-0282-1

Xiong, B., and Mao, Y.-d. (2005). Some Issues on 2.5-D Transient Electromagnetic Forward. *J. Cent. South. Univ. Technol.* 12, 177–182. doi:10.1007/s11771-005-0395-0

Xu, P., Li, M., Qian, H., Zhang, Q., Liu, F., and Hou, K. (2019). Hydrochemistry and Geothermometry of Geothermal Water in the central Guanzhong Basin, China: a Case Study in Xi'an. *Environ. Earth Sci.* 78 (3), 78–87. doi:10.1007/s12665-019-8099-1

Xu, S. G., and Guo, Y. S. (2009). *Geothermics Basis*. Beijing: Science Press, 37. (in Chinese).

Xun, Z., Juan, L., Haiyan, Z., Bin, F., Lan, Y., and Shijun, L. (2008). Increase in thermal Groundwater Due to a Flowing Well Near the Songshan Hot spring in Beijing, China. *Environ. Geol.* 53, 1405–1411. doi:10.1007/s00254-007-0749-z

Yan, B. Z., Xiao, C. L., Liang, X. J., and Jiang, H. Y. (2018). Characteristics and Genetic Model of the Basin Type Geothermal Water Recourses in Basalt Area of Changbai Mountain. *Geol. Rev.* 64 (5), 1201–1216. (in Chinese with English abstract). doi:10.16509/j.georeview.2018.05.012

Yan, X. X., Gan, H. N., and Yue, G. F. (2019). Hydrogeochemical Characteristics and Genesis of Typical Geothermal Flleds from Huangshadong to Conghua in Guangdong. *Geol. Rev.* 65 (3), 743–754 (in Chinese with English abstract). doi:10.16509/j.georeview.2019.03.018

Yang, L. W., Zhou, Y. C., Yu, Y., and Yang, W. G. (2018). Analysis on Genesis and Hydrochemical Characteristics Geothermal Water Qutan Area, Jianggangshan, Jiangxi Province. *Sci. Tech. Engieering* 18 (23), 8–13 (in Chinese with English abstract). doi:10.3969/j.issn.1671-1815.2018.23.002

Zhang, Q. J., Liu, R. D., and Lu, G. F. (2011). The Method for Forecasting Temperature of the Geothermal Field. *Geophys. Geochemical Exploration* 35 (3), 325–328. (in Chinese with English abstract).

Zhang, X., Guo, Q., Li, J., Liu, M., Wang, Y., and Yang, Y. (2015). Estimation of Reservoir Temperature Using Silica and Cationic Solutes Geothermometers: a Case Study in the Tengchong Geothermal Area. *Chin. J. Geochem.* 34 (2), 233–240. doi:10.1007/s11631-015-0037-7

Zhao, J. Y., Zhang, W., Zhang, H. X., Qu, Z. W., Li, M., and Yue, G. F. (2018). Hydrogeochemical Characteristics and Genesis of the Geothermal fields in Batang of Sichuan. *Hydrogeology Engineering Geology*. 46 (4), 16–23. (in Chinese with English abstract). doi:10.16030/j.cnki.issn.1000-3665.2019.04.11

Conflict of Interest: The authors declare that the research was conducted in the absence of any commercial or financial relationships that could be construed as a potential conflict of interest.

Publisher's Note: All claims expressed in this article are solely those of the authors and do not necessarily represent those of their affiliated organizations, or those of the publisher, the editors and the reviewers. Any product that may be evaluated in this article, or claim that may be made by its manufacturer, is not guaranteed or endorsed by the publisher.

frontiers | Frontiers in Earth Science

ORIGINAL RESEARCH
published: 23 May 2022
doi: 10.3389/feart.2022.864548

Study on the Thermophysical Properties and Influencing Factors of Regional Surface Shallow Rock and Soil in China

Xi Zhu[1,2]*, *Zongjun Gao*[3]*, *Tao Chen*[3], *Wanli Wang*[1,2], *Chuan Lu*[1,2] and *Qinglian Zhang*[4]

[1]Insitute of Hydrogeology and Environmental Geology, CAGS, Shijiazhuang, China, [2]Technology Innovation Center of Geothermal & Hot Dry Rock Exploration and Development, Ministry of Natural Resources, Shijiazhuang, China, [3]College of Earth Science and Engineering, Shandong University of Science and Technology, Qingdao, China, [4]School of Resources, Hebei GEO University, Shijiazhuang, China

Thermophysical properties of rock and soil are important parameters that affect the efficiency of shallow geothermal energy utilization. This paper analyzes the thermophysical parameters (specific heat capacity and thermal conductivity) and their influencing factors based on 6467 sample data in 24 provincial capitals, China. The statistical distributions of thermophysical properties are analyzed based on histogram plots. Linear regression analysis is conducted to investigate the correlation between thermophysical properties and lithology (classified as metamorphic rocks, igneous rocks, chemical sedimentary rocks, clastic sedimentary rocks, and loose sediments in this study)), density, and water content. The results show that the thermophysical properties are influenced predominantly by lithology. The measured values of thermophysical properties generally show normal distribution characteristics. The specific heat capacity of loose sediments is relatively high, the thermal conductivity of other four types are relatively high. The specific heat capacity is negatively correlated with density, positively correlated with water content, whereas thermal conductivity is positively correlated with density, and negatively correlated with water content. The findings obtained in this study provide evidence and guidelines for the investigation, evaluation, and development of shallow geothermal resources.

Keywords: thermophysical properties, shallow geothermal energy, influencing factors, density, water content

OPEN ACCESS

Edited by:
Dawei Hu,
Institute of Rock and Soil Mechanics (CAS), China

Reviewed by:
Magdala Tesauro,
Utrecht University, Netherlands
Xiting Long,
Shenzhen University, China

***Correspondence:**
Xi Zhu
zx19860727@163.com
Zongjun Gao
gaozongjun@126.com

Specialty section:
This article was submitted to Structural Geology and Tectonics, a section of the journal Frontiers in Earth Science

Received: *28 January 2022*
Accepted: *02 May 2022*
Published: *23 May 2022*

Citation:
Zhu X, Gao Z, Chen T, Wang W, Lu C and Zhang Q (2022) Study on the Thermophysical Properties and Influencing Factors of Regional Surface Shallow Rock and Soil in China. Front. Earth Sci. 10:864548. doi: 10.3389/feart.2022.864548

INTRODUCTION

Shallow geothermal energy is renewable and clean energy, which is characterized by being environmentally friendly, economical and applicable, widely distributed, convenient to use, and has great potential (Wang et al., 2012; Ran et al., 2014). For decades, the utilization of shallow geothermal energy has developed rapidly with the innovation of ground source heat pump technology. Since the United States established the first ground source heat pump system in the 1940s, universities in China began to study heat pump technology in the 1960s. Since the 1970s, the demonstration projects of shallow geothermal energy have been successively established in Switzerland, Netherlands and other countries. In the 1990s, the application of ground source heat pump systems was gradually progressed in China. At the beginning of the 21st century, ground source heat pump technology has developed rapidly. The annual growth rate of ground-source heat

pump market in China exceeds 30% since 2004, which is much higher than the world's average growth rate of 20–22% in the same period. It has now ranked second in the world (Zheng et al., 2010). According to the WGC 2020, geothermal (ground-source) heat pumps have the largest geothermal use worldwide, accounting for 71.6% of the installed capacity and 59.2% of the annual energy use. The number of countries with installations is 54, and over twice the number of units reported in 2010. The leaders in installed units (MWt) are China, United States, Sweden, Germany and Finland accounting for 77.4% of these units. Wang et al. (2017) conducted a new evaluation of the potential of shallow geothermal energy resources in China and the results showed that the shallow geothermal energy resources in 336 important cities could be extracted in an amount equivalent to 700 million t of standard coal per year. According to the survey, the actual heating and cooling area by shallow geothermal energy reached 1.6 billion m^3 in 2020 (Lund and Toth, 2020).

The capability of storing and conducting heat of the rock and soil depends on their thermal conductivity, specific heat capacity, and thermal diffusivity, which are collectively referred to as thermophysical parameters. Clauser and Huenges (1995) studied the thermal conductivity characteristics of different rocks. Their results showed that porosity is an important factor affecting the thermal conductivity of igneous and sedimentary rocks. Thermophysical parameters are also a key factor affecting the engineering design of ground source heat pumps (Lin et al., 2012). Many studies have carried out related topics (e.g., Middleton, 1994; Hartmann et al., 2008; Fuchs and Förster, 2014; Cheng and Yu, 2017; McDaniel et al., 2018; Naranjo-Mendoza et al., 2018; Ohta et al., 2018; Song et al., 2018; Miranda et al., 2021; Zeng et al., 2022). Midttømme et al. (1998) studied the thermal conductivity and its influencing factors of claystone and mudstone. The results showed that there is a correlation between grain size and thermal conductivity. Goto and Matsubayashi (2009) investigated the relation of the thermophysical properties to the porosity and mineral composition of clay and sandy sediments in the Juan de Fuca Ridge and built models that fitted with the observed data. Popov et al. (2011) analyzed the thermophysical property measurements on cores from the scientific drilling well Yaxcopoil-1 in Mexico and established correlations between the thermal conductivity and elastic wave velocities measured in the laboratory. Jorand et al. (2015) analyzed statistically the petrophysical properties of rocks of the northeastern Rhenish Massif and the Lower Rhine Embayment in Germany and found that the mineralogical compositions and water-filled pore volume control the thermophysical properties of rocks. Song et al. (2019) studied the characteristics and influencing factors of thermophysical properties of different rocks in the main strata in Guizhou Province, China. They found that the thermophysical properties of rocks are related to factors such as mineral composition, structure, and water content.

Such contributions are greatly helpful to understanding the characteristics of thermophysical parameters of rock and soil. However, the rock samples used in the related analysis are relatively small distributed in limited areas. Furthermore, the thermophysical parameters in most studies focus on thermal conductivity. Currently, few studies have focused on the distribution of thermophysical properties and their influencing factors nationwide in China. This study collected 6467 data from the survey and evaluation of shallow geothermal energy in 24 provincial capitals in China. The rock heat capacity and thermal conductivity are analyzed statistically. Their influencing factors are also analyzed and their correlation with rock type, rock density, and water content is investigate. The results provide a basis for the investigation, evaluation, development, and utilization of shallow geothermal energy.

TABLE 1 | The number of rock and soil samples for provincial capital cities.

City	Number	City	Number	City	Number
Jinan	384	Nanjing	588	Hefei	222
Taiyuan	148	Nanning	90	Kunming	265
Xi'an	106	Shanghai	733	Nanchang	136
Lhasa	20	Wuhan	390	Yinchuan	169
Xining	88	Changsha	575	Changchun	126
Haikou	157	Chongqing	185	Guangzhou	1072
Chengdu	6	Harbin	136	Hangzhou	408
Fuzhou	228	Lanzhou	82	Wulumuqi	153

SAMPLES AND EXPERIMENTAL METHODS

In 2014–2019, the shallow geothermal energy exploration and evaluation work had been completed in 31 provincial capital cities in China including Beijing, Tianjin, and Shanghai. To investigate the overall distribution characteristics of rock thermophysical parameters and their influencing factors in provincial capital cities, the sample data are checked and filtered, which are distributed in 24 provincial capital cities in China. It is mainly collected in strata of Carboniferous, Permian, Jurassic, Neogene, and Quaternary. The sampling depth is basically within 200 m. There are a total of 6467 samples. The number of rock samples for different cities is listed in **Table 1**.

The thermophysical properties are tested in the laboratory. The method of testing is followed by the Geotechnical Test Method Standard, GB_T50123-1999, China (GB/T 50123-1999; Ministry of Construction of the People's Republic of China, 1999). Samples were obtained from the different formations using a borehole sampler. After collecting rock and soil samples from the boreholes and sending them to the laboratory, and use special testing equipment to conduct thermophysical properties of rocks are tested by specific equipment and the testing results can thus be obtained directly. The microscopic characteristics of soil sample grains are observed by the optical stereo microscope method (magnification 30 -100). The rock density is measured by the volume ring gauge method (electronic balance 0.01 g, volume ring gauge, etc.). The specific gravity of rocks is measured by the standard pycnometer method plus vacuum pumping. The water content is evaluated by the standard drying method (electronic balance 0.1 mg, standard drying oven) 105°C, etc.). The thermal

TABLE 2 | Lithology classification and number of samples.

Lithology		The number of samples		Overall
Metamorphic rock	Phyllite	12	220	6467
	Slate	110		
	Gneiss	92		
	Quartzite	1		
	Skarn	5		
Clastic sedimentary rock	Shale	45	1929	
	Mudstone	745		
	Sandstone	1012		
	Conglomerate	127		
Chemical sedimentary rock	Limestone	599	682	
	Dolomites	83		
Igneous rock	Granite	141	204	
	Diorite	34		
	Gabbro	20		
	Andesite	7		
	Basalt	2		
Loose sediment	Clay	1793	3432	
	Mud	82		
	Silt	504		
	Sand	1002		
	Pebble	25		
	Shell layer	26		

conductivity, specific heat, thermal diffusivity are measured by the unsteady heat transfer method, in line with ASTM D5334-00 standard.

RESULTS AND DISCUSSION

The thermophysical properties of rock and soil are related to the origin and geological time when they formed, and the geological environment where they are located. These aspects are generally intuitively reflected in their lithology, mineral composition, texture, structure, density, porosity, water content, saturation, pressure, temperature, degree of weathering, etc (Kim et al., 2002; Hartmann et al., 2005; Muhieddine et al., 2012; Jorand et al., 2015; Oktay et al., 2015; Fuchs, 2018; Pimienta et al., 2018). Therefore, the thermophysical characteristics can be further investigated regarding these related factors.

The classification and the number of samples are shown in **Table 2**. The loose sediments and clastic sedimentary rocks accounted for most of samples, roughly 83% of the total number of samples. A small portion of residual slope soil and fill soil is classified as silt. Nearly 92% of the metamorphic rocks are slate and gneiss. Limestone accounts for a higher proportion of chemical sedimentary rocks, nearly 88%. For igneous rocks, granite accounts for the highest proportion of 69%.

The histograms of thermophysical parameters, including thermal conductivity and specific heat of rock and soil for various rock types are shown in **Figure 1**, showing a relatively centered distribution in general. The specific heat capacity for loose sediments is higher than those of metamorphic and igneous rocks. Metamorphic rocks, chemical sedimentary rocks, and igneous rocks have a higher thermal conductivity than clastic sedimentary rocks and loose sediments. As can be seen from **Table 2**, the values of the thermophysical parameters of these groups of rocks are strongly influenced by those of the prevalent lithotype, such as of the slate and gneiss among the metamorphic, rocks, sandstone and mudstone among the clastic sedimentary rocks, sandstone and mudstone among the clastic sedimentary rocks, limestone among the chemical sedimentary rocks, granite among the igneous rocks, clay and sand among the loose sediments. (**Figure 1**).

The Impact of Lithology on Thermophysical Properties

Lithology is a general concept, which is a comprehensive manifestation of rock's mineral composition, texture, physical and chemical properties. Rock lithology is comprehensively affected by their minerals, and the thermophysical parameters of different minerals vary (Wang et al., 1979; Han et al., 2017; Tiwari et al., 2021). The physical properties vary with the rock and soil types. For samples from 24 provincial capitals in China, based on the basic type of metamorphic rocks, sedimentary rocks, igneous rocks, and loose sediments, samples are further classified according to their lithology (**Table 2**). Further statistical analysis of the thermophysical parameters for different rocks types is conducted as shown in **Figure 2**, which gives clues for the influences of rock lithology on their thermophysical parameters. The median specific heat capacity of different types ranges roughly from 0.5 to 1.5 KJ/(kg•K), and the median thermal conductivity is from 1 to 4 W/(m•K) **(Figures 2A,B)**. In this study, most selected measure data are the average values for the specified rock type in a certain study area, the anisotropic effects are diminished in data processing. The object of this study is to investigate the relative magnificent of heat

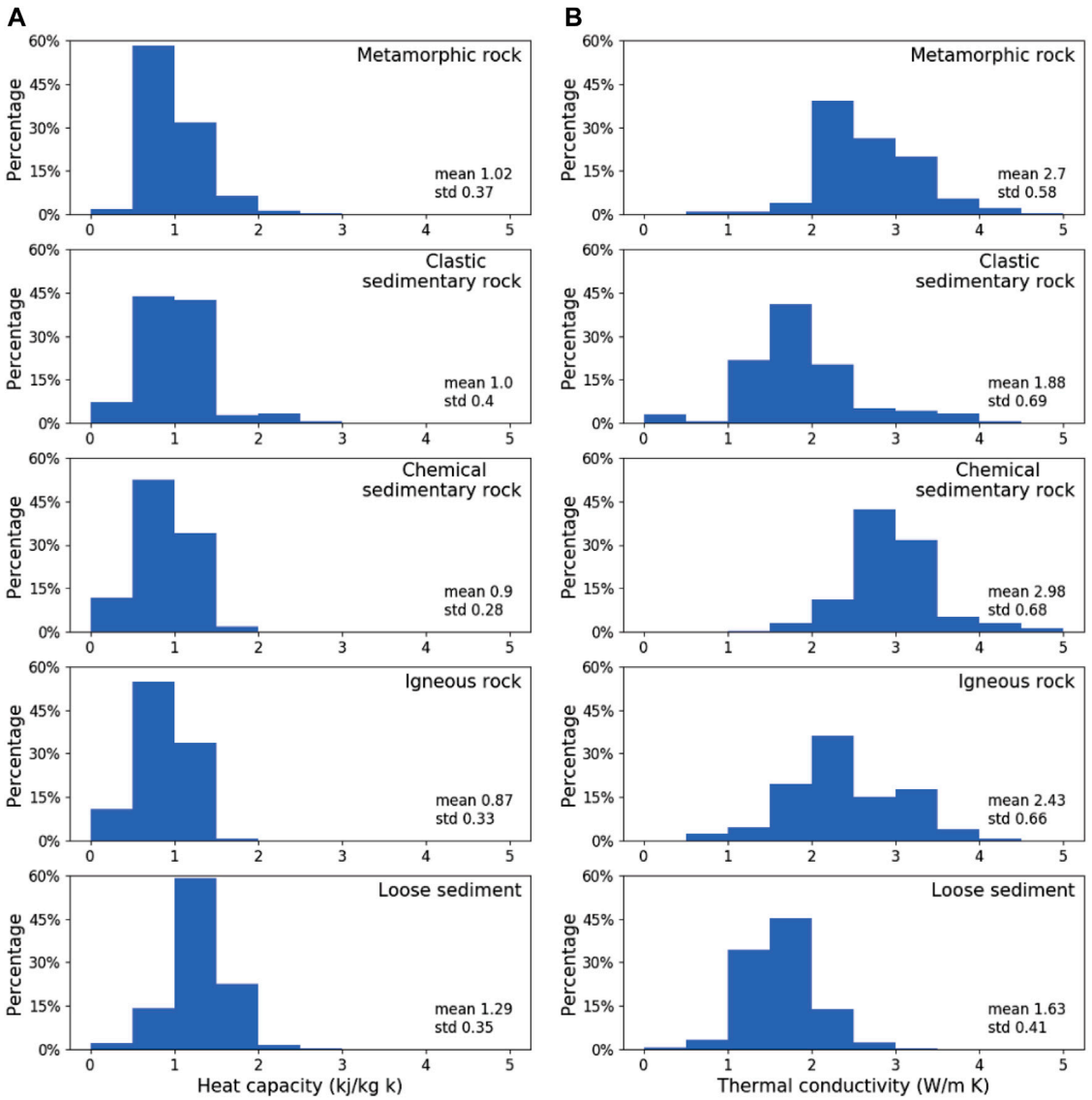

FIGURE 1 | Histograms of heat capacity **(A)** and thermal conductivity **(B)** of different rock and soil mass samples. (The y axis displays the percentage given by the samples number within the specified interval over the total number of the rock and soil samples.).

conductivity and capacity of different type of rocks and their influence factors. Hence, the anisotropic effect are omitted.

Rocks, including igneous rocks, sedimentary rocks, and metamorphic rocks, have a higher thermal conductivity than loose sediments being characterized by lower porosity (**Figure 2B**). For metamorphic rocks, the thermal conductivity for phyllite is highest, with a median value of 3.9 W/(m•K), while it is the lowest for skarn, with a median value of 1.1 W/(m•K). The variation of rock thermal conductivity is small for slate, with a median value of 2.39 W/(m•K). The median thermal conductivity of sedimentary rocks ranges from 1.8 to 2.8 W/(m•K). The chemical sedimentary rocks (limestone and dolomite) have a higher thermal conductivity than clastic sedimentary rocks (sandstone, mudstone, etc.). Sandstone and mudstone are the most widely distributed rock samples for clastic sedimentary rocks. The median thermal conductivity of sandstone is 1.86 W/(m•K) and mudstone is 1.79 W/(m•K). For igneous rocks, the rock thermal conductivity for granite is highest of 2.4 W/(m•K), the gabbro is lowest of 1.8 W/(m•K). The rock thermal conductivity for andesite has a larger variation range of 2–3 W/(m•K) than other igneous rocks. The median thermal conductivity of loose sediments is 1–2.1 W/(m•K), in which gravel is higher, sand and silt are in the middle, mud and clay are lower, shell layer is the lowest, and the thermal conductivity of gravel has a larger variation. The thermal conductivity of loose sediments generally shows an increasing trend with grain size, which result is consistent with the result of Midttømme et al. (1998).

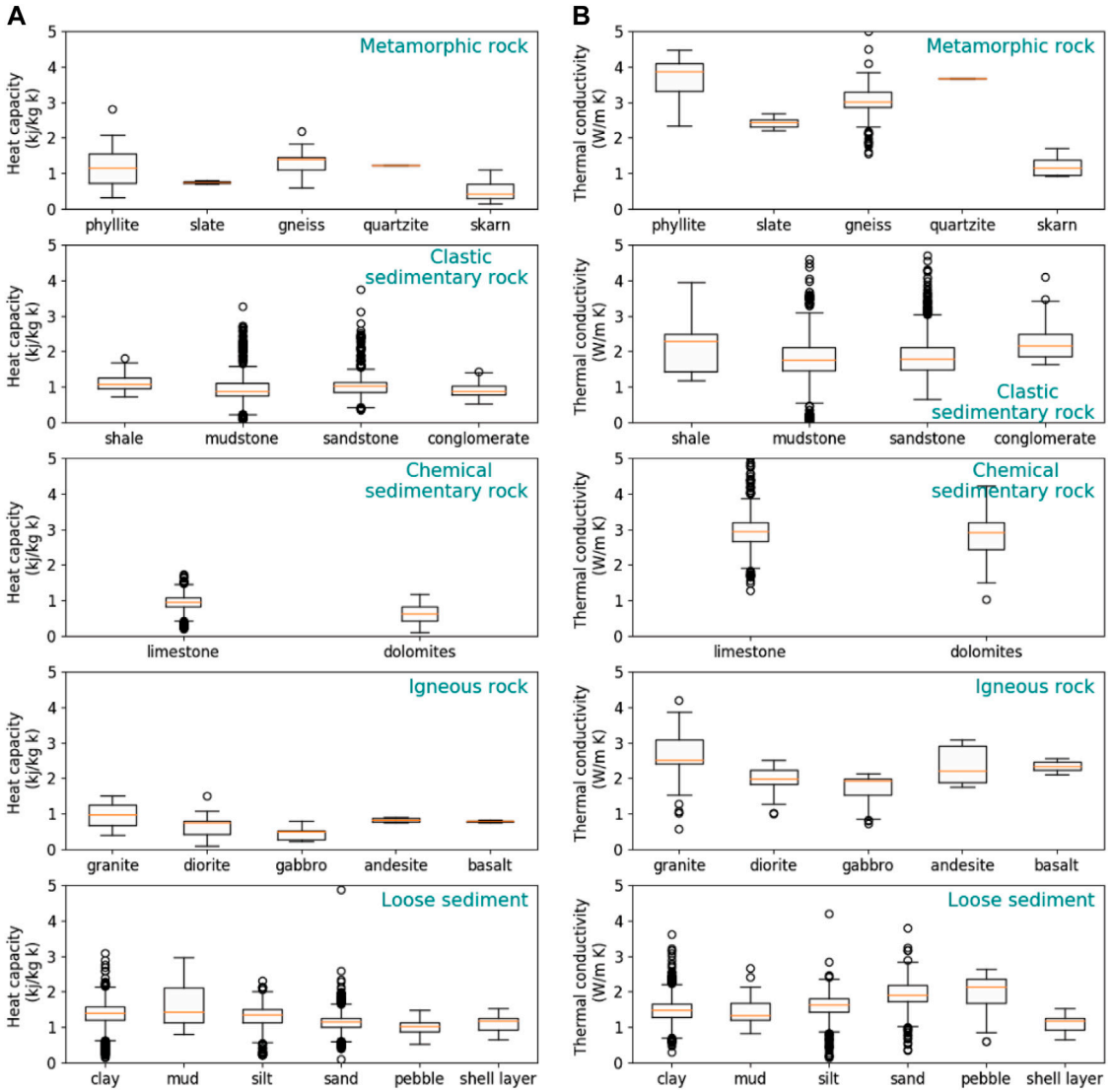

FIGURE 2 | Boxplots of heat capacity **(A)** and thermal conductivity **(B)** of rock and soil samples, having different lithology. (Boxes represent the quartile, red lines the median, whiskers–maximum data range, black circles the outliers.).

The variations of specific heat capacity with rock types are opposite to those of thermal conductivity, looser sediments have higher specific heat capacities and rocks, including igneous rocks, sedimentary rocks, and metamorphic rocks (**Figure 2A**). Clay, mud, and silt have the highest specific heat capacity, which is about 1.35KJ/(kg•K). Sand, pebbles, and shells have a relatively low specific heat capacity of about 1.18 KJ/(kg•K). The median value of clastic sedimentary rocks is relatively stable, ranging from 0.8 to 1.1 KJ/(kg•K), and the specific heat capacity of mudstone is relatively low. However, there are certain abnormal values in sandstone and mudstone, with the lowest of 0.2 KJ/(kg•K) and the highest of 3.5 KJ/(kg•K).

For igneous rocks, gabbro's specific heat capacity is the lowest of 0.46KJ/(kg•K), and the granite's specific heat capacity varied greatly from 0.7 to 1.2 KJ/(kg•K), followed by the diorite ranges from 0.5 to 0.7 KJ/(kg•K). The specific heat capacity of limestone is higher than that of dolomite, about 1 KJ/(kg•K), and the variation range of dolomite is relatively larger (has a bigger box in the plot) than that of limestone with 0.35–0.75 KJ/(kg•K). The specific heat capacity of metamorphic rocks has a large variation ranging from 0.3 to 1.4 KJ/(kg•K), which is the lowest for skarn, and the highest for gneiss. The specific heat capacity of phyllite varies greatly from 0.7 to 1.35 KJ/(kg•K).

In general the finer the particles of the loose sediment, the greater the porosity. Most samples are collected below the hydrostatic surface, so it can be assumed saturated with water whose thermal conductivity is lower and specific heat capacity is higher than most minerals. The comparisons of thermophysical parameters for different rocks show that the denser the rock-soil

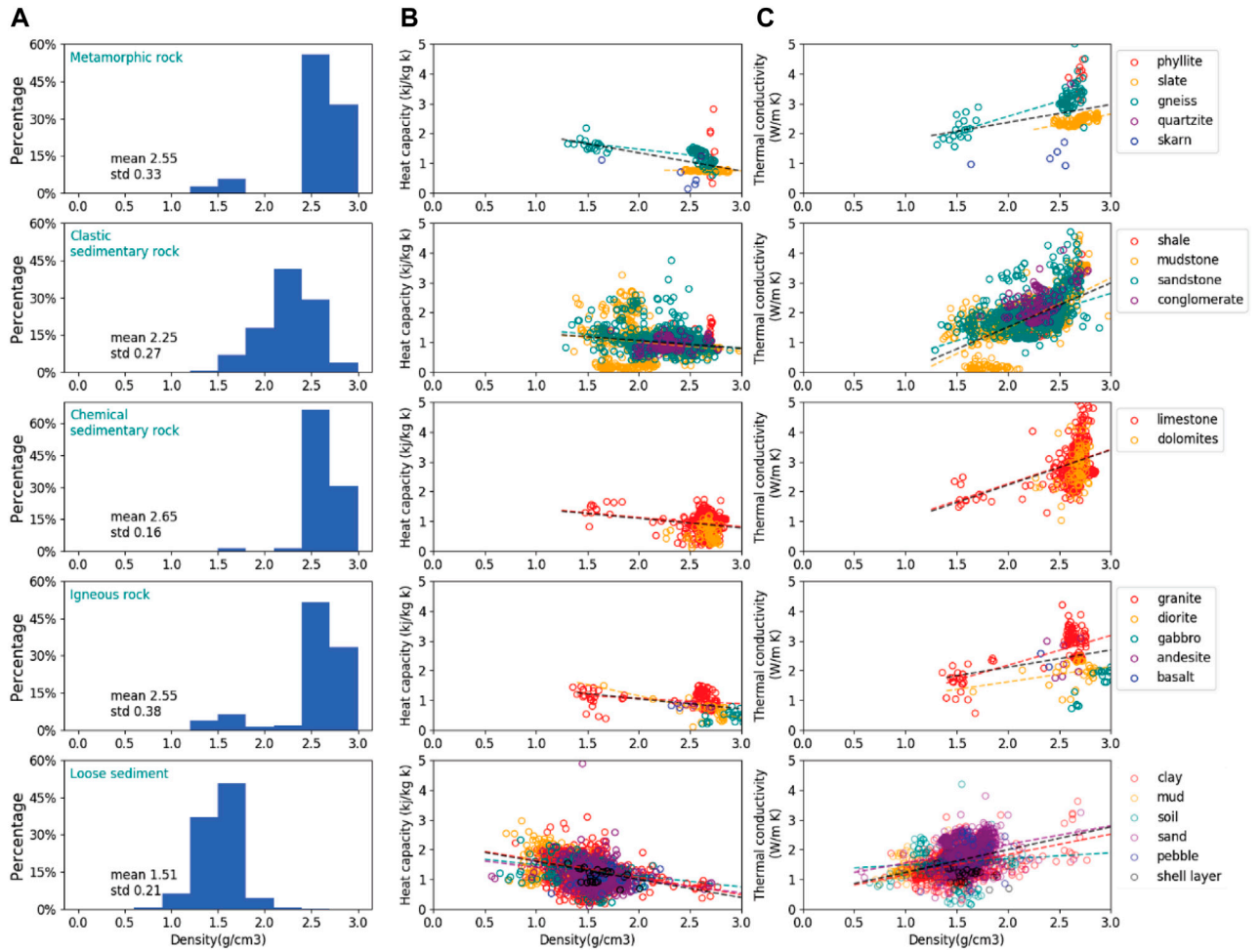

FIGURE 3 | Histograms of density **(A)** and its regression analysis with respect to heat capacity **(B)** and thermal conductivity **(C)** of rock and soil samples.

structure, the greater the thermal conductivity; the looser, the smaller the thermal conductivity, which indicating the combined effects of porosity and water content. The specific heat capacity is opposite, as it is generally larger for Quaternary loose layer than that for bedrock, and it is generally larger for clay than that for sandy soil and pebble layer.

The specific heat capacity of each soil body in the Quaternary loose overburden is quite different. Because the clay has a high porosity and water content, its specific heat capacity is relatively higher than that of the gravel and pebbles. It shows that silt and clay have a great ability to absorb or release heat. The thermal conductivity of pebble and sandy soil is better than that of silt and clay (**Figure 2**). These characteristics indicate that the heat absorption effect of the rock is better than that of the loose sediments, and the soil layer has a better heat storage capability than the rock layer due to the larger water content. Coarse-grained rock and soil have a better heat-releasing effect, but poor heat storage capability. On the contrary, fine-grained sediment has a better heat storage effect, but a poor heat-releasing effect. From the perspective of the development and utilization of shallow geothermal energy resources, the rock and soil are required to have good heat release performance for improving the efficiency of conducting heat.

The Impact of Density on Thermophysical Properties

Density is the basic physical property of rock and soil, which are composed of solid, liquid, and gas phases with a decreasing trend in density. Experience data shows that among the three-phase composition, the thermal conductivity of solid is the largest, followed by that of liquid, and that of gas is the smallest. Histograms of density for different rocks types are shown in **Figure 3**, column A. The density of metamorphic rocks, chemical sedimentary rocks, and igneous rocks are relatively higher than those of clastic sedimentary rocks and loose sediments. Whereas few samples of metamorphic rocks, chemical sedimentary rocks, and igneous rocks (row 1, 3, and 4) have low measured densities due to weathering. As a large number of rock samples for clastic

TABLE 3 | Regression analysis results for thermophysical properties and density.

Lithology		Specific heat capacity			Thermal conductivity		
		Slope	Intercept	R^2	Slope	Intercept	R^2
Metamorphic rock	Slate	−0.02	0.82	0.01	0.69	0.57	0.38
	Gneiss	−0.39	2.26	0.41	1.03	0.51	0.61
	Overall	−0.61	2.57	0.28	0.60	1.18	0.11
Clastic sedimentary rock	Mudstone	−0.31	1.63	0.04	1.69	−1.92	0.49
	Sandstone	−0.31	1.74	0.05	1.06	−0.53	0.17
	Overall	−0.26	1.58	0.03	1.47	−1.43	0.34
Chemical sedimentary rock	Limestone	−0.31	1.75	0.04	1.15	−0.03	0.08
	Overall	−0.32	1.74	0.03	1.17	−0.12	0.08
Igneous rock	Granite	−0.18	1.42	0.06	1.00	0.19	0.46
	Diorite	−0.75	2.65	0.39	0.51	0.61	0.10
	Overall	−0.34	1.73	0.15	0.58	0.96	0.11
Loose sediment	Clay	−0.58	2.22	0.12	0.68	0.47	0.20
	Silt	−0.37	1.86	0.05	0.20	1.28	0.01
	Sand	−0.43	1.83	0.06	0.62	0.92	0.07
	Overall	−0.61	2.21	0.14	0.76	0.47	0.15

sedimentary rocks and loose sediments, they show highly centered distributions.

By correlating the thermophysical properties, thermal conductivity and specific heat capacity, and density of all rock types, it shows that the thermal conductivity is positively related to rock density (black dashed lines in **Figure 3**, Column 3) but the specific heat capacity is negative to rock density (black dashed lines in **Figure 3**, Column 2). These results are in line with the previous studies (e.g., Hartmann et al., 2005; Oktay et al., 2015). The rock type is further classified according to its lithology. The regression analysis was conducted and the fitted parameters are shown in **Table 3**. The correlation between thermophysical properties and density for each rock type keep similar (colored dashed lines in **Figure 3**, Columns 2 and 3). For a given type of rock and soil, the thermal conductivity is positively correlated with the density. It is inversely proportional to the density (**Figure 3**, colored dashed line).

For metamorphic rocks, the specific heat capacity and thermal conductivity of slate vary slightly with density (a small slope), and the variation of gneiss is relatively large (a big slope). The changes of thermophysical properties with density are relatively similar for clastic sedimentary rocks. Compared with the specific heat capacity, the thermal conductivity has a strong correlation with density (a relatively high R^2). The density of chemical sedimentary rocks concentrates between 2.6 and 2.8 g/m3, and the weathered rocks with low density may slightly change the slopes. For igneous rocks, the specific heat of diorite varied obviously with density (the slope and R^2 are large), and the thermal conductivity of granite changes apparently with density. Similar to clastic sedimentary rocks, the thermophysical parameters of different loose sediments varied similarly with the density changes. The thermophysical parameters of clay (including specific heat and thermal conductivity) show a strong correlation with density.

For a specific rock type, higher density usually implies lower porosity if their mineralogy are identical, hence their thermal conductivity has an increasing trend with the density. Since the thermal conductivity is closely related to the grain configurations, the closely compacted mineral grains i.e., low porosity, increase the capability of conducting heat and thus a high thermal conductivity. The main effect of density on the difference in thermophysical properties lies in the "degree of compactness". For a given saturated soil, if the mineral composition and texture are basically the same, the difference in density results from the difference in the structure, porosity, water content, and other factors. Accordingly, the varied density may reflect the characteristics of porosity and water content to some extent and thus result in a change in thermophysical properties.

The Impact of Water Content on Thermophysical Properties

The water content is calculated as the percentage of the mass of free water in the total mass of the rock and soil (Li et al., 2007; Jorand et al., 2011; Kim and Oh, 2019). The water content of metamorphic rocks, chemical sedimentary rocks, and igneous rocks are small in general, less than 10% overall, and mostly concentrated between 0 and 5%, except for a few weathered rocks with high water content. The water content of clastic sedimentary rocks ranges roughly from 0 to 30%. As the water content increases, the number of samples gradually decreases. The water content of loose rocks concentrates around 20% and shows a nearly normal distribution (**Figure 4**).

For metamorphic rocks, the correlation between thermophysical parameters and water content for slate is not obvious compared to gneiss, which is similar to the previous results. For clastic sedimentary rocks, compared to sandstone, thermophysical parameters have a strong correlation with water content (a high R^2 in **Table 4**), and there are many mudstone samples with low specific heat capacity and low thermal conductivity. The thermophysical parameters of chemical sedimentary rocks have relatively low correlations with water content and exhibit a small change (small slopes as listed in **Table 4**).

Analysis of all the rock sample data shows that the specific heat capacity is directly proportional to water content (**Figure 4** and

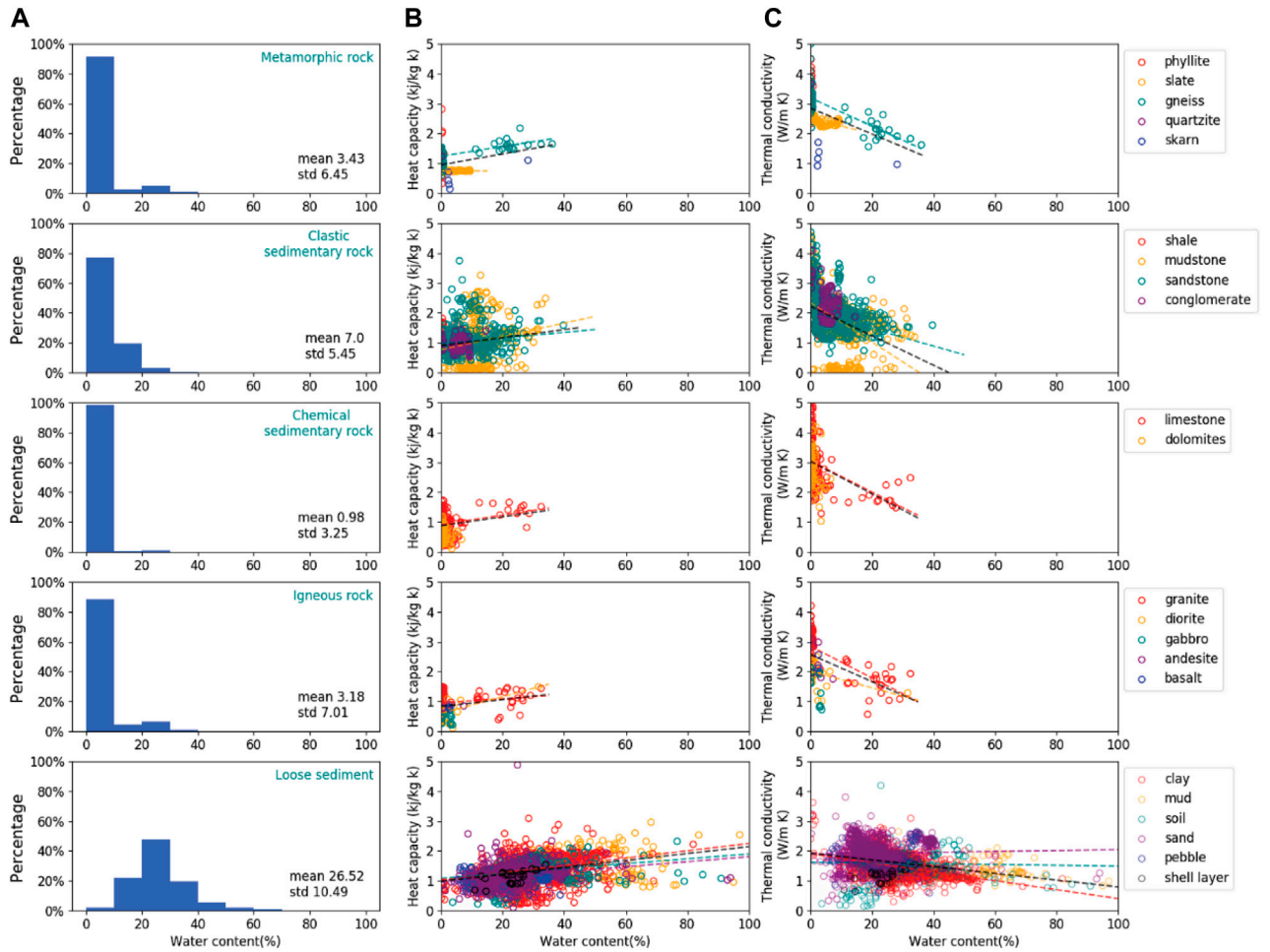

FIGURE 4 | Histograms of water content **(A)** and its regression analysis with respect to heat capacity **(B)** and thermal conductivity **(C)** of rock and soil samples.

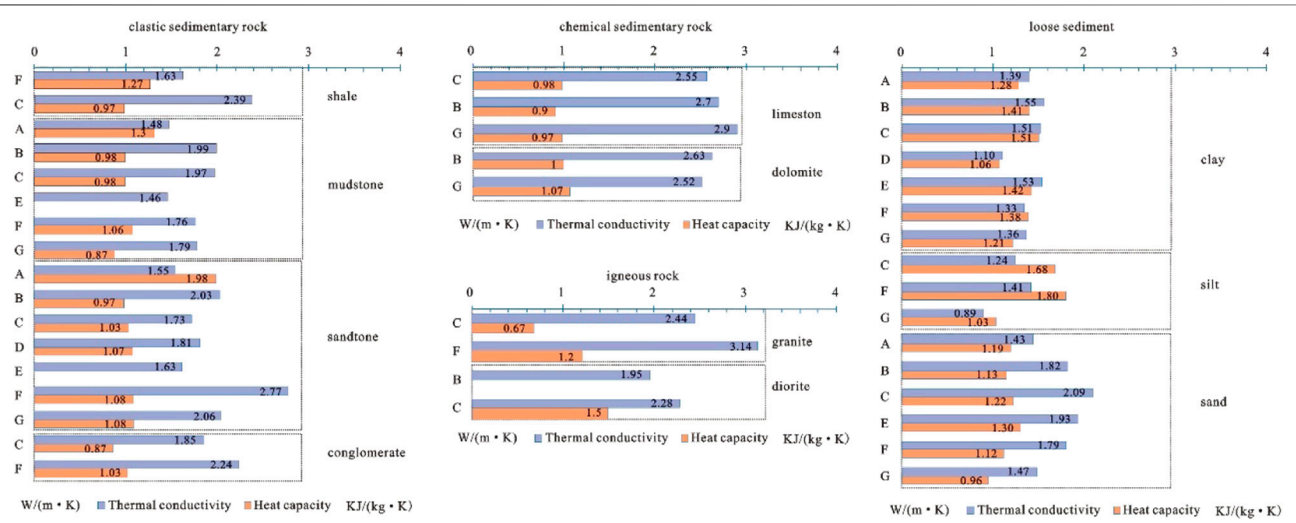

FIGURE 5 | Relationship between the thermal and physical parameters of each lithology in different regions.

TABLE 4 | Regression analysis results for thermophysical properties and water contents.

Lithology		Specific heat capacity			Thermal conductivity		
		Slope	Intercept	R^2	Slope	Intercept	R^2
Metamorphic rock	Slate	0.00	0.76	0.00	–0.02	2.49	0.31
	Gneiss	0.02	1.25	0.30	–0.05	3.19	0.56
	Overall	0.02	0.95	0.10	–0.04	2.85	0.23
Clastic sedimentary rock	Mudstone	0.02	0.77	0.07	–0.07	2.35	0.25
	Sandstone	0.01	0.97	0.02	–0.03	2.05	0.06
	Overall	0.01	0.90	0.03	–0.05	2.22	0.15
Chemical sedimentary rock	Limestone	0.02	0.92	0.04	–0.05	3.05	0.07
	Overall	0.01	0.88	0.03	–0.05	3.04	0.07
Igneous rock	Granite	0.01	0.96	0.04	–0.05	2.85	0.48
	Diorite	0.03	0.60	0.29	–0.03	2.01	0.17
	Overall	0.01	0.83	0.06	–0.05	2.57	0.23
Loose sediment	Clay	0.01	1.03	0.09	–0.01	1.90	0.16
	Silt	0.01	1.09	0.07	0.00	1.62	0.00
	Sand	0.01	0.96	0.07	0.00	1.89	0.00
	Overall	0.01	0.99	0.12	–0.01	1.92	0.08

Table 4), which is consistent with the results of Kim and Oh (2019). For igneous rocks, the water content greatly influences the thermal conductivity of granite and specific heat capacity of diorite. For loose sediments, the thermal conductivity and specific heat capacity of clay are greatly influenced by water content, while slit and sand are relatively unaffected by water content. As the particle size of the different sediments decreases, their thermal conductivity decreases and their thermal energy storage capacity increases.

The specific heat capacity mainly depends on the content of water and air. Since the specific heat capacity of water is much larger than that of air, the greater the water content in the rock and soil, the greater its specific heat capacity and vice versa. The data above indicates that specific heat capacity is positively correlated with water content, consistent with other studies.

In addition, some studies show that thermal conductivity is directly proportional to water content (Kim and Oh, 2019). Nevertheless, the analysis in this study shows that the thermal conductivity is negatively correlated with the water content (**Figure 4**; **Table 4**). The main reason may lie in that the relationship between thermophysical parameters and water content is not a simple linear relationship, and their correlation is also restricted by other factors such as lithology, density, etc. For example, considering silt and clay with large porosity, their density tends to be small, and yield a high water content. Their small contact area between the soil skeleton, and thus more pore water involved in transferring the heat, which results in a small thermal conductivity and a large specific heat capacity. Since the soils have different degree of cementation, the effect of porosity on the thermal properties is more complex, which is reflected in the different statistical patterns of these properties of sand and bedrock.

Other Influencing Factors

In terms of spatial distribution, except for structural factors, the distribution of thermophysical parameters could also be influenced by geological formation conditions and hydrogeological conditions. Tectonic faults affect heat transfer for crystalline rocks, due to the complexity and lack of commonality of these mechanisms, this aspect is not discussed in this paper.

Because the thermal conductivity of rocks is generally greater than that of loose sediments, the thicker and the larger the underlying bedrock, the higher thermal conductivity and the lower the specific heat capacity for the area. On the contrary, if the greater the thickness and area of loose sediments, e.g., silt and clay, the lower the thermal conductivity and the higher the specific heat capacity.

From the viewpoint of geomorphology, the high thermal conductivity area tends to be distributed in the mountains and the area where the bedrock is shallowly buried. By contrast, the thermal conductivity of the plain area is generally lower than that of the mountainous area (This part will be discussed further in the next section). Furthermore, the granite, dolomite, limestone, and shale areas in the bedrock area are also larger than the sandstone and mudstone areas. In the plain area, the thermal conductivity is slightly higher in river terraces and alluvial fans (where the lithology of strata is mainly coarse sand and gravel sand) than in the wind and slope deposition areas (where the lithology of strata is mainly clay and silty clay). The distribution characteristics of high and low specific heat capacity are roughly opposite to that of the thermal conductivity.

Hydrogeological conditions and temperature region are closely related to the thermophysical parameters of rock and soil. Different temperature regions have different climates and different weathering processes in the surface layer, affecting parameters such as lithology, grain size and water content of the loose sediments, influencing the thermophysical parameters in turn. The distribution of thermal conductivity of samples collected in most cities is correlated with the hydraulic characteristics. For instance, the high thermal conductivity area in Hohhot distributes in the pre-mountain plain area near the mountain, where is in well hydraulic conditions with coarse grains in strata; the thermal conductivity is low in the Daheihe plain area where is in poor hydraulic conditions with fine grains in strata. For the same rock formation in the urban area of Jinan, the better the groundwater runoff conditions, the stronger the water richness, and the greater the

TABLE 5 | Temperature region analysis results for thermophysical properties.

Temperature region	Region	City	Water content (%)	Density (g/cm^3)	Specific heat capacity KJ/(kg°C)	Thermal conductivity W/(m•°C)	Litho-logy
cold temperate zone	Songliao Plain	haerbin	23.47	1.86	1.34	1.42	clay
Mesothermal	Inner Mongolia, Shaanxi-Gansu Loess Plateau	taiyuan	21.34	2.01	1.41	1.56	clay
Subtropical	Tropical coastal plain area	fuzhou	29.31	1.85	1.06	1.84	clay
cold temperate zone	Songliao Plain	haerbin	24.04	1.72	1.20	1.40	sand
Subtropical	Tropical coastal plain area	fuzhou	26.07	1.92	1.00	1.88	sand

thermal conductivity. The high-value thermal conductivity is distributed in the south of Haikou City where is the groundwater recharge area, and the low-value is in the northern coastal plain, where is the groundwater discharge area. The distribution of specific heat capacity is opposite to that of the thermal conductivity. This reflects the influence of hydrogeological conditions on thermophysical parameters. Accordingly, the main factor that affects the thermophysical parameters is the hydrodynamic conditions. Areas with good hydrodynamic conditions generally have the characteristics of large water volume and rapid flow rate, which has a positive effect on heat transfer, whereas, in areas with poor hydrodynamic conditions, the groundwater moves slow and thermal transfer tend to small.

Data from the clay and sand of Harbin, Taiyuan and Fuzhou, from the cold temperate, mesothermal and subtropical zones, are listed in **Table 5**. There are small differences in water content and density regularity of clay, without meaningful trend. The thermal conductivity of the samples elevate with increase of regional temperature and the specific heat capacity shows a roughly decreasing trend. For sand in areas with high regional temperatures, the samples had higher water content, density and thermal conductivity and lower specific heat capacity. Overall, among samples with small differences in water content and density, the thermal conductivity of the rock/soil is positively correlated with the regional temperature and precipitation, while the specific heat capacity is the opposite.

Regional Characteristics

The thermal conductivity of clay in the Huang-Huai-hai Plain is small, but the median value tends to be the same in other regions, except for very large and very small values, which were mainly caused by the change of water content. The mean thermal conductivity of clay is 1.48 W/mK. In sand and clay, the thermal conductivity reflects regional differences. It is lower in the Songliao Plain, higher in the hilly mountains of eastern and central China, and the mean values in the Huang- Huai-hai Plain and the Loess Plateau of Inner Mongolia and Shaanxi-Gansu are relatively close to each other, with the median mean values ranging from 1.60 to 2.00 W/mK from the clay to the sands. The variability of regional thermal conductivity in bedrock is more evident, with distributions between 1.46 and 3.00 W/mK. The density, porosity and permeability of rocks in different regions, the nature and content of fluids in the pores of rocks, as well as the differences in temperature and pressure, all have an effect on the thermal conductivity (**Table 6**).

The regional variation of specific heat capacity is not clear. In the clay, slit, sand and shale in Quaternary, Neoproterozoic and Paleoproterozoic strata, the specific heat capacity in the karst hills of southwest China is generally lower than that in other areas of the earth, and that in the hills of east and central China is slightly higher than that in other areas. The median values range from 0.88 to 1.48 kJ/kgK. Among the rocks, the median specific heat capacity is concentrated around 1.00 kJ/kgK. The specific heat capacity of mudstone in the Songliao Plain is high, with a median value of 1.30 kJ/kgK, and the specific heat capacity of shale in southeast and south China marine climate is higher, with a median value of 1.27 kJ/kgK.

The thermal conductivity and heat capacity of the clastic sedimentary rock in plains, plateaus, mountains and hills are approximately similar. About the mudstone, the lowest thermal conductivity is found in the loess plateau, maybe due to the low water content. The thermal conductivity of sandstone in Tropical coastal plain area is 1.7 times of those in Songliao Plain, while the specific heat capacity is only 1/2. Similar features are found of the conglomerate, the formation of sedimentary strata containing smaller particles is more favorable in the Songliao Plain than in the coastal areas.

For the chemical sedimentary rock, the characteristics of the thermal and physical parameters tend to be consistent and do not correlate significantly with their locations.

For the igneous rocks, data are only available in Huang-Huai-Hai Plain, East China - Central China Hilly Mountainous Region and Tropical coastal plain area. The thermal conductivity of the granite in Tropical coastal plain area is 3.14, the highest value among those of the region.

Loose sediment is very heterogeneous, including clay, silt and sand widely distribute in seven different areas. For clay, only the thermal conductivity and specific heat capacity of Northwest Interior Basin are significantly lower than those of other areas, while the other six areas are basically the same. For silt, the thermal conductivity and specific heat capacity of Southwest karst hills are significantly lower than those of East China–Central China Hilly Mountainous Region and Tropical coastal plain area, and the thermal conductivity of sand shows a trend of gradually decreasing from mountain–plateau–plain (**Figure 5**).

Generally speaking, from the hilly areas to the middle of the basin or plain, as the altitude decreases, the lithology gradually changes

TABLE 6 | Statistical results of thermal and physical parameters of each lithology in different regions.

Code name	Region	Lithology		Mean thermal conductivity	Mean heat capacity
C	East china–central china hilly mountainous region	Clastic sedimentary rock	Shale	2.39	0.97
F	Tropical coastal plain area			1.63	1.27
A	Songliao Plain		Mudstone	1.48	1.30
B	Huang-huai-hai plain			1.99	0.98
C	East china–central china hilly mountainous region			1.97	0.98
E	Inner mongolia, shaanxi-gansu loess plateau			1.46	
F	Tropical coastal plain area			1.76	1.06
G	Southwest karst hills			1.79	0.87
A	Songliao Plain		sandstone	1.55	1.98
B	Huang-Huai-Hai Plain			2.03	0.97
C	East china–central china hilly mountainous region			1.73	1.03
D	Northwest interior basin			1.81	1.07
E	Inner mongolia, shaanxi-gansu loess plateau			1.63	
F	Tropical coastal plain area			2.77	1.08
G	Southwest karst hills			2.06	1.08
C	East china–central china hilly mountainous region		Conglomerate	1.85	0.87
F	Tropical coastal plain area			2.24	1.03
B	Huang-huai-hai plain	Chemical sedimentary	Limestone	2.70	0.90
C	East china–central china hilly mountainous region	rock		2.55	0.98
G	Southwest karst hills			2.90	0.97
B	Huang-Huai-Hai Plain		Dolomites	2.63	1.00
G	Southwest karst hills			2.52	1.07
C	East china–central china hilly mountainous region	Igneous rock	Granite	2.44	0.67
F	Tropical coastal plain area			3.14	1.20
B	Huang-huai-hai plain		Diorite	1.95	
C	East china–central china hilly mountainous region			2.28	1.50
B	Huang-huai-hai plain		Gabbro	1.93	
C	East china–central china hilly mountainous region		Andesite	1.54	0.91
A	Songliao plain	Loose sediment	Clay	1.39	1.28
B	Huang-huai-hai plain			1.55	1.41
C	East china–central china hilly mountainous region			1.51	1.51
D	Northwest interior basin			1.10	1.06
E	Inner Mongolia, Shaanxi-Gansu Loess Plateau			1.53	1.42
F	Tropical coastal plain area			1.33	1.38
G	Southwest karst hills			1.36	1.21
C	East China - Central China Hilly Mountainous Region		silt	1.24	1.68
F	Tropical coastal plain area			1.41	1.80
G	Southwest karst hills			0.89	1.03
A	Songliao Plain		sand	1.43	1.19
B	Huang-huai-hai plain			1.82	1.13
C	East china–central china hilly mountainous region			2.09	1.22
E	Inner mongolia, shaanxi-gansu loess plateau			1.93	1.30
F	Tropical coastal plain area			1.79	1.12
G	Southwest karst hills			1.47	0.96
F	Tropical coastal plain area		Shell layer	1.18	1.19

from sand, pebbles and gravels to silt and clay interlayers. The lithology change is accompanied by a gradual decrease of the thermal conductivity and increase of heat capacity, according to the gradual grain size decrease and porosity increase of the rock/soil's.

CONCLUSION

In this study, the thermophysical properties of 6467 rock and soil samples collected from 24 provincial capitals in China are analyzed and correlated with the lithology, density, water content. The thermal conductivity of the bedrock is generally greater than that of the Quaternary loose sediments. Dolomite, shale, and granite have a higher thermal conductivity than gabbro, sandstone, and mudstone for the bedrock. For the loose sediments, the thermal conductivity of pebble and gravel is larger than that of the clay and silt, which shows a decreasing trend with the grain sizes. For the specific heat capacity, which is opposite to the thermal conductivity, it is generally lower in the bedrock than that in the Quaternary loose sediments. Density and water content affect thermophysical parameters, thermal conductivity increases with density and decrease with water content, while specific heat capacity decreases with density and increase with water content.

To summarize, during the development and utilization of shallow geothermal energy, it is necessary to consider the local conditions such as geological formation, hydrogeological settings to

representatively collect measurement samples to determine thermophysical properties, in order to assess the applicable resource amount, optimize ground source heat pumps systems to maximize the utilization of shallow geothermal energy. The finding of this study provides data basis and variation analysis for the resource assessments and modeling, provides insights for the site selections of shallow geothermal energy development and utilization.

DATA AVAILABILITY STATEMENT

The raw data supporting the conclusions of this article will be made available by the authors, without undue reservation.

AUTHOR CONTRIBUTIONS

XZ Collected and collated the data listed in the manuscript and completed the main sections of the manuscript, ZG Provided methods of data analysis, TC analysed data and produced graphs, WW collected and collated primary data, CL provided methods for data analysis, QZ reviewed the literature and collated the current state of research.

FUNDING

This study was financially supported by the Natural Science Foundation of Hebei Province, China (Grant No. D2021504041), The National Key Research and Development Program of China (Grant No. 2019YFB1504101), Geological Survey Project (DD20221676).

ACKNOWLEDGMENTS

The authors acknowledge the reviewer for carefully reading and giving critical comments on this manuscript.

REFERENCES

Cheng, C., and Yu, W. (2017). Research Progress and Development Tendency about Thermal Physical Properties of Rocks. *Adv. Earth Sci.* 32 (10), 1072–1083. (in Chinese with English abstract). doi:10.11867/j.issn.1001-8166.2017.10.1072

Clauser, C., and Huenges, E. (1995). "Thermal Conductivity of Rocks and Minerals," in *Rock Physics and Phase Relations: A Handbook of Physical Constants*. Editor T.-J Ahrens (Hannover, Germany: American Geophysical Union), 3, 105–126.

Fuchs, S., and Förster, A. (2014). Well-log Based Prediction of Thermal Conductivity of Sedimentary Successions: A Case Study from the North German Basin. *Geophys. J. Int.* 196 (1), 291–311. doi:10.1093/gji/ggt382

Fuchs, S. (2018). The Variability of Rock Thermal Properties in Sedimentary Basins and the Impact on Temperature Modelling - A Danish Example. *Geothermics* 76, 1–14. doi:10.1016/j.geothermics.2018.06.006

Goto, S., and Matsubayashi, O. (2009). Relations between the Thermal Properties and Porosity of Sediments in the Eastern Flank of the Juan de Fuca Ridge. *Earth Planet Sp.* 61 (7), 863–870. doi:10.1186/bf03353197

Han, J., Sun, Q., Xing, H., Zhang, Y., and Sun, H. (2017). Experimental Study on Thermophysical Properties of Clay after High Temperature. *Appl. Therm. Eng.* 111, 847–854. doi:10.1016/j.applthermaleng.2016.09.168

Hartmann, A., Pechnig, R., and Clauser, C. (2008). Petrophysical Analysis of Regional-Scale Thermal Properties for Improved Simulations of Geothermal Installations and Basin-Scale Heat and Fluid Flow. *Int. J. Earth Sci. (Geol Rundsch)* 97 (2), 421–433. doi:10.1007/s00531-007-0283-y

Hartmann, A., Rath, V., and Clauser, C. (2005). Thermal Conductivity from Core and Well Log Data. *Int. J. Rock Mech. Min. Sci.* 42 (7-8), 1042–1055. doi:10.1016/j.ijrmms.2005.05.015

Jorand, R., Clauser, C., Marquart, G., and Pechnig, R. (2015). Statistically Reliable Petrophysical Properties of Potential Reservoir Rocks for Geothermal Energy Use and Their Relation to Lithostratigraphy and Rock Composition: The NE Rhenish Massif and the Lower Rhine Embayment (Germany). *Geothermics* 53, 413–428. doi:10.1016/j.geothermics.2014.08.008

Jorand, R., Fehr, A., Koch, A., and Clauser, C. (2011). Study of the Variation of Thermal Conductivity with Water Saturation Using Nuclear Magnetic Resonance. *J. Geophys. Res.* 116 (B8), 1–12. doi:10.1029/2010jb007734

Kim, D., and Oh, S. (2019). Relationship between the Thermal Properties and Degree of Saturation of Cementitious Grouts Used in Vertical Borehole Heat Exchangers. *Energy Build.* 201, 1–9. doi:10.1016/j.enbuild.2019.07.017

Kim, S., Kim, M. C., and Kim, K. Y. (2002). An Integral Approach to the Inverse Estimation of Temperature-Dependent Thermal Conductivity without Internal Measurements. *Int. Commun. Heat Mass Transf.* 29 (1), 107–113. doi:10.1016/s0735-1933(01)00329-3

Li, H. X., Xia, Z. Q., and Ma, G. H. (2007). Effects of Water Content Variation on Soil Temperature Process and Water Exchange. *J. Hohai Univ. (Natural Sciences)* 35 (2), 172–175. (in Chinese with English abstract). doi:10.3321/j.issn:1000-1980.2007.02.012

Lin, W. J., Wu, Q. H., and Wang, G. L. (2012). Shallow Geothermal Energy Resource Potential Evaluation and Environmental Effect in China. *J. Arid Land Resour. Environ.* 26 (3), 57–61. (in Chinese with English abstract).

Lund, J. W., and Toth, A. (2020). "Direct Utilation of Geothermal Energy 2020 Wordwide - 27 April, 2020," in World Geothermal Congress 2020, Reykjavik, Iceland, 27 April, 2020.

McDaniel, A., Tinjum, J., Hart, D. J., Lin, Y.-F., Stumpf, A., and Thomas, L. (2018). Distributed Thermal Response Test to Analyze Thermal Properties in Heterogeneous Lithology. *Geothermics* 76, 116–124. doi:10.1016/j.geothermics.2018.07.003

Middleton, M. F. (1994). Determination of Matrix Thermal Conductivity from Dry Drill Cuttings. *AAPG Bull.* 78 (11), 1790–1799. doi:10.1306/a25ff297-171b-11d7-8645000102c1865d

Midttømme, K., Roaldset, E., and Aagaard, P. (1998). Thermal Conductivity Claystones and Mudstones of Selected from England. *Clay Min.* 33 (1), 131–145.

Ministry of Construction of the People's Republic of China (1999). *GB/T 50123-1999 Standard for Soil Test Methods*. Beijing: Chinese Plan Publishing House.

Miranda, M. M., Velez Márquez, M. I., Raymond, J., and Dezayes, C. (2021). A Numerical Approach to Infer Terrestrial Heat Flux from Shallow Temperature Profiles in Remote Northern Regions. *Geothermics* 93, 102064. doi:10.1016/j.geothermics.2021.102064

Muhieddine, M., Canot, É., and March, R. (2012). Heat Transfer Modeling in Saturated Porous Media and Identification of the Thermophysical Properties of the Soil by Inverse Problem. *Appl. Numer. Math.* 62 (9), 1026–1040. doi:10.1016/j.apnum.2012.02.008

Naranjo-Mendoza, C., Wright, A. J., Oyinlola, M. A., and Greenough, R. M. (2018). A Comparison of Analytical and Numerical Model Predictions of Shallow Soil Temperature Variation with Experimental Measurements. *Geothermics* 76, 38–49. doi:10.1016/j.geothermics.2018.06.003

Ohta, K., Nishihara, Y., Sato, Y., Hirose, K., Yagi, T., Kawaguchi, S. I., et al. (2018). An Experimental Examination of Thermal Conductivity Anisotropy in Hcp Iron. *Front. Earth Sci.* 6, 176. doi:10.3389/feart.2018.00176

Oktay, H., Yumrutaş, R., and Akpolat, A. (2015). Mechanical and Thermophysical Properties of Lightweight Aggregate Concretes. *Constr. Build. Mater.* 96, 217–225. doi:10.1016/j.conbuildmat.2015.08.015

Pimienta, L., Klitzsch, N., and Clauser, C. (2018). Comparison of Thermal and Elastic Properties of Sandstones: Experiments and Theoretical Insights. *Geothermics* 76, 60–73. doi:10.1016/j.geothermics.2018.06.005

Popov, Y., Romushkevich, R., Korobkov, D., Mayr, S., Bayuk, I., Burkhardt, H., et al. (2011). Thermal Properties of Rocks of the Borehole Yaxcopoil-1 (Impact Crater Chicxulub, Mexico). *Geophys. J. Int.* 184 (2), 729–745. doi:10.1111/j.1365-246x.2010.04839.x

Ran, W. Y., Li, N. B., Yang, J. W., and Yu, Y. (2014). Some Enlightenment Gained from City Shallow Geothermal Energy Investigation and Evaluation. *Urban Geol.* 9 (Z1), 1–3. (in Chinese with English abstract). doi:10.3969/j.issn.0001-5717.2019.08.018

Song, X. Q., Jiang, M., Peng, Q., and Xiong, P. W. (2019). Thermal Property Parameters and Influencing Factor Analysis of Main Rock Strata in Guizhou Province. *Atca Geol. Sin.* 93 (8), 2092–2103. (in Chinese with English abstract).

Song, X., Zheng, R., Li, G., Shi, Y., Wang, G., and Li, J. (2018). Heat Extraction Performance of a Downhole Coaxial Heat Exchanger Geothermal System by Considering Fluid Flow in the Reservoir. *Geothermics* 76, 190–200. doi:10.1016/j.geothermics.2018.07.012

Tiwari, R., Boháč, V., Dieška, P., and Götzl, G. (2021). The Non-planar Surface of Carbonate Rock Sample Affecting the Behaviour of Thermal Response and the Measurement of Thermophysical Parameters by Pulse Transient Technique. *Therm. Sci. Eng. Prog.* 24, 100927. doi:10.1016/j.tsep.2021.100927

Wang, G. L., Lin, W. J., and Zhang, W. (2012). Evaluation on Utilization Potential of Shallow Geothermal Energy in Major Cities of China. *Build. Sci.* 28 (10), 1–3, 8 (in Chinese with English abstract). doi:10.12029/gc20170602

Wang, W. L., Wang, G. L., Zhu, X., and Liu, Z. M. (2017). Characteristics and Potential of Shallow Geothermal Resources in Provincial Capital Cities of China. *Geol. China* 44 (6), 1062–1073. (in Chinese with English abstract).

Wang, Y., Rajeshwar, K., Nottenburg, R. N., and Dubow, J. B. (1979). Thermophysical Properties of Oil Shale Minerals. *Thermochim. Acta* 30 (1-2), 141–151. doi:10.1016/0040-6031(79)85049-2

Zeng, Y., Ji, B., Zhang, Y., Feng, J., Luo, J., and Wang, M. (2022). A Fractal Model for Effective Thermal Conductivity in Complex Geothermal Media. *Front. Earth Sci.* 10, 786290. doi:10.3389/feart.2022.786290

Zheng, K., Han, Z., and Zhang, Z. (2010). Steady Industrialized Development of Geothermal Energy in China Country Update Report 2005-2009. *Proc. World Geotherm. Congr. Bali, Indonesia* 136, 1–11.

Conflict of Interest: The authors declare that the research was conducted in the absence of any commercial or financial relationships that could be construed as a potential conflict of interest.

Publisher's Note: All claims expressed in this article are solely those of the authors and do not necessarily represent those of their affiliated organizations, or those of the publisher, the editors and the reviewers. Any product that may be evaluated in this article, or claim that may be made by its manufacturer, is not guaranteed or endorsed by the publisher.

frontiers | Frontiers in Earth Science

ORIGINAL RESEARCH
published: 31 May 2022
doi: 10.3389/feart.2022.893969

Experimental Study on the Effect and Mechanism of Chemical Stimulation on Deep High-Temperature Granite

Zhenpeng Cui[1,2], *Shuantong Shangguan*[3], *Fabrizio Gherardi*[4], *Xiaofei Qi*[3], *Jianan Xu*[1,2], *Siqing He*[1,2] *and Bo Feng*[1,2]*

[1]Key Laboratory of Groundwater Resources and Environment, Ministry of Education, Jilin University, Changchun, China, [2]Engineering Research Center of Geothermal Resources Development Technology and Equipment, Ministry of Education, Jilin University, Changchun, China, [3]No.2 Exploration Team, Hebei Bureau of Coal Geological Exploration, Xingtai, China, [4]Institute of Geosciences and Earth Resources, Italy National Research Council, Pisa, Italy

Chemical stimulation has been increasingly applied to improve the performance of geothermal reservoirs since early 1980s. The potential for the successful application of this technique to high-temperature reservoirs hosted in granitic rocks is still uncertain, and one of the keys to assess this potential is to investigate experimentally the geochemical reactivity induced *via* chemical stimulation on relevant rock specimens. On this premise, we combined high-temperature and high-pressure dynamic simulation and static corrosion experiments to explore the effect of different chemical stimulants on the permeability of granite samples from the Baimiao formation (Hebei Province, China). Experimental results show that NaOH-dominated alkaline stimulants cause only weak dissolution patterns on primary feldspar and quartz, and they do not sensitively affect the original amount of chlorite. The overall effect is a negligible enhancement of the original permeability of all the granite specimens analyzed. Conversely, a large increase in permeability is observed when an acid mixture of 10wt% HCl + 1.5wt% HF is used as a stimulant, with an observed maximum magnifying effect of about 27 times, due to the effective dissolution of feldspar and chlorite. Though quartz appears not to be affected by dissolution, a relatively large amount of secondary neo-formed amorphous silica is also documented.

Keywords: laboratory experiment, mechanism analysis, enhanced geothermal system, chemical stimulation, permeability modification, secondary precipitation

OPEN ACCESS

Edited by:
Wenjing Lin,
Chinese Academy of Geological Sciences, China

Reviewed by:
Xianzhi Song,
China University of Petroleum, Beijing, China
Yanlong Kong,
Chinese Academy of Sciences (CAS), China

***Correspondence:**
Bo Feng
fengbo234@126.com

Specialty section:
This article was submitted to Geochemistry, a section of the journal Frontiers in Earth Science

Received: *11 March 2022*
Accepted: *01 April 2022*
Published: *31 May 2022*

Citation:
Cui Z, Shangguan S, Gherardi F, Qi X, Xu J, He S and Feng B (2022) Experimental Study on the Effect and Mechanism of Chemical Stimulation on Deep High-Temperature Granite. Front. Earth Sci. 10:893969. doi: 10.3389/feart.2022.893969

1 INTRODUCTION

Owing to the latest generation technology, geothermal energy is considered clean, renewable, and economically exploitable on a large scale (e.g., among many others, Liao et al., 2006). Due to its huge reserves and wide distribution, geothermal energy has become one of the most important alternative new energy sources after coal and oil and has attracted extensive research and development all over the world (Xu, 2005). It is estimated that if just 1% of the geothermal potential in the earth's crust might be fully utilized, the world energy requirement for 2,800 years would be provided at the current energy consumption rate (Olasolo et al., 2016; Alegria et al., 2022).

Enhanced geothermal systems (EGSs) are engineered geothermal reservoirs developed to commercially mine heat from hot rocks that have limited pathways through which operation fluids can flow (e.g., among many others, Wang et al., 2020). The key to the successful operation of

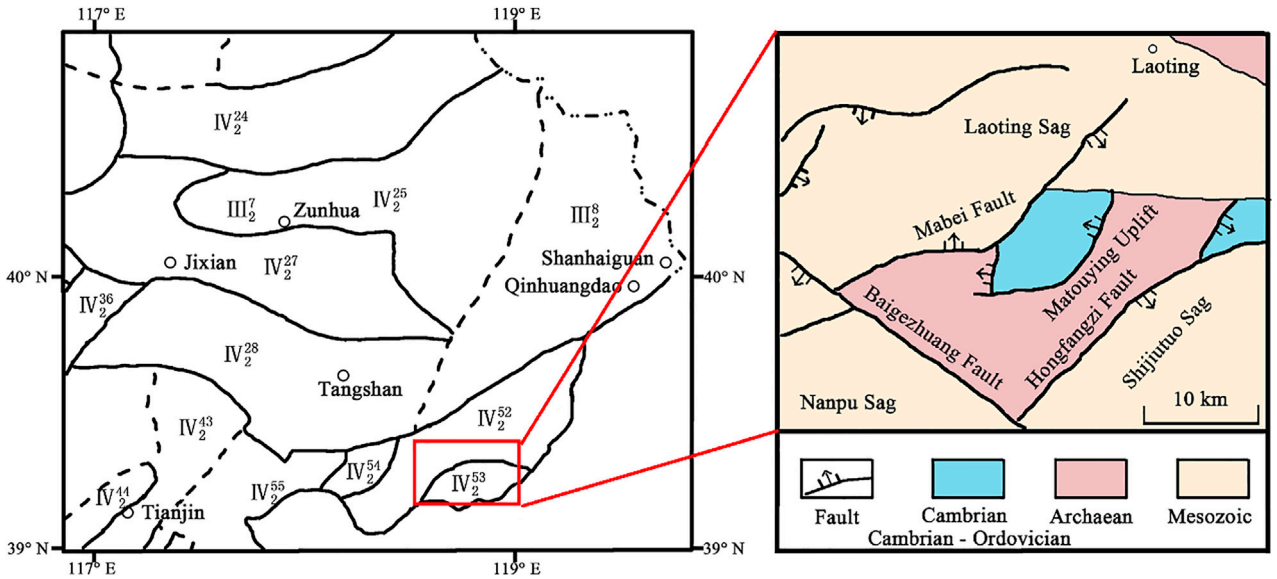

FIGURE 1 | Structural location of the study area. III_2^7: Malanyu compound anticline; III_2^8: Shanhaiguan anticline; IV_2^{24}: Kuancheng concave fold bundle; IV_2^{25}: Zunhua fornix fold bundle; IV_2^{27}: Jixian concave fold bundle; IV_2^{28}: Kailuan depressional platform; IV_2^{36}: Dachang uplift; IV_2^{43}: Panzhuang depression; IV_2^{44}: Dacheng depression; IV_2^{52}: Nanpu uplift; IV_2^{53}: Matouying uplift; IV_2^{54}: Baigezhuang uplift; IV_2^{55}: Beitang depression.

the EGS lies in the artificial creation of a network of hydraulically transmissive fractures in the low permeability rock (reservoir reconstruction), with the ultimate goal to establish a large volume of the water storage layer, to increase the contact area between the fluid for heat exchange and the high-temperature rock, and to establish a good hydraulic connection between the injection well and production well (e.g., Xu et al., 2018; Feng et al., 2019). At present, the main methods of stimulating artificial reservoirs include hydraulic fracturing, thermal stimulation, and chemical stimulation (Wang et al., 2012). Among them, hydraulic fracturing and thermal stimulation have some problems in practical application, such as unsatisfactory reconstruction effect, poor stability, and ease in inducing microseisms. As a kind of soft stimulation technology, chemical stimulation has the potential to enhance reservoir permeability without the abovementioned drawbacks associated with hydraulic and thermal stimulation practices (Luo et al., 2018).

Chemical stimulation relies on the injection of chemically reactive agents at a pressure lower than the formation fracture pressure. Reservoir permeability enhancement occurs through mineral dissolution. It is a method originally developed for, and widely applied in, oil and gas applications (Smith and Hendrickson, 1965; Economides and Nolte, 1989; Schechter, 1992; Liu et al., 2016). Any conventional chemical stimulation program is usually divided into three stages: pre-flush, main flush, and post-flush (Portier et al., 2009; Yang, 2012). The main purpose of the pre-flush stage is to prepare for the main stimulation stage by dissolving and expelling some mineral components (for example carbonates) that have the potential to hamper the stimulation effect *via* geochemical buffering. The main purpose of the post-flush stage is to keep the permeability of the reservoir stable by discharging the residual acid (or alkali) and reactive minerals in the fracture.

The effectiveness of the chemical stimulation sensitively depends on the type of stimulants and their reaction mechanism with formation minerals (Perthuis et al., 1989; Davies et al., 1994). The chemical agents commonly used in EGS practices comprise acidic and alkaline compounds. Acidic stimulants typically include conventional and retarded acid systems, mud acid (HCl + HF), chelating acids, and CO_2 (Portier and Vuataz, 2010; Yang, 2012). Alkaline stimulants mainly include NaOH, Na_2CO_3, and chelating bases (Evanoff et al., 1997; Sarda, 1977). Recent research developments have focused on the experimental study of the impact of HF and organic acid mixtures on the structure of sandstone rocks (Yang, 2012), and on the integration of experimental and numerical techniques to assess the performance of CO_2 as a chemical stimulant in EGS reservoirs (Na et al., 2014). In addition, the influence of high-concentration mud acid on the hydraulic characteristics of fractured granite has been recently addressed (Luo et al., 2018). The results of these laboratory experiments show that the permeability of fractured granite samples can be greatly improved after the static reaction with high-concentration mud acid. Finally, the reaction kinetics between soil acid and granite has been explored in some detail through static dissolution experiments and numerical modeling (Yue et al., 2020).

Despite all these efforts, the performance of chemical stimulation practices under field conditions still remain highly uncertain and inherently difficult to predict. For instance, both duration and mode of interaction between chemical stimulants and rocks are expected to be significantly different from laboratory conditions due to the inherently high complexity of

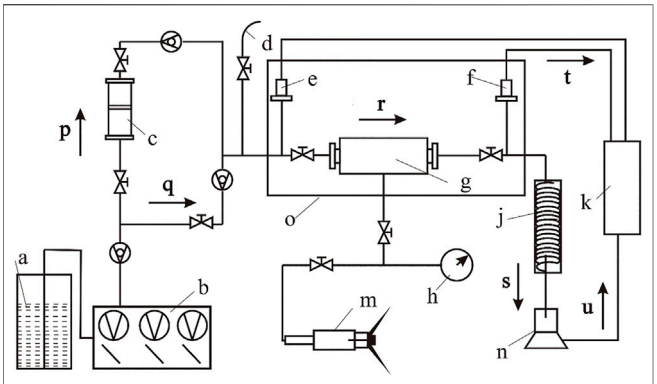

FIGURE 2 | Structure diagram of the core flow instrument. a, Ultrapure water; b, constant speed and pressure pump; c, intermediate container; d, safety valve; e, inlet pressure; f, outlet pressure; g, core holder; h, confining pressure gage; j, condenser; k, data acquisition device; m, hand pump; n, electronic balance; o, blast oven; p, ultrapure water; q, chemical stimulant; r, injected fluid; s, residual liquid; t, pressure data; u, velocity data.

the spatial distribution of fractures at the reservoir scale and the large variability of fluid–rock interaction conditions. For example, at the end of the injection stage, part of the chemical stimulant is expected to remain in the reservoir fractures, providing the driving force for additional mineral/dissolution processes, which may have side effects on reservoir reconstruction.

To account for all these complexities, in this study, we performed dynamic and static experiments on granite samples under high-temperature and high-pressure conditions. Dynamic experiments were carried out to explore the effect of different chemical stimulants during the injection phase. A set of prolonged static corrosion experiments were carried out under the same reaction conditions to explore "residual" reaction mechanisms likely associated with the late stages of the chemical stimulation. Granite rocks of the Baimiao formation of the Archean Dantazi Group in the Matouying uplift area (Hebei Province, China) are the target of our experiments.

2 GEOLOGICAL AND GEOTHERMAL SETTING

The study area is located in the Matouying uplift area in the eastern part of Hebei Province, China (**Figure 1**). The Matouying uplift is a secondary structural unit in the northern margin of Huanghua depression of North China fault depression, surrounded by Laoting depression, Nanpu depression, and Shijiutuo depression, bordering Bozhong depression in the southeast and Yanshan fold belt in the north. Both mantle-derived heat and radioactive heat contribute to the terrestrial heat flow of the study area. Deep and large faults exist in the region, which act as preferential pathways for heat and mass ascent through the crust (e.g., Cangdong and Tanlu fault zones; Zhang et al., 2020).

Regional geology is characterized by the occurrence of lithologies of the Archean to Quaternary age. Cenozoic formations, mainly represented by variable grain-sized sandstones and clay rocks, act as the local caprock. The Matouying uplift is characterized by a heat flow larger than 75 mW/m^2, slightly higher than the global average heat flow value (Wang et al., 1990), associated with a geothermal gradient generally comprised between 30 and 50°C/km, and up to a maximum of about 70°C/km in the middle of the area (Shangguan, 2017; Qi et al., 2020).

The target reservoir of this study is the metamorphosed granite of Baimiao formation of the Archean Dantazi Group. The surface of this granite is between 1200 and 1900 m b.g.l, whereas the bottom is generally deeper than 4000 m b.g.l, which corresponds to an approximate thickness of 1500–2,500 m. The maximum temperature is slightly above 150°C, which is considered appealing for geothermal applications (Qi et al., 2018). The main mineralogical constituents are K-feldspar (30%), plagioclase (33%), quartz (20%), chlorite (15%), and biotite (2%).

3 METHODS

3.1 Dynamic Simulation Experiment

3.1.1 Experimental Purpose and Principle

This experiment aims at reproducing the dynamics of the injection phase of the chemical stimulant in the reservoir. The variations in the equivalent permeability of the rock specimens were used as the master variable to monitor the impact of the stimulants on the granite structure. The equivalent permeability was calculated by applying **Eq. 3** along with instantaneous information on pressure and liquid outflow collected during the experiment. **Eq. 3** was deduced from Darcy's Law (**Eq. 1**) and the relationship between permeability and permeability coefficient (**Eq. 2**).

$$Q = K \times A \times \frac{H_1 - H_2}{L}, \tag{1}$$

$$k = K\frac{\mu}{\rho g}, \tag{2}$$

$$k = \frac{Q\mu L}{A(P_1 - P_2)}. \tag{3}$$

In **Eqs. (1–3)**, k [m^2] is the equivalent permeability, Q [m^3/s] is the liquid flow through the core, μ [Pa·s] is the dynamic viscosity coefficient of the liquid, L [m] is the core length, A [m^2] is the cross-sectional area of the core, P_1 [Pa] and P_2 [Pa] are, respectively, the inlet and outlet port pressure, K [m/d] is the permeability coefficient, H_1 [m] and H_2 [m] are the inlet and outlet head, respectively, ρ [kg/m^3] is the liquid density, and g [m/s^2] is the acceleration of gravity.

Further insights on the reaction mechanisms induced by the different stimulants were obtained by monitoring the chemical concentration of K^+, Na^+, Mg^{2+}, Al^{3+}, and soluble silicon. By applying mass conservation principles, the degree of progress of different mineral dissolution/precipitation processes was assessed with respect to the stoichiometry of the primary minerals.

3.1.2 Experimental Equipment and Samples

This experiment was carried out with the high-temperature and high-pressure core flow instrument of **Figure 2**. This instrument comprises a constant speed and pressure pump, a blast oven, an

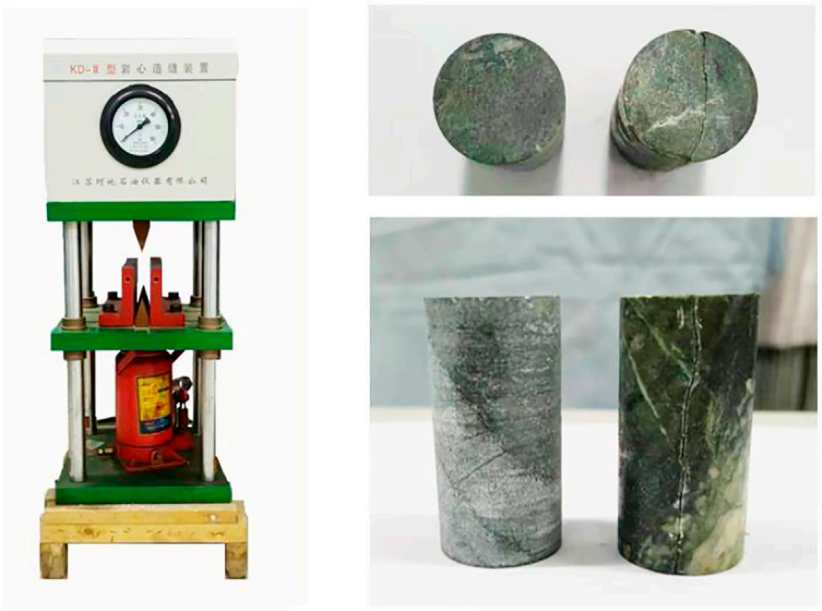

FIGURE 3 | Device for artificially creating fractures and cores before and after splitting.

intermediate container, a core holder, a hand pump, a condenser, and a data acquisition device (**Figure 2**). The constant speed and constant pressure pump is used to control the flow rate or injection pressure of the fluid. The blast oven, the core holder, and the hand pump are used to simulate temperature and pressure conditions in the actual EGS reservoir. The intermediate container is used to complete the transition between chemical stimulants and ultrapure water. The condenser is used for the collection of the residual liquid. The data acquisition device is used to record instantaneous flow information and pressure at the inlet and outlet ports.

Rock specimens used in the tests were cylindrical samples with 2.5 cm diameter and 5 cm length artificially fractured before the experiment. The device used to fracture the rock specimens is shown in **Figure 3**, along with cores before and after fracturing.

3.1.3 Experimental Schemes

NaOH and mud acid (HCl + HF) were selected as reference stimulants, and their relative concentration was set according to relevant literature (Na et al., 2017; Guo et al., 2020). In order to avoid excessive secondary precipitation in the reaction systems when alkaline chemical stimulants are used, two stable and efficient chelators, ATMP and PESA, were added in schemes D1 and D2, respectively, to chelate the metal ions produced by chemical stimulation and inhibit secondary precipitation. In scheme D3, HCl mainly plays the role of maintaining low pH. No chelating agent was added in this scheme because metal ion chelating agents are not effective under low pH conditions (**Table 3**).

Ultrapure water was used in the pre-flush and post-flush stages and main flush of the blank control experiment. The duration of the core flow experiment is 3 h in which the pre-flush stage and post-flush stage last 0.5 h as the main flush stage lasts 2 h. To make the reaction conditions closer to the actual formation, the temperature is set at 150°C, the confining pressure is set at 10 MPa, and the injection flow rate is set at 2 ml/min.

The artificially fractured cores were wrapped by a rubber sleeve resistant to high temperature and acid–base corrosion and transferred into the core holder. Ultrapure water was injected at a constant speed as soon as the temperature inside the oven and the pressure were stabilized at 150°C and 10 MPa, respectively. The valves of the intermediate container were rotated at 0.5 and 2.5 h to complete the transition between ultrapure water and the stimulant. The instantaneous data of inlet and outlet port pressure and liquid outflow were collected in the whole process of the experiment, and the discharged liquid was collected at 0.5, 1, 1.5, 2, 2.5, and 3 h, and each sampling lasts for 0.5 h.

3.2 Static Corrosion Experiment

3.2.1 Experimental Purpose and Principle

Chemical stimulants are expected to stay longer within the fractures under field conditions compared to laboratory conditions. Chemical agents remaining in the fractures likely continue to react with reservoir rocks, possibly causing additional precipitation/dissolution processes that might negatively affect reservoir reconstruction. On this premise, a number of static dissolution experiments were performed under the same P,T conditions of the dynamic experiment to explore geochemical reactivity over longer timescales.

3.2.2 Experimental Equipment and Samples

Static experiments were carried out with a high-temperature, high-pressure reactor (ML-0.3). As shown in **Figure 4**, the overall structure of the instrument can be divided into three parts:

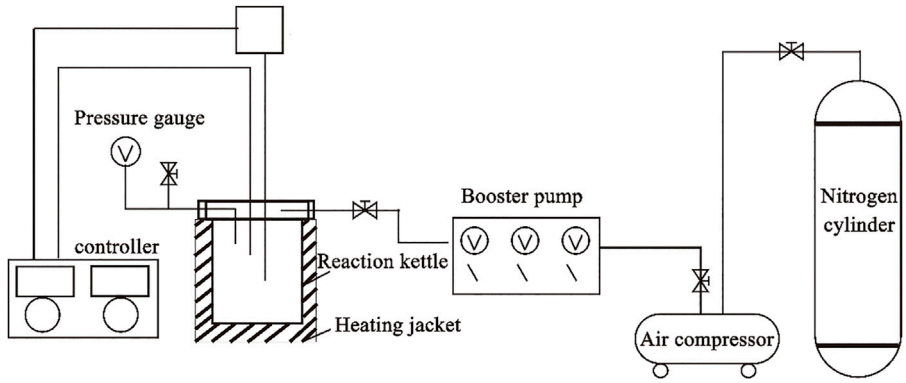

FIGURE 4 | Structural diagram of the high-temperature and high-pressure reactor.

TABLE 1 | Scheme of the dynamic simulation experiment.

Scheme number	Pre-flush (0.5 h)	Main flush (2 h)	Post-flush (0.5 h)
Blank scheme	Ultrapure water	Ultrapure water	Ultrapure water
D1	Ultrapure water	10wt% NaOH+3wt% ATMP	Ultrapure water
D2	Ultrapure water	10wt% NaOH+1wt% PESA	Ultrapure water
D3	Ultrapure water	10wt% HCl+1.5wt% HF	Ultrapure water

TABLE 2 | Schemes of the high-temperature and high-pressure static corrosion experiment.

Scheme number	Formula of the stimulant	Mass ratio (stimulant to rock powder)	Sampling time point (h)
S1	10wt% NaOH + 3wt% ATMP	10:1	1, 2, 4, 6, 12
S2	10wt% NaOH + 1wt% PESA	10:1	1, 2, 4, 6, 12
S3	10wt% HCl + 1.5wt% HF	10:1	1, 2, 4, 6, 12

heating device, pressurization system, and reactor body. The heating device comprises a heating sleeve and a controller. The pressurization system consists of a booster pump, an air compressor, and a nitrogen cylinder. The main body of the reactor is Hastelloy, which has strong corrosion resistance. The standard capacity of the reactor is 500 ml, and the maximum working temperature and pressure are 400°C and 12 MPa, respectively. Granite samples were pulverized and sieved (100–200 mesh), and the rock powder was sub-packed.

3.2.3 Experimental Schemes

For the sake of consistency, the same T,P conditions of the dynamic experiment (150°C and 10 MPa) were applied. To ensure that the content of the chemical stimulant was enough to maintain full contact between the sample and the stimulant over relatively long times, the chemical stimulant and the prepared rock powder were mixed in the mass ratio 10:1. During the experiment, the autoclave was opened for sampling after 1, 2, 4, 6, and 12 h reaction time, and the contents of K+, Na+, Mg2+, Al3+, and soluble silicon in the residual acid/alkaline were analyzed. The amounts of dissolved/precipitated minerals, along with the variations in the chemical composition of the reaction residue, were measured after washing, filtering, and drying. XRD mineral composition analysis and scanning electron microscope test of the rock powder residue after the reaction were carried out according to the experimental scheme of **Table 2**.

4 RESULTS AND DISCUSSION

4.1 Dynamic Effect of Chemical Stimulants on Permeability of Cores

Time variations of the equivalent permeability of the cores are shown in **Figure 5** for different experimental setups, during the dynamic experiment. The main features of the dynamic experiment are listed below.

During the whole process of injection of ultrapure water, the equivalent permeability of the core gradually decreased and finally approached a plateau, suggesting that ultrapure water had no effect on improving core permeability.

In addition, the NaOH-dominated alkaline chemical stimulants had minimal impact on the permeability of the specimen. Under both D1 and D2 conditions, the permeability was not sensitively modified during the early and late stages of the main flush, and just some abrupt changes were observed during the intermediate stage, after about 1 h. Though some larger

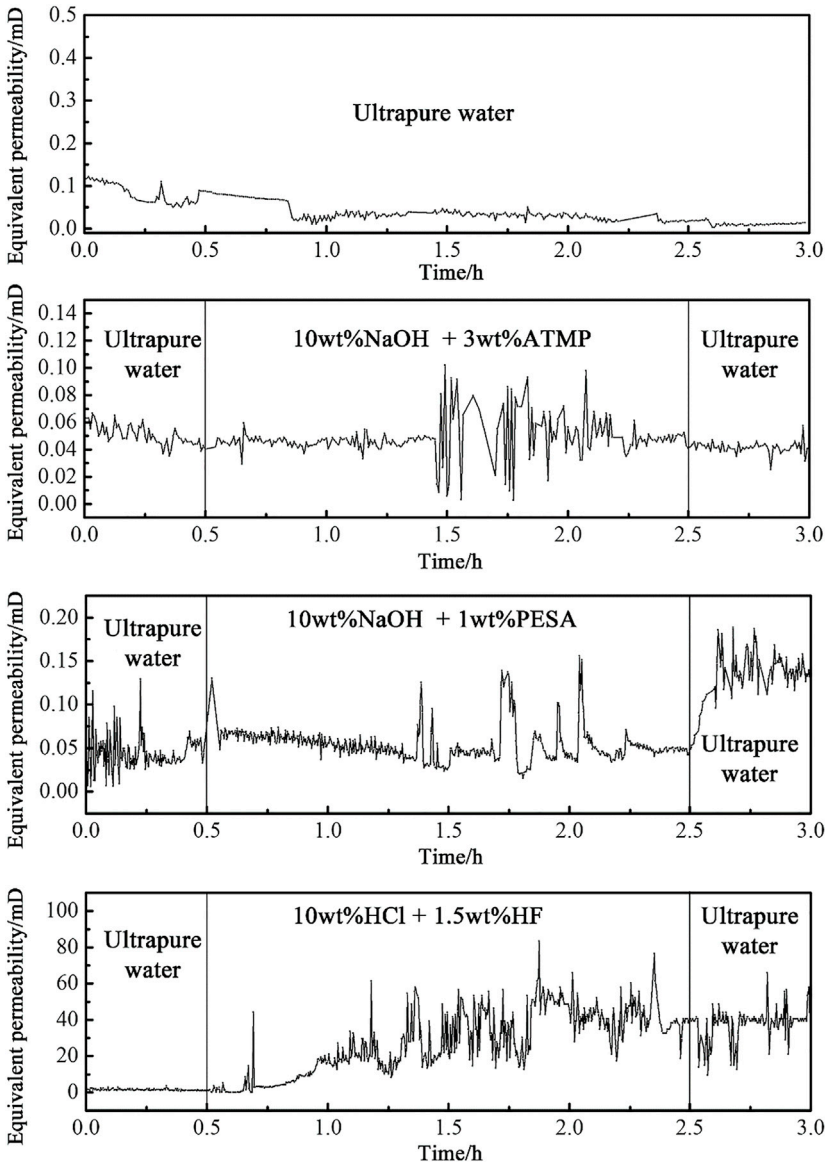

FIGURE 5 | Change of equivalent permeability of the cores with time.

increase in permeability was observed under D2 conditions, this result was interpreted as an evidence for the occurrence of similar reaction mechanisms under the two stimulation schemes.

The use of the alkaline 10wt% NaOH + 3wt% ATMP agent, after the completion of the flushing with ultrapure water, caused the permeability to slightly decrease below the average value of the pre-flush stage. The injection of the 10wt% NaOH + 1wt% PESA stimulant led to an increase of the equivalent permeability up to a plateau at about 2.83 times the initial value. Compared with 10wt% NaOH + 3wt% ATMP, 10wt% NaOH + 1wt% PESA played a positive role in improving equivalent permeability, but the effect was still not obvious. In this scheme, the improvement of equivalent permeability mainly occurred in the post-flush stage, and there was no stable and continuous increase during the main flush. Based on these evidences, we conclude that the 10wt% NaOH + 1wt% PESA system did not cause effective mineral corrosion in the fracture. The increase of equivalent permeability in the post-flush stage was due to the change of injected fluid viscosity and the scouring of ultrapure water on the secondary precipitated particles produced in the main flush stage.

Conversely, the application of the 10wt% HCl + 1.5wt% HF system led to a more significant and rapid impact on core equivalent permeability, compared to the alkaline system. In this scheme, the time pattern of the equivalent permeability was characterized by a steady increase after 0.4 h of the main flush stage, with significant fluctuations before and after 1 h reaction time, and with steady, high-permeability values after 1.6 h. During the post-flush stage, the equivalent permeability quickly recovered the level at the end of the main flush stage, before stabilizing at about 39.41mD, that is, more than 27 times the initial equivalent

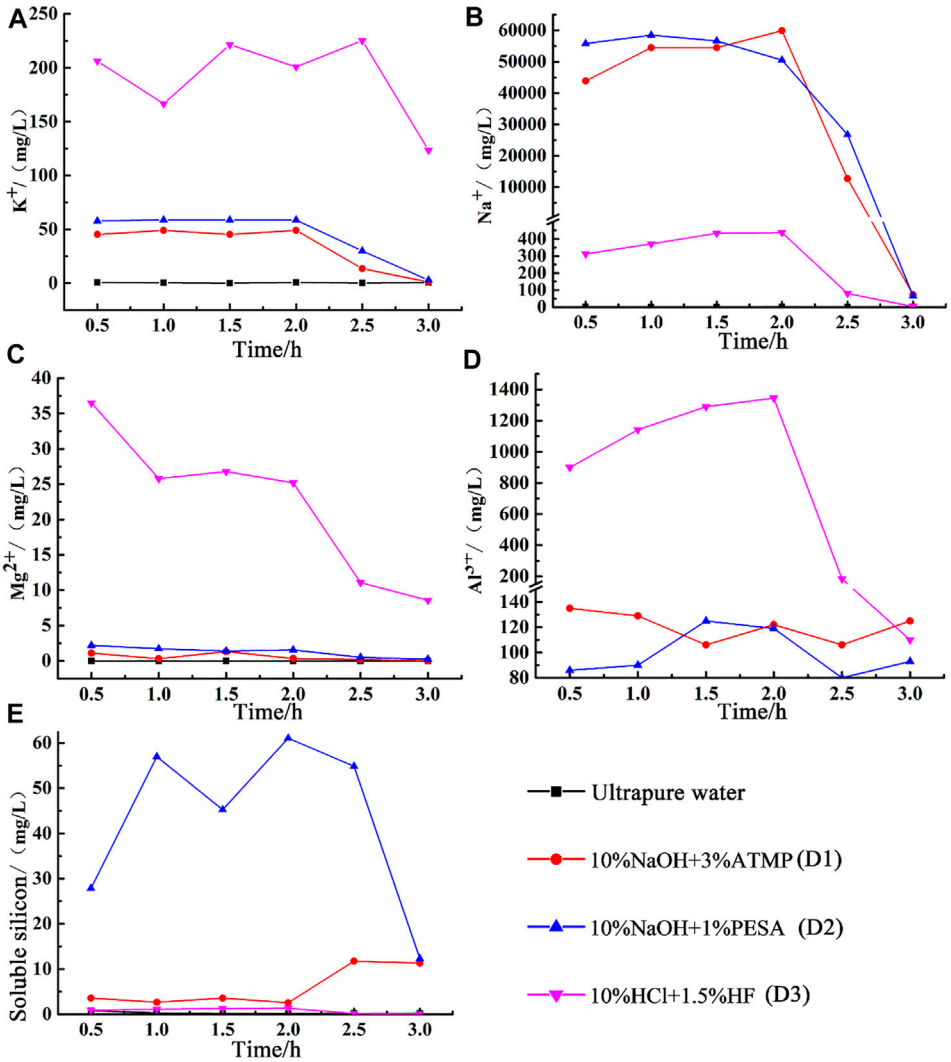

FIGURE 6 | Changes of chemical composition of the dynamic experiment. **(A)** Concentration of K^+; **(B)** concentration of Na^+; **(C)** concentration of Mg^{2+}; **(D)** concentration of Al^{3+}; **(E)** concentration of soluble silicon.

value. The effectiveness of the treatment based on the 10wt% HCl + 1.5wt% HF system was partially ascribed to the small scale of this laboratory experiment, in the sense that the limited length of the core (5 cm) allowed for a complete penetration of the stimulant throughout the specimen. For the same reason, also the particles produced in the early stage of main flush were likely removed by the injected fluid and likely discharged out of the fractured specimen along with the residual acid.

4.2 Reaction Mechanism Analysis of Chemical Stimulation

4.2.1 Changes of Chemical Components of Residual Stimulants

The chemical composition of residual stimulants under dynamic conditions is shown in **Figure 6**. During the injection of ultrapure water, the concentration of the main chemical components in the residual liquid remained close to zero because ultrapure water did not boost any dissolution process. Under this configuration, the observed decline in permeability was, thus, ascribed to the gradual increase in fracture tightness, driven by the high value of the confining pressure (10 MPa).

Very similar Na^+, K^+, Mg^{2+}, and Al^{3+} concentrations patterns were observed in the residual solution when either the 10wt% NaOH + 3wt% ATMP or the 10wt% NaOH + 1wt% PESA systems were used for chemical stimulation. No significant fluctuation in the dissolution rate was observed during the stimulation process, as testified by the invariably low Mg^{2+} concentration (2.2 mg/L and 1.3 mg/L).

Since the increase in Na^+ and K^+ concentration can be ascribed with reasonable confidence to plagioclase and potassium feldspar dissolution processes in our experimental setup and the increase in Mg^{2+} concentration to chlorite dissolution, we claimed that NaOH-dominated alkaline chemical stimulants had the potential

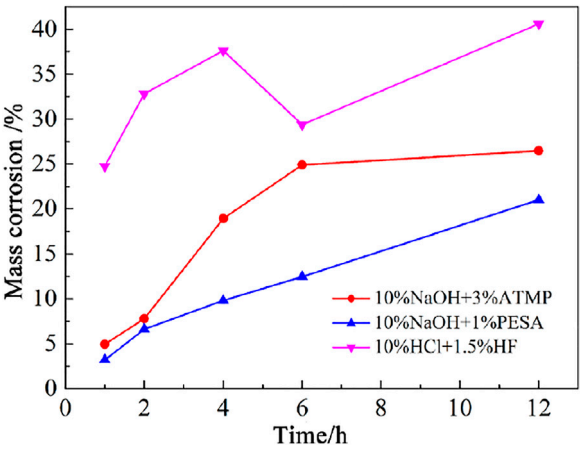

FIGURE 7 | Change of the mass corrosion rate of rock powder.

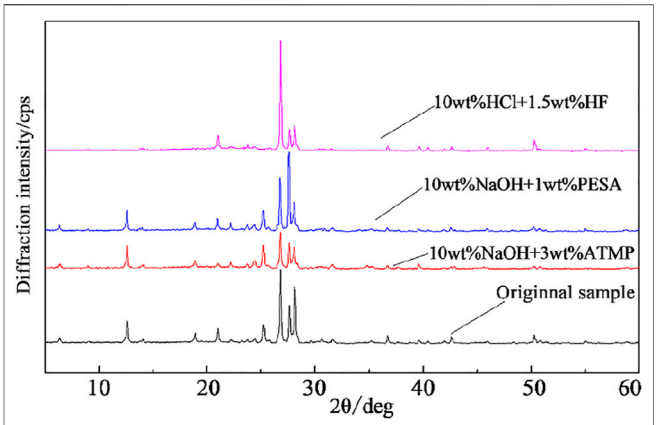

FIGURE 8 | XRD diffraction curves of residual samples after reaction for 12 h.

to slowly dissolve plagioclase and albite, while it had virtually no impact on chlorite stability. From the perspective of the chemical composition of the residual stimulants, the two stimulation schemes manly differed in terms of soluble silicon concentration (**Figure 6E**), a parameter which mirrored differences in quartz dissolution efficiency (see large fluctuation in cores permeability in the late stage of the main flush; **Figure 5**).

Similar and relatively high Na^+, K^+, and Al^{3+} concentrations were observed in the reaction residue after treatment with both NaOH-dominated alkaline and the 10wt% HCl + 1.5wt% HF acid solutions. Na^+ concentration increased gradually in the whole main flush stage, and the concentration of K^+ fluctuated between 174.2 and 227.5 mg/L, reflecting the capacity of these stimulants to induce substantial dissolution of feldspar and plagioclase. Mg^{2+} concentration increased up to about 36.5 mg/L at the beginning of the main stage and then gradually decreased with the progress of the experiment.

Based on differences in Mg^{2+} concentration, we noticed that under dynamic conditions, the 10wt% HCl + 1.5wt% HF configuration showed the best performance in terms of chlorite dissolution efficiency, in agreement with the recognized acid-sensitive behavior of chlorite (e.g., Tang et al., 2007; Kamal et al., 2019). The unexpected low Mg^{2+} concentration produced during this experiment was then interpreted as an effect of the low initial content of chlorite in the processed specimen.

With an average of only about 0.8 mg/L, the soluble silicon concentration did not increase significantly, reflecting the scarce reactivity of quartz with respect to low-concentration mud acids. Similar conclusions have been drawn in other studies based on evidences from scanning electron microscope analysis (Guo et al., 2020).

Overall, we noted that the 10wt% HCl + 1.5wt% HF configuration preferentially affect, reducing it, feldspar and chlorite concentration, leaving almost intact the primary quartz fraction. The initial increase in permeability noticed during the early stage of the main flush was then attributed to the availability of fresh, reactive surface area of primary feldspar and chlorite. As soon as the interaction progressed, this area progressively reduced, and the equivalent permeability first started to oscillate and then gradually stabilized in the post-flush stage.

4.2.2 Results of Prolonged Static Corrosion experiment

4.2.2.1 Sample Corrosion

The time variation of the dissolution rate of the rock samples under static conditions is shown in **Figure 7**. A gradual increase in the dissolution rate was observed when granite specimens were allowed to react with both 10wt% NaOH + 3wt% ATMP and 10wt % NaOH + 1wt% PESA agents, with the only relevant difference between the two experimental setups that under 10wt% NaOH + 3wt% ATMP conditions, some flattening of this trend was noticed after 4 h reaction time. Under 10wt% NaOH + 1wt% PESA conditions, dissolution patterns flattened after 2 h. It emerged that PESA was an effective chelating agent when associated with alkaline chemical stimulants.

Different from the results of the dynamic stimulation experiment, under static conditions, the 10wt% NaOH + 3wt% ATMP agent turned out to be very effective in driving the dissolution of primary minerals. This behavior was tentatively explained in terms of the dependency of the performance of NaOH-dominated alkaline stimulants on the hydrodynamic conditions of the fracture (Guo et al., 2020). In particular, it has been observed that the occurrence of an irregular flow of the stimulant may led to the accumulation of small mineral particles within the fracture, resulting in a decline of the equivalent permeability of the core. The application of the 10wt% NaOH + 1wt% PESA agent was then associated with a lesser accumulation of particles in the fracture that finally resulted in a more efficient reservoir reconstruction, compared to the 10wt% NaOH + 3wt% ATMP case.

The 10wt% HCl + 1.5wt% HF acid system efficiently performed (i.e., better than alkaline stimulants) during the first stage of the reaction path, up to a maximum dissolution rate of

TABLE 3 | XRD results after reaction for 12 h (%).

Scheme number	Quartz	K-Feldspar	Plagioclase	Chlorite	Biotite	Amorphous state
Original sample	20	30	33	15	2	—
S1	13	22	15	15	2	33
S2	15	51	17	15	2	—
S3	40	23	16	—	2	19

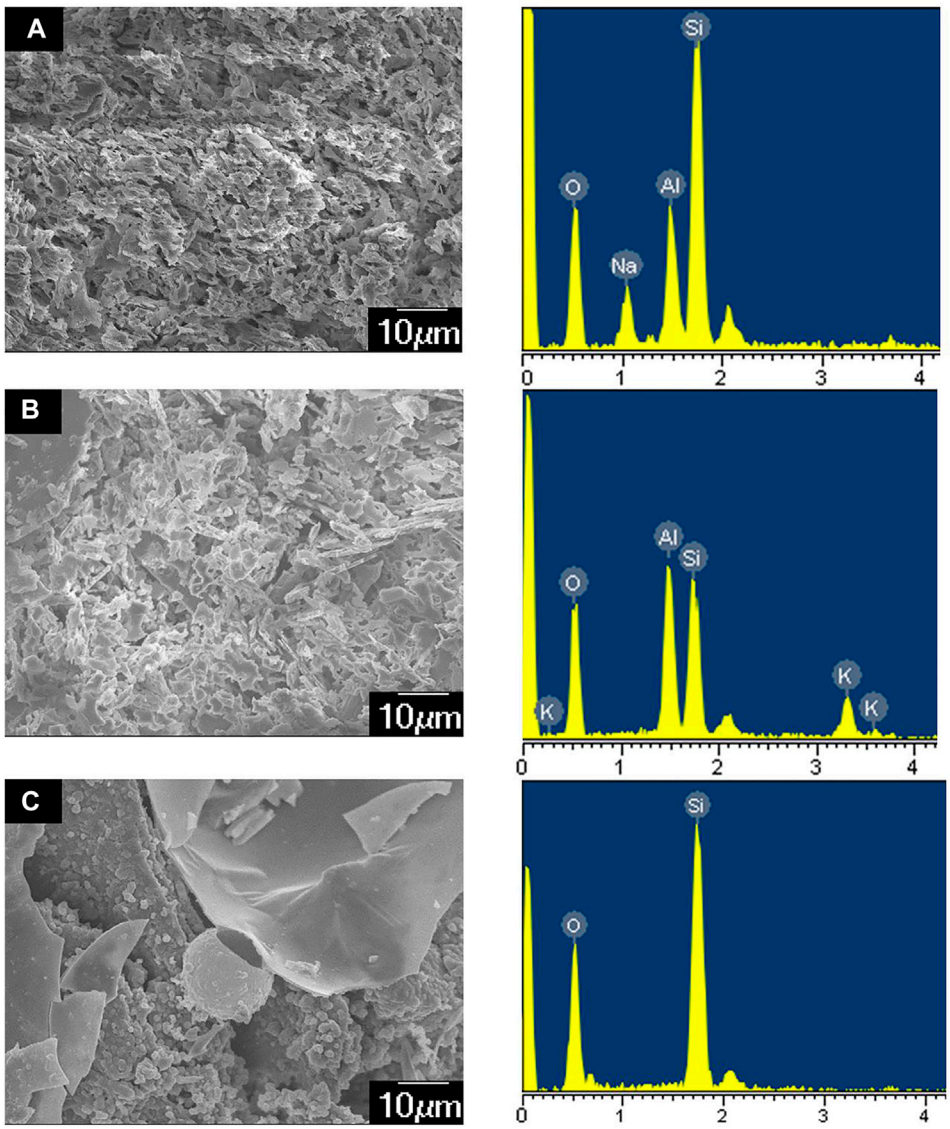

FIGURE 9 | SEM images of secondary precipitation. **(A)** Secondary plagioclase; **(B)** secondary potassium feldspar; **(C)** amorphous silica.

37.6% after 4 h interaction. Then, a minimum value of 29.4% was estimated after 6 h. A relatively large amount of secondary precipitates was observed during this time interval. According to XRD results (**Figure 8** and **Table 3**) and scanning electron microscope tests (**Figure 9**), during this stage, the main newly formed solids were quartz and amorphous silica. The mass dissolution rate of primary minerals increased again during the 6–12 h time span, up to the maximum value of 40.6% after 12 h of reaction. These features indicated that the dissolution effect driven by the stimulant overwhelmed the

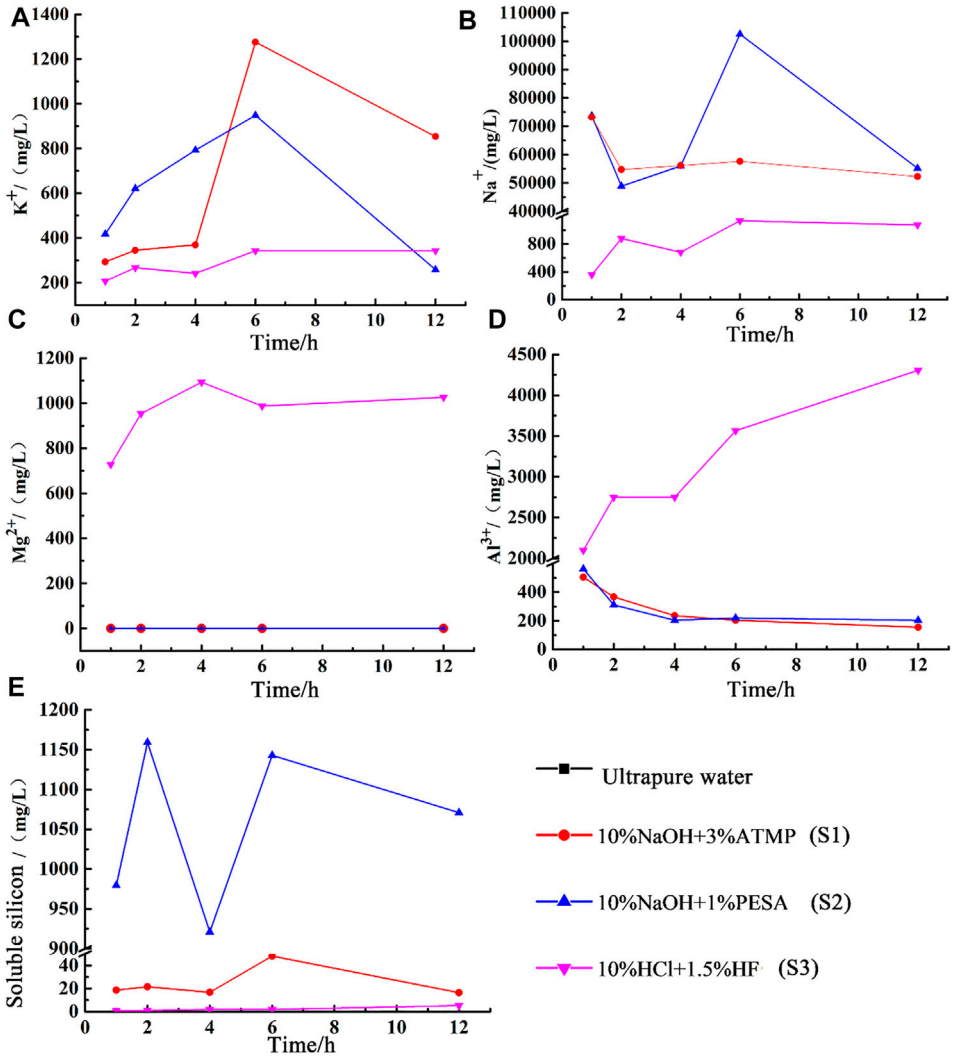

FIGURE 10 | Changes of chemical composition of the static experiment. **(A)** Concentration of K^+; **(B)** concentration of Na^+; **(C)** concentration of Mg^{2+}; **(D)** concentration of Al^{3+}; **(E)** concentration of Soluble silicon.

counter effect of the formation of secondary mineral/amorphous phases, testifying about the effectiveness of this formula.

4.2.2.2 Chemical Composition of Residual Stimulants

The chemical composition of residual stimulants under static conditions is shown in **Figure 10**. K^+ concentration increased during the first 2-h reaction when 10wt% NaOH + 3wt% ATMP and 10wt% NaOH + 1wt% PESA configurations were used, while Na^+ and Al^{3+} concentrations showed a minor decrease, indicating the possible formation of secondary plagioclase. The concentration of Na^+ and K^+ in the 10wt% NaOH + 3wt% ATMP residue increased significantly during the 2–6h interval, while the Na^+ and K^+ concentration increased slightly in the 10wt% NaOH + 1wt % PESA residue. After 12h, Na^+, K^+, and Al^{3+} concentrations decreased significantly in the 10wt% NaOH + 1wt% PESA case. Combined with XRD and SEM results (**Figure 10A**), these evidences were interpreted as an indication for K-feldspar and plagioclase precipitation. Conversely, during the same period, negligible feldspar dissolution/precipitation was observed under the 10wt% NaOH + 3wt% ATMP configuration.

XRD results and chemical patterns of **Figure 10C** indicated that the very low Mg^{2+} residual concentration associated with the interaction with alkaline agents likely mirrored the very low reactivity of chlorite under these experimental conditions.

Silicon emerged as a key parameter to trace variable quartz dissolution rates under alkaline conditions. As shown in **Figure 10E**, the soluble silicon concentration in the 10wt% NaOH + 1wt% PESA reaction residue was set up to 921–1143 mg/l, whereas it did not exceed 16.5–48.1 mg/l under 10wt% NaOH + 3wt% ATMP conditions.

When 10wt% HCl + 1.5wt% HF was used as the stimulant, the concentrations of K^+, Na^+, and Mg^{2+} showed an overall upward trend in the first 6 h of the reaction, with Na^+ being the only element decreasing over the 2–4 h interval. It is noteworthy that

the sample dissolution rate increased by 4.8% during this period. Combined with the change in Mg^{2+} concentration and with XRD results, chlorite dissolution was identified as the most relevant mineralogical transformation associated with this stage. The concentration of K^+ decreased significantly over the 6–12 h interval. It is speculated that a certain amount of K-feldspar precipitation was produced during this period. While K^+ concentration fluctuates greatly (**Figures 10A,B**), Na^+ concentration did not change significantly after 2 h, suggesting a relatively fast stabilization of albite.

Figure 10C shows that chlorite effectively dissolved upon reaction with 10wt% HCl + 1.5wt% HF, but the dissolution rate decreased gradually over time due to the decrease of chlorite content and the increase of ion concentration in the residual solution. The direct relationship between the progressively reduced amount of primary chlorite and the decrease of its dissolution rate was related to the fact that the overall dissolution rate of each mineral is directly proportional to its total reactive surface area, which in turns linearly depends on the total amount of the mineral and on its specific reactive area (e.g., Lasaga, 1984). As a result, the dissolution effect of the stimulant gradually weakens during the advancement of the reaction. **Figure 10E** indicates that despite a steady tendency to increase over time, silicon concentration remained at low concentration values (5.3 mg/l at 12 h) after interaction with 10wt% HCl + 1.5wt% HF. This chemical stimulant had a very limited dissolution capacity on quartz, consistent with experimental evidences from the literature (Luo et al., 2018).

To sum up, NaOH-dominated alkaline stimulants had the potential to slightly dissolve feldspar and quartz in the fractures, but they were not able to dissolve chlorite. The main difference in the performance of the two alkaline configurations can be recast in terms of a different impact on quartz concentration and formation of secondary minerals. The 10wt% HCl + 1.5wt% HF acid system is more effective in dissolving primary feldspar and chlorite, but this mechanism has the side effect of inducing the precipitation of significant amounts of secondary quartz.

4 CONCLUSION

Laboratory experiments were conducted on cylindrical granite samples from Baimiao formation to characterize its coupled hydraulic and geochemical response to chemical stimulation with different agents. The emphasis was on the static and dynamic behavior of the granite under T,P conditions (150°C, 10 MPa) relevant for the possible development of an EGS in the Matouying uplift area (Hebei Province, China). The main conclusions are as follows.

1) Acid stimulants based on HF and HCl performed better than NaOH-based alkaline agents to enhance the permeability of Baimiao granite cores. In particular, the 10wt% HCl + 1.5wt% HF configuration led to a maximum permeability increase of more than 27 times and the 10wt% NaOH + 1wt% PESA configuration to an increase of about 2.8 times, while the 10wt % NaOH + 3wt% ATMP agent did not show any impact on core permeability.
2) NaOH-dominated alkaline stimulants led to only minor feldspar and quartz dissolution. These agents induced the formation of secondary plagioclase but did not induce any chlorite dissolution. Alkaline chemical stimulants coupled with different chelating agents had variable impacts on quartz dissolution and precipitation of secondary phases. PESA emerged as the best-performing chelating agent to be coupled with NaOH-based alkaline stimulants.
3) The 10wt% HCl + 1.5wt% HF acid system showed significant potential to dissolve primary feldspar and chlorite of the Baimiao granite. Under laboratory conditions, this process was accompanied by relatively large amounts of newly formed amorphous silica, which were unaccompanied by an equivalent dissolution of primary quartz. This chemical agent proved to be effective in reconstructing the target rock, and under field conditions, its penetration performance can be likely optimized through the combined use of corrosion inhibitors and other components that might enhance its inhibition speed.

Overall, the laboratory experiments of this study set the baseline for the assessment of the field performance of a possible chemical stimulation program in a granite-hosted EGS reservoir. However, due to scale effects and the inherent complex distribution of fractures under field conditions, these results should be considered a preliminary support reference frame. Site-scale numerical simulations and field tests need to be carried out in the follow-up research to complement the current experimental approach.

DATA AVAILABILITY STATEMENT

The original contributions presented in the study are included in the article/Supplementary Material, further inquiries can be directed to the corresponding author.

AUTHOR CONTRIBUTIONS

SS and XQ completed the collection of regional data and the collection and preparation of the samples; BF and GF provided the overall idea and schemes; SH and JX completed part of the experiment; and ZC completed part of the experiment and finished this manuscript.

FUNDING

This work was jointly supported by the National Key R&D Program of China (No. 2018YFB1501802), Key Department Construction Project of Hebei Bureau of Coal Geological Exploration (No.205A4101H), Single Well Heat Extraction and Surface Comprehensive Heat Utilization Technology of HDR (No.19274102D), and College of New Energy and Environment

of the Jilin University and the Institute of Geosciences and Earth Resources (IGG) of the National Council of Italy (CNR) partnered in the Frame of the MOD-GRE (MODelling Conventional and Unconventional Geothermal Resources in Italy and China) Collaborative Project, Jilin Province Science and Technology Development Project (Grant No. 20200403147SF).

REFERENCES

Alegria, P., Catalan, L., Araiz, M., Rodriguez, A., and Astrain, D. (2022). Experimental Development of a Novel Thermoelectric Generator without Moving Parts to Harness Shallow Hot Dry Rock Fields. *Appl. Therm. Eng.* 200, 117619. doi:10.1016/j.applthermaleng.2021.117619

Davies, D. R., Faber, R., Nitters, G., and Ruessink, B. H. (1994). A Novel Procedure to Increase Well Response to Matrix Acidising Treatments. *SPE Adv. Technol. Ser.* 2 (1), 5–14.

Economides, M. J., and Nolte, K. G. (1989). *Reservoir Stimulation*. 2nd ed. Upper Saddle River, NY, USA: Prenitce Hall, 440.

Evanoff, J., Yeager, V., and Spielamn, P. (1997). Stimulation and Damage Removal of Calcium Carbonate Scaling in Geothermal Wells: A Case Study. *Energ. Sourc.* 19 (1), 2481–2485.

Feng, B., Xu, J., Xu, T., Li, S., Song, D., and Chen, M. (2019). Application and Recent Progress of Chemical Stimulation on Hot Dry Rock Reservoir Modification. *J. Earth Sci. Environ.* 41 (5), 577–591. doi:10.3969/j.issn.1672-6561.2019.05.006

Guo, Q., He, T., Zhuang, Y., Luo, J., and Zhang, C. (2020). Expansion of Fracture Network in Granites via Chemical Stimulation: A Laboratory Study. *Earth Sci. Front.* 27 (1), 159–168. doi:10.13745/j.esf.sf.2019.12.2

Kamal, M. S., Mahmoud, M., Hanfi, M., Elkatatny, S., and Hussein, I. (2019). Clay Minerals Damage Quantification in sandstone Rocks Using Core Flooding and NMR. *J. Petrol. Explor Prod. Technol.* 9 (1), 593–603. doi:10.1007/s13202-018-0507-7

Lasaga, A. (1984). Chemical Kinetics of Water-Rock Interactions. *J. Geophys. Res.* 89, 4009–4025. doi:10.1029/JB089iB06p04009

Liao, Z., Zhang, Y., Chen, W., Peng, Z., and Xiong, X. (2006). Available Persist Exploitation and Utilization of Geothermal Resourses. *China Mining Mag.* 15 (10), 8–11. doi:10.3969/j.issn.1004-4051.2006.10.003

Liu, M., Zhuang, Y., Zhou, C., Zhu, M., Zhang, C., Zhu, Y., et al. (2016). Application of Chemical Stimulation Technology in Enhanced Geothemal System: Theory, Practice and Expectation. *J. Earth Sci. Environ.* 38 (2), 267–276. doi:10.3969/j.issn.1672-6561.2016.02.014

Luo, J., Zhu, Y., Guo, Q., Tan, L., Zhuang, Y., Liu, M., et al. (2018). Chemical Stimulation on the Hydraulic Properties of Artificially Fractured Granite for Enhanced Geothermal System. *Energy* 142, 754–764. doi:10.1016/j.energy.2017.10.086

Na, J., Xu, T., Wu, Y., Feng, B., and Bao, X. (2017). Effectiveness of Using Mud Acid as Stimulation Agent for Enhanced Geothermal Systems (EGS) Reservoir. *J. Cent. South Univ. (Science Technology)* 48 (1), 247–254. doi:10.11817/j.issn.1672-7207.2017.01.033

Na, J., Feng, B., Lan, C., Xu, T., and Bao, X. (2014). Effectiveness of Using Supercritical CO2 as Stimulation Agent for Enhanced Geothermal Systems. *J. Cent. South Univ. Technol.* 45, 2447–2458.

Olasolo, P., Juárez, M. C., Morales, M. P., D´Amico, S., and Liarte, I. A. (2016). Enhanced Geothermal Systems (EGS): A Review. *Renew. Sustain. Energ. Rev.* 56, 133–144. doi:10.1016/j.rser.2015.11.031

Perthuis, H., Touboul, E., and Plot, B. (1989). "Acid Reactions and Damage Removal in Sandstones: A Model for Selecting the Acid Formulation," in SPE International Symposiumon Oilfield Chemistry, Houston, Texas, February 8–10, 1989 (Houston: Society of Petroleum Engineers). doi:10.2118/18469-ms

Portier, S., and Vuataz, F. D. (2010). Developing the Ability to Model Acid-Rock Interactions and Mineral Dissolution during the RMA Stimulation TEST Performed at the Soultz-Sous-Forêts EGS Site, France. *Comptes Rendus Geosci.* 342 (7/8), 668–675. doi:10.1016/j.crte.2010.04.002

Portier, S., Vuataz, F.-D., Nami, P., Sanjuan, B., and Gérard, A. (2009). Chemical Stimulation Techniques for Geothermal Wells: Experiments on the Three-Well EGS System at Soultz-Sous-Forêts, France. *Geothermics* 38, 349–359. doi:10.1016/j.geothermics.2009.07.001

Qi, X., Zhang, G., Shangguan, S., Su, Y., Tian, L., Li, X., et al. (2018). A Brief Analysis of Hot and Dry Rock Geothermal Resource Hosting and Distribution in Hebei Province. *Coal Geology. China* 30 (11), 47–73. doi:10.3969/j.issn.1674-1803.2018.11.11

Qi, X., Shangguan, S., Zhang, G., Pan, M., Su, Y., Tian, L., et al. (2020). Site Selection and Developmental Prospect of a Hot Dry Rock Resource Project in the Matouying Uplift,Hebei Province. *Front. Earth Sci.* 27, 94–102. doi:10.13745/j.esf.2020.1.11

Sarda, J. P. (1977). "Chemical Leaching," in The 2nd NATA-CCMS Information Meeting on Hot Dry Rock Geothermal Entergy, Los Alamos, NM, United States, June 28–30, 1977 (Los Alamos: Institute of Geophysics ETH Zurich).

Schechter, R. S. (1992). *Oil Well Stimulation*. Englewood Cliffs, NJ, USA: Prentice-Hall, 640.

Shangguan, S. (2017). Occurrence Conditions of Hot-Dry-Rock Geothermal Resources and Development Prospects in Matouying Area. *China Energ. Environ. Prot.* 39 (5), 155–165. doi:10.19389/j.cnki.1003-0506.2017.05.032

Smith, C. F., and Hendrickson, A. R. (1965). Hydrofluoric Acid Stimulation of sandstone Reservoirs. *J. Pet. Technol.* 17, 215–222. doi:10.2118/980-pa

Tang, H., Zhao, F., Li, G., Wang, C., and Xie, X. (2007). Experimental Study on the Reaction of Chlorite with Mud and Fluoroboric Acids. *Oilfield Chem.* 24 (4), 307–309. doi:10.19346/j.cnki.1000-4092.2007.04.005

Wang, G., Liu, Y., Zhu, X., and Zhang, W. (2020). The Status and Development Trend of Geothermal Resources in China. *Earth Sci. Front.* 27 (01), 1–9.

Wang, J., Huang, S., Huang, G., and Wang, J. (1990). *Basic Characteristics of Geothermal Distribution in China*. Beijing: Seismological Press.

Wang, X., Wu, N., Su, Z., and Zeng, Y. (2012). Progress of the Enhanced Geothermal systems(EGS)development Technology. *Prog. Geophys.* 27 (1), 355–362. doi:10.6038/j.issn.1004-2903.2012.01.041

Xu, J. (2005). China's Geothermal Resources and its Sustainable Development and Utilization. *China Popul. Resour. Environ.* 15 (2), 139–141. doi:10.3969/j.issn.1002-2104.2005.02.032

Xu, T., Hu, Z., Li, S., Jiang, Z., Hou, Z., Li, F., et al. (2018). Enhanced Geothermal System: International Progress and Research Status of China. *Acta Geologica Sinica* 92 (09), 1936–1947. doi:10.3969/j.issn.0001-5717.2018.09.012

Yang, F. (2012). *Acidizing Sandstone Reservoirs Using HF and Organic Acids*. College Station, Texas: Texas A&M University.

Yue, G., Li, X., Gan, H., and Wang, G. (2020). A Study on the Reaction Kinetics of Regular Mud Acid and Granite. *Acta Geol. Sin.* 94, 2108–2114. doi:10.19762/j.cnki.dizhixuebao.2020214

Zhang, B., Li, Y., Gao, J., Wang, G., Li, J., Xing, Y., et al. (2020). Genesis and Indicative Significance of Hot Dry Rock in Matouying, Hebei Province. *Acta Geologica Sinica* 94 (7), 2036–2051. doi:10.3969/j.issn.0001-5717.2020.07.012

Conflict of Interest: The authors declare that the research was conducted in the absence of any commercial or financial relationships that could be construed as a potential conflict of interest.

Publisher's Note: All claims expressed in this article are solely those of the authors and do not necessarily represent those of their affiliated organizations, or those of the publisher, the editors and the reviewers. Any product that may be evaluated in this article, or claim that may be made by its manufacturer, is not guaranteed or endorsed by the publisher.

frontiers | Frontiers in Earth Science

ORIGINAL RESEARCH
published: 08 June 2022
doi: 10.3389/feart.2022.854232

Lithospheric Thermal Structure in Jinggangshan City: Implications for High Geothermal Background

Yuzhong Liao[1,2], *Yanguang Liu*[1,2]*, *Feng Liu*[1,2], *Shuaichao Wei*[1,2] *and Hexiao Duan*[1,2]

[1]Institute of Hydrogeology and Environmental Geology, Chinese Academy of Geological Sciences, Shijiazhuang, China, [2]Technology Innovation Center for Geothermal and Hot Dry Rock Exploration and Development Ministry of Natural Resources, Shijiazhuang, China

Jinggangshan City, which is located in the southwestern part of Jiangxi Province, is rich in hot springs. However, lack of geothermal studies has limited the exploration and utilization of the geothermal resources in this city. This study estimated the terrestrial heat flow in Jinggangshan City through well logging and analyses of rock thermal conductivity and heat production. Based on this and the surrounding geoscience transect and the Crust 1.0 model, this study constructed a one-dimensional lithospheric thermal structure by solving the steady-state heat conduction equation. Furthermore, the deep temperature distribution in Jinggangshan City was obtained to better understand the geodynamic condition of the geothermal resources in this city. The results show that the heat flow in this city is around 83.52 mW/m^2, indicating the high heat background for the formation of geothermal resources. According to the lithospheric thermal structure of Jinggangshan City, the mantle contributes more to the terrestrial heat flow ($q_m/q_c > 1$) than the crust. The temperature of the Mohorovicic discontinuity (the Moho) is 671.7°C, which is consistent with that below the Tanlu deep fault (620–690°C). Moreover, the calculated depth of the Curie surface (585°C) is 27 km, which is consistent with the Curie isotherm depth estimated from aeromagnetic data. This consistency verifies the validity of the lithospheric thermal structure of Jinggangshan City constructed in this study. In summary, the high heat background plays an important role in the formation of geothermal resources in Jinggangshan City.

Keywords: Jinggangshan City, geothermal gradient, heat flow, lithospheric thermal structure, moho temperature

OPEN ACCESS

Edited by:
Dawei Hu,
Institute of Rock and Soil Mechanics, (CAS), China

Reviewed by:
Xianchun Tang,
Chinese Academy of Geological Science, China
Funda Bilim,
Cumhuriyet University, Turkey

***Correspondence:**
Yanguang Liu
gaoyuanzhixing@163.com

Specialty section:
This article was submitted to Solid Earth Geophysics, a section of the journal Frontiers in Earth Science

Received: *13 January 2022*
Accepted: *13 April 2022*
Published: *08 June 2022*

Citation:
Liao Y, Liu Y, Liu F, Wei S and Duan H (2022) Lithospheric Thermal Structure in Jinggangshan City: Implications for High Geothermal Background. Front. Earth Sci. 10:854232. doi: 10.3389/feart.2022.854232

1 INTRODUCTION

Lithospheric thermal structure plays a significant role in the potential assessment and exploration of geothermal energy (Sclater et al., 1980; Davies and Davies, 2010; Liu et al., 2016; Li et al., 2017). It integrates information on crustal and mantle heat flow, ground temperature distribution, and thermal conductivity and heat productivity of rocks (Liu et al., 2017; Zhang et al., 2018). Terrestrial heat flow density (also referred to as heat flow) is a key parameter used to constrain the lithospheric thermal structure (Jaupart and Mareschal, 2015; Jiang et al., 2019; Prol-Ledesma and Moran-Zenteno, 2019). It is the heat flux per unit time per unit area flowing from the interior to the surface of the Earth (unit: mW/m^2 (Furlong and Chapman, 2013; Wang et al., 2015) and comprises crustal and mantle heat flow (Jaupart and Mareschal, 2015; Liu et al., 2021).

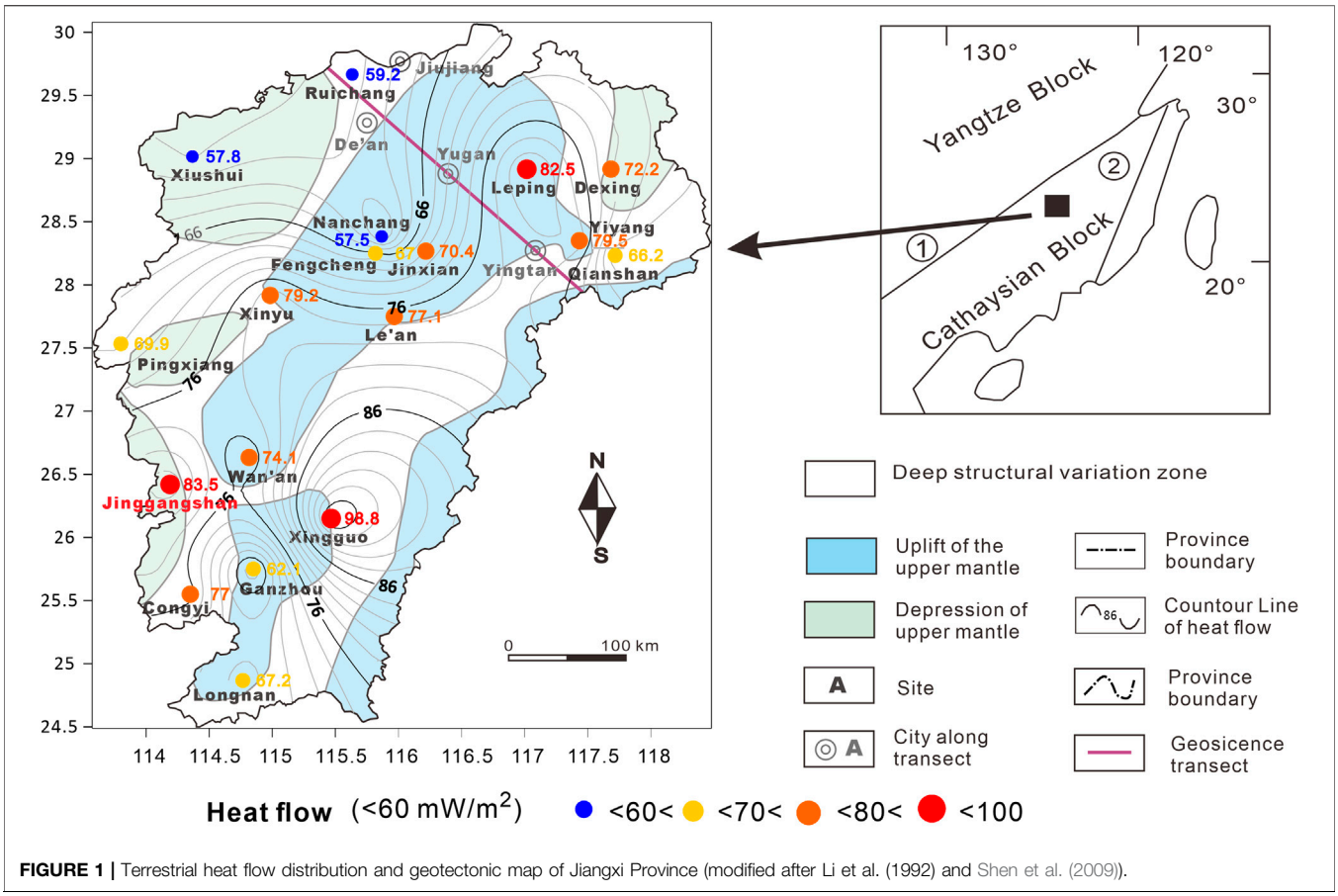

FIGURE 1 | Terrestrial heat flow distribution and geotectonic map of Jiangxi Province (modified after Li et al. (1992) and Shen et al. (2009)).

Jiangxi Province, which lies in the geothermal district of Southeast China, is rich in hot springs ((Zhu and Zhu, 1992). The geothermal resources in this province are predominantly controlled by faults and have middle–low temperatures (Xiao et al., 2018; Li, 2019). Since heat flow distribution is closely related to geological structures, previous heat flow values in Jiangxi Province were discussed based on the tectonic setting (Hu et al., 1992; Li et al., 1992; Jiang et al., 2019). For example, the heat flow in deep structural variation zones has a high average of 71.9 (n = 14) mW/m^2, whereas that in uplifts of the upper mantle has a similar average of 70.2 mW/m^2 but a relatively wide range of 56.4–98.8 mW/m^2, and that in depressions of the upper mantle (only that in Xiushui, northeastern Jiangxi Province has been measured) is 57.8 mW/m^2 (**Figure 1**). Therefore, deep structural variation zones have the highest heat flow background, with an average of 71.9 mW/m^2, which is higher than that of continental China (60.4 ± 12.3 mW/m^2 (Jiang et al., 2019)). On the other hand, the geothermal resources in Jiangxi Province, which mostly consists of uplifts and mountains, are predominantly controlled by the distribution of the NE–NNE-trending faults (Zhang, 2017; Li, 2019). The southeastern part of Jinggangshan City is intersected by the Huang'ao Fault—a deep NE-trending fault (**Figure 2**). Although Jinggangshan City in southwestern Jiangxi Province is located in the depression of the upper mantle, its location in an NE deep fault indicates high potential of high heat flow background (Li et al., 1992). Thus, the southeastern part of Jinggangshan City has great potential for the formation of geothermal resources (Zhu, 2007; Yang et al., 2018). Furthermore, Huang'ao Fault in Jinggangshan City belongs to Tanlu (Tancheng-Lujiang) deep fault (>3,000 km), extending NE along eastern China (Lin, 1992). The Tanlu fault, which experienced multistage deformation events since the Mesozoic, is inferred to be a channel for the percolation of melt and fluid and controls the lithosphere evolution in eastern China (Deng et al., 2013). As exhibited in **Figure 2**, massive Yanshanian granite (Mesozoic) is distributed along the Huangao fault in the southern part of Jinggangshan City (Fan et al., 2014). The study of the lithospheric thermal structure in Jinggangshan City, therefore, shed light on the heat flow anomaly led by Tanlu fault and its impact on the formation of geothermal resource.

This study focuses on Huang'ao and Qutan villages in the southeastern part of Jinggangshan City. The heat flow in the study area was acquired through well temperature logging and analyses of rock thermal properties and heat generation rates. Furthermore, by combining the geophysical studies of surrounding areas, the crustal thermal structure of Jinggangshan City was analyzed. The results provide insights into the genesis of the geothermal resources and have important implications for geothermal exploration in Jiangxi Province.

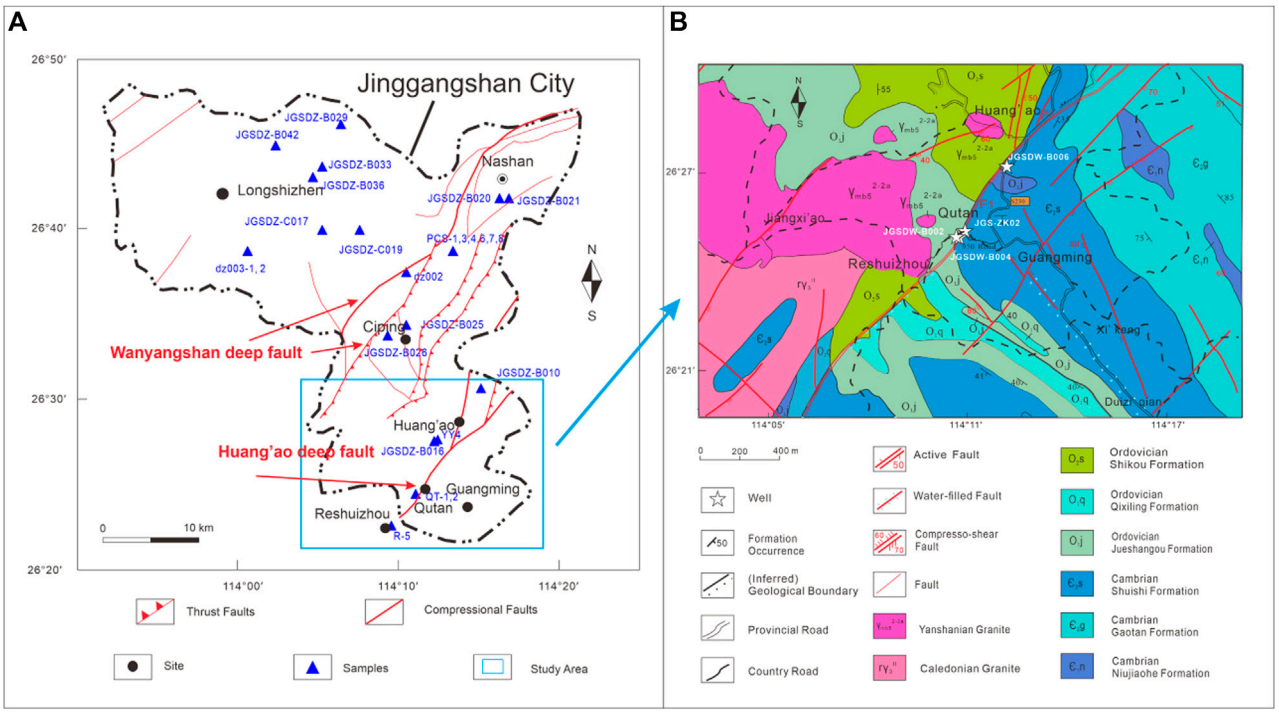

FIGURE 2 | Schematic geological map of Jinggangshan area and distribution of sampling locations.

2 GEOLOGICAL SETTING

Jinggangshan City is located in the middle part of the Caledonian South China orogenic belt bordering the Neoproterozoic Jiangnan Orogenic Belt (**Figure 1**; Shen et al. (2009)). As shown in **Figure 2**, Huang'ao and Qutan villages, which are situated in the southeastern part of Jinggangshan City, are intersected by the regional deep Huang'ao fault (Fan et al., 2014; Liu et al., 2018). The Huang'ao deep fault is an NE-trending (~45°C) compressional fault with a dip angle of 60°. Its width decreases from the southwest (Qutan village) to the northeast (Huang'ao village), as shown in **Figure 2**. Several types of alteration have extensively developed in this fault zone, including siliconization, schistosity, mylonitization, and brecciation. The Huang'ao deep fault is a geological boundary between the granites on its west side and the metamorphic rocks on its east side. The granites comprise Caledonian and Yanshanian granites (**Figure 1**). The Caledonian granites are grayish-white, medium-to-fine-grained equigranular biotite granites, containing quartz (~35 vo1%), plagioclase (~30 vol %), alkali feldspar (~25 vo1%), and biotite (~5 vol%). The Yanshanian granites are grayish-white, fine-grained, equigranular two-mica granites with a mineral composition similar to that of the Caledonian granites. The strata in the study area are dominated by Precambrian and Ordovician metamorphic rocks, which are subjected to strong folding (Zhu, 2007; Yang et al., 2018). The Precambrian strata mainly consist of the Niujiaohe (Є1n), Gaotan (Є2g), and Shuishi (Є3s) formations. The Niujiaohe formation comprises feldspar–quartz sandy slates, metamorphic sandstones, lamellate silicalites, and organic carbon-bearing phyllites. The Gaotan formation comprisesmedium-to-fine-grained sandy slates and carbonaceous phyllites. The Shuishi formation mostly comprises interbeds consisting of metamorphic feldspar–quartz slates and metamorphic sandstones, with some lenticular limestones at the top. Ordovician strata include the Jueshangou, Qixiling, and Shikou formations. The Jueshangou formation comprises metamorphosed (sandy-silt) slates, the Qixiling formation consists of sericite-slate and feldspar–quartz sandstones, and the Shikou formation includes metamorphic slates and sandstones.

3 METHODS

3.1 Measurement of the Terrestrial Heat Flow

Instead of direct measurement, the surface terrestrial heat flow was calculated by multiplying the geothermal gradient by the thermal conductivity of corresponding rocks (Jaupart and Mareschal, 2015; Wang et al., 2015).

3.1.1 Temperature Measurement of Well

The temperature of well JGS-ZK02 was measured using the well logging system (PSJ-2) equipped with a well temperature probe PS2512, which has a measurement range of 0–65°C and an accuracy of 0.1°C. The temperature was measured according to the Chinese industrial standard DZ/T0080-

2010 *Coal Geophysical Logging Specification*. To ensure that the well temperature was in a (quasi-) steady state, the well temperature was repeatedly logged at a time interval of 12 h after its deviation was less than 0.5°C following the completion of drilling.

The temperature measurement of wells in Qutan and Huang'ao villages was carried out using WD-016A-embedded sensors and TD-016C data acquisition instruments. The embedded sensors have a temperature measurement range of -50–100°C and an accuracy of 0.1°C at 0–80 and 0.5°C at 50–0°C and 81–125°C. These temperature sensors (diameter: 11 mm) were implanted into a PVC cable (diameter: 12 mm) at an interval of 5 m (distance 0–50 m) or 10 m (>50 m).

3.1.2 Thermal Conductivity

Thermal conductivity (unit: W/(mK)) is a measure of a given material's ability to transfer heat, representing the transferred heat per unit area at per unit time when the temperature gradient is 1°C per unit length (Wang et al., 2015). The thermal conductivities of the rock samples were measured using thermal conductivity scanning (TCS) in the East China University of Technology, with a measurement range of 0.2–25 W/(mK) and an accuracy of 3%.

Anand et al. (1973) suggested that thermal conductivity would increase with a decrease in temperature. The temperature at the burial depth of rocks before sampling was probably different from room temperature (25°C), at which the thermal conductivity was measured. Therefore, the measured thermal conductivity at room temperature should be corrected according to the *in situ* temperature.

Regarding exposed rocks or rocks buried at a relatively shallow depth that could be obtained by drilling, the measured temperatures should be corrected according to their *in situ* temperature using the following empirical formulas (Sass et al., 1992):

$$K(0) = K(25)\left(1.007 + 25\left(\frac{0.0037 - 0.0074}{K(25)}\right)\right), \quad (1)$$

$$K(T) = \frac{K(0)}{\left(1.007 + \mathrm{T}\left(\frac{0.0036-0.0072}{k(0)}\right)\right)}, \quad (2)$$

where T denotes the *in situ* temperature of rock samples and K (0), K (25), and $K(T)$ denote the thermal conductivity values of rock samples at 0°C, 25°C, and the *in situ* temperature, respectively.

For the rocks buried at a depth that could not be acquired through drilling, their thermal conductivity was corrected using the following formula (Cermak et al., 1990; Zang et al., 2002; Xu et al., 2011):

$$K = \frac{k_0 * (1 + cz)}{(1 + b * T)}, \quad (3)$$

where k_0 is the thermal conductivity at the top surface of each rock stratum; c is 0.0015; z is the depth of each rock stratum; and b is 0.0015, 0.0001, and 0.0001 for the upper, middle, and lower crust, respectively.

3.2 Lithospheric Thermal Structure

3.2.1 Lithospheric Thermal Structure

The crust is generally divided into four layers: a sedimentary layer, and an upper, middle, and lower crust. Its lower boundary—the Moho—is the contact surface between the lower crust and the mantle.

As the primary seismic wave (P wave, V_p) is distinct in each layer due to different geophysical characteristics, the distribution of V_p in the crust provides evidence of the contact surface between adjacent crust layers and crust structure. In the case where no geophysical analysis of an area has been conducted, the model of Crust 1.0 (Laske et al., 2013) is effective in establishing the crust structure in the area (Liu et al., 2021). Crust 1.0 is a global crustal model specified on a 1 × 1 degree grid and can be used for compiling global artificial seismic data. It provides the crustal structure and related parameters of each crust layer, such as V_p, density and boundary depths.

Since no geophysical study has been carried out in Jinggangshan City, Crust 1.0 is an effective tool for establishing the crust structure of the city. Nevertheless, the Crust 1.0 model has low resolution. To better constrain the crust structure, the geophysical information from a surrounding geoscience transect was collected. The geoscience transect from Menyuan in Qinghang Province to Ningde in Fujian Province (perpendicular distance: ~340 km) is similar to that of Jinggangshan City (Editorial Committee of Geoscience Transect, 1994; Wang et al., 1995). Though this geoscience transect is a little far away from the study area, it provides more accurate geophysical information.

3.2.2 Vertical Distribution of Heat Flow

The surface heat flow (q_0), which is calculated according to the thermal gradient and thermal conductivity (as mentioned in **Section 3.1**), consists of the crustal heat flow (q_c) and mantle heat flow (q_m).

The crustal heat flow is the sum of the radioactive heat generated by the heat production elements in the crust (U, Th, and K). The layer-stripping method is usually used to quantitatively estimate the radioactive heat generated in each crust layer and the whole crustal heat flow. The calculation formulas are as follows:

$$q_i = D_i \cdot A_i, \quad (4)$$

$$q_c = \sum qi, \quad (5)$$

where q_i is the radioactive heat flow in each crust layer; D_i is the thickness of each crust layer; A_i is the heat production rate of each crust layer; and q_c is the crustal heat flow.

The heat production rate (A) is traditionally calculated based on the U, Th, and K concentrations of representative rock samples using the following formula (Rybach and Buntebarth, 1981; Artemieva et al., 2017):

$$A = \rho(0.0952\,C_U + 0.0348\,C_K + 0.0256\,C_{Th}), \quad (6)$$

where A is the heat production rate (μW/m^3); ρ is rock density (g/cm^3); and C_U (ppm), C_K (ppm), and C_{Th} (ppm) are the concentrations of U, Th, and K, respectively.

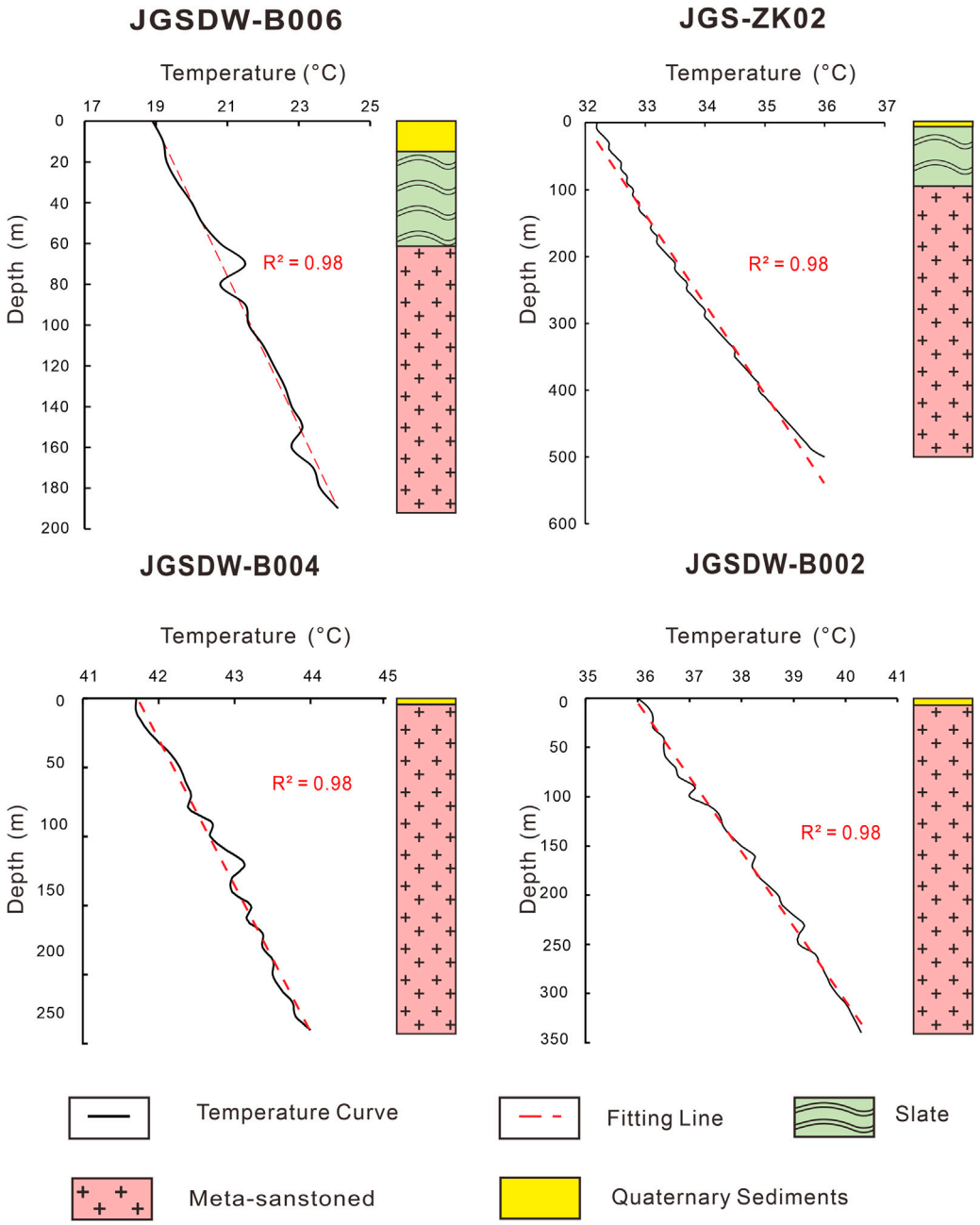

FIGURE 3 | Temperature–depth profiles for the wells in Huang'ao and Qutan villages.

The U, Th, and K contents of rock samples were determined by the Changsha Uranium Geology Research Institute. The K content was measured using a flame atomic absorption spectrophotometer, with a lower detection limit of 0.17%, and the U and Th contents were analyzed using the LA-ICP-MS method, with lower detection limits of 0.003 ug/g and 0.8 ug/g, respectively.

However, this method is not suitable for rocks at depths that are difficult to acquire through drilling. The heat production rate of these rocks can be estimated based on the functional relationship between V_p and A_i (Rybach and Buntebarth, 1984):

$$\mathrm{Ln}A = 13.7 - 2.17V_P, \tag{7}$$

where A is the heat production rate ($\mu W/m^3$) and V_p is the primary seismic wave (P wave). In this formula, the *in situ* seismic velocities should be corrected according to laboratory conditions (100 MPa, room temperature) using the method proposed by Rybach and Buntebarth (1984).

TABLE 1 | Temperature logging of geothermal wells in the study area.

JGSDW-B006		JGS-ZK02				JGSDW-B002		JGSDW-B004	
D	*T*	*D*	*T*	*D*	*T*	*D*	*T*	*D*	*T*
0	18.9	0	32.2	260	33.8	0	36.0	0	41.7
10	19.2	10	32.2	270	33.9	10	36.2	10	41.7
20	19.3	20	32.3	280	34	20	36.3	20	41.8
30	19.6	30	32.4	290	34	30	36.3	30	42.0
40	20	40	32.4	300	34.1	40	36.5	40	42.2
50	20.3	50	32.5	310	34.2	50	36.5	50	42.3
60	20.8	60	32.6	320	34.3	60	36.5	60	42.3
70	21.5	70	32.6	330	34.4	70	36.7	70	42.4
80	20.8	80	32.7	340	34.5	80	36.8	80	42.4
90	21.5	90	32.7	350	34.5	90	37.1	90	42.7
100	21.6	100	32.8	360	34.6	100	37.0	100	42.7
110	22	110	32.8	370	34.7	110	37.4	110	42.9
120	22.3	120	32.9	380	34.8	120	37.6	120	43.1
130	22.6	130	32.9	390	34.9	130	37.6	130	43.0
140	22.8	140	33	400	34.9	140	37.8	140	43.0
150	23.1	150	33.1	410	35	150	38.0	150	43.2
160	22.8	160	33.1	420	35.1	160	38.2	160	43.2
170	23.4	170	33.2	430	35.2	170	38.2	170	43.4
180	23.6	180	33.2	440	35.3	180	38.3	180	43.4
190	24.1	190	33.3	450	35.4	190	38.5	190	43.5
—	—	200	33.4	460	35.5	200	38.7	200	43.5
—	—	210	33.5	470	35.6	210	38.8	210	43.6
—	—	220	33.5	480	35.7	220	39.0	220	43.8
—	—	230	33.6	490	35.8	230	39.2	230	43.8
—	—	240	33.7	500	36	240	39.1	240	44.0
—	—	250	33.7	—	—	250	39.1	—	—
—	—	—	—	—	—	260	39.4	—	—
—	—	—	—	—	—	270	39.5	—	—
—	—	—	—	—	—	280	39.6	—	—
—	—	—	—	—	—	290	39.7	—	—
—	—	—	—	—	—	300	39.8	—	—
—	—	—	—	—	—	310	40.0	—	—
—	—	—	—	—	—	320	40.1	—	—
—	—	—	—	—	—	330	40.2	—	—
—	—	—	—	—	—	340	40.3	—	—

Note: D *denotes the depth of each well (unit: m) and* T *denotes the measured temperature (unit °C).*

The surface heat flow (q_0) minus the crustal heat flow (q_i) is the mantle heat flow (q_m). The mantle heat flow and the q_i/q_m ratio are important for understanding deep geodynamic processes (Wang et al., 2015; Zhang et al., 2018).

3.2.3 Deep Temperature Distribution

Well logging can be used to directly measure the temperature of shallow strata that can be unearthed by boreholes. By contrast, the temperature of deep strata should be calculated using the following one-dimensional steady-state heat conduction formula (Lachenbruch, 1970; Liu et al., 2021):

$$T_Z = T_0 + q \cdot D/k - A.D^2/(2.k), \tag{8}$$

where T_z (°C) is the temperature at depth z (m); T_0 and q are the temperature and heat flow (mW/m^2) at the top of each crust layer, respectively; and D, k (W/(mK)), and A are the thickness (km), thermal conductivity (μW·m^{-3}), and heat production rate of each crust layer, respectively.

4 RESULTS AND DISCUSSION

4.1 Terrestrial Heat Flow

4.1.1 Temperature Measurement and Geothermal Gradient

Temperature logging has been conducted for wells JGSDW-B006 and JGS-ZK02 in Huang'ao village and wells JGSDW-B002 and JGSDW-B004 in Qutan village (**Table 1**). The results are shown in **Figure 2**. Data fitting was completed using the linear least-squares regression method. The slope of the fitting line was numerically equal to the corresponding temperature gradient (**Figure 3** and **Table 2**). Well JGSDW-B006 had the highest thermal gradient of 26°C·km^{-1}, while well JGS-ZK02 had the lowest thermal gradient of 7.3°C·km^{-1}. The geothermal gradients of the two wells in Qutan village were 9.3°C·km^{-1} and 13.1°C·km^{-1}.

4.1.2 Thermal Conductivity

Five rock samples were collected in total to analyze thermal conductivity. These samples consisted of granites, metamorphic sandstones, slates, limestones, and quartz sandstones (**Figure 3**).

As shown in **Table 3**, the metamorphic sandstones had the highest thermal conductivity of 2.75–3.53 W/(mK) (average: 3.79 W/(mK)). Compared with metamorphic sandstones, the thermal conductivity of the Caledonian granites had a similar average of 3.42 W/(mK) but a relatively wider range of 2.06–5.15 W/(mK). The Yanshanian granites had the lowest thermal conductivity, with an average of 2.68 W/(mK). The limestones, sandstones, and slates had approximate thermal conductivity, with an average of 2.77 W/(mK), 2.86 W/(mK), and 2.72 W/(mK), respectively.

4.1.3 Surface Heat Flow

The heat flow was calculated based on the thermal gradient and thermal conductivity of the representative rocks (**Table 4**).

As presented in **Figure 3** and **Table 4**, the strata at valid depths of 0–190 m mainly consisted of metamorphic sandstones and slates, whose corrected thermal conductivity determined using **formulas (1)** and **(2)** was 3.8 W/(mK) and 2.73 W/(mK), respectively. By combining their thicknesses, their weighted thermal conductivity was estimated to be 3.57 W/(mK). The surface heat flow of well JGSDW-B006, which equaled the product of the geothermal gradient (26°C·km^{-1}) and the weighted thermal conductivity, was calculated to be 83.52 mW/m^2. This surface heat flow is much higher than the

TABLE 2 | Geothermal gradients and their depth ranges of temperature measurement.

Area	Well	*D* (m)	GG (°C·km^{-1})	*DRT* (m)
Huang'ao Country	JGSDW-B006	451.5	26	0–190
Qutan Country	JGS-ZK02	500	7.3	0–500
	JGSDW-B002	446	13.1	0–350
	JGSDW-B004	450	9.3	0–250

Note: D *denotes well depth;* GG *denotes the geothermal gradient of a well; and* DRT *denotes the depth range of temperature measurement.*

TABLE 3 | Heat conductivity of rocks in the study area.

Sample	Era	Lithology	Area	Longitude	Latitude	Heat Conductivity	Density	Average	N
JGSDZ-B010	Ordovician	Meta sandstone	Huang'ao	114°15	26°31′	3.44	2.78	3.24	3
JGSDZ-B029		Meta sandstone	Longshi Town	114°06	26°46′	3.53	3.08		
PCS-8		Meta sandstone	Nashan	114°13′	26°39′	2.75	3.25		
QT-1	Yanshanian	Granite	Huang'ao	114°11	26°25′	2.66	2.82	2.68	4
QT-2		Granite	Huang'ao	114°11	26°25′	2.62	3.5		
YY4		Granite	Huang'ao	114°12′	26°28′	2.55	2.57		
dz002		Granite	Nashan	114°10′	26°38′	2.9	2.7		
JGSDZ-B016	Caledonian	Granite	Huang'ao	114°12′	26°28′	3.57	2.67	3.42	8
dz003-1		Granite	Longshi Town	114°00′	26°39′	3.56	2.66		
dz003-2		Granite	Longshi Town	114°00′	26°39′	4.74	2.67		
JGSDZ-B033		Granite	Longshi Town	114°05′	26°44	3.55	2.7		
JGSDZ-B036		Granite	Longshi Town	114°04′	26°43′	2.26	3.11		
JGSDZ-B042		Granite	Longshi Town	114°03′	26°45′	2.45	2.62		
JGSDZ-C017		Granite	Longshi Town	114°05′	26°40′	5.15	2.68		
JGSDZ-C019		Granite	Longshi Town	114°08′	26°41′	2.06	2.97		
PCS-4	Devonian	Limestone	Nashan	114°14′	26°39′	2.81	3.43	2.77	4
PCS-6		Limestone	Nashan	114°14′	26°39′	2.81	2.77		
PCS-7		Limestone	Nashan	114°14′	26°39′	2.7	2.6		
PCS-1		Limestone	Nashan	114°14′	26°39′	2.78	3.28		
PCS-3	Ordovician	Metamorphic slate	Nashan	114°14′	26°39′	2.81	2.94	2.72	2
R-5		Metamorphic slate	Reshuizhou	114°12′	26°26′	2.63	2.56		
JGSDZ-B020	Devonian	Sandstone	Nashan	114°17′	26°42′	2.48	2.4	2.86	4
JGSDZ-B021		Sandstone	Nashan	114°17′	26°42′	2.41	2.41		
JGSDZ-B025		Sandstone	Nashan	114°10′	26°36′	2.99	2.67		
JGSDZ-B026		Sandstone	Nashan	114°10′	26°35′	3.54	3.01		

Note: the units of heat conductivity and density are W/(mK) and g/cm^3, respectively; average denotes the average of heat flux; and N denotes the number of heat flux values involved in the calculation of the average.

TABLE 4 | Calculated heat flow of each well in the study area.

Area	Well	*GG* (°C·km^{-1})	*DRT* (m)	*HC_C* (W/(m·K))	Heat flow (mW/m^2)
Qutan	JGSDW-B002	13.1	0–350	2.64	35.108
	JGSDW-B004	9.3	0–250	2.63	24.924
Shijiao Country	JGSDW-B006	26.6	0–190	3.14	83.52
Guangming Country	JGS-ZK02	7.3	0–500	3.53	25.77

Note: GG *denotes the geothermal gradient of a well;* DRT *denotes the depth range of temperature measurement; and* HC_C *denotes the corrected heat conductivity.*

average heat flow (60.4 ± 12.3 mW/m^2) of continental China. This finding indicates a high geothermal background in the study area, which is genetically associated to the formation of geothermal resources. In addition, the surface heat flow of wells JGSDW-B002, JGSDW-B004, and JGS-ZK02 was all low (24.9–35.1 mW/m^2), which was attributable to the disturbance of vertical water movement (Fan et al., 2014; Wang et al., 2015).

The surface heat flow value of well JGSDW-B006 (83.52 mW/m^2) is plotted in **Figure 1**, with the others in Jiangxi province. As shown in **Figure 1**, Jinggangshan City is located in the depression of the upper mantle where the heat flow background is expected to be low; however, the measured heat flow value (83.52 mW/m^2) there ranks second in all the measured values in Jiangxi Province. It is suggested that Huang'ao deep fault (NE trending) plays a key role in the high heat flow background. This deep fault is probably a channel of heat transfer from the heat source at a depth.

4.2 Crustal and Mantle Heat Flow

4.2.1 Boundaries of the Lithospheric Thermal Structure

The geoscience transect from the Menyuan area in Qinghai Province to the Ningde area in Fujian Province is shown in

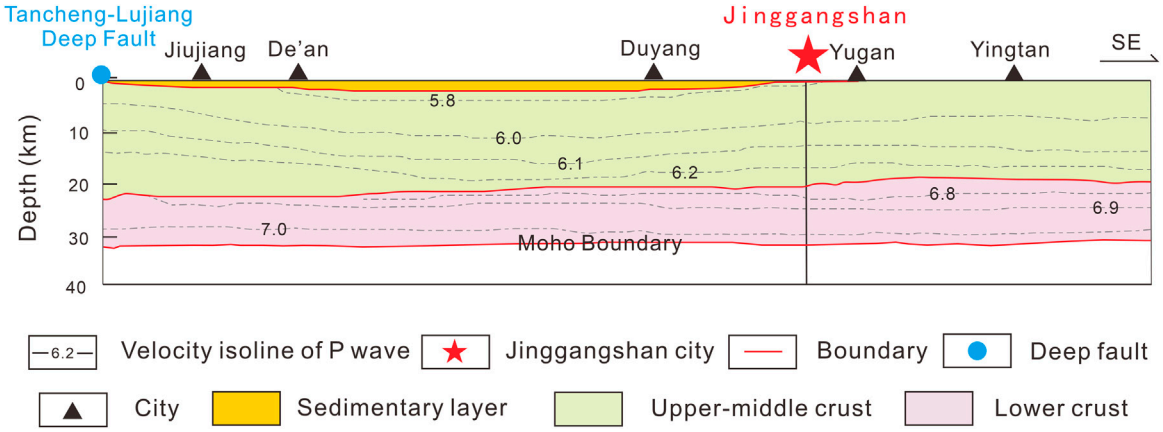

FIGURE 4 | Distribution of P-wave velocity in the geological transect from Menyuan to Ningde Zuoyi (modified after the Editorial Committee of Geoscience Transect C E a E, (1994); Wang et al. (1995); the location of the section line is defined in **Figure 1**).

TABLE 5 | Geothermal structure in Jinggangshan City.

Layer	*H* (km)	*D* (km)
Sedimentary layer	−0.62	0.62
Upper–middle crust	−20.97	20.35
Lower crust	−31.97	11

Note: H is the depth from the bottom of each layer to the ground surface in Jinggangshan City. The ground surface elevation is 330 m according to the logging of well JGSDW-B006. D is the thickness of each layer.

Figure 4. Jinggangshan City is located to the east of the Tanlu (Tancheng-Lujiang) deep fault, where the boundaries of the upper and the middle crusts have blurred due to the strong thrusting process (Editorial Committee of Geoscience Transect C E a E, 1994; Wang et al., 1995). Therefore, the crust was divided into a sedimentary layer and an upper–middle and lower layer. Based on the distribution of the V_p as shown in **Figure 4**, the depth of the interface between the middle and lower crusts in the study area was determined to be 20.97 km (**Table 5**). Similarly, the depth of the Moho was 31.97 km, and the lower boundary of the sedimentary layer was 0.62 km.

Based on the Crust 1.0 model, the depth of the interface between the middle and lower crusts was 22.06 km and the Moho depth was 32.9 km. By averaging the results calculated based on the V_p distribution and the Crust 1.0 model, the final depth of the interface between the middle and lower crusts was 21.52 km and the final depth of the Moho surface was 32.44 km (**Table 7**).

4.2.2 Layer-Stripping Calculation of Heat Flow

As mentioned in **Section 3.2.2**, the layer-stripping method can be used to calculate the crustal and mantle heat flow. The three layers of the crust (i.e., the sedimentary layer, the upper-middle crust, and the lower crust) were further divided into several portions according to the well logging (**Figure 3**) and the isolines of P-wave velocity (V_p; **Figure 4**). The thickness (D_i) represents the vertical distance between the top and bottom isolines of V_p.

For the sedimentary layer (thickness: 620 m), the well logging of well JGSDW-B006 (depth: 500 m) showed that this layer mainly consisted of slates and metamorphic sandstones (Fan et al., 2014), with the former located at a depth of < 62 m and the latter distributed at a depth of >62 m. Therefore, the sedimentary layer was subdivided into a slate layer and a metamorphic sandstone layer. The heat production rates (A_i) of these two sublayers were obtained based on the U, Th, and K contents of rock samples. Eleven samples were collected using a hammer to analyze the thermal conductivity (**Table 6**). The average heat production of the metamorphic slates and metamorphic sandstones was 3.63 μW/m^3 and 4.17 μW/m^3, respectively.

Regarding the upper–middle crust and the lower crust, $V_{p\text{-}layer}$ was the average velocity of the top and bottom isolines of V_p (**Table 7**). The heat flow on the top surface of each layer was calculated using **formulas (4)**, **(5)**, and **(7)**. It is noteworthy that the $V_{p\text{-}layer}$ of the middle and lower crust was corrected by multiplying the correction factor of 1.01 according to the laboratory conditions (Rybach and Buntebarth, 1984). The heat flow of the mantle and crust was 45.63 mW/m^2 and 37.89 mW/m^2, respectively. Therefore, the q_c/q_m ratio was less than 1 (0.83), suggesting a hot-mantle–cold-crust type of lithospheric thermal structure. In other words, the heat flow mainly originated from the heat contribution of the mantle. Based on **Table 7**, a conceptual model is constructed for the lithospheric thermal structure in the study area (**Figure 5**). As shown in this model, the values of heat flow and heat production rate in each layer could be easily identified and their changes between each other. The heat production and heat flow values in the upper–middle crust is obviously higher than those of the lower crust. Their values have a decreasing trend with increasing depth.

4.2.3 Deep Temperature Distribution

According to Fan et al. (2014), the constant temperature zone in Jinggangshan City (depth: 20 m) has a temperature of 15°C. The

TABLE 6 | Heat production of rocks in the study area.

Sample	Era	Lithology	Area	Longitude	Latitude	U	Th	K	Heat flux	Average	N
Dz001-1	Ordovician	Meta sandstone	Nashan	114°07′10.80″	26°37′19.10″	13.7	5.6	1.48	4.17	4.17	1
PCS-3	Ordovician	Metamorphic slate	Nashan	114°13′31.04″	26°39′21.25″	9.19	21.2	5.63	4.42	3.63	2
R-5		Metamorphic slate	Reshuizhou	114°12′00.83″	26°26′15.98″	7.1	10.9	2.05	2.84		

Note: the units of U, Th, K and heat flux are ppm, ppm, %, and μW/m^3, respectively; average denotes the average value of heat flux; and N denotes the number of heat flux values involved in the calculation of the average value.

TABLE 7 | Geoscience transect around the study area.

Layer		N	*Z*	*D*	*K*	$V_{p\text{-}b}$	$V_{p\text{-}layer}$	$V_{p\text{-}c}$	*A*	A_i	*q*	T_z
—			km	km	W/(m·K)	m·s^{-1}	m·s^{-1}	m·s^{-1}	μW/m^3	mW/m^2	mW/m^2	—
Sedimentary layer	CTZ		−0.02	—	—	—	—	—	—	—	83.52	15
	Slate	1	−0.062	0.042	2.73	—	—	—	3.63	0.15	83.37	16.3
	Meta-sandstone	2	−0.62	0.56	3.8	5.8	—	—	4.17	2.33	81.04	28.4
Upper–middle crust	—	3	−8.51	7.89	2.77	6	5.9	5.96	2.16	17.02	64.02	234.5
	—	4	−12.77	4.26	2.76	6.1	6.05	6.11	1.55	6.62	57.40	328.3
	—	5	−17.23	4.46	2.76	6.2	6.15	6.21	1.25	5.56	51.84	416.7
	—	6	−21.52	4.29	2.75	6.5	6.35	6.41	0.80	3.45	48.39	494.8
Lower crust	—	7	−23.25	1.73	2.84	6.8	6.65	6.72	0.42	0.72	47.66	524.0
	—	8	−25.64	2.39	2.86	6.9	6.85	6.92	0.27	0.64	47.02	563.6
	—	9	−30.52	4.88	2.91	7	6.95	7.02	0.22	1.05	45.97	641.6
	—	10	−32.44	1.92	2.93	7.1	7.05	7.12	0.17	0.33	45.63	671.7

Note: CTZ denotes the constant temperature zone; N denotes the sequence number of the layer; Z denotes the bottom depth of each layer; D denotes the thickness of each layer; K denotes the thermal conductivity of each layer; $V_{p\text{-}b}$ denotes the P-wave velocity at the bottom of each layer; $V_{p\text{-}layer}$ denotes the P-wave velocity of each layer, numerically equal to the average of v_p values of the top and bottom of each layer; $V_{p\text{-}c}$ denotes the corrected Vp *(correction factor is 1.01) (Rybach and Buntebarth, 1984); A denotes the heat production rate of each layer; A_i denotes the heat production of each layer; q denotes the heat flow at the bottom of each layer; and T_z denotes the temperature at depth Z.*

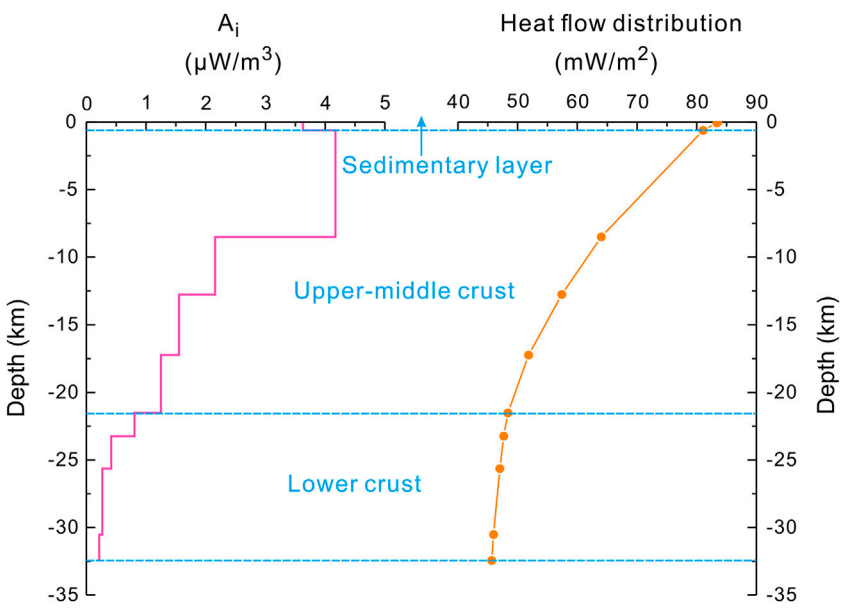

FIGURE 5 | Conceptual model constructed for the lithospheric thermal structure in the study area.

temperature below the constant temperature zone was thereby calculated using **formulas (1)**, **(2)**, **(3)**, and **(8)**. As shown in **Table 7**, the crust was divided into 10 layers to estimate the deep temperature distribution. The calculated temperature of the Moho was 671.7°C, which is consistent with the estimated temperature of the Moho below the Tanlu deep fault (620–690°C (He et al., 2006)).

The Curie temperature isotherm is the basal surface of the magnetite crust consisting of magnetitic minerals and corresponds to the temperature at which magnetic minerals become paramagnetic (Xiong et al., 2016; Yu-fei et al., 2021). Ilmenites and pyrrhotites lose their ferromagnetism at a temperature of 300–350°C. The demagnetized temperature of magnetite is 585°C (Ross et al., 2006), while that of Co–Ni–Fe–bearing minerals is up to 760–800°C. The Curie temperature isotherm is an important parameter of the lithospheric thermal structure since it can be used to estimate the temperature at a depth (Mayhew, 1985; Ross et al., 2006; Yang, 2015). It is a supplement to heat flow in constructing the lithospheric thermal structure. The Curie point isotherm in China (Xiong et al., 2016) shows that the Curie surface in the study area is at a depth of 19–30 km. Based on the deep temperature distribution of the lithospheric thermal structure listed in **Table 7**, the Curie surface depth corresponding to the demagnetized temperature of magnetite (585°C) was estimated to be 27 km using the interpolation method. The consistency of the Curie surface depth further dominates the validity of the lithospheric thermal structure and deep temperature distribution in Jinggangshan City.

5 CONCLUSION

This study is the first comprehensive investigation of the lithospheric thermal structure in Jinggangshan City, contributing to a better understanding of the genesis and exploitation potential of the geothermal resources therein. Based on the abovementioned analyses, the following conclusions can be drawn:

1) The heat flow of Jinggangshan City is 83.52 mW/m^2, which is much higher than the average heat flow (60.4 ± 12.3 mW/m^2) of continental China. The high heat flow indicates a high geothermal background in the study area.
2) As estimated from the lithospheric thermal structure of Jinggangshan City, q_c and q_m are 37.89 mW/m^2 and 45.63 mW/m^2, respectively. Therefore, the q_c/q_m ratio is less than 1, indicating that the terrestrial heat flow in Jinggangshan City mainly originates from the mantle.
3) As shown in the deep temperature distribution calculated using the one-dimensional steady-state equation, the temperature of the Moho in Jinggangshan City is 671.7°C, which is consistent with the temperature of the Moho below the Tanlu deep fault. Furthermore, the calculated depth of the Curie temperature isotherm in Jinggangshan City is 27 km, which is consistent with the depth estimated based on aeromagnetic data. The consistency verifies the validity of the lithospheric thermal structure established in this study.
4) The high heat flow background, which mainly originates from the heat supply of the mantle, contributes significantly to the formation of the geothermal resources in Jinggangshan City.

DATA AVAILABILITY STATEMENT

The original contributions presented in the study are included in the article/Supplementary Material, further inquiries can be directed to the corresponding author.

AUTHOR CONTRIBUTIONS

YL: ideas, field investigation, data analysis, picture drawing, creation of models, manuscript writing, and revision; YL: ideas, field investigation, review, and financial support; FL: field investigation, review, and financial support; SW: field investigation; and HD: picture drawing.

FUNDING

This work was financially supported by the China Geological Survey Project (DD20190128, 20190505, and DD20160190), the Basal Science Research Fund from the Institute of Hydrogeology and Environmental Geology (Grant Nos. SK202008 and SK202104), the S&T Program of Hebei China (No. 20374201D), and the Natural Science Foundation of Hebei Province China (No. D2019330003).

ACKNOWLEDGMENTS

The authors would like to thank Xiaoxue Yan, Haonan Gan, Lingxia Liu, Ruoxi, Yuan, Liu Tao, and Ronghua Hu for their assistance in field work.

REFERENCES

Anand, J., Somerton, W. H., and Gomaa, E. (1973). Predicting Thermal Conductivities of Formations from Other Known Properties. *Soc. Petroleum Eng. J.* 13, 267–273. doi:10.2118/4171-PA

Artemieva, I. M., Thybo, H., Jakobsen, K., Sørensen, N. K., and Nielsen, L. S. K. (2017). Heat Production in Granitic Rocks: Global Analysis Based on a New Data Compilation Granite2017. *Earth-Science Rev.* 172, 1–26. doi:10.1016/j.earscirev.2017.07.003

Cermak, V., Bodri, L., Rybach, L., and Buntebarth, G. (1990). Relationship between Seismic Velocity and Heat Production: Comparison of Two Sets of Data and Test of Validity. *Earth Planet. Sci. Lett.* 99 (1), 48–57. doi:10.1016/0012-821X(90)90069-A

Davies, J. H., and Davies, D. R. (2010). Earth's Surface Heat Flux. *Solid earth.* 1 (1), 5–24. doi:10.5194/se-1-5-2010

Deng, Y., Fan, W., Zhang, Z., and Badal, J. (2013). Geophysical Evidence on Segmentation of the Tancheng-Lujiang Fault and its Implications on the Lithosphere Evolution in East China. *J. Asian. Earth. Sci.* 78 ,263-276. doi:10.1016/j.jseaes.2012.11.006

Editorial Committee of Geoscience Transect C E a E (1994). *Geoscience Transect from Menyuan*, Qinghai Province to Ningde, Fujian Province: Seismological press.

Fan, B., Liu, X., Ye, H., Xv, L., and Yu, S. (2014). *Geothermal Water Survey Report in Qutan, Xiaqi Country, Jinggangshan City, Jiangxi Province*. Nanchang: Jiangxi Institute of Geo-Environment Monitoring.

Furlong, K. P., and Chapman, D. S. (2013). Heat Flow, Heat Generation, and the Thermal State of the Lithosphere. *Annu. Rev. Earth Planet. Sci.* 41 (1), 385–410. doi:10.1146/annurev.earth.031208.100051

He, L., Hu, S., Yang, W., Wang, J., Yang, S., Yuan, Y., and Cheng, Z. (2006). Heating Generation Model for the Continental Crust Based on the Main Hole of the Chinese Continental Scientific Drilling Project. *Acta Petrol. Sin.* 22 (11), 7

Hu, S. B., Xiong, L. P., Wang, J. Y., Shen, J. Y., and Li, J. L (1992). The First Group of Heat Flow Data from Jiangxi Province. *Chin. Sci. Bull.* 19, 1791.

Jaupart, C., and Mareschal, J. C. (2015). "6.05 - Heat Flow and Thermal Structure of the Lithosphere." in *Treatise on Geophysics*. Editors G. Schubert (Amsterdam: Elsevier), 217–251

Jiang, G., Hu, S., Shi, Y., Zhang, C., Wang, Z., and Hu, D. (2019). Terrestrial Heat Flow of Continental China: Updated Dataset and Tectonic Implications. *Tectonophysics* 753, 36–48. doi:10.1016/j.tecto.2019.01.006

Lachenbruch, A. H. (1970). Crustal Temperature and Heat Production: Implications of the Linear Heat-Flow Relation. *J. Geophys. Res.* 75 (17), 3291–3300. doi:10.1029/JB075i017p03291

Laske, G., Masters, G., Ma, Z., and Pasyanos, M. E. (2013). *Update on Crust1.0 - a 1-Degree Global Model of Earth's Crust*. United States: Jolla

Li, J. (2019). A Discussion on the Symbolic Role of Secondary Fault Structure in Geothermal Prospecting in Southern Mountainous Areas - to Take the Longgui Mountain Geothermal Field in Ningdu County, Jiangxi Province as an Example. *J. Geol. Hazards Environ. Preserv.* 030 (4), 85

Li, X., Shi, X., Zhou, W., Sun, Z., Zhang, W., Niu, X., et al. (1992). Terrestrial Heat Flow in Jiangxi Province. *Sci. Geol. Sin.* A12, 383

Li, Z., Zuo, Y., Qiu, N., and Gao, J. (2017). Meso-Cenozoic Lithospheric Thermal Structure in the Bohai Bay Basin, Eastern North China Craton. *Geosci. Front.* 8 (5), 977–987. doi:10.1016/j.gsf.2016.09.003

Lin, Z. (1992). *Geological Transects from Menyuan in Qinghang to Ningde in Fujian*. Beijing: Seismological Press.

Liu, C., Chen, L., and Wang, Z. (2018). Geological Characteristics of Yangkeng Tungsten Ore Deposit in Jinggangshan City, Jiangxi Province. *Min. Eng.* 16 (6), 9

Liu, F., Lang, X., Lu, C., Lin, W., Tong, J., and Wang, G. (2017). Thermophysical Parameters and Lithospheric Thermal Structure in Guide Basin, Northeast Qinghai-Tibet Plateau. *Environ. Earth Sci.* 76 (5), 199. doi:10.1007/s12665-017-6503-2

Liu, F., Wang, A., Wang, G., Zhang, W., Liao, Y., and Tong, J. (2021). Characteristics of Terrestrial Heat Flow and Lithospheric Thermal Structure in Typical Intermountain Basin at the Eastern Foot of Yanshan Mountain, North China. *Front. Earth Sci.* 9, 758605. doi:10.3389/feart.2021.758605

Liu, Q., Zhang, L., Zhang, C., and He, L. (2016). Lithospheric Thermal Structure of the North China Craton and its Geodynamic Implications. *J. Geodyn.* 102, 139–150. doi:10.1016/j.jog.2016.09.005

Mayhew, M. A. (1985). Curie Isotherm Surfaces Inferred from High-Altitude Magnetic Anomaly Data. *J. Geophys. Res.* 90 (B3), 2647–2654. doi:10.1029/JB090iB03p02647

Prol-Ledesma, R. M., and Morán-Zenteno, D. J. (2019). Heat Flow and Geothermal Provinces in Mexico. *Geothermics* 78 (MAR.), 183–200. doi:10.1016/j.geothermics.2018.12.009

Ross, H. E., Blakely, R. J., and Zoback, M. D. (2006). Testing the Use of Aeromagnetic Data for the Determination of Curie Depth in California. *Geophysics* 71 (5), L51–L59. doi:10.1190/1.2335572

Rybach, L., and Buntebarth, G. (1984). The Variation of Heat Generation, Density and Seismic Velocity with Rock Type in the Continental Lithosphere. *Tectonophysics* 103 (1-4), 335–344. doi:10.1016/0040-1951(84)90095-7

Rybach, L., and Buntebarth, G. (1981). Heat-Generating Radioelements in Granitic Magmas. *J. Volcanol. Geotherm. Res.* 10 (4), 395–404. doi:10.1016/0377-0273(81)90088-3

Sass, J. H., Lachenbruch, A. H., Moses, T. H., and Morgan, P. (1992). Heat Flow from a Scientific Research Well at Cajon Pass, California. *J. Geophys. Res.* 97, 5017–5030. doi:10.1029/91JB01504

Sclater, J. G., Jaupart, C., and Galson, D. (1980). The Heat Flow through Oceanic and Continental Crust and the Heat Loss of the Earth. *Rev. Geophys.* 18 (1), 269–311. doi:10.1029/RG018i001p00269

Shen, W., Ling, H., Shu, L., Zhang, F., and Xiang, L. (2009). Sm-Nd Isotopic Compositions of Cambrian-Ordovician Strata at the Jinggangshan Area in Jiangxi Province: Tectonic Implications. *Sci. Bull.* 54 (010), 1750–1758. doi:10.1007/s11434-009-0214-3

Wang, C. Y., Lin, Z. Y., and Chen, X. B. (1995). Comprehensive Study of Geophysics on Geoscience Transect from Menyuan, Qinghai Province, to Ningde, Fujian Province, China. *Chin. J. Geophys.*14, 58

Wang, J., Pang, Z., Hu, S., He, L., Huang, S., and Qiu, N. (2015). *Geothermics and its Application*. Zealand: Supports open access

Xiao, Z., Wang, J., and Hou, H. (2018). Analysis of Characteristics and Causes of Geothermal Water in the East of Southern Jiangxi Province. *J. East China Univ. Technol.* 41 (3), 58

Xiong, S., Yang, H., Ding, Y., and Li, Z. (2016). Characteristics of Chinese Continent Curie Point Isotherm. *Chin. J. Geophys.* 59 (10), 14. doi:10.6038/cjg20161008

Xu, M., Zhu, C., Rao, S., and Hu, S. (2011). Difference of Thermal Structure between Eastern Edge of Tibet Plateau and Weasten Sichuan Basin. *Chin. J. Geol.* 46 (1), 203–212. doi:10.1007/s11769-011-0451-7

Yang, H. (2015). *Characteristics of Chinese Continental Curie Point Isotherm*. Sichuan, Chengdu: Chengdu University of Technology

Yang, L., Zhou, Y., Yu, Y., and Yang, W. (2018). Analysis on Genesis and Hydrochemical Characteristics of Geothermal Water in Qutan Area,Jinggangshan,Jiangxi Province. *Sci. Technol. Eng.* 18 (23), 13–18. doi:10.1007/s12665-021-09577-8

Yu-Fei -, X., Ya-Bo -, Z., and Yuen, - D. (2021). Geothermal Structure Revealed by Curie Isothermal Surface under Guangdong Province, China. *J. Groundw. Sci. Eng.* 9, 114. doi:10.19637/j.cnki.2305-7068.2021.02.003

Zang, S., Liu, Y., and Ning, J. (2002). Thermal Structure of the Lithosphere in North China. *Chin. J. Geophys.* 45 (1), 56–66. doi:10.1002/cjg2.216

Zhang, C., Jiang, G., Shi, Y., Wang, Z., Wang, Y., Li, S., Jia, x., and Hu, S., (2018). Terrestrial Heat Flow and Crustal Thermal Structure of the Gonghe-Guide Area, Northeastern Qinghai-Tibetan Plateau. *Geothermics* 72, 182–192. doi:10.1016/j.geothermics.2017.11.011

Zhang, Z. (2017). *Hydrogeochemistry of Nitric Hot Springs in Southern Jiangxi Province*. Fuzhou, China: East China University of Technology

Zhu, B., and Zhu, L. (1992). *Geochemical Exploration of Geothermal Fields*. Bath, UK: Geological Publishing House.doi:10.1016/S0375-6505(97)00012-6

Zhu, Z. (2007). Hot-Spring in the Reshuizhou Region of Jiangxi Province. *Geol. Mineral Resour. South China* 03, 63

Conflict of Interest: The authors declare that the research was conducted in the absence of any commercial or financial relationships that could be construed as a potential conflict of interest.

frontiers | Frontiers in Earth Science

ORIGINAL RESEARCH
published: 14 June 2022
doi: 10.3389/feart.2022.858814

Heat Accumulation Mechanism of the Gaoyang Carbonatite Geothermal Field, Hebei Province, North China

Baojian Zhang[1,2], Siqi Wang[1,2], Fengxin Kang[3]*, Yanqiu Wu[4], Yanyan Li[1,2], Jun Gao[1,2], Wenzhen Yuan[1,2] and Yifei Xing[1,2]*

[1]Chinese Academy of Geological Sciences, Beijing, China, [2]Technology Innovation Center of Geothermal and Hot Dry Rock Exploration and Development, Ministry of Natural Resources, Beijing, China, [3]Shandong Provincial Bureau of Geology and Mineral Resources, Jinan, China, [4]School of Water Resources and Environment, China University of Geosciences (Beijing), Beijing, China

From 2019 to 2021, we constructed two high-productivity geothermal wells with wellhead temperatures of 109.2 and 123.4°C in the Gaoyang geothermal field. Based on the two wells, it was proved that Gaoyang is a medium-temperature carbonate geothermal field with great development potential. The article reported the latest exploration achievements of deep buried hill geothermal resources in the geothermal field. The productivity of D34 and D35 geothermal wells were evaluated by James end-pressure method: the total flow of steam–water mixture was 234.59–331.92 (t/h), the dryness was 1.36–2.03%, and the single-well power generation potential was 2.10–2.55 MW. Combined with those results, the heat control factors and heat accumulation mechanism of the deep carbonatite geothermal field were confirmed. The westward subduction of the Pacific plate caused obvious damage to the eastern North China Craton and greatly reduced the thickness of the lithosphere and crust. This process facilitated the conduction of mantle-derived heat to shallow crust. Deep strike-slip faults (e.g., Maxi fault) cut through the lithosphere, leading the deep mantle-derived heat and magma to migrate into the crust. The heat accumulated from the depression with low thermal conductivity to the uplift with high thermal conductivity. Groundwater was heated up by deep cycle and convection along faults. The catchment of regional karst groundwater also had a certain effect on the heat accumulation. The Gaoyang geothermal field was formed by these factors.

Keywords: Gaoyang geothermal field, medium-temperature geothermal resources, heat accumulation mechanism, development potential, capacity of geothermal well

OPEN ACCESS

Edited by:
Wenjing Lin,
Chinese Academy of Geological Sciences, China

Reviewed by:
Haibing Shao,
Helmholtz Association of German Research Centres (HZ), Germany
Jiexiang Li,
Henan Polytechnic University, China
Xi zhu,
Chinese Academy of Geological Sciences, China

****Correspondence:***
Baojian Zhang
zbjsddk@126.com
Fengxin Kang
kangfengxin@126.com

Specialty section:
This article was submitted to Structural Geology and Tectonics, a section of the journal Frontiers in Earth Science

Received: *20 January 2022*
Accepted: *05 May 2022*
Published: *14 June 2022*

Citation:
Zhang B, Wang S, Kang F, Wu Y, Li Y, Gao J, Yuan W and Xing Y (2022) Heat Accumulation Mechanism of the Gaoyang Carbonatite Geothermal Field, Hebei Province, North China. Front. Earth Sci. 10:858814. doi: 10.3389/feart.2022.858814

1 INTRODUCTION

The study area is within the northeastern Gaoyang geothermal field located in Xiong'an New Area, central Hebei Province. The shallow-seated carbonate thermal reservoirs include the Niutuo and Rongcheng geothermal fields, which are less than 1,000 m, and their development and utilization are simple and large scale with many years of history (Chen et al., 1982). However, the depth of carbonate reservoir of the Gaoyang geothermal field is more than 3,000 m and its development is small scale due to the relatively complex mining technology. The China Geological Survey of the Natural Resources Ministry has conducted a series of exploration and research work of the geothermal resources with the authors to make improvements in this area and has made great progress in the detection of new formations and deep bedrock thermal reservoirs (Wang et al., 2018;

Wu et al., 2018) since the foundation of Xiong'an New Area in 2017. The Chinese Academy of Geological Sciences discovered the highest temperature (123.4°C) geothermal well in the North China basin in 2020 after the foundation of the most productive geothermal well with a temperature of 109.2°C in 2019 in Gaoyang geothermal field. The exploration results show that the geothermal field with medium temperature (>90°C) has great development and utilization potential.

Regarding the heat accumulation mechanism of the ancient buried hill geothermal field in the North China basin, Chen (1988), Chen (1992) has found that the geothermal anomaly in the uplift of the North China basin is trigged by the redistribution of the relatively uniform heat flow in deep crust to the surface during the upward conduction. Pang et al. (2017) propose a new geothermal genesis model (heat accumulation of binary sources) of the Niutuo geothermal field and points out that the abundant geothermal resources in Xiong'an New Area are formed under dual mechanism, that is, rock thermal conductivity and basin-scale groundwater circulation. Yue et al. (2020) summarize the geothermal accumulation of the ancient buried hills in Xiong'an New Area as a four-element (heat conduction, structural uplift, deep fractures, and convection within the reservoir) model by heat conduction simulation (Yue et al., 2020). However, the key issue about how the heat sourced from mantle and deep crust migrated to the shallow crust remains poorly understood. Wang et al. (2017) report that the obvious thinning of the lithosphere, crustal deformation, earthquakes, and magmatic activities caused by the destruction of the North China crust (NCC) have promoted the production of geothermal resources. Wang and Lin (2020) assign the genetic model of geothermal systems in China as "homologous symbiosi-crust and mantle heat generation-tectonic heat accumulation" and point out that the high-temperature subcrust matter can flow up to the shallow crust along deep fractures. Zhang et al. (2020) confirm that the upwelling of deep mantle-derived thermal matter is a favorable factor for the formation of hot dry rocks in Matouying, Hebei Province (Zhang et al., 2020). Wang et al., 2021 comprehensively analyze the heat accumulation mechanism of deep ancient buried hill geothermal resources in the northeastern Gaoyang geothermal field and discuss the controlling effects of the deep geological structure on the heat distribution in the ancient buried hills (Wang et al., 2021).

Based on the earlier discussion, the heat accumulation mechanism of the buried hill geothermal field in the large sedimentary basin is established. It is the redistribution of the relatively uniform heat flow in deep crust to the surface during the upward conduction (Chen, 1988; Chen, 1992). Under the differential effect of rock thermal conductivity, the heat flow accumulates from the depression with low thermal conductivity to the uplift with high thermal conductivity, and the geothermal water heated by deep cycle from the recharge area to the discharge area and the upper crust fracture upwells after undergoing basin-scale groundwater circulation. This type of geothermal resource can be called "low–medium temperature convective–conductive geothermal system" (Wang et al., 2015). The deep-cycle heating of groundwater along faults generally occurred within a depth of 10 km. Therefore, the deep geothermal anomaly caused by the deep crust or mantle heat upwelling and its activity mechanism is worth further discussion. Based on previous studies, this article reports the latest exploration achievements of geothermal resources in the Gaoyang geothermal field, proposes the heat accumulation mechanism, and estimates its development potential. The productivity and resource potential of Gaoyang carbonate were evaluated. It could provide geological basis and technical support for efficient development and utilization of deep medium-temperature geothermal resources in the Gaoyang geothermal field and elsewhere worldwide with the same geological setting.

2 GEOLOGIC SETTING

2.1 Geological Structure

The study area is located in the middle-west of the Jizhong depression within the Bohai Bay basin. The Jizhong depression is mainly the secondary tilted block, half-graben depression and buried hill structural units, which are composed of a series of normal faults or inverted normal faults formed under Mesozoic compression and Cenozoic extension. The geothermal field has two structural units (the Gaoyang low uplift and the Lixian slope), which are distributed in NE direction strips as a whole. It is separated from the Rongcheng uplift and the Niutuo uplift by the Anxin-Wen'an structural transfer zone in the NWW–SEE direction in the north, and it is connected to the Xingheng uplift by the Hengshui-Wuji structural transfer zone in the NW–SE direction in the south, with the Baoding depression in the west, and the Raoyang depression in the east, respectively (**Figure 1**). The carbonate geothermal reservoir at the top of the Gaoyang uplift is buried at a depth of 3,000–3,500 m and gradually deepens to below 4,000 m in the depressions on the east and west sides, respectively (**Figure 2**).

The main Gaoyang-Boye fault occurs along the axis of the Gaoyang low uplift with NE trending. Its fault distance in the north is relatively small, and the activity is significantly weakened after the Paleogene. However, faults developed in the structural transfer zone at the north and south ends of the geothermal field. The Anxin-Wen'an structural transfer zone is mainly composed of a series of echelon faults such as the Anxin fault and the Niunan fault. "Transfer zone" is derived from the study of the fold-thrust fault in the compression deformation of the Canadian Rocky Mountains, which is an adjustment structure that can enable the amount of shortening is more nearly constant (Dahlstrom, 1970). This concept of transfer zone was later applied to extensional structures and strike-slip structures (Morley et al., 1990; Faulds and Varga, 1998; Qi, 2007; Yang, 2009). Transfer zone is a favorable tectonic regime for formation of oil, gas, and geothermal resources, as its development is of multi-level faults.

The N–S trending Maxi strike-slip fault has gone through weak extensional activities and sedimentation-controlling effect due to the influence of the Anxin-Wen'an structural transfer zone in the north. The fault is part of a large basement strike-slip fault and the Tangshan-Hejian-Cixian fault (Qi, 2004). The Niudong Maxi strike-slip structural system composed of the Maxi fault and

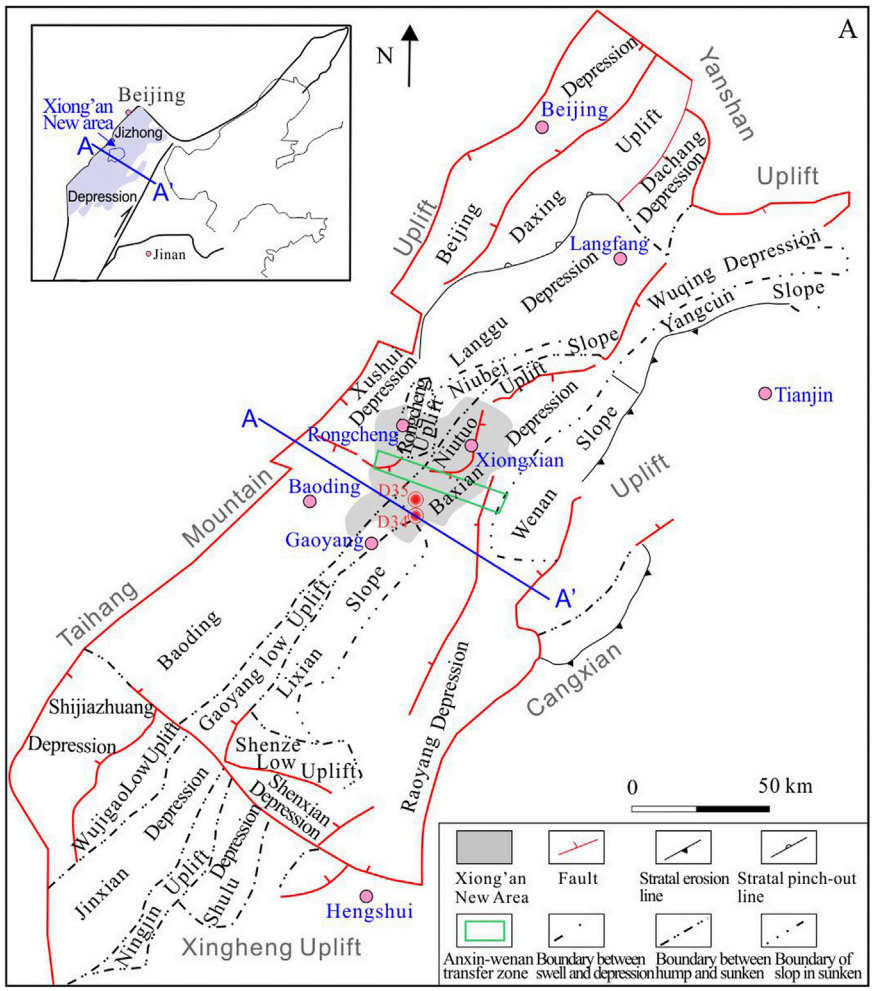

FIGURE 1 | Structural location of Xiong'an New Area in the Jizhong depression.

the Niudong fault is considered to be the result of right-lateral strike-slip activities of deep faults that cut through the basement in the Cenozoic. This is direct evidence that deep tectonic stress is transferred to the shallow crust through the lower crust (Xiao et al., 2000).

2.2 Deep Geological Structure

The western Pacific plate subducted to northwest in the Early Jurassic and retreated in the Early Cretaceous. The subduction, rollback, and retreat of the western Pacific plate eventually led to the stagnation of the slab in the mantle transition zone—the big mantle wedge under eastern Asia. This process (craton destruction) may significantly change the physical properties and viscosity of that section and the overlying mantle, resulting in nonsteady flow of the overlying mantle wedge, and may further dramatically give rise to the increase of melt/fluid contents in the lithospheric mantle, lower viscosity, the stretch/decompression of the lithosphere, and the transformation from the old cratonic lithosphere to the young mantle (Zhu and Xu, 2019). Groundwater played an important role in the destruction of the NCC lithosphere. During the subduction of the plate, a large amount of water was released into the cratonic lithospheric mantle and caused strong hydration. As a result, the mantle convection system in the eastern NCC destabilized and the overlying lithosphere was metasomatized, melted, and weakened, which led to lithospheric thinning and cratonic destruction (Xia et al., 2013).

The thermal erosion *via* mantle convection and peridotite-melt interaction within the big mantle wedge resulted in significant thinning of the NCC lithosphere during the Mesozoic. Due to the retreat of the subducting plate, the lithosphere extended and further thinned, accompanied by the passive upwelling of the asthenosphere, which led to the development of the Bohai Bay sedimentary basin in the Cenozoic as well as the increase in the surface heat flow. In the late Cenozoic, under the effect of thermal attenuation, the lithosphere gradually thickened, but still maintained a thin state and high heat flow (He and Qiu, 2014). As the thickness of the lithosphere changed, the lithosphere of the Bohai Bay basin transformed its thermal structure from "cold mantle but hot

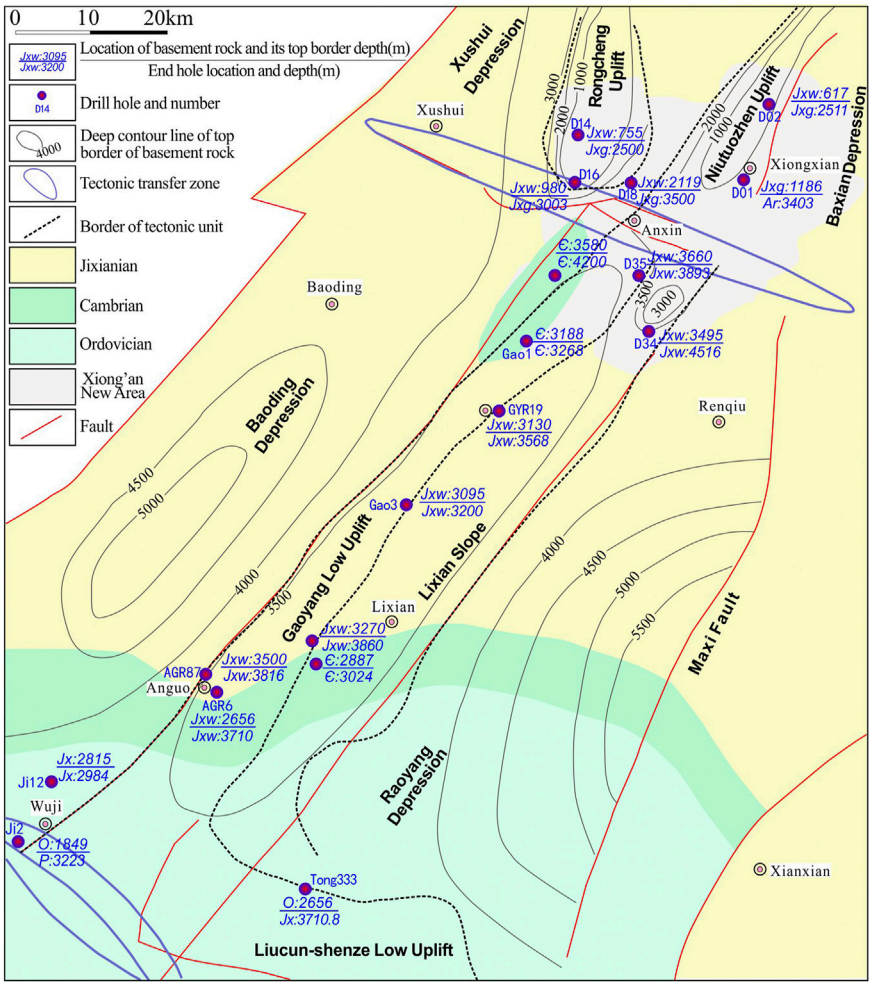

FIGURE 2 | Contour map of the buried depth of the top boundary of the Gaoyang geothermal field and the surrounding bedrock heat reservoir.

crust" in the Triassic–Jurassic to "hot mantle but cold crust" stage in the Cretaceous–Cenozoic (Zuo et al., 2013). It can be concluded that thermal erosion is a factor deduced from the thinning of the NCC lithosphere. The thinning of the lithosphere made the eastern NCC at a high degree heat flow (60–68 mW/m^2).

2.3 Neotectonics and Its Dynamic Mechanism

Neotectonic movements are not well developed in the study area, whereas the Maxi fault in the eastern Raoyang depression is a large strike-slip fault in the Cenozoic, which is a part of the Tangshan-Hejian-Cixian active tectonic zone. It is a new-born seismotectonic zone consisting of the Cixian-Handan fault, Xinhe fault, Tangshan fault, and Maxi fault. Most of them are right-lateral normal with NE trending. The earthquakes in this area are strong today. About 4 M > 7.0 earthquakes were recorded, including the 1966 Xingtai M7.2 earthquake and the 1976 Tangshan M7.8 earthquake. The focal rupture is dominated by the right lateral strike-slip fault, and a steep dip was formed during the process (Xu et al., 1996).

Neotectonic movements in North China are controlled by the interaction of two lithospheric structures, that is, the far-field effect of India–Eurasia collision and the upwelling of lithospheric mantle. First, the eastward push in the northeastern Qinghai–Tibet resulted in compressional and strike-slip deformation occurring along the Tanlu fault zone in the eastern North China. Furthermore, the upwelling of deep mantle caused by the subduction of the Pacific plate dominated regional thermal subsidence and Quaternary mantle-derived volcanic activity in the eastern North China. These two lithospheric tectonic forces alternated in time and space, controlling the differential evolution history of neotectonic landforms in North China (Zhang et al., 2019). The surface crust is mainly controlled by the collision and push of the Indian plate, while the deep crust is affected by the westward subduction of the Pacific plate, providing an energy source for shallow movement and controlling super-large earthquakes on the surface. The regional deep strike-slip faults constitute the main channels

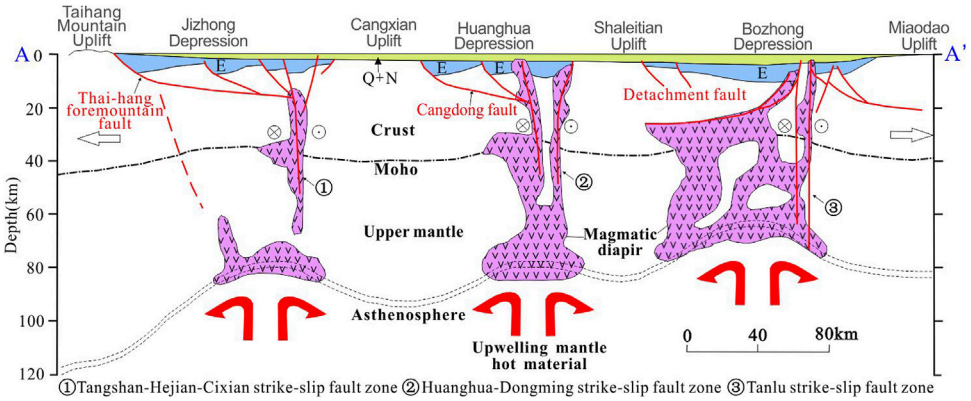

FIGURE 3 | Schematic diagram of the tectonic section of the Bohai Bay basin (see **Figure 2** for the content of the section line, after Xia et al., 2012; see **Figure 1** for section).

for the upwelling of the mantle heat (Xia et al., 2012; **Figure 3**). The high heat flow zone is closely related to the distribution of deep basement faults (Zuo et al., 2014).

2.4 Features of Geothermal Reservoir

The main strata of the Gaoyang geothermal field are Archean, Changcheng, Jixian, Cambrian, Ordovician, Paleogene (in depression and low uplift), Neogene, and Quaternary. The thermal reservoirs are mainly composed of the Jixian Wumishan, Changcheng, and Gaoyuzhuang formations. Above the Wumishan Formation, there is a thin Cambrian–Ordovician reservoir in the south of the geothermal field.

2.4.1 Jixian Wumishan Formation Reservoir

The Jixian Wumishan Formation reservoir consists of dolomite rocks located on the top of the Gaoyang low uplift and the Yanling buried hill in the northern Lixian slope. The depths of the top boundary and low boundary are 3,000–3,500 m and 3,500–4,000 m, respectively. The thickness of the Wumishan Formation is about 1,000–1,400 m, and the average thickness ratio is about 19%. The rock porosity is generally less than 6%, and the maximum and the average are 22.4% and 3.39%, respectively. The permeability ranges from 0.01 to 1,000 mD, most (87.8%) distributed between 0.01 and 100 mD (Dai et al., 2019). The depth of D35 is 3,853 m, revealing 218.5 m of the Wumishan Formation reservoir (not penetrated). The main lithology is gray-white and light gray dolomite rocks with argillaceous. The lower segment contains blue-gray, brown intrusive diorite porphyrite and structural breccia, and the upper segment is highly weathered with well-developed fractured karst. The thickness of the fractured aquifer is 43 m, accounting for 19.68% of the formation.

2.4.2 Changcheng–Gaoyuzhuang Formation Reservoir

Several wells were drilled to the Changcheng–Gaoyuzhuang Formation with thickness over 1,000 m in the study area. The lithology is dominantly gray dolomite intercalated with argillaceous and siliceous dolomite with flint. The porosity is 2–6% and with permeability varying from 0.1 to 160 mD. The temperature of the formation is generally around 75–95°C. The yield and TDS of well water are ~45–80 m^3/h and 3,000 mg/L, respectively. The depth of D34 is 4,507.43 m, revealing 814.43 m of the Changcheng–Gaoyuzhuang Formation (not penetrated). The main lithology is gray and off-white dolomite rocks with a lot of flint and a small amount of calcite particles and quartz. The overlying Yangzhuang Formation (209.19 m) and Wumishan Formation (29 m) are composed of purple-red and off-white gravel-bearing dolomite rocks and off-white dolomite, respectively. The thickness of the fractured aquifer in the Gaoyuzhuang Formation is 173 m, accounting for 21.24% of the total formation.

2.4.3 Cambrian–Ordovician Reservoir

The Cambrian–Ordovician reservoir is mainly distributed in Anguo-Boye-Lixian-Anping on the southern Gaoyang geothermal field. The top boundary has karst fissures with a depth of 2,800–3,500 m. The Ordovician Formation accounts for 32% in total reservoir thickness, whereas the ratio of Cambrian Formation is 16.5%. AGR50 reveals 460 m of the Cambrian reservoir, and the depth of the top boundary is 3,000 m.

The top boundary of the Jixian Formation in the buried hill of Anxin-Wen'an transfer zone is buried at a depth of 2,500–3,500 m and the depression bedrock with a depth more than 4,000 m. While outside the study area, the depth of the depression bedrock can reach to 5,000 m. The maximum depth of the bedrock in the Raoyang depression is more than 6,500 m, and that in the Baxian depression is above 10,000 m. The Anxin-Wen'an transfer zone is the direction of fluid (oil and gas) migration and a favorable place for fluid (oil and gas) accumulation in the Raoyang depression and Baxian depression.

3 METHODS

3.1 Deep Geological Structure

For analyzing the upwelling of hot materials from the mantle or deep crust and the influence of their activity mechanism on the deep geothermal anomaly, the deep geological structure of the

study area is researched. We collected previous magnetotelluric soundings and artificial seismic soundings of the study area (Liu and Liu, 1982; Dai et al., 1995; Lu et al., 1997; Xu 2003) to determine the depth of the asthenosphere and the undulation shape of the top surface and Moho surface of the circle. The multilayer structure, the interlayer active surface, and the active structure of the crust in the study area are further identified and the upwelling mechanism and channel of deep thermal materials analyzed.

3.2 Method of Correction of Earth's Heat Flow

Heat flow refers to the heat transferred from the interior of the earth to the surface by heat conduction per unit area and unit time and then dissipated into space. Under one-dimensional steady-state conditions, the heat flow is the thermal conductivity of the rock and the vertical temperature product of gradients (Lin W. J. et al., 2021).

Based on the Fourier's law, the heat flow value was calculated by multiplying the geothermal gradient with the thermal conductivity value (**Eq. 1**) (Bullard and Schonland, 1939). The surface heat flow value can also be calculated by combining the basal heat flow value at the bottom of the formation with the heat flow value contributed by radiogenic heat production within the overlying formation (**Eq. 2**) (Morgan, 1984).

$$Q = \lambda \frac{dT}{dZ} \tag{1}$$

$$Q_b = Q_0 - A \cdot \Delta Z \tag{2}$$

where Q is the heat flow in $mW \cdot m^{-2}$, dT/dZ is the temperature gradient in $^{\circ}C \cdot km^{-1}$, λ is the thermal conductivity, Q_b and Q_0 are the heat flows at the bottom and top of the formation, ΔZ is the formation thickness in km, and $A \cdot \Delta Z$ is the heat flow value, which was contributed by the overlying formation.

The "baking" effect of higher-temperature hot water formed by hydrothermal convection from deep dolomite geothermal reservoirs and the influence of lateral convergence of heat flow on regional normal heat flow needs to be eliminated. Based on the heat transfer due to the heat flow of the metamorphic bedrock layer in Well D01 and the heat flow values generated by the heat generation rate of the upper rock layer, combined with the formation information of different wells in the study area and the heat generation rate data of different rock layers, the heat flow value in the Xiong'an New Area is recalculated, to analyze and evaluate the size of the real heat flow value in this area (Wang et al., 2021).

3.3 Test of Productivity on Geothermal Storage

For evaluating the productivity of the D34 and D35 geothermal wells, a high-temperature and high-pressure well test experiment was conducted in this research. The working pressure of the pressure sensor is 0–100 MPa, and the working temperature is 0–150°C. When it is put down to 350 m depth of the well, the probe records the pressure and temperature every 10 s. Then the probe is raised and the data are read (**Figure 4**). The pressure and temperature of the three trips are verified with the manually measured water level. After pumping, the end pressure is tested at the discharge port with a pressure gauge installed at the wellhead. Compared with the manually measured temperature, pressure, and flow data, the errors are all within 3%, indicating that the obtained data are accurate. The total flow and steam flow of the mixture were roughly calculated using the James end-pressure method.

The productivity parameters of D34 and D35 geothermal wells constructed in this research are shown in **Table 1**. Combined with the data of the surrounding carbonate geothermal wells, the wellhead temperature of the carbonate geothermal wells buried below 4,500 m is generally 95–120°C, with the bottom hole temperature being 105–140°C of the Gaoyang geothermal field. It is assigned to the middle-temperature geothermal resources. The total flow of the steam–water mixture in a single well is 234.59–331.92 t/h, the steam flow is 4.51–4.76 t/h, the dryness is 1.36–2.03%, and the single-well power generation potential is 2.10–2.55 MW, which has a good development potential.

3.4 Comprehensive Logging

For obtaining the porosity, permeability, and other aquifer properties of the carbonate geothermal reservoirs of D34 and D35, full hole logging is carried out by SKD-3000B numerical control logging tool. The logging items include well temperature, well diameter, well deviation, resistivity, natural potential, natural gamma, and time difference of acoustic wave. The average relative errors of natural gamma ray, 2.5 m gradient resistivity, and 0.5 m potential resistivity are 4.5, 4, and 4.5%, respectively. All the logging quality meets the specification requirements. The logging data are processed by forward exploration logging interpretation platform.

According to the results of logging interpretation and core logging, it is concluded that the geothermal reservoir of D34 is mainly Gaoyuzhuang Formation of Jixian and that of the D35 is mainly Wumishan Formation. The performance parameters of the geothermal reservoir aquifer of the geothermal well are shown in **Table 2**. The logging results show that Wumishan and Gaoyuzhuang formations on the depth of the study area are carbonate geothermal reservoir aquifers with fracture karst or karst fractures, with relatively developed voids and strong permeability, which ensure the high productivity of Jixian system geothermal reservoir in deep depth. Among them, the well temperature is measured after standing for 120 h after the well test, for ensuring steady-state well temperature data. According to the well temperature measurement results, the steady-state temperature measurement curve of geothermal well is drawn (**Figure 5**).

4 RESULTS AND DISCUSSION

4.1 Heat Control of the Lithosphere, the Moho Uplift

The Pacific plate subducted westward in the Early Jurassic and subducted toward the NW low-angle plate in the Late Jurassic–Early Cretaceous (~170 Ma), causing the subduction

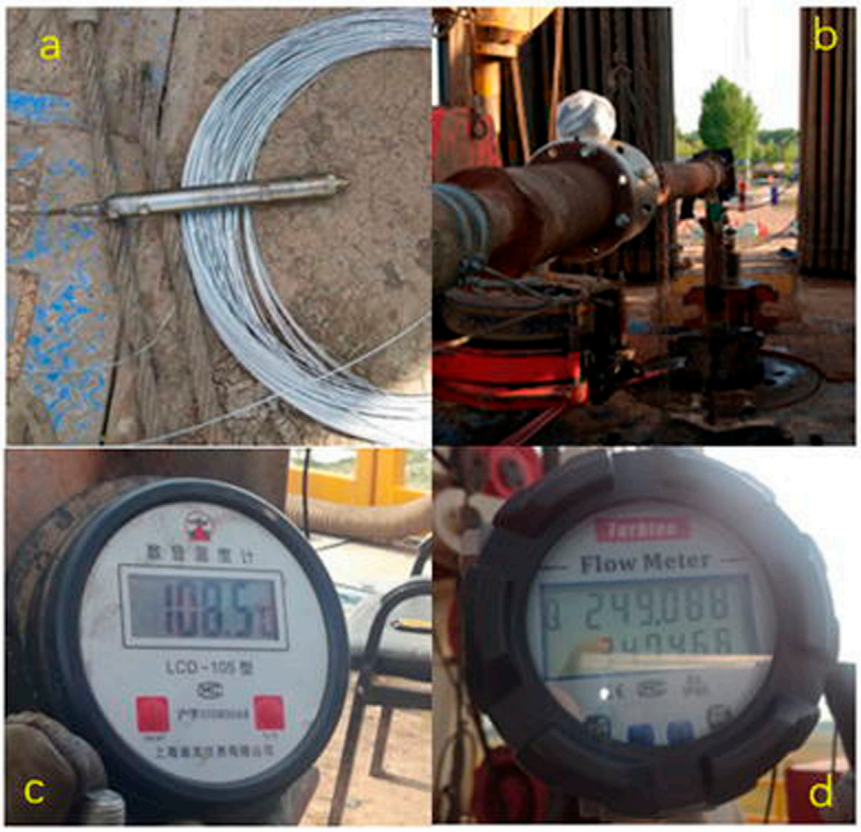

FIGURE 4 | Well test equipment: **(A)** CEP2 high-temperature probe; **(B)** end-pressure gauge; **(C)** thermometer; **(D)** flow meter.

TABLE 1 | Parameters of geothermal well thermal reservoir capacity evaluation of D34 and D35.

No.	Formation of water intake	Depth of water intake (m)	Wellhead temperature (°C)	Average temperature of geothermal reservoir (°C)	Diameter of discharge pipe (cm)	End pressure of discharge pipe (bar)	Total flow of steam–water mixture (t/h)	Steam flow (t/h)	Dryness (%)	Power generation potential of single well (MW)
D34	Gaoyuzhuang	3,458.78–4,507.43	123.4	133	15	2.2	234.59	4.76	2.03	2.10
D35	Wumishan	3,660–3,853	109.2	116	15	3.1	331.92	4.51	1.36	2.55

TABLE 2 | Properties of aquifer in the carbonate heat reservoir.

No.	Hydrothermal reservoir	Aquifer thickness (m)	Space form	Porosity (%)	Mean of porosity (%)	Permeability (mD)	Mean of permeability (mD)
D34	Gaoyang Formation of Jixian	10–57	Karst fissure	1.29–3.49	1.81	0.11–1.56	0.33
D35	Wumishan Formation of Jixian	2.3–8.30	Karst cave, solution crack	1.85–7.20	3.93	0.24–9.93	3.16

zone to migrate to the interior of the North China Craton (Ling et al., 2009; Ling et al., 2013). The massive thinning of the lithosphere caused by the NCC destruction has been confirmed based on large amounts of geophysical exploration results. Driven by the subduction of the western Pacific plate, the asthenospheric molten material moved to both sides, causing

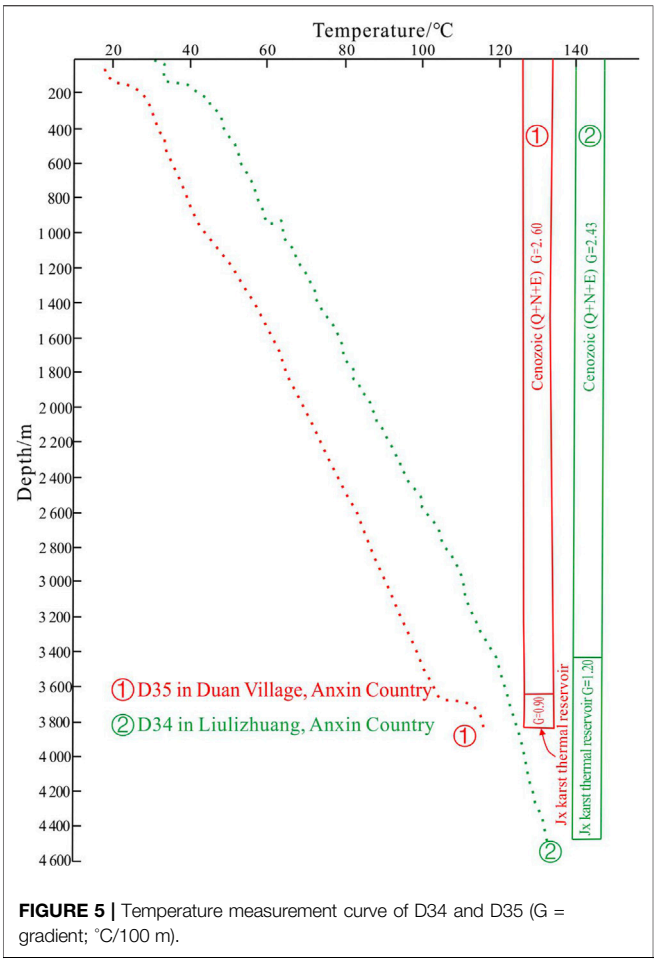

FIGURE 5 | Temperature measurement curve of D34 and D35 (G = gradient; °C/100 m).

obvious damage to the eastern NCC. In the eastern NCC, the Moho depth is 33 km, and the lithosphere and the crust are significantly thinner than in the central and western NCC. The massive thinning of the lithosphere promotes the conduction of mantle-sourced heat and facilitates deep thermal energy to enter the shallow crust (Wang et al., 2017).

According to the research of Liu and Liu (1982), it can be concluded that the depth of the top surface of the asthenosphere is the consistent position of the high-conductivity layer on the mantle and the low-velocity zone in earthquake. Due to the upwelling of the asthenosphere caused by the destruction of the North China Craton, the lithosphere in the Bohai Bay Basin is obviously thinner, and the lithosphere in the Jizhong depression is thinned to 50–70 km (**Figure 6A**), which is more than 10 km thinner than the surrounding uplift. At the same time, the thickness of the Moho surface in the Jizhong depression is reduced to 32 km, which is 2–4 km thinner than the surrounding uplift (**Figure 6B**). It can be recognized that there is a clear mirror image relationship between the large depression basement and the Moho uplift (Dai et al., 1995; Xu 2003), which means that the asthenosphere and the Moho uplift, the uplift of high-conductivity and low-velocity layers in the crust, the differential movement in the fault block, the basement fault, the strong magma, and other deep activities are relatively well developed in areas with thinner lithosphere. Therefore, the heat flow and temperature of the depression are higher than that of the uplift at the same depth below the Heat Flow Equilibrium Line.

4.2 Upwelling and Pathways of Deep Heat

Driven by the subduction of the western Pacific plate in the Early Jurassic, a large amount of slab fluid or melt was released into the overlying mantle wedge (**Figure 7A**). During the Early Jurassic, the Paleo-Pacific plate subducted westward and then turned into a low-angle northwestward flat plate subduction in the Late Jurassic–Early Cretaceous (~170 Ma), causing the subduction zone to migrate into the NCC (Ling et al., 2009; Ling et al., 2013), and large amount of slab fluid or melt was released into the overlying mantle wedge (**Figure 7A**). The retreat of the subducted plate in the Early Cretaceous (~130 Ma) caused large amounts of asthenospheric mantle upwelling, which induced the formation of large-scale intraplate magma with high oxygen fugacity (fO_2) (**Figure 7B**). The subduction and retreat of the western Pacific plate caused the asthenospheric heat upwelling in the eastern NCC, reaching the top of the upper mantle and intruding into the crust along the existing supercrust faults (such as the Maxi fault), which resulted in the dehydration of hydrous minerals in the upper mantle and lower crust to produce fluids. From previous studies, the water content of the mantle below the NCC exceeded 1,000 ppm at about 120 Ma and was significantly higher than that of other cratons during the same period, which in turn may have led to the formation of low-velocity and high-conductivity layers in the crust and upper mantle (Xia et al., 2013).

The crust of the Jizhong depression basement has a multilayer structure and interlayer active surfaces, which can generally be divided into high-velocity and low-conductivity upper crust, low-velocity and high-conductivity middle crust, and high-velocity and low-conductivity lower crust (**Figure 8**), evidenced by artificial seismic and magnetotelluric sounding data. The high-conductivity layer is about 15–22 km deep between the middle and lower crust and it is also the location of the deep interlayer sliding surface. The shallow normal faults mostly end in this low-velocity zone (Liu et al., 1984; Lu et al., 1997). Seismic sources mostly occur at the bottom of the upper crust and in the low-velocity middle crust, whereas medium-strong earthquakes mostly occur near the top of the low-velocity middle crust. This indicates that the low-velocity and high-conductivity layer of the middle crust is tectonically active, which is conducive to connect the mantle heat and become a channel for the upwelling of deep mantle-derived heat by cooperating with the deep faults that cut through the crust and even lithosphere. The upwelling geothermal fluids and eruption magma along the deep faults are the main controlling factors for the formation of deep linear (stripe) and beaded thermal anomalies. At the same time, the upwelling mantle-derived heat can also promote the activation of deep fractures or the formation of new fractures and upwelling other heat (Zhang et al., 2020). The characteristic of He isotope of gas reservoirs in the Hejian section of the Maxi fault has an anomalous zonal distribution (R/Ra>1) (Dai et al., 1995), indicating that mantle-derived material may migrate to the shallow crust along the Maxi fault. The contribution of mantle-derived He is between 5 and 8%,

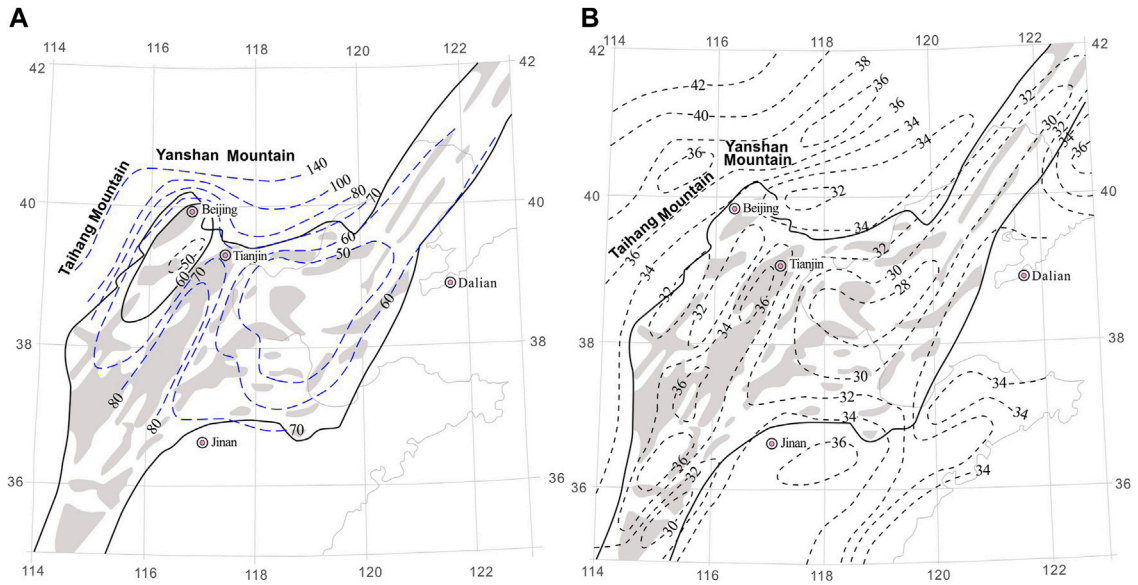

FIGURE 6 | The top surface of the asthenosphere **(A)** and the Moho isobaths **(B)** in the Bohai Bay basin (modified from Liu and Liu, 1982).

showing that deep faults are regional heat-controlling structures and channels for deep fluid convection into shallow reservoirs (Pang et al., 2018). The D34 and D35 have relatively high temperature, which are 20 km away from the Maxi fault. Furthermore, the Anxin-Wen'an structural transfer zone has faults that directly intersect the Maxi fault, which is conducive to connect deep heat sources.

4.3 Distribution of Heat Flow in the Shallow Crust

4.3.1 Heat Control of the Uplift and the Depression

As the thermal conductivity of the bedrock in the uplift is significantly higher than that of the Cenozoic sediments in the depression, the uplift and depression are favorable for distribution and redistribution of heat flow (Xiong and Zhang, 1984; Chen, 1988). Therefore, the deep heat flow is more likely to accumulate to the uplift with high thermal conductivity. The Niutuo geothermal field is well known because of its shallow geothermal anomaly formed by a high geothermal gradient. However, it is just for the shallow crust. For the deep crust, the heat flow accumulates from the depression to the uplift below the horizontal Heat Flow Equilibrium Line (Xiong and Gao, 1982), and above the line when the trend of the accumulation is opposite. Mao (2019), Mao (2018) also studied temperature distribution characteristics and controlling factors in geothermal field and referred to the phenomenon similar to the Heat Flow Equilibrium Line as the High Conductivity Homogenization Depth (Mao, 2019; Mao, 2018). The reasons for this phenomenon may be as follows: first, the thinner lithosphere in the depression is conducive to the upward conduction of deep heat sources; second, deep strike-slip faults tend to spread along the bottom of the depression, which is conducive to the deep heat upwelling; third, the thermal conductivity of the Cenozoic loose sediments in the depression is lower than that of the base rock in the uplift. These factors cause the temperature at the bottom of the Cenozoic to be significantly higher than that of the uplift at the same depth. The thickness of the Cenozoic is more than 5,000 m in the Baoding depression in the western Gaoyang geothermal field, more than 6,000 m in the Raoyang depression in the east, and can reach to 10,000 m in the Baxian depression in the northeast. As a result, the temperature at the bottom of the Cenozoic around the Gaoyang geothermal field is maintained at 130–300°C and makes it a stable heat source for continuously heating the carbonate reservoirs in the Gaoyang geothermal field.

Combined with the basic heat flow values in the metamorphic rock of well D01 and the heat flow values contributed by the radiogenic heat production of the overlying strata, the surface heat flow values of the Xiong'an New Area were recalculated and the heat flow contour map was drawn (**Figure 9**). It can be seen from **Figure 9A** that before the heat flow correction, the calculated terrestrial heat flow values of the Niutuozhen uplift are significantly higher than those of the Rongcheng uplift and Gaoyang uplift, and the terrestrial heat flow values of the Rongcheng uplift is significantly higher than those of the Gaoyang uplift. These are mainly caused by the difference in thermal conductivity, which leads to the lateral accumulation of the depression area and the section with a large burial depth of carbonate geothermal reservoir to a high bulge with a small thermal storage burial depth. **Figure 9B** shows that the corrected heat flow of the Gaoyang uplift is slightly higher than that of the Niutuozhen uplift and the Rongcheng uplift, which is mainly due to the larger thickness of the Cenozoic in the Gaoyang uplift. The Rongcheng uplift is mainly metamorphic

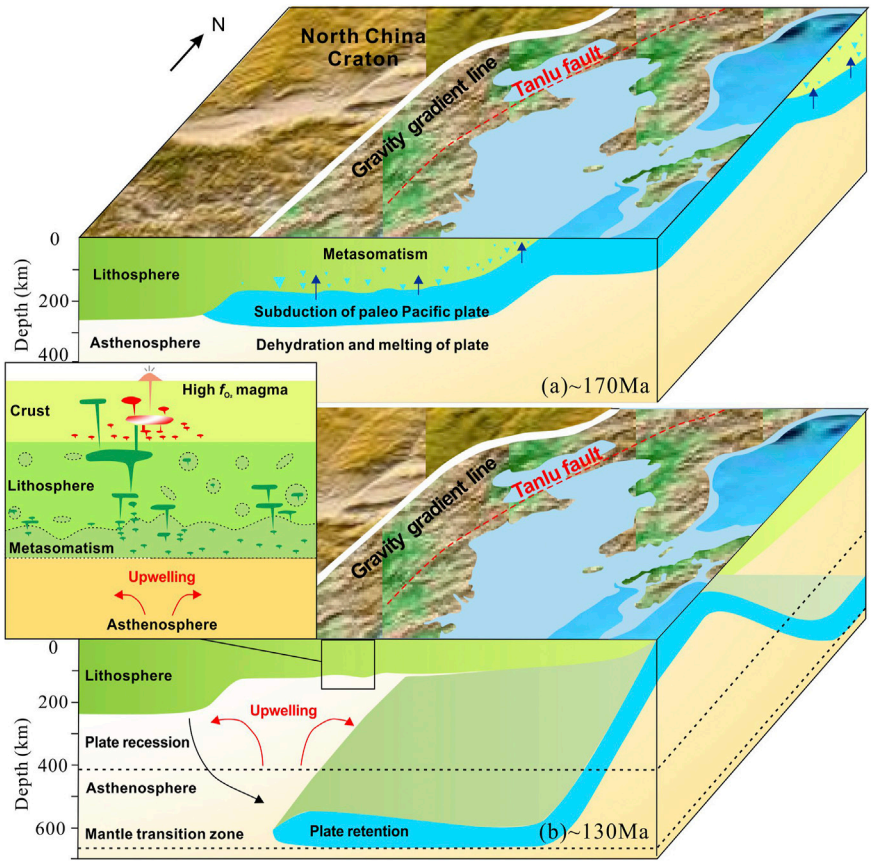

FIGURE 7 | The upwelling mechanism of the mantle-derived thermal material caused by the subduction and retraction of the Paleo-Pacific plate. **(A)** The subduction of the Paleo-Pacific plate may have started in the Early Jurassic. Northwestward flat subductions began in the Late Jurassic to Early Cretaceous, which may have reached the inner land and was responsible for the destruction of the NCC (Ling et al., 2009, 2013). Much slab fluid and melt releases into the overlying mantle wedge. **(B)** The retreat of the (Paleo)-Pacific plate resulted in the upwelling of the asthenospheric mantle and triggered the formation of large-scale high fO_2 intraplate magmas.

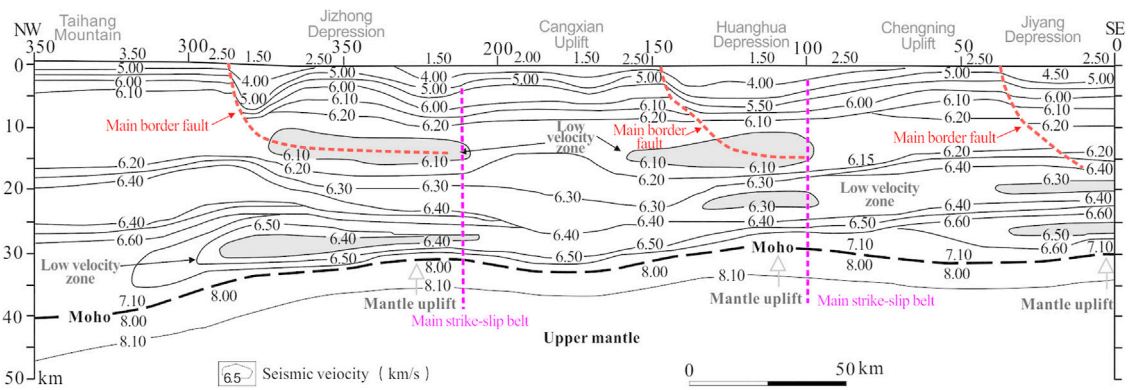

FIGURE 8 | Sectional view of the deep structure in North China (according to Liu et al., 1984).

rocks below the depth of 3,000 m, while the Gaoyang uplift still has carbonate geothermal reservoir of about 1,000 m, and there is still a certain degree of deep circulation convection of hot water.

Numerous concealed basaltic rocks are developed in the Jizhong depression (Wang et al., 2012), and hypabyssal intrusive rocks are distributed in the uplift and the

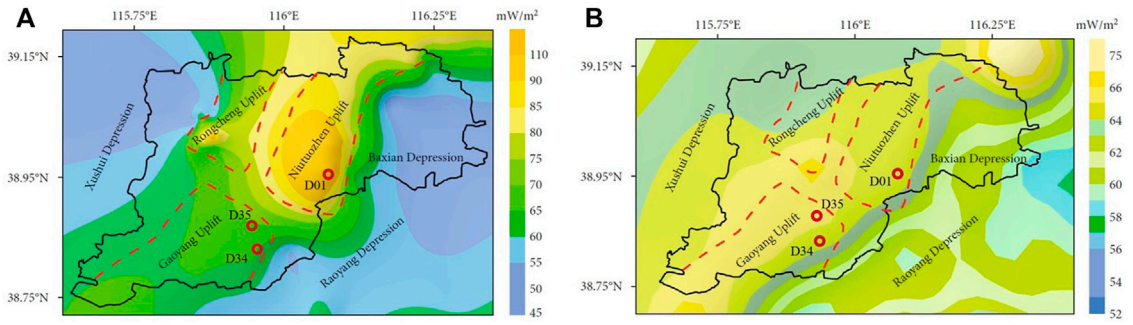

FIGURE 9 | Comparison of the heat flow map before **(A)** and after correction **(B)** (according to Wang Z. et al., 2021).

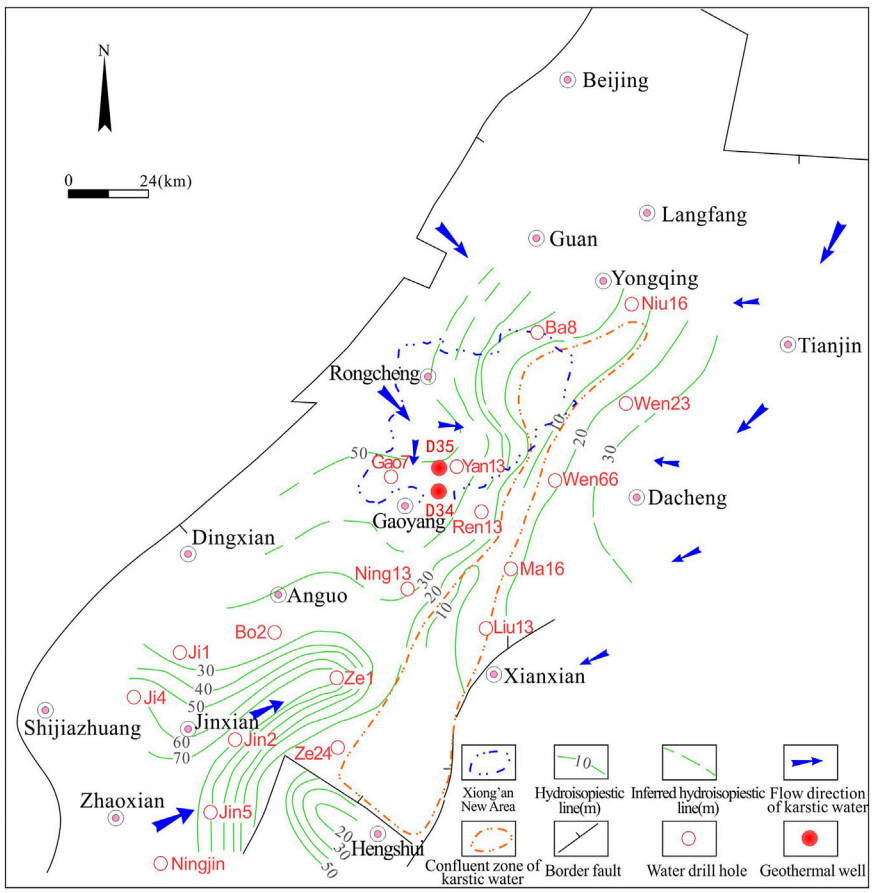

FIGURE 10 | Contour map of the phreatic pressure level elevation in the Jizhong depression (according to Yan and Yu, 2000).

depression in the study area. This area is dominated by Paleogene intrusive rocks. According to the research about D19 in the northwestern Anxin, it is confirmed that the 120 m thick metamorphic basalt is exposed below 3,000 m, and a small amount of blue-gray, brown intrusive diorite porphyry in the Wumishan Formation is also exposed in the lower interval of D35. Although the residual heat retained by early magmatic activities is very small, basalt and diorite porphyry with low thermal conductivity reduce the upward conduction of heat flow. Large-scale layered intrusive rocks can form a "cotton" effect, which makes local geothermal anomalies.

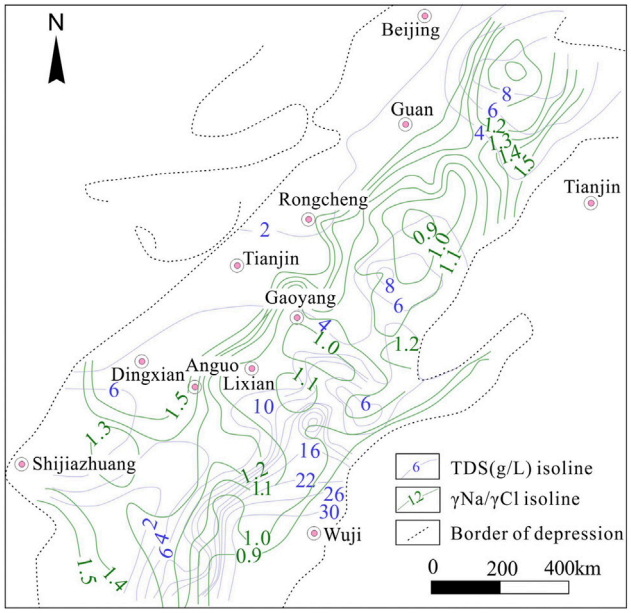

FIGURE 11 | Contour maps of TDS and γNa/γCl of carbonate geothermal water in the Jizhong depression (according to Yan and Yu, 2000).

4.3.2 Deep Circulation Convection Heating of Groundwater Along Faults

Fault structures and caprock conditions also strongly control the accumulation and dissipation of subsurface heat (Lin W. et al., 2021). The faults in the study area control the development of karst and karst paleomorphology. Structural rupture and deformation produce cracks and fractures, forming storage spaces and seepage channels for heat reservoirs. The fractures and faults are conducive to groundwater activity and development of dissolution pores and karstification and finally form a pore–cavity–fracture system. The fault structures and karsts facilitate the groundwater rise after being heated by deep circulation and convection in carbonate rocks, making it easier for deep heat sources to reach the shallow crust to form local shallow thermal anomalies. Therefore, these fault zones are often the areas with well-developed heat reservoirs (Dai et al., 2019). The Cenozoic geothermal gradient (about 2.5°C/100 m) is significantly higher than that of the Jixian carbonate rocks (about 1.0°C/100 m) (**Figure 5**), indicating that the deep circulation and heat convection of groundwater in carbonate rocks below 3,500 m is still relatively strong. The development of fault in the study area provides a channel for the deep circulation heating of carbonate groundwater.

4.3.3 Influence of Hydrodynamic Field on Geothermal Field

Decades of geothermal water exploitation history and the influence of oilfield water injection activities have caused significant changes in the geothermal hydrodynamic field of bedrocks in and around Xiong'an New Area. The present geothermal water hydrodynamic field can no longer reflect the geothermal water recharge, runoff, and discharge conditions in the bedrocks' natural state. Therefore, we use the earlier hydrodynamic field characteristics (Yan and Yu, 2000) to illustrate the bedrock geothermal water recharge, runoff, and discharge conditions.

The bedrock geothermal water in the Jizhong depression is mainly recharged from Taihang Mountains in the west of the study area and Yanshan Mountains in the north (**Figure 10**). The groundwater level of bedrocks in the Anxin-Wen'an structural transfer zone is slightly higher than that in the uplift on the northern and southern sides. This may be due to a series of NWW–SEE faults in the Anxin-Wen'an structural transfer zone connecting the piedmont faults on the eastern foot of Taihang Mountains, making it easily recharge from the piedmont of Taihang Mountains. The Cangxian uplift is connected to the Yanshan Mountains in the northeast. The karst fissures of shallow carbonate reservoirs are developed and the recharge conditions are better. As a result, the groundwater level of bedrocks in the Cangxian uplift is significantly higher than that in the Jizhong depression on the western side. At the same time, the relatively shallow bedrocks in the Anxin-Wen'an structural transfer zone (the maximum depth is about 5,000 m) are favorable for groundwater derived from the Cangxian uplift to migrate west along the Anxin-Wen'an structural transfer zone. Groundwater from the east and west forms a hydrodynamic balanced zone on the western Renqiu (Zhang et al., 2015) and then flows slowly to the Raoyang and Baxian depressions on the northern and southern sides. In the southeastern Raoyang depression and the western Baxian depression, two confluence centers of regional bedrock groundwater (low potential areas) are formed under the condition of slow movement of groundwater, and heat accumulates to form high-temperature areas. The northeastern Gaoyang geothermal field is close to these two confluence areas, so its temperature is also high.

Contours of total dissolved solids (TDS) and metamorphic coefficient (γNa/γCl) of carbonate geothermal water in the Jizhong depression (Wang et al., 2010; **Figure 11**) show that the TDS in the southeastern Raoyang depression is above 10 g/L, and the metamorphic coefficient is lower than 0.90. TDS in the western Baxian depression is above 6 g/L, and the metamorphic coefficient is lower than 1.0, which respond well to the confluence center of the regional carbonate geothermal water. TDS of D35 is 2.6 g/L, and the metamorphic coefficient is 1.19. TDS of D34 is 2.98 g/L, and the metamorphic coefficient is 1.16. Refer to the carbonate geothermal hydrochemistry data in the Niutuo and Rongcheng geothermal fields; the closer to the confluence area of carbonate geothermal water, the larger the TDS and the lower the metamorphic coefficient, which are more conducive to heat accumulation.

4.4 Heat Accumulation Mechanism

Overall, the heat accumulation mechanism of the Gaoyang medium-temperature geothermal field can be summarized as follows (**Figure 12**). Affected by the westward subduction of the Pacific plate, the eastern NCC was significantly damaged, and the thickness of the lithosphere and crust was greatly reduced. The Moho surface obviously uplifted at the bottom of the depression, which caused the upwelling of asthenospheric

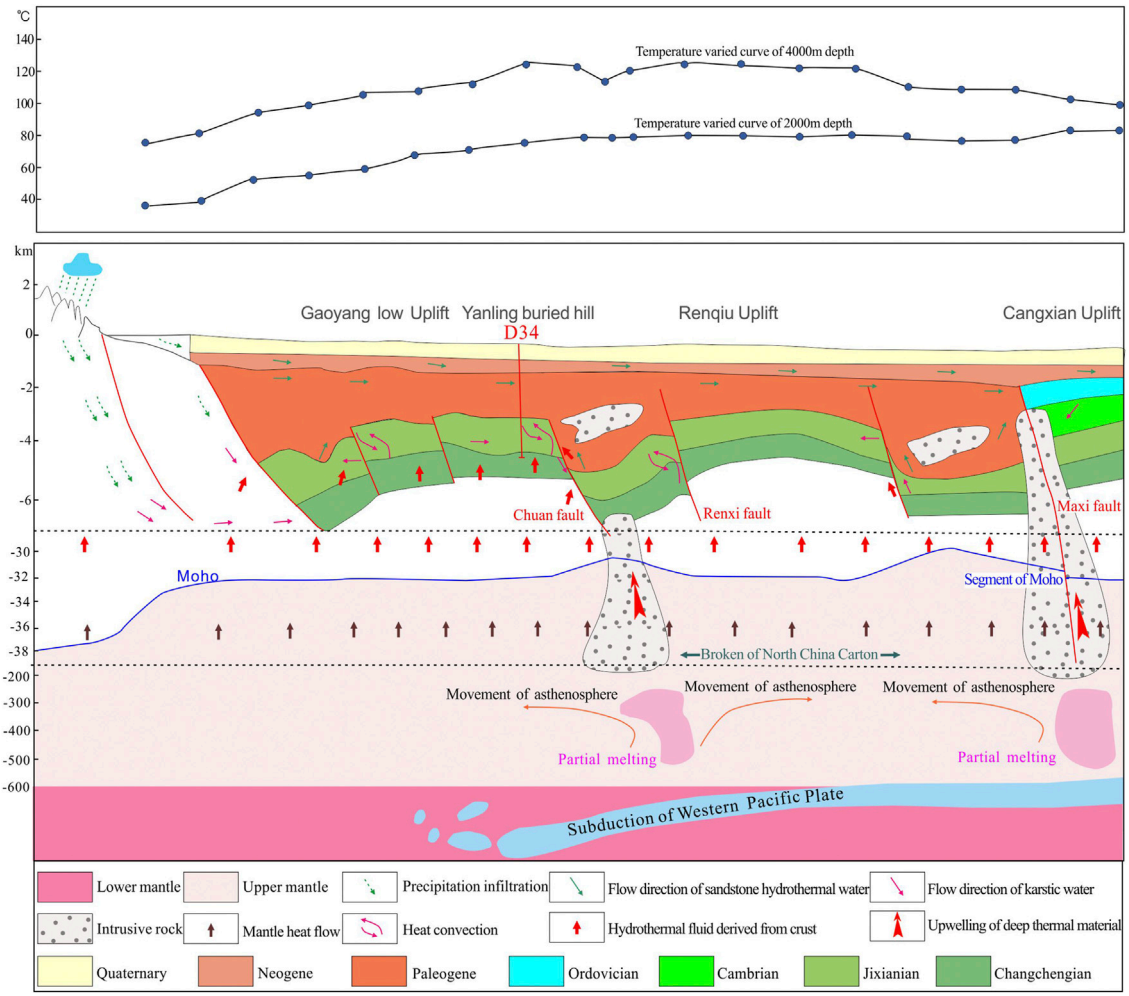

FIGURE 12 | Heat accumulation model of deep ancient buried hill in the northeast of the Gaoyang geothermal field.

mantle. When it reached to the top of the upper mantle, the super-crust faults (such as the Maxi fault) invaded into the crust. As a result, hydrous minerals in the top of the upper mantle and the lower crust dehydrated to produce fluids intruding into the crust with the deep magma. The thickness of the Cenozoic depression around the study area can reach up to 5,000–10,000 m, and the temperature is at 130–300°C at the bottom, which make it a stable source for continuous heating of the carbonate reservoirs in the Gaoyang geothermal field. Under the effect of "thermal refraction," the heat flow accumulates from the depression with low thermal conductivity to the uplift with high thermal conductivity. Moreover, large-scale intrusive rocks with high thermal conductivity in some sections also contribute to heat flow. Meanwhile, the groundwater is heated by deep cycle and convection along the Chuan fault, and the confluence area of regional karst groundwater also has a certain heat accumulation effect. Under the influence of these favorable factors, the Gaoyang medium-temperature carbonatite geothermal field was formed.

5 CONCLUSION

Combining deep geological structure and geodynamic processes in the deep lithosphere, this article discusses the heat accumulation mechanism and the development and utilization potential of geothermal resources in the Gaoyang medium-temperature carbonatite geothermal field.

1) The thermal reservoirs in the northern Gaoyang geothermal field are the Jixian Wumishan Formation, the Gaoyuzhuang Formation, and the Cambrian–Ordovician reservoir in the south. The fractured karst and karst fractures of the Jixian carbonate reservoir are relatively developed, and aquifers account for about 20% of the stratum. As for the carbonate reservoir in the geothermal field, its buried depth is generally 3,000–4,000 m; its geothermal temperatures at the top and in the middle are 95–115°C and 110–135°C, respectively. The total flow of steam–water mixture in a single well is 234.59–331.92 t/h, the steam flow is 4.51–4.76 t/h, the

dryness is 1.36–2.03%, and the single-well power generation potential is 2.10–2.55 MW.

2) The westward subduction of the Pacific plate caused obvious damage to the eastern NCC and great reduction to the thickness of lithosphere and crust, which promote the conduction of mantle-derived heat to the shallow crust. Deep strike-slip faults such as the Maxi fault cut through the lithosphere facilitate the deep mantle-derived heat and deep magma intruding into the crust. Besides, the heat flow accumulates from the depression with low thermal conductivity to the uplift with high thermal conductivity. Groundwater is heated by deep cycle and convection along the Chuan fault, and the confluence area of the regional karst groundwater also has a certain heat accumulation effect. The Cenozoic with a thickness of more than 3,000 m and good thermal insulation effect in the Gaoyang geothermal field are favorable factors for the high temperature of the bedrock thermal reservoir. Under the influence of these factors, the Gaoyang medium-temperature carbonatite geothermal field was formed.

DATA AVAILABILITY STATEMENT

The raw data supporting the conclusion of this article will be made available by the authors, without undue reservation.

AUTHOR CONTRIBUTIONS

BZ was responsible for the overall conception and main contents of the paper; SW participated in the main contents of the paper; FK participated in the introduction and main contents of the paper; YW was responsible for the preliminary writing of the paper in English; YL was responsible for the production of illustrations and the verification of English; JG participated in writing the hot storage part of the paper; WY participated in the writing of the geological structure part of the paper; YX participated in the calculation of geothermal resources.

FUNDING

This research was financially supported by the National Natural Science Foundation of China (Nos. U1906209, 42072331, and 41902310), Project of China Geological Survey (Nos. DD20189114 and DD20190132), and the Scientific Research Fund project of Hunan Geological Institute (No. hngstp202102).

ACKNOWLEDGMENTS

The editor, associate editor and reviewers are thanked for their constructive comments that helped greatly improve the paper.

REFERENCES

Bullard, E. C., and Schonland, B. F. J. (1939). Heat Flow in South Africa. *Proc. R. Soc. Lond. Ser. A. Math. Phys. Sci.* 173 (955), 474–502.

Chen, M. X. (1992). Advances of Studies of Geothermal Resources in China. *Adv. Earth Sci.* 7 (3), 9–14.

Chen, M. X. (1988). *Geothermal in North China*. Beijing: Science Press.

Chen, M. X., Huang, G. S., Zhang, W. R., Zhang, R. Y., and Liu, B. Y. (1982). The Temperature Distribution Pattern and the Utilization of Geothermalwater at Niutuozhen Basement Protrusion of Central Hebei Province. *Sci. Geol. Sin.* 17(3), 239–252.

Dahlstrom, C. D. A. (1970). Structural Geology in the Eastern Margin of the Canadian Rocky Mountain. *Bull. Can. Petroleum Geol.* 18, 332–406. doi:10.35767/gscpgbull.18.3.332

Dai, J. X., Song, Y., Dai, C. S., Chen, A. F., Sun, M. L., and Liao, Y. S. (1995). *Inorganic Gas and its Reservoir Forming Conditions in Eastern China*. Beijing: Science Press.

Dai, M. G., Lei, H. F., Hu, J. G., Guo, X. F., Ma, P. P., and Zhang, J. Y. (2019). Evaluation of Recoverable Geothermal Resources and Development Parameters of Mesoproterozoic Thermal Reservoir with the Top Surface Depth of 3500 M and Shallow in Xiong'an New Area. *Acta Geol. Sin.* 93 (11), 2874–2888. doi:10.1111/1755-6724.13979

Faulds, J. E., and Varga, R. J. (1998). "The Role of Accommodation Zones and Transfer Zones in the Regional Segmentation of Extended Terranes,". Geological Society of America Special Paper in *Accommodation Zones and Transfer Zones: Regional Segmentation of the Basin and Range Province*. Editors J. E. Faulds and J. H. Stewart, 323, 1–46. doi:10.1130/0-8137-2323-x.1

He, L. J., and Qiu, N. S. (2014). Heating and Craton Destruction. *Chin. J. Geol.* 49 (3), 728–738. doi:10.3969/j.issn.0563-5020.2014.03.002

Lin, W. J., Wang, G. L., Gan, H. N., Wang, A. D., Yue, G. F., and Long, X. T. (2021). Heat Generation and Accumulation for Hot Dry Rock Resources in the Igneous Rock Distribution Areas of Southeastern China. *Lithosphere* 2021 (Special 5), 2039112. doi:10.2113/2022/2039112

Lin, W., Wang, G., Zhang, S., Zhao, Z., Xing, L., Gan, H., et al. (2021). Heat Aggregation Mechanisms of Hot Dry Rocks Resources in the Gonghe Basin, Northeastern Tibetan Plateau. *Acta Geol. Sin. Eng.* 95 (6), 1793–1804. doi:10.1111/1755-6724.14873

Ling, M.-X., Li, Y., Ding, X., Teng, F.-Z., Yang, X.-Y., Fan, W.-M., et al. (2013). Destruction of the North China Craton Induced by Ridge Subductions. *J. Geol.* 121, 197–213. doi:10.1086/669248

Ling, M.-X., Wang, F.-Y., Ding, X., Hu, Y.-H., Zhou, J.-B., Zartman, R. E., et al. (2009). Cretaceous Ridge Subduction along the Lower Yangtze River Belt, Eastern China. *Econ. Geol.* 104, 303–321. doi:10.2113/gsecongeo.104.2.303

Liu, G. D., and Liu, C. Q. (1982). Crust and Upper Mantle Tectonics in Northern North China and Their Relationship with Cenozoic Tectonic Activity. *Sci. China Ser. B* 12 (12), 1132–1140.

Liu, G. D., Shi, S. L., and Wang, B. J. (1984). The High Conductive Layer in the Crust of North China and its Relationship with Crustal Tectonic Activity. *Sci. China Ser. B* 14 (9), 839–848.

Lu, K. Z., Qi, J. F., Dai, J. S., Yang, Q., and Tong, H. M. (1997). *Structural Model of Cenozoic Petroliferous Basin in Bohai Bay*. Beijing: Geological Publishing House, 1–251.

Mao, X. P. (2019). Characteristics of Temperature Distribution and Control Factors in Geothermal Field. *Acta Geol. Sin. Ed.* 92 (2), 96–98. doi:10.1111/1755-6724.14209

Mao, X. P. (2018). Genetic Mechanism and Distribution Characteristics of High Temperature Anomaly in Geothermal Field. *Acta Geosci. Sin. Ed.* 39 (2), 216–224. doi:10.3975/cagsb.2018.012201

Morgan, P. (1984). The Thermal Structure and Thermal Evolution of the Continental Lithosphere. *Phys. Chem. Earth* 15 (12), 107–193. doi:10.1016/0079-1946(84)90006-5

Morley, C. K., Nelson, R. A., and Patton, T. L. (1990). Transfer Zones in the East African Rift System and Their Relevance to Hydrocarbon Exploration in Rifts. *AAPG Bull.* 74, 1234–1253. doi:10.1306/0c9b2475-1710-11d7-8645000102c1865d

Pang, J. M., Pang, Z. H., Lv, M., Tian, J., and Kong, Y. L. (2018). Geochemical and Isotopic Characteristics of Fluids in the Niutuozhen Geothermal Field, North China. *Environ. Earth Sci.* 77 (1), 12.1–12.21. doi:10.1007/s12665-017-7171-y

Pang, Z. H., Kong, Y. L., Pang, J. M., Hu, S. B., and Wang, J. Y. (2017). Geothermal Resources and Development in Xiongan New Area. *Bull. Chin. Acad. Sci.* 32 (11), 1224–1230.

Qi, J. F. (2007). Structural Transfer Zones and Significance for Hydrocarbon Accumulation in Rifting Basins. *Mar. Orig. Pet. Geol.* 12 (4), 43–50. doi:10.3969/j.issn.1672-9854.2007.04.007

Qi, J. F. (2004). Two Tectonic Systems in the Cenozoic Bohai Bay Basin and Their Genetic Interpretation. *Geol. China* 31 (1), 15–22.

Wang, G. L., Li, J., Wu, A. M., Zhang, W., and Hu, Q. Y. (2018). A Study of the Thermal Storage Characteristics of Gaoyuzhuang Formation, A New Layer System of Thermal Reservoir in Rongcheng Uplift Area, Hebei Province. *Acta Geosci. Sin.* 39 (5), 533–541. doi:10.3975/cagsb.2018.071901

Wang, G. L., and Lin, W. J. (2020). Main Hydro-Geothermal Systems and Their Genetic Models in China. *Acta Geol. Sin.* 94 (7), 1923–1937. doi:10.1111/1755-6724.14469

Wang, G. L., Zhang, W., Lin, W. J., Liu, F., Zhu, X., Liu, Y. G., et al. (2017). Research on Formation Mode and Development Potential of Geothermal Resources in Beijing-Tianjin-Hebei Region. *Geol. China* 44 (6), 1074–1085. doi:10.12029/gc20170603

Wang, J. Y., Pang, Z. H., Hu, S. B., He, L. J., Hang, S. P., and Qiu, N. S. (2015). *Geothermics and its Applications*. Beijing: Science Press.

Wang, P. X., Yang, X., and Bian, X. D. (2012). Petrologic and Geochemical Characteristics of Igneous Rock in Jizhong Depression. *Geol. Sci. Technol. Inf.* 31 (4), 4–13.

Wang, S., Zhang, H. D., Sun, J. C., Guo, G. P., Jing, J. H., and Tian, G. S. (2010). *Modeling of Formation and Evolution of Deep Water and Hydrocarbon Migration and Accumulation in the Basin*. Beijing: Geological Publishing House.

Wang, S. Q., Zhang, B. J., Li, Y. Y., Xing, Y. F., Yuan, W. Z., Li, J., et al. (2021). Heat Accumulation Mechanism of Deep Ancient Buried Hill in the Northeast of Gaoyang Geothermal Field, Xiong'an New Area. *Bull. Geol. Sci. Technol.* 40 (3), 12–21. doi:10.19509/j.cnki.dzkq.2021.0319

Wang, Z., Gao, P., Jiang, G., Wang, Y., and Hu, S. (2021). Heat Flow Correction for the High-Permeability Formation: A Case Study for Xiong'an New Area. *Lithosphere* 2021 (Special 5), 9171191. doi:10.2113/2021/9171191

Wu, A. M., Ma, F., Wang, G. L., Liu, J. X., Hu, Q. Y., and Miao, Q. Z. (2018). A Study of Deep-Seated Karst Geothermal Reservoir Exploration and Huge Capacity Geothermal Well Parameters in Xiongan New Area. *Acta Geosci. Sin.* 39 (5), 523–532. doi:10.3975/cagsb.2018.071104

Xia, Q.-K., Liu, J., Liu, S.-C., Kovács, I., Feng, M., and Dang, L. (2013). High Water Content in Mesozoic Primitive Basalts of the North China Craton and Implications on the Destruction of Cratonic Mantle Lithosphere. *Earth Planet. Sci. Lett.* 361, 85–97. doi:10.1016/j.epsl.2012.11.024

Xia, Q. L., Tian, L. X., Zhou, X. H., Wang, Y. B., Yu, Y. X., and Lu, D. Y. (2012). *Tectonic Evolution and Deformation Mechanism of Bohai Sea Area*. Beijing: Petroleum Industry Press.

Xiao, S. B., Gao, X. L., Jiang, Z. X., and Qiao, H. S. (2000). Cenozoic Dextral Strike-Slip Motion in Bohai Bay Basin and its Meaning to Petroleum Geology. *Geotect. Metallogenia* 24 (4), 321–328. doi:10.3969/j.issn.1001-1552.2000.04.004

Xiong, L. P., and Gao, W. A. (1982). Characteristics of Geotherm in Uplift and Depression. *Chin. J. Geophys.* 25 (5), 60–68.

Xiong, L. P., and Zhang, J. M. (1984). Mathematical Simulation of Refraction and Redistribution of Heat Flow. *Chin. J. Geol.* 19 (4), 445–454.

Xu, C. F. (2003). Lithospheric Structure, Basin Structure and Hydrocarbon Migration in Mainland China. *Earth Sci. Front.* 10 (3), 115–127.

Xu, J., Han, Z. J., Wang, C. H., and Niu, L. F. (1996). Preliminary Study on Two Newly-Generated Seismotectonic Zones in North and Southwest China[J]. *Earthq. Reserch China* 10 (4), 393–401.

Yan, D. S., and Yu, Y. T. (2000). *Evaluation and Utilization of Geothermal Resources in Beijing Tianjin Hebei Oil Region*. Wuhan: China University of Geosciences Press.

Yang, M. H. (2009). Transfer Structure and its Relation to Hydrocarbon Exploration in Bohai Bay Basin. *Acta Pet. Sin.* 30 (6), 816–823. doi:10.3321/j.issn:0253-2697.2009.06.004

Yue, G. F., Wang, G. L., and Ma, F. (2020). The State and Convergence Mechanism of Geothermal Energy in the Buried Hills in Xiong'an New Area. *Geotherm. Energy* (2), 14–19.

Zhang, B. J., Gao, Z. J., Zhang, F. Y., Hao, S. H., Liu, F. Y., and Zang, J. J. (2015). Hydrodynamic Condition and Response of Formation Water Chemical Fields of Geothermal Water in North China Basin. *Earth Sci. Front.* 22 (06), 217–226. doi:10.13745/j.esf.2015.06.017

Zhang, B. J., Li, Y. Y., Gao, J., Wang, G. L., Li, J., Xing, Y. F., et al. (2020). Genesis and Indicative Significance of Hot Dry Rock in Matouying, Hebei Province. *Acta Geol. Sin.* 94 (7), 2036–2051. doi:10.19762/j.cnki.dizhixuebao.2020226

Zhang, Y. Q., Shi, W., and Dong, S. W. (2019). Neotectonics of North China: Interplay between Far-Field Effect of India- Eurasia Collision and Pacific Subduction Related Deep-Seated Mantle Upwelling. *Acta Geol. Sin.* 93 (5), 971–1001. doi:10.1111/1755-6724.14187

Zhu, R., and Xu, Y. (2019). The Subduction of the West Pacific Plate and the Destruction of the North China Craton. *Sci. China Earth Sci.* 62, 1340–1350. doi:10.1007/s11430-018-9356-y

Zuo, Y. H., Qiu, N. S., ChangHao, J. Q. Q., Li, Z. X., Li, J. W., Li, W. Z., et al. (2013). Meso-Cenozoic Lithospheric Thermal Structure in the Bohai Bay Basin. *Acta Geol. Sin.* 87 (2), 145–153.

Zuo, Y., Qiu, N., Hao, Q., Zhang, Y., Pang, X., Li, Z., et al. (2014). Present Geothermal Fields of the Dongpu Sag in the Bohai Bay Basin. *Acta Geol. Sin. - Engl. Ed.* 88 (3), 915–930. doi:10.1111/1755-6724.12246

Conflict of Interest: The authors declare that the research was conducted in the absence of any commercial or financial relationships that could be construed as a potential conflict of interest.

Publisher's Note: All claims expressed in this article are solely those of the authors and do not necessarily represent those of their affiliated organizations, or those of the publisher, the editors and the reviewers. Any product that may be evaluated in this article, or claim that may be made by its manufacturer, is not guaranteed or endorsed by the publisher.

frontiers | Frontiers in Earth Science

ORIGINAL RESEARCH
published: 15 June 2022
doi: 10.3389/feart.2022.872620

Effects of Seawater Recharge on the Formation of Geothermal Resources in Coastal Areas and Their Mechanisms: A Case Study of Xiamen City, Fujian Province, China

Chunlei Liu[1,2], *Yasong Li*[1,2], *Shengwei Cao*[1,2], *Wanli Wang*[1] *and Jing Li*[3]*

[1]The Institute of Hydrogeology and Environmental Geology, Chinese Academy of Geological Science, Shijiazhuang, China, [2]Fujian Provincial Key Laboratory of Water Cycling and Eco-Geological Processes, Xiamen, China, [3]Faculty of Environment, China University of Geosciences, Wuhan, China

The southeast coastal areas of China have abundant geothermal resources. Most especially, seawater-recharged geothermal systems in the coastal areas have large quantiles of recharge but suffer water salinization and low water temperature. Moreover, the geothermal water development in these areas may induce seawater intrusion. Understanding the genetic patterns of geothermal resources is significant for rational exploration and protection. This study analyzed the hydrochemical and environmental isotopic characteristics of geothermal water, groundwater, and surface water samples collected in the area with geothermal resources in Xiamen Province in the southeast coastal areas of China. Based on this, the recharge of geothermal water circulation and the genetic patterns of geothermal resources were revealed. The results of this study indicate that the geothermal water in mountainous areas and piedmonts in Xiamen is mainly recharged by rainfall infiltration. In contrast, the geothermal water in coastal areas in Xiamen is recharged by seawater mixing to different extents, as indicated by hydrochemical types, isotopic characteristics, and the C1-/Br- ratio of geothermal water. As revealed by the calculation results using the Cl^- mixing model, 10 of 13 geothermal fields in Xiamen are recharged by seawater mixing, with a mixing ratio of up to 73.20% in the Pubian geothermal field. After being recharged by rainfall in the low mountainous areas, geothermal water migrates toward deep parts along NW-trending faults. Then, it converges with regional NE-trending deep faults to absorb heat conducted from deep parts to form deep geothermal reservoirs. The deep geothermal reservoirs were estimated to be 185–225°C using the silica-enthalpy mixing model. The geothermal water is mixed with cold water or seawater while rising along faults. The temperature of shallow geothermal reservoirs was estimated to be 71–145°C using SiO_2 geothermometers.

Keywords: geothermal water, environmental isotope, geochemical geothermometer, seawater recharge, genesis of geothermal resources

OPEN ACCESS

Edited by:
Dawei Hu,
(CAS), China

Reviewed by:
Walter D'Alessandro,
National Institute of Geophysics and Volcanology, Section of Palermo, Italy
Kunal Singh,
Geological Survey of India, India

***Correspondence:**
Jing Li
lijing915@cug.edu.cn

Specialty section:
This article was submitted to Geochemistry, a section of the journal Frontiers in Earth Science

Received: *09 February 2022*
Accepted: *23 May 2022*
Published: *15 June 2022*

Citation:
Liu C, Li Y, Cao S, Wang W and Li J (2022) Effects of Seawater Recharge on the Formation of Geothermal Resources in Coastal Areas and Their Mechanisms: A Case Study of Xiamen City, Fujian Province, China. Front. Earth Sci. 10:872620. doi: 10.3389/feart.2022.872620

1 INTRODUCTION

Geothermal resources are new green energy resources that integrate heat, water, and minerals. They are rich and cause low-level environmental pollution compared to fossil energy resources. However, geothermal water with high salinity and high concentrations of As, Hg, F, and H_2S also poses risks of environmental pollution (Giggenbach, 1988; Ozgener and Kocer, 2004; Armienta et al., 2014). In the southeast coastal areas of China, which are in great demand for energy resources, the development and utilization of geothermal energy is an important measure for promoting sustainable urban development (Lin, 2007; Lin et al., 2016; Lin et al., 2020). The hydrothermal systems in southeast coastal areas of China circulate as follows. Faults develop in the low-permeability granite basement, and the atmospheric precipitation is heated through deep circulation in these faults and then rises to the Earth surface (Han and Zhuang, 1988; Hu and Xiong, 1990; Xiong et al., 1990; Liao, 2012; Gan, 2017; Gan et al., 2020). However, geothermal water in some coastal areas in Southeast China shows noticeable salinization and is rich in heavy isotopes, indicating the recharge by seawater mixing (Gao et al., 2009; Wang, 2018). Any changes in interactions between groundwater and seawater—the primary recharge factors of geothermal systems in coastal areas—will directly affect the quantity and quality of geothermal resources in coastal areas. The increase in mixed seawater may lead to a significant increase in the salinization and a decrease in the temperature of the geothermal water. By contrast, the decrease in the mixed seawater may lead to the depletion of geothermal resources. In this case, the exploitation of large amounts of geothermal water may cause the high salinization of geothermal water and seawater intrusion. The depletion and water quality deterioration of geothermal resources induced by the exploration of geothermal reservoirs in the southeast coastal areas of China can be effectively prevented by studying the formation conditions of seawater-recharged hot water systems and the genetic patterns of geothermal water and deeply understanding the formation and evolutionary patterns of low-medium temperature convective geothermal systems in these areas.

Southeast coastal areas are among the geothermal active areas with the most considerable potential for the development and utilization of geothermal resources in South China. These areas have widely distributed Mesozoic volcanic rocks and granites (Xiong et al., 1991; Zhang et al., 2018; Lin, 2022), abundant regional geothermal resources, and a ternary heat accumulation pattern consisting of the radioactive heat production by acidic rocks, heat transfer by faults, and heat retention by cap rocks (Li et al., 2020). Geothermal anomalous areas in southeast coastal areas are all located in low-lying areas such as intermountain basins, stream valleys, and plains. As indicated by the characteristics of the geothermal field in the geothermal anomalous areas, as well as the features of pores in strata, rock joints, and tectonic fractures (Qiu, 2018), the geothermal fields in the Southeast coastal areas lie at the intersections of NNW- and NE/NEE-trending faults (Han and Zhuang, 1988; Fan et al., 1993; Zhang et al., 2020). Among them, the NE -trending faults are major regional geothermal-controlling structures, while NEE- and EW-trending tensional faults serve as major regional water-conducting structures (Ma et al., 2021). As calculated using no-steam loss quartz thermometers, the hot springs in Zhangzhou-Xiamen areas have geothermal reservoir temperatures of 106–149°C and circulation depths of approximately 3400–5100 m (Lin et al., 2020). The recharge and salinization of geothermal water in coastal areas have always been controversial. The chemical and isotopic studies show that, in the Zhangzhou area, which is adjacent to the study area, the atmospheric precipitation mixes with seawater in the deep parts of geothermal fields, leading to a significant increase in the salinity of geothermal water and accordingly the formation of saline water (Pang, 1987). Existing studies are mainly focused on the genesis of geothermal resources from the regional structures and hydrochemical isotopic characteristics of geothermal fields and the estimation of geothermal reservoir temperature. However, few studies have been conducted on the genesis of geothermal sources and the recharge, runoff, and discharge conditions of geothermal fluids. Most especially, the contribution of seawater recharge to the formation of geothermal resources is yet to be ascertained. This study revealed the recharge mechanisms of geothermal water circulation and the genetic patterns of geothermal resources and will assist in effectively preventing and controlling the resource and environment problems such as geothermal water salinization, seawater intrusion, and the decrease in the geothermal water caused by geothermal water exploration and utilization.

2 REGIONAL GEOLOGICAL BACKGROUND

The study area lies in the coastal area in southeastern Fujian Province. It has a subtropical monsoon climate, with an average annual temperature of 20.8°C, an extreme maximum temperature of 38.4°C, and average annual rainfall of 1347.8 mm. Xiamen City lies at the eastern margin of the Cathaysia block of the South China Plate and in the zone where the southeastern margin of the Eurasian Plate interacts with the Pacific Plate (Wang et al., 1993). Because of the intensive and frequent Yanshanian magmatic activities, polyphasic rock masses were formed and widely distributed in the study area. Moreover, the Late Jurassic magmatic activities occurred on the largest scale among the Yanshanian magmatic activities. As a result, highly radioactive acidic Late-Jurassic and Early-Cretaceous granites are widely developed in the study area (Wang et al., 1996). Because of the large-scale Yanshanian magmatic activities, the deep Zhenghe-Dapu Fault Zone and the coastal deep Dongshan Island—Nan'ao Island Fault Zone extend from hundreds of kilometers to more than 1000 km in the NE and NNE directions. They have a long history of multi-stage orogenic activities and are increasingly active in areas closer to the coast (Wang, 1985). The movement of the Philippine Plate in the NW direction caused these deep faults to slide leftward or suffer compression and torsion, leading to the formation of a

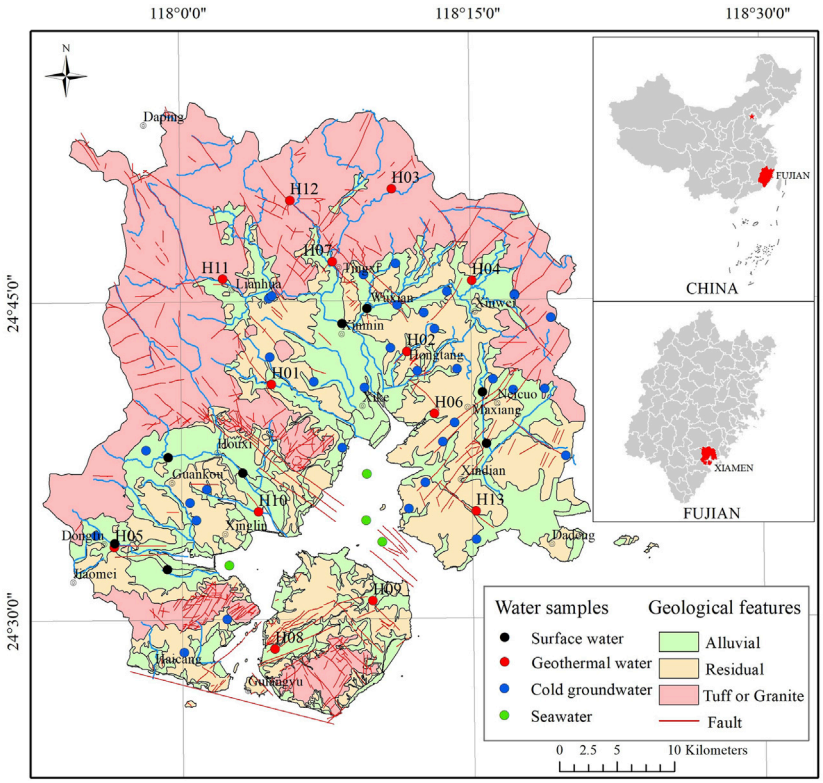

FIGURE 1 | Geological sketch of Xiamen and the distribution of sampling points.

set of tensional or transtensional faults in the NW direction (**Figure 1**).

The study area shows sporadic hydrogeological units, most of which are independent or semi-independent. The groundwater in these hydrogeological units is mainly recharged by atmospheric precipitation and discharges into the sea through short runoff. It can be divided into water in loose-rock porous rocks, water in mesh fractures of weathered zones, and water in bedrock fractures. The former two types of water are primarily distributed in shallow alluvial-diluvial and weathered eluvial strata. The water in bedrock fractures mainly occurs in joints and tectonic cracks in Yanshanian granites and Jurassic volcanic rocks.

3 SAMPLE COLLECTING AND TESTING

Thirteen water samples were collected from geothermal wells with depths of 48.6–500.8 m in the study area. Thirty-four water samples were collected from cold groundwater along the runoff direction of groundwater in the hydrological units of geothermal wells, including 26 samples of water in loose porous rocks (corresponding well depth: 3–25 m) and eight samples of water in bedrock fractures (corresponding well depth: 31–120 m). In addition, eight surface water samples were collected from rivers in the main recharge and discharge areas of groundwater and four samples were collected from seawater (**Figure 1**). The water temperature, pH, and electrical conductivity were measured on-site using the portable Eureka Manta2 water quality recorder. Water samples were stored in clean polyethylene bottles after being filtered using Millipore membrane filters with a pore size of 0.45 μm. Then, they were tested for anions, cations, and hydrogen and oxygen isotopes at the Key Laboratory of Groundwater Science and Engineering, Ministry of Natural Resources. Cations and anions SO_4^{2-} and Br^- were tested using the ICP-OES spectrometer (iCAP-6300) and the Dionex ICS-1500 ion chromatography system, respectively, with testing accuracy of 1% and charge-balance error of 5% or less. Anion Cl^- was tested using the titrimetric method, and SiO_2 was tested using UV-2550 spectrophotometer according to the silicon molybdenum yellow spectrophotometry. Using the method of wavelength-scanned optical cavity ring-down spectroscopy, hydrogen and oxygen isotopes were detected at a temperature of 22°C and relative humidity of 40% with the Picarro L2130-i isotope analyzer. The detection accuracy was 0.2‰ for δ18O and 2‰ for δ^2H. The testing results are shown in **Table 1**.

4 RESULTS AND ANALYSE

4.1 Hydrochemical Characteristics

The temperature of the hot water exposed in the study area is 37.6–88.9°C, and that of the cold groundwater in the area is 23.4–26.8°C. The pH of the geothermal water and surface water

TABLE 1 | List of hydrochemical characteristics of groundwater in Xiamen.

No.	Type	Well depth	T	pH	TDS	K^+	Na^+	Ca^{2+}	Mg^{2+}	Cl^-	SO_4^{2-}	HCO_3^-	CO_3^{2-}	Br^-	SiO_2	δ^2H	$\delta^{18}O$
		m	(°C)		(ppm)	(ppm)	(ppm)	(ppm)	(ppm)	(ppm)	(ppm)	(ppm)	(ppm)	(ppm)	(ppm)	(‰)	(‰)
G01	Cold Groundwater	3.0	26.2	7.02	550	46.3	33.3	96.8	11.1	34	70.3	285	0	<0.10	34.5	−33	−5.4
G02	Cold Groundwater	10.0	24.5	6.4	433	7.06	52	50.1	17.4	61.3	35.2	121	0	<0.10	29	−41	−6.5
G03	Cold Groundwater	44.0	25.4	6.78	248	4.68	14.3	59.6	4.15	17.5	31.5	170	0	<0.10	23.3	−33	−5.1
G04	Cold Groundwater	24.0	25.9	5.88	179	12.9	27.7	11.5	2.48	38.4	20.7	17.7	0	<0.10	28.3	−42	−6.4
G05	Cold Groundwater	11.0	24.6	4.55	222	0.86	27.1	31.3	3.83	40.3	14.1	6.07	0	<0.10	7.81	−38	−5.9
G06	Cold Groundwater	10.0	24.7	7.14	132	1.28	10.7	25.7	2.22	8.73	14.6	88.5	0	<0.10	19.6	−33	−4.7
G07	Cold Groundwater	10.0	24.8	5.35	174	3.2	19.6	21.8	4.06	30.5	9.36	18.2	0	<0.10	14.1	−38	−5.9
G08	Cold Groundwater	10.0	25.9	7.41	555	2.01	64.2	113	13.5	89.3	80.2	309	0	<0.10	22.3	−32	−5.2
G09	Cold Groundwater	38.0	26.8	6.72	98.3	3.75	9.33	4.46	0.92	5.24	3.13	30.5	0	<0.10	49.2	−42	−6.5
G10	Cold Groundwater	10.0	25.7	5.5	181	3.22	11.8	29.3	4.1	15.8	1.91	54.6	0	<0.10	20.6	−43	−6.6
G11	Cold Groundwater	25.0	25.9	6.17	71.5	4.44	9.48	4.08	0.3	8.73	2.47	18.3	0	<0.10	17.7	−34	−5.3
G12	Cold Groundwater	25.0	25.4	6.82	422	5.47	45.5	74.7	8.04	64.8	32.8	150	0	<0.10	11.9	−36	−5.6
G13	Cold Groundwater	13.0	25.1	6.28	244	29.3	36.7	18.4	2.44	41.9	48.3	55.5	0	<0.10	19.2	−37	−5.8
G14	Cold Groundwater	10.0	24.8	6.31	324	52.9	41.3	18.3	3.25	47.9	57.4	30.5	0	<0.10	4.42	−39	−5.9
G15	Cold Groundwater	9.5	25.5	5.86	107	6.04	12	7.98	1.09	15.4	4.87	24.3	0	<0.10	26	−37	−5.8
G16	Cold Groundwater	9.5	26.1	5.79	84	3.53	7.36	9.35	1.43	12.6	4.09	6.07	0	<0.10	10.4	−40	−6.1
G18	Cold Groundwater	9.0	25	6.61	399	4.32	33.6	69.8	9.25	51	38.2	101	0	<0.10	19	−35	−5.6
G19	Cold Groundwater	31.0	25.8	6.35	348	6.78	60.7	30.1	7.15	102	17.9	48.8	0	<0.10	40.2	−39	−6.1
G20	Cold Groundwater	11.3	25.9	7.08	306	7.88	36.1	45.9	4.39	46.5	41.9	82.4	0	<0.10	21.6	−34	−5.3
G21	Cold Groundwater	9.5	24.5	7.51	366	15.6	47.6	41.1	9.12	59.4	28.5	97.6	0	<0.10	25.9	−38	−5.9
G22	Cold Groundwater	10.0	25.6	7.67	132	5.74	17	6.02	1.63	16.1	3.52	31.7	0	<0.10	47.6	−42	−6.4
G23	Cold Groundwater	15.0	24.5	5.35	236	1.98	47.1	17.7	3.24	61.8	12.5	7.32	0	<0.10	13.2	−42	−6.5
G24	Cold Groundwater	11.0	25.4	7.59	414	26.6	44.6	51.1	9.45	60.4	35.1	98.9	0	<0.10	22	−40	−6.2
G26	Cold Groundwater	10.0	25.9	6.71	279	10.7	33.5	44	3.48	40.2	33.2	99.5	0	<0.10	11.1	−33	−5.2
G27	Cold Groundwater	8.0	25.7	6.88	708	4.96	86.5	131	14.7	114	87.9	250	0	<0.10	7.77	−36	−5.6
G28	Cold Groundwater	11.2	24.7	6.42	339	18.3	36.3	39.6	11.9	40.9	56.1	104	0	<0.10	20.3	−32	−5.2
G29	Cold Groundwater	14.4	24.8	6.3	344	2.53	47.3	37.5	15.2	64.6	54.6	64.1	0	<0.10	12.3	−39	−6.1
G30	Cold Groundwater	100.0	24.3	7.23	249	1.37	22.5	49	5.3	8.03	8.46	190	0	<0.10	52.1	−42	−6.3
G31	Cold Groundwater	120.0	25	6.9	186	2.39	17.3	29.3	4.06	9.43	6.48	122	0	<0.10	45.4	−43	−6.5
G32	Cold Groundwater	105.0	25.2	7.36	172	0.96	14.5	32.2	3.6	4.89	13.9	122	0	1.73	36.4	−47	−7.3
G33	Cold Groundwater	100.0	23.4	7.51	171	0.85	14.8	32.2	3.49	4.89	14.5	122	0	<0.10	36.4	−46	−7.2

(Continued on following page)

TABLE 1 | (*Continued*) List of hydrochemical characteristics of groundwater in Xiamen.

No.	Type	Well depth	T	pH	TDS	K^+	Na^+	Ca^{2+}	Mg^{2+}	Cl^-	SO_4^{2-}	HCO_3^-	CO_3^{2-}	Br^-	SiO_2	δ^2H	$\delta^{18}O$
		m	(°C)		(ppm)	(ppm)	(ppm)	(ppm)	(ppm)	(ppm)	(ppm)	(ppm)	(ppm)	(ppm)	(ppm)	(‰)	(‰)
G34	Cold Groundwater	100.0	25.1	7.92	251	0.71	58.6	25.8	0.54	21.7	33.5	140	0	<0.10	37.9	−47	−7
H01	Geothermal water	200.4	56.8	7.34	2300	15.9	619	237	0.71	1210	130	33.6	0	3.94	64.1	−48	−7.3
H02	Geothermal water	140.0	51.7	7.36	1100	8.62	332	53.9	0.23	459	108	104	0	1.17	75.4	−43	−6.4
H03	Geothermal water	48.6	48	8.91	301	1.36	85.2	2.84	0.08	14.7	55.8	73.2	18	<0.10	73.2	−51	−7.7
H04	Geothermal water	110.0	37.6	8.07	326	1.71	86	16.4	0.47	56.6	69	88.5	0	<0.10	49.3	−43	−6.5
H05	Geothermal water	150.6	80	7.11	3640	33.4	828	496	1.3	1950	216	48.8	0	6.4	83.4	−42	−6.2
H06	Geothermal water	151.1	47	6.92	8000	59.9	1830	1060	4.17	4630	297	36.6	0	16.5	84.7	−40	−5.9
H07	Geothermal water	160.0	45.5	7.82	391	2.81	112	14.8	0.26	52.4	73.8	142	0	<0.10	56.3	−43	−6.4
H08	Geothermal water	202.0	38.2	6.94	19300	86.4	4040	2940	185	11100	866	45.8	0	35.3	65.9	−29	−4.2
H09	Geothermal water	150.0	53.6	6.65	17600	127	4320	1870	118	10400	609	84.8	0	38.7	79.1	−29	−4.2
H10	Geothermal water	500.8	88.9	6.86	13800	95.3	3520	1410	129	7550	690	67.1	0	27	107	−32	−4.8
H11	Geothermal water	151.5	47.5	8.68	345	1.43	101	4.4	0.35	16.8	101	55.5	18	<0.10	65.3	−49	−7.5
H12	Geothermal water	51.8	48.5	7.17	443	5.72	99.2	16.2	1.9	11.2	136	110	0	<0.10	114	−47	−7
H13	Geothermal water	151.0	68.3	6.5	21100	201	4650	2810	54.9	12500	447	48.8	0	49.2	98.9	−26	−3.8
S01	Surface Water	-	33.1	8.24	279	12.5	36.5	43.1	5.38	40.9	44.8	140	0	<0.10	19.3	−37	−5.7
S02	Surface Water	-	34.9	9.41	1100	14	147	99.1	2.78	321	49.6	85.4	0	0.92	27.9	−36	−5.3
S03	Surface Water	-	30.7	7.4	121	5.73	11.6	18	2.38	11.9	11	73.2	0	0.12	21	−37	−5.7
S04	Surface Water	-	34.7	7.89	330	12.6	64.6	34.8	7.92	88.7	39.6	122	0	<0.10	16.1	−36	−5.5
S05	Surface Water	-	34.1	7.8	94.9	4.07	9.08	12	1.38	6.99	8.5	48.8	0	<0.10	20.5	−41	−6.4
S06	Surface Water	-	32.6	8.04	147	6.37	15.5	19.8	2.84	17.8	17	61	0	<0.10	20.7	−37	−5.9
S07	Surface Water	-	33.4	9.03	359	14.2	48.9	50.8	7.36	70.6	43.2	177	0	<0.10	27.3	−33	−4.9
S08	Surface Water	-	33.8	8.73	386	14.2	58.8	47.2	7.07	69.2	45	201	0	<0.10	33.4	−32	−4.8
SW01	Seawater	-	28.1	7.86	31300	385	9910	353	1140	17200	2330	138	0	55.7	2.92	-	-
SW02	Seawater	-	28.8	7.87	32700	386	10100	369	1190	17400	2390	133	0	57.3	2.43	-	-
SW03	Seawater	-	31.7	8.2	32400	385	10000	351	1170	17800	2480	134	0	59.2	<1.00	-	-
SW04	Seawater	-	28.5	7.8	29800	352	9330	336	1100	16000	2230	132	0	53.1	3.58	-	-

is 6.50–8.68 and 7.4–9.41, respectively, indicating slightly alkaline water. The pH of the groundwater is 4.55–7.92, suggesting neutral and meta-acidic water.

The salinity of the geothermal water tends to increase from the surrounding mountainous areas to the coastal areas in Xiamen. It is 300–443 mg/L for geothermal water exposed in mountainous and piedmont alluvial-diluvial plains (i.e., samples H03, H04, H07, H11, and H12), 1100–3640 mg/L for those exposed to groundwater runoff areas of alluvial-diluvial plains and eroded platforms (i.e., samples H01, H02, and H05), and 8000–21000 mg/L for those exposed in sea-land intersections (i.e., samples H06, H08, H09, H10, and H13).

According to the Piper trilinear diagram of water samples (**Figure 2**), the cations and anions in the surface water mainly include Ca^{2+}, Na^+, and HCO^{3-}. For the cold groundwater, the cations and anions are dominated by Na^+, Ca^{2+}, HCO^{3-}, and Cl^- and the hydrochemical types mainly include Ca•Na-HCO_3 and Ca•Na-HCO_3•Cl. For the geothermal water in the hilly mountainous areas and the piedmont alluvial-diluvial plains, the cations and anions mainly include Na^+, Ca^{2+}, HCO^{3-}, and SO_4^{2}, and the hydrochemical types are dominated by Ca•Na-HCO_3•SO_4. For the geothermal water in the coastal areas, the cations and anions are dominated by Na^+ and Cl^-, respectively, with the water type of Na-Cl, and the hydrochemical types feature abrupt changes.

Cl^- is not liable to form mineral salts nor is absorbed on mineral surfaces in natural water-rock systems. Moreover, it is hardly affected by water-rock interactions even in a high-temperature environment. Therefore, Cl^- is frequently used to trace the origins of materials in geothermal water and its systems that are closely correlated with Cl^- (Cartwright et al., 2004; Arnórsson and Andrésdóttir, 1995). In the study area, there is a negative correlation between SiO_2 and Cl^- in cold groundwater and the geothermal water H03, H04, H07, H11, and H12 in the

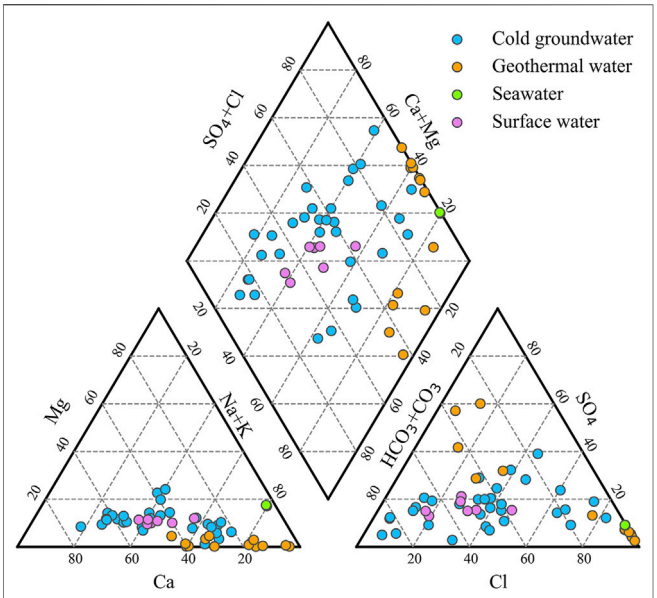

FIGURE 2 | Piper trilinear diagram of water samples from Xiamen.

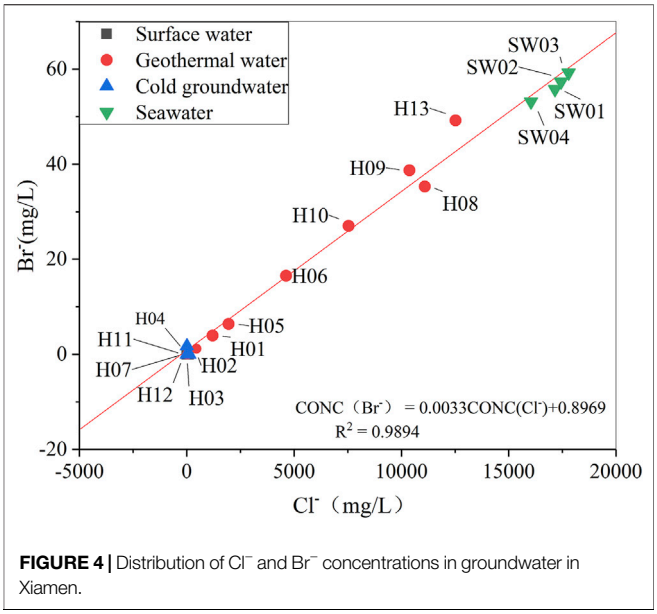

FIGURE 4 | Distribution of Cl^- and Br^- concentrations in groundwater in Xiamen.

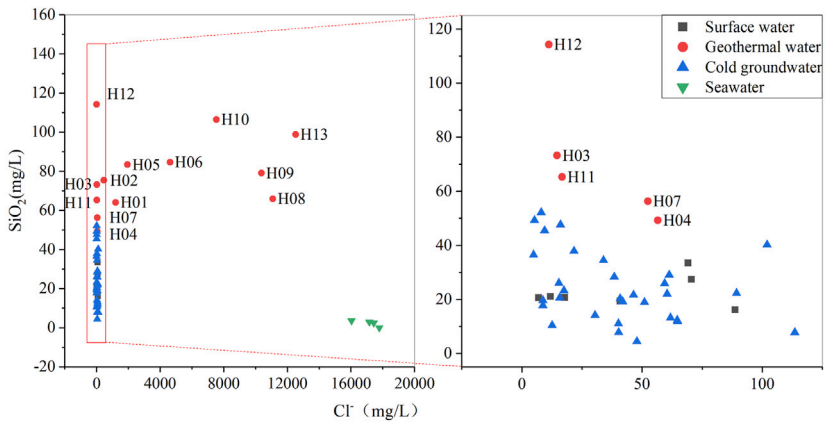

FIGURE 3 | Distribution of SiO_2 and Cl^- concentrations in groundwater in Xiamen.

hilly mountainous areas and piedmont alluvial-diluvial plains, while there is no close correlation between SiO_2 and Cl^- in the nearshore geothermal water (**Figure 3**). These phenomena indicate that the SiO_2 and Cl^- concentrations in the cold groundwater and the geothermal water in the hilly mountainous areas and piedmont plains are controlled by water-rock interactions, while the SiO_2 and Cl^- concentrations in nearshore geothermal water are possibly mainly affected by seawater infiltration (Wang et al., 1986).

4.2 Mixing Ratio of Seawater in Geothermal Water

The Piper trilinear diagram and the isotopic characteristics of groundwater all indicate that the nearshore geothermal water in Xiamen is affected by seawater. **Figure 4** illustrates the Cl^- and Br^- concentrations in the geothermal water. The Br^- concentration of the groundwater in the study area is relatively low and is mostly below the detection limit, while that in the nearshore geothermal water is relatively high. The linear relationship between Cl^- and Br^- concentrations reveals that the salinity of the geothermal water originates from seawater and is controlled by the quantity of mixed seawater. The mixing ratio of seawater in the geothermal water was calculated based on the Cl^- concentration in geothermal water (**Table 2**). Specifically, the Cl^- concentration in seawater was taken as 17100 mg/L, which was the average Cl^- concentration of seawater samples collected from the local sea in Xiamen City. Meanwhile, the Cl^- concentration in geothermal water before seawater mixing was taken as 17.90 mg/L, which was the average Cl^- concentration in

TABLE 2 | Mixing ratio of seawater in geothermal water in Xiamen.

No.	Landform type	Cl^-(mg/L)	Mixing ratio of seawater %
H03	Bedrock	14.67	0.00
H11		16.77	0.00
H12		11.18	0.00
H01	Alluvial residual plain	1209	6.97
H02		459.3	2.58
H04		56.58	0.23
H07		52.39	0.20
H05		1947	11.29
H06	Alluvial marine floodplain	4628	26.99
H08		11090	64.82
H09		10374	60.63
H10		7545	44.06
H13		12522	73.20

oxygen isotopes of geothermal fields show obvious zonation. Geothermal waters H01, H03, H11, and H12, which are distributed in low mountains, hills, and river valleys, have relatively negative water isotopes and low temperatures due to the recharge of water from high altitude areas. The elevation of the mountain is about 1175 m in the study area. In addition, groundwater could be recharged during the glacial period, contributing to the depleted water isotopes. The ^{14}C ages of waters H06 and H13 are greater than 18 ka. The temperature of geothermal water tends to be higher and the isotopes of geothermal water tend to approximate those of seawater near the coast (Cai, 2003; **Figure 5**). When the seawater has a maximum $\delta^{18}O$ value of −1.29, the $\delta^{18}O$ values at the freshwater endmember of geothermal water were calculated to

TABLE 3 | δ^2H and $\delta^{18}O$ of coastal seawater in Xiamen.

Sample	Sampling timing	$\delta^2H\ V_{SMOW}$ (‰)		$\delta^{18}O_{VSMOW}$ (‰)	
		1998–11-06	1998–12-06	1998–11-06	1998–12-06
Seawater	H	−15.9 ± 0.6	−10.2 ± 0.3	−1.94 ± 0.02	−1.29 ± 0.03
	L	−17.8 ± 0.4	−12 0.6 ± 0.1	−2.35 ± 0.05	−1.53 ± 0.02

"H" denotes high tide and "L" denotes low tide.

groundwater in the bedrock mountainous areas. The calculation results show that the geothermal water H3, H4, H7, H11, and H12 exposed in the piedmont areas is not affected by seawater mixing, while the nearshore geothermal water is affected by seawater mixing at different levels. The geothermal water H13 in the Pubian geothermal field shows the highest mixing ratio of seawater, which is up to 73.20%.

4.3 Environmental Isotopic Characteristics of Groundwater

In the study area, the $\delta^{18}O$ and δ^2H values of hot water are −7.7 to −3.8‰ and −51 to −26‰, respectively, and those of cold water are −7.3 to −4.7‰ and −47 to −32‰, respectively.

The local meteoric water line (LMWL) of Xiamen approximates the global meteoric water line (GMWL; Yurtsever, 1975), with the slope and y-intercept of the former being greater than those of the latter (Chen et al., 2016). The delta values of hydrogen and oxygen isotopes in the surface water, groundwater, and geothermal water in the study area are distributed on both sides of the local atmospheric precipitation line, indicating that the water in the area is mainly recharged by atmospheric precipitation. The seawater in the Xiamen Bay is greatly affected by the Jiulong River with a total annual runoff of 8.22 billion m^3 and the surface water and groundwater surrounding Xiamen. Large amounts of surface water and groundwater mix with seawater in the Xiamen Bay, causing the seawater to be rich in negative water isotopes. As shown by the testing data, the seawater in the Xiamen Bay has $\delta^{18}O$ values of −2.35 to −1.29 and thus is rich in negative water isotopes compared to open ocean water (**Table 3**). The hydrogen and

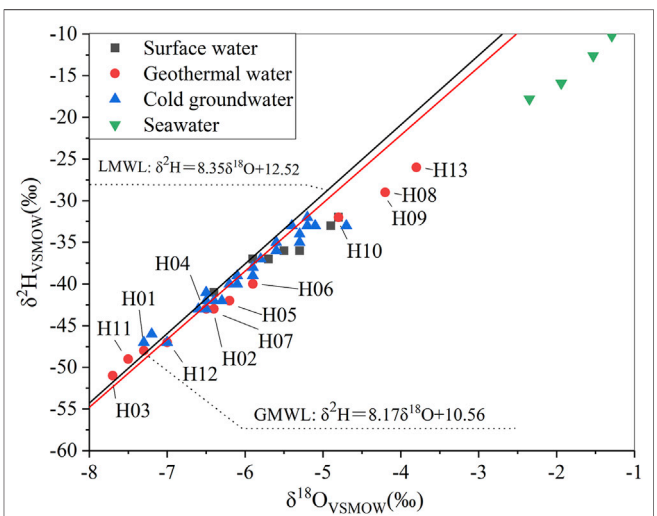

FIGURE 5 | Distribution of stable hydrogen and oxygen isotopes in geothermal water in Xiamen.

be −10.66 to −6.4 (average: −7.7) based on the mixing ratio of seawater. For example, Pubian (H13) is rich in negative water isotopes, with a $\delta^{18}O$ value of −10.66. When the seawater has a minimum $\delta^{18}O$ of −2.35, the calculated $\delta^{18}O$ values at the freshwater endmember of geothermal water were −7.7 to −6.4. The $\delta^{18}O$ values at freshwater endmember of geothermal water approximate to those of the precipitation in the study area, indicating that the freshwater endmember of geothermal water was recharged by atmospheric precipitation. In addition, the

TABLE 4 | Estimated temperatures of geothermal reservoirs in Xiamen.

No.	Temperature of water	Quartz thermometer (°C, no-steam loss)	Chalcedony thermometer (°C)
H01	56.8	114	85
H02	51.7	122	94
H03	48.0	121	92
H04	37.6	101	71
H05	80.0	127	100
H06	47.0	128	100
H07	45.5	107	78
H08	38.2	115	86
H09	53.6	125	97
H10	88.9	141	114
H11	47.5	115	86
H12	48.5	145	119
H13	68.3	137	110

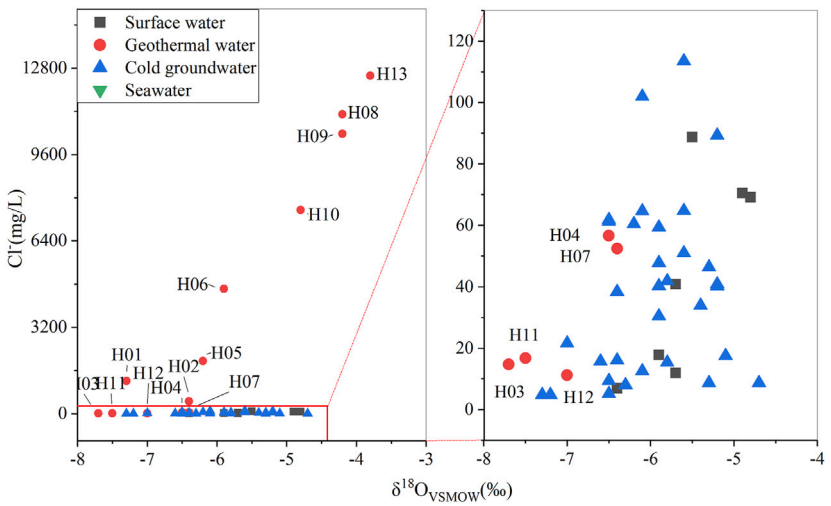

FIGURE 6 | Relationship between the distribution of Cl^- concentration and $\delta^{18}O$.

groundwater in the geothermal water Pubian (H13) has a ^{14}C age of 19.7 ka, indicating that the freshwater endmember of groundwater in the hot spring could be recharged during the glacial period.

According to the relationships between Cl^- concentration and $\delta^{18}O$ values (**Figure 6**), Cl^- is poorly correlated with $\delta^{18}O$ for cold groundwater and the geothermal water in mountainous areas in Xiamen. In contrast, there is a significantly positive correlation between Cl^- and $\delta^{18}O$ for the geothermal water in coastal areas, indicating a marine origin of Cl^- in geothermal water. The geothermal water circulation in offshore areas could be affected by the paleo-seawater trapped in the marine sediments or modern seawater. The regional geological tectonism in Xiamen is dominated by crustal uplift, with merely a small number of thin marine sedimentary strata. In this case, paleo-seawater cannot be stored. Therefore, it can be inferred that the geothermal water in coastal areas in Xiamen is mainly recharged by modern seawater.

5 DISCUSSION

5.1 Water-Rock Equilibrium State

The Na-K-Mg ternary diagram can be used to distinguish different types of water samples based on the equilibrium state of geothermal water (**Figure 7**). The ternary diagram shows three zones, namely the zones of fully equilibrated water, partially equilibrated water, and immature water. It is applied on the basis that K and Na concentrations can reach equilibrium faster than Mg and K concentrations (Giggenbach, 1988). The geothermal water in the study area is partially equilibrated water, except for H04 and H12, which are immature water. The water-rock interactions in the study area have not yet reached the fully equilibrated state, and dissolution still continues. The geothermal water may originate from a hotter environment and is mixed and diluted by shallow cold water during its deep circulation and rise. As a result, the contents of chemical components in hot water change. The high salinity and

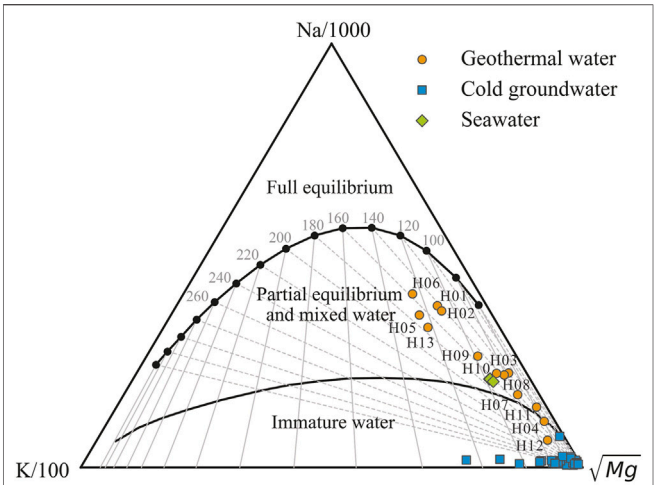

FIGURE 7 | Na-K-Mg ternary diagram of geothermal water samples in Xiamen.

Cl^- concentration of geothermal water originate from seawater mixing, which brings abundant ions such as Na^+ and K^+ besides Cl^-. Meanwhile, the Na-K-Mg ternary diagram shows that all cold groundwater samples lie near the Mg endmember at the lower right corner. This phenomenon indicates that the temperature of water-rock equilibrium is low and Na and K minerals in hot water do not reach equilibrium. The Na/K ratios of the partially equilibrated waters indicate a possible equilibration temperature range of 140–180°C. This result suggests that the high-temperature geothermal water that undergoes deep circulation is mixed with shallow cold water, thus forming partially equilibrated or immature water.

5.2 Estimation of Geothermal Reservoir Temperature

Geochemical geothermometers can be used to calculate the temperature of underground geothermal reservoirs based on the concentrations of chemical components in geothermal water. In the geothermal system, the migration of hot water from deep to shallow parts tends to be accompanied by the dissolution and precipitation reactions of various minerals. If a certain mineral concentration shows a relationship with the fluid temperature when it reaches the reaction equilibrium in the solution, the mineral concentration can be used to deduce the temperature of mineral equilibrium (i.e., the ambient temperature) (Craig, 1953; Li et al., 2022). Geothermal geothermometers generally include SiO_2, gas, isotopic, and cation geothermometers. The cation geothermometers are related to components such as Na, K, and Mg. This study revealed that a large amount of seawater is mixed into the geothermal water in Xiamen. As a result, the concentrations of key cations in the geothermal water have the same orders of magnitude as those in the cold groundwater, making it difficult to conduct correction using the mixing ratio. In other words, the seawater mixing makes the essential application conditions of cation geothermometers unavailable (Fournier, 1977; Fournier and Potter, 1982). SiO_2 geothermometers are devised based on the concentrations of SiO_2 minerals in geothermal water since the solubility of SiO_2 minerals is the function of temperature. Moreover, pressure and the increase in salts (leading to the change in salinity) have small effects on the solubility of quartz and non-crystalline silica when the geothermal reservoir temperature is less than 300°C (Verma and Santoyo, 1997).

Most geothermal water in the study area is partially equilibrated water, and only Dongtang (H04) and Tangli (H12) are immature water. Moreover, geothermal water H01, H02, H05, H06, H07, H08, H09, H10, and H13 is mixed with seawater at different levels. Seawater can enter the geothermal water in the deep or shallow parts. When seawater mixing occurs in deep parts, water-rock interactions reach the equilibrated state after seawater mixing and thus cation geothermometers are applicable. However, in the case of seawater mixing in shallow parts, water-rock interactions have not reached the equilibrated state after seawater mixing and thus cation geothermometers are inapplicable. It is difficult to determine whether seawater enters the geothermal water in the deep or shallow parts using currently available data. Moreover, partially equilibrated water (H03, H11) highly approaches immature water, possibly leading to large errors in the temperature calculated using cation geothermometers.

SiO_2 geothermometers are devised based on the solubility of the SiO_2 minerals including quartz, chalcedony, and amorphous non-crystalline silica (Fournier and Rowe, 1966; Fournier and Truesdell, 1973). At a temperature range of 0–250°C, the results calculated using the formulas of quartz geothermometers are very close to the solubility of quartz under the vapor pressure of solutions (Fournier et al., 1980). Therefore, the calculation results of geothermometers are accurate at this temperature range. However, the geothermal reservoir temperature in the study area is generally less than 250°C as revealed by relevant research results. In general, quartz and chalcedony determine the SiO_2 concentration at temperatures of > 180°C and < 110°C, respectively, but the minerals that control the SiO_2 concentration at a temperature of 110–180°C are still unknown (Arnorsson, 1975). This study selected quartz and chalcedony geothermometers. Quartz geothermometers can be divided into no-steam loss geothermometers and maximum steam loss geothermometers. Since the temperature at geothermal wellheads is significantly lower than the local boiling point, the no-steam loss quartz thermometer and chalcedony geothermometer was used in this study (Fournier, 1977). As revealed by the geothermal temperatures calculated using SiO_2 geothermometers, the quartz geothermometer and the chalcedony geothermometer yielded geothermal reservoir temperatures of 101–145°C, and 71–119°C (**Table 4**).

5.3 Mixing Model

Given that the geothermal water in the study area is mixed with cold water and seawater in shallow parts, this study used the silica-enthalpy mixing model to determine the mixing ratio of hot water with shallow cold water and to obtain the original temperature of the geothermal reservoirs (Fournier and Truesdell,

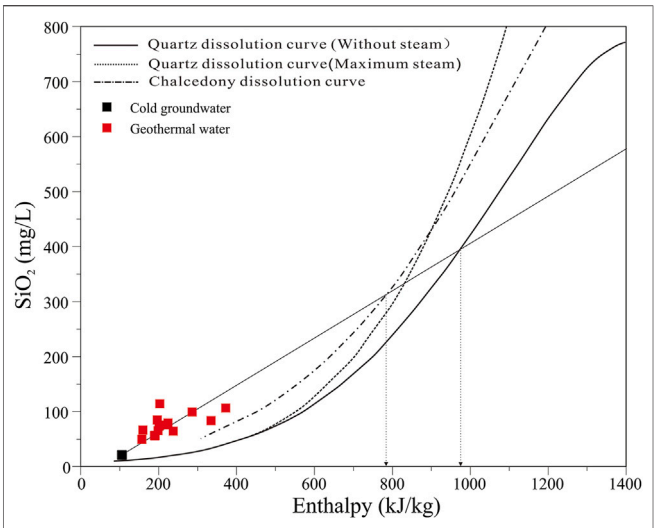

FIGURE 8 | Silica-enthalpy illustration method.

5.4 Formation Mechanisms of Geothermal Resources

The low-medium temperature geothermal systems in the study area are affected by deep mantle-derived materials to a limited extent, and their He isotopic ratios show typical crustal metamorphic characteristics (Tian et al., 2021). The heat in the study area mainly originates from the heat transfer of EW-trending deep faults and the radioactive heat production of granites. The shallow groundwater or seawater surrounding geothermal anomalous areas infiltrates downward along the fractures of NW-trending structures while continuously absorbing heat (heating, expanding, and specific gravity decreasing). When it infiltrates to heat sources, where the geothermal water is about 185–225°C, the pressure difference formed by the temperature difference between the heat sources and their surrounding areas pushes the geothermal water to rise along tensional fractures and then release thermal energy. Meanwhile, the surrounding low-temperature groundwater continuously infiltrates and recharges the geothermal water. As a result, the shallow

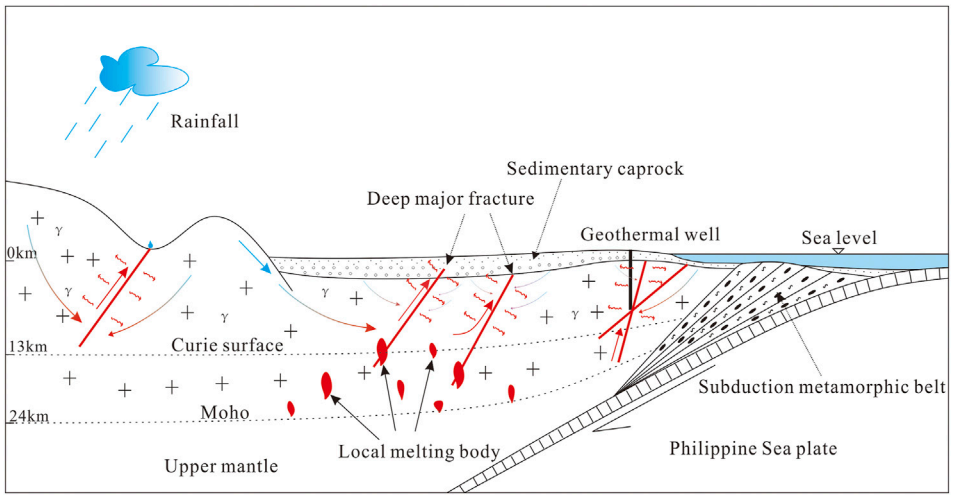

FIGURE 9 | Diagram showing the genetic model of geothermal resources in igneous rock areas in the southeast coastal areas of China.

1973). In this study, the average temperature of cold water samples was used as the cold water endmember (t = 21°C, SiO_2 = 20.64 mg/L). In the silica-enthalpy mixing model, assuming no steam or heat loss, the hot water endmember and the cold water endmember were projected into the silica-enthalpy diagram (**Figure 8**). Then, the temperature range of deep geothermal reservoirs was determined by the temperatures corresponding to three points of intersection of the line passing the hot water points and the cold water point and the solubility curves of quartz and chalcedony (Alcicek et al., 2018), and the mixing ratio range of cold water is the proportions of the distance between the hot water point and the intersection points along the line. Using the silica-enthalpy illustration method, it can be estimated that deep geothermal reservoirs in Xiamen have enthalpy values of 775–975 kJ/kg and temperatures of 185–225°C and that the mixing ratio of cold water is 63–91%.

geothermal reservoirs in the study area have a temperature of 71–149°C. The temperature difference between the heat sources and their surrounding areas continues pushing the geothermal water to constantly rise, leading to the formation of the convective geothermal systems in igneous rock areas in southeast coastal areas of China (**Figure 9**).

6 CONCLUSION

The geothermal water exposed in Xiamen has a temperature of 37.60–88.90°C. It is slightly alkaline water, and its hydrochemical types mainly include Ca•Na-HCO_3 and Ca•Na-HCO_3•Cl. From piedmont areas to the coastal areas, the salinity of the geothermal water constantly increases. Moreover, the geothermal water in the

coastal areas has a hydrochemical type of Na-Cl, showing an abrupt change compared with the cold groundwater.

The geothermal water in coastal areas in Xiamen is recharged by seawater mixing to different extents according to the hydrochemical types, isotopic characteristics, and the C1-/Br- ratio of geothermal water. As revealed by the calculation results using the Cl^- mixing model, 10 of 13 geothermal fields in Xiamen are recharged by seawater mixing. The geothermal water in the Pubian geothermal field (H13) shows the highest mixing ratio of seawater, which is up to 73.20%. Furthermore, the freshwater recharge endmember of the deep geothermal water in Xiamen could be recharged during the glacial period.

The geothermal resources in Xiamen mainly have low-medium temperatures. The geothermal fields in piedmont areas are recharged by rainfall infiltration, while those in the coastal areas are recharged by rainfall and seawater mixing. The quartz and chalcedony geothermometers yielded geothermal reservoir temperatures of 101–145°C and 71–119°C, respectively.

The NE-trending faults in Xiamen have significant impacts in deep parts and constitute channels that allow deep heat to rise. The NW- and near-EW-trending faults are mainly tensional and constitute the recharge, runoff, and discharge circulation channels of geothermal water. Atmospheric precipitation infiltrates downward along the NW- and near-EW-trending faults to the NE-trending faults, and groundwater temperature reaches 185–225°C subject to deep heat transfer. The temperature difference results in the pressure difference, which causes the geothermal water to rise along tensional fractures and the surrounding cold water to continuously infiltrate and recharge the geothermal water. As a result, the mixing ratio of cold water is up to 63–91%, and the shallow geothermal reservoirs in Xiamen have temperatures of 71–145°C.

DATA AVAILABILITY STATEMENT

The original contributions presented in the study are included in the article/Supplementary files, further inquiries can be directed to the corresponding author.

AUTHOR CONTRIBUTIONS

All authors listed have made a substantial, direct, and intellectual contribution to the work and approved it for publication. CL: Conceptualization, Writing-original draft, Visualization, Funding acquisition. YL: Methodology, Resources, Project administration. SC: Investigation, Data curation. JL: Formal analysis, Writing-review and editing, Supervision.

FUNDING

This work was supported by China Geological Survey project (DD20190303).

REFERENCES

Alçiçek, H., Bülbül, A., Brogi, A., Liotta, D., Ruggieri, G., Capezzuoli, E., et al. (2018). Origin, Evolution and Geothermometry of the Thermal Waters in the Gölemezli Geothermal Field, Denizli Basin (SW Anatolia, Turkey). *J. Volcanol. Geotherm. Res.* 349, 1–30. doi:10.1016/j.jvolgeores.2017.07.021

Armienta, M. A., Rodriguez, R., Ceniceros, N., Cruz, O., Aguayo, A., and Morales, P. (2014). Groundwater Quality and Geothermal Energy. The Case of Cerro Prieto Geothermal Field, Mexico. *Renewable Energy* 63, 236–254.

Arnórsson, S., and Andrésdóttir, A. (1995). Processes Controlling the Distribution of Boron and Chlorine in Natural Waters in Iceland. *Geochimica Cosmochimica Acta* 59 (20), 4125–4146. doi:10.1016/0016-7037(95)00278-8

Arnorsson, S. (1975). Application of the Silica Geothermometer in Low Temperature Hydrothermal Areas in Iceland. *Am. J. Sci.* 275 (7), 763–784. doi:10.2475/ajs.275.7.763

Cai, M. (2003). The Study of Hydrogen and Oxygen Isotopes of Coastal Groundwater in Xiamen Island. *Mar. Sci.* 27 (9), 1–6. doi:10.3969/j.issn.1000-3096.2003.09.001

Cartwright, I., Weaver, T. R., Fulton, S., Nichol, C., Reid, M., and Cheng, X. (2004). Hydrogeochemical and Isotopic Constraints on the Origins of Dryland Salinity, Murray Basin, Victoria, Australia. *Appl. Geochem.* 19 (8), 1233–1254.

Chen, Y., Du, W., Chen, J., and Xu, L. (2016). Composition of Hydrogen and Oxygen Isotopic of Precipitation and Source Apportionment of Water Vapor in Xiamen Area. *Acta Sci. Circumstantiae* 36 (2), 667–674. doi:10.13671/j.hjkxxb.2015.046410.5846/stxb201408251674

Craig, H. (1953). The Geochemistry of the Stable Carbon Isotopes. *Geochimica Cosmochimica Acta* 3 (2-3), 53–92. doi:10.1016/0016-7037(53)90001-5

Dezi, W., Qijiang, R., Jiansheng, Q., Kerong, C., Zhaowen, X., and Jiahu, Z. (1996). Characteristics of Volcanic Rocks in the Shoshonite Province, Eastern China, and Their Metallogenesis. *Acta Geol. Sin. Ed.* 9 (3), 246–259. doi:10.1111/j.1755-6724.1996.mp9003003.x

Fan, W., Menzies, M. A., Yi, H. X., Chen, X., and Zhou, H. (1993). Nature and Processes of the Lower Lithosphere of the Southeast China Coast. *Geotect. Metallogenia* 17 (1), 27–34.

Fournier, R. O. (1977). Chemical Geothermometers and Mixing Models for Geothermal Systems. *Geothermics* 5 (1-4), 41–50. doi:10.1016/0375-6505(77)90007-4

Fournier, R. O., and Potter, R. W., II (1982). A Revised and Expanded Silica (Quartz) Geothermometer. *Geotherm. Resour. Counc. Bull.* 11 (10), 3–12.

Fournier, R. O., and Rowe, J. J. (1966). Estimation of Underground Temperatures from the Silica Content of Water from Hot Springs and Wet-Steam Wells. *Am. J. Sci.* 264 (9), 685–697. doi:10.2475/ajs.264.9.685

Fournier, R. O., Thompson, J. M., and Austin, C. F. (1980). Interpretation of Chemical Analyses of Waters Collected from Two Geothermal Wells at Coso, California. *J. Geophys. Res.* 85 (B5), 2405–2410. doi:10.1029/JB085iB05p02405

Fournier, R. O., and Truesdell, A. H. (1973). An Empirical NaKCa Geothermometer for Natural Waters. *Geochimica Cosmochimica Acta* 37 (5), 1255–1275. doi:10.1016/0016-7037(73)90060-4

Gan, H., Lin, W., Yan, X., Yue, G., Zhang, W., and Wang, G. (2020). Analysis of Geothermal Occurrence Characteristics and Origin of the Thermal Anomalies in the Hidden Igneous Rock Area in the Central Guangdong. *Acta Geol. Sin.* 94 (7), 2096–2106. doi:10.19762/j.cnki.dizhixuebao.2020215

Gan, H., Lin, W., Yue, G., Wang, X., Ma, F., and Wang, G. (2017). Research on the Fault Controlling Mechanism of Geothermal Water in Zhangzhou Basin. *J. Groundwater Sci. Eng.* 5 (4), 326–335.

Gao, F., Yang, X., Wu, A., Fu, Y., and Chen, Y. (2009). Characteristics of Thermal Springs and Genesis of Thermal Underground Waters in Hainan Island. *J. Jilin Univ.* 39 (2), 281–287. doi:10.3969/j.issn.1671-5888.2009.02.016

Giggenbach, W. F. (1988). Geothermal Solute Equilibria. Derivation of Na-K-Mg-Ca Geoindicators. *Geochimica Cosmochimica Acta* 52 (12), 2749–2765. doi:10.1016/0016-7037(88)90143-3

Han, Q., and Zhuang, Q. (1988). On the Source and Pathway of Hot Water in Zhangzhou Basin, Fujian. *Sci. J. Earth Sci.* 13 (3), 271–277.

Hu, S., and Xiong, L. (1990). Reservoir Modelling of Zhangzhou Low Temperature Fracture Zone System, Fujian, China. *Geol. Sci. Technol. Inf.* 9 (4), 65–71.

Li, J., Zhang, L., Ruan, C., Tian, G., Sagoe, G., and Wang, X. (2022). Estimates of Reservoir Temperatures for Non-magmatic Convective Geothermal Systems: Insights from the Ranwu and Rekeng Geothermal Fields, Western Sichuan Province, China. *J. Hydrology* 609 (3), 127668. doi:10.1016/j.jhydrol.2022.127668

Li, T., lin, W., Gan, H., Yue, G., Zhang, D., and Wang, G. (2020). Research on the Genetic Model and Exploration Progress of Hot Dry Rock Resources on the Southeast Coast of China. *J. Geomechanics* 26 (2), 187–200. doi:10.12090/j.issn.1006-6616.2020.26.02.018

Liao, Z. (2012). Deep-Circulation Hydrothermal Systems without Magmatic Heat Source in Fujian Province. *Geoscience* 26 (1), 85–98. doi:10.3969/j.issn.1000-8527.2012.01.009

Lin, S. (2007). Characteristics, Exploitation and Utilization of Geothermal Resources in the Xinglinwan Area of Xiamen City. *Geol. Fujian* 27 (2), 249–253. doi:10.3969/j.issn.1001-3970.2008.02.021

Lin, W., Chen, X., Gan, H., and Yue, G. (2020). Geothermal, Geological Characteristics and Exploration Direction of Hot Dry Rocks in the Xiamen Bay-Zhangzhou Basin, Southeastern China. *Acta Geol. Sin.* 94 (7), 2066–2077. doi:10.19762/j.cnki.dizhixuebao.2020223

Lin, W., Gan, H., Wang, G., and Ma, F. (2016). Occurrence Prospect of HDR and Target Site Selection Study in Southeastern of China. *Acta Geol. Sin.* 90 (8), 2043–2058. doi:10.3969/j.issn.0001-5717.2016.08.031

Lin, W. J., Wang, G. L., Gan, H. N., Wang, A. D., Yue, G. F., and Long, X. T. (2022). Heat Generation and Accumulation for Hot Dry Rock Resources in the Igneous Rock Distribution Areas of Southeastern China. *Lithosphere* 2021 (5), 2039112. doi:10.2113/2022/2039112

Ma, Z., Ma, Y., Zhang, P., Si, F., Huo, Q., and Chu, L. (2021). Application of Wide Area Electromagnetic Method in Geothermal Exploration of Hongtang Town, Fujian Province. *Mineral. Explor.* 12 (3), 661–667. doi:10.3969/j.issn.1674-7801.2021.03.019

Ozgener, O., and Kocer, G. (2004). Geothermal Energy Utilization in Jordanian Deserts. *Energy Sources* 26 (4), 353–360. doi:10.1080/00908310490424105

Pang, Z. (1987). *Zhangzhou Basin Geothermal System–Genesis Model, Energy Pottential and the Occurrence of Thermal Water*. Beijing: Institute of Geology and Geophysics, 270.

Qiu, Z. (2018). *Study on Geothermal Resources and its Causes in Xiamen*. Beijing: China University of Geosciences.

Tian, J., Li, Y., Zhou, X., Pang, Z., Li, L., Xing, L. Z., et al. (2021). Geochemical Characteristics of Hydrothermal Volatiles from Southeast China and Their Implications on the Tectonic Structure Controlling Heat Convection. *Front. Earth Sci.* 9, 1–13. doi:10.3389/feart.2021.786051

Verma, S. P., and Santoyo, E. (1997). New Improved Equations for Na/K, Na/Li and SiO2 Geothermometers by Outlier Detection and Rejection. *J. Volcanol. Geotherm. Res.* 79 (1-2), 9–23. doi:10.1016/S0377-0273(97)00024-3

Wang, D., Zhang, R., and Shi, Y. (1986). *General Hydrogeology*. Beijing: Geological Publishing House.

Wang, J. (1985). Distributions and Formation of the Geothermal Field along the Coast, Southeastern China. *Seismol. Geol.* 7 (1), 49–58.

Wang, P., Chen, Y., Cao, B., Pan, J., and Wang, C. (1993). Crust-upper Mantle Structure and Deep Structure Setting of Fujian Province. *Geol. Fujian* 12 (2), 79–158.

Wang, X. (2018). *Formation Conditions and Hydrogeochemical Characteristicsof the Geothermal Water in Typical Coastal Geothermal Field with Deep Faults*. Wuhan: Guangdong Province , China University of Geosciences.

Xiong, L., Wang, J., and Pang, Z. (1990). Convective and Conductive Heat Flows in Zhangzhou Geothermal Field, Fujian Province, China. *Chin. J. Geophys.* 33 (6), 702–711. doi:10.1016/0009-2541(90)90098-R

Xiong, S., Jin, D., Sun, K., Zou, Z., Fan, S. Y., Du, B. X., et al. (1991). Some Characteristics of Deep Structure of the Zhangzhou Geothermal Field and It's Neighbourhood in the Fujian Province. *Chin. J. Geophys.* 34 (1), 55–63. doi:10.1007/BF02919155

Yurtsever, Y. (1975). Worldwide Survey of Stable Isotopes in Precipitation. International Report. Vienna: IAEA.

Zhang, J., Wang, B., Tang, X., Dong, M., and Ai, Y. (2018). Temperature Structure and Dynamic Background of Crust and Mantle beneath the High Heat Flow Area of the South China Continental Margin. *Chin. J. Geophys.* 61 (10), 3917–3932. doi:10.6038/cjg2018L0448

Zhang, Y., Luo, J., and Feng, J. (2020). Characteristics of Geothermal Reservoirs and Utilization of Geothermal Resources in the Southeastern Coastal Areas of China. *J. Groundwater Sci. Eng.* 8 (2), 134-142. doi:10.19637/j.cnki.2305-7068.2020.02.005

Conflict of Interest: The authors declare that the research was conducted in the absence of any commercial or financial relationships that could be construed as a potential conflict of interest.

Publisher's Note: All claims expressed in this article are solely those of the authors and do not necessarily represent those of their affiliated organizations, or those of the publisher, the editors and the reviewers. Any product that may be evaluated in this article, or claim that may be made by its manufacturer, is not guaranteed or endorsed by the publisher.

frontiers | Frontiers in Earth Science

ORIGINAL RESEARCH
published: 17 June 2022
doi: 10.3389/feart.2022.885197

Genetic Mechanism of Geothermal Anomaly in the Gaoyang Uplift of the Jizhong Depression

Qingzhuang Miao[1,2,3], Guiling Wang[2,3], Shihua Qi[1], Linxiao Xing[2,3], Hailiang Xin[4] and Xiaoni Zhou[2]*

[1]State Key Laboratory of Biogeology and Environmental Geology, School of Earth Sciences and Resources, China University of Geosciences, Wuhan, China, [2]Institute of Hydrogeology and Environmental Geology, Chinese Academy of Geological Sciences, Shijiazhuang, China, [3]Technology Innovation Center of Geothermal and Hot Dry Rock Exploration and Development, Ministry of National Resources, Shijiazhuang, China, [4]Geophysical Exploration Center, China Earthquake Administration, Zhengzhou, China

The Gaoyang uplift is rich in geothermal resources, but there are few studies on the regional geothermal genetic mechanism. A large number of geothermal wells fail in position calculation because of a shortage of basis. By using the methods of P-wave velocity structure imaging and magnetotelluric sounding, it draws the following conclusions: 1) The crustal thickness in the Gaoyang uplift area is relatively thin, about 32 km; 2) The cutting depth of the Gaoyang East fault exceeds 28 km and has reached the bottom of the lower crust. It is a large tensile fault that provides a channel for mantle heat flow into the shallow crust; 3) The Gaoyang uplift and its surrounding depressions form a concave-convex base fluctuation mode, which is conducive to the accumulation of heat flow to the uplift; 4) The deep carbonate thermal reservoir in the Gaoyang uplift is overlaid with Cenozoic sand and mudstone strata, with a thickness of more than 3000 m and low thermal conductivity, which is conducive to the preservation of thermal storage heat. Therefore, the shortening of the heat conduction path caused by regional crustal thinning, convective heat conduction of large faults, concave-convex structure, and thick Cenozoic caprock are the reasons why the heat reservoir temperature in the Gaoyang uplift is higher than that around, which provides a theoretical basis for geothermal development and utilization.

Keywords: p-wave, magnetotelluric sounding, depression, heat convection, Gaoyang uplift

OPEN ACCESS

Edited by:
Biao Shu,
Central South University, China

Reviewed by:
Sayantan Ganguly,
Indian Institute of Technology Ropar, India
Kunal Singh,
Geological Survey of India, India

****Correspondence:***
Guiling Wang
ihegwangguiling@sina.com

Specialty section:
This article was submitted to Solid Earth Geophysics, a section of the journal Frontiers in Earth Science

Received: *27 February 2022*
Accepted: *09 May 2022*
Published: *17 June 2022*

Citation:
Miao Q, Wang G, Qi S, Xing L, Xin H and Zhou X (2022) Genetic Mechanism of Geothermal Anomaly in the Gaoyang Uplift of the Jizhong Depression. Front. Earth Sci. 10:885197. doi: 10.3389/feart.2022.885197

INTRODUCTION

With the transformation of energy, geothermal energy as a green energy source has been confirmed by its actual utilization in China (Wang et al., 2017a). Nowadays, the continuous development of traditional non-renewable energy is gradually drying up, but the geothermal resources in the crust are rich in China. The total amount of hydrothermal geothermal resources in China is equivalent to 1.25 trillion standard tons of coal (Wang et al., 2020a). Although it cannot be compared with traditional energy at present, its influence will gradually become important because of carbon peak and carbon neutral. Therefore, it is increasingly becoming the concern of the majority of geological work. The direct utilization of geothermal energy has many benefits. The utilization of geothermal energy as a new energy source has been put forward for many years, which is of great significance for alleviating air pollution in China (Wang et al., 2017b).

The genetic mechanism of the geothermal field remains to be studied. Many scholars have done a lot of research on the abnormally high temperatures in geothermal fields (Chapman and

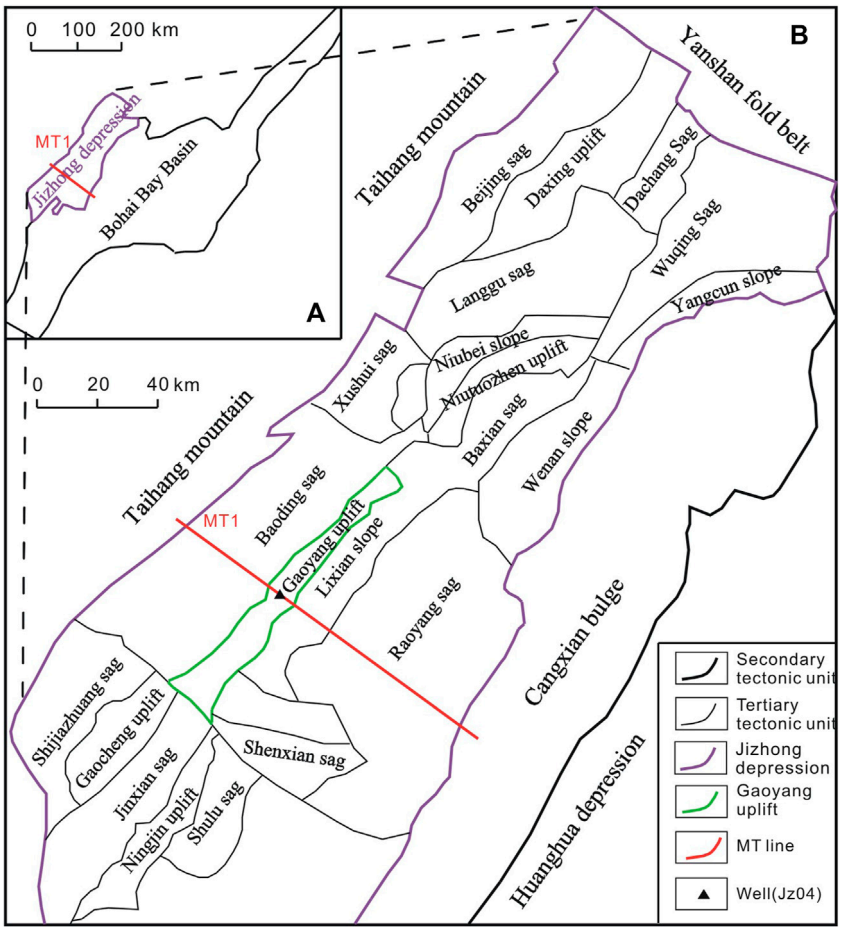

FIGURE 1 | (A) Location map of the Jizhong depression. **(B)** Schematic diagram of tectonic units in the Jizhong depression.

Rybach, 1985; Cermark and Rybach, 1989; Wang et al., 2001; Wang et al., 2017b; Lin et al., 2020). At present, it is generally believed that faults, radioactive heat generation, and mantle activity are the main causes of geothermal anomalies (Jaupart et al., 2015). Most scholars believe that the fault plays the role of a channel for thermal convection (Villas and Norton, 1977; Turcote and Schubert, 1982; Lin et al., 2020). High-temperature fluid in the deep can be obtained through the fault. Gao Z summarized the cause of abnormal geothermal temperatures according to practical experience, which is attributed to thermal convection with material exchange (Gao et al., 2009). Chen Moxiang and Deng Xiao believe that the underground heat flow in sedimentary basins always tends to have high thermal conductivity (Chen and Deng, 1990). It is suggested that the uplift zone has a high temperature, and the height of the geothermal field has a positive correlation with basement fluctuation. Aside from the aforementioned factors, many scholars also put forward that magmatic activity is the main factor in the geothermal field and believe that magmatic activity provides a steady stream of heat for the geothermal field (Urzua et al., 2002; Oskooi et al., 2005).

In recent years, several geothermal wells have been drilled in the Gaoyang uplift, and their temperatures are the highest (about 116°C) in North China Plain (Wang et al., 2020b). The Gaoyang uplift has geothermal heating and cascading utilization potential (Wu et al., 2018). However, there is little research on the genetic mechanism of geotherms in the Gaoyang uplift. This article intends to discuss the genetic mechanism of the high geothermal anomaly in the Gaoyang uplift by using geophysical methods.

GEOLOGICAL CONDITION

Gaoyang uplift belongs to the third structural unit in the Jizhong depression (class II) of the North China Basin (class I), which is located in the south central part of the Jizhong depression (**Figure 1**). The Gaoyang uplift is adjacent to the Lixian slope, with Baoding sag in the west, Raoyang sag in the east, Niutuozhen uplift and Baxian sag in the north and northeast, and Wuji-Gaocheng uplift and Jinxian sag in the southwest. The buried hill roof is deeply buried, and the main body is between 2.8 and 4 km, with a region of about 70 km^2.

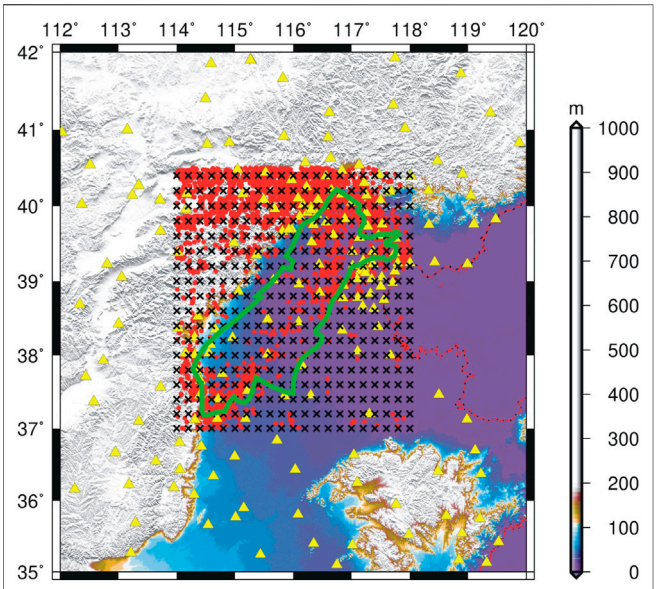

FIGURE 2 | Seismic events (red dots) and stations (yellow triangles). Grid points of 0.2° (black oblique cross) and the green frame (Jizhong depression).

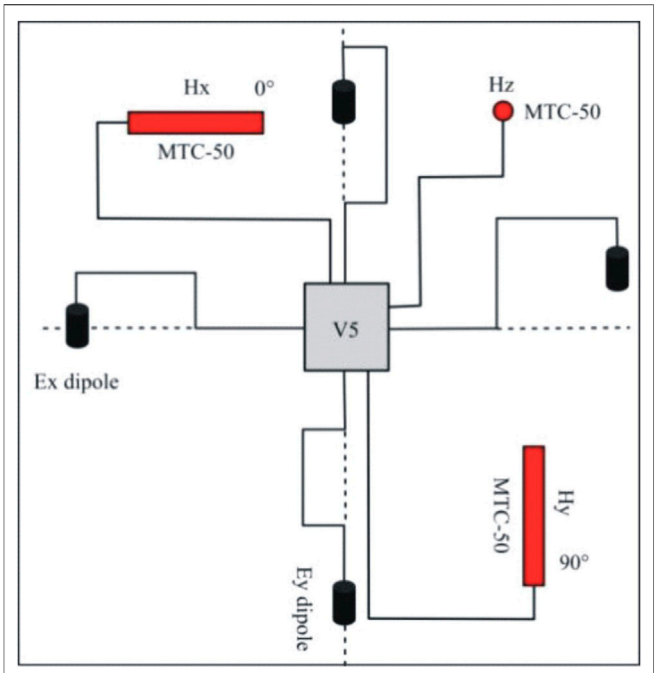

FIGURE 3 | Diagram of the MT station layout in the Jizhong depression.

The karst thermal reservoir dominated by marine carbonate rocks of the Proterozoic Wumishan formation is thick and widely distributed (Ye, 1983).

The Yanshan movement is the most important tectonic movement in this area, and a series of NE, NWW, and EW trending inherited tensile faults have been developed. The Taihang Mountain in the west and the Yanshan Mountain in the northwest are uplifted, and the Jizhong depression subsides as a whole. However, the interior of the Jizhong depression is uneven and distributed in the NE-SW direction, accompanied by a large number of secondary faults and folds (Yan et al., 2000).

Near NE trending faults such as the Gaoyangdong fault, the Anguo fault and other small faults mainly grew in the main part of the Gaoyang uplift. The Gaoyangdong fault is a group of reverse-slope normal faults with strikes similar to that of NE that form the boundary between the Gaoyang uplift and Lixian slope (Jin et al., 2017). Regionally, the Gaoyang uplift is distributed in the NE direction. The strata of the Paleogene and Jixian systems are in angular unconformity contact, forming an unconformity surface. Deep faults and unconformities are channels for fluid migration. The main thermal reservoir of the Gaoyang uplift is dolomite of the Wumishan formation, and the caprock is sandstone and mudstone of the Quaternary, Neogene, and Paleogene.

From the early to later stages, the strata of the Gaoyang uplift include Archean (Ar), Changcheng system (Ch), and Jixian system (Jx) of Middle and Lower Proterozoic; Cambrian-Ordovician (Є-O) of Lower Paleozoic, Jurassic-Cretaceous (J-K) of Mesozoic; and Paleogene (E), Neogene (N), and Quaternary (Q) of Cenozoic. The buried hill carbonate strata are mostly made of Wumishan, as well as some Cambrian and Ordovician formations. The caprocks of thermal reservoirs are generally sandstone and mudstone of the Paleogene, Neogene, and Quaternary. The Paleogene is in angular unconformity contact with Jixian, Cambrian, or Ordovician strata.

GEOPHYSICAL METHODS

P-wave velocity imaging and magnetotelluric sounding were used for this study.

P-Wave Velocity Imaging

The data for P-wave velocity imaging were natural seismic events recorded by fixed observation stations during 2008 and 2019 in the study area and its adjacent area. Seismic events occurring in 114–118°E and 37–40.5°N with travel time residual≤0.5 S and seismic stations located in 112–120°E and 35–42°N were selected for the study. In order to obtain the pair of seismic data, we selected the control parameters of seismic phase data. The controlling parameters were set as follows. Firstly, the number of pairs for each earthquake is no more than 20 earthquakes. Secondly, the distance from the earthquake to the station is no more than 600 km. Thirdly, the distance between each pair of earthquakes is between 1 and 10 km. Finally, the number of seismic phases required for each pair is between 8 and 50. After screening, there are 6,036 seismic events and 90,980 primaries of P-wave from 193 stations used (**Figure 2**).

The initial velocity model of one dimension, which was established through multiple inversion tests based on the inversion results of the velocity structure in North China (Yu et al., 2010; Duan et al., 2016), was used.

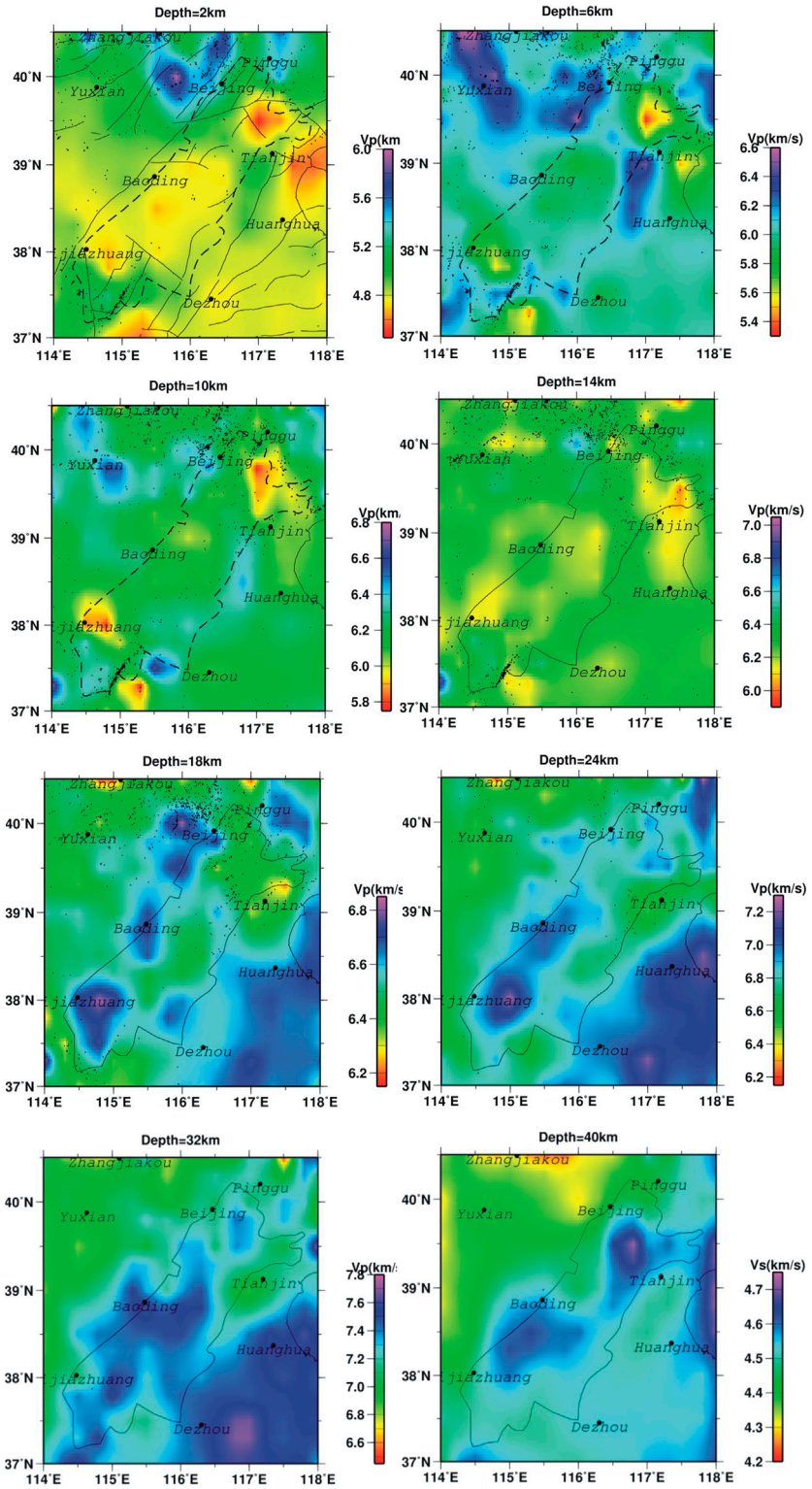

FIGURE 4 | P-wave velocity imaging at different depths in the Jizhong depression and its surroundings.

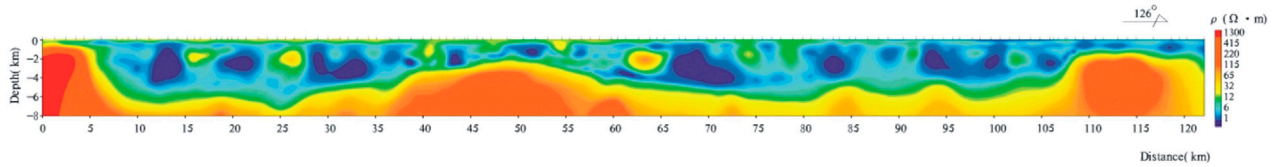

FIGURE 5 | 2D magnetotelluric inversion map.

Magnetotelluric Sounding

One section named MT01 was arranged for magnetotelluric sounding (**Figure 1**), with an average dot pitch of 1 km and a length of about 122 km. It crosses multiple geological structural units (Zhang et al., 2008), and a total of 122 points were recorded. In order to ensure the length of the apparent resistivity and impedance phase, the recording time of all measuring points that were collected at night was more than 12 h. Besides, reference stations are arranged to eliminate relevant noise.

A networked multifunctional electrical instrument, named V5, developed by Phoenix Geophysical Corporation of Canada, was selected for this study. The instrument contains a portable and solid acquisition system and a GPS synchronization system by which all recording units are synchronized within ±0.2 microseconds. The frequency range of the system is 10,000~0.000005 Hz. The frequency range of this study was 10,000~0.001 Hz in order to obtain information from depths of 6,000 to 10,000 m. Besides, the tensor observation method was adopted (**Figure 3**).

We used the imaging software system (MTSoft2d 2.4) with functions of two-dimensional magnetotelluric processing and inversion interpretation to preprocess data such as decoding and conversion, data editing, smoothing, polarization mode discrimination, and static correction. The preprocessed data were first inversed for one-dimensional inversion by using the method named Occam. The result was taken as the initial model to carry out two-dimensional nonlinear conjugate gradient (NLCG) to obtain the two-dimensional profile of magnetotelluric inversion.

GEOPHYSICAL RESULTS

P-Wave Velocity Imaging

Based on the velocity results of the seismic sounding profile in the working area (Duan et al., 2016), the initial velocity model was comprehensively constructed, for which the grid space in the horizontal dimension was $0.2^{\circ} \times 0.2^{\circ}$ and the depth of the grid in the vertical dimension was 0, 2, 6, 10, 14, 18, 24, 32, and 40 km. The P-wave of crust in the study area was fitted by using the Heda method.

In general, the travel time residuals of P-waves are distributed in the range of -1–1s after inversion. The P-wave velocity imaging maps of 2, 6, 10, 14, 18, 24, 32, and 40 km in the vertical dimension were obtained (**Figure 4**). It can be seen that the velocity of P-wave has an obvious lateral difference at the same depth, and the velocity of P-wave increases and then decreases with the increase of depth.

Magnetotelluric Sounding

The result of the magnetotelluric profile (**Figure 5**) shows that it is non-homogeneous for electrical structure in the Jizhong depression, and there are three layers for electrical structure in the longitudinal direction. The surface layer shows low resistance with high frequency, which is inferred to be the Quaternary incompact layer. The middle layer is characterized by low resistance (lower than the surface resistance) with medium frequency, which is inferred to be the interbedding of Neogene and Paleogene sandstone and mudstone. The deep layer is characterized by high resistance with medium and low frequency, which is inferred to be Mesozoic or Paleozoic limestone or carbonate rock. In the horizontal direction, it shows that the terrain of high resistance with medium and low frequency is undulating. High resistance buried shallow is the convex area, while high resistance buried deep is the concave area.

ANALYSIS AND DISCUSSION

Regional Crustal Thickness

According to the slice of P-wave velocity imaging at 2 km depth, the P-wave velocity decreased significantly after entering the North China Plain from the uplift of the Taihang Mountain. In the area where Paleozoic strata and Precambrian bedrock are widely exposed in the Taihang Mountain, it shows a high-speed anomaly. While in the Jizhong depression, which is located in the North China Plain, it shows a P-wave velocity anomaly that is consistent with the previous research results (Li et al., 2006; Qi et al., 2006; Lei et al., 2008).

As the depth increases to 20 km, the high-speed and low-speed anomalies are distributed alternately, and the corresponding relationship with the surface tectonic unit weakens. The velocity in the Jizhong depression still presents a low-speed anomaly, but the velocity value increases.

At a depth of 40 km, the change of P-wave velocity is as high as 6%, taking the Taihang piedmont fault as the boundary. The Taihang Mountain located in the west of the Taihang fault shows a low-speed anomaly (Wang et al., 2003), while the Jizhong

TABLE 1 | Resistivity of regional formation.

Number	Age	Resistivity (Ω·m)
1	Q	20
2	N, E	3–9
3	O, Є	200–300
4	J_{xw}	1,000

TABLE 2 | Geologic framework of JZ04.

Number	Depth(m)	Age	Lithology
1	0–455	Q	Mud, sand
2	455–1950	N	Mudstone, sandstone
3	1950–3,070	E	Mudstone, sandstone
4	3,070	J_{xw}	Dolomite

depression located in the east shows high-speed anomaly. The low-velocity anomaly at the depth of the Taihang Mountain may be caused by the upwelling, intrusion, or crustal warming of thermal materials in the upper mantle. Moreover, the heterogeneity of material composition in the crust–mantle transition zone is also a factor causing the heterogeneity of velocity.

The depth fluctuation of the Moho surface is inversely related to the fluctuation of the Cenozoic sedimentary basement. In the Jizhong depression located east of the Taihang piedmont fault, the buried depth of the Moho surface is relatively shallow, and it is mantled at a depth of 40 km. According to the deep reflection data of artificial seismic, the depth of the Moho surface in the Jizhong depression is about 32 km, which gradually deepens westward into the Taihang Mountain, and the maximum depth is about 42 km in the Taihang Mountain (Duan et al., 2016).

Tectonic Fracture

According to P-wave velocity imaging at different depths, there is an obvious velocity difference between the Taihang uplift and Jizhong depression in the North China Plain because of the sedimentary layers. The Taihang piedmont fault is the boundary of the Jizhong depression, which has a tendency toward the northeast. Because of its influence, P-wave velocity below the sedimentary layer in the Jizhong depression is still a low-speed anomaly. As the depth increases, the low-speed anomaly range expands to the southeast. When the depth reaches 18 km, the speed of the low-speed abnormity increases a bit. We can conclude that the speed at 18 km is not affected by the Taihang piedmont fault. Therefore, it can be inferred that the cutting depth of the Taihang piedmont fault is about 18 km, which does not reach the Moho surface and does not belong to a deep fault (Xu et al., 2001; Yang et al., 2002; Xu et al., 2010). Wang Chunyong (Wang et al., 1994) also concluded that the Taihang piedmont fault is not a deep fault by analyzing the deep seismic reflection profiles cutting through different sections of the fault. He considered it to be a shovel slip fault with a steep upper and a slow lower.

The Northeast P-wave low-velocity anomaly appears at a depth of 14 km in the Jizhong depression. As the depth increases, the region of P-wave low-velocity anomaly expands all the way down to 32 km. It is considered to be caused by the reduction of formation wave velocity by a series of faults. The faults at that location are the Niudong fault and the Gaoyangdong fault. We conclude that the Niudong fault and the Gaoyangdong fault are deep faults. It is generally believed that the Niudong fault controls the Niutuozhen uplift, while the Gaoyangdong fault controls the Gaoyang uplift. The main activity period of the faults is later than the secondary fault of the depression (Zhou et al., 2010).

Due to the dislocation of the strata on both sides caused by the fault, the fracture zone is generated, which makes the fault appear as a banded resistivity anomaly zone on the resistivity profile. Based on this, we identified the Taihang piedmont fault, Gaoyang west fault, Gaoyang east fault, Suning fault, Hejian fault, and so on according to the two-dimensional inversion profile of magnetotelluric resistivity. But small- and medium-sized faults in the Cenozoic caprock could not be identified because of the large distance between points measured by the magnetotelluric method. The multi-stage and multi-level spatial inherited faults of tectonic activities and the karst fissures in the Wumishan formation of the Jixian system are channels for thermal convection of deep fluids.

Stratigraphic Strata and Basement Undulation

According to the electrical characteristics of magnetotelluric sounding, the variation of low-high or low-high-low-high in the profile corresponds to the difference in electrical values of different lithologic strata, and the dense spacing of resistivity isolines shows the lithologic interface. After studying the logging data of 7 oil wells in the Jizhong depression (Shi et al., 2018), the resistivity of the regional formation was obtained (**Table 1**). It can be seen that among the sedimentary strata in the Jizhong depression, the resistivity of the Proterozoic Jixian system is the highest, followed by the Ordovician, Cambrian, and Qingbaikou systems, and the resistivities of the Neogene and Paleogene are the lowest. It should be noted that the resistivity obtained is the direct current resistivity, which is different from the magnetotelluric resistivity. However, the relative resistivity of different formations does not change. **Table 1** can still be used to explain the magnetotelluric profile in this study.

In the magnetotelluric profile, the Proterozoic Jixian system is the highest resistivity layer that belongs to the regional marker bed. The lithology of JZ04 is as follows (**Table 2**). The geological interpretation of the profile in the Jizhong depression (**Figure 6**) is compiled and combined with the JZ04 borehole. The profile is divided into 6 structural units, including the Taihang piedmont plain, Baoding sag, Gaoyang uplift, Lixian slope, Baxian sag, and Cangxian bulge. This forms a concave-convex structural pattern. The Gaoyang uplift belongs to low uplift, which is controlled by the Gaoyangdong fault. The buried depth of high resistivity carbonate rock at the section is 2,800~3300 m. Baoding sag

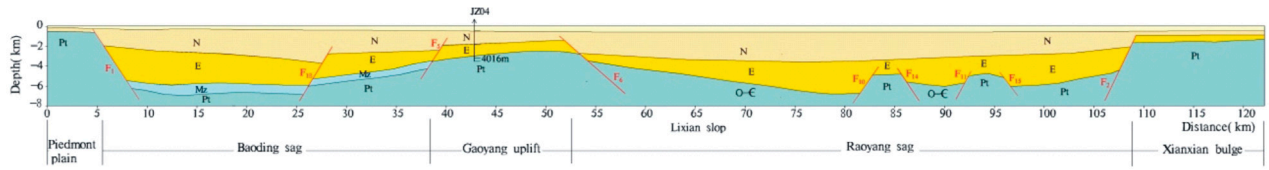

FIGURE 6 | Geological interpretation of MT.

is located in the west of the Gaoyang uplift, which is controlled by the Gaoyang fault. The buried depth of high resistivity in the sag is about 6 km. The east of the Gaoyang uplift is the Lixian slope, whose high resistivity is more than 4 km. To the east is Raoyang sag, whose depth of high resistivity is 4~6.5 km.

ANALYSIS OF THE HEAT SOURCE MECHANISM

The terrestrial heat flow of a sedimentary basin is made up of two parts (Birch et al., 1968). One part is crustal heat flow, whose heat comes from the decay of radioactive elements such as U, Th, and K in the shallow crust. The other part is the mantle heat flow, which comes from the deep mantle. Qiu Nansheng (Qiu et al., 2000) believes that the mantle heat flow accounts for more than 60% of the earth's heat flow according to the calculation of 10 km of sedimentary caprock in the North China Basin. As the Gaoyang uplift is located at the secondary unit of the Jizhong depression in the North China basin, so the deep mantle heat flow is the main heat source.

The North China Craton resulted in a massive thinning of the lithosphere. Seismic tomography results show that the thickness of the crust in the Jizhong depression is about 32 km. The thinner crust thickness reduces the distance for deep fluid to convert into the shallow crust, and that provides good conditions for deep heat energy to enter the shallow crust (Wang et al., 2017).

In recent years, helium derived from mantle was found in geothermal wells that indicated the invasion of materials from the mantle along the fault zone (Yang et al., 2018). Furthermore, the regional radon in the soil near the Xiadian fault is abnormally high (Miao et al., 2020), indicating the deep convection of fluid in the fault. According to the measurement of isotope gas geotemperature in the Niutuozhen geothermal field, the deep temperature of the Wumishan reservoir in the Jixian system is between 141 and 165°C. The contribution of helium derived from the mantle to the total helium content is 5~8%, indicating that the deep fault is a regional thermal control structure along which deep fluids are convecting into shallow reservoirs (Pang et al., 2018). The results of seismic tomography show that the cutting depth of the Gaoyangdong fault controlling the Gaoyang uplift reaches 28 km. The Gaoyangdong fault, which belongs to the tensile fault, is a deep fault. As an important channel, the fluid convection brings the deep heat flow to the shallow due to the difference in thermal potential.

There are sags on either side of the Gaoyang uplift. It forms a pattern of concave-convex structure which is conducive to the distribution and redistribution of heat flow in the Gaoyang uplift (Xiong and Gao, 1982). The pattern results in the formation temperature at the same depth being higher than that on both sides.

In addition, the thermal conductivity of Cenozoic sand and mudstone in the Gaoyang uplift is less than that of deep Jixian carbonate. Its thickness is more than 3000 m. The extremely thick caprock plays a good role in thermal insulation, which is the basic condition for the deep Jixian thermal reservoir to maintain a high temperature.

CONCLUSIONS

In this study, P-wave tomography and magnetotelluric sounding were used to probe the mechanism of high temperature in Gaoyang uplift, and the following conclusions were drawn:

1) The thickness of the crust in the Jizhong depression, where the Gaoyang uplift is located, is about 32 km. Compared with the Taihang Mountain uplift and Yanshan tectonic belt, the thickness of the crust is thinner, facilitating the heat flow of mantle into the shallow crust.
2) Each side of the Gaoyang uplift are sags. The concave-convex structure of the carbonate rock basement is convenient for heat flow to collect in the uplift area.
3) The thickness of Cenozoic sandstone and mudstone caprock in the Gaoyang uplift is about 3 km, which plays a good role in thermal insulation.
4) The cutting depth of the Gaoyang East fault is about 28 km, which is a large fault and provides a channel for convection of heat flow from the mantle to enter the shallow crust.

Comprehensive analysis shows that the crustal thickness in the Jizhong depression reducing, the tectonic pattern with concave and convex intersections, and the thickness of Cenozoic cap are the important conditions for the formation of regional geotherms. Compared with other uplifts in the Jizhong depression, the most important condition for high-temperature anomaly of heat storage in the Gaoyang uplift is that the Gaoyang East fault is a regional large fault, which provides conditions for deep geothermal fluid entering the shallow crust. Therefore, geothermal exploitation and utilization should be focused on the vicinity of the Gaoyang East fault and its intersecting faults in the future.

DATA AVAILABILITY STATEMENT

The raw data supporting the conclusions of this article will be made available by the authors without undue reservation.

AUTHOR CONTRIBUTIONS

QM studied the two methods and wrote the paper, GW provided suggestions for the structure of the paper, SQ studied the geology of the profile, LX studied the drill of JZ04, HX studied the P-wave velocity, and XZ studied the regional geology.

FUNDING

This study was financially supported by the grants from the geothermal survey project of the China Geological Survey (Grant No. DD20190555).

REFERENCES

Birch, F., Roy, R. F., and Decker, E. R., (1968). *Heat Flow and Thermal History in New York and New England: Studies of Appala Chian Geology: Northern and Maritime*. Editors E. Zen, W. S. White, J. B. Hadley, and J. B. Thopson (New York: Interscience), 437–451.

Cermark, V., and Rybach, L. (1989). Vertical Distribution of Heat Production in the Continental Crust. *Tectonophysic* 159, 217–230.

Chapman, D. S., and Rybach, L. (1985). Heat Flow Anomalies and Their Interpretations. *J. Geodyn.* 4 (1), 3–37. doi:10.1016/0264-3707(85)90049-3

Chen, M. X., and Deng, X. (1990). The Map of Geothermal Gradient of Cenozoic Sedimentary Cover in the North China Plain and its Brief Explanation. *Sci. Geol. Sin.* 3, 270–277. (in Chinese with English abstract).

Duan, Y., Wang, F., Zhang, X., Lin, J., Liu, Z., Liu, B., et al. (2016). Three dimensional Crustal Velocity Structure Model of the Middle-Eastern North China Craton (HBCrust1.0). *Sci. China Earth Sci.* 59, 1477–1488. doi:10.1007/s11430-016-5301-0

Gao, Z. J., Wu, L. J., and Cao, H. (2009). The Summarization of Geothermal Resources and its Exploitation and Utilization in Shandong Province. *J. Shandong Univ. Sci. Technology-Natural Sci.* 28 (2), 1–7. (in Chinese with English abstract). doi:10.16452/j.cnki.sdkjzk.2009.02.006

Jaupart, C., Labrosse, S., Lucazeau, F., and Mareschal, J.-C. (2015). Temperatures, Heat, and Energy in the Mantle of the Earth. *Earth Syst. Environ. Sci.* 7, 223–270. doi:10.1016/b978-0-444-53802-4.00126-3

Jin, F. M., Cui, Z. Q., Wang, Q., Li, L., Ren, C. L., Cui, M. Y., et al. (2017). Distribution Characteristics and Main Controlling Factors of Stratigraphic-Lithologic Reservoirs in Jizhong Depression. *Lithol. Reserv.* 29 (2), 19–27. doi:10.3969/j.issn.1673.8926.2017.02.003

Lei, J. S., Xie, F. R., Lan, C. X., Xing, C. Q., and Ma, S. Z. (2008). Seismic Images under the Beijing Region Inferred from P and P_mP Data. *Phys. Earth Planet Interi* 168 (3-4), 134–146. doi:10.1016/j.pepi.2008.06.005

Li, Z. W., Xu, Y., Hao, T. Y., Liu, J. S., and Zhang, L. (2006). Seismic Tomography and Velocity Structure in the Crust and Upper Mantle Around Bohai Sea Area. *Chin. J. Geophys.* 49 (3), 797–804. (in Chinese). doi:10.1002/cjg2.884

Lin, W. J., Chen, X. Y., Gan, H. N., and Yue, G. F. (2020). Geothermal, Geological Characteristics and Exploration Direction of Hot Dry Rocks in the Xiamen Bay-Zhangzhou Basin, Southeastern China. *Acta Geol. Sin.* 94 (7), 2066–2077. doi:10.19762/j.cnki.dizhixuebao.2020223

Miao, Q. Z., Wang, G. L., Xing, L. X., Zhang, W., Zhou, X. N., and Wang, W. Q. (2020). Study on Application of Deep Thermal Reservoir by Using Geophysical and Geochemical Methods in the Jizhong Depression Zone. *Acta Geol. Sin.* 94 (7), 2147–2156. doi:10.19762/j.cnki.dizhixuebao.2020225

Oskooi, B., Pedersen, L. B., Smirnov, M., Árnasonb, K., and Manzellac, A.the DGP Working Group (2005). The Deep Geothermal Structure of the Mid-Atlantic Ridge Deduced from MT Data in SW Iceland. *Phys. Earth Planet. Inter.* 150 (1-3), 183–195. doi:10.1016/j.pepi.2004.08.027

Pang, J. M., Pang, Z. H., and Lu, M. (2018). Geochemical and Isotopic Characteristics of Fluids in the Niutuozhen Geothermal Field, North China. *Environ. Earth Sci.* 77 (1), 1–12. doi:10.1007/s12665-017-7171-y

Qi, C., Zhao, D. P., Chen, Y., Chen, Q. F., and Wang, B. S. (2006). 3-D P and S Wave Velocity Structures and Their Relationship to Strong Earthquakes in the Chinese Capital Region. *Chin. J. Geophys.* 49 (3), 805–815. (in Chinese). doi:10.3321/j.issn:0001-5733.2006.03.024

Qiu, N. S. (2000). Discussion on Genesis Models of Thermal Evolution in Different Sedimentary Basins. *Petroleum Explor. Dev.* 27 (2), 15–17. doi:10.3321/j.issn:1000-0747.2000.02.005

Shi, Z., Zhang, H., and Duan, T. (2018). Investigation of Oil and Gas Reservoir in Jizhong Depression Based on Time-Frequency Electromagnetic Method. *Glob. Geol.* 37 (02), 585–594. (in Chinese with English abstract). doi:10.3969/j.issn.1004-5589.2018.02.025

Turcote, D. L., and Schubert, G. (1982). *Geodynamics: Application of Continuum Physics to Geological Problems*. New York: John Wiley and Sons.

Urzua, L., Powell, T., Cumming, W. B., and Dobson, P. (2002). *Apacheta, A New Geothermal Prospect in Northern Chile*, 26. US: Transactions-Geothermal Resources Council.

Villas, R. N., and Norton, D. (1977). Irreversible Mass Transfer between Circulating Hydrothermal Fluids and the Mayflower Stock. *Econ. Geol.* 72 (8), 1471–1504. doi:10.2113/gsecongeo.72.8.1471

Wang, C. Y., Zhang, X. K., Wu, Q. J., and Zhu, Z. P. (1994). Seismic Evidence of Detachment in North China Basin. *Chin. J. Geophys.* 37 (5), 613–620. (in Chinese).

Wang, G. L., Gao, J., Zhang, B. J., Xing, Y. F., Zhang, W., and Ma, F. (2020b). Study on the Thermal Storage Characteristics of the Wumishan Formation and Huge Capacity Geothermal Well Parameters in the Gaoyang Low Uplift Area of Xiong'an New Area. *Acta Geol. Sin.* 94 (7), 1970–1980. doi:10.19762/j.cnki.dizhixuebao.2020235

Wang, G. L., Liu, Y. G., and Zhu, X. (2020a). The Status and Development Trend of Geothermal Resources in China. *Earth Sci. Front.* 27 (1), 001–009. doi:10.13745/j.esf.2020.1.1

Wang, G. L., Zhang, W., Liang, J. Y., Lin, W. J., Liu, Z. M., and Wang, W. L. (2017b). Evaluation of Geothermal Resources Potential in China. *Acta Geol. Sin.* 38 (4), 449–459. doi:10.3975/cagsb.2017.04.02

Wang, G. L., Zhang, W., Lin, W. J., Liu, F., Zhu, X., Liu, Y. G., et al. (2017a). Research on Formation Mode and Development Potential of Geothermal Resources in Beijing-Tianjin-Hebei Region. *Geol. China* 44 (6), 1074–1085. (in Chinese with English abstract). doi:10.12029/gc20170603

Wang, S. Y., Xu, Z. H., and Pei, S. P. (2003). Velocity Structure of Upper Most Mantle beneath North China from P_n Tomography and its Implications. *Sci. China Ser. D Earth Sci.* 33 (2), 130–140. doi:10.1002/cjg2.431

Wang, Y., Wang, J. Y., Xiong, L. P., and Deng, J. F. (2001). Lithospheric Geothermics of Major Geotectonic Units in China Mainland. *Acta Geosci. Sin.* 22 (1), 17–22. (in Chinese with English abstract). doi:10.3321/j.issn:1006-3021.2001.01.004

Wu, A. M., Ma, F., Wang, G. L., Liu, J. X., Hu, Q. Y., and Miao, Q. Z. (2018). A Study of Deep-Seated Karst Geothermal Reservoir Exploration and Huge Capacity Geothermal Well Parameters in Xiong'an New Area. *Acta Geosci. Sin.* 39 (5), 523–532. (in Chinese with English abstract). doi:10.3975/cagsb.2018.071104

Xiong, L. P., and Gao, W. A. (1982). Characterics of Geotherm in Uplift and Depression. *Chin. J. Geophys.* 25 (5), 60–68. (in Chinese with English abstract).

Xu, J., Gao, Z. W., Sun, J. B., and Song, C. Q. (2001). A Preliminary Study of the Coupling Relationship between Basin and Mountain in Extensional Environments. *Acta Geol. Sin.* 75 (2), 165–174. doi:10.3321/j.issn:0001-5717.2001.02.004

Xu, M.-C., Gao, J.-H., Rong, L.-X., Wang, G.-K., and Wang, X.-J. (2010). Seismic Analysis of the Active Character of the Taihang Mountain Piedmont Fault. *Appl. Geophys.* 7 (4), 392–398. doi:10.1007/s11770-010-0265-x

Yan, D. S., and Yu, Y. T. (2000). *Evaluation and Utilization of Geothermal Resources in Beijing-Tianjin-Hebei Oil Region*. (Beijing: China University of Geosciences Press), 8–95. (in Chinese).

Yang, M. H., Liu, C. Y., Yang, B. Y., and Zhao, H. G. (2002). Extensional Structures of the Paleogene in the Central Hebei Basin,China. *Geol. Rev.* 48 (1), 58–67. doi:10.16509/j.georeview.2002.01.011

Yang, Q. Y., Wu, Q. J., Sheng, Y. R., Gao, J. Y., Song, J., and Di, L. (2018). Regional Seismic Body Wave Tomography and Deep Seismogenic Environment beneath Zhangbo Seismic Belt and its Adjacent Area. *Chin. J. Geophys.* 33 (8), 3251–3262. (in Chinese with English abstract). doi:10.6038/cjg2018L0628

Ye, L. J. (1983). *North China Platform Sedimentary Formation*. Beijing: Science Press. (in Chinese).

Yu, X. W., Chen, Y. T., and Zhang, H. (2010). Three-dimensional Crustal P-Wave Velocity Structure and Seismicity Analysis in Beijing-Tianjin-Tangshan Region. *Chin. J. Geophys.* 53 (8), 1817–1828. (in Chinese). doi:10.3969/j.issn.0001-5733.2010.08.007

Zhang, W. C., Yang, X. D., Chen, Y. J., Qian, Z., Zhang, C. W., and Liu, H. F. (2008). Sedimentary Structural Characteristics and Hydrocarbon Distributed Rules of Jizhong Depression. *Acta Geol. Sin.* 82 (8), 1103–1112. (in Chinese with English abstract). doi:10.16509/j.georeview.2002.01.011

Zhou, C. A., Li, X. P., Xin, W. J., Li, H. L., Wu, G. Q., Wu, X. L., et al. (2010). Research on Hydrocarbon Accumulating Conditions of Internal Buried Hills Exploration in Niutuozhen Uplift in Jizhong Sag. *China Pet. Explor.* 2010 (2), 29–32. doi:10.3321/j.issn:0001-5717.2008.08.011

Conflict of Interest: The authors declare that the research was conducted in the absence of any commercial or financial relationships that could be construed as a potential conflict of interest.

frontiers | Frontiers in Earth Science

ORIGINAL RESEARCH
published: 20 June 2022
doi: 10.3389/feart.2022.895604

Genetic Analysis of Abnormally High Ground Temperature From the Existence of Magmatic Rock Beneath Pingdingshan Coalfield

*Qi Wang[1], Jiajia Liao[2], Dongxu Zhou[1], Quanlin Hou[3] and Xinyi Wang[2,4,5]**

[1]College of Geosciences and Engineering, North China University of Water Resources and Electric Power, Zhengzhou, China, [2]Institute of Resources & Environment, Henan Polytechnic University, Jiaozuo, China, [3]College of Earth Science, University of Chinese Academy of Sciences, Beijing, China, [4]Collaborative Innovation Center of Coalbed Methane and Shale Gas for Central Plains Economic Region, Jiaozuo, China, [5]Collaborative Innovation Center of Coal Work Safety and Clean High Efficiency Utilization, Jiaozuo, China

Studies on the genetic mechanisms of abnormally high ground temperatures in coalfields are of great significance for the efficient mining of coal mines and the development and utilization of geothermal water. Therefore, we measured the temperature of 45 Cambrian limestone groundwater samples, thermal conductivity values of 11 Cambrian limestone samples, and the contents of uranium, thorium, and potassium-40 of 40 rock samples, aiming to ascertain the heat source of the abnormally high ground temperature in the Pingdingshan coalfield. The results show that the average geothermal gradient in the coalfield is about 3.32°C/100 m, and the calculated values of the average ground heat flow are about 104.28 mW/m^2, which demonstrate the abnormally high ground temperature in Pingdingshan coalfield. We also concluded that the whole radiogenic heat generation in sedimentary and magmatic rocks is 1.53 mW/m^2, whose contribution rate to the local geothermal flow is only 1.47%. Hence, we can infer that magmatic rocks exposed in or near the coalfield area may supply the heat source for the abnormally high ground temperature beneath Pingdingshan coalfield. A comprehensive analysis further shows that the latest intrusion time of the magmatic rock mass in the coalfield was 35 Ma; its lava temperature was 900°C, its cooling rate is 20.0°C/Ma, and the calculated residual temperature is more than 200.0°C. These values support the idea that the magmatic rocks may be the primary cause of the abnormally high ground temperature in the Pingdingshan coalfield.

Keywords: terrestrial heat flux, radionuclide exothermic, magmatic heat generation, residual temperature, Pingdingshan mining area

OPEN ACCESS

Edited by:
Wenjing Lin,
Chinese Academy of Geological Sciences, China

Reviewed by:
Zhuting Wang,
China University of Mining and Technology, China
Fengxin Kang,
Shandong Provincial Bureau of Geology and Mineral Resources (SPBGMR), China

****Correspondence:***
Xinyi Wang
wangxy@hpu.edu.cn

Specialty section:
This article was submitted to Geochemistry, a section of the journal Frontiers in Earth Science

Received: *14 March 2022*
Accepted: *16 May 2022*
Published: *20 June 2022*

Citation:
Wang Q, Liao J, Zhou D, Hou Q and Wang X (2022) Genetic Analysis of Abnormally High Ground Temperature From the Existence of Magmatic Rock Beneath Pingdingshan Coalfield. Front. Earth Sci. 10:895604. doi: 10.3389/feart.2022.895604

1 INTRODUCTION

Monitoring data have shown that the average geothermal gradient of the Pingdingshan coalfield is 3.32°C/100 m. At a buried depth of 1,000 m, the temperature can reach as high as 49.57°C in the rocks or groundwater. Hence, it is an area with an abnormally high ground temperature compared to other zones in Henan Province. Affected by the higher surrounding rock temperature and roof-pouring (gushing) water, the ambient temperature and air humidity of the underground mining space are

very high so that it not only increases the cost of coal mining, but also affects the physical and mental health and labor efficiency of the workers. Therefore, in this study an analysis of the genetic mechanism responsible for the abnormally high coalfield ground temperature seems to be of great significance.

In recent years, many scholars have focused on researching the heat-source mechanism of different geothermal areas via studying the heat production of radioisotopes and magmatic rocks. Burns et al. (2015) studied the steep permeability drop and low heat flow anomaly of a middle plateau aquifer system on the Columbia Plateau, which contains a heat flow regime at depths of 600–900 m. Their research showed that the steep permeability drop is related to hydrothermal transformation and pore-refilling minerals in the volcanic area. Peng et al. (2015) studied the geothermal field in the Linhuan mining area of the Huaibei coalfield and concluded that the high geothermal gradient mainly occurs in areas containing intensively developed anticlines and faults, and a high-temperature anomaly also occurs mainly in areas with intensively developed folds, uplifts, and faults (Jun et al., 2015). Ren et al. (2017) calculated the heat generation rate of coal-measure sedimentary rocks and magmatic rocks based on the natural gamma (GR) logging values of 6,208 coal-measure rocks taken from 36 boreholes in the Zhuji coalfield, Huainan, China. Generally speaking, the contribution of radiogenic heat generation of coal-measure rocks to terrestrial heat flow in the area is small, but the high heat generation rate of magmatic rocks has changed the heat generation structure of the rock strata greatly. Hasterok et al. (2018) analyzed the radiogenic heat generation of 204,000 whole rock geochemical data. Their research showed that the radiogenic heat generation of igneous and metamorphic igneous rocks increases with an increase of SiO_2 and K_2O, and decreases with an increase of Fe_2O_3, MgO, and CaO; meanwhile, the heat production of sedimentary and metamorphic rocks increases with an increase of Al_2O_3, FeO, TiO_2, and K_2O, but decreases with an increase of CaO. According to 39,933 and 6,465 Precambrian rock samples collected in Sweden and Finland, Veikkolainen et al. (2019) measured the concentrations of radioactive uranium, thorium, and potassium and calculated the heat generation rate. Their calculations showed that the average radiogenic heat generation rate of Precambrian rock samples in Sweden and Finland is $2.4 \pm 1.6\ \mu W/m^3$ and $1.42 \pm 1.41\ \mu W/m^3$, respectively; hence, the heat-production rate in Sweden is much higher than that in Finland (Veikkolainen and Kukkonen, 2019). Scharfenberg et al. (2019) tested and performed calculations of a Bohemia block in Germany, showing that the radiogenic heat generation rate in the granite is 3.9–8.9 $\mu W/m^3$, with an average of 4.9 $\mu W/m^3$, implying a medium-to-high heat-generation rate. The contribution of radiogenic heat generation should be considered in simulations of geothermal genetic mechanism. Erbek and Dolmaz (2019) showed that the heat flow to the southeast of the Aegean Sea and western Turkey is 50–125 mW/m^2, while the radiogenic heat generation rate is 0.21–0.51 $\mu W/m^3$. They found that the high heat flow value is closely related to seismic and tectonic activity in this area. Wang et al. (2019) analyzed the thermal state and geothermal potential of the lithosphere in the Xiong'an New Area, and their results showed that the average heat flux in the study area is 70.5 mW/m^2, higher than that on the Chinese mainland, which is 61.5 mW/m^2, and the crustal temperature at a depth of 40 km is 750–1,100°C.

Zhao et al. (2020) studied the geothermal mechanism of the hot dry rock (HDR) area in the Gonghe Basin, and they found that magma chambers and molten granite in the upper crust may be important heat sources for the HDR in Gonghe Basin, and that heat is transmitted through the near formation fractures, making Gonghe Basin a potential geothermal area. Song et al. (2020) calculated the radiogenic heat generation rate of a magmatic rock mass in southeast Jiangxi. Their research showed that the heat generation rate increases as the age of the rock mass decreases, and the heat generation rate of the Yanshanian magmatic rocks shows an obvious law of high in the south, low in the north, high in the west, and low in the east (Lu-sheng et al., 2020). Zhang et al. (2020a) calculated the heat production of radioactive elements of granitoids in the Gonghe Basin and Qinghai Tibet Plateau, and found that the abnormal heat flow in the Gonghe Basin may be a result of the combined action of radioactive element radiation heat generation in the thick crust and local thermal anomalies. According to the research of Sun et al. (2020), the ground heat flow value in southeast Guangxi is between 80 and 100 mW/m^2, and the temperature gradient is higher than 30°C/km. They concluded that the higher radionuclide content in the Indosinian granite in the area is the basis of the stable heat source. Based on the radiogenic heat generation rate data of 98 rock samples collected from the Gonghe Basin, Zhang et al. (2020b) analyzed the distribution characteristics of the radiogenic heat generation rate of main lithologic rocks in the basin and established a genetic model of the HDR geothermal resources in the area. Luo et al. (2020) calculated 6,094 radiogenic heat generation rates in the sedimentary layers in the Tarim Basin, finding an average value of $1.17 \pm 0.336\ \mu W/m^3$. Mudstone has the highest heat generation rate, followed by sandstone, dolomite, and limestone, and lithology is the main factor affecting the heat generation rate. It was estimated that the heat flow contribution from radiogenic heat generation is 9.36 mW/m^2, accounting for about 21% of the total surface heat flow. The radiogenic heat generation also has an impact on the geothermal field in the Tarim Basin. Ogunsanwo et al. (2021) calculated the radiogenic heat production rate for 30 rock samples from 10 quarries in Ogun State, Nigeria, which showed a range of values of 0.549–3.122 $\mu W/m^3$, in which uranium contributes the most and thorium contributes the least. Weinert et al. (2021) calculated the radionuclide heat production rate based on 30 Triassic, Silurian, Ordovician, and Devonian intrusive rocks extracted from a complex in the Gonghe Basin. Their study showed that the heat production rate of radioactive elements in this area is less than 1 $\mu W/m^3$ in biotite granite, and greater than 5 $\mu W/m^3$ in syenogranite. Ma et al. (2021) found that the deep heat source of a geothermal abnormity in the eastern Himalayan structural junction area mainly comes from the Yarlung Zangbo River junction zone and nearby deep faults, and the surface heat is mainly controlled by secondary tension and torsion faults on both sides of the junction zone (Xin et al., 2021).

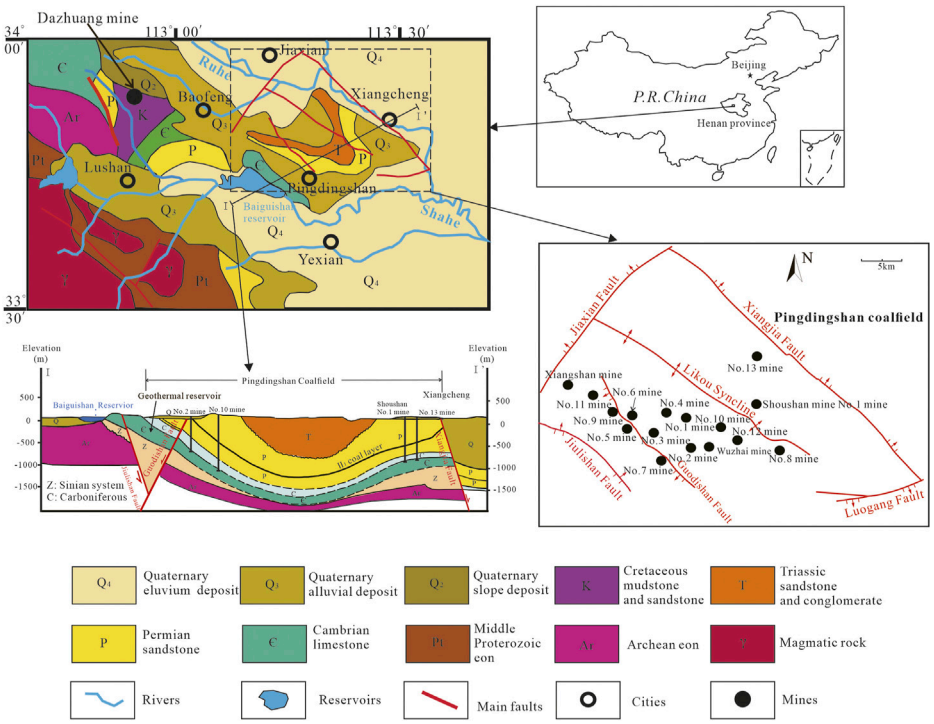

FIGURE 1 | Geological setting and mine positions in the Pingdingshan coalfield.

Regarding the abnormally high ground temperature in Pingdingshan coalfield, Zhang et al. (2000) analyzed the influence of groundwater migration on the temperature field based on the silica temperature scale method and isotope method, and expounded the causes of the uneven temperature distribution in the geothermal field. Based on an analysis of the distribution characteristics of the geothermal field in the Pingdingshan coalfield, Cao et al. (2014) clarified that the abnormal high-temperature area has the characteristics of a dense development of faults and fractures and fold uplift. The geothermal distribution is affected by the regional geological structure, groundwater activities, rock properties, and caprock properties (Bingqi et al., 2014).

Overall, studies on the abnormity of the ground temperature and its influencing factors in the Pingdingshan coalfield have been extensive, but there has been less research regarding the genetic mechanism of the abnormally high ground temperature. Therefore, based on field-measured data and geological setting conditions, we further studied the heat source of the abnormally high ground temperature in the Pingdingshan coalfield. The conclusions in this study may provide support for preventing and controlling mine heat damage, and promoting the development and utilization of geothermal water in the future.

2 GEOLOGICAL AND GEOTHERMAL CHARACTERISTICS

The Pingdingshan coalfield is located on an uplift fault block surrounded by the Jiaxian Fault, Xiangjia Fault and Luogang Fault, with an east–west length of 40 km and a north–south width of 10–20 km, and the mining area is about 650 km^2 (**Figure 1**). At present, Pingdingshan coalfield mainly mines the II_1 coal bed with a depth ranging from 680 to 1,000 m, which represents a deep mining state.

The strata of the Pingdingshan coalfield includes an Archean metamorphic rock series, Archaean, upper Proterozoic Sinian, lower Paleozoic Cambrian, upper Paleozoic Carboniferous and Permian, Mesozoic Triassic, Cenozoic Neogene and Quaternary (**Figure 1**). A histogram of the stratum lithology in Pingdingshan coalfield is shown in **Figure 2**. The geothermal reservoirs in the Pingdingshan abnormity area are thick limestone composed of an upper Cambrian Gushan Formation and middle Zhangxia Formation. For buried stratum depths less than 420 m, karst caves of different sizes and shapes are densely distributed and karst is relatively developed. For buried depths greater than 420 m, the distributions of karst layers are variable, and there are no karst caves. Generally, the karst is not as developed as in the upper part, but at the intersection of structural development zones and faults, karst pores, karst gaps, and fractures are relatively developed.

The main structure in the area is a wide and gentle compound Likou syncline with many secondary folds located to the south and north of the Likou syncline axis. There also exists some large and medium-sized faults in Pingdingshan coalfield, such as Guodishan Fault, and most of them are blocking faults. The simple geological setting of the Pingdingshan coalfield is shown in **Figure 1**.

Rock stratigraphic units				Thickness (m)	Lithological description
Erathem	System	Formation	Designator		
Cenozoic	Quaternary		Q	0~430	Gravel, pebbles and sand dominate.
	Neogene		N	0~200	The lower part is sandstone and the middle and upper part is sandy mudstone.
Mesozoic	Triassic	Ermaying	T_{2E}	0~250	Feldspathic quartz sandstone and feldspathic sandstone.
		Liujiagou	T_{1l}	0~250	Medium and fine-grained sandstone interspersed with calcareous siltstone.
Upper Paleozoic	Permian	Shiqianfeng	P_{22}	0~312	Sandstone and sandy mudstone.
		Upper-Shihezi	P_{21}	0~390	Sandstone, sandy mudstone and thin coal seams.
		Lower-Shihezi	P_{12}	0~397	Sandstone, sandy mudstone, mudstone and coal seams.
		Shanxi	P_{11}	84	Sandstone, sandy mudstone and coal seams.
	Carboniferous	Taiyuan	C_{3t}	30~80	Limestone, sandstone, sandy mudstone and coal seams.
		Benxi	C_{2b}	0~20	Limonite, oolitic aluminous mudstone and very unstable thin coal seams.
Lower Paleozoic	Cambrian	Fengshan	$\in_{3f}$	0~38	Cryptocrystalline dolomitic limestone, thinly bedded mudstone and grey dolomite.
		Changshan	$\in_{3ch}$	0~66	Dolomitic limestone, mudstone and dolomite.
		Gushan	$\in_{3g}$	25~32	Fine-grained dolomite and oolitic dolomite.
		Zhangxia	$\in_{2zh}$	60~220	Oolitic dolomite.
		Xuzhuang	$\in_{2x}$	50~250	Medium-thickly bedded muddy-striped limestone, dolomitic limestone.
		Maozhuang	$\in_{2m}$	90~140	Siltstone.
		Mantou	$\in_{13}$	220	Shale and limestone.
		Xinji	$\in_{11}$	55~210	Medium to coarse grained quartz sandstone, leopard skin limestone and dolomitic limestone.
Upper Proterozoic	Sinian	Luoquan	Z_{3l}	100	The lower part is an ice-covered sandy conglomerate and the upper part is a sandy mudstone.
		Luoyukou	Z_{3ly}	320	Thickly bedded siliceous streaked dolomite.
		Sanjiaotang	Z_{3s}	100	Thickly bedded medium to fine-grained quartz sandstone.
		Cuizhuang	Z_{3c}	290	Sandy shale.
		Beidajian	Z_{2bd}	241~280	Thickly bedded fine and medium grained quartz sandstone.
		Baicaoping	Z_{2b}	166~180	Muddy siltstone and sandy mudstone.
		Yunmengshan	Z_{2y}	177~533	Quartz sandstone.
		Majiahe	Z_{1m}	1,580~2,220	Metamorphic andesite.
Archaean		Zhaoanzhuang	A_{rz}	>2,950	Plagioclase gneisses and hornblende gneisses.

FIGURE 2 | Histogram of stratum lithology.

3 DATA AND METHODS

In order to ascertain the heat source of Pingdingshan geothermal abnormal area, a total of 45 temperature values were measured at the outlets of geothermal wells and drains in the Pingdingshan coalfield, and the locations, measured temperatures, and corresponding geothermal gradients are shown in **Table 1**.

In the Pingdingshan coalfield and neighboring Ruzhou coalfield, 11 limestone samples were collected from the Cambrian strata, and the values of the thermal conductivity were determined by Chinese Academy of Geological Sciences using thermal conductivity scanning (TCS), with a determining range of 0.20–25 W/(mK). The uncertainty of measured results was about 3%, and the results are shown in **Table 2**.

To obtain the radionuclide contents (uranium, thorium, and potassium-40) in the stratum of the Pingdingshan coalfield, 40 rock samples were collected from surface rock belts and geological drilling holes. At Beijing Research Institute of Uranium Geology (BRIUG), the contents of uranium and thorium were both measured by inductively coupled plasma mass spectrometry (ICP-MS; PerkinElmer Elan DCR-e), and the uncertainties were lower than 10% with a determining range of 0.05×10^{-6} to $1{,}000 \times 10^{-6}$ mg/kg. The content of potassium-40 was determined by atomic absorption spectroscopy (z-2000) with an uncertainty lower than 2%. The densities of the rock samples were measured with a densitometer (AKD-120A) with a measurement precision and uncertainty of 0.0001 g/cm^3 and 2%, respectively, in the laboratory of Henan Polytechnic University. All the measured values are shown in **Table 3**.

TABLE 1 | Geothermal gradient of cap rock in different mines.

Locations	Depth (m)	Well head temperature (°C)	Geothermal gradient (°C/100 m)
Special return air roadway of No. 2 mine	508	27	2.03
31,010 air roadway of No. 2 mine	790	41	3.11
Lower concentration roadway of No. 2 mine	818.7	40	2.87
Downhill drilling of geng-1 belt in No. 2 mine	916	41.5	2.73
Cambrian hydrological hole of No. 3 mine	690	42	3.73
Geng-1 Drainage hole of No. 4 mine	627	40	3.79
Downhill 18# hole of No.4 mine	902.5	43.5	3.00
G18 + 3 m drainage hole of No. 4 mine	1,017	43	2.60
Drainage hole in F19 of No. 4 mine	1,055	48	2.99
Shimen water inrush point of No. 5 mine	616	40	3.86
320 water inrush point of No. 5 mine	622	45	4.66
Ji-2 water bunker of No. 5 mine	975	46	3.03
The downhill in the geng-2 area of No. 7 mine	355	21.5	1.30
13,141 cut hole of No. 8 mine	465	36	4.27
Ji-3 return air roadway of No. 8 mine	513	37	4.06
11,032 drain hole of No. 8 mine	585	40.7	4.20
13,011 drain hole of No. 8 mine	598	40.7	4.10
13,022 drain hole of No. 8 mine	590	38	3.68
West roadway 1# hole of No. 8 mine	680	49	4.85
West roadway 2# hole of No. 8 mine	760	49	4.33
West roadway 3# hole of No. 8 mine	843	52	4.25
West roadway 4# hole of No. 8 mine	850	49	3.85
West roadway 5# hole of No. 8 mine	860	49	3.81
West roadway 6# hole of No. 8 mine	875	49	3.74
West roadway 7# hole of No. 8 mine	925	49	3.53
Ji-2 lower extension sump of No. 8 mine	1,179	47	2.58
-618 hydrological hole of No. 9 mine	893	37.5	2.34
Ji-4 water bunker of No. 10 mine	1,106.8	51	3.12
Hydrological hole of No. 11 mine	543	23	1.12
Hydrological hole 2 of No. 12 mine	1,091	54	3.45
5# drain hole of No. 12 mine	1,119	52	3.18
7# drain hole of No. 12 mine	1,114	54	3.38
Hydrological hole of No. 13 mine	580	45	5.01
Inrush point 1# of No. 13 mine	584	38	3.72
Inrush point 2# of No. 13 mine	660	27	1.54
Inrush point 3# of No. 13 mine	590	27	1.73
Inrush point 4# of No. 13 mine	627	42	4.12
Inrush point 5# of No. 13 mine	823	53	4.49
Ji-3 bunker mouth of No. 13 mine	822	49	3.99
Hydrological hole of Xiangshan mine	293	22	1.79
Hydrological hole of Wuzhai mine	438	26	2.13
2# hole in transportation roadway of Wuzhai mine	457.2	26	2.03
-7,604 hole of Shoushan No.1 mine	633	51	5.56
-769 sump of Shoushan No.1 mine	891.7	50	3.78
Civil well near to Jiaxian	421	25	1.97
Mean Value			3.32

4 RESULTS AND DISCUSSION

4.1 Characteristics of the Geothermal Gradient

The temperature of the constant-temperature zone in Pingdingshan is 17.2°C, and the depth of the constant temperature zone is about 25 m. According to the measured temperatures of the 45 groundwater samples of Cambrian limestone, the geothermal gradient of the Pingdingshan coalfield was calculated, and the calculated results for the different mines are shown in **Table 1** and **Figure 3**. It can be seen that the geothermal gradient is 1.12–5.56 °C/100 m, with an average of 3.32°C/100 m, inferring that the Pingdingshan coalfield is an area with an abnormally high ground temperature. It is interesting that the areas between the No. 13 mine and Shoushan No.1 mine show a high geothermal gradient.

The cap rock geothermal gradients are controlled by the buried depth of the Cambrian limestone reservoir. The results are shown in **Table 4**. In general, the geothermal gradient at buried depths less than 550 m is relatively low, with an average of 2.01°C/100 m. The geothermal gradient at buried depths of 600–850 m is relatively high, with an average of 3.96°C/100 m. The geothermal gradient at buried depths of more than 900 m is also low, with an average of 2.93°C/100 m.

TABLE 2 | Thermal conductivity of the Cambrian limestone (W/mK).

Coalfields	Locations	Sratum	Lithology	Thermal conductivity	Average
Pingding shan	Cambrian limestone exposed area	Zhangxia Formation in Cambrian system	Dolomite	3.050	3.837
	No. 11 mine			3.241	
	Shoushan No.1 mine			4.166	
	No. 2 mine			4.889	
	Xiangshan mine	Gushan Formation in Cambrian system	Dolomite limestone	1.501	2.420
	No. 11 mine			2.871	
	No. 9 mine			2.560	
	Shengli bridge			2.448	
	No. 13 mine			2.680	
	No. 5 mine			2.461	
	Average			2.987	
Ruzhou	Well 1 of Chaochuan mine	Zhangxia Formation in Cambrian system	Dolomite	3.036	

TABLE 3 | Measured contents of radionuclides in the different strata.

Times	Lithology	N_U (μg/g)	N_{Th} (μg/g)	N_K (%)	P (g/cm^3)
Quaternary	Clay	2.91	16.20	3.48	1.72
Neogene	Marl	2.18	11.60	1.51	1.47
Triassic Liujiagou formation	Sandstone	1.05	6.10	2.76	2.46
Permian Qianfeng formation	Sandstone	1.57	6.71	1.79	2.58
Upper Shihezi Formation of Permian	IV_2 coal	2.21	6.99	0.19	1.41
	V_2 coal	1.41	3.69	0.10	1.45
Lower Shihezi Formation of Permian	Mudstone	3.57	15.90	1.59	2.49
	Sandstone	1.80	8.68	1.72	2.63
Permian Shanxi Formation	Sandy mudstone	2.28	12.55	1.97	2.62
	II_1 coal	1.30	5.42	0.11	1.40
Carboniferous Taiyuan Formation	Sandstone	1.64	9.86	3.03	2.69
	Thin limestone	1.85	0.26	0.04	2.70
	Bauxite mudstone	2.93	16.40	4.46	2.65
	I_5 coal	1.99	3.65	0.09	1.32
Cambrian Gushan formation	Dolomitic limestone	2.96	5.12	3.06	2.68
Cambrian Zhangxia formation	Oolitic dolostone	2.77	1.36	0.29	2.75
Late Yanshanian magmatic rocks	Andesite	1.10	3.47	2.63	2.43
Mean Value		2.09	7.88	1.70	2.20

4.2 Calculating the Terrestrial Heat Flow

The Earth heat flux can be estimated by the Fourier formula:

$$q = 10 \times \lambda \times \theta \quad (1)$$

where q is the geothermal flow (mw/m^2), λ is the thermal conductivity of the surrounding rock (w/(mk)), and θ is the geothermal gradient (°C/100 m).

Based on the measured thermal conductivity of the limestone in the Cambrian system (**Table 2**), the average thermal conductivity of the oolitic dolomite of the Cambrian Zhangxia Formation in the Pingdingshan coalfield is 3.837 W/mK (**Table 5**), and that of the dolomitic limestone in the Gushan Formation is 2.420 W/m·K; the former is significantly higher than the latter. The average thermal conductivity of the Cambrian limestone throughout the whole coalfield is 2.987 W/m·K.

Because the areas near the southwest of the Guodishan Fault and northwest of the No. 13 mine are recharge areas of the Cambrian limestone, we may infer that the relatively low geothermal gradient is due to the influence of groundwater flow; so these areas were not used to calculate the ground heat flow. The calculations of the average geothermal gradient in different mines are shown in **Table 5**, where the heat flow value of each mine was obtained from **Eq. 1**. The mean values of the ground heat flow in the Pingdingshan coalfield is an abnormally high heat flow of 104.28 mW/m^2, which is much higher than the value of 65.88 mW/m^2 in the No. 1 well of the Chaochuan mine in the Ruzhou coalfield, 58.49 mW/m^2 in the Kaifeng Depression, and 62.63 mW/m^2 in the Tongxu Uplift.

4.3 Radiogenic Heat Generation in the Strata

4.3.1 The Computational Formula

The rock radiogenic heat generation rate refers to the heat generated in the decay process of radionuclides contained in rock per unit volume (or unit weight) per unit time. Uranium

TABLE 4 | Geothermal gradients at different burial depths (°C/100 m).

Buried depth the cambrian limestone reservoir (m)	Geothermal gradient	Buried depth the cambrian limestone reservoir (m)	Geothermal gradient	Buried depth the cambrian limestone reservoir (m)	Geothermal gradient
300 ± 25	1.79	600 ± 25	3.87	900 ± 25	3.08
350 ± 25	1.30	650 ± 25	3.75	950 ± 25	3.03
400 ± 25	1.97	700 ± 25	4.29	1,000 ± 25	2.60
450 ± 25	2.81	750 ± 25	4.33	1,050 ± 25	2.99
500 ± 25	3.05	800 ± 25	3.62	1,100 ± 25	3.28
550 ± 25	1.12	850 ± 25	3.91	1,150 ± 25	2.58
Average	2.01	Average	3.96	Average	2.93

TABLE 5 | Calculated heat flow in Pingdingshan and neighboring mining areas (mw/m^2).

Coalfield	Locations	Geothermal gradient (°C/100m)	Thermal conductivity (W/m·K)	Terrestrial heat flux	Average value
Pingding shan	Wuzhai mine	2.08	2.987	62.13	104.28
	No. 2 mine	2.69		80.35	
	No. 4 mines	3.10		92.60	
	No. 10 mines	3.12		93.19	
	No. 12 mines	3.34		99.77	
	No. 3 mines	3.73		111.42	
	No. 5 mines	3.85		115.00	
	No. 8 mines	4.06		121.27	
	No. 13 mines	4.27		127.54	
	Shoushan No.1 mine	4.67		139.49	
Ruzhou	Well 1 of Chaochuan mine	2.17	3.036	65.88	

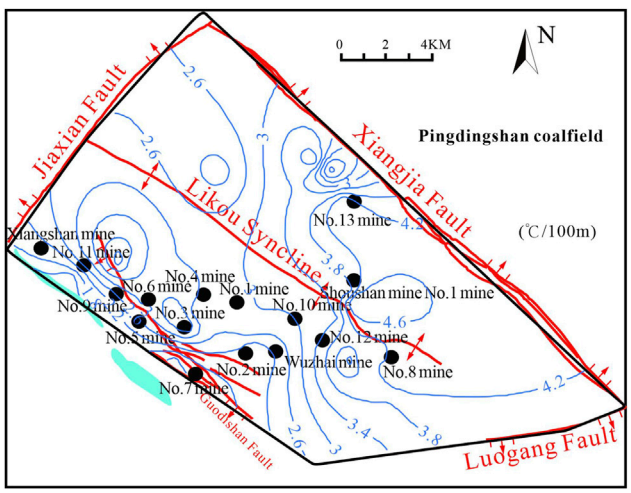

FIGURE 3 | Contour map of the geothermal gradient in the Pingdingshan coalfield.

($^{238}_{92}U$), thorium ($^{232}_{90}Th$), and potassium ($^{40}_{19}K$) in crustal rocks are three radionuclides that play an important role in the ground temperature because of their high abundances and high heat generation rates. Their half-lives (4.47×10^9 year, 1.40×10^{10} year, and 1.26×10^9 year, respectively) are equivalent to the Earth's age (4.55×10^9 year).

Based on the content of the radionuclides uranium, thorium, and potassium, and rock densities of the tested rock samples, the heat generation rate of radionuclides and the corresponding heat release can be calculated by using the Rybach formulas as:

$$Q_A = 0.01 \times \rho \times (9.52 \times N_U + 2.56 \times N_{Th} + 3.48 \times N_K) \quad (2)$$

$$Q = 0.001 \times \overline{Q_A} \times M \quad (3)$$

where Q_A is the heat generation rate of radionuclides in the rocks ($\mu W/m^3$), $\overline{Q_A}$ is the heat generation rate of radionuclides in the rock formation ($\mu W/m^3$), N_U is the U content in the rock ($\mu g/g$), N_{Th} is Th content in the rock ($\mu g/g$), N_K is the K content in the rock (%), $\boldsymbol{\rho}$ is the rock density (g/cm^3), Q is the radiogenic heat generation in the rock formation (mW/m^2), and M is the stratum depth (m).

4.3.2 Content of Radionuclides

According to the measured values of uranium, thorium, and potassium in the 40 rock samples collected from the Pingdingshan coalfield, their contents calculated as a function of time are shown in **Figures 4–6**, respectively. Obviously, the largest content of uranium, thorium, and potassium-40 in the Pingdingshan coalfield are, respectively, in the mudstone of the Lower Shihezi Formation, the bauxite mudstone of the carboniferous Taiyuan Formation, and the bauxite mudstone of the Carboniferous Permian Taiyuan Formation. The lowest contents are found in the sandstone of the Liujiagou Formation,

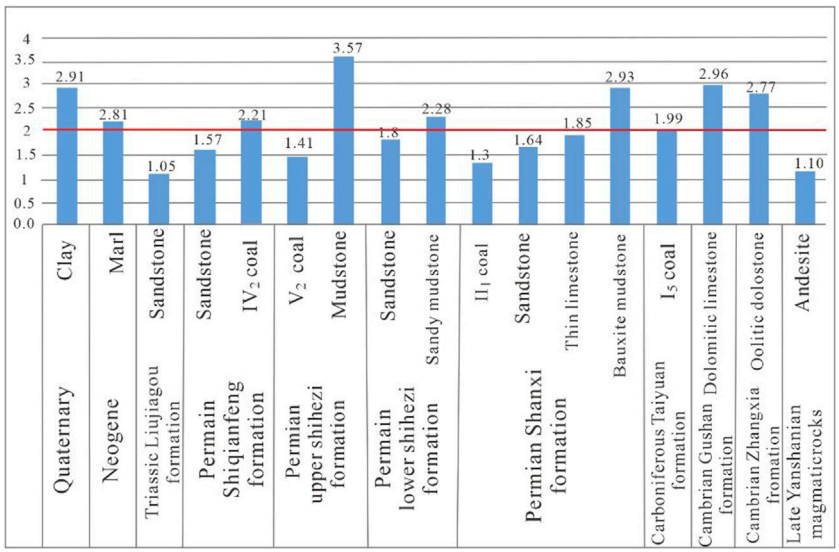

FIGURE 4 | Uranium content in the different strata (μg/g).

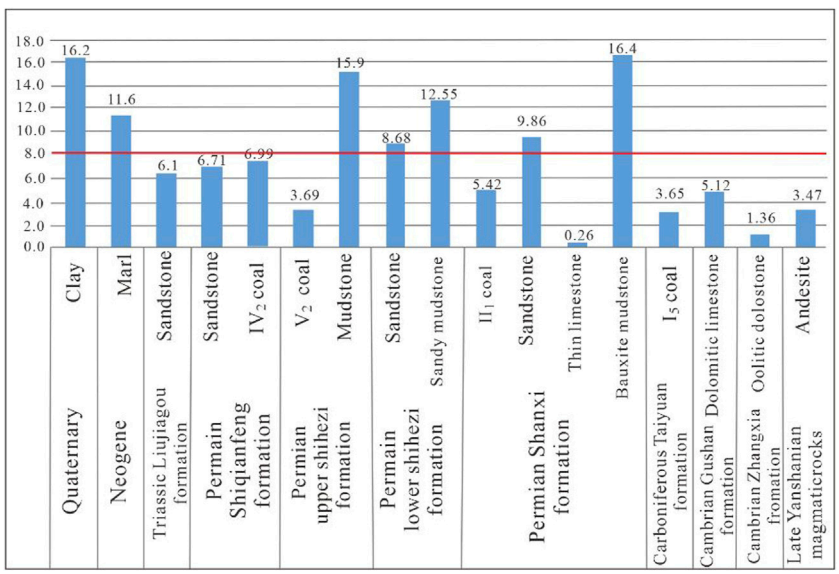

FIGURE 5 | Thorium content in the different strata (μg/g).

the limestone of the carboniferous Taiyuan Formation, and the limestone of carboniferous Triassic Taiyuan Formation, respectively. **Figures 4–6** show that the content of radionuclides in the magmatic rocks is at a relatively low level.

4.3.3 Radiogenic Heat Generation

The heat generation rate of radionuclides of different lithologies in the Pingdingshan coalfield (**Figure 7**) can be obtained using **Eq. 2**. The highest heat generation rate was found for the bauxite mudstone of the carboniferous Taiyuan Formation, followed by the mudstone of the Permian Lower Shihezi Formation, and the lowest heat generation rates were measured in 52 coal samples obtained from the Permian upper Shihezi Formation and 15 coal samples taken from the carboniferous Taiyuan Formation. The order of heat generation rate of the various lithology is mudstone > clay > thick limestone > sandstone > marl > andesite > thin limestone > coal seam; that is, the higher the argillaceous composition, the greater the heat generation rate.

The average radiogenic heat generation rate of the late Cambrian strata in the Pingdingshan coalfield is 1.05 $\mu W/m^3$, the thickness of which is about 800 m. The average heat generation rate of radionuclides in the Cambrian strata is

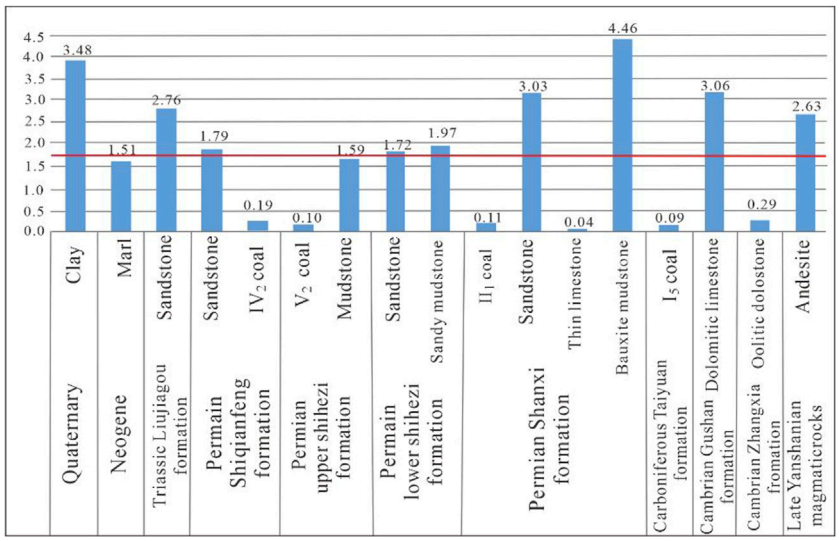

FIGURE 6 | Potassium-40 content in the different strata (%).

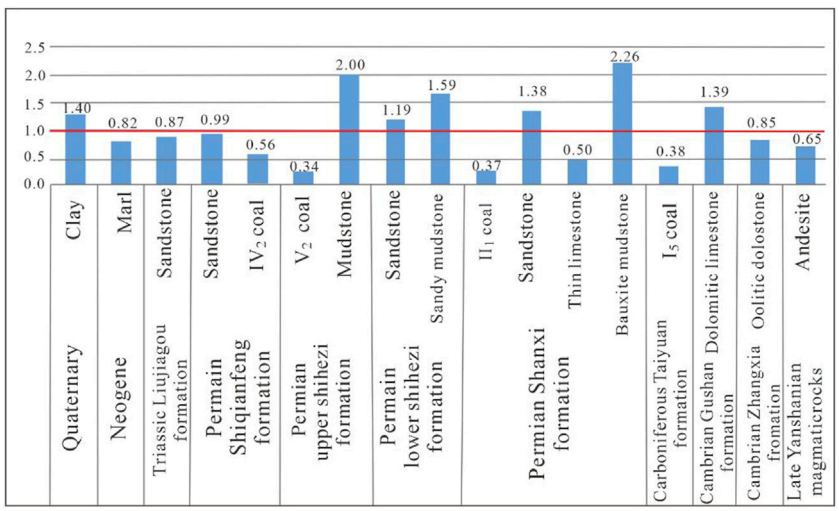

FIGURE 7 | Rate of radiogenic heat generation in the different strata (μW/m^3).

1.12 μW/m^3, whose thickness is about 300 m. The heat generation rate of radionuclides in the magmatic rock is 0.69 μW/m^3, for a thickness of 500 m. The radiogenic heat generation rates in the late Cambrian strata, Cambrian strata, and magmatic rocks in the coalfield are 0.84, 0.34, and 0.35 mW/m^2, respectively, where the sum of the three is 1.53 mW/m^2.

Overall, the contribution rate of the radiogenic heat generation in the sedimentary rocks and magmatic rocks in the Pingdingshan coalfield is only 1.47% of the local large geothermal flow value of 104.28 mW/m^2, which is at a very low level. Therefore, we may infer that the abnormally high ground temperature in the Pingdingshan coalfield is not caused by the radiogenic heat generation in the sedimentary strata or magmatic rocks.

4.4 Heat Release of Magmatic Rocks

4.4.1 Distribution of Magmatic Rocks

A magmatic rock intrusion was found during coal seam mining of the No. 13 coal mine in the Pingdingshan coalfield. The main lithology is neutral diorite porphyrite and basic diabase. The rock mass strikes northeast, with a length of 860 m and a maximum width of 60 m. A dyke intruded into the coal bearing strata, resulting in the existence of natural coke in the second group of coal seams.

TABLE 6 | Temperature of the ejected lava in the different volcanic areas (°C).

Types	Compositions	T	Locations	Source
Acidic	Rhyolite (lava, fused tuff, pumice flow)	735–780	Taupo, New Zealand	Ewart et al. (1971)
	Pyroxene rhyolite (pumice flow)	860–890	Taupo, New Zealand	Ewart et al. (1971)
	Rhyolitic dacite pumice	880	New Britain in the Western Pacific	Herming and Carmichael (1973)
	Rhyolitic dacite Obsidian	900–925	Iceland	Carmichael (1967)
Neutral	Dacite lava and pumice	925	New Britain in the Western Pacific	Herming and Carmichael (1973)
	Andesitic pumice	940–990	New Britain in the Western Pacific	Herming and Carmichael (1973)
Basic	leucite basalt	1,095	Muragira, Congo	Verhoogen (1948)
	Basaltic andesite	1,020–1,110	Parikuting, Mexico	Zies (1946)
	Tholeiitic basalt	1,150–1,225	Kilauea, Hawaii	Wright et al. (1968)

Magmatic rocks are exposed in the Dongshan area of the Dazhuang mine, Shilong District, Pingdingshan City, with an area of about 2 km^2 and a maximum thickness of 337.9 m, showing in **Figure 1**. The lithology mainly includes neutral andesite and andesite porphyrite. The magmatic rock mass in the coal-bearing strata is mainly shallow intrusive bedrock, dyke, and stock. From the perspective of the magma intrusion into different coal bearing sections and Neogene strata, the latest activity age should be the Neogene. Judging from the fact that the dyke was cut by the Yanshanian Liuzhuang Fault, the magmatism already formed in the Yanshanian Period.

In addition, a large area of magmatic rocks is exposed in the mountainous area of Lushan County, Pingdingshan City (**Figure 1**). The lithology is mainly late Yanshanian alkaline aegirine syenite, while acid granite porphyry and granite are also exposed locally. Shangtang, Zhongtang, Xiatang, and Jianchang hot springs are distributed along the Checun Fault that cuts through the magmatic rocks from top to bottom, and the temperatures of the springs are 71°C, 63°C, 64°C, and 35°C, respectively, indicating that there is also an abundant heat source in this zone.

4.4.2 Heat Generation of the Magmatic Rocks

The latest active age of the magmatic rocks exposed in the Dazhuang mine was during the Neogene, and its age is estimated to be about 35 Ma. In Mogou, southeast of Song County, Henan Province, which has the same age and lithology as Lushan's magmatic rocks, Mao et al. (2010) extracted intrusive alkaline rock samples of late Yanshan Cretaceous aegirine gabbro syenite and Indosinian syenite, and determined their ages to be 108 Ma and 194 Ma, respectively, using shrimp zircon. At the same site, Ren et al. (2001) and Lu et al. (2013) measured the ages of Indosinian syenites to be 208.5 ± 6.2 Ma and 245.5 ± 8.0 Ma, respectively (Fugen et al., 2001; Ren et al., 2013). In addition, Hou et al. (2007) measured the age of Late Mesozoic magmatic rocks from ^{40}Ar and ^{39}Ar isotopes in Dabie Mountain, finding 125–190 Ma (Hou et al., 2007). In conclusion, the activity of the intrusive neutral diorite porphyrite and basic diabase in the Pingdingshan coalfield began in the late Yanshanian Cretaceous and ended in the Himalayan Neogene, and has an age of 35–108 Ma.

The temperature of modern volcanic eruption lava measured directly on site shows that the magma composition is from acidic to basic, and the temperature of eruption lava was 735°C–1,225°C (**Table 6**) (Xu and Qiu, 2012). The intrusive magmatic rocks in the Pingdingshan coalfield are neutral diorite porphyrite and basic diabase. It is speculated that the lava temperature was more than 900°C.

At present, there have been a few literature studies on the cooling rate of neutral diorite porphyrite and basic diabase. Therefore, this paper compares the cooling rates of magmatic rocks in the Pingdingshan coalfield with the cooling rates of magmatic rocks with the same or similar lithology. Hourgian et al. (2004) found that the cooling rate of neutral syenite is 20°C/Ma in Kamchatka, Russia. For the basic cave granite in the late Yanshanian period in Zhangzhou, Fujian Province, studies by Shen et al. (2000) have shown, according to the isotope dating results and the closed temperature data in the different isotope systems, that igneous rocks always have changing cooling rates during the various geologic periods, such as, 103.0–97.1 Ma, 97.1–63.1 Ma, 63.1–57.5 Ma, 57.5–54.7 Ma corresponding to 16.9°C/Ma, 7.3°C/Ma, 8.9°C/Ma, and 53.6°C/Ma, respectively, with an average of 11.3°C/Ma. Therefore, it is estimated that the cooling rate of neutral diorite porphyrite and basic diabase in the Pingdingshan coalfield ranges from 11.3 to 20°C/Ma (Shen et al., 2000).

The latest intrusion time of the magmatic rock mass in the Pingdingshan coalfield is 35 Ma; with a lava temperature of 900°C. Therefore, assuming the cooling rate was 20°C/Ma, it is estimated that the residual temperature of the magmatic rock mass is more than 200°C. The higher residual temperature of the magmatic rock may cause its heat to be continuously transmitted upward through the rock strata or upward through faults, which provided a foundation for the high geothermal flow in the Pingdingshan coalfield. The conceptual model of abnormally high ground temperature caused by magmatic rocks is shown in **Figure 8**. Of course, the distribution of the ground temperature in the Pingdingshan coalfield seems to be uneven, which may be mainly controlled by the distributions of the different geological structures, intrusive rock mass distribution, Cambrian limestone groundwater migration, rock stratum structure, overburden performance, and other factors; however, further investigation of the effects of these structures and formations on the ground temperature distribution in the Pingdingshan coalfield is beyond the scope of the current study.

4.5 Discussion

In this study, we measured the outlet temperature values of 45 geothermal wells and water drains, and the thermal conductivity of 11 rock samples in the Cambrian layer. The measuring and sampling locations in the Cambrian layers with different burial depths are well-distributed, so the calculated geothermal gradient and

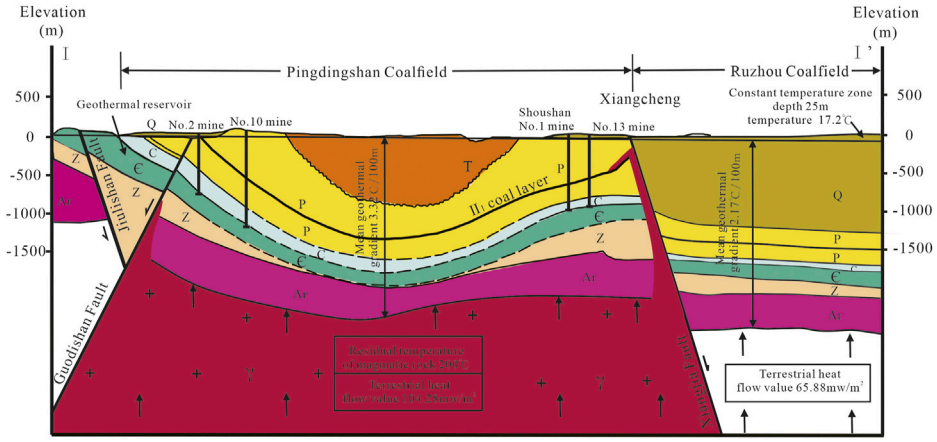

FIGURE 8 | Conceptual model diagram of geothermal genesis.

geothermal heat flow values can represent the true conditions in the abnormal Pingdingshan geothermal area. Based on the contents of the main radionuclides, the amounts of radiogenic heat production and their contributions for terrestrial heat flow were calculated quantificationally, and radiogenic heat production only has a 1.47% proportion of the whole terrestrial heat flow in the Pingdingshan area, which allows us to conclude that the influence of radiogenic heat generation on the abnormally high geothermal temperature in the Pingdingshan coal field can be excluded. In view of the intrusion of magmatic rocks in the 13 mines of the Pingdingshan coalfield and the neighboring area (Dazhuang Mine), it is can be inferred that the abnormally high ground temperature may likely be caused by the continuous heat release of magmatic rocks, and the conclusion that the residual temperature of the magmatic rock body is more than 200°C seems to be credible, agreeing with relevant research at similar conditions.

In the future, gravity prospecting and 3D seismic method can be further used to explore the characteristics of deep rock structure and fault distribution. A geothermal, geologic, hydrogeologic, and mathematical model will be constructed to ascertain the heat production and locate the high temperature target areas and layers in Pingdingshan. The geothermal wells (boreholes) will be constructed in the remained spaces after excavating coal, and the mathematical models can also be calibrated to predict the reservoir temperatures at different locations and depths accurately, providing technical support for the protecting the reservoirs in Pingdingshan coalfield and exploiting the deep geothermal energy.

5 CONCLUSION

Based on the discussions above, we can obtain the following conclusions:

1) The geothermal gradients of the Pingdingshan coalfield range from 1.12 to 5.56°C/100 m, with an average value of 3.32°C/100 m. The calculated values of heat flow in this coalfield is 62.13–139.49 mW/m^2, with an average value of 104.28 mW/m^2. Therefore, we can conclude that the Pingdingshan coalfield belongs to an abnormal geothermal area.
2) The radiogenic heat generation rates of the late Cambrian strata, Cambrian strata, and magmatic rocks in the coalfield are 0.84 mW/m^2, 0.34 mW/m^2, and 0.35 mW/m^2, respectively, with a sum of 1.53 mW/m^2. The contribution rate of the radiogenic heat generation to the local large geothermal flow value is only 1.47%, which is at a very low level.
3) Neutral diorite porphyrite and a basic diabase intrusion were found during mining in the No. 13 coal mine, while neutral andesite and andesite porphyrite were exposed in the Dazhuang coal mine near the Pingdingshan coalfield. The heat release of magmatic rock may be the primary heat source causing the abnormally high ground temperature in Pingdingshan.
4) In the Pingdingshan area, the intrusion time of the magmatic rock mass is about 35 Ma and the lava temperature is about 900°C. Assuming the cooling rate is 20°C/Ma, we can obtain the residual temperature of the magmatic rock mass, which is more than 200°C. The relatively high residual temperature of the magmatic rock may be the main heat source of the abnormally high ground temperature in this coalfield.

DATA AVAILABILITY STATEMENT

The original contributions presented in the study are included in the article/Supplementary Material, further inquiries can be directed to the corresponding author.

AUTHOR CONTRIBUTIONS

All authors listed have made a substantial, direct, and intellectual contribution to the work and approved it for publication.

FUNDING

This work was supported by the National Natural Science Foundation of China (41802186, 41972254), the Innovation

Scientists and Technicians Troop Construction Projects of Henan Province (Grant CXTD2016053), and the Fundamental Research Funds for the Henan Polytechnic University (NSFRF200103).

REFERENCES

Bingqi, C., Xinyi, W., and Jiale, Z. (2014). Analysis on Temperature Distribution and Influencing Facators in Pingdingshan Coal Field. *Coal Technol.* 33 (07), 73–75. doi:10.2514/6.2008-2309

Burns, E. R., Williams, C. F., Ingebritsen, S. E., Voss, C. I., Spane, F. A., and DeAngelo, J. (2015). Understanding Heat and Groundwater Flow through Continental Flood Basalt Provinces: Insights Gained from Alternative Models of Permeability/depth Relationships for the Columbia Plateau, USA. *Geofuilds* 15, 120–138. doi:10.1002/9781119166573.ch13

Erbek, E., and Dolmaz, M. N. (2019). Investigation of the Thermal Structure and Radiogenic Heat Production through Aeromagnetic Data for the Southeastern Aegean Sea and Western Part of Turkey. *Geothermics* 81, 113–122. doi:10.1016/j.geothermics.2019.04.011

Fugen, R., Yanjie, Y., Shuangbao, L., and Jianong, Z. (2001). The Coupling Character between Isotopic Geochronology of Indosinian Epoch in Xiong'er Fault Basin. *Bull. Mineralogy, Petrology Geochem.* 2001 (04), 286–288. doi:10.3969/j.issn.1007-2802.2001.04.022

Hasterok, D., Gard, M., and Webb, J. (2018). On the Radiogenic Heat Production of Metamorphic, Igneous, and Sedimentary Rocks. *Geosci. Front.* 9 (6), 1777–1794. doi:10.1016/j.gsf.2017.10.012

Hou, Q., Liu, Q., Li, J., Zhang, H., and Zhang, X. (2007). Late Mesozoic Shear Zones and its Chronology in the Dab Ie Mountains, Central China. *Chin. J. Geol. Sci. Geol. Sinica)* 2007 (01), 114–123. doi:10.1155/2012/291467

Hourgian, J. K., Soloviev, A. V., and Ledneva, G. V. (2004). Timing of Syenite Intrusions on the Eastern Slope of Sredinnyi Range, Kamchatka: Rate of Accretionary Structure Exhumation. *Geochem. Int.* 42 (2), 131–141. doi:10.1144/1467-7873/03-024

Jun, P., Wen, W. J., and Tao, P. (2015). Distribution Characteristics and Abnormal Factors of Geothermal Field in Linhuan Mine Area. *Coal Eng.* 47 (01), 88–91. doi:10.11799/ce201501028

Lu-sheng, S., Qiu-xiang, H., and Shan-shan, C. (2020). Characteristics of Radioactive Heat Generatio Rate of Granites in the Southeastern Jiangxi Province. *J. East China Univ. Technol. Sci.* 43 (06), 514–520. doi:10.3969/j.issn.1674-3504.2020.06.002

Luo, X., Zhu, C., Zhang, B., Boning, T., and Tiange, C. (2020). Heat Production Rate Calculation Using Gamma-Raylogging of the Sedimentary for Mation in the Tarimbasin,Northwest China. *Acta Geol. Sin.* 94 (07), 2078–2088. doi:10.19762/j.cnki.dizhixuebao.2020219

Mao, J.-W., Xie, G.-Q., Pirajno, F., Ye, H.-S., Wang, Y.-B., Li, Y.-F., et al. (2010). Late Jurassic-Early Cretaceous Granitoid Magmatism in Eastern Qinling, Central-Eastern China: SHRIMP Zircon U-Pb Ages and Tectonic Implications. *Aust. J. Earth Sci.* 57, 51–78. doi:10.1080/08120090903416203

Ogunsanwo, F. O., Adepitan, J. O., Ayanda, J. D., Giwa, K. W., Falayi, E. O., and Adejimi, A. I. (2021). Radiogenic Heat Production in Crustal Quarry Rocks of Ogun State, South-Western, Nigeria. *Environ. Earth Sci.* 80 (7), 1–15. doi:10.1007/s12665-021-09578-7

Ren, L., Tao, L., Fengjun, B., and Xinxiang, L. (2013). LA-ICP-MS U-Pb Zircon Age and Hf Isotope Composition of Mogou Syenite, Western Henan Province. *Geol. Rev.* 59 (02), 355–368. doi:10.3969/j.issn.0371-5736.2013.02.017

Ren, Z., Wu, J., and Peng, T. (2017). Radiogenic Heat Production of Magmatic Rock of Coal Measure Strata Based on Natural Gamma-Ray Logging in Zhuji Mine Field of Huainan Coal Field. *Coal Geol. Explor.* 45 (03), 49–53+58. doi:10.3969/j.issn.1001-1986.2017.03.009

Scharfenberg, L., Regelous, A., and De Wall, H. (2019). Radiogenic Heat Production of Variscan Granites from the Western Bohemian Massif, Germany. *J. Geosciences* 64 (4), 251–269. doi:10.3190/jgeosci.293

Shen, W., Ling, H., Li, H., Li, W., Wang, D, et al. (2000). Thermal Evolution History of Xincun Cave Granite in Fujian Province. *Chin. Sci. Bull.* 2000 (14), 1538–1543. doi:10.3321/j.issn:0023-074X.2000.14.016

Sun, M., Liu, D., Kang, Z., Guan, Y., Liang, G., Huang, X., et al. (2020). Analysis of Hot-Dry Geothermal Resource Potential in Southeastern Guangxi. *Earth Sci. Front.* 27 (01), 72–80. doi:10.13745/j.esf.2020.1.9

Veikkolainen, T., and Kukkonen, I. T. (2019). Highly Varying Radiogenic Heat Production in Finland, Fennoscandian Shield. *Tectonophysics* 750, 93–116. doi:10.1016/j.tecto.2018.11.006

Veikkolainen, T., Kukkonen, I. T., and Näslund, J.-O. (2019). Radiogenic Heat Production Analysis of Fennoscandian Shield and Adjacent Areas in Sweden. *Geophys. J. Int.* 218 (1), 640–654. doi:10.1093/gji/ggz186

Wang, Z., Jiang, G., Zhang, C., Hu, J., Shi, Y., Wang, Y., et al. (2019). Thermal Regime of the Lithosphere and Geothermal Potential in Xiong'an New Area. *Energy Explor. Exploitation* 37 (2), 787–810. doi:10.1177/0144598718778163

Weinert, S., Bär, K., Scheuvens, D., and Sass, I. (2021). Radiogenic Heat Production of Crystalline Rocks in the Gonghe Basin Complex (Northeastern Qinghai–Tibet Plateau, China). *Environ. Earth Sci.* 80 (7), 1–19. doi:10.1007/s12665-021-09558-x

Xin, M. A., Lei, F., and Tiefeng, L. I. (2021). Analysis of Geothermal Origin in Eastern Himalayan Syntaxis. *Geoscience* 35 (01), 209–219. doi:10.19657/j.geoscience.1000-8527.2021.016

Xu, X., and Qiu, J. (2012). *Igneous Petrology*. Beijing: Science Press.

Zhang, C., Hu, S., Song, R., et al. (2020). Genesis of the Hot Dry Rock Geothermal Resources in the Gonghe Basin: Constraints from the Radiogenic Heat Production Rate of Rocks. *Chin. J. Geophys.* 63 (7), 2697–2709. doi:10.6038/cjg2020N0381

Zhang, C., Hu, S., Zhang, S., Li, S., Zhang, L., Kong, Y., et al. (2020). Radiogenic Heat Production Variations in the Gonghe Basin, Northeastern Tibetan Plateau: Implications for the Origin of High-Temperature Geothermal Resources. *Renew. Energy* 148, 284–297. doi:10.1016/j.renene.2019.11.156

Zhang, F., Wang, G., and Hou, X. (2000). An Analysis of the Formation of Geothermal Resources and the Effects of Groundwater Circulation on the Wall Rock Temperature Field –Taking the Pingdingshan Mining Field as an Example. *Acta Geosci. Sin.* 2, 142–146. doi:10.3321/j.issn:1006-3021

Zhao, X., Zeng, Z., Huai, N., and Wang, K. (2020). Geophysical Responses and Possible Geothermal Mechanism in the Gonghe Basin, China. *Geomechanics Geophys. Geo-Energy Geo-Resources* 6 (1), 1–12. doi:10.1007/s40948-020-00141-5

Conflict of Interest: The authors declare that the research was conducted in the absence of any commercial or financial relationships that could be construed as a potential conflict of interest.

Publisher's Note: All claims expressed in this article are solely those of the authors and do not necessarily represent those of their affiliated organizations, or those of the publisher, the editors and the reviewers. Any product that may be evaluated in this article, or claim that may be made by its manufacturer, is not guaranteed or endorsed by the publisher.

frontiers | Frontiers in Earth Science

ORIGINAL RESEARCH
published: 22 July 2022
doi: 10.3389/feart.2022.905852

Isotopic and Hydrogeochemical Characteristics and Genesis of Warm Springs in the Jiangcang Basin, Qinghai, China

Lingxia Liu[1,2,3], *Shihua Qi*[1], *Yongbin Zhang*[4], *Ming Gao*[2], *Jing Hu*[5] *and Wenzhong Wang*[1,2]*

[1]School of Environmental Studies, China University of Geosciences, Wuhan, China, [2]Institute of Hydrogeology and Environmental Geology, Chinese Academy of Geological Sciences, Shijiazhuang, China, [3]Technology Innovation Center for Geothermal & Hot Dry Rock Exploration and Development, Ministry of Natural Resources, Shijiazhuang, China, [4]New Energy Geological Team of Hebei Coalfield Geological Bureau, Xingtai, China, [5]Jiangsu University of Science and Technology, Zhenjiang, China

OPEN ACCESS

Edited by:
Wenjing Lin,
Chinese Academy of Geological Sciences, China

Reviewed by:
Kunal Singh,
Geological Survey of India, India
Jianfei Yuan,
Chengdu Geological Survey Center, China

***Correspondence:**
Wenzhong Wang
308200378@qq.com

Specialty section:
This article was submitted to Geochemistry, a section of the journal Frontiers in Earth Science

Received: 28 March 2022
Accepted: 03 June 2022
Published: 22 July 2022

Citation:
Liu L, Qi S, Zhang Y, Gao M, Hu J and Wang W (2022) Isotopic and Hydrogeochemical Characteristics and Genesis of Warm Springs in the Jiangcang Basin, Qinghai, China. Front. Earth Sci. 10:905852. doi: 10.3389/feart.2022.905852

The Jiangcang Basin is a Cenozoic faulted basin, where many low-temperature warm springs are exposed, with the highest temperature being 36.6°C. The study of the hydrogeochemical characteristics of the geothermal fluids of these warm springs can effectively clarify the genetic mechanisms of the geothermal resources in the Jiangcang Basin and thus is of great significance for the development and utilization of geothermal resources in the Qinghai Province. Using the geothermal and geological conditions of the Jiangcang Basin, this study analyzed the hydrochemical and isotopic characteristics of water samples collected from cold water and from four warm springs in the Jiangcang Basin, obtaining the following results. The four warm springs have the hydrochemical types of HCO_3-Ca·Mg, HCO_3-Ca·Na·Mg, and HCO_3·SO_4-Na·Ca and total dissolved solids (TDSs) of 720.4–1,663 mg/L. Moreover, no significant positive correlation is found between Cl^- and other ions in the warm springs. The results of isotopic analysis show that the warm springs are mainly recharged by atmospheric precipitation and meltwater from ice and snow, with a recharge elevation of 4,401–4,501 m. Furthermore, the geothermal reservoirs in the Jiangcang Basin have temperatures of 51–83°C and circulation depths of 1,848–2,610 m. Atmospheric precipitation and the meltwater from ice and snow infiltrate downward in high mountain areas and form runoffs along the tectonic channels in the basin. After being heated through deep circulation, they migrate upward along fault fracture zones under the influence of faults and the water blocking of mudstones, during which they cool by thermal conduction and mixing with shallow cold groundwater. Finally, the mixed water is exposed in the form of low-temperature tectonic warm springs. The results of this study can provide data for the exploitation and utilization of geothermal resources in the Qinghai Province.

Keywords: Jiangcang Basin, hydrogeochemistry, Silica geothermometers, geothermal reservoir temperature, geothermometer, isotope

1 INTRODUCTION

Eco-friendly and sustainable development is the common pursuit of all human beings. Geothermal resources, a source of renewable new clean energy that can be directly utilized, have great potential for development. China is rich in geothermal resources, with 2,334 discovered warm spring outcrops and 5,818 existing geothermal exploitation wells (Wang G. L. et al., 2017). In recent years, many researchers have investigated geothermal resources in China, especially with reference to their occurrence regularity, hydrogeochemical characteristics, and genetic modes (Guo et al., 2015; Du et al., 2012; Wang G.L. et al., 2017; Yuan et al., 2020).

The Qinghai Province, located in the northeast of the Qinghai-Tibet Plateau, features complex geological structures and strong neotectonic movements. It is rich in geothermal resources due to its numerous geothermal anomalous areas, including more than 200 geothermal sites (Zhang, 1999). Much work has been conducted on the geothermal resources in Qinghai. For example, Zhang et al. (2007) analyzed the genetic mechanisms of the geothermal water in the Dujiazhuang geothermal field in Xining, Qinghaim using the Langelier-Ludwig diagram combined with isotopic and hydrological analyses. The results show that geothermal water from the Dujiazhuang geothermal field is of meteoric origin and is recharged by modern water. Moreover, the geothermometers indicate that there are geothermal reservoirs in the Dujiazhuang geothermal field whose temperature is far higher than that of geothermal well DR 2005 (i.e., 62.5°C). Li et al. (2007) analyzed the recharge sources and genesis of Yaoshuitan warm spring based on hydrochemical characteristics and stable isotopes. Sun et al. (2019) obtained the circulation mechanisms of the geothermal water in the Xining Basin based on the study of the dynamic, chemical, and geothermal fields of groundwater, as well as the isotopic characteristics. Sun et al. (2022) determined the genetic mechanisms for the high TDS of different geothermal water bodies in the Xining Basin through the TDS and hydrochemical analyses. Wang (2009) systematically studied the hydrochemical characteristics of geothermal water in the Qiabuqia area and their regional distribution. They also estimated the geothermal reservoir temperature in this area using geochemical geothermometry, thus providing basic data and a scientific basis for the exploitation of geothermal resources in this area. Li (2016) analyzed the hydrogeochemical and isotopic characteristics and the genesis of the geothermal water in the Qiabuqia area. They inferred that the geothermal water in the Qiabuqia area originates from the confined water in the west and the meltwater from ice in the high mountains in the north, and the heat is mainly derived from the mantle through thermal conduction. Tang et al. (2020) analyzed the tectonic background and heat source mechanisms of the Gonghe Basin in Qinghai using isotope chronology and hydrogeochemistry. Consequently, they proposed a ternary heat accumulation model of hot dry rocks in the Gonghe Basin. Ma et al. (2020) analyzed the migration pattern and genetic mechanisms of geothermal fluids in the Gonghe Basin through hydrogeochemical analysis. Lang et al. (2016) analyzed the hydrochemical and stable isotopic characteristics of the geothermal fluids in the Guide Basin. They also estimated the temperature and circulation depth of the geothermal reservoirs in the geothermal fields in the Guide Basin and identified the genetic mechanisms of the geothermal fields. Li et al. (2016a) investigated the characteristics of the geothermal reservoirs and the geothermal field, as well as the hydrogeochemical characteristics of geothermal water in the Guide Basin. Based on these characteristics, they summarized the occurrence regularity and the geological genetic modes of the geothermal resources in the Guide Basin. Jiang et al. (2019) developed an isotopic migration module based on the water-heat-rock coupling model. Using this module, they simulated the isotopic fractionation of δ^2H and $\delta^{18}O$ induced by advection, diffusion, and water-rock interaction and analyzed the recharge sources and rates and the temperature of geothermal water in the basin. Dai (2020) investigated convective geothermal water along five faults in the Guide Basin. Then, they analyzed the genetic mechanisms of the geothermal resources in the basin, based on the hydrochemical and stable isotopic characteristics to deepen the understanding of the circulation process of the geothermal water in the basin.

Studies of the geothermal resources in the Qinghai Province focus on basins with a low elevation (<3,000 m), such as the Gonghe, Xining, and Guide basins, while the geothermal resources in the basins with a high elevation (>3,800 m), such as the Jiangcang and Reshui basins, lying in the upper reach of the Datong River, have been scarcely concerned. Previous surveys reveal that four warm springs are exposed in the Jiangcang Basin. Among them, the Muliqugu warm spring located on the south slope of the Tuolai Nanshan Mountain on the north bank of the Datong River has the highest temperature of 36.6°C (Li et al., 2016b). According to the report entitled Current Status Assessment and Zoning of Geothermal Resources in Qinghai Province (2015), the Jiangcang Basin has considerable potential for exploration and has been explored recently (Yang et al., 2015). Given this, this study analyzed the chemical composition and recharge sources and revealed the genetic mechanisms of the geothermal water in the Jiangcang Basin based on the hydrogeochemical characteristics of the geothermal water. The purpose is to provide a scientific basis for the future exploitation and utilization of the geothermal resources in Qinghai.

2 OVERVIEW OF THE STUDY AREA

The Jiangcang Basin is located in the northeast of the Qinghai Province and lies at the junction of Gangcha County, Qilian County, and Tianjun County, Haixi. This basin features abundant resources, large grasslands, a sparse population, and an underdeveloped economy and non-mainstream culture. The Tibetans living have a nomadic economy. The study area has a typical plateau continental climate, which is characterized by indistinct seasons, cold climate, and large temperature variations. This basin has an average annual temperature of −1.93–0.5°C, average annual precipitation of 463 mm, and average annual evaporation of 1,261 mm. Moreover, the period from June to August is the rainy season and the period from January to May is

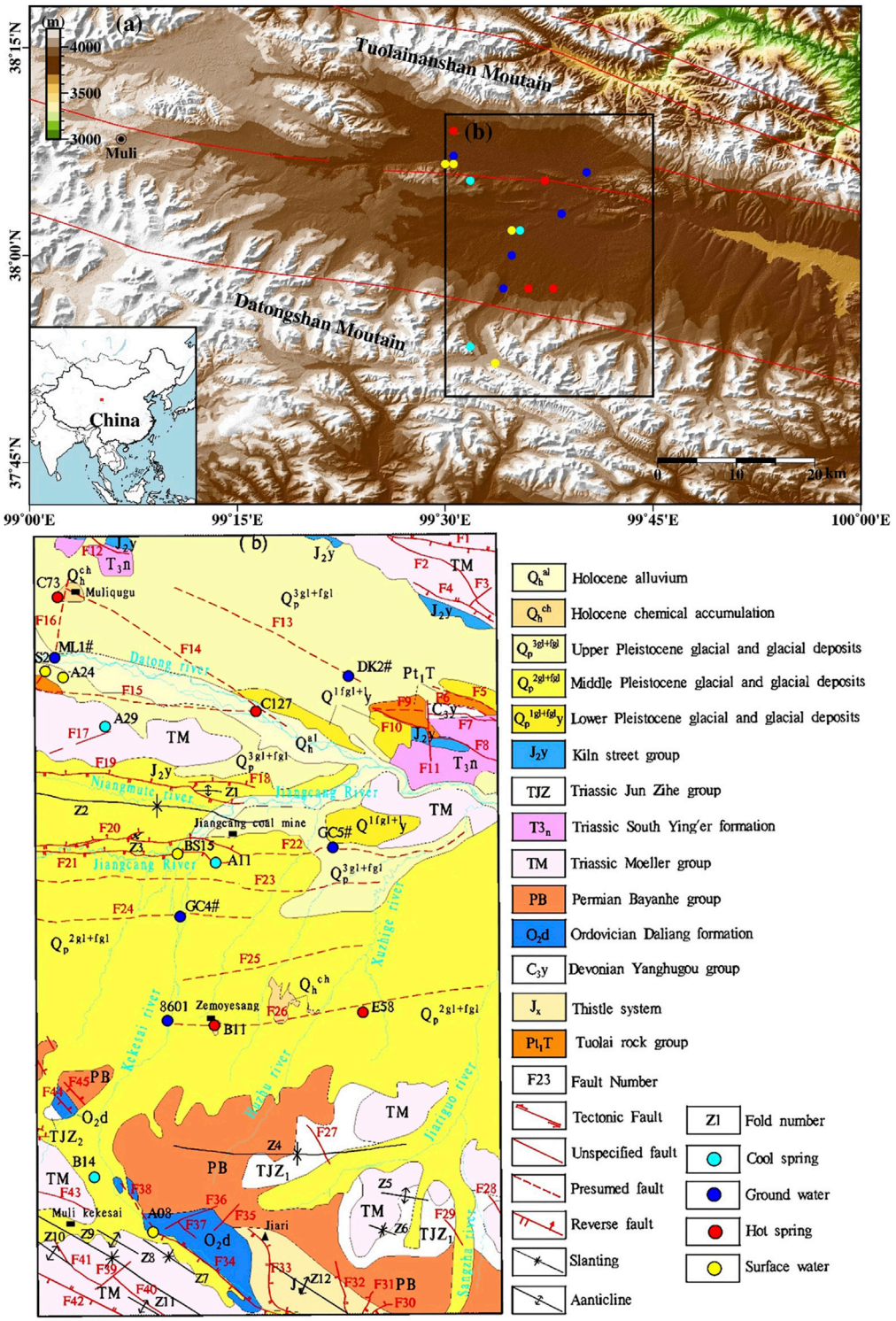

FIGURE 1 | (A) Geological sketch and sampling point location map of the study area. **(B)** After hydrogeological and environmental geological survey of Qinghai energy.

dominated by snow. This basin suffers from inconvenient transportation, with only the west-east Reshui Industrial Park—Jiangcang and the north-south Gangca-Jiangcang highways passing through it.

The study area is a part of the middle part of the Proterozoic Qilian paleocontinental block in the western craton. It is sandwiched between large fault zones, with one extending from the south slope of the Tuolai Mountain to Lenglongling and the other from the Shule Nanshan Mountain to Datong Mountain (**Figure 1A**), and it lies in the Muli-Jiangcang-Reshui basin (also referred to as the MJR Basin). The crystalline basement of the study area consists of Paleozoic mesometamorphic rocks, and the cap rock is a set of Carboniferous-Jurassic clastic sedimentary suites. The folds of the MJR Basin are a synclinorium with an axial direction of NW-SE, approximately the same as the strike of the Qilian Mountains overall.

Under the influence of regional tectonism, the structures in the major areas of the Jiangcang Basin are dominated by faults, followed by folds. Specifically, there are 45 faults and 12 folds in the study area (**Figure 1B**). Among these, faults F13, F14, and F15, on both banks of the Datong River, and faults F34, F40, and F42, on the southwest side of the study area, extend NW-SE strike, which is the same as the direction of the regional tectonic line. The faults from the south of the Datong River to the north of the Zemoyesang Spring show a west-east strike. The major faults between the Datong Rive and the Jiangcang mining area are dominated by reverse faults, including F18, F19, F20, and F21. Moreover, several inferred deep faults, namely F22, F23, F24, F25, and F26, exist between the Jiangcang mining area and the Zemoyesang Spring. Faults F34 and F42, lying in the southwest, serve as the boundary faults of the central Qilian uplift zone and the southern Qilian geosyncline zone. These two faults have a large scale and show long-term activity. Each of them has a total regional length of hundreds of km and extends eastward. They are intruded by Caledonian mafic rocks and thus cut deeply (Li, 1952).

Muliqugu warm spring C73 and the C127 warm spring in a floodplain of the Datong River extend in the NWW direction along fault F14. Among them, C73 is exposed at the junction of F14—a major compressive deep fault with a NWW strike—and F16—a NNE-strike compressive fault; C127 is exposed in the superimposition part of two NWW-strike major compressive fractures F14 and F15. Warm springs B11 and E58, which have a NEE-SWW strike, are exposed in F26, a concealed regional fault with a strike of approximately 5° at the junction of the Jiangcang Basin and the Datong Mountains. There are six spring vents along this fault at the early stage (Xie et al., 1987), with a large amount of sinter exposed on the surface. Cold springs A11 and A29 are exposed in fault zones F21 and F17, respectively.

The outcrops in the study area include Proterozoic, Sinian, Ordovician, Carboniferous, Permian, Triassic, Jurassic, Paleogene, Neogene, and Quaternary strata, among which the Triassic and Jurassic strata are well preserved and widely distributed.

3 SAMPLES AND EXPERIMENTAL METHODS

A total of 21 sets of water samples were collected in this study, including four sets from warm springs, three sets from cold spring waters, six sets from surface water, four sets from groundwater, and three sets of snow samples (**Figure 1A**). Before the sampling, field physical and chemical parameters, such as pH, water temperature (T), and electrical conductivity (EC), were measured *in situ*. Samples were collected after these parameters became stable. All of the samples were stored in polyethylene bottles, kept refrigerated, and sent to labs for analyses in time.

The total analysis, trace element analyses, and δ^2H and $\delta^{18}O$ measurements of the water samples were carried out at the Key Laboratory of Groundwater Science and Engineering, Ministry of Land and Resources, Institute of Hydrogeology and Environmental Geology, Chinese Academy of Geological Sciences. Major anions (K^+, Na^+, Ca^{2+}, and Mg^{2+}) and trace components were determined using a Perkin Elmer Optima 8000 inductively coupled plasma optical emission spectrometer (ICP-OES; ± 1%). Cl^-, SO_4^{2-}, and F^- were measured using a Dionex ICS-1100 ion chromatography system, with a testing error of ±1%. The HCO_3^- concentration was analyzed using the reagent titration method, with an analytical precision of ±2%. Moreover, silicates were determined using a SHIMADZU UV-2550 spectrophotometer, with testing errors of less than 0.0003%. All the water samples were tested for cation-anion balance. As a result, all the samples yielded charge-balance errors of within ±5%, except for B14, which had a charge-balance error of 5.61%, thus meeting the demands for testing precision. δ^2H and $\delta^{18}O$ measurements were conducted using a high-precision Picarro L2130-I isotope analyzer, with a measurement precision of 0.025% (**Table 1**).

4 RESULTS AND DISCUSSION

4.1 Hydrochemical Characteristic

4.1.1 TDS

TDS intensively reflects the major ions in groundwater and is an important indicator of the chemical characteristics of groundwater. The TDS of water samples from the surface water was 227.1–388.5 mg/L (average: 262.1 mg/L), and that of water samples from the groundwater was 178.1–354.6 mg/L (average: 258.3 mg/L). As for the cold springs in the study area, water samples from B14 had high TDS, while those from the A11 and A29 had TDS of 270.4 mg/L and 356.8 mg/L, with an average of 313.6 mg/L. Water samples from warm springs C73, C127, E58, and B11 in the study area had a TDS range of 720.4–1,663 mg/L, with an average of 1,234.6 mg/L. Therefore, the warm springs have the highest TDS, followed by the cold springs and surface water, while the surface water have the lowest TDS in the study area (**Table 1**).

TABLE 1 | Chemical composition and hydrogen and oxygen isotope composition of water samples.

Type	Sample ID	pH	Temperature(°C)	Hydrochemical composition/(mg/L)											Hydrochemical type	Isotope/‰		Charge balance (%)
				Ca^{2+}	Mg^{2+}	Na^{+}	K^{+}	HCO_3–	SO_4^{2}–	Cl^{-}	F^{-}	TDS	H_2SiO_3	Li	Sr		δD	$\delta^{18}O$	
Hot spring	C73	5.93	36.6	105.10	38.87	91.08	12.78	612.90	29.70	71.78	2.00	720.4	51.61	0.146	0.692	HCO_3-Ca·Na·Mg	–60	–8.9	–0.12
	C127	6.46	6.9	267.60	92.50	172.50	74.55	1,474.00	56.74	165.30	1.10	1,663.0	52.13	0.975	2.854	HCO_3-Ca·Mg	–60	–8.3	1.45
	E58	6.66	19.5	166.80	68.40	202.10	33.41	836.50	320.30	79.48	2.40	1,322.0	26.88	0.708	2.196	HCO_3·SO_4-Na·Ca	–59	–9.1	3.98
	B11	5.94	24.0	141.30	73.89	163.20	18.79	770.10	321.10	59.8	1.40	1,233.0	32.81	0.466	1.143	HCO_3-Ca·Mg	–63	–10.0	–1.30
Cold spring	A11	6.80	1.8	40.68	9.00	41.94	1.11	147.80	90.05	3.27	0.20	270.4	7.96	0.014	0.231	HCO_3·SO_4-Ca·Na	–42	–7.1	3.75
	A29	6.40	2.4	61.53	15.14	45.23	1.52	239.30	97.67	5.55	—	356.8	9.67	0.008	0.466	HCO_3·SO_4-Ca·Na	–42	–6.3	2.87
	B14	6.97	1.4	3.48	0.96	867.40	0.89	29.85	1,680.00	15.03	—	2,583.0	—	—	—	SO_4-Na	–51	–8.7	5.61
Surface water	A24	7.62	—	26.85	8.66	39.30	1.02	104.70	87.19	2.29	—	227.1	9.78	0.007	0.470	SO_4·HCO_3-Na·Ca	—	—	–2.24
	A08	7.34	—	34.02	8.14	34.25	0.82	104.70	85.29	4.63	—	228.0	5.51	—	0.167	SO_4·HCO_3-Ca·Na	—	—	1.36
	S2	7.90	—	68.39	16.56	26.53	1.83	233.70	83.75	8.75	0.16	345.9	4.54	0.021	0.461	HCO_3·SO_4-Ca	–48	–7.6	–2.14
	BS15	7.61		63.07	10.37	64.38	0.85	232.80	115.80	7.52	0.12	388.5	9.15	—	0.233	HCO_3·SO_4-Ca·Na	–27	–4.6	1.55
	BS19	7.50		39.04	5.44	49.91	0.82	131.30	101.00	4.10	0.12	238.7	5.41	—	0.207	HCO_3·SO_4-Na·Ca	–43	–7.1	0.92
	AS03	7.34		34.02	8.14	34.25	0.82	104.70	85.29	4.63	<0.1	228.0	5.51	—	0.167	SO_4·HCO_3-Ca·Na	–50	–8.4	1.36
Groundwater	DK2#	7.27	—	63.73	13.54	5.32	1.42	233.7	13.99	9.10	0.18	240.3	12.21	0.011	0.303	HCO_3-Ca·Mg	–46	–6.8	1.87
	GC4#	7.65	—	41.62	14.57	21.17	4.07	150.80	30.36	23.10	0.22	260.1	27.14	0.011	0.348	HCO_3-Ca·Mg	–32	–4.9	2.32
	GC5#	7.76	—	56.53	17.18	45.22	2.88	199.4	88.45	35.36	0.12	354.6	8.06	0.360	56.53	HCO_3·SO_4-Ca·Na	–58	–9.0	2.62
	ML1#	7.61	—	47.19	14.63	5.13	1.76	214.0	6.92	4.90	0.38	178.1	8.38	0.030	0.197	HCO_3-Ca·Mg	–49	–8.0	–0.31
Snow	A-19	7.17	—	10.46	0.60	302.00	0.34	47.76	599.40	5.13	—	942.3	—	—	—	SO_4-Na	–38	–6.4	2.14
	ADX-02	6.45	—	1.57	0.17	86.83	0.06	8.63	167.10	1.78	0.10	266.0	5.41	—	—	SO_4-Na	–32	–7.2	1.27
	ADX-03	6.57	—	1.99	0.21	101.30	0.08	11.51	214.40	1.78	—	325.9	—	—	—	SO_4-Na	–42	–7.2	–4.06

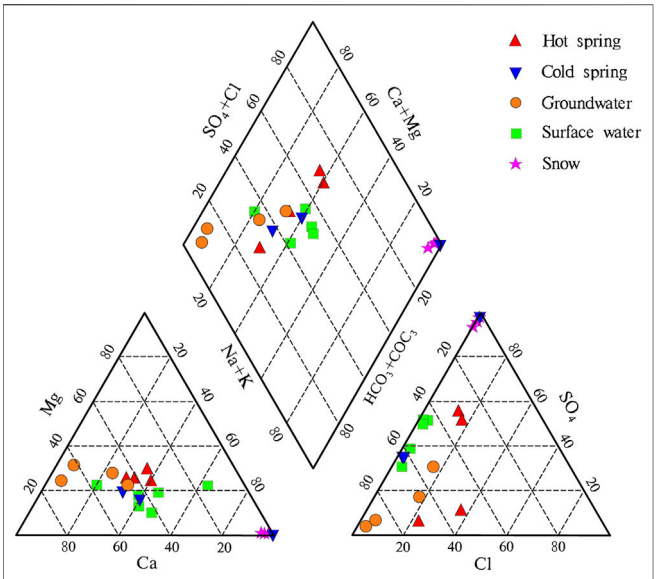

FIGURE 2 | Piper trilinear diagram of the water samples from the Jiangcang Basin.

4.1.2 Hydrochemical Types

The hydrochemical types of groundwater can comprehensively reflect the primary hydrogeochemical environment of groundwater, including occurrence conditions of groundwater, water-rock interaction, and recharge-drainage circulation. To understand the hydrochemical characteristics of warm springs and their genetic mechanisms, the authors determined the hydrochemical types of different types of water bodies using the Shukalev classification method. The Piper trilinear diagram was plotted according to hydrochemical data (**Figure 2**). This plot can effectively reflect the differences in the hydrochemical types of warm spring water, cold water, and meltwater from snow.

Water samples from the four warm springs had pH of 5.94–6.66, with an average of 6.20, indicating that they were weakly acidic. As for the warm springs from the study area, the water samples from C127 and B11 yielded hydrochemical types of HCO_3-Ca·Mg, and those from C73 and E58 yielded hydrochemical types of HCO_3-Ca·Na·Mg and HCO_3·SO_4-Na·Ca, respectively. The water samples from cold springs A11, A29, and B11 had pH values of 6.408.05, with an average of 7.08. The water samples from A11 and A29 showed a hydrochemical type of HCO_3·SO_4-Ca·Na, and those from B14 located in the front of the Datong Mountains had a hydrochemical type of SO_4-Na. The surface water samples had pH of 7.34–7.90, with an average of 7.48. The surface water samples close to the piedmont had hydrochemical types of SO_4·HCO_3-Na·Ca and SO_4·HCO_3-Ca·Na, while those close to the center of the Jiangcang Basin had hydrochemical types of HCO_3·SO_4-Ca·Na, HCO_3·SO_4-Na·Ca, and HCO_3·SO_4-Ca. The groundwater samples had pH of 7.61–7.76, with an average of 7.69. Water samples from wells DK2#, GC4#, and ML1#, all of which had depths greater than 100 m showed a hydrochemical type of HCO_3-Ca·Mg, while those from well GC5# with a small depth of 13.5 m had a hydrochemical type of HCO_3·SO_4-Na·Ca. The three meltwater samples from snow had a hydrochemical type of SO_4-Na. Because these samples were collected around the Jiangcang mining area, it is inferred that they were affected by coal dust.

The analysis indicated that most of the surface water, shallow groundwater, and cold spring water in the study area had similar hydrochemical types, and they are mainly recharged by atmospheric precipitation and meltwater from ice and snow. Moreover, due to the short circulation pathway, they are renewed at a high rate. Cold spring B14, which is close to the piedmont, have the same hydrochemical type as the meltwater from snow, indicating that B14 is mainly recharged by the meltwater from snow. Warm springs C127 and B11 have the same hydrochemical type as the deep groundwater—HCO_3-Ca·Mg, indicating that C127, B11, and the deep groundwater are deeply circulating confined water. Warm spring E58 has similar hydrochemical type to the cold springs. However, the warm springs have significantly higher Cl^- concentration than cold springs and generally higher TDS than cold water (i.e., water other than warm spring water).

The differences in the hydrochemical types and TDS of the geothermal water indicate differences in the degree of water-rock interaction. Specifically, the water-rock interaction in the geothermal water is greater than that the cold water.

4.1.3 Characteristics of the Trace Elements

The trace elements in the water samples from the warm springs mainly included fluorine (F), metasilicic acid, lithium (Li), and strontium (Sr). As shown in **Table 1**, water samples from the cold and warm springs showed F^- concentrations of 0–0.38 mg/L (average: 0.18 mg/L) and 1.10–2.40 mg/L (average: 1.73 mg/L), respectively, with the latter 9.6 times the former. They had metasilicic acid concentrations of 4.54–27.14 mg/L (average: 9.89 mg/L) and 26.88–52.13 mg/L (average: 40.86 mg/L), with the latter 4.1 times the former. Moreover, they had Li concentrations of 0.007–0.030 mg/L (average: 0.015 mg/L) and 0.146–0.975 mg/L (average: 0.574 mg/L), with the latter 38.3 times the former. Therefore, the warm springs have higher trace element concentrations than the shallow cold springs overall, reflecting that they feature deep circulation. Moreover, the metasilicic acid and Li with high concentrations are the indicators of warm spring water. As for the warm springs in the study area, their Sr concentrations meet the criterion for natural mineral water, the F^- concentrations of C73 and E58 meet the criteria for natural mineral water, and the Li concentrations of them except for C73 meet the criterion for natural mineral water. Overall, C127 has the highest water quality among the warm springs. However, all the warm springs are not suitable to use as natural mineral water.

4.1.4 Correlation Between Icons and TDS

As indicated by the analyses of the correlation between the major ions and TDS of the warm springs in the Jiangcang Basin (**Figure 3**), there was a high correlation between icons Mg^{2+}, Ca^{2+}, HCO_3^-, and K^+ and TDS, with a correlation coefficient (R^2) of greater than 0.75. Moreover, Mg^{2+} showed a high R^2 of up to 0.96, while Na^{2+} showed a low R^2 of 0.65. These results reflect the ion composition of medium- and low-temperature thermal

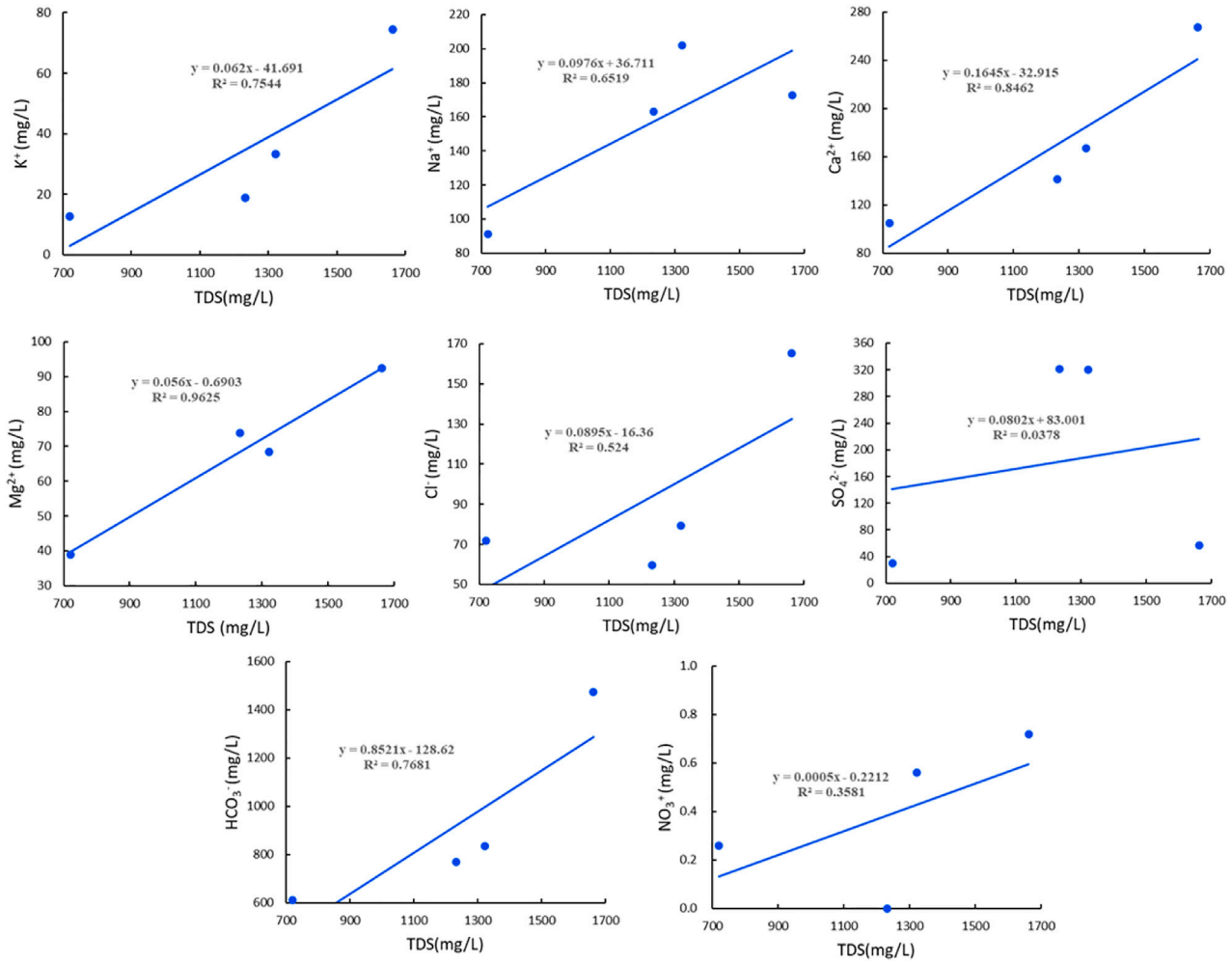

FIGURE 3 | Curves showing the correlation between ions and TDS of water samples from warm springs in the Jiangcang Basin.

springs. Correlation analyses suggested a low correlation between anions and TDS, except for HCO_3^-, which showed an R^2 of 0.77. Moreover, SO_4^{2-} showed the lowest R^2 of 0.04. These results indicate significantly reduced direct recharge by the surface water and the shallow groundwater containing high SO_4^{2-} concentrations, and this significantly enhanced the effects of deep water-rock interaction on the salinity.

Cl^- in groundwater mainly originates from the dissolution of salt or other chlorides in sedimentary rocks, the weathering and dissolution of chlorides in magmas, seawater, the leaching of materials erupting from volcanoes, and man-made pollution. Cl^- is stable since it is not liable to be absorbed or react with other minerals. Therefore, Cl^- can be used to trace other ions to which it is closely related in order to analyze groundwater runoff.

As shown by the analyses of the correlation between Cl^- and other ions (**Figure 4**), there was no significant positive correlation between Cl^- and other ions. This result indicates that the trace elements in the warm springs in the Jiangcang Basin mainly originate from the dissolution of relevant minerals. Moreover, there was a positive correlation between the Na^+ concentration and the length of the runoff pathways of groundwater. Specifically, a higher Na^+ concentration corresponds to longer runoff pathways in the warm springs (e.g., E58). Metaboric acid (HBO_2) widely exists in the formation and migration of groundwater, and the precipitation and dissolution of boron-bearing minerals in water-rock interaction are closely related to groundwater runoff. In detail, the boron content decreases with increased runoff intensity of geothermal fluids (Yuan. 2010). The water samples from the warm springs in the Jiangcang Basin had a high HBO_2 content, 60 times that of the water samples from the cold springs. This finding indicates that the geothermal water in the basin features small and low-rate runoff. Moreover, the high TDS also indicates strong water-rock interaction.

4.2 Characteristics of Stable Hydrogen and Oxygen Isotope

4.2.1 Recharge Sources of Warm Springs

Stable hydrogen and oxygen isotopes (δ^2H, $\delta^{18}O$) help distinguish groundwater origin, identify the hydraulic

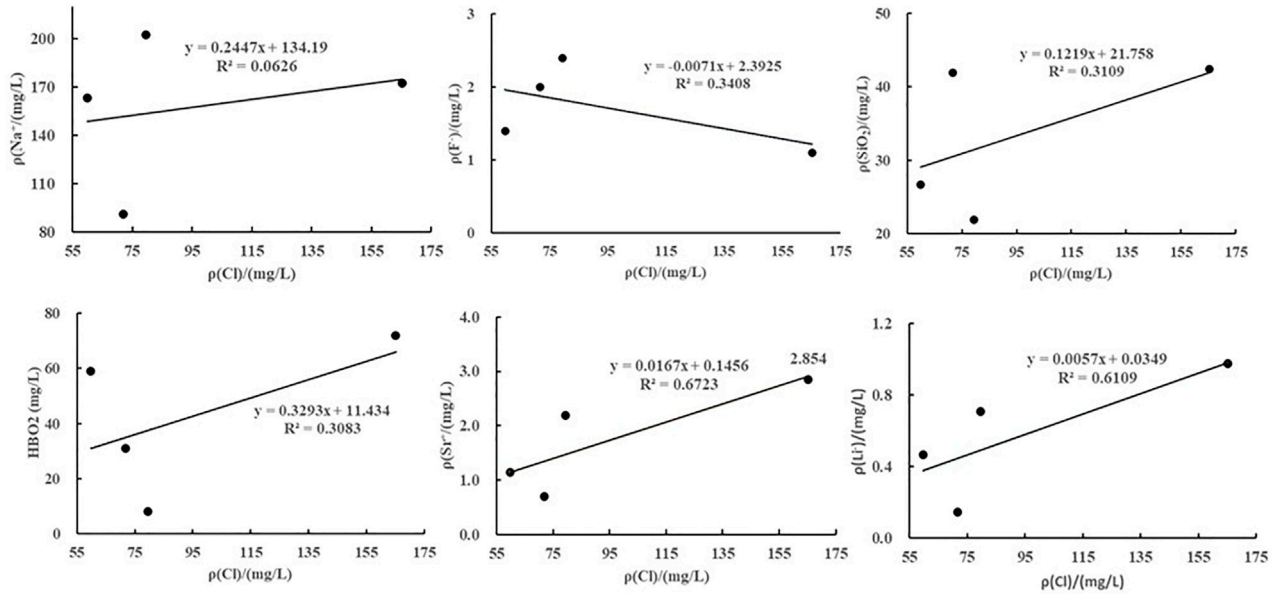

FIGURE 4 | Curves showing the relationships between the ions and Cl^- in the warm springs in the Jiangcang Basin.

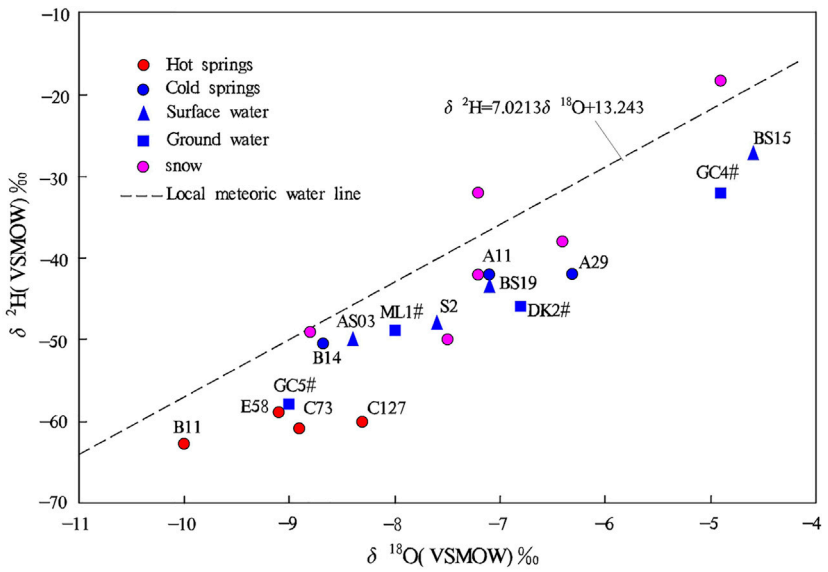

FIGURE 5 | δ^2H vs. $\delta^{18}O$ relationship of water samples from the Jiangcang Basin.

connections among atmospheric precipitation, surface water, and groundwater, trace groundwater recharge conditions, and explore groundwater circulation pathways. ^2H and ^{18}O are rich in liquid but depleted in gas due to their low vapor tension. As a result, the composition of hydrogen and oxygen isotopes are different in different groundwater circulations (Zhang, 1988). Besides being slightly affected by mixing, the δ^2H value of groundwater is mainly determined by recharge temperature and elevation, while the $\delta^{18}O$ value of groundwater mainly depends on the degree of water-rock interaction and the water-rock ratio (Ni et al., 2016).

Through the 1-D linear regression analyses of δ^2H and $\delta^{18}O$ values of the atmospheric precipitation in the study area, the local meteoric water line (LMWL) equation of the Jiangcang Basin was fitted as follows: $\delta^2H = 7.0213\delta^{18}O + 13.243$ (R2=0.8935, n=7), which approximates the LMWL equation for the Qilian Mountain (Sun et al., 2019) $\delta^2H = 7.77\delta^{18}O + 13.03$ (R2=0.99, n=127). This similarity indicates

that the fitted MWL equation of the Jiangcang Basin is reasonable.

The δ^2H vs. $\delta^{18}O$ curve was plotted based on the data on water samples from the warm springs, cold springs, surface water, groundwater, and precipitation, as shown in **Figure 5**. According to this figure, water samples from the thermal water had δ^2H values of −63‰–−59‰ (average: −60.8‰) and $\delta^{18}O$ values of −10‰–−8.3‰ (average: −9.1‰), and those from the cold springs had δ^2H values of −51‰–−42‰ (average: −45‰) and $\delta^{18}O$ values of −8.7‰–−6.3‰ (average: −7.4‰). Moreover, water samples from the surface water had δ^2H values of −50‰–−27‰ (average: −39.2‰) and −8.4‰–−2.8‰ (average: −6.1‰), and those from the groundwater had δ^2H values of −53‰–−32‰ (average: −45‰) and $\delta^{18}O$ values of −8.3‰–−4.9‰ (average: −7.0‰). As shown in **Figure 5**, all the samples were distributed along the LMWL, indicating that they were mainly recharged by atmospheric precipitation and the meltwater from snow. However, the points of the δ^2H and $\delta^{18}O$ values of all the water samples were located to the right of the LMWL, indicating that $\delta^{18}O$-shift occurred. The surface water samples were close to the LMWL, suggesting that they were mainly recharged by modern atmospheric precipitation across short circulation pathways and with a high rate of renewal. Most groundwater samples were plotted close to the LMWL, and their average δ^2H and $\delta^{18}O$ values were close to those of the surface water samples, suggesting that the groundwater was of meteoric and surface water origin. For example, well GC4# lies in the floodplain of the Kekesaiqu area, and surface river water BS15 is also in this area. **Figure 5** shows that GC4# was recharged by BS15. In addition, water samples from ML1# and DK2# were distributed close to those from cold springs A11 and A29 and surface water S2 and BS19, indicating that the groundwater has similar circulation pathways to cold springs and a higher renewal rate. The groundwater at ML1# and DK2# is mainly recharged by atmospheric precipitation, and it is mixed with large amounts of surface water. Compared with other water samples, samples from the warm springs showed more significant $\delta^{18}O$-shift. In general, the δ^2H value cannot be significantly affected by the hydrogen isotope exchange between water and surrounding rocks. However, the $\delta^{18}O$ value can be increased by the oxygen isotope exchange between water and surrounding rocks, and the rate of the oxygen isotope exchange increases rapidly with increased temperature. Therefore, the degree of $\delta^{18}O$-shift depends on and reflects not only the degree of the oxygen isotope exchange between water and surrounding rocks but also the temperature during the water-rock interaction (Zhang et al., 2021). The average annual $\delta^{18}O$ value of the local atmospheric precipitation is −9.2‰ (Yang, 2019), which is lower than the average $\delta^{18}O$ values of water samples from the cold springs, surface water, and groundwater. This result indicates that cold springs, surface water, and groundwater experienced evaporation. The $\delta^{18}O$ value of the water samples from the warm springs was roughly the same as the average annual $\delta^{18}O$ value of the local atmospheric precipitation, suggesting that the $\delta^{18}O$-shift of the warm springs is caused by water-rock interaction.

TABLE 2 | Calculated elevation of the recharge areas of warm springs.

Warm spring	Sample elevation (m)	δ^2H (‰)	Recharge elevation (m)
C73	3,831	−61	4,451
C127	3,771	−60	4,426
E58	3,851	−59	4,401
B11	3,891	−63	4,501

4.2.2 Recharge Elevation of Warm Springs

In general, the δ^2H and $\delta^{18}O$ values for atmospheric precipitation are linearly related to the temperature. The elevation effect refers to the phenomenon that, with increased elevation, the temperature of air decreases and, accordingly, the δ^2H and $\delta^{18}O$ values of water also decrease (Sun et al., 1992). The reasons are as follows. The air temperature decreases, and the water vapor in air condenses as the elevation increases. Moreover, the increased elevation corresponds to the decreased pressure and volume expansion of air, which also lead to the decreased temperature and the condensation of water vapor in air. The water vapor condensation will cause isotopic fractionation and decreased raindrop evaporation. As a result, precipitation increases on the windward side of a mountain, resulting in the formation of an overtopping precipitation area. Accordingly, the isotope content of clouds decreases with increased elevation, and thus the elevation effect is formed (Chen et al., 2019). The elevation effect of isotopes in the atmospheric precipitation can be used to determine the recharge sources for groundwater and their elevation. However, a $\delta^{18}O$ shift tends to occur in geothermal water due to the water-rock interaction during the deep circulation of geothermal water. As a result, the recharge elevation calculated using $\delta^{18}O$ values will deviate from its actual value. Therefore, in this study, the recharge elevation of the warm springs was determined based on δ^2H values in this study.

The relationship between the δ^2H value and recharge elevation was fitted using the δ^2H and $\delta^{18}O$ values of atmospheric precipitation at different elevation values. The fitted equation is:

$$H = -24.995\,\delta^2H + 2926 \quad (1)$$

where H is recharge elevation.

The fitted equation approximates the elevation effect equation proposed by (Li et al., 2016a), that is, $H=-25.47\,\delta^2H + 2{,}827.68$.

As shown in **Table 2**, the recharge elevation of the four warm springs in the study area was calculated as 4,401–4,501 m, which is approximately 600 m greater than the elevation of the sampling sites. As shown by comparison and analysis based on the terrain and fault distribution in the study area, the recharge areas of the four warm springs are mainly located in the Tuolai Nanshan Mountain and the Datong Mountain, which lie on the north and south sides of the Jiangcang Basin, respectively. In these recharge areas, precipitation and meltwater from snow infiltrate and then are exposed along faults after deep circulation.

4.3 Estimation of Geothermal Reservoir Temperature

The geothermal reservoir temperature is a critical parameter in assessing the formation mechanism of geothermal resources and

TABLE 3 | Formulas for calculation of cationic geothermometers.

Geothermometer	Calculation formula
Na/K	T=1,217/(log(Na/K)+1.483)–273.15
K/Mg	T=4,410/(13.95–log(K^2/Mg))–273.15
Na-K-Ca	$T = \frac{1647}{\log(\frac{Na}{K})+\beta(\log(\frac{\sqrt{Ca}}{Mg})+2.06)+2.47} - 273.15$ β=4/3(when t<100°C)or β=1/3(when t>100°C)

TABLE 4 | Temperature of warm springs in the Jiangcang Basin calculated using geothermometers.

Warm spring	Temperature (°C)	$T_{Na/K}$ (°C)	$T_{K/Mg}$ (°C)	$T_{Na-K-Ca}$ (°C)	No-steam loss quartz thermometer (°C)	Chalcedony geothermometer (°C)	Multi-mineral equilibrium (°C)	Temperature (°C)
C73	36.6	247.9	57.8	163.5	91.4	60.7	96	83
C127	6.9	385.6	89.2	229.2	91.8	61.2	53	69
E58	19.5	264.2	73.1	173.5	64.7	32.7	55	51
B11	24	229.4	59.2	154.9	72.4	40.7	85	66

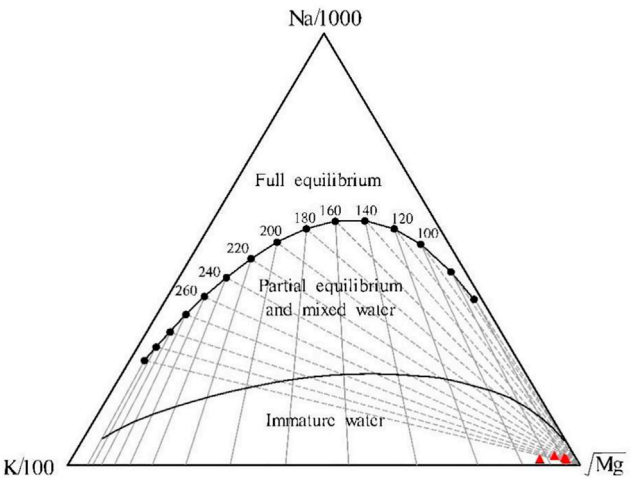

FIGURE 6 | Na-K-Mg ternary diagram of warm springs in the Jiangcang Basin.

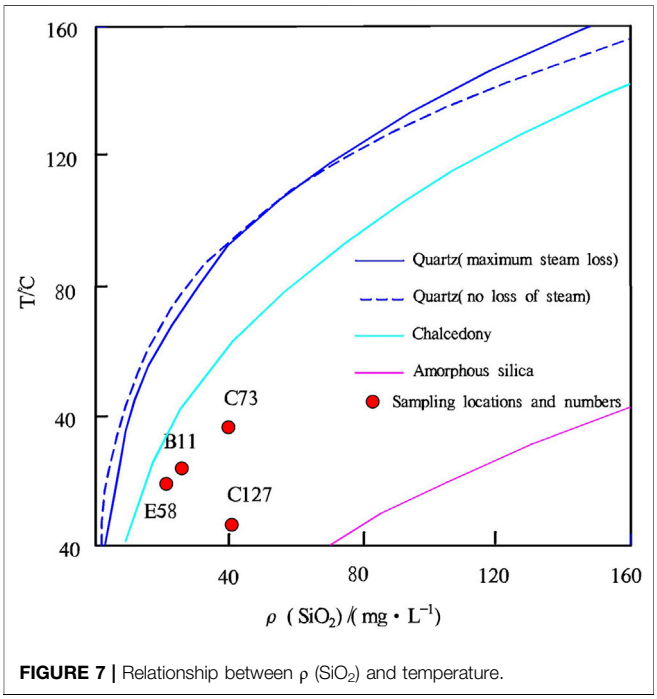

FIGURE 7 | Relationship between ρ (SiO_2) and temperature.

their potential for exploitation and utilization. Geothermometers developed based on the chemical equilibrium of minerals in geothermal fluids can be used to accurately estimate the geothermal reservoir temperature. In this study, the geothermal reservoir temperature in the Jiangcang Basin was estimated using cationic geothermometers, silica geothermometers, and the multi-mineral equilibrium method. Then, properly calculated results were selected for the geothermal reservoir temperature in the basin, based on the analysis of the water-rock mineral equilibrium.

4.3.1 Cationic Geothermometers

Cationic geothermometers are designed to obtain the geothermal reservoir temperature by establishing the relationship between the temperature and the ratio of cations in geothermal water. Commonly used cationic geothermometers include Na-K, K-Mg, and Na-K-Ca geothermometers (Zhao, 1988; Xu and Guo, 2009). The formulas are shown in **Table 3**.

The test results of water samples collected from the four warm springs, the geothermal reservoir temperature was estimated using different cationic geothermometers (Na-K, K-Mg, and Na-K-Ca geothermometers) according to the temperature of spring vents, and the results are listed in **Table 4**. The data in this table show that the calculated results differ too greatly, and thus it is necessary to analyze the applicability of these cationic geothermometers.

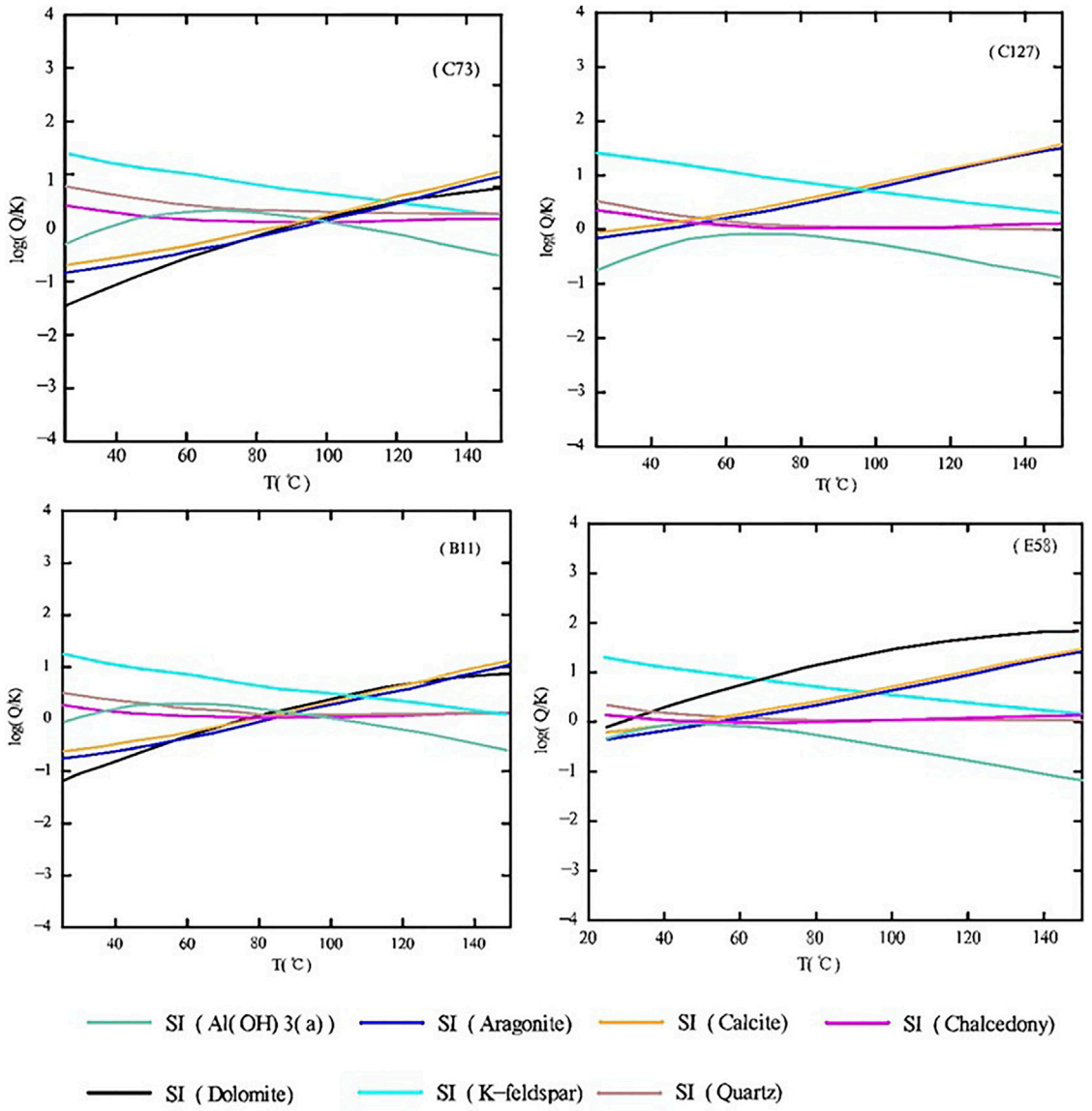

FIGURE 8 | SI-T curves of various minerals in the warm spring water in the Jiangcang Basin.

Different cationic geothermometers should be used in different conditions. The Na-K geothermometer applies to high-temperature geothermal water (temperature >150°C) that is depleted in calcium. Since the warm springs of the Jiangcang Basin feature low temperatures and relatively high Ca^{2+} concentrations (Zhao, 1988), the Na-K geothermometer is not usable. The K-Mg geothermometer applies to low-temperature groundwater. The temperature estimated using the K-Mg geothermometer is generally higher than the temperature of water yielded from a geothermal well and is considered the temperature that can be possibly obtained by drilling toward deep parts (Giggenbach, 1988). A Na-K-Ca geothermometer can be used for medium- and low-temperature Ca-rich water or shallow hot water. This means that the Na-K-Ca geothermometer is the most appropriate for the geothermal reservoirs in the Jiangcang Basin. However, the warm spring water has a generally high Mg^{2+} content, of 38.87–92.5 mg/L. For medium- and low-temperature water rich in Mg^{2+}, the results estimated using the Na-K-Ca geothermometer also significantly deviated from the actual temperatures. Therefore, it is necessary to further correct the estimated results according to the Mg^{2+} content (Rybach and Muffer, 1986).

A geothermometer can be used to estimate the geothermal reservoir temperature on the premise that the minerals in the geothermometer and the minerals in the geothermal reservoir reach equilibrium (Shi et al., 2018). The Na-K-Mg ternary diagram developed based on the Na-K and K-Mg geothermometers can be used to assess the water-rock equilibrium and distinguish different types of water samples. As shown in the Na-K-Mg ternary diagram (**Figure 6**), the water

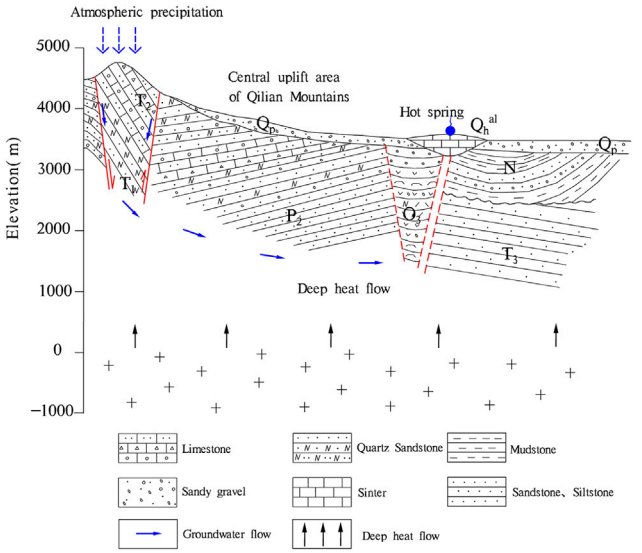

FIGURE 9 | Genetic model of warm spring B11 in the Jiangcang Basin.

samples from the four warm springs in the Jiangcang Basin all fall into the immature water zone. This result indicates that the water-rock interaction in the warm springs has not yet reached an equilibrated state or that the warm spring water is mixed with large amounts of shallow cold water as it rises. In this case, the warm spring water is not sufficiently saturated regarding ion concentrations. Therefore, the geothermal reservoir temperature determined using cationic geothermometers will experience large errors and thus can only be used as a reference.

4.3.2 Silica Geothermometers

Silica geothermometers are used to calculate the temperature of a geothermal reservoir according to the concentrations of silica minerals in hot water since the solubility of silica minerals is a function of temperature. When the temperature is below 300°C, changes in the pressure and salinity have minor effects on the solubility of quartz and amorphous silicon. Moreover, other ions and complexes generally do not affect dissolved silica in water at a temperature of less than 300°C. Therefore, silica geothermometers are one of the most commonly used and effective geothermometers (Zheng and Guo, 1996).

The solubility curves of silica can be used to determine the minerals that control the mass concentration of silica in a solution. There are many types of silica minerals in nature, among which quartz, chalcedony, and amorphous silicon are of primary importance in geothermal study. Based on the relationship between the silica concentration and temperature, as well as the solubility curves of silica (**Figure 7**), the water samples from the warm springs in the study area all fall below the dissolution curves of quartz and chalcedony in the theoretically equilibrated state. This phenomenon indicates that the quartz and chalcedony were oversaturated, but amorphous silicon was not equilibrated in the water samples. Therefore, the silica concentration in the warm springs is possibly controlled by quartz and chalcedony, which can be used to estimate the temperature of deep geothermal reservoirs, as ideal geochemical geothermometers.

Quartz geothermometers can be divided into two types, namely, quartz-no steam loss and quartz-maximum steam loss. Because the study area is at high elevation, 80°C can be considered the boiling point in the area. Given that the four warm springs have a maximum temperature of 36.6°C, the geothermometer of quartz-no steam loss was employed to calculate the temperature of the warm springs in this study, and the equations are as follows:

For geothermometer of quartz-no steam loss: $T=1{,}309/(5.19-\log SiO_2)-273.15$.

For chalcedony geothermometer: $T=1{,}032/(4.69-\log SiO_2)-273.15$.

The calculated results are shown in **Figure 4**.

4.3.3 Multi-Mineral Equilibrium Method

The multi-mineral equilibrium method can be used to determine the chemical equilibrium state of minerals in geothermal fluids. It is designed as follows. Firstly, the dissolution states of multiple minerals in geothermal fluids are expressed as a function of temperature. Then, if several minerals reach equilibrium (saturation index=0) at a certain temperature, the minerals whose equilibrium curves (i.e., the curves formed by connecting the solubility values at different temperatures) converge can be used as geothermometers (Reed and Spycher, 1984; Wu and Sun, 2000), and the temperature obtained is the geothermal reservoir temperature (Chai, et al., 2010). The saturation index (SI) can be used to determine the degree of saturation of minerals. Specifically, values of SI=0, >0, and <0 of minerals indicate that the minerals are saturated, oversaturated, and undersaturated in a solution (Guo and Song, 2005).

The PREEQC software can be used to calculate the SIs of various minerals. Because the rocks in the Jiangcang Basin are dominated by sandstone and are interbedded with shales and limestones, minerals including quartz, chalcedony, K-feldspar, calcite, aragonite, gibbsite, and dolomite were selected to calculate the geothermal reservoir temperature in this study. Then, the SI vs. temperature curves of minerals and geothermal fluids were plotted (**Figure 8**). In this manner, the geothermal reservoir temperature of the study area was obtained (**Table 4**).

As shown in **Figure 8**, K-feldspar and gibbsite curves poorly converge, while the curves of the remaining six minerals converge at a narrow temperature interval and roughly intersect at one point. Moreover, the trend curves of quartz and chalcedony more approximate the curve of SI=0, and the intersection points between the curves of the quartz, chalcedony, and aragonite roughly lie on the curve of SI=0. Therefore, the intersection point of the three types of minerals was used to estimate the geothermal reservoir temperature, and the estimated results are shown in **Table 4**.

The geothermal reservoir temperature, estimated using the multi-mineral equilibrium method was close to that determined using the quartz and chalcedony geothermometers. Because the results obtained using various methods all contain errors, the averages of these results were taken as the temperatures of deep

geothermal reservoirs of the warm springs in the Jiangcang Basin, as shown in **Table. 4**.

4.4 Circulation Depth of Geothermal Water

To obtain a detailed understanding of the genesis of the warm springs in the Jiangcang Basin, the circulation depth of geothermal water was estimated. Geothermal water is usually heated by deep heat sources during deep circulation. The circulation depth of a warm spring can be roughly estimated using the following equation:

$$H = \frac{t - t_0}{k} + H_0 \quad (5)$$

where T is the geothermal reservoir temperature, t_0 is the local average multi-year temperature, k is the geothermal gradient, and H_0 is the thickness of the constant temperature zone. Relevant data reveal that the average annual temperature in the Jiangcang Basin is −5.6°C. As mentioned in the regional hydrogeologic report of the Zhimahe Map Sheet, the logging and temperature data of borehole 8601 lying approximately 2 km to the west of warm spring E58 (No. 958) (i.e., to the west of the Kekesaiqu area) show a temperature gradient of 4.2°C/100m and a thickness of the constant temperature zone of approximately 50 m (Xie et al., 1987). The circulation depths of the geothermal water of warm springs C73, C127, E58, and B11 were calculated to be approximately 2,610 m, 2,276 m, 1848 m, and 2,205 m, respectively. Therefore, all the warm springs in the Jiangcang Basin feature deep circulation, and the warm spring water is mixed with shallow cold water as it rises to the ground surface. In addition, the permafrost in the Jiangcang area has a thickness of up to 86.65 m, causing the geothermal water to cool through conduction as it rises. As a result, the water at the spring vents has a low temperature.

4.5 Genesis Models of Warm Springs

The Jiangcang Basin is a Cenozoic faulted basin, where many warm springs are exposed. The genetic model of the warm springs is exemplified by warm spring B11 (**Figure 9**). B11 is recharged by the atmospheric precipitation and the meltwater from snow and ice in the high mountainous areas on the southwest side of the Jiangcang Basin. The atmospheric precipitation and meltwater from snow and ice infiltrate and migrate downward along regional deep fault F42, which penetrates deep heat sources. The groundwater enters the deep thermal reservoirs through infiltration and recharge by lateral runoff. Then, it is heated by terrestrial heat flow after a long-term and slow deep circulation, forming deep geothermal resources. Faults serve as pathways with effective hydraulic conductivity. There are more than 30 faults and folds of various sizes in the study area. Influenced by faults and the water blocking of the Nanyinger Formation (T3n) and Paleogene (N) mudstones, geothermal water rises along faults and is mixed with shallow groundwater as it rises. Finally, the mixed water is exposed as a low-temperature warm spring in the muddy gravels (Q2) of the moraine mound zone in the piedmont.

The geothermal water of B11 mainly originates from the heat flow conduction of deep granites and natural geothermal gradients. As indicated by the isotopic analysis, the geothermal water of B11 is primarily recharged by atmospheric precipitation and meltwater from snow, with a recharge elevation of 4,401–4,501 m and a circulation depth of up to 1,848–2,610 m. Tectonic fractures of Triassic sandstones serve as the water-bearing media of the geothermal water of B11. The water in these tectonic fractures is characterized by long circulation pathways, strong water-rock interaction, and high TDS. The deep geothermal water is mixed with the shallow cold water and is cooled by the upper permafrost through conduction. Finally, the mixed water is exposed as the Zemoyesang low-temperature warm spring.

5 CONCLUSION

(1) The warm springs in the Jiangcang Basin have hydrochemical types of HCO_3-Ca·Mg, HCO_3-Ca·Na·Mg, and HCO_3·SO_4-Na·Ca. Hydrochemical analyses show a high correlation between $Mg^{2+}$and TDS, with a correlation coefficient of up to 0.96. By contrast, there is a low correlation between Na^{2+} and TDS, with a correlation coefficient of 0.65. These results reflect the ion composition characteristics of medium- and low-temperature thermal springs. Moreover, there is no significant positive correlation between Cl^- and other ions in the warm springs, indicating that the trace elements in the warm springs mainly originate from the dissolution of relevant minerals.

(2) The points of δ^2H and $\delta^{18}O$ values of water samples from the Jiangcang Basin all fall below the LMWL, indicating different degrees of $\delta^{18}O$-shift. By comparison with the average $\delta^{18}O$ value of the local atmospheric precipitation, the $\delta^{18}O$-shift of the cold water is mainly affected by evaporation, while that of the warm springs is primarily caused by deep water-rock interactions.

(3) The temperature of the deep geothermal reservoirs in the Jiangcang Basin is 51–83°C, with an average of 67°C. The results of the calculations of the hydrogen and oxygen isotopes show that the recharge elevation of the warm springs is 4,401–4,501 m (average: 4450 m), which is similar to the elevation of the Tuolai Nanshan Mountain and the Datong Mountain on the north and south sides of the Jiangcang Basin, respectively. Therefore, the warm spring water in the study area is mainly recharged by atmospheric precipitation and meltwater from snow of the piedmont. In addition, the circulation depth of the geothermal water is 1,848–2,610 m.

(4) The atmospheric precipitation and meltwater from ice and snow infiltrate downward through the deep fault fracture zones in the high mountainous areas and then form runoff in the basin along the tectonic channels. Then, they are heated through deep circulation and then rise along faults under the influence of fault structures and the water blocking of mudstones. As they rise, they are mixed with the shallow groundwater and cool by the upper permafrost through

conduction. Finally, the mixed water is exposed as low-temperature tectonic warm springs.

DATA AVAILABILITY STATEMENT

The original contributions presented in the study are included in the article/supplementary material, and further inquiries can be directed to the corresponding author.

AUTHOR CONTRIBUTIONS

LL was responsible for numerical simulation and drafting the paper. WW put forward the research idea. YZ and MG helped with the field survey and sampling. SQ gave guidance regarding the genetic model of the warm springs. JH assisted in data analysis.

FUNDING

This research was supported by the Natural Science Foundation of China (41502336), the China Geological Survey Grant (DD20221676), and the S&T Program of Hebei Province, China (No. 20374201D).

ACKNOWLEDGMENTS

We would like to extend our gratitude to Researcher Xiangquan Li and Senior Engineer Zhenxing Wang from the Institute of Hydrogeology and Environmental Geology, Chinese Academy of Geological Sciences, for their assistance in data and materials. Our thanks also go to Researcher Wenjing Lin, Associate Researcher Zhaoxian Zheng, and Associate Researcher Xiaojiao Guo for their great assistance in mapping and article polishing.

REFERENCES

Chai, R., Wang, H., and Liu, Y. (2010). Application of Multimineral Balance Method to Estimation of Geothermal Temperature. *Coal Sci. Technol.* 38 (4), 100–103. doi:10.13199/j.cst.2010.04.107.chair.001 (in Chinese with English abstract).

Chen, L. (2019). Isotopic Characteristics Analysis of Hydrogenoxygen Environment in Geothermal Water in Fujian Province. *Geology of Fujian* 1, 61–68. (in Chinese with English abstract).

Dai, M. (2020). "The Hydrogeochemical Characteristics and the Evolution of Geothermal Water in Guide Area, Qinghai," (Beijing: China university of geosciences). Master's thesis.

Du, G. L., Cao, W. H., and Zhai, B. (2012). Genesis of Baoquantang Hot Spring and its Influence on Fault and Seismicity in Weihai City. *Mar. geology&Quaternary Geol.* 32 (5), 67–72. doi:10.3724/SP.J.1140.2012.05067

Giggenbach, W. F. (1988). Geothemal Solute Equilibria. Derivation of Na-K-Ca Geoindicators. *Geochim. Cosmochim. Acta* 52, 2749–2765. doi:10.1016/0016-7037(88)90143-3

Guo, Z. J., and Song, H. Z. (2005). Chemical Components in Groundwater and its SI Values. *Resources Environment & Engineering* 19 (3), 200–202.

Guo, Z. J., Wang, J. G., Chen, Z., and Shi, J. H. (2015). Discussion on the Formation Mechanism of Wenshui Longtan Hot Spring in Xishan, Heqing, Yunnan Province. *Geotech. Investig.* 5, 43–48.

Jiang, Z. J., Xu, T. F., Dirk, M., Tian, H., and Owen, D. D. R. (2019). Numerical Modelling of Stable Isotope (2H and 18O) Transport in a Hydro-Geothermal System: Model Development and Implementation to the Guide Basin, China. *J. Hydrology* 569 (2), 93–105. doi:10.1016/j.jhydrol.2018.11.065

Lang, X. J., Lin, W. J., Liu, Z. M., Xing, L. X., and Wang, G. L. (2016). Hydrochemical Characteristics Water in Guide Basin. *Earth Sci.* 41 (10), 1723–1734.

Li, H. D., Zhang, S. Q., Bai, J. Q., Zhou, J. Y., Shi, W. D., and Zhao, Y. (2007). Hydrochemistry and Origin of the Yaoshuitan Geothermal Field, Xining, Qinghai. *Acta Geol. Sin.* 81 (9), 1299–1304.

Li, X. Q., Hou, X. W., Wang, Z. X., Liu, L. X., Gao, M., Ma, J. F., et al. (2016a). *Institute of Hydrogeology and Environmental Geology*. China: Chinese Academy of Geological Sciences. 1:50,000 hydrogeological map manual of the Jiariguorixue.

Li, X. Q., Wang, Z. X., Hou, X. W., Chen, J., Liu, L. X., Gao, M., et al. (2016b). *Institute of Hydrogeology and Environmental Geology*. China: Chinese Academy of Geological Sciences. Hydrogeology and environmental geology survey report of important energy base in Qinghai province.

Li, L. L. (1952). "Research on the Preservation Law and Genetic Model of Geothermal Resources in Guide Basin , Qinghai Province," (China: East china university of technology). Master's thesis.

Li, Y. G. (2016). "Hydrogeochemical Characteristics and its Origin Analysis of Geothermal Water in the Qia Bu-Qia Area, Gonghe Basin, Qinghai Province," (China: East china university of technology). Master's thesis.

Ma, Y. H., Tang, B. C., Su, S. Y., Zhang, S. S., and Li, C. Y. (2020). Geochemical Characteristics of Geothermal Fluids and Water-Rock Interaction in Geothermal Reservoirs in and Around the Gonghe Basin, Qinghai Province. *Earth Sci. Front.* 27 (1), 123–133. doi:10.13745/j.esf.2020.1.14

Ni, G. Q., Zhang, H., Wei, Y. T., and Hu, Y. Z. (2016). Hydrogeochemical and Isotope Characteristics of Geothermal Fluid in Sichuan. *Adv. New Renew. Energy* 4 (3), 184–194. doi:10.3969/j.issn.2095-560X.2016.03.004

Reed, M., and Spycher, N. (1984). Calculation of pH and Mineral Equilibria in Hydrothermal Waters with Application to Geothermometry and Studies of Boiling and Dilution. *Geochimica Cosmochimica Acta* 48 (7), 1479–1492. doi:10.1016/0016-7037(84)90404-6

Rybach, L., and Muffler, L. J. P. (1986). *Geothermal Systems - Principles and Analysis of Typical Geothermal Systems*. China: Department of Geology, Peking University. Translated by the Geothermal Research Unit.

Shi, J., Nai, W. H., Li, M., Wang, S., Ma, X. J., and Zhang, J. (2018). Hydrogeochemical Characteristics of High Temperature Geothermalfield of the Quman Geothermal Field in Xinjiang. *Hydrogeology & Engineering Geol.* 45 (3), 165–172. doi:10.16030/j.cnki.Issn.1000-3665.2018.03.23

Sun, Z. X., Li, X. L., and Shi, W. J. (1992). Isotopic Hydrogeochemistry of Mid-low Temperature Geothermal Water in Jiangxi Province. *J. East China Geol. Inst.* 15 (3), 243–248.

Sun, C. J., Zhang, Z. Y., Chen, W., Li, W., Chen, R. X., School of Geographical Science, et al. (2019). Spatial Distribution of Precipitation Stable Isotopes in the Alpine Zones in Central Asia. *Arid Zone Res.* 36 (01), 19–28. doi:10.13866/j.azr.2019.01.03

Sun, H. L., Wang, G. L., and Lin, W. J. (2022). Distribution Characteristics and Enrichment Mechanism of TDS Geothermal Water in Xining Basin. *Bull. Geol. Sci. Technol.* 41 (1), 278–287. doi:10.19509/j.cnki.dzkq.2021.0079

Tang, X. C., Wang, G. L., Ma, Y., Zhang, D. L., Liu, Z., Zhao, X., et al. (2020). Geological Model of Heat Source and Accumulation for Geothermal Anomalies in the Gonghe Basin, Northeastern Tibetan Plateau. *Acta Geol. Sin.* 94 (7), 2052–2065. doi:10.1111/1755-6724.14541

Wang, G. L., Zhang, W., Liang, J. Y., and Lin, W. J. (2017a). Evaluation of Geothermal Resources Potential in China. *Acta Geosci. Sin.* 38 (4), 449–459. doi:10.3975/cagsb.2017.04.02

Wang, G. l., Zhang, W., Lin, W. J., Liu, F., and Zhu, X. (2017b). Research on Formation Mode and Development Potential of Geothermal Resources in Beijing-Tianjin-Hebei Region. *Geol. China* 44 (6), 1074–1085. doi:10.12029/gc20170603

Wang, R. J. (2009). Geochemical Characteristics and Resource Evaluation of Underground Hot Water in the Chabcha Geothermal Zone of the

Republican Basin, Qinghai Province. (China: Chang'an University). Master's thesis.
Wu, H. M., and Sun, Z. X. (2000). Calculation of the Fluid-Rock Equilibrium State in the Geothermal System. *J. east china Geol. Inst.* 23 (1), 39–42.
Xie, C. J., Liu, Z. F., Xu, X. C., and Zhang, S. Q. (1987). *Second Hydrogeological Team of Qinghai Province*. 1:200,000 regional hydrogeological survey report of the zhihema.
Xu, S. G., and Guo, Y. S. (2009). *Fundamentals of Geothermics*. Beijing: Science Publishers.
Yang, S. K., Luo, Y. F., Zhao, Z., Zhang, S. S., Zhang, Z. X., A., H. J., et al. (2015). Report on the Evaluation and Zoning of the Current Situation of Geothermal Resources in Qinghai Province. Xining: Qinghai Bureau of Environmental Geology Exploration.
Yang, Y. F. (2019). "Precipitation and Runoff Process in Shaliu River Basin of Qinghai Lake Based on Hydrogen-Oxygen Stable Isotope Technique," (China: Qinghai Normal University). Master's thesis.
Yuan, X. f., Wang, J., Huo, G., Song, M. z., and Wang, J. l. (2020). Hydrochemistry and Genesis of the Hongshuilantang Hot Spring in the Jiaodong Peninsula. *Geol. Explor.* 56 (2), 427–437. doi:10.12134/j.dzykt.2020.02.017
Yuan, J. (2010). "Transport of Boron in the Aquatic Environment of the Yangbajing Geothermal Field, Tibet," (China: China University of Geosciences). Master's thesis.
Zhang, S. Q., Li, H. D., Xu, G. C., Shi, W. D., Zhou, J. Y., and Shang, X. G. (2007). Geochemical Characteristics of Groundwater in the Du Jia Zhuang Geothermal Field in the South of xining、Qinghai. *Front Earth Science*. 21 (1), 163–169.
Zhang, C. C., Li, X. Q., Ma, J. F., Fu, C. C., and Bai, Z. X. (2021). Formation Pattern of Geothermal Water in Chaya of Tibet Based on Hydrochemistry and Stable Isotopes. *Geoscience* 35 (1), 1–22. doi:10.19657/j.geoscience.1000-8527.2021.013
Zhang, X. G. (1988). Application of Isotopic Geochemistry in Geothermal Exploration. *Hydrogeology Eng. Geol.* 1, 28–31.
Zhang, Z. (1999). Rich Geothermal Resources in Qinghai. *Earth* 6, 11.
Zhao, Q. S. (1988). The Application of Geothermometers in the Exploration of Hydrothermal Resources in Western Sichuan. *J. chengdu Univ. Sci. Technol.* 37 (1), 44–50.
Zheng, X. L., and Guo, J. Q. (1996). Silica Geothermal Temperature Scale and its Related Treatment Methods. *Groundwater* 18 (2), 85–88.

Conflict of Interest: The authors declare that the research was conducted in the absence of any commercial or financial relationships that could be construed as a potential conflict of interest.

The handling editor WL declared a shared affiliation with the authors LL, MG, and WW at the time of review.

frontiers | Frontiers in Earth Science

TYPE Original Research
PUBLISHED 09 January 2023
DOI 10.3389/feart.2022.895530

OPEN ACCESS

EDITED BY
Wenjing Lin,
Chinese Academy of Geological Sciences, China

REVIEWED BY
Wei Shi,
Chinese Academy of Geological Sciences (CAGS), China
Dawen Zhang,
Zaozhuang University, China

*CORRESPONDENCE
Feng Qingda,
fengqingda@mail.cgs.gov.cn
Li Fucheng,
lifucheng@mail.cgs.gov.cn

SPECIALTY SECTION
This article was submitted to Structural Geology and Tectonics, a section of the journal Frontiers in Earth Science

RECEIVED 14 March 2022
ACCEPTED 05 August 2022
PUBLISHED 09 January 2023

CITATION
Yang Z, Qingda F, Fucheng L, Linyou Z, Chao Z, Senqi Z, Dunpeng L, Zhen Y, Jian S, Lei F and Zhaoxuan N (2023), Insights into the late Cenozoic structural deformation and tectonic stress field of the Qiabuqia region, Gonghe Basin, northeastern Qinghai–Tibetan Plateau. *Front. Earth Sci.* 10:895530. doi: 10.3389/feart.2022.895530

Insights into the late Cenozoic structural deformation and tectonic stress field of the Qiabuqia region, Gonghe Basin, northeastern Qinghai–Tibetan Plateau

Zhang Yang[1], Feng Qingda[1]*, Li Fucheng[1]*, Zhang Linyou[1], Zhang Chao[2], Zhang Senqi[1], Li Dunpeng[3], Yan Zhen[4], Song Jian[1], Fu Lei[1] and Niu Zhaoxuan[1]

[1]Center For Hydrogeology and Environmental Geology Survey, China Geological Survey, Baoding, China, [2]College of Energy, Chengdu University of Technology, Chengdu, China, [3]Zijin Mining College, Fuzhou University, Fuzhou, China, [4]Institute of Geology, Chinese Academy of Geological Sciences, Beijing, China

In addition to overall uplift of the Qiabuqia region during the Late Cenozoic, three deformation stages can be identified in the northeastern Qinghai–Tibet Plateau. Specifically, these deformation stages were recognized in areas east of the Gonghe Basin that surrounds Waliguan Mountain and include: 1) Late Miocene to Late Pliocene deformation—dominated by thrust napping with dextral strike-slipping; 2) Early Pleistocene to late middle period of Pleistocene deformation—fault structures were dominated by the dextral strike-slipping with thrust napping; and 3) end of Late Pleistocene to Middle Holocene deformation—thrust napping slowed down and finally braked, while the shallow surface began to loosen and extend at Qiabuqia region's rear-edge. DR4 borehole drilling data indicate that the Xiangshuihe Formation's buried depth is ~1,000 m. The Xianshuihe Formation's top section is characterized by normal fault–type (NF) tectonic stress, while the maximum principal tectonic stress (σ1) is perpendicular and the minimum principal tectonic stress (σ3) is horizontal. In contrast, the deep basement is characterized by thrust fault (TF) and strike-slip (SS) tectonic stress, while the σ1 is in the NE-SW direction, ranging from 20.1° to 75.3° with an average of 40.0°. Based on the aforementioned observations, it can be inferred that there are three sets of hidden faults in the basement of the Qiabuqia region: 1) the NW–NNW trending compressional–torsional faults; 2) the NE trending tensional–torsional faults; and 3) the NWW trending compressional–torsional faults. The findings in this study can potentially offer a robust geological basis for exploring and utilizing hot, dry rock resources within the Gonghe Basin.

KEYWORDS

thrust nappe, strike-slip fault, normal fault, tectonic stress field, hot dry rock, Late Cenozoic, Gonghe Basin

1 Introduction

The concentration of geostress in the rocks surrounding the borehole wall affects how compression fractures in the borehole walls will open, while the far-field minimum principal geostress direction determines compression fractures' extensional mode. In summary, the hydraulic fractures' extensional direction is generally perpendicular to that of the minimum principal stress (Wu et al., 2014; Zhang et al., 2017; Zeng et al., 2019). Therefore, drilling along the direction of maximum principal stress is beneficial for constructing artificial reservoirs and connecting injection and production wells. In highly heterogeneous reservoirs punctuated by fault structures, hydraulic fracture formation and distribution is governed by both the current geostress field and spontaneous fractures resulting from the paleotectonic stress field. In addition, active faults can indicate the arrangement/direction of hot, dry rock geothermal wells, as they frequently indicate where energy is concentrated, which in turn can be followed to the high-temperature geothermal reservoir (Yang et al., 2017). Consequently, accurately analyzing the deep paleotectonic stress field and deducing the direction and characteristics of hidden fault structures within the basement is a key process in exploring and utilizing hot, dry rock resources.

Extensive compressional and strike-slip structures are dispersed throughout the Gonghe Basin and surrounding orogenic belts; thus, they have received widespread attention (Wang et al., 1988; Yuan et al., 2004a; Jiang et al., 2008; Chang et al., 2009; Craddock, 2011; Craddock et al., 2011; Craddock et al., 2014). In contrast, normal faults that are distributed throughout the basin, and are also characterized by small displacement, are often overlooked. In recent years, seven groups of stepped and horst–graben–shaped normal fault structural assemblages have been identified in the Qiabuqia area of the northeastern Gonghe Basin. Contrarily, thrust nappe and strike-slip structures developed at Waliguan Mountain, east of the Qiabuqia region. As such, both vertical and horizontal structural changes resulting from tectonic stress must be considered to accurately characterize hidden fault structures.

It has been established that geological bodies that affect and record geological structural histories become progressively younger as the targeted underground engineering area is approached. Thus, a direction analysis of stress generated by modern geostress has a higher reliability. To fill the resulting gap, this work focuses on analyzing the brittle tectonic deformation and neotectonic components that cut across the older deformational fabrics, which includes evaluating the folds, faults, and arrangement of quartz or calcite veins based on Triassic geological bodies in the Qinghai South Mountain–Waliguan Mountain area. This study locale was selected because it is close to Qiabuqia town. Moreover, Late Miocene and younger sedimentary strata in the study area were also analyzed to obtain numerous types of structural information. Simultaneously, all non-tectonic influence factors were excluded. The process described before provides a strong foundation for determining the tectonic stress field and deep basement fault structures that have developed since the Late Cenozoic.

In summary, this study combined field geological surveys, fault analysis, remote sensing imagery interpretation, and geochronological analysis to 1) determine the formation sequences of the thrust nappe structures and small displacement normal faults and 2) ascertain study area's tectonic setting and evolutionary history. Next, the results from the Late Cenozoic tectonic deformation analysis were implemented, and the Qiabuqia area's deep tectonic stress field and hidden basement faults were simulated using Anderson's theory of faulting (Anderson, 1951), Riedel shear model (Harding, 1974), and bow-and-arrow rule (Elliott, 1976).

2 Regional geological setting

The Gonghe Basin is located in the northeastern region of the Qinghai–Tibetan Plateau. Tectonically, it is part of Qinghai–Tibet Plateau's extensional front edge, which leads toward the intra-continents (Yuan et al., 2004b). The Gonghe Basin is situated on the central–eastern part of an active crustal block that is surrounded by three giant left-lateral strike-slip faults—the NEE-trending Altyn fault, NWW-trending Qilian Mountain–Haiyuan fault, and approximately EW-trending East Kunlun fault (Yuan et al., 2004b; Li et al., 2010). Since the Late Cenozoic, the Qinghai–Tibetan Plateau's northeastern margin has undergone significant deformation in response to the Indo–Asian plate collision and subsequent orogeny. Thus, the area's folds, thrusts, and strike-slip faults are extensively developed. These structural deformation characteristics indicate that this region is undergoing crustal shortening and strike-slip shearing, as well as the clockwise rotation associated with vertical uplift (Deng et al., 2002; Zhang et al., 2006a).

The Qiabuqia area is located on the Gonghe Basin's northeastern margin, nestled on the southwestern side of the ZongWuLong–Qinghai South Mountain tectonic belt (Figure 1A). The most striking fault structures on the belt's northeastern side include a fault (F2) with anti-S arc bending at northeastern Dongwaliguan, fault (F3) at the ZongWuLong–Qinghai South Mountain's southern margin, and Duolonggou curviplanar fault (F4) (Figure 1B). Most previous studies suggest that these arcuate tectonic belts are 1) a consequence of structural deformation during the Late Cenozoic and 2) correlated with the Qinghai–Tibetan Plateau's uplift and eastward extrusion (Zhang et al., 2006a; Wang et al., 2006; Yin, 2010). Extrusion of these blocks was accommodated by strike-slip activity that occurred within the

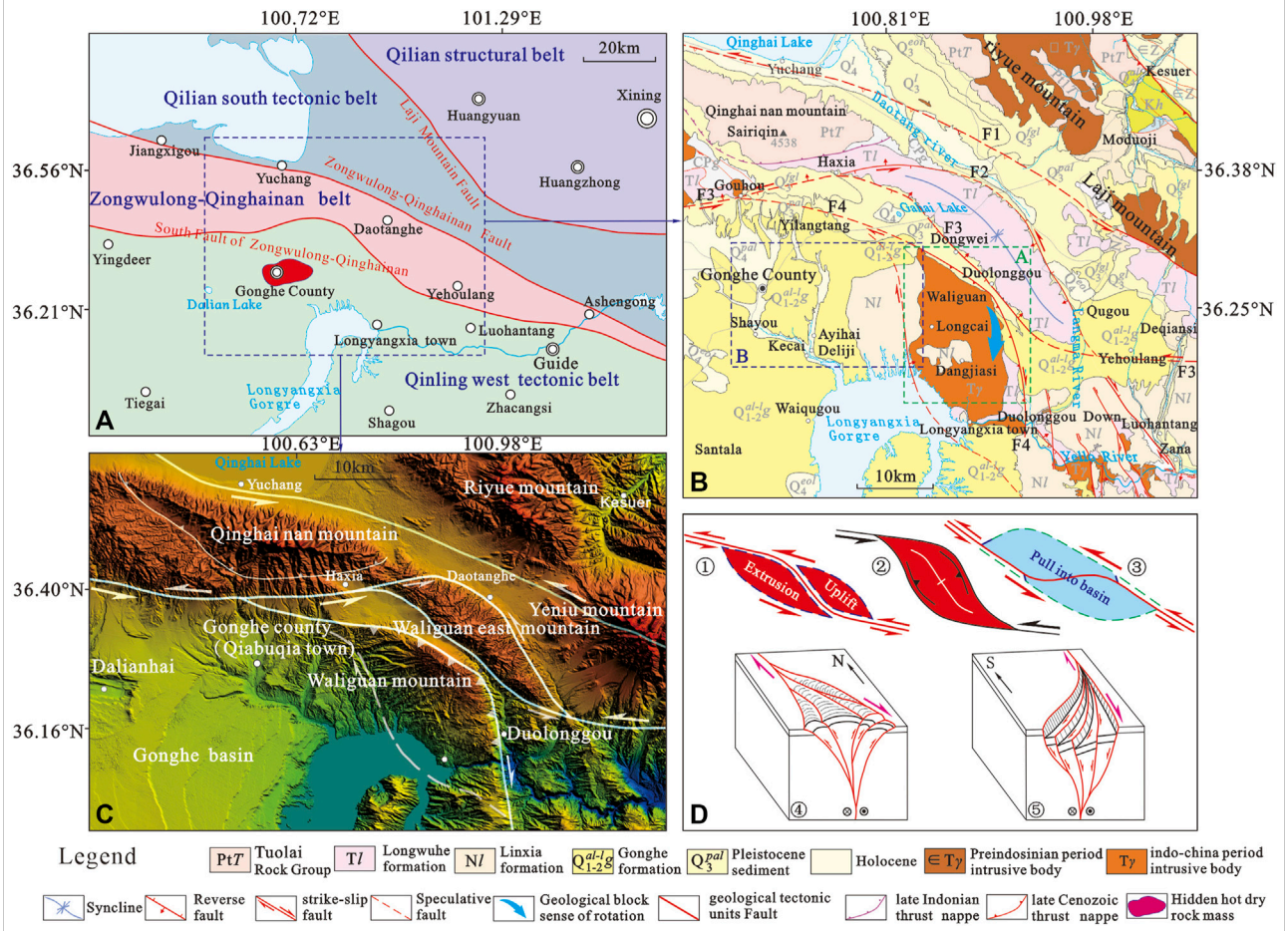

FIGURE 1
(A) Geological map of the Qiabuqia area showing major tectonic unit divisions; **(B)** regional geological map of the Qiabuqia area; **(C)** digital elevation model (DEM) and distribution map depicting main boundary faults; and **(D)** diagram of geomorphological changes caused by strike-slip fault bending (① restricted bending of the left strike-slip fault to form the strike-slip-squeezing uplift at Yeniu Mountain, ② strike-slip-squeezing uplift caused by paired low-curvature restricted bending of the Waliguan and East Waliguan Mountains, ③ fusiform–rhombus composite pull-apart basin formed when the left-lateral strike-slip fault bending stress was released, and ④ + ⑤ horsetail structure at the end of the strike-slip fault: ④ compressional horsetail structure and ⑤ stretching the horsetail structure).

interior of the arcuate tectonic belts and at the marginal faults (Zhang et al., 2004; Zhang et al., 2006b).

The arcual faults mentioned before each behave differently in response to structural location. To accommodate the local contraction, some portions of the arcual faults produced strike-slip–extrusion uplift, resulting in restricted bending, as well as rotation along the vertical axis (Luyendyk et al., 1980; Westaway, 1995; Cowgill et al., 2004). Other parts of the arcual faults were formed when bending stress was released, which produced the strike-slip, pull-apart basin to accommodate extensional bending (Figure 1D) (Crowell and Dickinson, 1974; Christie-Blick and Biddle, 1985). Furthermore, two or more strike-slip faults depicting lip-shaped strikes are referred to as “paired bending” (Mann, 2007)—a feature similar to the arcuate bending fractures seen along Waliguan Mountain and the East Waliguan Mountain boundary (Figure 1C). “Paired bending” commonly occurs in strike-slip systems and probably reflects crustal thickening and uplift at the restricted bending site and volumetric balance between crustal thinning and basin formation at the site where bending stress was released (Woodcock and Fischer, 1986). The tail ends of the strike-slip faults are commonly scattered as horsetail shapes, forming positive and negative flower structures, respectively (Lowell, 1972; Sylvester and Smith, 1976; Harding, 1985; Dooley et al., 1999). Consequently, the strike-slip bending faults were ultimately absorbed and adjusted by oblique and dip-slip faulting (McClay and Bonory, 2001).

Based on regional geological investigation and drilling data, the sedimentary cover in the Qiabuqia area primarily

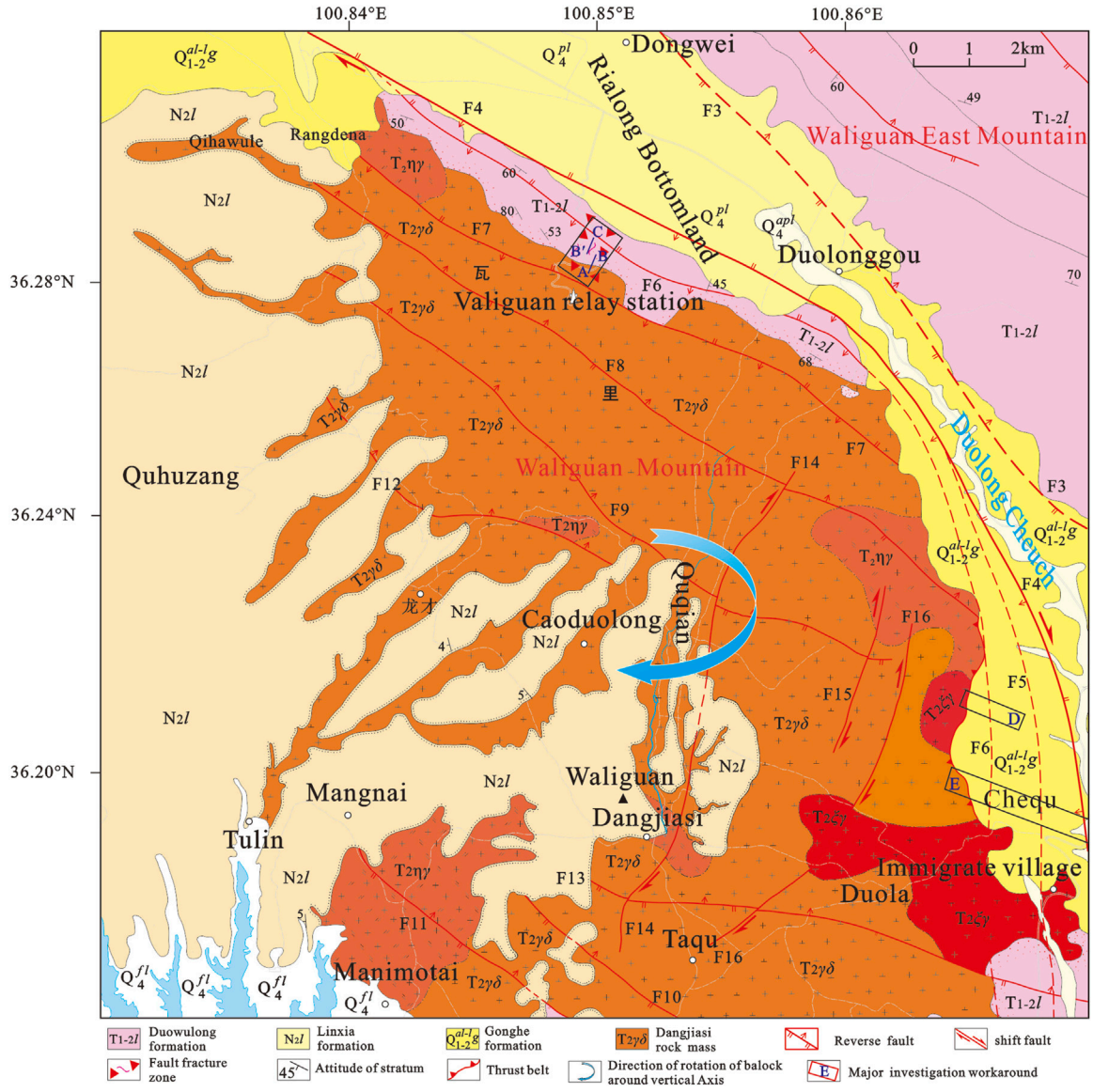

FIGURE 2
Geologic map of the thrust nappe at Waliguan Mountain (Area A in Figure 1B) (Chen et al., 2016).

includes the Miocene Xianshuihe Formation (N1x), Pliocene Linxia Formation (N2l), Early–Middle Pleistocene Gonghe Formation ($Q^{al-l}_{1-2}g$), Middle–Late Pleistocene Yellow River alluvial sand and gravel strata (Q_{2-3}^{al}), and other Quaternary strata (Figure 1B). Emplacement time studies indicate that the Xianshuihe and Linxia formations are 20.8–7.8 Ma and 7.8–2.6 Ma, respectively (Fang et al., 2005; Fang et al., 2007). The top interfaces of both formations show diachroneity. Furthermore, the Gonghe Formation and Yellow River alluvial strata show an emplacement time of 2.24–0.10 Ma (Xu et al., 1984) and 174.5–91.0 ka (Sun et al., 2007), respectively.

3 Geological characteristics of the strike-slip–thrust nappe at Waliguan Mountain

The strike-slip–thrust nappe at Waliguan Mountain is located at the northern part of the Xinjie–Waliguan strike-slip–extrusion uplift zone and constitutes the front part of the Gonghe quasi-thrust nappe (Zhang et al., 2020). Situated ~25 km east of Qiabuqia town, the thrust nappe is a NW–SN–trending arcuate mountain measuring ~12 km in width (east to west) and ~28 km in length (south to north). It mainly consists of Middle Triassic Dangjiasi pluton (T2γδ) and Early–Middle Triassic

LongWuHe Formation. The thrust nappe's geomorphology is described as "tilt-up on the east and being subducted on the west". The thrust nappe's western slope is relatively long and flat, whereas the eastern slope is relatively steep and short. The eastern boundary is defined by the NE-extruding Duolonggou curviplanar fault (F4) (Figure 1B). On the eastern side, the thrust nappe and dextral strike-slip structures overlie the Gonghe Formation and the Middle–Late Pleistocene Yellow River alluvial strata. On the western side, the thrust nappe is unconformably overlain by the Pliocene Linxia Formation (Figure 2).

To the west of Waliguan Mountain, the bottom of the Gonghe Basin's Linxia Formation overlies the western Dangjiasi magmatic body creating an angular unconformity. The boundary is marked by the presence of basal conglomerate–like granitic weathered sands that show poor sorting, low degree of rounding, and *in situ* transportation and accumulation. Apatite fission track (AFT) thermochronological data suggests that the strike-slip–thrust nappe started in the Late Miocene and ended in the Middle–Late Pleistocene period.

3.1 The Duolonggou arc–shaped strike-slip–thrust nappe (F4)

The Duolonggou strike-slip–thrust nappe (F4) serves as the major fault boundary associated with the Waliguan Mountain thrust nappe and forms a NE-extruding arc shape that peaks at Duolonggou Hamlet. This nappe's northwestern section strikes to the NWW, although most of it remains hidden. In the northwestern section, the Gonghe Formation and Middle–Late Pleistocene Old Yellow River alluvial gravel deposit jointly formed an eroded hilly landform, which was superimposed by a diluvial fan during the latter part of the Late Pleistocene–Holocene. All these features indicate that the northwestern section of this arc formed during a relatively earlier time. The southern portion extends in the S-N direction and is a dextral strike-slip and thrust nappe with a west dipping fault plane and a dip angle of 60°–70°. The 0.05- to 1.0-km-wide broken belt is mainly composed of cataclasites and fault gouges. Many branch faults in the southern section of the Duolonggou curviplanar fracture (F4) developed within the Gonghe Formation. The footwall of the local main fault also has very thick deposits of autochthonous granitic weathered sands, indicating that this fault (F4) underwent intense impulse-type thrust napping during the Early–Middle Pleistocene. Consequently, rapid uplift and erosion occurred at Waliguan Mountain. In addition, the fact that the branch faults developed on the west side of the southern Duolonggou arc's main fault and the Middle–Late Pleistocene Yellow River alluvial deposit is the youngest affected stratum suggest that the southern section continued to move until the middle of the Late Pleistocene. The geological features of three structural profiles controlling this fault are described as follows:

(1) Structural profile along the road paralleling Waliguan relay station's eastern foot

This profile was measured along a part of the Waliguan relay station that is located at the artificial excavation slope on the northern side of a highway near the mountain pass. During data collection, point B shifted northward to point B′ due to the impact of the Holocene slope deposits east of the A–B section. The A–B and B′–C sections make up the structural section shown in the A–C area of Figure 2 and comprise a total length of 0.43 km.

The profile was constructed by carrying out all measurements within the intrusive contact line and fault fractural zone of the Dangjiasi rock mass (Figure 3D). While the LongWuHe Formation captures the uneven sizes distributed throughout the Dangjiasi rock mass, it also depicts granitic apophyses and veins, all of which were cut and destroyed by joint cracks and fractured rocks associated with later stage brittle faults (Figures 3B,C,F). In addition, alternating occurrences of strong and weak strain bands in the brittle deformational provinces are also presented in this profile (Figures 3B,C,F). Individual fault bands have a width of 0.1–10 m and are mainly composed of cataclasites, fault gouges, and tectonic lenses. The brick-red color also developed locally due to iron dissemination (Figures 3B,F,G). The dragged tectonic lenses and the hanging and foot walls indicate thrusting to the NE-E, with the fault plane dipping to the SW-W at a 38°–70° angle. Plagiotropous striations superimposed on late-stage joint surfaces illustrate the dextral strike-slip attributes and indicates that there was a substantial SSE-trending horizontal displacement component during the late stage (Figures 3A,E). Due to the presence of Holocene slope washes covering the area, this profile only controls the local part (about 0.43 km) of the Duolonggou arc fault zone's middle region. However, it can be inferred that the entire fault fracture zone is wider than 1.0 km.

(2) Structural profile along the Duolonggou South Mountain's eastern foot.

The second profile was measured along the eastern foot of the Duolonggou South Mountain (Area D in Figure 2). At the profile's western end, the Dangjiasi rock masses thrust westward over the Gonghe Formation. Due to the overlying Holocene slope deposits, no nappe interface outcroppings are visible. The fault plane is believed to dip to the NWW at ~60° (Craddock et al., 2014). The footwall (Gonghe Formation) has been tilted and distorted in response to Waliguan Mountain thrusting. As a consequence, the dip angle has dropped from 20° to 50° in the western portion to 6°–10° a few kilometers to the east.

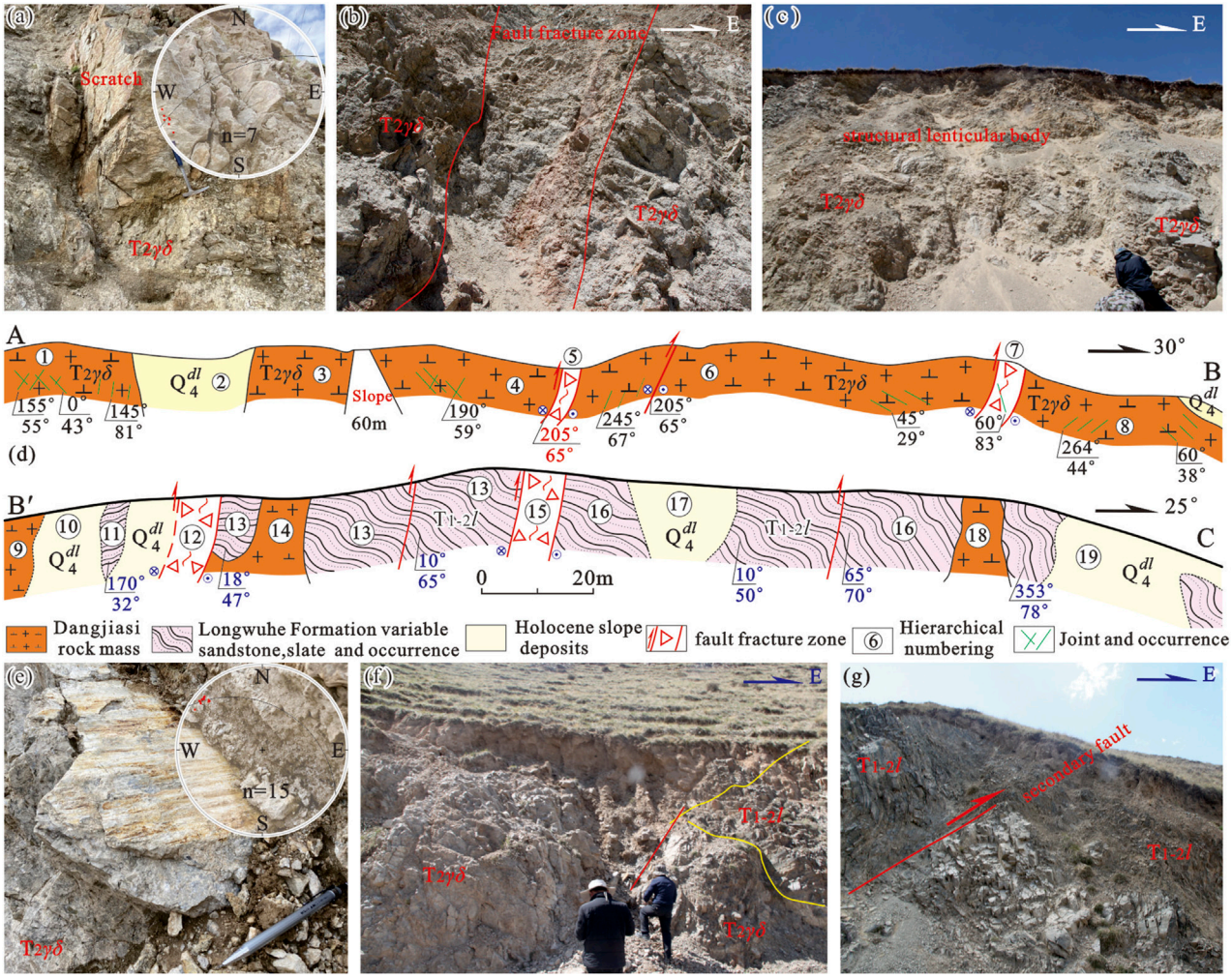

FIGURE 3
Measured structural profile along the road paralleling Waliguan relay station's eastern foot. **(d)** Coordinate of starting point A: E100°53′56″, N36°17′28″; coordinate of end point B: E100°53′56″, N36°17′28″; coordinate of starting point B′: E100°53′65″, N36°17′33″; coordinate of end point C: E100°53′59″, N36°17′40″.

Notably, there's an ~80 m high outcrop at the profile's western segment, where the dip angles of the Gonghe Formation's growth strata gradually reduce from bottom to up. The strata, which dip to the SEE at a 31° angle, are unconformably covered by a stratum that also dips to the SEE but with a dip angle of 22°. Likewise, the eastern segment has fan-inclined Gonghe Formation growth strata that are also unconformably covered by overlying strata (Craddock et al., 2014). This phenomenon suggests that 1) the Duolonggou arc fault may have undergone impulse-type thrust nappe activities during sedimentation of the Gonghe Formation in the Early to Middle Pleistocene and 2) East Waliguan Mountain may have hedged westward, resulting in the Duolonggou ramp valley experiencing compressional stress and the Gonghe Formation undergoing folding deformation.

(3) Structural profile of the Chiqugou

A profile of the main fracture comprising the Duolonggou curviplanar fracture (F4) is visible ~50 m west of the Chiqugou culvert along the Gonghe–Gahaitan–Longyangxia roadway (Region E in Figure 2). In the profile, the Dangjiasi rock mass thrusted onto the Gonghe Formation's Middle–Late Pleistocene Yellow River alluvial deposit at a high angle (Figure 4C). This dextral strike-slip and thrust fault strikes roughly south to north and is characterized by a fault plane dipping to the west at a 60°–70° angle. The fracture zone is 50–100 m wide and is primarily composed of clastic granite and fault breccia. Fault scratches are clearly visible on the K-feldspar located within the hanging wall's granite veins (Figure 4E). Thick layers of granitic weathered sands were deposited on the fault's footwall,

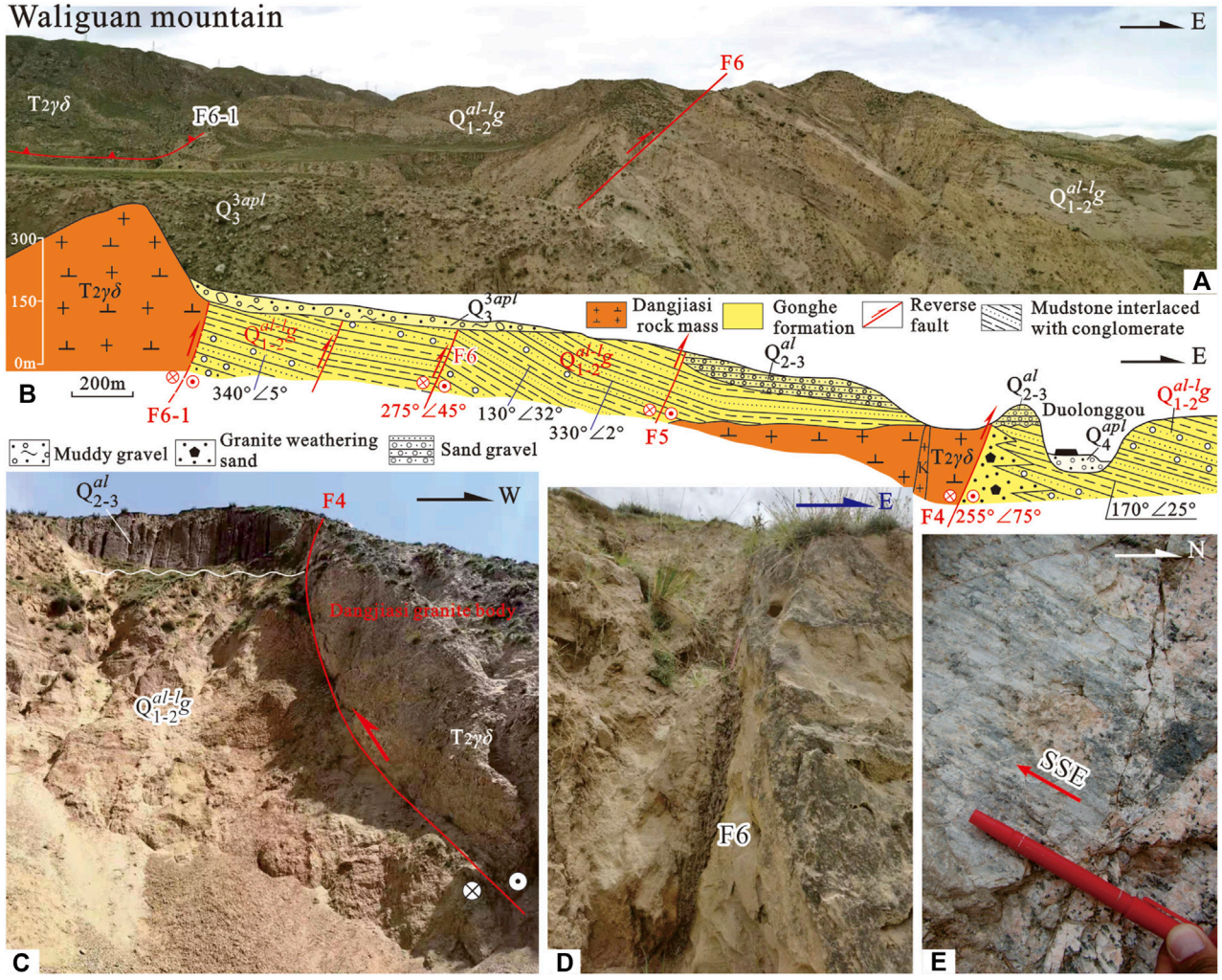

FIGURE 4
(A,B) Photo and profile of the Chiqugou route.

representing syntectonic denudation deposits induced by the hanging wall's strong thrust nappe and structural uplift. The Gonghe Formation has been tilted and distorted due to faulting activity, as evidenced by its attitude of 170°∠25°. Thermoluminescence dating of the low-order fault gouge indicates that the last activity occurred ~110,000 years ago, during the early stage of the Late Pleistocene. This suggests that the major fault in the southern portion was mostly active in the Early–Middle Pleistocene. During the later period, the branch faults continued to move westward.

F4, F5, and a series of secondary faults are all present in the western Gonghe Formation. Thus, grey-yellow, grey-white, grey-green, and grey-black mudstone; argillaceous siltstone mixed with multicolored, medium-coarse grained sandstone; and poorly cemented sandy conglomerates are found along this profile. The F5 fracture zone characteristics cannot be discerned due to collapse and overlying slope deposits, while F6 depicts a fault plane attitude of 275°∠45° and a 0.04–0.10 m wide fault fracture zone (Figures 4A,D). The bottom portion of this profile is comprised of a secondary, steeply inclined reverse fault, with a fault plane attitude of 260°∠88°. Due to the high degree of weathering, this fault is categorized as a thrust fault, based on the fault gouge and the dislocation direction of the upper and lower plates. The Gonghe Formation's footwall was impacted by F6 and is clearly inclined and distorted. In this area, the strata's dip angle steadily decreases eastward from F6 to F5 (Figure 4A). Specifically, the lower plate's attitude changes from 275°∠45° at F6, to 130°∠32° midway between F6 and F5, to 150°∠2° on the western side of F5 (Figure 4B). The F6 upper plate's attitude is indecipherable, due to landslide events and slope deposit cover. The most recent Dangjiasi thrust interface (F6-1) in the western part of the Chiqugou route section does

not outcrop, as it is buried under Late Pleistocene alluvial deposits.

In addition, geologic evidence reflecting the LongWuHe Formation's thrust over the Middle–Late Pleistocene Yellow River alluvial strata is observable in a gully west of Duolonggou village. On the northern bank of the South Yellow River, the Dangjiasi rock mass was thrusted onto the Gonghe Basin's Linxia Formation (Perrineau et al., 2011). This resulted in the Linxia Formation west of Waliguan Mountain standing 200 m higher than its counterpart in the eastern Qunaihai sub-sag.

As discussed before, the Middle–Late Pleistocene Yellow River alluvial gravel deposit is the youngest strata impacted by the Waliguan Mountain thrust nappe, which indicates that the thrust napping activity distinctly weakened during the middle of the Late Pleistocene. In the south, the activity is stronger and the duration is longer, as compared to the north. The northern section is dominated by thrusting with dextral strike-slip in the early stage, whereas the southern section depicts occasional dextral strike-slip activity with thrusting occurring during the Late epoch.

3.2 Strike-slip–thrust nappe structure and spatiotemporal evolution

AFT thermochronology is commonly used to determine the uplift history of shallow crustal mountains (5–8 km) (Sobel and Dumitru, 1997; George et al., 2001; Sobel et al., 2003; Zheng et al., 2003). Previous AFT thermochronological studies on bedrock from mountains throughout the Gonghe Basin suggest that Ela Mountain, which is located in the southwest, started to uplift and become rapidly exposed ~25 Ma (Lu et al., 2012). In contrast, the northern Qinghai Nanshan and the southern Guinan Nanshan began to rapidly uplift 11–9 Ma and 10–7 Ma, respectively (Craddock, 2011). AFT thermal chronology results from Dangjiasi rock mass samples show rapid uplift was initiated in this area ~8–5 Ma (unpublished data). On the west of Waliguan Mountain, the bottom of the Linxia Formation is bordered by a layer of granitic weathered sands with basal conglomerate features. This stratum forms an angular unconformity west of the Dangjiasi rock mass. This phenomenon indicates that Waliguan Mountain was swiftly elevated and thrusted to the NE during deposition of the Linxia Formation.

The front margin of the strike-slip–thrust nappe structure belt at Waliguan Mountain consists of three imbricate strike-slip–thrust faults. From east to west, these include the Duolonggou Arc Fault (F4), Shangjiangou Fault (F6), and Waliguan Fault (F7). These faults, in combination with three additional NE-dipping faults on the west slope—F8, F9, and F10—constitute Waliguan Mountain's thrust nappe system, which depicts a positive flower structure. Waliguan Mountain has a large-scale thrust structure that is influenced by the boundary faults on the east and west sides.

Considering the north–south direction, there are significantly more branch faults in the south, as F4 and F6 primarily confine the branch faults in the north. The LongWuHe Formation and Dangjiasi rock mass comprise this nappe, while Late Pleistocene–Holocene alluvial fans cover the majority of the lower plate. To date, the most recent stratum impacted by the branch faults in the north remains undetermined. Oblique scratches are occasionally found in the fracture zone, which is thought to have been active throughout the Pliocene. These branch faults are primarily distinguished by the presence of thrust nappes. Contrarily, the southern part of Waliguan Mountain's thrust nappe belt is characterized by multibranch faults comprised of fault bundles—such as F4, F5, and F6. There are numerous oblique scratches in the Dangjiasi rock mass fracture zone, which suggests dextral strike-slip behavior. The F5 sliced through the Gonghe Formation. Ancient Yellow River alluvial deposits are the most recent stratum impacted by the footwall. These observations suggest that the southern section of the nappe, which became active in the Early Pleistocene to Middle–Late Pleistocene, is characterized primarily with dextral strike-slip movement accompanied by a thrust nappe from west to east.

The previously described phenomena demonstrates that as the thrust nappe and dextral strike-slip movements developed, the northwest section of this nappe continued to compress and shift northeastward in response to the clockwise rotation around Waliguan Mountain's vertical axis. In addition, the front fault's strike gradually shifted from NW to NNW, while the fracture zone was simultaneously narrowed. The most recent stratum impacted by this tectonic activity was continually buried beneath the footwall. In contrast, thrust nappe activity in the southern part of the nappe continued to develop with a backward expansion from east to west. Although the fracture zone for a single fault is narrower in the south than in the north, the southern area has more branch faults and oblique scratches within the Gonghe Formation. These observations suggest that Waliguan Mountain thrust nappe was dominated by thrust napping and dextral strike-slip movement during the Pliocene and primarily dextral strike-slip movement from the Early Pleistocene to the middle stage of the Late Pleistocene.

3.3 Analyzing the direction of maximum principal tectonic stress based on the strike-slip–thrust nappe structure

3.3.1 Depicting the direction of maximum principal tectonic stress based on the archery principle

When determining the direction of maximum principal tectonic stress (σ_1), the thrust nappe can be considered a structural style created by an extrusion system comprised of imbricate thrust faults. The imbricate thrust faults are a common

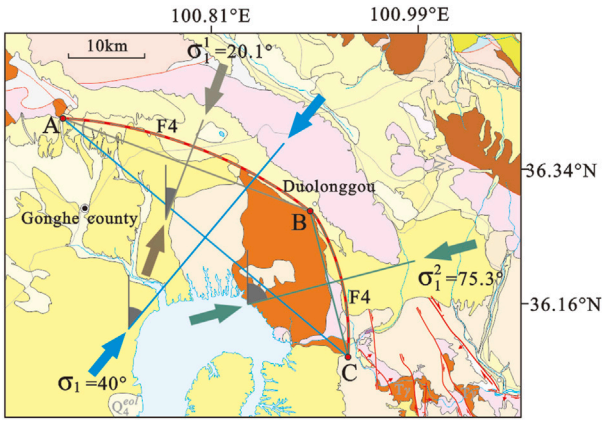

FIGURE 5
Determination of maximum principal tectonic stress (σ1) based on the Archery principle.

fault combination produced under a primarily horizontal tectonic stress field (Li et al., 2017). The tectonic extrusion direction is perpendicular to the strike of the leading-edge fault, namely the macroscopic tectonic direction. Therefore, the arching concept can be utilized to determine the maximum tectonic stress direction (σ_1). Applying the arching concept to the bow-shaped fault within the Duolonggou arc fault, the bow-shaped fault's two extremities were connected with a string. Subsequently, a vertical line was drawn from the string's midpoint to the top of the arc. This line represents the direction of maximum principal tectonic stress (σ1). The directions of minimum (σ3) and middle principal tectonic stress (σ2) are parallel and perpendicular to the string, respectively.

For diagramming purposes, the figure is split into AB, BC, and AC arcs based on the different distinguishing features between the northern and southern arcs in Duolonggou village. The top arcs AB, BC, and AC indicate the direction of maximum principal tectonic stress (σ1 1) during the early-stage thrust nappe, the maximum principal tectonic stress (σ2 1) during the late-stage thrust nappe, and the intermediate value of the maximum principal tectonic stresses (σ_1) during the early and late stages, respectively. The results from this study show that σ1 1, σ2 1, and σ1 in the study area equal 20.1°, 75.3°, and 40.0°, respectively (Figure 5).

The intermediate value (σ1) obtained before approximates that of the nearest Longyangxia dam area (Ma and Qi, 1993) and the Laxiwa hydropower station (Dong and Chen, 2003), indicating that this method is suitable for analyzing the Late Cenozoic tectonic stress field in the Qiabuqia area.

3.3.2 Tectonic stress field determination based on the fault's slickenside

Systematic sampling of obvious fault slickensides throughout the structural profile on the eastern foot of the Waliguan relay station indicated that the fault planes that formed during the early stage dipped to the SW at a 35° angle. Furthermore, well-developed slickensides and lineations showed that thrusting occurred in the NE direction (Figure 3A). Early-stage NW-trending thrust faults are crosscut by later-stage strike-slip faults that are striking SN and dipping at ~60°. Slickensides and lineations on the fault planes show dextral strike-slip activity (Figure 3D).

To obtain the triaxial stress orientation, STEREO.EXE software (Table 1) was used to reflect the tectonic stress field for a dextral oblique fault that lies within the southern Duolonggou arc fault and is characterized by clear slickensides. The results show that the σ1, σ2, and σ3 attitudes are 214.0°∠2.5°, 349.9°∠86.5°, and 108.7°∠1.7°, respectively. In summary, the stress associated with σ1, which strikes from 34°–214°, is nearly horizontal.

4 Geological characteristics of normal faults

In the study area, normal faults with small fault displacement are primarily found in the Linxia Formation (N_2l), Gonghe Formation ($Q_{1-2}^{al-l}g$), Middle–Late Pleistocene Yellow River alluvial strata (Q_{2-3}^{al}), and the Middle–Late Pleistocene alluvial–diluvial–swamp accumulation layers (Q_3^{2apl-l}) (Figure 6). However, these faults were all observed at outcrop scales and do not cut through modern slope alluvium. Consequently, the surface fault traces are difficult to recognize.

4.1 Geological features of the primary normal faults

4.1.1 Normal faults within the Linxia Formation

The stepped fault system west of Tulin (Fn1): Fn1 is in the Linxia Formation (N_2l), which is located east of the Qiabuqia Town–Longyangxia Highway and west of the Longyangxia Forest Geopark (Figure 7). The southern fault (Fa) has an attitude of 145°∠65°, and the grey-green mudstone marker bed is dislocated downward along the dip for 0.6 m. Similarly, the northern fault (Fb) has an attitude of 125°∠70°, with the grey-green mudstone marker bed dislocated downward along the dip for 0.55 m (Figures 7A,C). Oblique fault slickensides can be evident along the fault plane, suggesting that this fault is part of the normal–dextral strike-slip fault.

Using the third layer as the marker bed, the Fa fault offset measured 0.60 m. Joint fissures accompanied by the drag structure are prevalent around the fault, indicating that the fault be classified as normal. Using the second layer as the marker bed, the Fb fault offset measured 0.60 m (Figures 7C,D). In addition, joint fissures are commonly found to the south (Figure 7B), and the fault slickensides demonstrate dextral oblique thrust.

TABLE 1 Results of the tectonic stress field reflection using fault slickensides in the southern Duolonggou Arc Fault.

Postion	Number of the outcrop	Number of scratches/band	σ_1		σ_2		σ_3	
			Dip/°	Dip direction/°	Dip/°	Dip direction/°	Dip/°	Dip direction/°
Duolonggou	S717	8	220.9	11.2	316.3	25.3	89.0	55.1
	S718	8	34.6	16.1	142.8	47.3	275.2	31.9
	S722	5	248.0	1.7	342.5	70.0	165.9	19.9
	S724	8	183.4	15.1	261.5	62.9	274.6	23.2
Waliguan Moutain	S717	29	214.0	2.5	249.9	86.5	108.7	1.7
	S718							
	S722							
	S724							

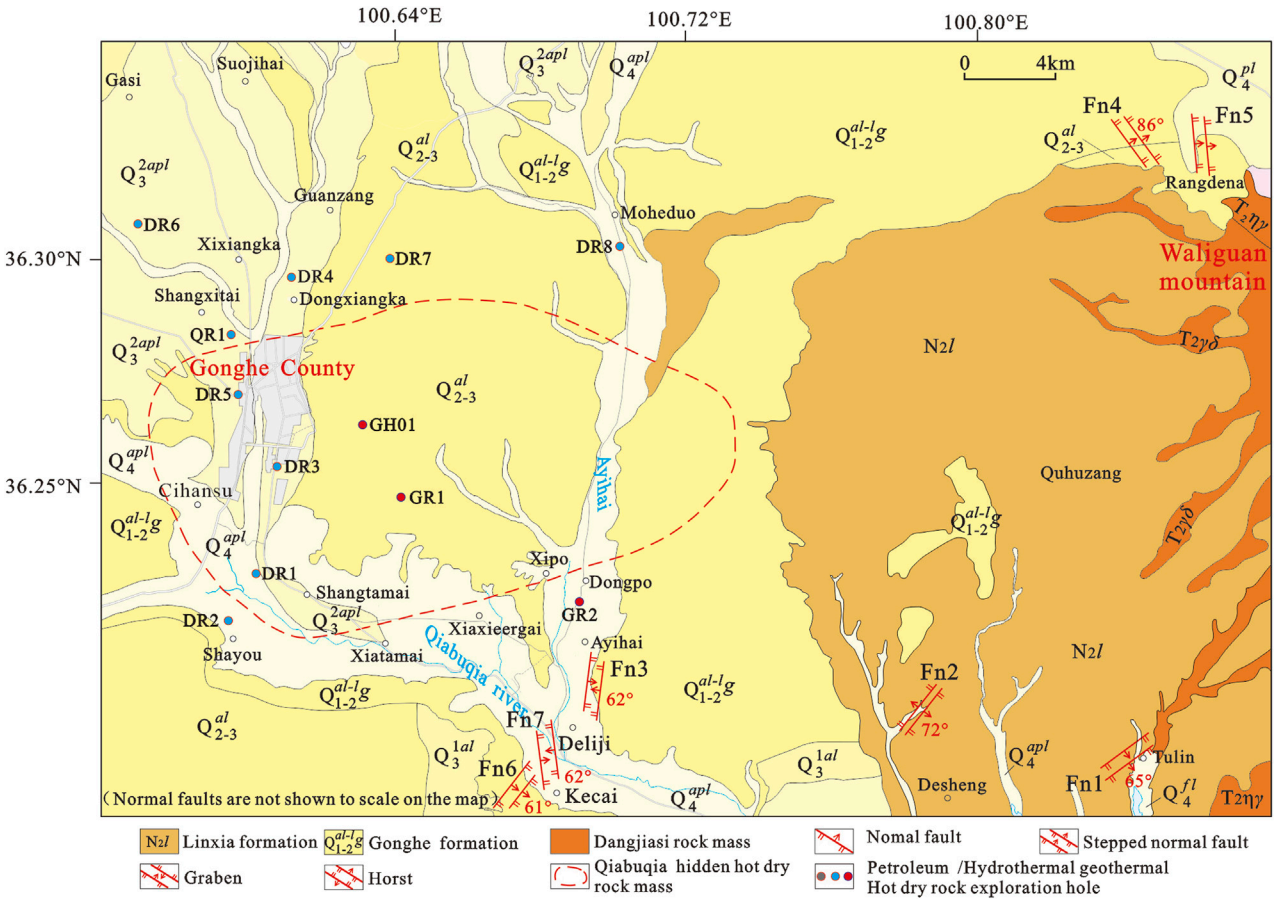

FIGURE 6
Distribution of normal faults in the Qiabuqia area (Area B in Figure 1B).

4.1.2 Normal faults in the Gonghe Formation (Fn2)

Normal faults in the Gonghe Formation are dominated by a graben-type structural framework. In the north central part of Ayihai gully, five typical faults with opposite dips were observed in the mudstone section of the Gonghe Formation. From northwest to southeast, the faults have attitudes of 295°∠75°, 300°∠70°, 305°∠70°, 125°∠60°, and 140.0°∠70°, and the associated

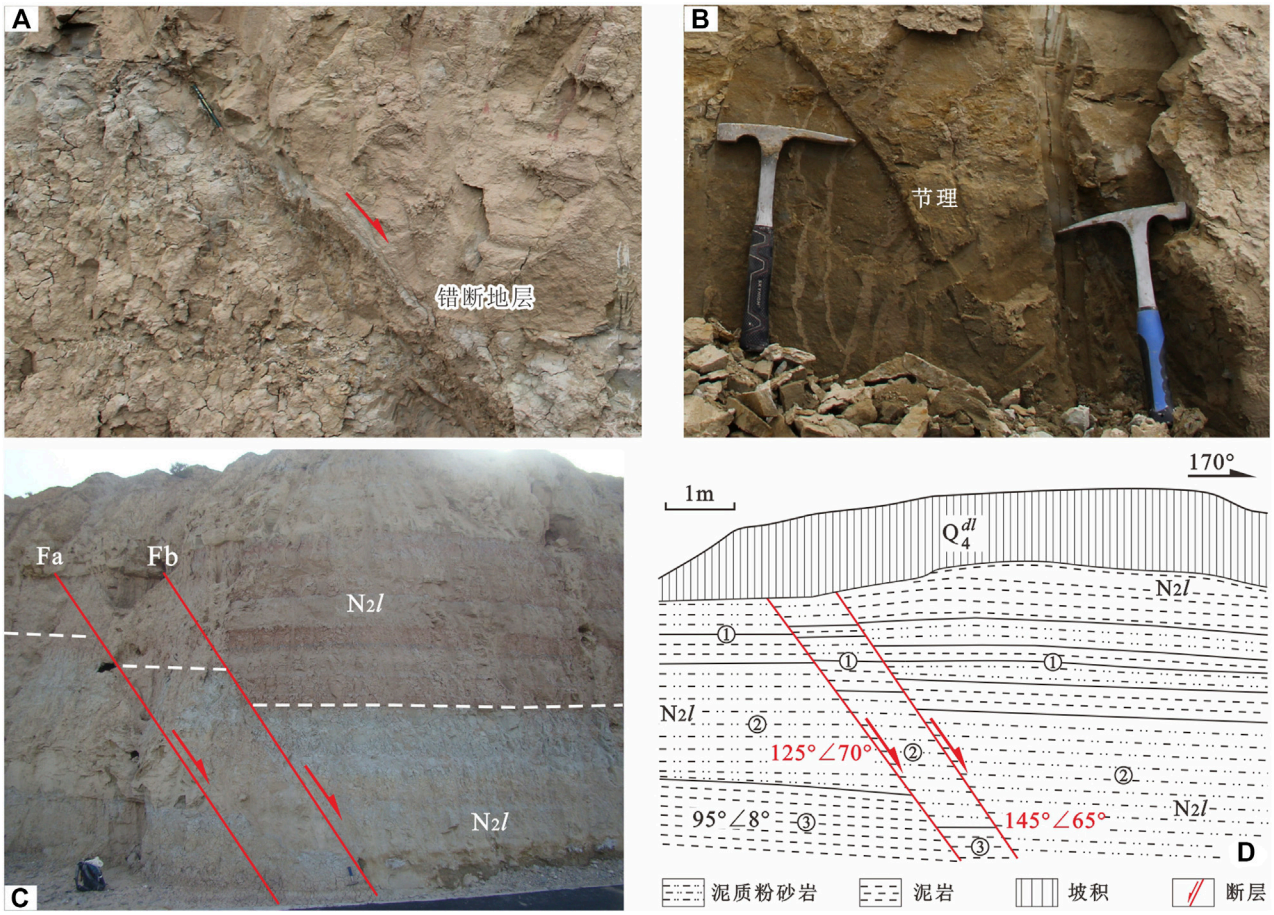

FIGURE 7
Step fault system west of Tulin (Fn1).

strata's attitudes range from 280°∠15° to 310°∠18°. Due to the absence of unique maker beds, the fault displacements were not measurable. However, the presence of vertical down-slip slickensides on the fault planes suggests that they are normal faults (Figures 8A,B).

The T1 terrace, which is located in the middle of Ayihai gully, is characterized by an evident ~0.05 m wide fault gouge and a secondary gypsum layer depicting S-shaped deformation (Figures 8C,D). The attitudes of the fault plane and associated stratum are 320°∠72° and 340.0°∠18°, respectively. The presence of clear downward-gliding slickensides on the fault plane suggests it's a normal fault.

In the Gonghe Formation located in the north central part of Ayihai gully, four normal faults with opposite dips were discovered under modern riverbed gravel deposits. From west to east, these faults have attitudes of 272°∠65°, 110°∠60°, 140.0°∠58°, and 295°∠72°, respectively (Figure 8C). The attitude of the associated stratum is 250°∠20°. The horizontal distance between adjacent faults from west to east is ~7, 3, and 10 m, respectively. The conglomerate marker bed successively dislocated downward along the dip for 0.50, 0.80, 0.05, and 1.0 m, respectively. The vertical downward-slipping slickensides on the fault planes demonstrate that they are also normal faults.

Similar graben structures that extend nearly south to north are common throughout many localities in north Deliji Village at the gully entry to Ayihai Valley (Figure 8F). The grabens are made up of two or more normal faults (Fn2) with the same characteristics; that is, they strike nearly parallel but dip in opposite directions. In profiles A and B, which span north–south, the Fa and Fb normal faults control the same graben structure (Figures 9A,B). The Fa fault has an attitude ranging from 97°∠58° to 101°∠62°, whereas the Fb fault's attitude is 283°∠62°. In profile A, the two faults are 3.10 m apart, yet in profile B the separation increased to 8.5 m.

As shown in profile B, the strata on both sides of the Fa fault are clearly dislocated, and the echelon shear joints are well developed (Figures 9C,D). These characteristics are typical of

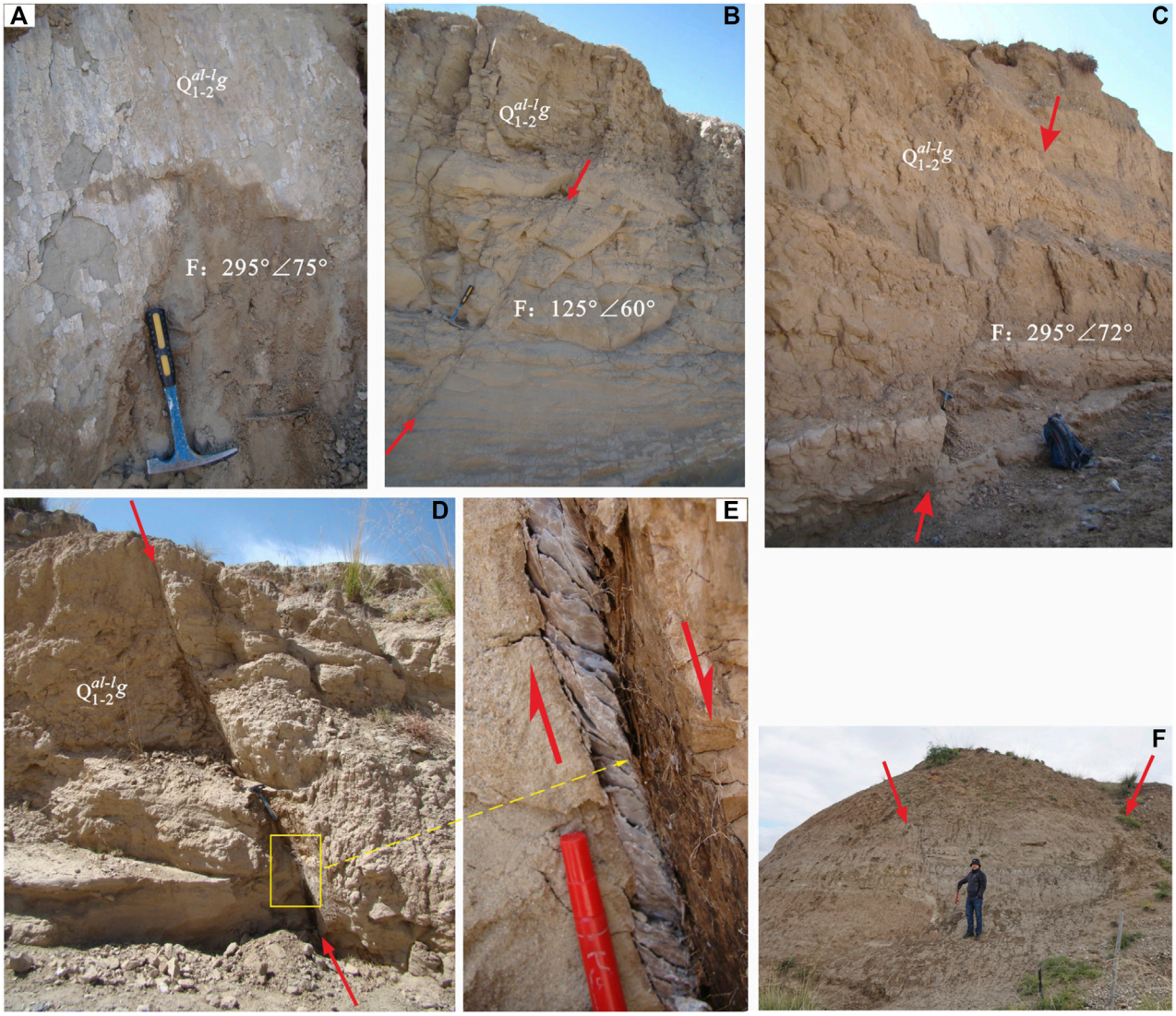

FIGURE 8
NS-trending normal faults along Ayihai gully. **(A,B)** Normal faults in northern Ayihai Valley. **(C,D,E)** Normal faults and S-shaped shear joints in central Ayihai Valley. **(F)** Combination of graben normal faults north of Dejilicun in southern Ayihai Valley.

normal faults. In profile A, the strata in the upper and lower plate of the Fa fault are also obviously dislocated and somewhat dragged (Figure 9E); features that are also commonly associated with normal faults. The Fb fault in profile A cuts across the Gonghe Formation strata. On both sides of the fault, the strata have distinct coloring and lithologies. From the bottom up, the upper plate is characterized with brown-red-yellowish silty mudstone, brown-red mudstone with grey-green mudstone, grey-green sandy mudstone, and grey-white sandy mudstone. The footwall consists of maroon mudstone, green fine siltstone, and grayish-yellow medium fine sandstone (Figures 9F,G). The strata's drag phenomena is indicative of the normal fault's behavior. While both the Fa and Fb faults lack comparable marker beds, it is assumed that these two faults have relatively large displacements.

4.1.3 Normal faults within the Middle–Late Pleistocene Yellow River alluvial strata

(1) Stepped normal fault system west of the Randena sand mining field (Fn3):

Two normal faults separated by 2–3 m were observed in an artificial profile of the Middle–Late Pleistocene Yellow River alluvial layer (Figures 10E,F). These faults do not cut through the overlying modern humus layer. The eastern fault consists of two wedge-shaped secondary faults that dip in opposite

10.3389/feart.2022.895530

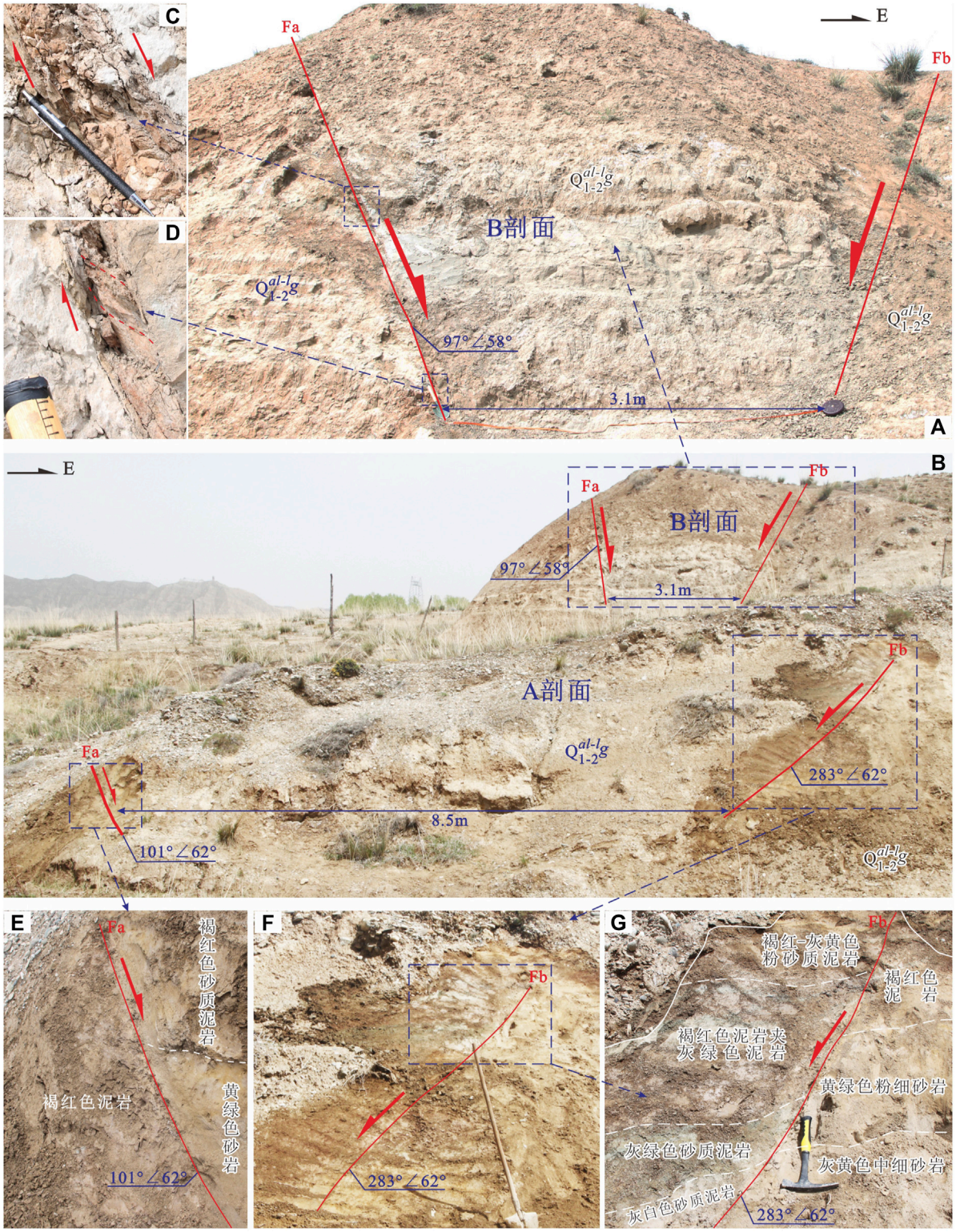

FIGURE 9
Graben-type normal fault framework north of Deliji village (Fn2).

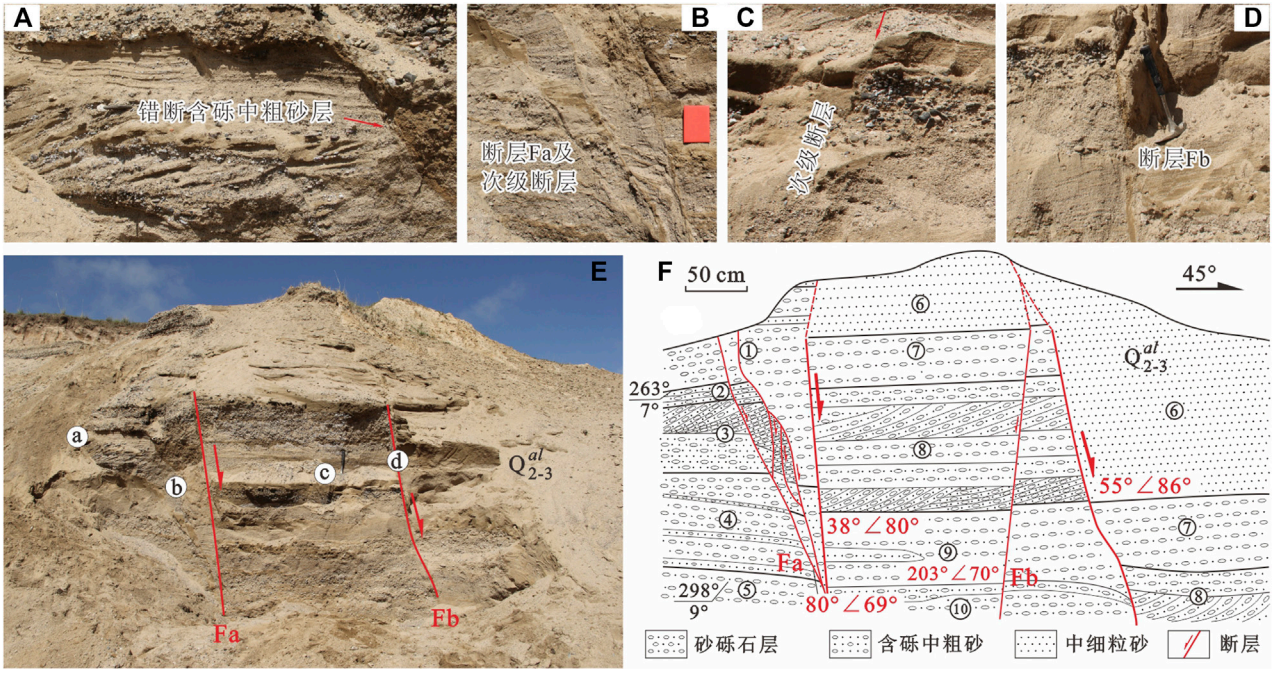

FIGURE 10
Stepped normal fault system west of the Rangdena sand mining field (Fn3).

directions. The fault's attitude is 55°∠86°, and the fault zone is 0.01–0.02 m wide and filled with sand. The marker bed in the upper plate moved downward more than 1.50 m. The western fault has an attitude of 203°∠70°, and is characterized with a 0.01–0.02 m wide fault zone. The marker bed on the upper plate dislocated downward ~0.05–0.10 m.

The western fault is composed of three secondary faults. Among them, the eastern and western branch faults have attitudes of 38°∠80° and 30°∠69°, respectively. The eastern branch fault has a 0.01–0.02 m wide fault zone that is filled with sands. Moreover, the marker bed in the upper plate is estimated to have moved downward for more than 1.50 m. Similarly, there is also a 0.01–0.02 m wide fault zone, with the marker bed of the upper plate being moved downward for about 0.05–0.10 m. A 0.05–0.20 m wide crumpled band developed in the sliding blocks that are controlled by the western, eastern, and middle branch faults. Here, the marker bed moved downward ~0.11 m. From SW to NE, the fault structures in the sedimentary layer have the following characteristics:

The Fa fault, is characterized by a 0.05–0.07 m wide disturbance zone and a fault plane attitude of 38°∠80°. The fault displacement is inferred to be >1.90 m, based on the corresponding relationships of the sedimentary assemblages. Four sets of secondary normal faults are on the west side of the fault; the lower ends of which intersect with the primary F1 fault. The marker beds are defined by medium-coarse pebbled sand and medium-coarse gravel sand with horizontal and oblique bedding (Figures 10C,D). From SW to NE, the fault displacements are 0.08, 0.04, 0.020, and 0.17 m, respectively. The Fb fault is characterized by 0.07–0.08 m wide fault gouges/sands and a fault plane attitude of 55°∠86°. Sand, gravels, and medium-coarse grained pebbled sand layers with oblique bedding served as marker beds and suggest a fault distance of ~1.50 m (Figure 10A). Between the principal Fa and Fb faults is a minor secondary normal fault with a fault plane attitude of 203°∠70° and a fault displacement of 0.055 m. Given the attitude of this secondary fault, it cut across different sedimentary layers (Figure 10B).

(2) Stepped normal fault system north of the Rangdena sand mining field (Fn4):

Fn4 consists of two normal faults separated by 0.60–1.20 m. The eastern fault has an attitude of ~82°∠45° and does not cut through the ~1.00 m thick alluvial gravel deposit at the top. In addition, the hanging wall's conglomerate marker bed moved upward ~0.05 m. Similarly, the western fault has an attitude of 70°∠68°, and also does not cut through the ~0.6 m thick alluvial gravel deposit at the top. In this case, the conglomerate marker bed on the hanging wall moved downward ~0.58 m. There is no evidence that the fault may extend deeper into Earth's interior.

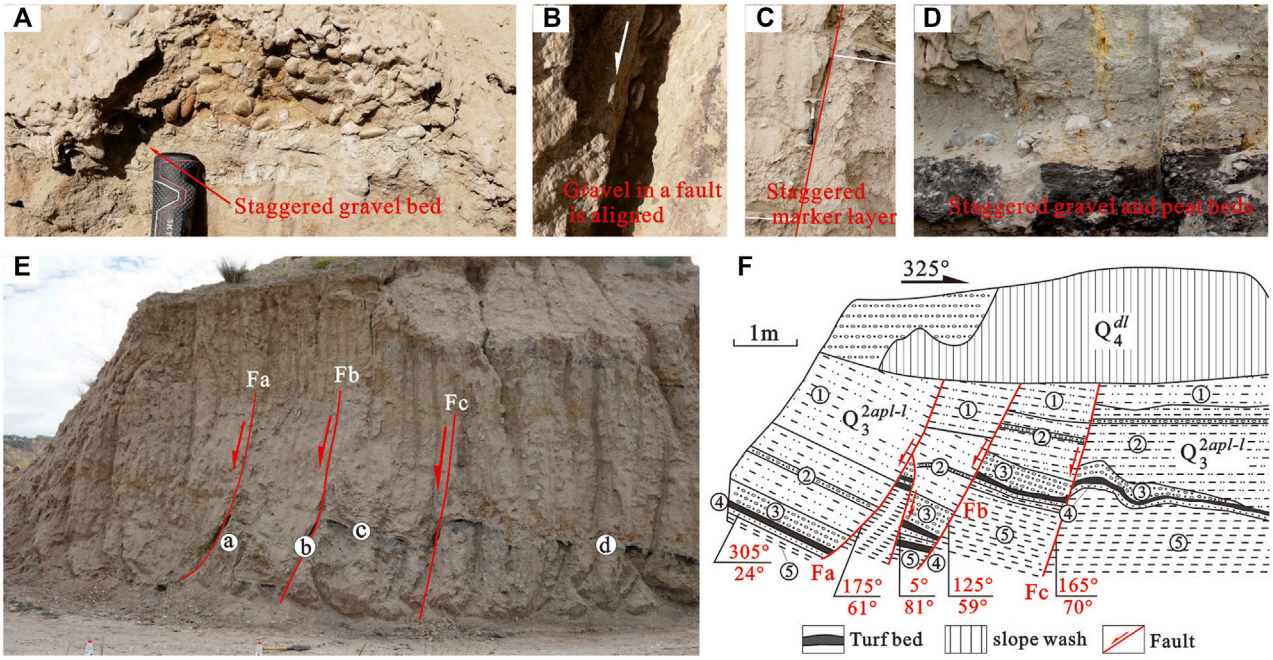

FIGURE 11
Stepped normal fault system in northwestern Kecai village (Fn5).

4.1.4 Normal faults in alluvial–flood strata intercalated with marsh strata during the Middle to Late Pleistocene

Stepped normal fault system northwest of Kecai Village (Fn5): The Fn5 profile is located northwest of Kecai Village, in front of a high terrace on the west side of the Qiabuqia River. Along the artificial cutting slope north of the makeshift road is a ~10 m long and 4.50 m high exposed profile composed of Late Pleistocene alluvial–flood accumulation strata intercalated with the marsh accumulation strata (Q_3^{2apl-l}). Two sets of normal faults were observed in the Late Pleistocene conglomerate/peat interlayers. One of those sets is characterized by an overall NE-NNE strike and SE dip, and consists of 3–4 secondary faults (Figures 11E,F). The other set generally strikes NE and dips SE, and is comprised of 3–4 secondary faults with attitudes of 135°∠40.0°, 128°∠58°, and 170°∠55°, respectively. The conglomerate marker beds are dislocated downward by 0.70, 0.95, and 0.50 m, respectively, demonstrating that it is a normal fault.

The Fa fault clearly cuts through the sand gravel, argillaceous silt, and peat layers. Along the fault fracture zone, the sand gravel shows directional alignment with the flat horizontal surface, and thus, is parallel to the fault plane, which has an attitude of 175°∠61° (Figure 11A). Using the gravel layer as the marker bed, the measured fault displacement is 0.93 m. A small secondary fault that cuts through the sand gravel, argillaceous silt, and peat layers is visible north of the Fa fault. The sand gravel along this fault fracture zone is also oriented with the flat horizontal surface and therefore is parallel to the fault plane, which has an attitude of 5°∠81°. Again, using the gravel layer as the marker bed, the measured fault displacement on this secondary fault is 0.60 m.

The Fb cuts across the sand gravel and peat strata. As observed in the Fa fault, the gravel shows directional alignment with the flat horizontal surface, and thus, is parallel to the fault plane, which has an attitude of 125°∠59° (Figure 11B). Using the gravel layer as a marker bed, the measured fault displacement is 1.15 m.

The Fc has a fault plane attitude of 165°∠75° and is comprised of gravel layers (Figure 11C). The measured fault displacement is 0.40 m. A secondary fault on the north section of Fc clearly dislocated the gravel and peat layers (Figure 11D).

4.2 Analysis of a normal fault's tectonic environment and formation time

Normal faults can be formed in multiple tectonic environments due to a myriad of geologic processes. Specifically, these include: 1) passive continental margin and rifting extensional environments (Qian, 1994); 2) fault bending in strike-slip fault systems and lateral jointing in local extensional environments (Woodcock and Fischer, 1986); 3) wedge extrusion structures or tunnel flows (Yin, 2006; Wang et al., 2016); 4)

refolding of thrust folds (fake 'normal fault') (Boyer and Elliott, 1982; Xiao et al., 2013; Thornton et al., 2018); 5) macroscopic anticline neutral outer arc extensional environments (Ramsay and Huber, 1987); and 6) alternating pressure–tension environments. In the latter case, once a symbiotic nappe and slippery nappe undergoing deformation show extrusion features, the "pushing first and sliding then" mechanism is initiated and relaxation/extension cyclicity occurs. As a result, during later extension, the thrust fault created during the extrusion deformation period develops such that the dip slip is opposite to the thrust direction. During this time, new normal faults may develop. Furthermore, as the temperature rises in the deep crust, the stress field undergoes horizontal tension in the upper crust and horizontal compression in the deeper crust. Tensile and compressive stresses are proportional to temperature gradients. This type of tensile stress can result in the formation of tensile structures. The surface tensile stress is greatest above the temperature-increasing zone, while the tension rapidly decreases on both sides and changes to compressive stress (Wang et al., 1999). Therefore, typical normal faults can form in a variety of situations. As such, because normal faults form in so many varied environments, and they cannot be exclusively used to decipher the geologic history.

In the Qiabuqia region, normal faults with a small degree of displacement generally show a similar set of characteristics. Specifically, normal faults with dispersed development positions are mostly found in sedimentary layers within the Linxia Formation and in Middle–Late Pleistocene period layers between Qiabuqia Town and Waliguan Mountain. Surface observations show that these normal faults have extremely short extensional lengths along the strike and small fault displacements along the dip, indicating that they are quite minor. Stepped and horst to graben structures are all observed in typical fault systems, while the profile structures are distinct and unrelated to one another. NE–SW, NW–SE, and near E–W strikes are all visible in the field outcrops. These fault planes show the distribution directions that are incompatible with one another, and they differ from the representative radial or zonal normal fault systems generated by the deep thermal dome structure (Liu, 2010). According to the statistical analysis results, only the graben-type normal fault systems that depict a roughly S-N extension in the Kecai–Deliji villages–Ayihai region extend relatively further. However, the scale and formation time of these normal faults' is significantly smaller than those of the graben system in the southern Qinghai–Tibetan Plateau, and thus are not regional. Regional geological surveys have shown that normal faults in the Gonghe Basin are mostly concentrated in the vicinity of Qiabuqia Town, west of Waliguan Mountain. Moreover, the deep basement structure demonstrates the presence of a relatively stable west-dipping slope belt. The possibility that this area was influenced by a nearly south–north extrusion associated with the Qinghai's southern mountain cannot not be excluded. The consistency of the tectonic stress system that caused the normal faults to develop in the Qiabuqia region remains unknown.

Based on the results presented before, this study divides the short displacement normal faults in the Qiabuqia region into two potential categories: 1) The Kecai village–Ayihaigou fault, which is associated with the Fn3 and Fn7 graben-type normal faults. This association came about due to the "brake" effect following the intense thrust nappe–dextral strike-slip activities of the Waliguan Mountain thrust nappe during the Middle–Late Pleistocene period. This "brake" effect caused the Qiabuqia region's shallow section on the trailing edge to relax and extend, resulting in the development of these new normal faults. 2) The Fn4 and Fn5 faults in the Rangdena area, northwest of Waliguan Mountain; and the Fn1 and Fn2 faults in the Tulin–Desheng village area, southwest of Waliguan Mountain. These associations were generated during the clockwise rotation around the vertical axis of the late Waliguan Mountain thrust nappe's right lateral strike slip. Under the tensional tectonic environment in the northwest and compressional tectonic environment in the southwest, the result is comparable to the pressure shadow trailed on both ends of the rotational speckles.

4.3 Direction of maximum principal tectonic stress analysis based on normal fault structural interpretation

4.3.1 Analyzing the direction of maximum principal tectonic stress based on the Anderson fault model

When using the Anderson fault model (Craddock et al., 2014) to analyze the stress state of a fault, it is generally believed that the fault plane of a brittle fault, on (near to) the surface, is a shear fracture plane. Thus, the σ_1 and σ_3 directions are consistent with acute and obtuse angle bisectors between two shear fracture planes. The plate where σ_1 is located will slide to the acute angular point, meaning the fault's upper and lower plates slide perpendicular to the σ_2 direction. The stress states of a normal fault consist of: maximum principal stress (σ_1), which is vertical; intermediate (σ_2) and minimum (σ_3) principal stresses, which are horizontal, while the σ_2 direction is consistent with the fault's strike. A Mohr's circle diagram depicting the stress states associated with normal fault formation shows that horizontal stretching and vertical uplifting are the most suitable stress states to form a normal fault. Under these circumstances, the maximum (σ_1) or minimum (σ_3) principal stresses gradually increase vertically or decrease horizontally. Therefore, according to the Anderson fault model, the σ_1, σ_2, and σ_3 directions in the Qiabuqia area are perpendicular, consistent, and horizontal, respectively, to the normal fault's strike.

TABLE 2 Tectonic stress field results for normal faults in the Qiabuqia area, as reflected by slickensides.

Outcrop location	Number of the outcrop	Number of slickensides/band	σ_1		σ_2		σ_3	
			Dip/°	Dip direction/°	Dip/°	Dip direction/°	Dip/°	Dip direction/°
Ayihai gully	S705	10	106.4	82.6	212.2	2.0	302.6	10.8
	S706	5	179.7	81.3	44.3	6.2	313.9	3.6
	S707	5	30.1	86.9	223.5	3.1	133.3	4.6
	S708	5	151.8	80.6	51.5	1.7	321.1	11.5
	S709	8	38.0	82.3	199.8	7.3	290.4	4.8
	S710	5	73.1	81.1	214.4	6.9	305.5	9.0
	S705–S710	38	98.0	85.4	215.9	2.2	306.2	6.2
Upper Qiabuqia River	S711	8	118.4	77.4	210.3	0.4	300.3	10.3
Data merging	S701–S711	46	106.3	83.9	214.6	1.9	304.8	7.2

4.3.2 Reflecting the maximum principal tectonic stress direction based on the normal fault slickensides

In this case, STEREO.EXE software was used to reflect the tectonic stress field's (σ1, σ2, and σ3) triaxial stress orientations of 46 sets of slickenside data obtained from normal faults in the Qiabuqia area (Table 2). The results show that the attitudes of σ_1, σ_2, and σ_3 are 106.3°∠83.9°, 214.6°∠1.9°, and 304.8°∠7.2°, respectively. The σ_1 direction is nearly vertical, whereas the σ_2 and σ_3 directions are both nearly horizontal. The fault's strike varies from 34.6° to 214.6°, while the direction of minimum principal stress, that is, the tensile stress, ranges from 124.8° to 304.8°.

5 Inference of the deep fault structure and analysis of the tectonic stress field

5.1 Inference of the deep basement fault structure in the Qiabuqia area

Although there is a NNW–SN-trending fault in the northern Nanshan–Gouhou Reservoir near Qiabuqia Town, it is cut off by a nearly E–W trending fault on the southern margin of Nanshan Mountain. This latter fault underwent dextral strike-slip during the Late Triassic–Cretaceous and has undergone left-lateral strike slip since the Paleogene. Therefore, the comparable southern *in situ* fault system is less likely to extend deep into the Qiabuqia area. As a result, the deep fault structure in the Qiabuqia region is related to the fault structure formed east of Waliguan Mountain.

The Riedel shear model (Figure 12) recognized four sets of faults in the Waliguan Mountain region (Figure 2), including the Duolonggou arc-shaped fault (F4) in the main displacement zone (PZD), four NW–NNW trending compression–torsion faults (F8–F11)—i.e., Riddell same-trending secondary faults (P), three NNE–NE-trending tension–torsion faults (F14–F16)—i.e., Riedel local tensional (T) rupture, and three NWW compression–torsion faults (F13–F14)—i.e., conjugate Riedel (R′) reverse strike-slip faults. The Qiabuqia region's deep section is thought to contain three sets of the primary hidden

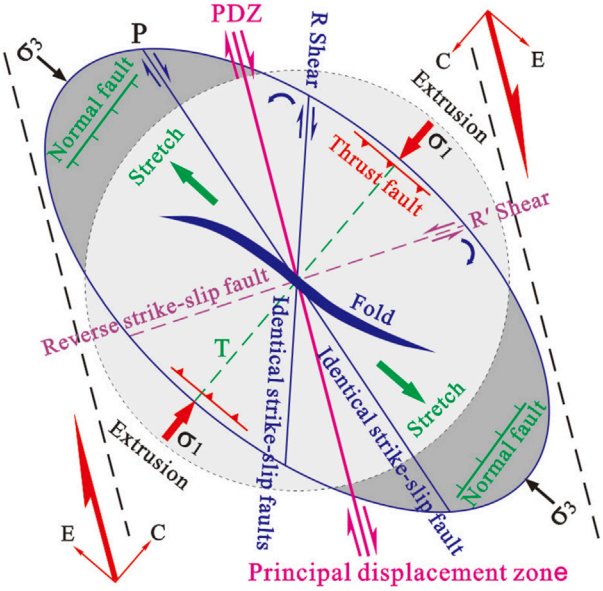

FIGURE 12
Illustration of the Riedel shear mode of the right strike-slip fault (Harding, 1974). *C, compression vector; E, extension vector; R, Riedel shear or same-directional strike-slip fault; R′, conjugate Riedel shear or reverse strike-slip fault; P, same-directional shear or secondary same-direction fault; T, local extension with shear; σ_1, maximum principal stress with a N-E direction; σ_2, intermediate principal stress with a vertical direction; σ_3, minimum principal stress with a N-W direction

fault structures: the NW–NNW compression–torsion faults, the NE compression–torsion faults, and the NWW compression–torsion faults.

5.2 Analysis of the relationship between the cover and the basement fault

Geophysical investigation showed that the contact interface between the Qiabuqia hidden granite and the top of the Triassic metamorphic basement has a gentle slope form and gradually inclines to the west. There is no large-scale structural activation or arch deformation of the basement >20 m in length. Normal faults in the granitic body are characterized with a NE-NNE strike and are common in the north and east, but less so in the south and west. In the top sedimentary cover, a limited number of normal faults formed in the hanging wall of the NE-NNE trending basement thrust fault showed a "Y" shape. These faults have a fault displacement of <20 m and are parallel to the underlying basement structure, with more in the higher portion and less in the lower. Most of them do not cut through the Xianshuihe Formation. In the shallow level above the Xianshuihe Formation, there are normal faults scattered in all directions. However, in the deep level below the Xianshuihe Formation, normal faults are rare and mainly in the NE-NNE direction.

According to the aforementioned analysis, the top interface of the Xianshuihe Formation, controlled by the representative DR4 hole, may be buried at a depth of ~1,000 m. The top part of the Xianshuihe Formation shows tectonic stress states associated with a normal fault (NF), whereas in the deep basement, the tectonic stress states associated with a reversal fault (TF) accompanied by strike-slip (SS) movement are dominant. The Xianshuihe Formation's top interface is analogous to the "neutral plane" that presents as "tension at the top and thrust and strike-slip in the bottom" (Figure 13). As a result, the NE–NNE trending normal fault formed inside Qiabuqia's hidden granite body due to a tensile–torsional structural plane that formed concurrently with the Riedel shear mode T rupture. However, the normal faults visible on the surface extend only to a limited depth and cannot be used as a basis for judging the deep tectonic stress field.

5.3 Tectonic evolution and stress variation during the Late Cenozoic

Under the influences of the Qinghai–Tibetan Plateau uplift and the accompanying eastward extrusion of its northeast margin, as well as the far-field effect of the Indo–Asian plate collision, the Late Cenozoic tectonic evolution and stress variation in the Qiabuqia area can be divided into the following three periods:

(1) Thrust nappe accompanied by dextral strike-slip movement during the Late Miocene to Late Pliocene:

The *in situ* "granite weathered sand" layer with the basal conglomerate features at the bottom of the Pliocene Linxia Formation shows that Waliguan Mountain thrusted over and uplifted out of the surface during this period, similar to a peninsula stretching southeastward. While the area northeast of Waliguan Mountain lacks sedimentary records, fluvial-lacustrine deposits belonging to the Linxia Formation can, for the most part, be found in the west, south, and southeast parts. The mountain's eastern border has continually risen, owing to the fast uplift of the thrust nappe along the Duolonggou arc-shaped fault. Simultaneously, NNE-trending tensile–torsional faults, that is, Riedel local tension (T) rupture, NW-trending compressive–torsion faults that is, Riedel secondary syn-trending faults (P), and NWW-trending compressive–torsion faults have been revived or regenerated. The (σ1 1) direction was NNE 20.1° during this period.

(2) Dextral strike-slip accompanied by thrust nappe movement during the Early Pleistocene to the Middle–Late Pleistocene period:

During this time, the extent of uplift in Waliguan Mountain, generated by the thrust, continually increased. The Gonghe Formation sedimentation was almost completely surrounding Waliguan Mountain. Meanwhile, the Linxia Formation on the west part of Waliguan Mountain rose, whereas the Linxia Formation on the east dropped ~200 m below the Gonghe Formation. This might have resulted in simultaneous uplift and emplacement of the Qiabuqia hidden hot dry rock mass. During the Late Pleistocene, from the early to middle period, the magnitude of the dextral strike-slip and the clockwise rotation around the vertical axis of Waliguan Mountain progressively increased. The NW portion of the Duolonggou arc fault compressed and contracted, while the south segment pushed and napped. Within the Gonghe Formation, at least three fault bundles extended southward. This tectonic activity also caused these strata to tilt and formed local dips up to 45°.

The growth layers within the Gonghe Formation suggest that the Early–Middle Pleistocene thrust nappe event had a pulse development pattern. The thrust nappe event has most recently influenced the Middle–Late Pleistocene alluvial deposit from the ancient Yellow River. It is believed that the thrust nappe activity began to decline around the Middle–Late Pleistocene. The maximum principal tectonic stress direction shifted from NNE 20.1° during the early period to SSE 75.3° during the late

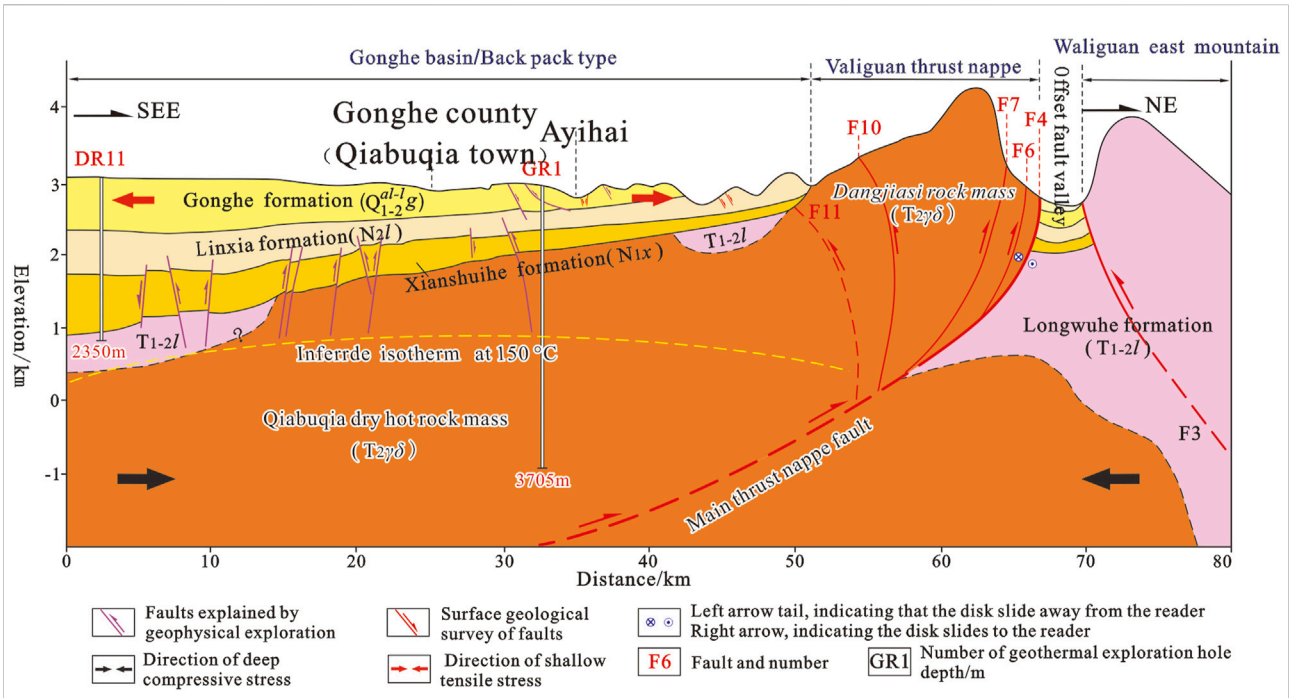

FIGURE 13
Structural profile of the Dalianhai–Waliguan and vertical structural changes of the tectonic stress field.

period, due to the Duolonggou arc fault's progressive transformation from thrust nappe to dextral strike-slip movement. Waliguan Mountain started to rotate clockwise along the vertical axis as the regional stress field shifted from NNE to SSE. Meanwhile, dextral strike-slip movement was introduced to regulate the eastward expansion of Waliguan Mountain. It may also have resulted in the formation of Fn4 and Fn5 in the Rangnade area, as well as Fn1 and Fn2 normal faults in the Tulin–Desheng Village area.

(3) Late Pleistocene to Middle Holocene—the "brake" period for the thrust nappe in Waliguan Mountain and relaxational extension for the shallow part of the trailing edge:

This geological body experienced a significant thrust nappe from the Early Pleistocene to the middle of the Late Pleistocene. However, the thrust nappe activity ceased in the Late Pleistocene, resulting in a "brake" effect for the trailing edge. Meanwhile, the surface of the western Qiabuqia region began to relax and stretch, forming a graben-type normal fault system with a roughly S–N trend in the Kecai–Deliji Village–Ayihai gully area.

In summary, using the buried depth of ~1,000 m at the top interface of the Xianshuihe Formation, the vertical structure of the tectonic stress field in the Qiabuqia area is a normal fault–type (NF) tectonic stress state for the upper part and a reverse fault–type (TF) plus strike-slip-type (SS) tectonic stress state for the lower part. The top interface of the Xianshuihe Formation is equivalent to a structural "neutral plane," depicting "tension at the upper part, but thrust and strike-slip at the lower part."

6 Conclusion

The following major conclusions can be drawn from the present study:

1. During the Late Cenozoic, the Qiabuqia region, which resides in the northeastern margin of the Gonghe Basin, experienced three stages of evolution: 1) thrust napping with occasional dextral strike-slipping during the Late Miocene–Late Pliocene; 2) occasional dextral strike-slipping with thrusting during the Early Pleistocene to Middle Pleistocene; and 3) "braking" of the thrust nappe in Waliguan Mountain, as well as relaxing and stretching of the shallow part in the trailing edge during the Late Pleistocene to Middle Holocene.
2. As demonstrated by the DR4 borehole, the Xianshuihe Formation is buried to a depth of ~1,000 m. The top part of this Formation is characterized by a normal fault–type (NF) tectonic stress state, whereas the reverse fault–type (TF) + strike-slip type (SS) tectonic stress state dominates in the deep basement. The upper normal fault's σ1 and σ3 are vertical and horizontal, respectively. As for the deep reverse fault + strike-slip, the σ1 is in the NE–SW direction and varies from 20.1° to 75.3°, yielding an average of 40.0°.

3. Based on the Riedel shear model, three types of hidden fault structures developed in the Qiabuqia region, that is, the NW–NNW trending compressional–torsional fault, the NE-trending tensional–torsional fault, as well as the NWW-trending compressional–torsional fault.

Data availability statement

The original contributions presented in the study are included in the article/Supplementary Material; further inquiries can be directed to the corresponding author.

Author contributions

ZY: The conception or design of the work, field investigation and analysis by synthesis, drafting and revising the work. Q: Field investigation, analysis by synthesis, map compilation and revising the work. FL: Analysis by synthesis, drafting and revising the work. ZC: Analysis by synthesis. ZL: Field investigation and analysis by synthesis. ZS: The conception or design of the work, field investigation and analysis by synthesis, map compilation. LD: Analysis by synthesis. YZ: Analysis by synthesis. SJ: Map compilation. FL: Analysis by synthesis. NZ: Field investigation.

Funding

This work was supported by the National Key Research and Development Program of China (No. 2018YFB1501801) and China Geological Survey Project (No. DD20190131).

Conflict of interest

The authors declare that the research was conducted in the absence of any commercial or financial relationships that could be construed as a potential conflict of interest.

Publisher's note

All claims expressed in this article are solely those of the authors and do not necessarily represent those of their affiliated organizations, or those of the publisher, the editors, and the reviewers. Any product that may be evaluated in this article, or claim that may be made by its manufacturer, is not guaranteed or endorsed by the publisher.

References

Anderson, E. M. (1951). The dynamics of faulting and dyke formation with application to Britain. *J. Geol.* 62 (4), 417. doi:10.1086/626182

Boyer, S. E., and Elliott, D. (1982). Thrust systems. *Am. Assoc. Petroleum Geol. Bull.* 66 (9), 1196–1230. doi:10.1306/03B5A77D-16D1-11D7-8645000102C1865D

Chang, H., Jin, Z. D., and An, Z. S. (2009). Sedimentary evidences of the uplift of the Qinghai Nanshan (the mountains south to Qinhai Lake) and its implication for tructural evolution of the Lake Qinghai-Gonghe basin. *Geol. Rev.* 55 (1), 49–57. (in Chinese with English abstract).

Chen, F. W., Wu, Z. Z., and Li, S. H. (2016). Three 1:50,000 regional geological and mineral survey reports of J47E022019, J47E022020, and J47E023020 in Dongba area, Gonghe County, Qinghai Province. Xining. Qinghai Provincial Department of Natural Resources Archives.

Christie-Blick, N., and Biddle, K. T. (1985). Deformation and basin formation along strike-slip faults. *Strike-Slip Deformation, Basin Form. Sediment.*, 1–34. doi:10.2110/pec.85.37.0001

Cowgill, E., Yin, A., Arrowsmith, R., Feng, W., and Shuanhong, Z. (2004). The akato tagh bend along the Altyn tagh fault, northwest tibet, 1: Smoothing by vertical-axis rotation and the effect of topographic stresses on bend-flanking faults. *Geol. Soc. Am. Bull.* 116, 1423–1442. doi:10.1130/b25359.1

Craddock, W. H., Eric, K., Huiping, Z., Marin, K. C., Jean-Daniel, C., and Daoyang, Y. (2014). Rates and style of cenozoic deformation around the Gonghe Basin, northeastern Tibetan plateau[J]. *Geosphere* 10 (6), 1255–1282. doi:10.1130/ges01024.1

Craddock, W. H., Kirby, E., and Zhang, H. (2011). Late Miocene-Pliocene range growth in the interior of the northeastern Tibetan Plateau[J]. *Lithosphere.* 3 (6), 420–438. doi:10.1130/l159.1

Craddock, W. H. (2011). *Structural and geomorphic evolution of the Gonghe basin complex, northeastern Tibet: Implications for the timing of plateau growth[D].* Pennsylvania, United States: The Pennsylvania State University.

Crowell, J. C. (1974). "Origin of late cenozoic basins of southern California,". Editor W. R. Dickinson (Oklahoma, United States: SPEM Special Publications), 22, 190–204. Tectonics and Sedimentation.

Deng, Q. D., Zhang, P. Z., Ran, Y. K., Yang, X. P., He, W., and Chu, Q. Z. (2002). Basic characteristic of active tectonics of China. *Sci. China (Ser D)* 32 (12), 1020–1030. (in Chinese with English abstract). doi:10.3321/j.issn:1006-9267.2002.12.007

Dong, L. F., and Chen, W. Y. (2003). Study on characteristics of *in-situ* stress field in laxiwa hydropower station. *Chin. J. Rock Mech. Eng.* 22 (S2), 2544. (in Chinese with English abstract). doi:10.3321/j.issn:1000-6915.2003.z2.002

Dooley, T., Mcclay, K., and Bonora, M. (1999). 4D evolution of segmented strike-slip fault systems: Applications to NW europe. *Geol. Soc. Lond. Pet. Geol. Conf. Ser.* 5, 215–225. doi:10.1144/0050215

Elliott, D. (1976). The energy balance and deformation mechanisms of thrust sheet. *Phil. Trans. R. Soc. Lond.* 238, 289–312. doi:10.1098/rsta.1976.0086

Fang, X. M., Song, C. H., Dai, S., Zhu, Y. T., Gao, J. P., and Zhang, W. L. (2007). Cenozoic deformation and uplift of the NE Qinghai-Tibet Plateau: Evidence from high-resolution magnetostratigraphy and basin evolution. *Earth Sci. Front.* 14 (1), 230–242. (in Chinese with English abstract). doi:10.3321/j.issn:1005-2321.2007.01.022

Fang, X. M., Yan, M. D., Voo, R. V. D., Rea, D. K., Song, C. H., Josep, M. P., et al. (2005). Late cenozoic deformation and uplift of the NE Tibetan plateau: Evidence from high-resolution magnetostratigraphy of the guide basin, Qinghai province, China. *Geol. Soc. Am. Bull.* 117 (9–10), 1208–1225. doi:10.1130/b25727.1

George, A. D., Marshalsea, S. J., Wyrwoll, K. H., Jie, C., and Yanchou, L. (2001). Miocene cooling in the northern Qilian Shan, northeastern margin of the Tibetan Plateau, revealed by apatite fission-track and vitrinite - reflectance analysis. *Geol.* 29 (10), 939–942. doi:10.1130/0091-7613(2001)029<0939:mcitnq>2.0.co;2

Harding, P. T. (1974). Petroleum traps associated with wrench faults. *AAPG Bull.* 58 (7), 1290–1304. doi:10.1306/83d91669-16c7-11d7-8645000102c1865d

Harding, T. P. (1985). Seismic characteristics and identification of negative flower structures, positive flower structures, and positive structural inversion. *AAPG Bull.* 69, 582–600. doi:10.1306/AD462538-16F7-11D7-8645000102C1865D

Jiang, R. B., Chen, X. H., Dang, Y. Q., Yin, A., Wang, L. Q., Jiang, W. M., et al. (2008). Apatite fission track evidence for two phases Mesozoic-Cenozoic thrust

faulting in eastern Qaidam Basin, 2008. *Chin. J. Geophys.* 51 (1), 116–124. (in Chinese with English abstract). doi:10.3321/j.issn:0001-5733.2008.01.015

Li, P., Su, S. R., Ma, C., Zhang, C. Y., and Chen, Y. H. (2017). Distribution law of crustal stress in different combina-tions of imbricate reverse faults. *J. Eng. Geol.* 25 (3), 637–647. (in Chinese with English abstract). doi:10.13544/j.cnki.jeg.2017.03.009

Li, Z. M., Tu, H. W., Tian, Q. J., Zhang, J. L., and Li, W. Q. (2010). The 2008 Ms 6.3 earthquake in the Dachaidan region, Qinghai Province and its seimotectonic setting. *Prog. Geophys.* 25 (3), 768–774. doi:10.3969/j.issn.1004-2903.2010.03.004

Liu, C. Y. (2010). Geologic and metallogenic or pool - forming effects of the thermodynamic process and their identification. *Oil Gas Geol.* 31 (6), 72. doi:10.11743/ogg20100605

Lowell, J. D. (1972). Spitsbergen tertiary orogenic belt and the spitsbergen fracture zone. *Geol. Soc. Am. Bull.* 83, 3091–3102. doi:10.1130/0016-7606(1972)83[3091:stobat]2.0.co;2

Lu, H. J., Wang, E. C., Shi, X. H., and Meng, K. (2012). Cenozoic tectonic evolution of the Elashan range and its surroundings, northern Tibetan Plateau as constrained by paleomagnetism and apatite fission track analyses. *Tectonophysics* 580, 150–161. doi:10.1016/j.tecto.2012.09.013

Luyendyk, B. P., Kammerling, M. J., and Terres, R. (1980). Geometrical model for Neogene crustal rotations in southern California. *Bull. Geol. Soc. Am.* 91, 211–217.

Ma, Q. C., and Qi, L. (1993). Three dimensional ground stress field and mechanism of fault zone at dam site of Longyangxia project. *Chin. J. Geotechnical Eng.* 15 (3), 1–8. (in Chinese with English abstract). doi:10.1007/BF02656947

Mann, P. (2007). *Global catalogue, classification and tectonic origins of restrainingand releasing bends on active and ancient strike-slip fault systems*, 290. London: Special Publications, 13–142. Geological Society.

McClay, K., and Bonory, M. (2001). Analog models of restraining stepovers in strike-slip fault systems. *AAPG Bull.* 85, 233–260. doi:10.1306/8626C7AD-173B-11D7-8645000102C1865D

Perrineau, A., Van Der Woerd, J., Gaudemer, Y., Jing, L. Z., Pik, R., Tapponnier, P., et al. (2011). Incision rate of the Yellow River in northeastern tibet constrained by 10Be and 26Al cosmogenic isotope dating of fluvial terraces: Implications for catchment evolution and plateau building. *Geol. Soc. Spec. Publ.* 353, 189–219. doi:10.1144/sp353.10

Qian, X. L. (1994). *Studies on extensional tectonics*. Beijing: Geological Publishing House, 166. (in Chinese with English abstract).

Ramsay, J. G., and Huber, M. I. (1987). *The techniques of modern structural geology: Volume 2 folds and fractures*. London: Academic Press, 309–700.

Sobel, E. R., and Dumitru, T. A. (1997). Thrusting and exhumation around the margins of the western Tarim Basin during the India-Asia collision. *J. Geophys. Res.* 102 (B3), 5043–5063. doi:10.1029/96jb03267

Sobel, E. R., Hilley, G. E., and Strecker, M. R. (2003). Formation of internally drained contractional basins by aridity-limited bedrock incision. *J. Geophys. Res.* 108 (B7), 2344. doi:10.1029/2002jb001883

Sun, Y. G., Fang, H. B., Zhang, K., Zhao, F. Y., and Liu, S. Y. (2007). Step-like landform system of the Gonghe Basin and the uplift of the Qinghai-Tibet Plateau and development of the Yellow River. *Geol. China* 34 (6), 1141–1147. (in Chinese with English abstract). doi:10.3969/j.issn.1000-3657.2007.06.021

Sylvester, A., and Smith, R. (1976). Tectonic transpression and basement controlled deformation in the San Andreas fault zone, Salton trough, California. *AAPG Bull.* 60, 2081–2102. doi:10.1306/C1EA3A73-16C9-11D7-8645000102C1865D

Thornton, J. M., Mariethoz, G., and Brunner, P. (2018). A 3D geological model of a structurally complex Alpine region as a basis for interdisciplinary research. *Sci. Data* 5, 180238. doi:10.1038/sdata.2018.238

Wang, J. M., Zhang, J. J., Liu, K., Zhang, B., Wang, X. X., Rai, S. M., et al. (2016). Spatial and temporal evolution of tectonometamorphic discontinuities in the central Himalaya: Constraints from P-T paths and geochronology. *Tectonophysics* 679, 41–60. doi:10.1016/j.tecto.2016.04.035

Wang, L. J., Ciu, J. W., and Wang, W. (1999). Tectonic deformation and thermal stress field in Qinghai - tibet plateau. *J. Geomechanics* 5 (3), 1–7. doi:10.3969/j.issn.1006-6616.1999.03.001

Wang, S. T., LiY, S., Su, D. G., and Wei, L. W. (1988). Engineering geological study of regional structural stability in the area of the Longyang Gorge hydro-electrical power station on the Huanghe (Yellow) river. *Acta Geol. Sin.* 62 (4), 361–372. (in Chinese with English abstract).

Wang, Z. C., Zhang, P. Z., Zhang, G. L., Li, C. Y., Zheng, D. W., and Yuan, D. Y. (2006). Tertiary tectonic activities of the north frontal fault zone of The west qinling mountains: Implications for the growth of the northeastern margin of the Qinghai-Tibetan plateau. *Earth Sci. Front.* 13 (4), 119–135. (in Chinese with English abstract). doi:10.3321/j.issn:1005-2321.2006.04.010

Westaway, R. (1995). Deformation around stepovers in strike-slip fault zones. *J. Struct. Geol.* 17, 831–846. doi:10.1016/0191-8141(94)00098-k

Woodcock, N., and Fischer, M. (1986). Strike-slip duplexes. *J. Struct. Geol.* 8, 725–735. doi:10.1016/0191-8141(86)90021-0

Wu, Y., Dai, J. S., Gu, Y. C., Shang, L., and Liu, Q. (2014). Numerical simulation of present geo-stress field and its effect on hydraulic fracturing of Fuyu reservoir in Gaotaizi oilfield. *J. Geomechanics* 20 (4), 363–371. (in Chinese with English abstract). doi:10.3969/j.issn.1006-6616.2014.04.004

Xiao, W., Windley, B. F., Allen, M. B., and Han, C. (2013). Paleozoic multiple accretionary and collisional tectonics of the Chinese Tianshan orogenic collage. *Gondwana Res.* 23 (4), 1316–1341. doi:10.1016/j.gr.2012.01.012

Xu, S. Y., Xu, D. F., and Shi, R. S. (1984). A discussion on the development of landforms and evolution of environments in the gonghe basin. *J. Lanzhou Univ.* 20 (1), 196–157. (in Chinese with English abstract).

Yang, L. Z., Sun, Z. X., Liu, J. H., Wang, A. D., and Wan, J. J. (2017). On deployment of high - temperature deep geothermal wells in typical areas with hot dry rock potential in China. *Geol. Explor.* 53 (2), 355–360. (in Chinese with English abstract). doi:10.12017/dzkx.2017.022

Yin, A. (2010). Cenozoic tectonic evolution of asia: A preliminary synthesis. *Tectonophysics* 488, 293–325. doi:10.1016/j.tecto.2009.06.002

Yin, A. (2006). Cenozoic tectonic evolution of the Himalayan orogen as constrained by along-strike variation of structural geometry, exhumation history, and foreland sedimentation. *Earth-Science Rev.* 76, 1–131. doi:10.1016/j.earscirev.2005.05.004

Yuan, D. Y., Zhang, P. Z., Liu, B. C., Gan, W. J., Mao, F. Y., Wang, Z. C., et al. (2004). Geometrical imagery and tectonic transformation of Late Quaternary active tectonics in northeastern margin of Qinghai-Xizang Plateau. *Acta Geol. Sin.* 78 (2), 270–278. (in Chinese with English abstract). doi:10.3321/j.issn:1005-2321.2004.04.006

Yuan, D. Y., Zhang, P. Z., Liu, X. L., Liu, B. C., Zheng, W. J., and He, W. G. (2004). The tectonic activity and deformation features during the Late Quaternary of Elashan Mountain active fault zone in Qinghai Province and its implication for the deformation of the northeastern margins of the Qinghai-Tibet Plateau. *Earth Sci. Front.* 11 (4), 393–402. (in Chinese with English abstract). doi:10.3321/j.issn:0001-5717.2004.02.017

Zeng, Z. P., Liu, Z., Ma, J., Zhang, C. L., Li, J., Liu, Z., et al. (2019). A new method for fracrability evaluation in deep and tight sandstone reservoirs. *J. Geomechanics* 25 (2), 223–232. (in Chinese with English abstract). doi:10.12090/j.issn.1006-6616.2019.25.02.021

Zhang, C. Y., Chen, Q. C., Qin, X. H., Hong, B., Meng, W., and Zhang, Q. F. (2017). *In-situ* stress and fracture characterization of a candidate repository for spent nuclear fuel in Gansu, northwestern China. *Eng. Geol.* 213, 218–229. doi:10.1016/j.enggeo.2017.10.007

Zhang, K., Liu, K., and Yang, J. (2004). Asymmetrical valleys created by the geomorphic response of rivers to strike-slip fault. *Quat. Res.* 62, 310–315. doi:10.1016/j.yqres.2004.07.003

Zhang, P. Z., Zheng, D. W., Yin, G. M., Yuan, D. Y., Zhang, G. L., Li, C. Y., et al. (2006). Discussion on Late Cenozoic growth and rise of northeastern margin of the Tibetan plateau. *Quat. Sci.* 26 (1), 5–13. (in Chinese with English abstract). doi:10.3321/j.issn:1001-7410.2006.01.002

Zhang, S. Q., Wu, H. D., Zhang, Y., Song, J., Zhang, L. Y., Xu, W. L., et al. (2020). Characteristics of regional and geothermal Geology of the reshuiquan HDR in guide county, Qinghai province. *Acta Geol. Sin.* 94 (5), 1591–1605. (in Chinese with English abstract).

Zhang, Y. Q., Liao, C. Z., Shi, W., and Hu, B. (2006). Neotectonic evolution of the peripheral zones of the Ordos basin and geodynamic setting. *Geol. J. China Univ.* 12 (3), 285–297. (in Chinese with English abstract). doi:10.3969/j.issn.1006-7493.2006.03.001

Zheng, D. W., Zhang, P. Z., Wan, J. L., Li, C. Y., and Cao, J. X. (2003). Late cenozoic deformation subsequence in northeastern margin of tibet: Detrital AFT records from Linxia basin. *Sci. China (Series D)* 33, 190–198. (in Chinese with English abstract). doi:10.3321/j.issn:1006-9267.2003.z1.021

Frontiers in Earth Science

Investigates the processes operating within the major spheres of our planet

Advances our understanding across the earth sciences, providing a theoretical background for better use of our planet's resources and equipping us to face major environmental challenges.

Discover the latest Research Topics

See more →

Frontiers

Avenue du Tribunal-Fédéral 34
1005 Lausanne, Switzerland
frontiersin.org

Contact us

+41 (0)21 510 17 00
frontiersin.org/about/contact